JOURNAL
OF
APPLIED PHYSICS

UNIVERSITY OF ILLINOIS
LIBRARY
AUG 16 1961
CHICAGO

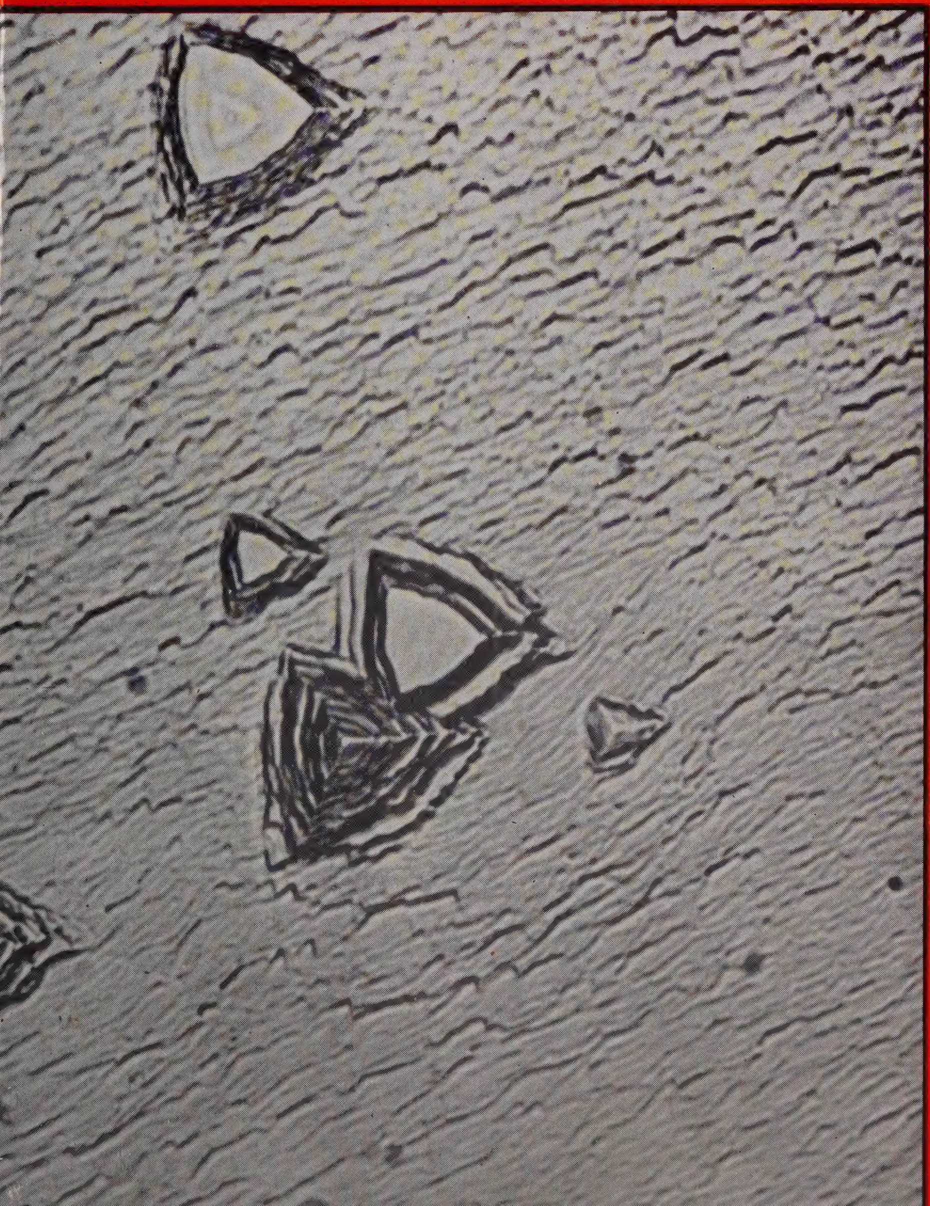

August
1961
Vol. 32 No. 8

Simple Dislocation Motion in Copper
See Page 1625

International Conference on the Nature of Solid Friction

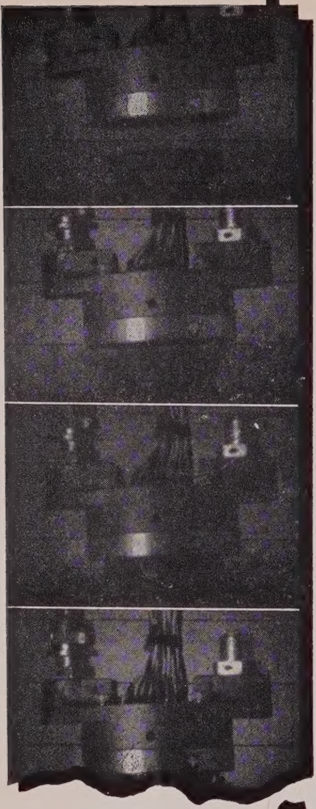

WHAT IS IT YOU NEED TO KNOW...

about the four winds?

Meteorology is one of the strong points in t
activity of the Research & Development Di
sion. The special instrument shown above w
created by this group to meet vertical-gu
iness-measurement needs of Dugway Provi
Ground of the U. S. Army Chemical Cor
Now in continuous service, this first-of-its-ki
instrument was produced, from concept to f
ished hardware, in a neat though admitte
hectic ninety days.

about energy and motion?

One of our product divisions packages up explosive energy into ingenious devices which turn, twist, chop, push, or pull things aboard missiles in flight. So naturally, the R&D people get involved in similar projects. Above is a series of Dynafax pictures of an explosive-actuated electrical disconnect in operation. This is known as playing both ends against the middle, since the facilities and knowledge of our own photo-instrumentation product department are brought into the situation as well.

Availability of such facilities as a Model 189 Framing Camera and related items has recently led R&D scientists into an investigation of electrets. This is one, at right. A charged plastic plate, 4 by 4 in., is punctured at the bottom center and the charge forms the pathway shown. One of the more interesting points is that it all happens in something less than 0.58 microseconds.

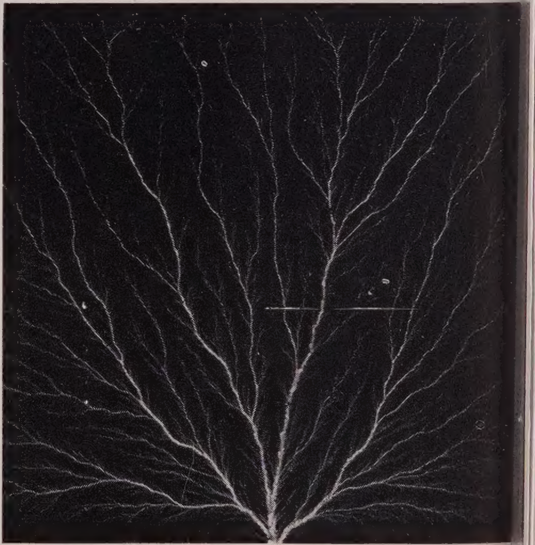

These are just a few of the things going on in
Beckman & Whitley Research & Development Divis
The combination of backgrounds, talents, and techn
facilities is available to government and industry
the solution of the unusual range of problems w
lie in these general areas. For specific details, con
Tom Holland, director.

about time resolved spectroscopy?

Temperature measurements in the 2,000°-20,000° K range of events resolved in time up to 3×10^{-8} seconds, and with sprectrum coverage from 2,000 to 9,000 angstroms. Such data is useful in work on radiated transients, concentration temperatures and composition of molecular species.

Beckman & Whitle

SAN CARLOS 8 • CALIFORNIA • U.S.A.

JOURNAL OF APPLIED PHYSICS

Vol. 32, No. 8 AUGUST, 1961

In This Issue

International Conference on the Nature of Solid Friction

Preface . . . 1407
Friction and Adhesion of Clean and Contaminated Mica Surfaces . . . Anita I. Bailey 1407
Recent Work on Solid Friction at the Research Laboratory for the Physics and Chemistry of Solids . . . Anita I. Bailey 1413
Single Contacts and Multiple Encounters . . . J. F. Archard 1420
Rolling Friction of Polymeric Materials. II. Thermoplastics . . . D. G. Flom 1426
Friction of Metals in Reciprocating Sliding . . . Yasukatsu Tamai 1437
Influence of Surface Energy on Friction and Wear Phenomena . . . E. Rabinowicz 1440
Lubrication of Polymers . . . C. Rubenstein 1445
Frictional Behavior of a Simple Rheological Material . . . R. T. Spurr 1450
Use of Graphite Whiskers in a Study of the Atmosphere Dependence of Graphite Friction . . . F. R. Rollins, Jr. 1454

Regular Articles

Electron Spin Resonance in Neutron-Irradiated Quartz . . . Robert H. Silsbee 1459
Grain-Boundary Diffusion . . . A. E. Austin and N. A. Richard 1462
Operation of the Field Ion Microscope with a Dynamic Gas Supply . . B. J. Waclawski and E. W. Müller 1472
Shock Wave Compression of Hardened and Annealed 2024 Aluminum . . . G. R. Fowles 1475
Scattering of Plane Waves by a Rigid Ribbon in a Solid . . . K. Harumi 1488
Surface Kinetics and Physics Investigation of the Reaction between Single-Crystal Germanium and Iodine . . . W. J. Heinecke and S. Ing, Jr. 1498
Back Scattering of Electrons . . . G. D. Archard 1505
Low-Angle X-Ray Diffraction of Crystalline Nonoriented Polyethylene and Its Relation to Crystallization Mechanisms . . . L. Mandelkern, A. S. Posner, A. F. Diorio, and D. E. Roberts 1509
An Approximate Solution of Fick's Diffusion Equation . . . T. Tsang 1518
Etch Pits in Electroluminescent Zinc Sulfide Crystallites . . . Paul Goldberg 1520
Nonlinear Damping Losses in YIG . . . Robert L. Conger 1525
Experimental Study of Arc Stability. II. An Investigation of Mercury Arc Stability . . . G. A. Farrall and G. H. Reiling 1528
Orientation-Dependent Dissolution of Lithium Fluoride . . . M. B. Ives 1534
Lattice Parameter Determinations with an X-Ray Spectrogoniometer by the Debye-Scherrer Method and the Effect of Specimen Condition . . . Henry M. Otte 1536
Temperature-Compensated Debye Temperature of Carbonyl Iron . . . Charles P. Gazzara and Raymond M. Middleton 1546
Acceleration of Rigid, Conducting, Diamagnetic Bodies by a Magnetic Field . . . R. U. Ayres 1549
Single-Crystal Tin Films . . . Richard W. Vook 1557
Ferromagnetic Nucleation Sources on Iron Whiskers . . . R. W. De Blois 1561
Optimization of Emission-Limited Thermionic Generators . . . Alfred Schock 1564
Increase in Dielectric Constant during Switching in Lithium Selenite and Triglycine Sulfate . . . Ennio Fatuzzo 1571
Dislocation Etch Pit Formation in Sodium Chloride . . . S. Mendelson 1579
Zero-, First-, and Second-Order Theories of a General Thermocouple . . . A. H. Boerdijk 1584
Nanosecond Triggering of Air Gaps with Intense Ultraviolet Light . . . Terry F. Godlove 1589
Study of Electron Bombardment of Thin Films . . . G. B. Gilbert, T. O. Poehler, and C. F. Miller 1597
Influence of Deformation and Temperature on the Cobalt Gamma Irradiation of Sodium Chloride. Evidence for Electrical Interaction between Dislocations and Point Defects . . . Rohn Truell 1601
X-Ray Diffraction Study of Interdiffusion in Cu-Ni Powder Compacts . Bertina Fisher and P. S. Rudman 1604
Electron Trajectories in a Nonuniform Axially Symmetric Magnetic Field . D. A. Dunn and R. E. Holaday 1612

Letters to the Editor:
- **Monotonic Trap Distributions** . . . Richard H. Bube 1621
- **Ferrimagnetic Resonance of Single-Crystal Barium Ferrite in the Millimeter Wave Region** . . . Franklin F. Y. Wang, Koryu Ishii, and James B. Y. Tsui 1621
- **Stored Energy in Fuel-Bearing Graphite** . . . A. H. Willis, J. M. Baugnet, and R. C. De Beukelaer 1622
- **Peltier Coefficient at High Current Levels** . . . John R. Reitz 1623
- **Maser Action in Emerald** . . . F. E. Goodwin 1624

Announcements . . . 1625
Cover Photograph . . . 1625
Proceedings of the Electron Microscope Society of America . . . 1626
Index to Advertisers . . . xxii

JOURNAL OF APPLIED PHYSICS

A journal of general physics and its applications to other sciences and to industry

Published by the
American Institute of Physics

GOVERNING BOARD

Members

Ralph A. Sawyer, *Chairman*
James G. Baker
R. H. Bolt
Wallace R. Brode
Harvey Brooks
Dirk Brouwer
J. H. Elliott
Herbert A. Erf
N. S. Gingrich
S. A. Goudsmit
W. W. Havens, Jr.
W. V. Houston
Winston E. Kock
R. Bruce Lindsay
David L. MacAdam
H. Victor Neher
Leonard O. Olsen
C. J. Overbeck
Ray Pepinsky
S. L. Quimby
Ralph A. Sawyer
Francis W. Sears
Frederick Seitz
C. Guy Suits
Mary E. Warga
William R. Willets

ADMINISTRATION

Elmer Hutchisson
Director

Wallace Waterfall
Secretary and Treasurer

Henry A. Barton
Administrative Consultant

W. C. Kelly
Director of Education

Eugene H. Kone
Director of Public Relations

Hugh C. Wolfe
Director of Publications

Kathryn Setze
Assistant Treasurer

James E. Mills
Supervisor, Editorial Department

Sistina Greco
Circulation Manager

Edward Tober
Manager, Production and Distribution

Theodore Vorburger
Advertising Manager

Emily Wolf
Manager, Special Services

Editor
J. H. Crawford, Jr.

Assistant Editor
Ethel McMillan

Editorial Board

J. E. Goldman
Herman A. Haus
Henry Hurwitz
J. L. Tuck
C. Lester Hogan
James A. Krumhansl
C. A. Wert
R. S. Rivlin
C. P. Slichter

THE JOURNAL OF APPLIED PHYSICS is devoted to general physics and its applications to other sciences, to engineering, and to industry. Previous to 1937, this journal was called PHYSICS.

The JOURNAL OF APPLIED PHYSICS welcomes articles of two distinct kinds: (1) Descriptions of new results in experimental or theoretical physics which are of general interest to physicists. The author should explain his contribution in such a way that a physicist or engineer in another field of specialization can appreciate its objectives and essential features. (2) Critical reviews of particular areas of physics or surveys of extensive investigations at a single laboratory. Authors contemplating writing such should correspond with the Editor before they begin writing.

The JOURNAL OF APPLIED PHYSICS welcomes Letters to the Editor which are short [approximately four (4) typewritten pages] communications without abstracts. Timeliness, briefness, and degree of current importance of the subject matter will be of primary concern in the publication of Letters. Letters should not be looked upon as partial publication or announcement of more comprehensive work, but rather self-contained presentations in themselves.

Manuscripts should be submitted to the Editor, J. H. Crawford, Jr., Solid State Division, Oak Ridge National Laboratory, Oak Ridge, Tennessee. Authors should read the "Information for Contributors," facing page 1 of the January issue, before writing articles or letters. The *Style Manual* of the American Institute of Physics is also helpful to writers preparing manuscripts for journals published by the American Institute of Physics. It can be obtained for $1.00 from the American Institute of Physics, 335 East 45 Street, New York 17, New York.

Corrected proofs and all correspondence concerning papers in the process of publication should be addressed to the Supervisor, Editorial Department, American Institute of Physics, 335 East 45 Street, New York 17, New York.

Subscriptions, renewals, and orders for back numbers should be addressed to the American Institute of Physics, 335 East 45 Street, New York 17, New York.

Subscription Price	U.S. and Canada	Elsewhere
To members of member organizations of the American Institute of Physics and Affiliated Societies ..	$12.00	$13.00
To all others	14.00	16.00

Back Number Prices

Yearly back number rate when complete year is available: $17.00.
Single copies: $1.75 each (exception: March, 1958—$3.00 each).

Changes of address should be sent to the American Institute of Physics.

Advertising rates supplied on request. Orders, advertising copy, and cuts should be sent to the American Institute of Physics.

The Journal of Applied Physics is published monthly at Prince and Lemon Streets, Lancaster, Pennsylvania.
Second-class postage paid at Lancaster, Pa.

What was Bell Telephone Laboratories doing
ON FRIDAY, JUNE 30, 1961?

It was exploring the communications possibilities of the gaseous optical maser — a device which generates continuous coherent infrared radiation in a narrow beam.

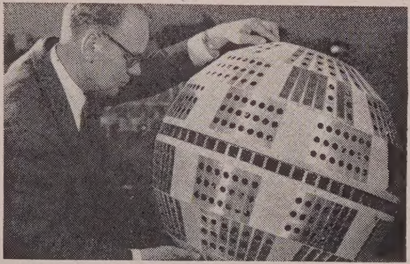

It was preparing an experiment in world-wide communications using "active" satellites powered by the solar battery, a Bell Laboratories invention.

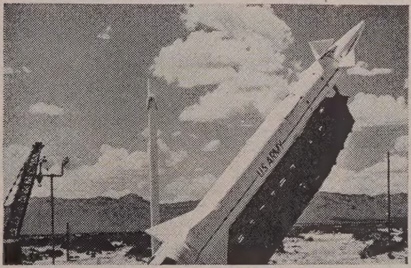

It was developing an anti-missile defense system designed to detect, track, intercept and destroy an enemy ICBM—in a matter of minutes.

It was demonstrating the potentialities of the superconducting compound of niobium and tin for generating, with little power, magnetic fields of tremendous strength.

It was experimenting with an electronic central office at Morris, Ill., which is capable of providing a wide range of new telephone services.

It was perfecting the card dialer which permits, through insertion of a punched card into a slot, the automatic dialing of most frequently used numbers.

Bell Laboratories scientists and engineers work with every art and science that can benefit communications. Their inquiries range from the ocean floor to outer space, from atomic physics to the design of new telephone sets, from the tiny transistor to massive transcontinental radio systems. The goal is constant—ever-improving Bell System communications services.

BELL TELEPHONE LABORATORIES

World center of communications research and development

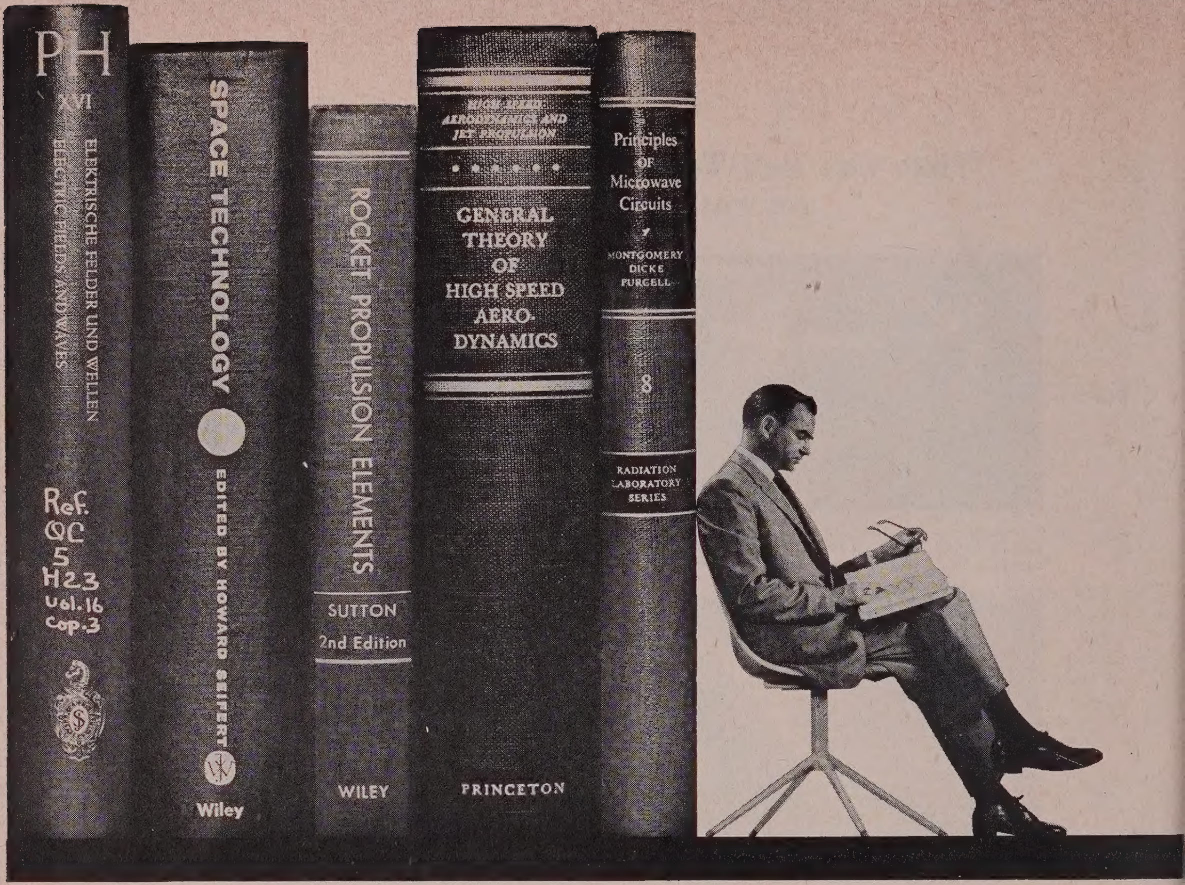
PH
XVI
ELEKTRISCHE FELDER UND WELLEN
ELECTRIC FIELDS AND WAVES
Ref.
QC
5
H23
Vol.16
Cop.3
SPACE TECHNOLOGY
EDITED BY HOWARD SEIFERT
Wiley
ROCKET PROPULSION ELEMENTS
SUTTON
2nd Edition
WILEY
HIGH SPEED AERODYNAMICS AND JET PROPULSION
GENERAL THEORY OF HIGH SPEED AERODYNAMICS
PRINCETON
Principles of Microwave Circuits
MONTGOMERY
DICKE
PURCELL
8
RADIATION LABORATORY SERIES

scientists and engineers in a unique leadership role

The frontiers of space science and technology are being expanded at Aerospace Corporation. The scientists and engineers of this leadership organization are the critical civilian link uniting government and the scientific-industrial team developing space systems and advanced ballistic missiles. In providing broad scientific and technical leadership to every element of this team, they are engaged in a balanced program of activities spanning the spectrum from basic research and forward planning through general systems engineering. Included in the latter are technical supervision, integration and review of the engineering, development and test operations of industry to the extent necessary to assure achievement of system concept and objectives in an economical and timely manner. These people are privileged to view both the state-of-the-art and system development in their totality. Now more men of superior ability are needed: highly motivated scientists and engineers with demonstrated achievement, maturity, and judgment, beyond the norm. Such men are urged to contact Aerospace Corporation, Room 123, P. O. Box 95081, Los Angeles 45, California.

Organized in the public interest and dedicated to providing objective leadership in the advancement and application of space science and technology for the United States Government.

AEROSPACE CORPORATION

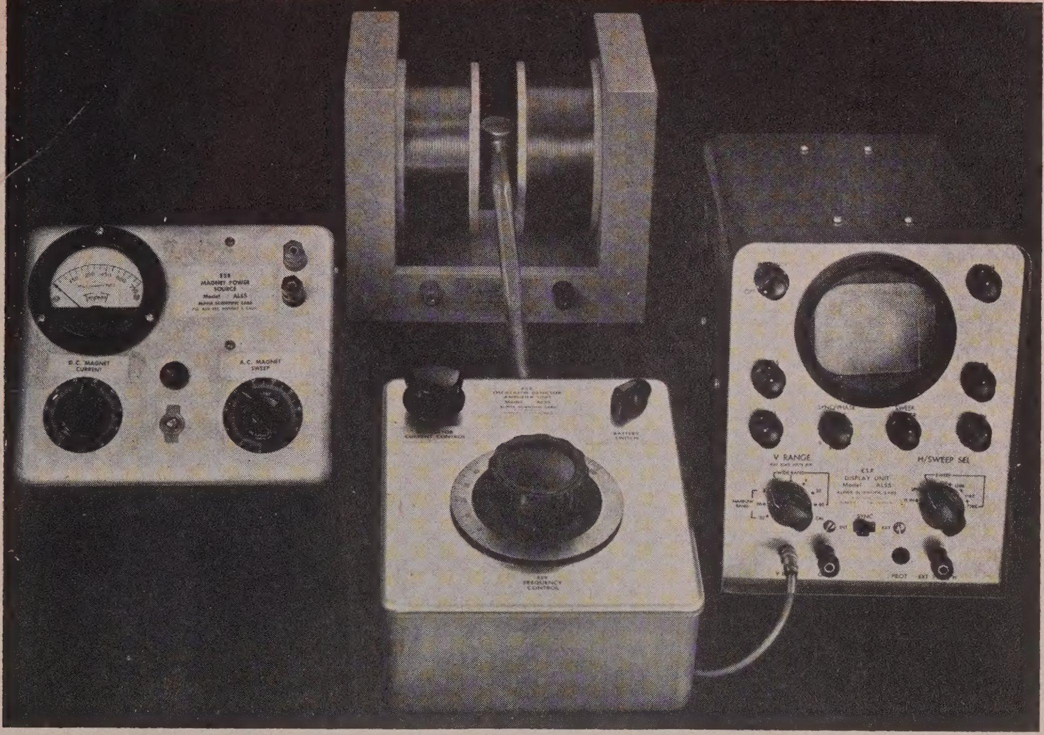

SPIN RESONANCE SPECTROMETERS

The model AL55 Electron Spin Resonance Spectrometer is designed especially for experimental use in the physics laboratories of colleges and universities. The complete instrument consists of a magnet power supply, magnetic field unit, an oscillator-detector-amplifier unit, a sample holder, and a matched oscilloscope display unit combined into a complete system for observing ESR in materials possessing a magnetic dipole moment due to electron spins.

Although designed for laboratories in teaching and research institutions, there are many additional applications in chemical and physical laboratories.

FEATURES

- Exhibits ESR absorption signals with samples smaller than 10 milligrams (approximately one ten-thousandth of a mole of a free radical or less).
- Kinetic reaction rates involving free radicals are observed by the changes in the ESR absorption line.
- Access to the sample is always available for addition of solvent or an additional substance to form a new compound. Rotation of samples while observing ESR absorption is very simply done.
- Very simple to operate. May be used in student laboratories or as a lecture demonstration system.
- Large or small samples can be utilized in ESR observations. The conventional sample holder takes samples approximately one cm long by four mm in diameter in a glass tube sample holder. Larger sample holders are also available.
- ESR absorption line widths are easily measured directly in frequency or magnetic field units as both the operating frequency and the magnetic field are variable.
- ESR line broadening and narrowing effects due to dissolving crystals in a solvent may be demonstrated and observed while the sample undergoes ESR absorption. The changes in line shape may be evaluated in terms of the time to dissolve.
- Power requirements are 115 Volts A.C. and a set of self-contained batteries. (Battery life is 500 hours of use.)
- Instructional manual and a laboratory experiment manual are included.

SYSTEM COMPONENTS

The AL55 ESR Spectrometer is composed of six items:

1. The Master Oscillator-Detector-Amplifier Unit.
2. The Sample Holder Unit and a supply of sample holder tubes.
3. The Magnetic Field Power Source and Sweep Supply.
4. The Magnetic Field Unit.
5. The Display Oscilloscope Unit.
6. The standard free radical sample for lining up the system.

Shipping weight . . . . 100 lbs. (approx.)
Delivery . . . . a limited number of AL55 units are presently in stock.

Specifications subject to modification without prior notice.

PLEASE WRITE OR USE THE COUPON FOR FURTHER DETAILS.

ESR SPECTROMETERS FROM

ALPHA SCIENTIFIC LABORATORIES, INC.

P. O. BOX 333
BERKELEY 1, CALIFORNIA

Name . . . .
Title . . . .
Company . . . .
Address . . . .
City and State . . . .

Original painting by Louis Ribak, Taos.

Man's accelerating progress toward mastering his environment is experiencing a startling thrust as a result of experimentation in nuclear space propulsion and controlled thermonuclear reactions.

Qualified applicants are invited to send resumes to:
Director of Personnel Division 61-68

los alamos
scientific laboratory
OF THE UNIVERSITY OF CALIFORNIA
LOS ALAMOS, NEW MEXICO

All qualified applicants will receive consideration for employment without regard to race, creed, color, or national origin. U.S. citizenship required.

Keithley Micro-microammeters

for low-level dc measurements

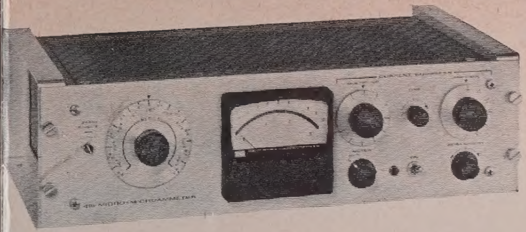

The 415 provides zero suppression up to 100 full scales, urrent detection of approximately 1 x 10^{-14} ampere, zero tability of better than 2% per day.

NEW MODEL 415 research micro-microammeter has a response time of less than 600 milliseconds to 90% of final value at 10^{-12} ampere where external circuit capacity is 50 $\mu\mu$f. It is ideal for current measurements in ion chambers, ionization gages. Useful with flame and Beta-ray ionization detectors; in gas chromatography, mass spectrometry. **$800.00***

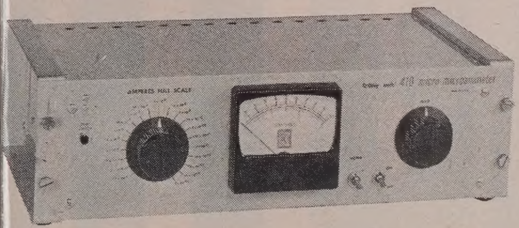

odels 410 and 411 provide high sensitivity, low switching ransients, high accuracy, fast response and low noise. rive 5 ma recorders or 50 mv potentiometer types.

MODEL 410 Recommended for research and control applications where source voltages exceed 300 millivolts. Twenty ranges cover ten decades from 10^{-3} to 10^{-13} ampere. **$490.00***

MODEL 411 Recommended where exceptional zero stability is required and source voltage exceeds 10 volts. Seventeen ranges cover eight decades from 10^{-3} to 10^{-11} ampere. **$535.00***

MODEL 414 Lowest cost instrument for monitoring installations, reactor control, production tests, experiments within its 17 ranges from 10^{-2} to 10^{-10} ampere. **$295.00***

MODELS 410C, 411C AND 414C Contact meters replace panel meters providing economical control or alarm circuitry.
410C—$625.00*; 411C—$670.00*; 414C—$430.00*

MODELS 412 AND 413 Stable log n amplifiers for fluctuating currents from 10^{-5} to 10^{-13} ampere. Uses include reactor monitoring, aerial surveying, film exposure studies. **$485.00***

*End Frames (pair for bench use) **$15.00**

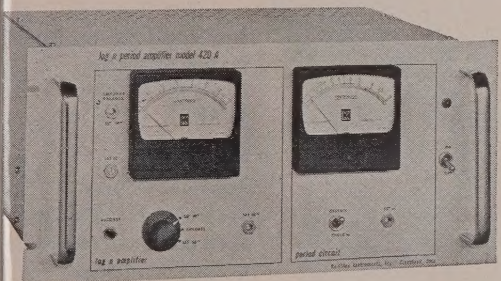

he log n circuit of the 420A has only three adjustments and e period circuit one adjustment. Period and current oututs unaffected by normal ambient changes.

MODEL 420A LOG N PERIOD AMPLIFIER A combined log n amplifier and period circuit for the most exacting reactor monitoring. This dual instrument measures current over a seven decade range, from 10^{-6} to 10^{-13} ampere, and reactor period from minus 30 to plus three seconds. Outstanding features are rapid warmup, 5-second recovery from overloads, unsurpassed stability, 10^{-13} ampere sensitivity, adjustable damping. Contact meter models on special order. **$1050.00**

ODEL	RANGE	ACCURACY	ZERO DRIFT	OUTPUT
0/410C†	10 x 10^{-4}, 3 x 10^{-4}, 10 x 10^{-5}, etc. to 3 x 10^{-13} amp f.s.	±2% f.s. on 10 x 10^{-4} to 10 x 10^{-9} ranges; within 4% on others.	After warmup, below 2% f.s. per 24 hours all ranges.	5 v f.s. up to 5 ma. Output noise below 1% of f.s.
1/411C†	10 x 10^{-4}, 3 x 10^{-4}, 10 x 10^{-5}, etc. to 10 x 10^{-12} amp f.s.	±2% f.s. on 10 x 10^{-4} to 10 x 10^{-8} ranges; within 4% on others.	Below 2% per week from cold start, input 10 v or more.	10 v f.s. up to 5 ma. Output noise below 1% of f.s.
2/413††	Single 10^{-7} to 10^{-13} amp, source voltage over 1 v.	Within 0.2 decade, with source voltage over 1 v.	Below 0.05 decade in 24 hours with source voltage over 1 v.	Zero at 10^{-13} amp to –6v at 10^{-7} amp; up to 5 ma.
4/414C†	17 ranges from 10^{-2} to 10^{-10} amp f.s.	Within 3% f.s. 10 ma to 10 mμa; 4% f.s. 3 mμa to 0.1 mμa.	2% per day with source voltage over 1 v.	5 v f.s. up to 1 ma. Output noise below 1% of f.s.
5	10^{-12}, 3 x 10^{-12}, 10^{-11} 3 x 10^{-11}, to 10^{-3} amp f.s.	±2% f.s. 10^{-3} thru 10^{-8} ranges; ±3% f.s. 3 x 10^{-9} thru 10^{-12}.	After warmup, below 2% f.s. per 24 hours all ranges.	1 v f.s. up to 5 ma. Noise below 20 mv rms.
0A g n MPLIFIER nd	Single, 10^{-6} to 10^{-13} amp, positive currents only.	Within 0.2 decade.	After warmup, below 0.05 decade in 24 hours.	High level—zero at 10^{-13} amp, –75 v at 10^{-6} amp. Recorder—50 mv f.s.
ERIOD ETER	Single, –30 to + three seconds.	3% at center scale.		High level — zero for 30 sec. period, 10 v for 3 sec. Recorder—50 mv f.s.

tact meter models have same specifications as standard units except for addition of a contact meter relay.
same as 412 except: RANGE, 10^{-5} to 10^{-11} ampere.

KEITHLEY INSTRUMENTS, INC.
12415 EUCLID AVENUE CLEVELAND 6, OHIO

BREADTH

A new facility, a new scientific community, and new and ambitious scientific goals—this is the Sperry Rand Research Center. Here academic curiosity, scientific objectivity and true interdisciplinary exchange will combine to fill broad and varied basic research needs of the many divisions of Sperry Rand Corporation in the following areas: Materials Sciences including solids, mechanics, magnetics, and physical chemistry; Radiation Sciences including microwave physics, plasmas, infrared, optics, energy conversion, and communications; Applied Mathematics and Theoretical Physics; Earth and Life Sciences.

Our immediate needs for top scientific talent are in the areas of:

- **Magnetics**
- **Resonance Physics**
- **Semiconductor Physics**
- **Fluid and Solid Mechanics**
- **Infrared and Optics**

If you are interested in fundamental research in any of the above fields, direct your communication in confidence to:

Frederick M. Swope, Jr.,
Sperry Rand
Research Center,
North Road,
Sudbury, Massachusetts

an important
word
at the new

SPERRY RAND RESEARCH CENTER

SUDBURY, MASSACHUSETTS

ANOTHER FIRST FROM VARIAN

ADJUSTABLE AIR GAP/ROTATABLE 6″ LABORATORY MAGNET

Rotate **and** adjust the air gap easily and precisely

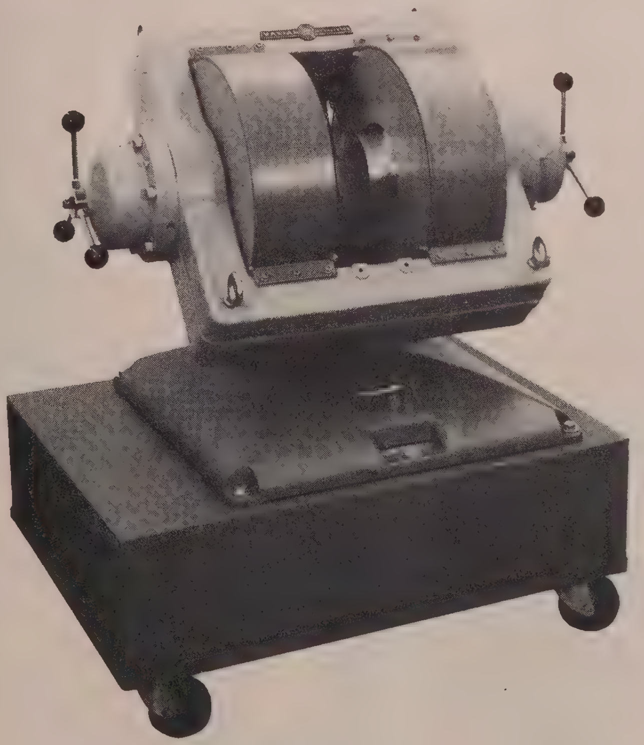

Continuously adjust air gap widths from zero to 6″, as well as rotate the magnetic field over a 200° arc with reference to the vertical, using the new Varian V-4007-2 laboratory magnet. Field homogeneity reproduces accurately after gap adjustment, since the gap-adjusting assembly maintains precise axial alignment and parallelism throughout total pole cap travel. Field strength and homogeneity can be quickly verified using the Varian F-8 Fluxmeter. Traditional Varian design foresight makes the gap-adjusting assembly compatible for fitting to all Varian 6″ rotatable magnets presently in use. And, of course, the new V-4007-2 can be converted to the V-4007-1 configuration when the homogeneity of this most rigid magnet is a requirement.

A complete magnet family with accessories

Varian's V-4007-1 rotatable and V-4007-fixed-azimuth 6″ magnets complement the new V-4007-2 to provide the most complete line of 6″ laboratory magnets available. Select the system that precisely matches your field-volume/strength/homogeneity needs from these three versatile 6″ types, and Varian's 4″ adjustable-gap, 12″ adjustable-yoke, 12″ rotator and new 22″ high-field laboratory magnets. Matching regulated power supplies, a wide range of pole cap options, a fluxmeter-control unit, rolling and rotating bases, support tables and other accessories, plus a world-wide service engineering organization, make Varian the logical choice for all your magnet needs.

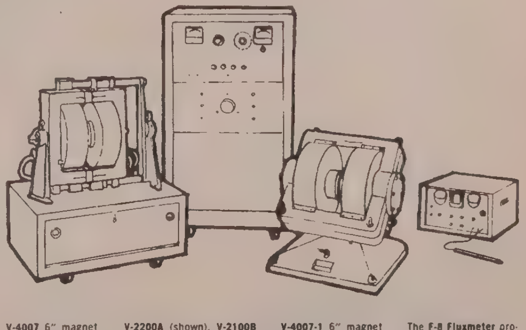

V-4007 6″ magnet yoke is adjustable about the horizontal axis. Air gap width is adjusted with precision yoke-separating spacer blocks

V-2200A (shown), **V-2100B** power supplies furnish precisely regulated power to Varian's 6″ and 12″ magnets. Matching regulated power supplies are available for the complete Varian magnet line.

V-4007-1 6″ magnet rotates around the vertical axis and uses pole caps of various thicknesses for air gap adjustment.

The **F-8 Fluxmeter** provides precise measurement and/or control of magnetic fields as an accessory to Varian magnet systems and readily adapts to other systems.

For further information, write Instrument Division

New Eastern office: *12 South Michigan Avenue*
Kenilworth, New Jersey • CHestnut 1-0200

VARIAN associates
PALO ALTO 36, CALIFORNIA

EPR SPECTROMETERS, MAGNETS, FLUXMETERS, GRAPHIC RECORDERS, MAGNETOMETERS, MICROWAVE TUBES, MICROWAVE SYSTEM COMPONENTS, HIGH VACUUM EQUIPMENT, LINEAR ACCELERATORS, RESEARCH AND DEVELOPMENT SERVICES

HIGH-RESOLUTION, ALL-PURPOSE JEM-6A ELECTRON MICROSCOPE FROM FISHER

Now, Fisher Scientific is your exclusive United States and Canadian source for electron microscopes, related instruments manufactured by Japan Electron Optics Laboratory Co., Ltd. Model JEM-6A gives you resolving power up to 8 Angstroms for physical, chemical and metallurgical work . . . 12 A is routine. **Direct magnification:** continuously variable from 600X to 200,000X, providing photographic magnifications above 1,000,000X. **Accelerating voltages** of 50, 80 and 100 KV are extremely stable. With accessories, you heat specimens to 1000° C; cool them to −140° C; put them under tensile stress while inside the JEM-6A. A 16-mm camera films changes in crystal structure. You can record electron diffraction patterns of 1-micron fields . . . make direct-reflection photographs of surface structure. **For full details,** call your Fisher branch, or write Fisher Scientific Company, 151 Fisher Building, Pittsburgh 19, Pa.

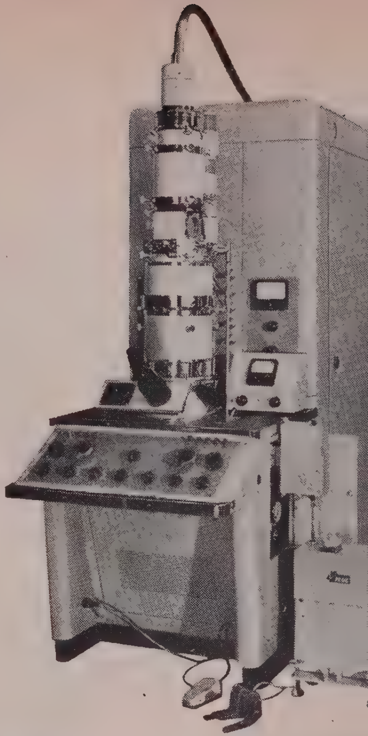

F-195

ZINC OXIDE SMOKE 80,000X

FISHER SCIENTIFIC

World's Largest Manufacturer-Distributor of Laboratory Appliances & Reagent Chemicals

Boston • Chicago • Ft. Worth • Houston • New York • Odessa • Philadelphia • Pittsburgh • St. Louis • Washington • Montreal • Toron

Specify "ARNOLD"
for your PERMANENT MAGNET requirements

ypical group of Arnold permanent magnets, both cast and sintered types.

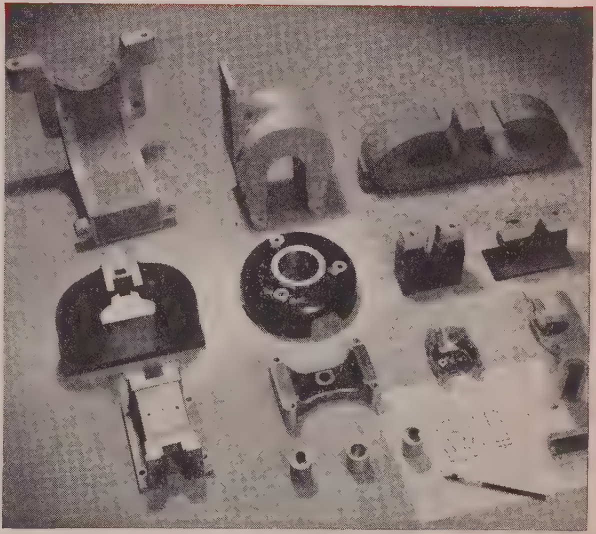

Typical group of permanent magnet assemblies, aluminum jacketed.

ALNICO MAGNETS

Arnold permanent magnets are available in all types Alnico material, in sizes ranging from large castings eighing over 80 pounds to very small sintered parts eighing less than one gram.

Alnico V can usually be depended upon to deliver the eatest energy product to the magnetic circuit per unit eight of magnet material. It is therefore generally the st choice for a magnetic material except where special ıysical considerations are paramount.

Special assemblies such as rotors, traveling wave tube magnets, magnetron magnets, etc. may be supplied in an aluminum jacket to facilitate mounting and supply an added protection to the magnet.

Large magnet assemblies may also be supplied for mass spectrometer and other measuring applications where a high degree of stability and uniformity of field is required.

Many sizes and types of Alnico magnets are carried in stock for immediate delivery. For more information, *write for Bulletin GC-106C.*

SPECIAL PERMANENT MAGNET MATERIALS

ARNOX III

Arnox III is a molded-type magnet having high coer- ve force and moderately low residual induction and ıergy product. Principal uses are for magnetic require- ents which are not stringent, and for a relatively short agnet of reasonable cross section. Accurate dimensions ıd close tolerances can be economically obtained. These agnets can be premagnetized before assembly, and have ery high resistance to demagnetization. Slightly better agnetic properties are obtained in the pressing direction han in other directions.

ARNOX V

Arnox V is a ceramic permanent magnet material com- osed of highly oriented barium ferrite. It has many times ie energy product of Arnox III and is comparable in any applications to Alnico V. Because of its high coer- ve force, its use is recommended in applications where a ort magnetic length is desirable or where extremely high emagnetizing forces may be encountered. In many appli- ations, it may be magnetized prior to assembly.

VICALLOY

Vicalloy is a carbon-free permanent magnet alloy containing about 10% vanadium, 50% cobalt and the balance iron.

Vicalloy may be fabricated in the form of castings, hot rolled bars and forgings, or cold rolled strip, wire and tubing. After suitable heat treatment, the material is quite readily machinable. Vicalloy is available on special order in bar, strip and thin tape for recording purposes. *For more information, write for "The Magneteer," Vol. 2, No. 1.*

CUNIFE

Cunife is a permanent magnet alloy of copper, nickel and iron which is malleable, ductile and machinable, after final heat treatment. The magnetic properties of Cunife are developed by cold working and are directional, with the best magnetic properties found only in the smaller sizes of rods or wires.

7506-A

ARNOLD

SPECIALISTS in MAGNETIC MATERIALS

THE ARNOLD ENGINEERING COMPANY, Main Office: MARENGO, ILL.
BRANCH OFFICES and REPRESENTATIVES in PRINCIPAL CITIES

Increased technical responsibilities in the field of range measurements have required the creation of new positions at the Lincoln Laboratory. We invite inquiries from senior members of the scientific community interested in participating with us in solving problems of the greatest urgency in the defense of the nation.

RADIO PHYSICS and ASTRONOMY

RE-ENTRY PHYSICS

PENETRATION AIDS DEVELOPMENT

TARGET IDENTIFICATION RESEARCH

SYSTEMS: Space Surveillance
Strategic Communications
Integrated Data Networks

NEW RADAR TECHNIQUES

SYSTEM ANALYSIS

COMMUNICATIONS: Techniques
Psychology
Theory

INFORMATION PROCESSING

SOLID STATE Physics, Chemistry, and Metallurgy

A more complete description of the Laboratory's work will be sent to you upon request.

All qualified applicants will receive consideration for employment without regard to race, creed, color or national origin.

Research and Development
LINCOLN LABORATORY
Massachusetts Institute of Technology
BOX 33
LEXINGTON 73, MASSACHUSETTS

For recording high-speed one-shot occurrences

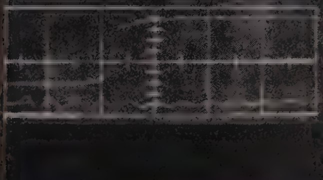

Avalanche test as illustrated may produce only one waveform of significance. The upper single-shot trace at 2 nanoseconds per centimeter displays approximately 0.4-nanosecond risetime. It is the result of the very first avalanche event.
The lower 1 gigacycle* timing trace illustrates sweep linearity.

NOW, you can see and record non-repetitive, high-speed phenomena with a standard oscilloscope—one that does not depend upon sampling techniques. On its distributed-deflection CRT, you can observe bright displays with 100-line-per-centimeter definition. You can photograph fractional-nanosecond signals with ease on its full 2 x 6 centimeter display area.

With a Tektronix Type 519 Oscilloscope and associated C-19 Camera, you can easily photograph a single transient at 2 nanoseconds per centimeter—as illustrated in the avalanche test.

You will find the Type 519 engineered for convenience . . . *Internally*—all circuit components of the complete unit fit compactly, yet are readily accessible for easy maintenance. A fixed signal-delay line plus variable sweep-delay control maintains the wide display passband and eliminates any need for adjusting delay-cable lengths.

Externally—the Type 519 features a minimum of controls and connectors for an instrument in this range. A carefully-coordinated front-panel layout facilitates your test setups and procedures, aids greatly in saving engineering time and effort.

You need no auxiliary equipment for many high-speed applications. In fact, for normal operation, you make two connections only: (1) you plug-in the power cord, (2) you couple-in the signal source.

With such operational ease—combined with its inherent Tektronix reliability—the Type 519 is an ideal laboratory oscilloscope for your high-speed measurements up to the gigacycle region and slightly beyond—especially those applications demanding a photographic record of one-shot occurrences.*

CHARACTERISTICS **Passband**—from dc, 3db point typically above 1 gigacycle. **Instrument Risetime**—less than 0.35 nanosecond (including trigger takeoff, delay line, CRT, and termination). **Synchronization**—200 mv peak-to-peak, 1 MC to 1 gigacycle. **Accelerating Potential**—24 kilovolts. **Sensitivity**—10 volts/centimeter, maximum, into 125 ohms. **Time Base**—linear 6-centimeter sweeps from 2 nanoseconds/centimeter to 1 microsecond/centimeter in 9 steps. **Sweep Delay**—through 35 nanoseconds. **Triggering**—jitter-free: **External**—3-microwatt (20-millivolt) pulse of 1-nanosecond duration. **Internal**—2-tracewidth pulse of 1-nanosecond duration. Signal waveform undisturbed by trigger takeoff. **Power and High-Voltage Supplies**—electronically regulated. **Calibration-Step Generator. Avalanche-Transistor Rate Generator.**

TEKTRONIX TYPE 519 Oscilloscope f.o.b. factory **$3800**

C-19 CAMERA

- **Full-Intensity Mirror Viewing.**
- **Direct Recording.**
- **One-Hand Portability.**
- **Lift-On Mounting.**
- **Swing-Away Hinging.**
- **Comfortable Viewing—with or without glasses.**

C-19 Camera **$650**
Includes f/1.5 lens with 1:0.5 (object-to-image ratio) complete with cable release, Focusing Back, Polaroid† Back, other accessories. †® *by Polaroid Corporation*

**1 gigacycle = 10^9 cycles.*

For a demonstration of these instruments in your own wide-band applications, please call your Tektronix Field Engineer.

ektronix, Inc. *P. O. BOX 500 · BEAVERTON, OREGON / Mitchell 4-0161 · TWX—BEAV 311 · Cable: TEKTRONIX*

KTRONIX FIELD OFFICES: Albuquerque, N. Mex. • Atlanta, Ga. • Baltimore (Towson) Md. • Boston (Lexington) Mass. • Buffalo, N.Y. • Chicago (Park Ridge) Ill. • Cleveland, Ohio • Dallas, Texas • Dayton, Ohio ıver, Colo. • Detroit (Lathrup Village) Mich. • Endicott (Endwell) N.Y. • Greensboro, N.C. • Houston, Texas • Indianapolis, Ind. • Kansas City (Mission) Kan. • Los Angeles, Calif. Area (East Los Angeles, cino • West Los Angeles) • Minneapolis, Minn. • Montreal, Quebec, Canada • New York City Area (Albertson, L.I., N.Y. • Stamford, Conn. • Union, N.J.) • Orlando, Fla. • Philadelphia, Pa. • Phoenix (Scottsdale) Ariz. ughkeepsie, N.Y. • San Diego, Calif. • San Francisco, Calif. Area (Lafayette, Palo Alto) • St. Petersburg, Fla. • Syracuse, N.Y. • Toronto (Willowdale) Ont., Canada • Washington, D.C. (Annandale, Va.).

KTRONIX ENGINEERING REPRESENTATIVES: Hawthorne Electronics: Portland, Oregon; Seattle, Washington • Kentron Hawaii Ltd., Honolulu, Hawaii. Tektronix is represented in twenty overseas countries qualified engineering organizations.

Europe please contact Tektronix International A.G., Terrassenweg 1A, Zug, Switzerland, Phone (042) 4-91-92, for the address of the Tektronix Representative in your country.

MEASURE VACUUM

10^{-3} to 10^{-10} Torr

ACCURATELY

. . . with NRC's Nottingham Vacuum Gauge

Recent research in the field of pressure measurement by Prof. Nottingham and NRC Equipment Corp. resulted in an improved ionization gauge . . . the only vacuum gauge offering all the features essential to knowing the actual pressures being measured in the ultra-high vacuum range.

NRC Model 751A provides:

- **Grounded shield coating . . .** on inside surface of gauge glass envelope prevents space charge electrostatic build-up . . . resulting in uniform stability at low pressures.
- **Grid structure closures at both ends . . .** prevent end-loss of ions, provides more efficient ion collection . . . resulting in more uniform sensitivity over a wider pressure range.
- **Two separate filaments . . .** electrically independent . . . resulting in use of the flash filament technique to measure pressures below normal gauge range — to 10^{-12} Torr. Extra filament lengthens useful life of gauge.
- **Low amplifier sensitivity with 100% negative feedback . . .** provides stable, 100% linear amplification, resulting in elimination of effect of stray lab signals . . . zero drift is negligible.

For pressure readings down to 10^{-12} Torr, use the NRC Model 751A Nottingham vacuum gauge.

For data sheet, specs or a quote, write Dept. 20H, 160 Charlemont St., Newton 61, Mass., or any NRC Sales Office. DEcatur 2-5800

NRC
EQUIPMENT
CORPORATION

A Subsidiary of National Research Corporation
160 Charlemont Street, Dept. 10F
Newton 61, Massachusetts
DEcatur 2-5800

Not necessarily in words and syllables
but in electronic impulses, relayed by orbital, lunar and
interplanetary communications systems.

Scientific advancement depends upon the ability of man to overcome the limitations of current knowledge. These limitations are being pushed aside at the Amherst Laboratories by new concepts for aerospace communications and instrumentation systems.

The role that microwave and millimeter wave technology will assume in future aerospace systems is being shaped through state-of-art advances achieved by our technical staff.

PROFESSIONAL STAFF AND MANAGEMENT OPPORTUNITIES *are unlimited for Physicists, Mathematicians and Electronic Engineers with advanced degrees and creative desire.*

All qualified applicants will receive consideration for employment without regard to race, creed, color or national origin.

You are invited to direct inquiries in confidence to Mr. H. L. Ackerman, Professional Employment,

AMHERST LABORATORIES • 1183 WEHRLE DRIVE • WILLIAMSVILLE, NEW YORK

SYLVANIA **ELECTRONIC SYSTEMS**
Government Systems Management
for ***GENERAL TELEPHONE & ELECTRONICS***

Welch High Form TRIPLE BEAM BALANCE

- High Sensitivity
- Stainless Steel

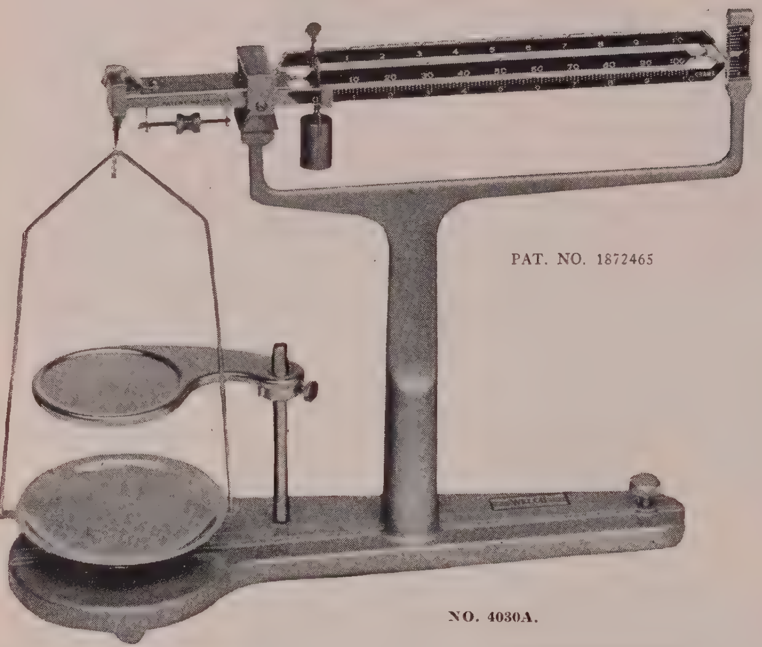

PAT. NO. 1872465

NO. 4030A.

• STAINLESS STEEL CONSTRUCTION

Every part except knife edges, bearings, and body casting made of highly corrosion-resistant stainless steel.

• ONE-PIECE BEAM (PATENTED)

Low beam weight plus good rigidity permits high balance sensitivity. The three scales are tiered for perfect eye-level readability. One-piece construction assures unchanging sensitivity.

• ELECTROPOLISHED SURFACES

All exposed stainless-steel surfaces are specially processed to clean easily, stay bright longer.

• COBALITE KNIFE EDGES

Ground with precision to eliminate friction, hard enough to remain sharp for a lifetime.

• REVERSE ETCHED SCALES

Lines and numerals on all scales are in sharp, clear contrast with black background for greater reading ease.

• AGATE BEARINGS

Widely spaced for stability, permanently set, carefully covered to keep foreign matter from critical surfaces.

• POSITIVE-SETTING SLIDING WEIGHTS

All of stainless steel, the two larger weights lift from notch to notch, discourage rough usage, promote long-lasting accuracy of calibration.

• CLEAN, UNCLUTTERED DESIGN

Note the simple functional appearance, the freedom from frills, the absence of dust-collecting corners and grooves. This balance looks clean—and stays clean with no effort.

Capacity: 111 grams.

Sensitive to 0.01 gram.

Includes adjustable platform for specific gravity determinations.

Over-all dimensions 14 x 4¼ x 11 inches high.
Net weight 2 lbs.
Shipping weight 3½ lbs.

4030A. TRIPLE BEAM BALANCE, High Form. Each, $27.50

4031. AUXILIARY WEIGHT. For increasing the capacity of No. 4030A Balance to 201 grams. Each, $1.50

4030C. PLASTIC COVER. For No. 4030A. Each, $1.60

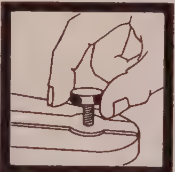

JUST ONE LEVELING SCREW TO ADJUST

You turn only one easily accessible leveling screw to place balance in instant adjustment.

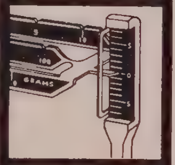

BEAM POSITION INDICATED BY GRADUATED END SCALE

You see at a glance the approximate adjustment of the centigram rider you need to complete the weighing.

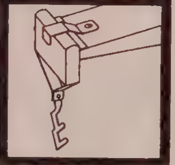

STIRRUP CAN'T FALL OFF

The Cobalite stirrup knife edge and its agate bearing have a protective cover with a retainer to prevent accidental stirrup removal.

THE WELCH SCIENTIFIC COMPANY

ESTABLISHED 1880

1515 SEDGWICK STREET, DEPT. C-1, CHICAGO 10, ILLINOIS, U.S.A.

Manufacturers of Scientific Instruments and Laboratory Apparatus

Journal of Applied Physics

Volume 32, Number 8 August, 1961

International Conference on the Nature of Solid Friction

Preface

The following articles on friction were presented at the International Conference on the Nature of Solid Friction, held at Midwest Research Institute, Kansas City, Missouri, September 26–28, 1960.

The conference was sponsored by the National Science Foundation, Office of Ordnance Research, Office of Naval Research, and Wright Air Development Division, and was chairmanned by T. B. Daniel of MRI.

A synopsis of the papers presented at this Conference can be found in Wear **4**, No. 2, 161-64 (1960).

Friction and Adhesion of Clean and Contaminated Mica Surfaces

Anita I. Bailey
Research Laboratory for the Physics and Chemistry of Solids, University of Cambridge, Cambridge, England

In order to determine the shear strength of boundary lubricants it is essential to use a substrate which is smooth on a molecular scale. An apparatus is described in which it is possible to apply normal and tangential loads to sheets of mica covered with monomolecular layers of boundary lubricant. The shear strength obtained from these experiments explains in part why frictional force and pickup are not reduced proportionately, in the presence of a boundary lubricant. The remaining difference is probably due to elastic hysteresis losses in the sliding solids. The surface energy of mica in air has also been measured by determining the force necessary to propagate a crack in the material. Cycles of opening and closing the crack have been performed and the difference in energy which is observed is attributed to the adsorption and migration of an interfacial film of air or water vapor. An electronmicrographic study of the structure of monolayers deposited by retraction from nonpolar solution is also described. This indicates that the area covered by the monolayer is only about $\frac{1}{3}$ the total surface area. This poor coverage arises from incorporation of solvent molecules in the monolayer, which later evaporate.

INTRODUCTION

When studying any phenomenon involving contact between solid surfaces, complications often arise owing to the difficulty of knowing the extent of true contact. As a result, many methods have been devised for measuring the real area of contact of two bodies placed together. These include the measurement of contact resistance for metals, methods involving the use of radioactive tracers, and the examination of light totally internally reflected from one of the solid surfaces in the case where at least one of the solids is transparent. Unlike nearly all other materials, mica can be smooth on a molecular scale so that, if it is clean, contact occurs all over the apparent area of contact rather than merely at the tops of asperities.

At Cambridge we have been using multiple-beam interference techniques to measure the area of contact between sheets of mica. The mica, when cleaved carefully, splits along the cleavage planes yielding sheets consisting of large parallel-sided facets. If such a sheet is silvered on both sides and examined using high dispersion Fizeau fringes, each facet is revealed as a region of constant tint and intensity. A sustained change in thickness can be revealed even if it is only a few angstroms in height. The specimens used in this work were usually cut from a single facet.

Copyright © 1961 by the American Institute of Physics.

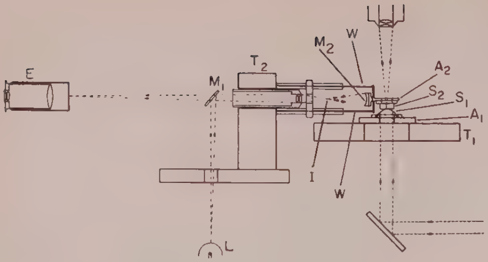

FIG. 1. Schematic diagram of the apparatus used to determine shear strength of boundary lubricants.

Clean mica adheres readily to itself and to many other surfaces. If two such sheets are stuck together, the high dispersion fringes indicate where the contact is intimate and show the presence of accidental contamination. These results were used in the design of an apparatus for the measurement of adhesion and the shear strength of a typical boundary lubricant.[1]

EXPERIMENTS

A schematic diagram of the apparatus is shown in Fig. 1. A_1 and A_2 are clamps which hold the specimens S_1 and S_2 in such a way that each is bowed up to form a section of a cylinder. The two cylindrical shells are mounted at right angles. This was done in order that the contact may be located away from the edges of the mica strips. A_1 is fixed to the stage T_1 of a microscope, while A_2 is supported by four equal silver steel wires W. The other ends of the wires were fixed to a block mounted on a movable table T_2 separate from the microscope. An optical system was used to measure the deflection of the upper specimen. A small frosted lamp L had a cross hair attached to it; by means of a mirror M_1 and the lens shown, an image of the cross hair was produced at I. This acts as object for a concave mirror M_2 attached to the back of the upper specimen holder, and is so arranged that it produces an image coincidental with I if no forces are applied to A_1. If, however, A_1 is displaced, the image produced by M_2 is also displaced. This displacement is magnified by the lens and observed using a micrometer eyepiece E. Normal and tangential loads were applied by vertical movement of T_2 and horizontal movement of T_1, respectively.

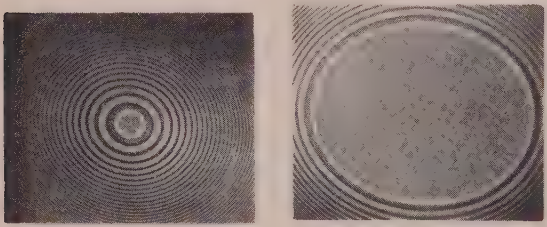
(a) (b)

FIG. 2. Areas of contact between mica surfaces obtained using high-dispersion Fizeau fringes.

The area of contact was observed by directing a collimated beam of light from a mercury lamp on to the specimens. The fringe pattern consisted of an area of uniform tint approximately circular in shape, surrounded by a system of concentric rings (Fig. 2). It was also found useful to use fringes of equal chromatic order in this examination. Examples of these fringes are shown in Fig. 3(a) and (b). The section of constant wavelength corresponds to the region of contact; Fig. 3(b) shows that, when the sheets of mica are coated with a monolayer of a fatty acid or soap, the nature of the contact is the same.

When a normal load is applied and then removed, it is found that the sheets still adhere and a reversed load must be applied to separate them. The maximum load required to separate the sheets was found to be independent of the initial load. From the measurement of the final area of contact and the maximum value of the tension, a value of 2 kg/mm² was obtained for the normal adhesion. This result is not of great precision because the final area was only of the order of 10^{-4} cm².

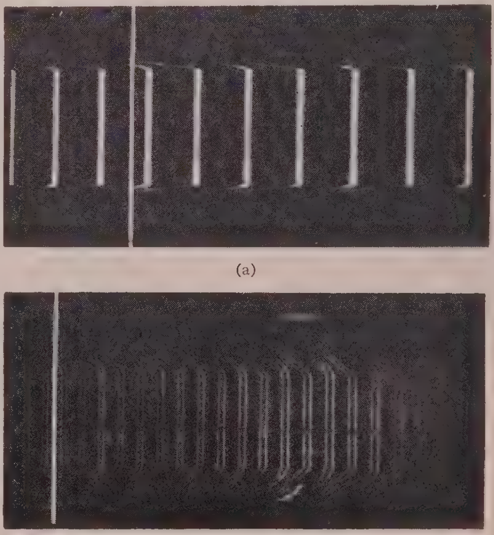
(a)

(b)

FIG. 3. Fringes of equal chromatic order showing thickness variation across area of contact. (a) Unlubricated mica. (b) Mica lubricated with monolayer of calcium stearate.

Although the adhesion did not vary with the size of the initial area, it did vary with the time for which the specimens were in contact. A greatly reduced value of the adhesion was obtained if the sheets had been in contact for less than about 20 sec. This reduction could be as great as 50%. If the specimens were left together for longer than this, the full value of the adhesion was always observed, even after they had been separated for as long as 10 min.

---

[1] A. I. Bailey and J. S. Courtney-Pratt, Proc. Roy. Soc. (London) **227A**, 500 (1955).

In order to determine the shear strength, tangential loads were applied and measured. The shear strength of freshly cleaved mica was usually fairly consistent for a given specimen, but varied quite a lot from specimen to specimen. The results yielding the highest value obtained are shown in Fig. 4. This was 10 kg/mm². There was a noticeable time effect. After about 2 hr the values of the shear strength decreased fairly rapidly to a value at least a factor of 10 lower. Since the observations were made in air, the surfaces would have been covered with a layer of adsorbed gas or water vapor, so that we would expect observations made *in vacuo* to give even higher values. We were also interested in the shear strength of monomolecular layers of boundary lubricants, and chose calcium stearate as a suitable material. The monolayers were deposited on the mica sheets using the Langmuir-Blodgett method, before mounting these in the clamps. The presence of the lubricant was found to cause a decrease in the size of the area of contact for similar specimens under given normal loads. As expected, they sheared much more readily. The results are shown in Fig. 5, the value of the shear strength being about 250 g/mm².

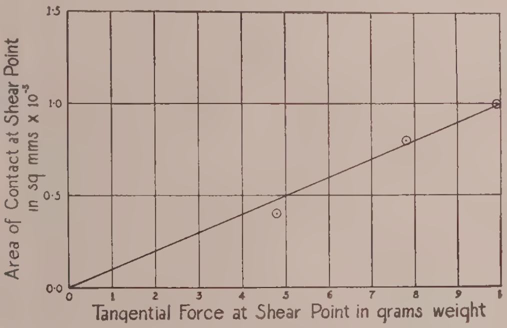

FIG. 4. Shear strength results for clean mica surfaces. Average value is 10 kg/mm².

This result is of interest in the interpretation of boundary friction results. It had been shown previously by Rabinowicz[2] that the presence of a single monolayer of a good lubricant on the surfaces of sliding metals caused a reduction in the friction force of a factor of about 10. When such an interface is sheared, the force must break junctions of the metal where penetration of the lubricant film has occurred, and it must also shear regions where lubricant is in contact with lubricant. Radioactive tracer techniques showed that in the presence of a good lubricant the area of metallic contact was reduced by an enormous factor—10 000 or more. Using the values of shear strength obtained, the shearing of the boundary lubricant will make some contribution towards this effect but will not account for it entirely. Recent work of Tabor[3] suggests that the remainder may be due to elastic hysteresis losses in the materials. If the surfaces are rough, losses will occur as asperities are deformed even if no penetration of the lubricant film takes place.

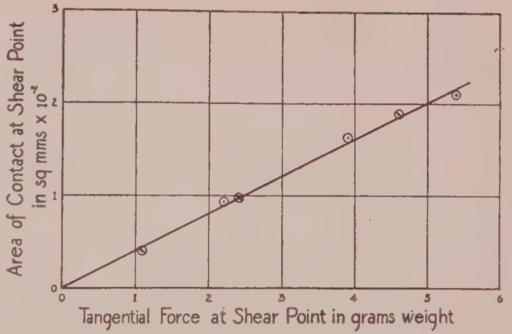

FIG. 5. Shear strength results for mica covered with a monolayer of calcium stearate. Average value is 250 g/mm².

Returning now to the measurement of adhesion, we required an experimental arrangement which involved the use of larger areas of contact, and we decided to measure adhesion in terms of the energy required to separate sheets of mica.[4] Consider a strip of mica of uniform thickness split symmetrically at one end (Fig. 6) so that the upper and lower sheets are of equal thickness. By application of the forces F, cleavage can be made to proceed. Supposing that the cleavage proceeds from A to B along the sheets, and that y is the separation at the open end, then the total work done during the cleavage process is

$$\int_{y_1}^{y_2} F dy.$$

Part of this work is stored as strain energy in the mica and part has been used in overcoming the force of adhesion between the sheets. For the purpose of determining the change in the strain energy, the sheets were treated as elastic beams. The shape used was chosen to give simple end conditions, and the sealed end was left free so that tension along the length of the sheets would be avoided.

The apparatus used was a modification of that already described. The four springs were replaced by a pair of horizontal leaf springs which allowed vertical movement

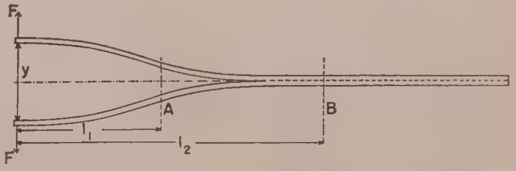

FIG. 6. Arrangement of mica for cleaving experiments.

---

[2] E. Rabinowicz, Proc. Roy. Soc. (London) **208A**, 455 (1951).
[3] D. Tabor (private communication).

[4] A. I. Bailey, Proc. 2nd Intern. Congr. Surface Activity, London **III**, 406 (1957).

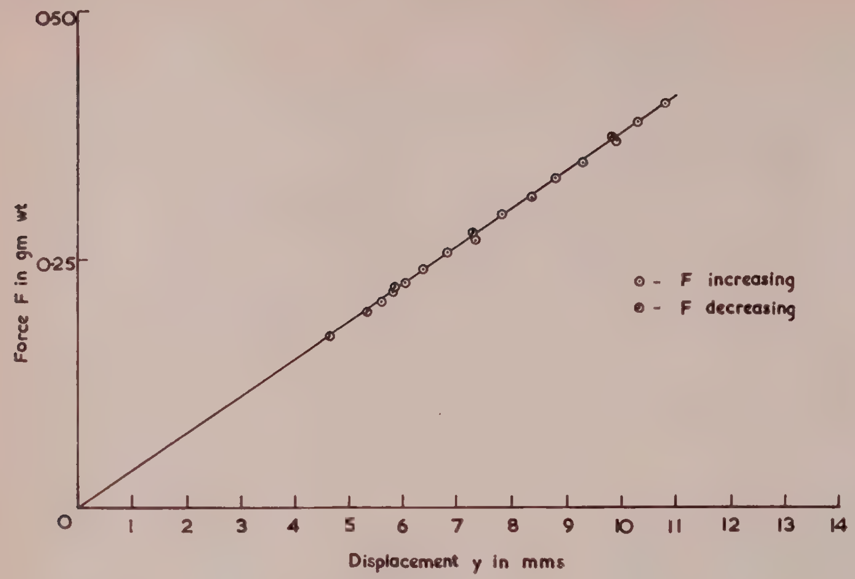

FIG. 7. Force-vs-displacement diagram for mica covered with particles of talc. No cleavage.

without twisting. The displacement y' was measured using a sensitive dial gauge, and the forces were measured using the same optical arrangement as before. The sheets were coated with a highly reflecting layer of silver before splitting, and the line of bifurcation was located using high-dispersion Fizeau fringes.

The $\int F dy$ represents the area under a plot of force vs displacement. These diagrams turned out to have a variety of interesting shapes. To test the reproducibility of the observations given by the experimental arrangements, a sheet of mica was split open over most of its length and the new surfaces thus exposed dusted with a little talc to prevent adhesion. F was plotted against y for this arrangement, and the results are shown in Fig. 7.

Figure 8 shows results obtained when cleaving a fairly thick sheet of mica. This jerky behavior was common at first, and is caused by interlocking of the sheets at the cut edges. Once the cleavage is halted by such interlocking, all the work done is put into strain energy in the mica and the F-vs-y diagram follows a straight line passing through the origin. This proceeds until the force at the bifurcation line is sufficient to overcome the restricting force and a sudden cleavage occurs without further increase of y. Sometimes the specimen continues to cleave on one edge while the other is stuck. This gives

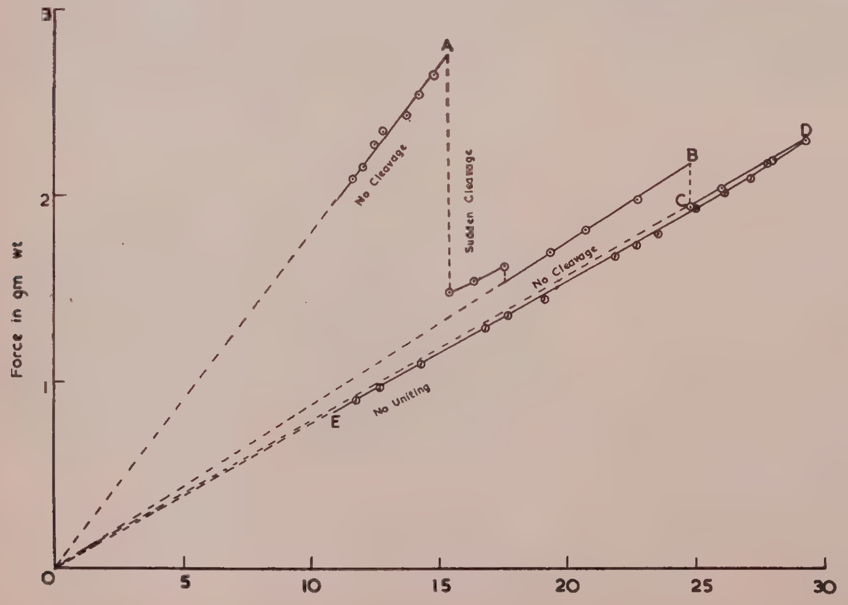

FIG. 8. Force-vs-displacement diagram. Abrupt cleaving of thick prestrained sheet of mica.

a line at a lower slope. The mica used here had considerable prestraining and would not stick together again when y was reduced.

Some specimens cleaved very smoothly. An example of such observations is shown in Fig. 9. The cleavage in all cases is allowed to proceed extremely slowly; i.e., about 1 or 2 mm/min. From the observations given in Fig. 9, the energy associated with cleaving unit length of sample was obtained. This represents the work used in the formation of 2 cm^2 of new surface, together with any which may have been dissipated in the process. Slow cleavage tends to minimize such losses. The spread on the results can be seen from Fig. 10, which gives a plot of length of sample cleaved against energy used. The energy is given in arbitrary units and the result obtained from the average slope. The upper line in the diagram is just too high, while the lower is just too low, to give a good representation of the points. The average slope gave a value of 300 erg/cm^2 for the energy required to produce unit area of new surface.

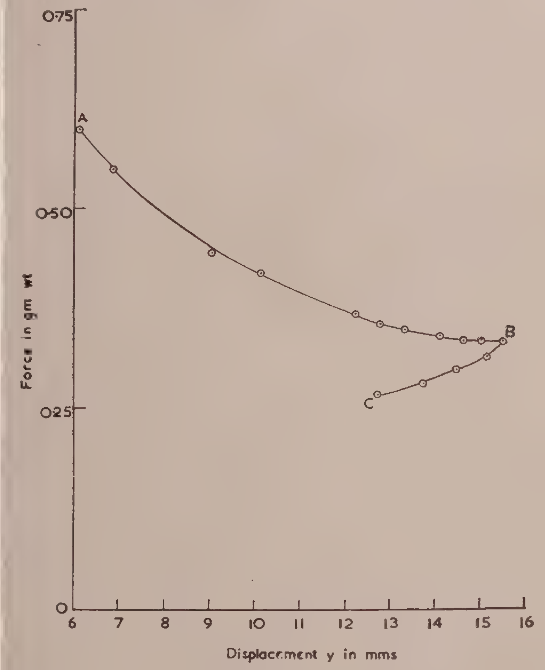

FIG. 9. Force-vs-displacement diagram for specimen showing smooth cleavage.

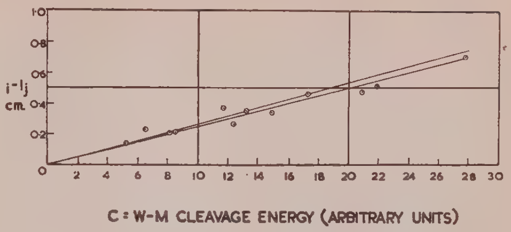

FIG. 10. Surface energy, virgin mica. Results for cleavage energy obtained using graph of Fig. 9. The slope gives a value of 310 erg/cm^2.

The sheets seal up again when the displacement y is decreased, and it is interesting to know what proportion of the energy is regained during this process. A cycle of opening and closing was therefore carried out. The method of splitting the mica in this experiment makes this easy since the surfaces are only subject to accidental contamination and are not damaged by the cleaving mechanism. Figure 11 shows such a cycle. Owing to the complex nature of this cycle, I will describe the physical process which was observed to occur as the various branches were being traced. The initial straight line AB shows that at first all the energy was stored as strain energy in the sheets, and no cleaving occurred. At B the mica cleaved suddenly without further increase in y and the force F dropped to the value corresponding to the point C. From C to D cleaving was relatively smooth, but was retarded at two points owing to slight imperfections in the cut edge. At D the direction of increase of y was reversed. Observations of the line of birfurcation showed that no sealing up occurred until the point E was reached. This proceeded to point F, when y was again increased. The mica was now being opened for the second time. In a similar way observations of the line of birfurcation showed that cleavage did not begin at once, so from F to G the work was stored as elastic strain energy in the mica. From G to H cleaving proceeded and the previously split region was again opened. The energy used or gained was obtained from the portions CD, EF, and GH giving the following values:

opening 1, energy used = 310 erg/cm^2;
closing, energy gained = 190 erg/cm^2;
opening 2, energy used = 250 erg/cm^2.

It is of interest to compare these results with those of Obreimoff.[5] He cleaved a thin sheet of mica from a thicker

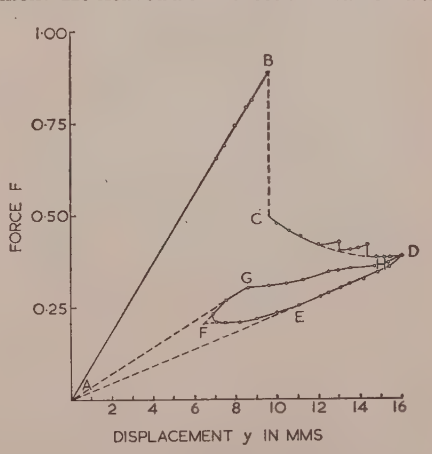

FIG. 11. Force-vs-displacement diagram for complete cycle of opening and closing. Virgin mica.

---

[5] J. W. Obreimoff, Proc. Roy. Soc. (London) 127A, 290 (1930).

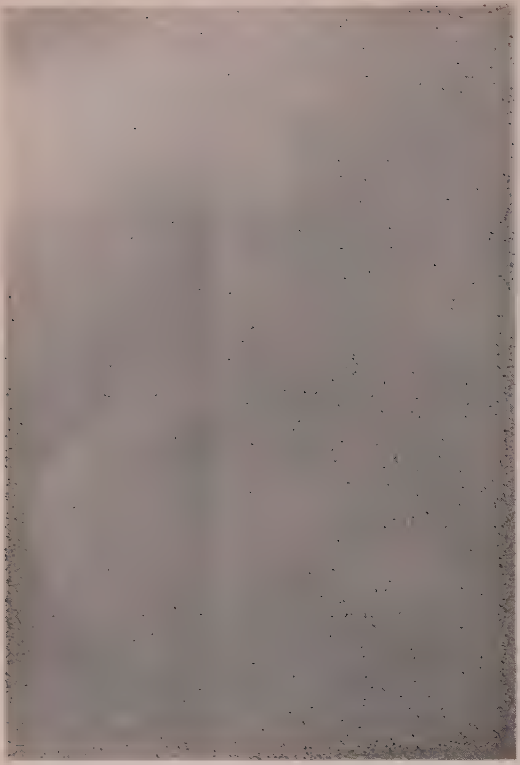

FIG. 12. Electron micrograph showing islands of fatty acid monolayer on mica surface.

sheet using a wedge, and obtained a value of 375 erg/cm^2 for mica cleaved in air. The values of 300–310 erg/cm^2 obtained here are in reasonably good agreement considering that mica is a natural product. These experiments have the advantage that the mechanism used for cleaving does not change the surfaces in any way and also shows whether or not the cleavage is confined to one single plane of atoms. The two results for opening the sheets are surprisingly close, showing that mica regains most of its strength even after having been exposed to the atmosphere. The difference between the results for opening and closing may be due to trapping a thin film of air between the surfaces. Such films have been observed, and found to become unstable and diffuse into rows of tiny air bells which give the mica a wrinkled appearance. An attempt has also been made to measure the thickness of the adsorbed film by cleaving part of an extremely thin facet of mica, about 2000–3000 A thick, and measuring the total thickness of cleaved and uncleaved portions. These observations gave a result of 6±2 A for the thickness of the interfacial film, after the bulk of the trapped air has migrated. The time effect observed with normal adhesion measurements also supports this migration hypothesis.

The presence of a monolayer of perfluorodecanoic acid greatly reduces the value of the separation energy. Exact figures are not yet available but are of the order of a factor of 10 lower.

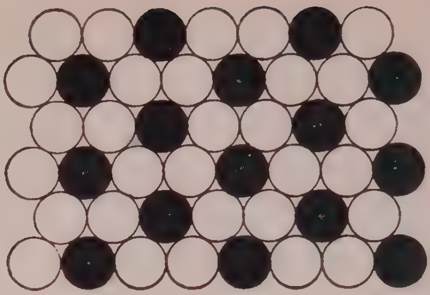

FIG. 13. Arrangement of solute and solvent molecules on the surface of mica. Dark circles represent fatty acid molecules and open circles those of the paraffin from which the monolayer was retracted.

To conclude, I would like to describe briefly some work which has been done by Mathieson[6] of this laboratory. This is concerned with the structure of monomolecular films of fatty acids when deposited by various methods. He deposited films using the well-known method of retraction from nonpolar solvent. The film was then preshadowed, a carbon replica of the surface made, and examined in the electron microscope. Figure 12 shows an electron micrograph obtained in this way. It can be seen that the stearic acid has formed little islands on the surface. If you measure the area occupied by the acid it turns out to be one-third the total area of the surface. It may be suggested that this poor coverage is due to evaporation of the film during the vacuum deposition of the shadowing material and the replica, but no such island structure was observed when the monolayer was retracted from the melt and subjected to the same treatment.

Mathieson suggests that, when stearic acid is retracted from a solution in a material like *n*-hexadecane, some of the solvent is incorporated in the monolayer. Figure 13 shows how this is possible. The *n*-hexadecane molecules orient themselves around those of the stearic acid, forming a sheath, and are held there by the lateral attraction between the molecules. The black circles in the diagram are the acid molecules and the open circles those of *n*-hexadecane. Each acid molecule is thus surrounded by six solvent molecules. Since the *n*-hexadecane has a higher vapor pressure than the stearic acid, these do evaporate during pumping out and the remaining film collapses into the island structure observed. Mathieson has obtained similar results with alcohols, amines, and amides dissolved in a long chain paraffin. All the paraffins behave in the same way down to dodecane. Decane and octane and various cyclic hydrocarbons do not appear to become incorporated. Hence, when studying the properties of monomolecular films, great care must be exercised in the method of deposition.

---

[6] R. T. Mathieson, Nature **183**, 1803 (1959).

JOURNAL OF APPLIED PHYSICS VOLUME 32, NUMBER 8 AUGUST, 1961

Recent Work on Solid Friction at the Research Laboratory for the Physics and Chemistry of Solids

ANITA I. BAILEY
Research Laboratory for the Physics and Chemistry of Solids, University of Cambridge, Cambridge, England

This paper is a review of some of the recent work which has been done in the Research Laboratory for the Physics and Chemistry of Solids, University of Cambridge. Three main topics are discussed: (a) The friction and wear of materials at very high rates of sliding. When a ball, spinning at high velocity, is brought into contact with a flat surface of a material such as bismuth, very rapid wear occurs as a result of melting on a large scale. For this to occur, the material should have a low melting point and a low thermal conductivity, as these properties together influence the rate at which the melted zone penetrates the solid. (b) Elastic hysteresis losses and rolling friction. A cylinder rolling over the surface of rubber causes the material under the roller to be subjected to a complex deformation cycle, partly torsion and partly tension. Experiments to investigate the hysteresis losses in such complex cycles are described and used in the interpretation of rolling friction results. (c) The effect of combined stresses and contamination on the growth of junctions between metal surfaces. The simple theory of friction treats the mean yield pressure and the maximum shear stress as independent strength properties. Plasticity theory suggests that the yielding of a junction should occur as the result of their combined action. The theory has been confirmed by experiment and used to explain the fact that small traces of contamination can reduce the very high values of friction observed with outgassed metals to normal values of 1 or 2.

INTRODUCTION

IN this paper three main topics will be discussed: (a) the friction and wear of materials at very high rates of sliding; (b) the part played by hysteresis losses in the rolling friction of rubber; and (c) the role of combined stresses and contamination on junction growth in metallic friction. Previous work of the research group has been described in a monograph by Bowden and Tabor[1]; its more recent work is described in a second monograph[2] which is in preparation.

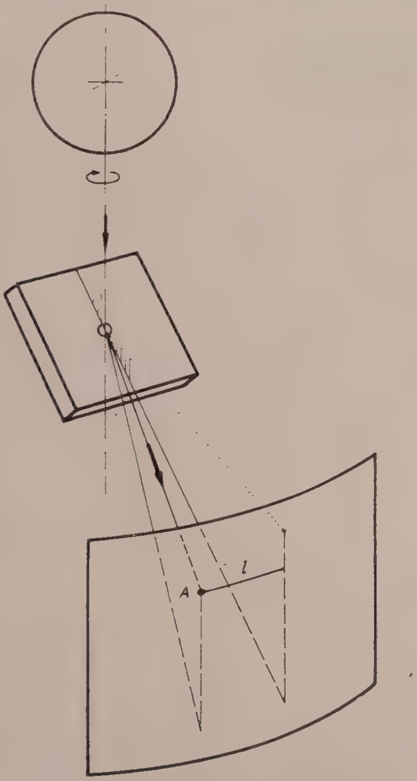

FIG. 1. A steel ball is suspended and rotated magnetically and then allowed to drop a few centimeters on to an inclined surface. The sideways deflection gives a measure of the frictional force.

FRICTION AND WEAR AT HIGH SPEEDS OF SLIDING

This work is a development of the experiments carried out by Bowden and Freitag.[3] They suspended a steel ball bearing magnetically and set it spinning in a vacuum using the method devised by Beams.[4] When the ball had attained a sufficiently high angular velocity, it was then trapped between three flat plates made from the material under investigation. The frictional force caused the ball to decelerate; by measuring

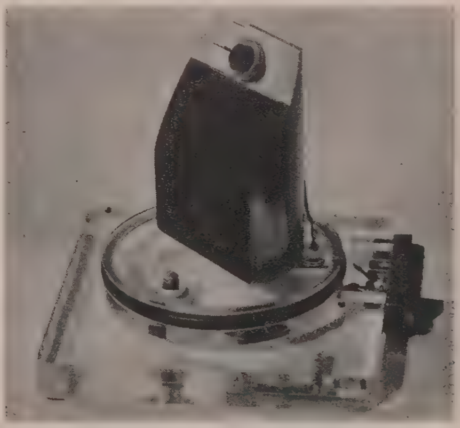

FIG. 2. The specimen holder.

---

[1] F. P. Bowden and D. Tabor, "Friction and lubrication of solids," Part I (Clarendon Press, Oxford, England, 1950).

[2] F. P. Bowden and D. Tabor, "Friction and lubrication of solids," Part II [Clarendon Press, Oxford, England (to be published)].

[3] F. P. Bowden and E. H. Freitag, Proc. Roy. Soc. (London) **A248**, 350 (1958).

[4] J. W. Beams, J. Wash. Acad. Sci. **37**, 221 (1947).

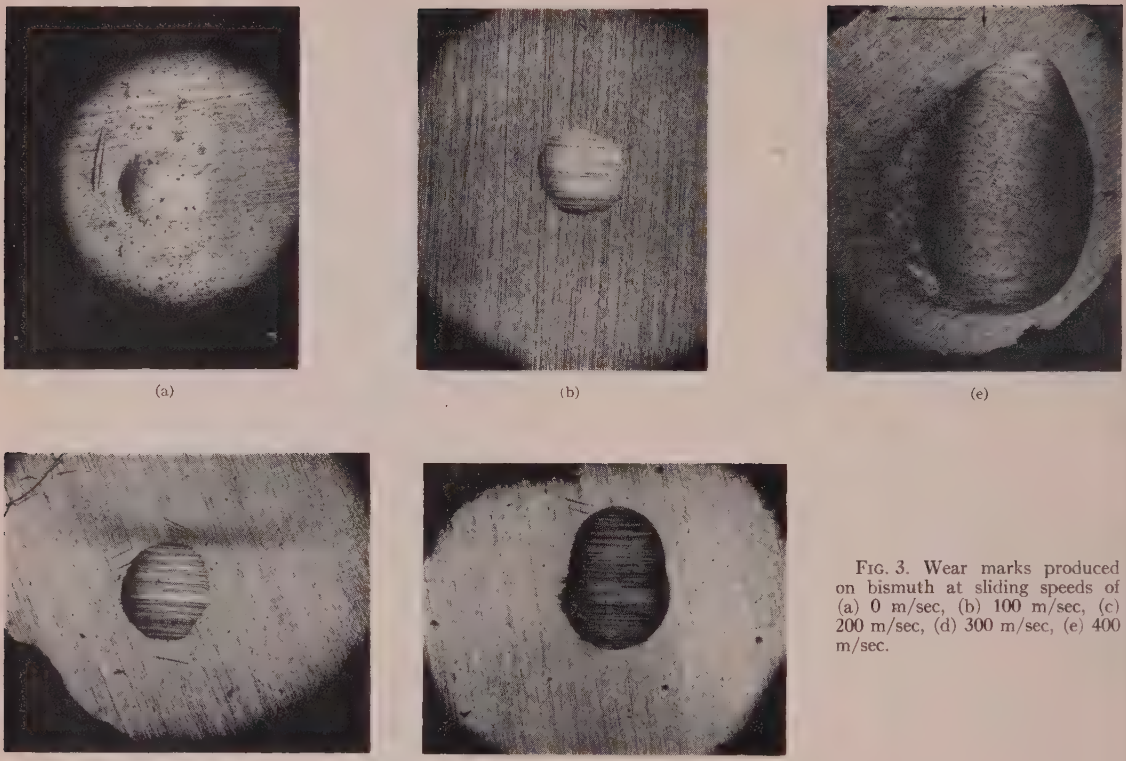

(a) (b) (e)

(c) (d)

FIG. 3. Wear marks produced on bismuth at sliding speeds of (a) 0 m/sec, (b) 100 m/sec, (c) 200 m/sec, (d) 300 m/sec, (e) 400 m/sec.

the retardation, they deduced the friction. It was found that the coefficient of friction decreased with increasing speed and this was attributed to localized melting of the surfaces.

One of the disadvantages of this setup is that, if melting occurs on a large scale, then the vessel becomes sprayed with molten material and it is no longer possible to pass a beam of light, used to stabilize the ball, through it. Bowden and Persson[5] therefore developed another piece of apparatus which is shown schematically in Fig. 1. In this arrangement the ball is suspended and rotated in the same manner as before, but is then allowed to drop a small distance (about 5 cm) onto a flat specimen which is set at an angle to the main axis of the apparatus. The spinning ball then bounces off and the sliding friction at the interface gives it a sideways deflection which is measured. Figure 2 shows the specimen holder which could be fitted with piezoelectric elements to allow the normal load or the friction force to be measured. Both measures of the friction force showed that it was independent of normal load.

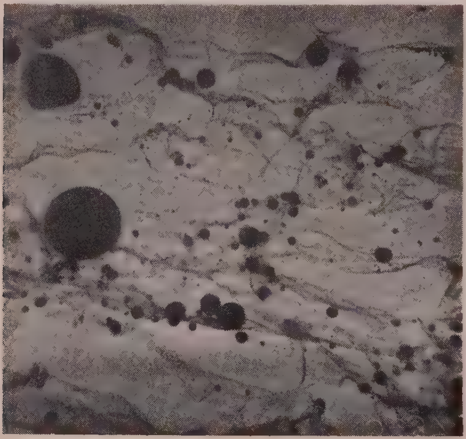

FIG. 4. Electron micrograph of wear material caught on a nitrocellulose film showing that the high wear is due to melting at the interface.

A number of materials were examined, both metals and nonmetals, at sliding speeds up to about 700 m/sec. As an example we may consider the behavior of bismuth (mp 271°C, thermal conductivity $k = 0.016$ cal cm^{-1} sec^{-1} °C^{-1}). Figure 3 shows the appearance of the wear mark produced by the ball at different speeds of sliding. Initially, there are indications of considerable plastic deformation followed by a softening and smear-

---

[5] F. P. Bowden and P. Persson, Proc. Roy. Soc. (London) (to be published).

TABLE I. Data affecting surface melting of solids at high rates of sliding.

Material	Melting point in °C	Thermal conductivity k in cal cm^{-1} sec^{-1} °C^{-1}
Bismuth	271	0.016
Lead	328	0.082
Tin	232	0.145
Wood's alloy	65	0.032
Copper	1080	0.91
Steel	1800	0.1
Nylon, terylene	~265	0.0006
Silver nitrate	210	0.002

ing of the material in the indentation. The wear marks at high speeds of sliding show obvious signs of melting. Various methods were used to catch the material as it was removed from the region of contact, and Fig. 4 is an electron micrograph of minute droplets caught on a nitrocellulose film.

It is quite clear that the wear occurring in this experiment is very high. The mechanism suggested by the observations is that the frictional heating causes a layer of molten material to be formed which is then removed by the spinning ball. The ball then penetrates deeper into the surface and the time of contact increases. If the film of liquid in the interface is to be stable, at least as much heat must be supplied by frictional heating as is carried away by conduction, suggesting that the thermal conductivity must play an important part in the process. In the case of bismuth the film is clearly stable and is formed at speeds of sliding as low as 50 m/sec. A combination of low melting point and low thermal conductivity seems to be what is required for the occurrence of melting on a large scale. These conclusions are borne out by observations on other materials, the relevant data for which are shown in Table I. Bismuth and Wood's alloy both showed large-scale melting even at low speeds of sliding. Lead and tin have higher values of thermal conductivity; their behavior resembled that of bismuth except that wear did not become appreciable until higher speeds had been reached. These were about 200 m/sec for lead and 120 m/sec for tin. Copper and steel both have high melting points and high values of thermal conductivity, and we should not expect large-scale melting to occur. Observations show that droplets are only picked up at the highest speeds of sliding.

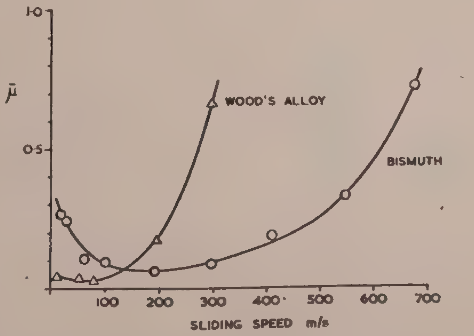

FIG. 5. Average coefficient of friction as a function of speed of sliding for Bi and Wood's metal.

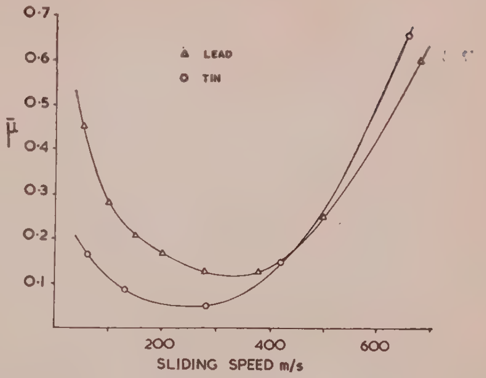

FIG. 6. Average coefficient of friction as a function of speed of sliding for Pb and Sn.

The friction in cases such as bismuth arises primarily from the shearing of the liquid layer. As this is wiped away by the spinning ball, the area of the film grows rapidly and we should expect a marked increase in friction. Figures 5 and 6 show the friction as a function of sliding speed for bismuth, Wood's alloy, lead, and tin. The coefficient of friction is the average value for the time of contact. All the graphs show a characteristic rise at the onset of large-scale melting, but for lead and tin, where the thermal conductivity is higher, this increase takes place at higher speeds of sliding. The friction for copper shows a steady decrease with increasing speed. Softening and subsequent melting occurs, but the underlying material remains hard and the load is supported on a relatively small area of film.

Table I also gives the data for several nonmetals. Silver nitrate shows a behavior very similar to that of bismuth but the polymers nylon and terylene showed a good resistance to wear in spite of low softening points and very low thermal conductivities. This high resistance to wear shown by the polymers appears to be due to the fact that these materials soften to form a very viscous film. A lot of heat is generated when this film is sheared, but this is used in raising the temperature and reducing the viscosity of the film itself before wear becomes appreciable and is not available for further melting. In this way a relatively thick film is maintained on the surface. Signs of decomposition of the polymers also occur. The friction shows a steady decrease (Fig. 7).

The important factors which govern wear at high rates of sliding are the melting point and the thermal conductivity. These together influence the rate at which the molten zone advances into the solid. If both are low,

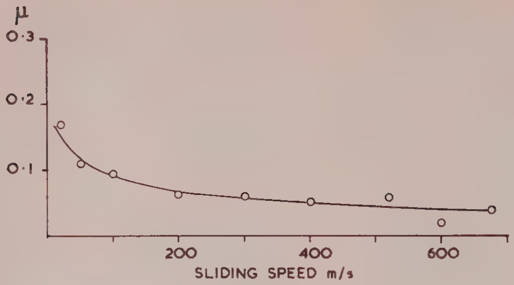

Fig. 7. Average coefficient of friction as a function of speed of sliding for terylene.

this rate is high except in the case where a highly viscous layer is formed.

ROLE OF ELASTIC HYSTERESIS LOSSES IN ROLLING FRICTION

Tabor *et al.*[6] have recently carried out a more detailed study of the rolling process. If we consider a cylinder rolling on a piece of rubber, then any theory of the rolling friction must account for three important observations. These are:

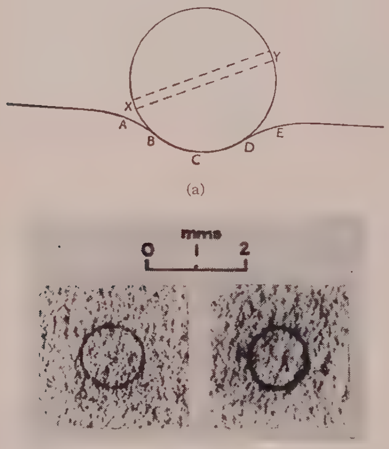

(a)

(b)

Fig. 8. A cylinder (a) having an inked hole through it is allowed to make (b) static (left) and rolling (right) imprints on rubber. The static imprint was made with a light load. The rolling imprint with a heavy load. As may be seen, the imprints show very little smearing, indicating that interfacial slip is negligible.

(a) The friction is independent of the condition of the surfaces. The presence of contamination and lubricants is found to have very little effect.

(b) Interfacial slip is extremely small. This may be seen by examining Fig. 8. A cylinder with a diametral hole in it was used to make static and rolling imprints on a piece of rubber by coating the hole with ink. As can be seen, the imprints, even under quite large loads, show little sign of smearing.

(c) If two rubbers are compared, it is found that the rolling friction is proportional to the hysteresis losses (Fig. 9). As has been suggested earlier by Tabor,[7] these observations suggest that the most important factor in rolling friction is the elastic hysteresis losses which occur in the material.

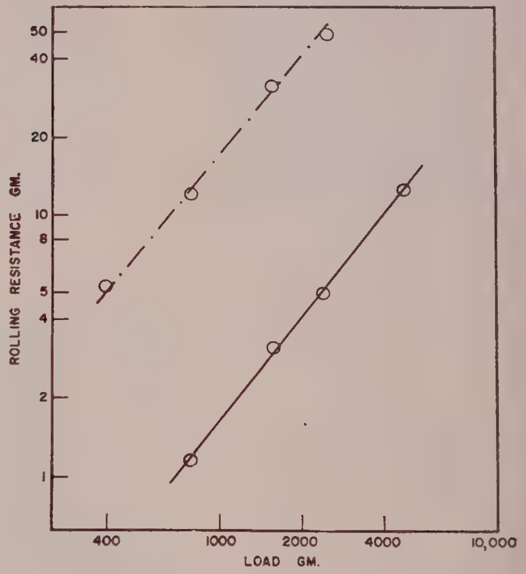

Fig. 9. Rolling friction for rubbers having different hysteresis losses. The broken curve is for a rubber having a hysteresis loss factor eight times as great as for the other rubber.

If we assume that hysteresis losses are a constant fraction α of the input energy, then if elastic energy/cm of rolling is designated by ϕ, the hysteresis losses/cm

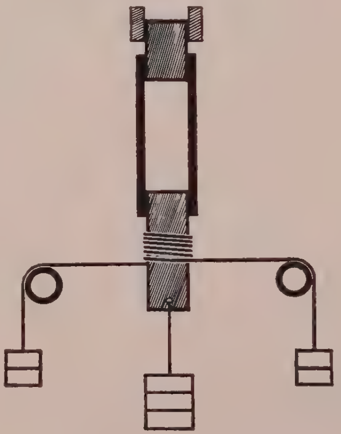

Fig. 10. Apparatus for examining hysteresis losses during cycles composed of a mixture of tension and torsion elements.

---

[6] D. Tabor, J. Greenwood, and H. Minshall, Proc. Roy. Soc. (London) **A259**, 480 (1961).

[7] K. Eldredge and D. Tabor, Proc. Roy. Soc. (London) **A229**, 181 (1955); D. Tabor, *ibid.* **A229**, 378 (1959).

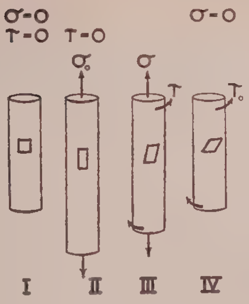

Fig. 11. States through which the specimen passed during complex strain cycles.

of rolling equal $\alpha\phi$. This may then be equated to the friction force F. Thus $F=\alpha\phi$. We can compare α with the hysteresis loss factor α_0 for a simple tension or torsion cycle. Experiment shows that $\alpha\approx 3\alpha_0$, and a mechanism to account for this numerical discrepancy is required.

α_0 is determined from simple tension or torsion cycles; i.e., under conditions of homogeneous uniform strain, but during the rolling process, the material under the roller is subjected to complex strain cycles and it is possible that this may account for the difference in the hysteresis losses.

To investigate this, Tabor *et al.*[6] studied the behavior of a thin-walled rubber tube when it was passed through various cycles. Figure 10 is a schematic diagram of the apparatus. By adding weights to the scale pans, cycles composed of varying amounts of torsion and tension could be devised. They found that a pure tension cycle yielded losses of about 8% of the input energy and that a pure torsion cycle yielded approximately the same amount. This result is not surprising since the only difference between torsion and tension is a hydrostatic component which does little work in this case (Poisson's ratio for rubber is approximately 0.5).

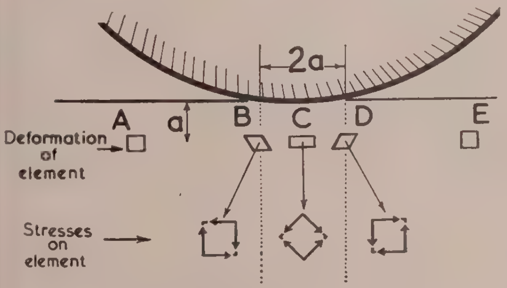

Fig. 12. Stress cycle applied to an element of rubber as a cylindrical roller passes over it.

During complex strain cycles, the rubber tube passed through the states indicated in Fig. 11. The most interesting case is that in which the elastic input energy remained constant between states II and IV. Under these conditions, energy was lost in both the tension and the torsion parts of the cycle; so, in this case, it is not useful to think in terms of the hysteresis loss factor as it is usually defined. The total loss was almost double that which occurred in a simple tension or torsion cycle of the same magnitude.

These considerations may be applied to the problem of a cylinder rolling over rubber. Figure 12 shows the stresses which are applied to an element, initially square, as a cylindrical roller passes over it. From A to B the element undergoes almost pure shear so that A to B and D to E constitute a simple shear cycle with an attendant hysteresis loss of α_0. It can be shown that from state B to C to D there is practically no change in the elastic energy content, but the direction of the shear is rotated through 45° followed by a further 45°. This is very like the shear torsion cycle applied to the rubber tube, so that we would expect this cycle to contribute losses of about $2\alpha_0$ to the rolling friction. Hence, the total losses during the cycle A to E will be about $3\alpha_0$, which is in good agreement with the experimental observations on rolling friction.

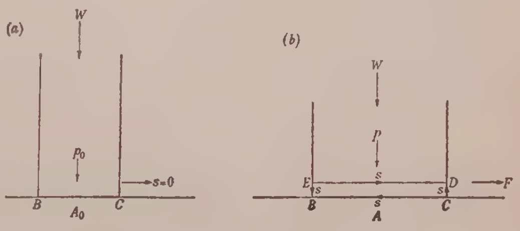

Fig. 13. Two-dimensional model illustrating effect of combined stresses in producing junction growth. (a) Contact under normal load W alone; (b) after application of tangential force F.

ROLE OF COMBINED STRESSES AND CONTAMINATION ON THE JUNCTION GROWTH IN METALLIC FRICTION[8]

On the simple theory of metallic friction, the frictional force arises primarily from the shearing of junc-

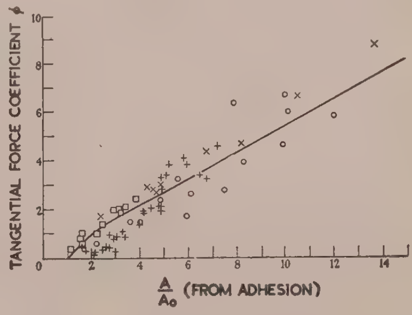

Fig. 14. Sliding of steel on indium. Effect of tangential force coefficient ϕ, before gross sliding occurs, on growth of area of contact. A/A_0 is the ratio of grown area to initial static area of contact. Experimental points: ○, 6-g load; +, 15-g load; □, 100-g load; ×, other loads. Continuous line represents Eq. 4 with $\alpha=3.3$.

---

[8] D. Tabor, Proc. Roy. Soc. (London) **A251**, 378 (1959).

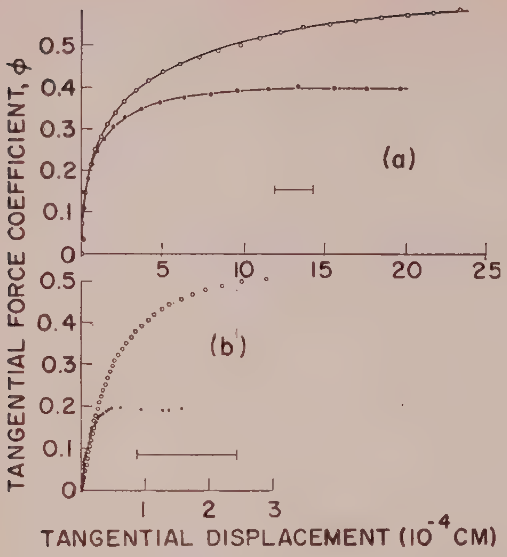

FIG. 15. Microdisplacements for lubricated and unlubricated metals: (a) platinum sliding on platinum; (b) steel sliding on steel. The lower curve in each case shows the effect of applying a lubricant. The scale mark represents 1/40 of the diameter of the region of contact.

tions formed in the interface between the sliding bodies. If one surface is much harder than the other, the asperities on the harder surface will plow grooves in the softer one and there will be an additional term in the equation for the friction force. In general the plowing term is small compared with the shearing term, and in what follows we shall assume that it is negligible. If A_0 is the area of real contact, p_0 the yield pressure of the metal, and s the specific shear strength of the interface, then we have the familiar relations $A_0=W/p_0$ and $F=Ws/p$. Hence the coefficient of friction μ is given by $\mu=F/W=s/p_0$. This assumes that s and p_0 are independent strength properties.

The theory of plasticity leads us, however, to expect that the yielding of a junction should be the result of the combined normal and tangential stresses. Consider the two-dimensional model shown in Fig. 13. We have an infinite two-dimensional slab of soft metal loaded onto a hard surface and we assume, for simplicity, that the whole area A_0 is in contact. Initially the load is W and the tangential force $F=0$ (i.e., tangential stress $s=0$). Then $p_0=W/A_0$.

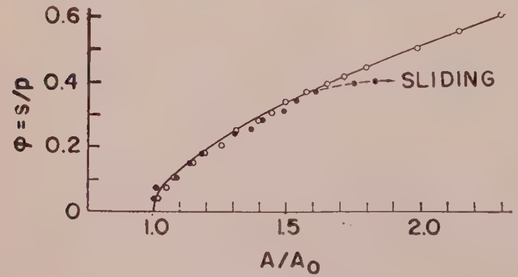

FIG. 16. The observations of Fig. 15 replotted as a variation of ϕ with A/A_0.

According to the criterion of plastic flow under combined stress,[9] the material will flow plastically when

$$p^2+3s^2=k^2. \qquad (1)$$

Initially $p=p_0$ and $s=0$; therefore $k^2=p_0^2$. Hence,

$$p^2+3s^2=p_0^2. \qquad (2)$$

If initially $p=p_0$, then the material in the interface is already plastic and the smallest tangential stress s will cause flow, and the area increases to A. The normal pressure is then W/A which is less than p_0 so that it cannot of itself cause plastic flow. Hence s must be increased to some larger value which again satisfies the relation above, before further flow will occur.

For a three-dimensional junction, no theoretical treatment is available, but we may expect a similar type of relation to hold. Let us assume that in this case,

$$p^2+\alpha s^2=k^2=p_0^2, \qquad (3)$$

where α is a constant. This expression may be reduced to the form

$$1+\alpha\phi=(A/A_0)^2, \qquad (4)$$

where ϕ is the tangential force coefficient defined by $\phi=F/W$ at any instant. The coefficient of friction μ is then the limiting value of ϕ for macroscopic sliding.

Figure 14 shows results obtained for indium. The continuous line is a plot of Eq. (4), where the value of α is 3.3. The values of A were obtained from measurements of adhesion. Similar results were obtained for Cu, Ni, Ag, and Pt by Bowden and Rowe.[10] They took great care to allow for released elastic stresses in their measurements of adhesion. For these materials $\alpha=3$.

So far we have no indication as to when the microdisplacement ends and macroscopic sliding begins. We obtain information on this from the experiments of Bowden and Young.[11] They carried out measurements

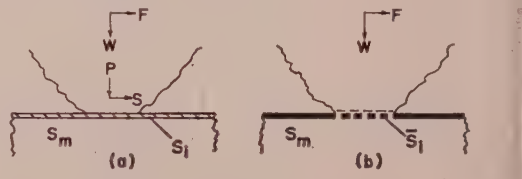

FIG. 17. (a) Schematic diagram showing that junction growth ceases when the shear stress reaches the critical shear stress s_i of an interfacial film. (b) Behavior when interface consists of ruptured oxide and metallic contact; mean critical shear stress of interface $=\bar{s}_i$.

---

[9] A. Nadai, *Plasticity* (McGraw-Hill Book Company, Inc., New York, 1931).

[10] F. P. Bowden and G. Rowe, Proc. Roy. Soc. (London) **A233**, 429 (1956).

[11] F. P. Bowden and J. E. Young, Proc. Roy. Soc. (London) **A208**, 311 (1951).

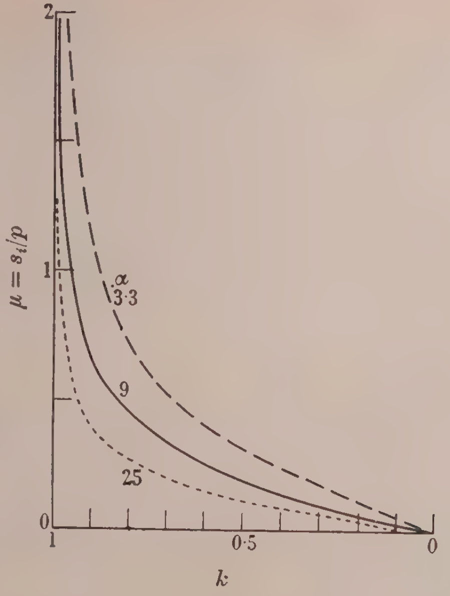

FIG. 18. Coefficient of friction μ as a function of $k=s_i/s_m$. The results are shown for three values of $\alpha=3.3$, $\alpha=9$, $\alpha=25$.

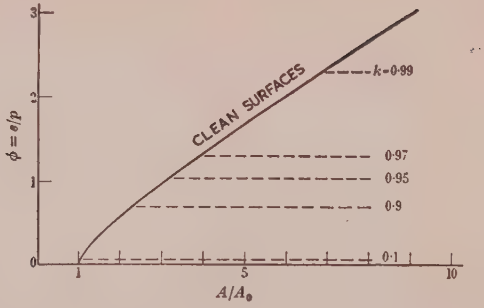

FIG. 19. The horizontal lines indicate the point at which junction growth ceases for interfacial films having shear strengths given by various values of k.

in high vacuum and showed that the friction for outgassed materials is extremely high, but that the introduction of a small trace of oxygen into the system causes the friction to drop to values of 1 or 2. We also get some information from the work of Courtney-Pratt and Eisner,[12] who measured the microdisplacements for platinum sliding on platinum and for steel on steel. Their results are shown in Fig. 15. The lower curves in each case show the effect of a good boundary lubricant. Note that the initial part of the curves is unaffected by the lubricant. The scale mark represents 1/40 of the diameter of the region of contact so that gross sliding is seen to occur after displacements which are very much less than the diameter of the region of contact. Figure 16 shows these results replotted as a function of A/A_0. The value of the area of contact in these experiments was determined from contact resistance measurements and the microdisplacements using a highly sensitive interference technique. The solid line is again a plot of Eq. (4), but here the value of α is 12. This figure shows clearly that the effect of the lubricant is primarily to cause sliding at smaller values of A/A_0.

The value of α in these experiments is higher, and theoretical considerations show that we should expect it to be even higher. In fact, as may be seen later, the exact value is not of great importance, and in what follows we shall take $\alpha=9$. For a material of this kind $p_0 \approx 3s_m$, where s_m is the critical shear stress of the material, so that

$$p^2+9s^2=9s_m^2. \qquad (5)$$

Now consider a junction separated from a surface by a thin film of critical shear stress $s_i<s_m$ (Fig. 17). In this case

$$p^2+9s_i^2=9s_m^2, \qquad (6)$$

and if we assume that $s_i=ks_m$, where $k<1$, we may show that

$$\mu=s_i/p=[3(k^{-2}-1)^{\frac{1}{2}}]^{-1}. \qquad (7)$$

Figure 18 shows μ plotted as a function of k. The three curves were obtained using for α the values 3, 9, and 25, as indicated, and their closeness shows why the exact value of α is not of prime importance. For $k=1$, $\mu=\infty$. This corresponds to gross seizure such as can only occur with outgassed metals. If, however, the interfacial film has a strength only 5% lower than that of the metals, it may be seen that the coefficient of friction drops to normal values, of the order of 1 ($k=0.95$, $\mu \approx 1$). Figure 19 shows another way of looking at the same effect. Here ϕ is plotted against A/A_0 and the solid line corresponds to clean surfaces; i.e., $k=1$. The horizontal lines show the point at which junction growth stops and macroscopic sliding takes place for various values of k.

The physical picture of the process which emerges from this discussion may be summarized as follows. If two clean metal surfaces are placed in contact, junction growth occurs which is governed by Eq. (4). This increase in area results in very high values of the coefficient of friction. If a thin film of lower shear strength is interposed between the metals, the initial growth of the contact region follows the same law. This is true only as long as the tangential stress is less than s_i. When, however, $s=s_i$, the film can no longer transmit these stresses, junction growth stops, and macroscopic sliding takes place.

---

[12] J. S. Courtney-Pratt and E. Eisner, Proc. Roy. Soc. (London) A238, 529 (1957).

JOURNAL OF APPLIED PHYSICS VOLUME 32, NUMBER 8 AUGUST, 1961

Single Contacts and Multiple Encounters

J. F. Archard
Research Laboratory, Associated Electrical Industries, Aldermaston, England

The analysis of wear experiments suggests that most of the events which occur in rubbing are contacts between protuberances which are deformed elastically and which separate without damage; an asperity encounter with damage is a relatively rare event. Apparatus for the study of isolated single contacts is described. A single contact which is deformed elastically does not obey Amontons's law, but an assembly of such contacts (multiple contact conditions) should do so. It is shown that under multiple contact conditions the load which can be borne by elastic deformation of the protuberances may be as much as a million times larger than that which can be borne by each individual asperity contact. Reflection electron microscopy shows that many irregularities on worn surfaces must bear their share of the load without plastic flow. Recent experiments suggest that, although a worn particle is produced very infrequently, it is nevertheless the direct consequence of the many preceding encounters which occurred without apparent damage.

I. INTRODUCTION

THIS paper presents a view of friction which arises from the work of a group[1] whose main interest has been the study of wear.

It is now well understood that the contact between rubbing surfaces occurs at a number of small areas and that the true area of contact, formed by the sum of these small areas, constitutes a small proportion of the apparent area of contact.[2,3] The unit event in friction and wear is therefore the contact and deformation of two protuberances on the opposing surfaces. Two questions immediately arise. First, what constitutes a typical unit event, and how can such a single contact be isolated and studied in the laboratory? Second, because most surfaces touch at a number of places, how is the behavior of rubbing surfaces affected by the existence of these multiple encounters?

II. EVIDENCE OF WEAR EXPERIMENTS

Wear rates and coefficients of friction have been measured with a pin and ring machine for a range of material combinations.[4] A typical selection of the results (Table I) shows that the rates of wear cover a range of nearly 10^5 but the coefficients of friction vary by less than five to one. Consider now an interpretation of these results in terms of asperity encounters.

Table I. Wear rates, coefficients of friction and values of K. Load 400 g; speed 180 cm/sec. Rings are hardened tool steel except where stated otherwise.

Material	Wear rate 10^{-10} cm³/cm	Coefficient of friction μ	K
Mild steel on mild steel	1570	0.62	7.0×10^{-3}
60/40 leaded brass	240	0.24	6.0×10^{-4}
P.T.F.E.	20	0.18	2.5×10^{-5}
Stellite	3.2	0.60	5.5×10^{-5}
Ferritic stainless steel	2.7	0.53	1.7×10^{-5}
Polythene	0.3	0.65	1.3×10^{-7}
Tungsten carbide on tungsten carbide	0.02	0.35	1.0×10^{-6}

Figure 1 is an idealized representation of one such unit event in which it is assumed that the encounter produces a worn particle of volume δV. The total worn volume V is the summation of all such particles. Wear theories[3,5,6] show that if every event produces a worn particle, then to a rough approximation

$$V = AL, \tag{1}$$

where A is the total true area of contact and L is the distance of sliding. This equation is comparable with the usually accepted relation

$$F = As, \tag{2}$$

where F is the frictional force and s is the effective shear strength of the junctions between the sliding members. However, there is one vital difference between friction and wear; all contacts must contribute to the friction but they may not all contribute to the wear. One assumes that a proportion K do so and that the rest are broken without damage. Equation (1) then becomes

$$V = KAL. \tag{3}$$

When this theory is compared with experiment it is found that only a small proportion of the contacts give rise to wear; from the results (Table I) it will be seen that K varies between 10^{-2} and 10^{-7}. More important still is the fact that each protuberance on the rubbing surfaces must be rubbed many times without being damaged. Such a protuberance may undergo plastic deformation at its first encounter with the other surface but in subsequent encounters under similar conditions it will bear the same load by elastic deformation only.[4]

Thus, wear experiments strongly suggest that the type of event shown in Fig. 1 is quite rare. Instead, the typical unit event in friction is an encounter between two protuberances which bear the required load by elastic deformation and which separate without giving rise to a worn particle.

---

[1] W. Hirst, Brit. J. Appl. Phys. **9**, 125 (1958).

[2] F. P. Bowden and D. Tabor, *The Friction and Lubrication of Solids* (Oxford University Press, London, 1954).

[3] R. Holm, *Electrical Contacts* (H. Gerbers, Stockholm, Sweden, 1946).

[4] J. F. Archard and W. Hirst, Proc. Roy. Soc. (London) **A236**, 397 (1956).

[5] J. T. Burwell and C. D. Strang, J. Appl. Phys. **23**, 18 (1952).

[6] J. F. Archard, J. Appl. Phys. **24**, 981 (1953).

III. AMONTONS'S LAW OF FRICTION

If a single spherical protuberance is deformed elastically, the area of contact A is proportional to the $\frac{2}{3}$ power of the load W and therefore, according to Eq. (2), $F \propto W^{\frac{2}{3}}$. Thus

$$\mu \propto W^{-\frac{1}{3}}, \tag{4}$$

where $\mu = F/W$ is the coefficient of friction. This result is inconsistent with Amontons's law, which states that the coefficient of friction is constant. On the other hand, if the deformation is plastic, $W = Ap_m$, where p_m is the flow pressure, and one obtains

$$\mu = F/W = s_f/p_m. \tag{5}$$

From Eq. (5) an explanation of Amontons's law follows.[2]

The above argument applies to a single contact, whereas for bodies touching at many regions the situation may be very different. Using models to represent the multiple contact conditions, it has been shown[7] that, even when the deformation is entirely elastic, A is very nearly proportional to W and Amontons's law can be explained without the necessity of assuming that the deformation is plastic.

The theoretical argument is summarized in Fig. 2, which shows the various models used and the deduced relationships between area of contact A and load W. The models are built up by the superposition of protuberances (assumed to be spherical caps) of various scales of size.

In general,

$$A \propto W^n, \tag{6}$$

and as the model becomes more complex and is, therefore, made to represent a closer approach to a real surface, n approaches unity. If $F \propto A$, the relationship between F and W moves towards direct proportionality parallel with the dependence of A upon W; it has been shown experimentally that this is so.[7] Because measurements of friction show a larger statistical variation than most physical measurements, the larger values of n shown in Fig. 2 are experimentally indistinguishable from direct proportionality.

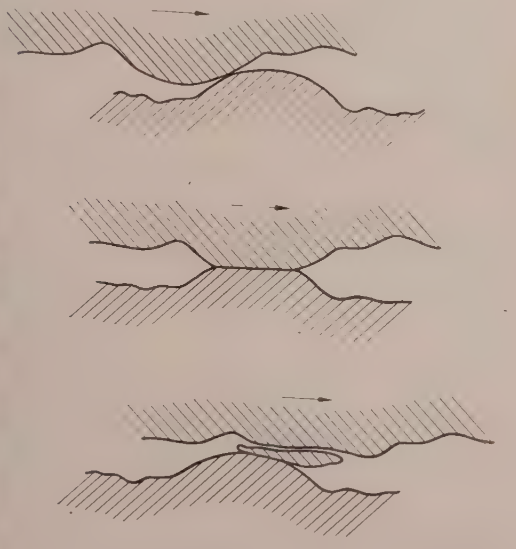

FIG. 1. Simplified representation of the contact of the two protuberances.

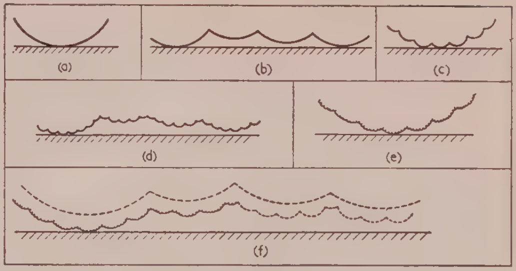

FIG. 2. Real area of contact under elastic conditions, models of surfaces in contact. The relations between the area of contact A and the load W are as follows: (a) $A \propto W^{2/3}$, (b) $A \propto W^{4/5}$, (c) $A \propto W^{8/9}$, (d) $A \propto W^{14/15}$, (e) $A \propto W^{26/27}$, (f) $A \propto W^{44/45}$.

The models are an imperfect representation of the complex topography of real surfaces. Consider, therefore, a treatment of the problem in terms of the number, N, and size, δA, of the individual areas which constitute the total true area of contact A. Assume first that all areas are of the same size δA and that they are all formed by elastic deformation of protuberances of the same radius of curvature. Both N and δA will increase with W and it will be assumed that

$$\delta A \propto W^{2\psi},$$

where ψ is a constant the significance of which will emerge later. The load per contact is (W/N) and since the deformation is elastic,

$$\delta A \propto (W/N)^{\frac{2}{3}}.$$

Also,

$$A = N\delta A.$$

It follows immediately that

$$\delta A \propto W^{2\psi}, \quad N \propto W^{(1-3\psi)}, \quad A \propto W^{(1-\psi)}. \tag{7}$$

It can be shown that Eqs. (7) also apply when the individual contact areas are not all the same size, but instead it is assumed that they have a size distribution. The only restriction is that the shape of the size distribution should be unaffected by the load. δA now represents any convenient characteristic of the size distribution, e.g., the average or maximum value of the individual contact areas.

Equations (7) demonstrate certain principles which are independent of the use of any model. Under multiple contact conditions an increase in the load can be utilized by increasing the size of existing areas, by bringing into contact new areas, or by both of these alternatives in

---

[7] J. F. Archard, Proc. Roy. Soc. (London) **A243**, 190 (1957).

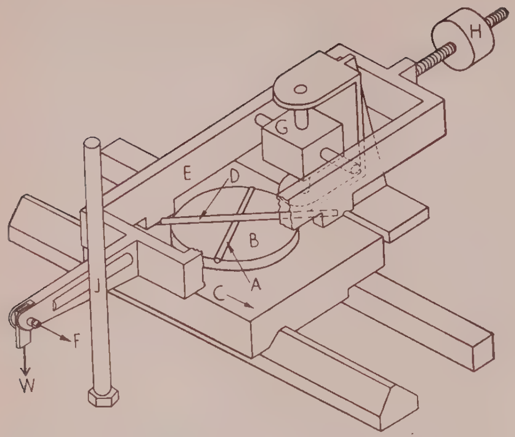

FIG. 3. The crossed-cylinders friction machine.

different proportions [in Eqs. (7) ψ is a measure of these proportions]. If an increase in the load is used mainly to enlarge existing areas, $\psi \rightarrow \frac{1}{3}$ and the relation between A and W approaches the single contact condition ($A \propto W^{\frac{2}{3}}$); whereas if the increased load is used mainly to create new areas, $\psi \rightarrow 0$, and A becomes nearly proportional to W. The models of Fig. 2 demonstrate the point at issue but they are necessarily rather abstract, whereas Eqs. (7) have the merit that they pose the problem in a form which might be checked experimentally. Certainly Dyson and Hirst[8] have demonstrated directly the division of the area of contact into a large number of small areas; they show, moreover, that the number of these areas increases with increasing load, but their size increases very little.

IV. EXPERIMENTAL METHODS FOR THE STUDY OF SINGLE CONTACTS

As a prerequisite for the study of distributed contacts, it is desirable to isolate and study the behavior of a single undamaged contact area. Experience shows that the widely used arrangement in which a sphere slides upon a flat surface has a number of limitations. Because one part of the sphere is always in contact, the experiment may be dominated by the aftereffects of damage occurring at or near the start of the sliding. In rubbing between nominally conforming surfaces such damage is quite rare, but when a sphere slides on a flat the damage is self-propagating and it thus assumes an unwarranted importance. Moreover, if damage occurs the contact conditions are changed and the bulk of the experiment is carried out under conditions different from those deduced from the original shape of the specimens.

These difficulties have been overcome and the experimental conditions made more precise in the crossed-cylinders friction machine[9] shown in Fig. 3. In the most usual arrangement the cylinders A and D are loaded together with their axes mutually at right angles and the lower specimen is moved slowly in a direction at 45° to the two specimen axes. The area of contact moves along both specimens so that fresh undamaged surfaces are continuously being encountered on both sliding members.

The crossed-cylinders friction machine is convenient for speeds lower than a few centimeters per second. To investigate the behavior of single contacts at higher speeds (up to about 1000 cm/sec) we have used[10] a crossed-cylinders machine with rotating specimens.

V. EXPERIMENTS WITH SINGLE CONTACTS AT SLOW SPEEDS

Even when the crossed-cylinders apparatus is used the conditions of a single contact will not be achieved if the surfaces of the cylinders are too rough. For over-all contact any surface protuberances must be shallow enough to be pressed into the general surface contour under the applied load.

Figure 4(a) shows the coefficient of friction for a single contact between polished Perspex specimens as a function of the load W. To a good approximation $\mu \propto W^{-0.26}$ or $F \propto W^{0.74}$; the experiments[7] also showed that within the limits of experimental error $A \propto W^{0.74}$. [Equation (4) is not obeyed because Perspex is not a perfectly elastic material.] The frictional force is proportional to the area of contact and this explains why the system does not obey Amontons's law.[11] Figure 4(b) shows the values of μ obtained when rougher Perspex cylinders are used. It is clear that at the heavier loads ($>$10 kg) the local asperities are flattened and a single contact is achieved. At lighter loads not all the asperities are flattened; therefore, the area of contact and the friction fall below the values obtained for a single contact. At the lightest loads the coefficient of friction approaches a constant value as forecast by the multiple contact theory.

It is more difficult to attain the conditions of a single contact with metal specimens because of their higher modulus of elasticity; smoother surfaces or heavier loads are required. However, sufficiently smooth surfaces were obtained[7] by running-in the specimens at a heavy load and then performing experiments at lighter loads. Figure 4(c) shows the value of μ thus obtained with lubricated cylinders of brass. The behavior is remarkably similar to that of the Perspex specimens shown in Fig. 4(b) and the explanation of the results is the same. It should be noted that at the heaviest loads the results with metal specimens conform to the relationship $\mu \propto W^{-\frac{1}{3}}$ forecast for perfectly elastic materials [Eq. (4)].

---

[8] J. Dyson and W. Hirst, Proc. Phys. Soc. (London) **B67**, 309 (1954).

[9] J. F. Archard, Wear **2**, 21 (1958).

[10] J. F. Archard and M. T. Kirk, Proc. Roy. Soc. (London) **A261**, 532 (1961).

[11] M. W. Pascoe and D. Tabor, Proc. Roy. Soc. (London) **A235**, 210 (1956).

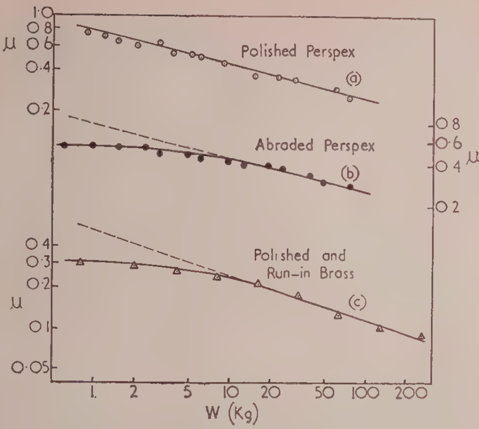

FIG. 4. Coefficients of friction μ as a function of the load W for single-contact regions.

VI. SURFACE TOPOGRAPHY AND ITS INFLUENCE UPON THE MODE OF DEFORMATION

It has been shown that the existence of multiple contacts allows one to reconcile Amontons's law of friction with the supposition of elastic deformation. The calculations to be described will show that the existence of multiple contacts also makes elastic deformation more likely; when only a single asperity is considered, plastic flow seems almost certain but with multiple contacts elastic deformation can be maintained up to enormous loads.

The profile shown in Fig. 5(a) is part of a model surface of the type shown in Fig. 2(e). It has a general curvature of 100 cm and has superposed upon it protuberances of radii 1 cm and 10^{-2} cm. The profile has been drawn as it would appear when using the highest magnification of the widely used Talysurf profilometer. For comparison, Figs. 5(b) and 5(c) show profiles of hardened steel surfaces used in wear experiments[12]; the horizontal and vertical magnifications are identical with those of Fig. 5(a). The model surface is, in general terms, rougher than the surfaces used in the wear experiment.

Consider therefore a hardened steel surface (VPN 800) of the form shown in Fig. 5(a). One of the smallest protuberances on this surface will start to flow plastically when it is bearing a load of about 10 g. The protuberance would not be pressed flat under this load but would be depressed to about 40% of its full height. This sort of calculation for a single protuberance suggests that the load required to start plastic flow would be quite small, even when surfaces of hardened steel were used. However, the theory of multiple contacts leads to very different conclusions; if the surface of Fig. 5(a) is pressed against an identical surface so that corresponding protuberances touch, no plastic flow occurs, even at the most heavily loaded protuberance, up to loads in excess of 10^7 g. Under multiple contact conditions, therefore, the capacity of the surface to support a load elastically becomes more than a million times greater than that of a single contact.

If protuberances of a smaller radius of curvature are considered, the loads required to cause plastic flow are reduced but the general conclusions remain unaffected. Thus, let the surface of Fig. 5(a) be covered by a close packed array of protuberances of radius of curvature 10^{-4} cm, each of such a shape that plastic flow starts when the protuberance is pressed flat into the local surface level. One such protuberance would bear a load of only 10^{-3} g without plastic flow, but, using the same argument as before, the whole surface of Fig. 5(a) would then be bearing a load of 8 kg. It is of interest to note that under this load the areas of contact would be grouped within a circle of diameter $D[\approx 1.3$ mm, Fig. 5(a)] and that the center of this region would be depressed by a distance $h[\approx 4\times 10^{-5}$ cm, Fig. 5(a)]. If the profiles under consideration formed part of two nominally flat surfaces prepared with normal engineering accuracy, this depression would be sufficient to bring other regions into contact; this would cause yet wider distribution of the load and delay the onset of plastic flow even further.

Comparison between the model surface [Fig. 5(a)] and the profiles of the surfaces used in the wear experiments [Figs. 5(b) and 5(c)] suggest that in the experiments many of the protuberances must have been deformed elastically although some features such as the one indicated in Fig. 5(c) would clearly give rise to plastic flow.

VII. EXAMINATION OF SURFACES BY REFLECTION ELECTRON MICROSCOPY[13]

Plastic deformation of the surface irregularities will not occur if they can be pressed flat into the general surface level by elastic deformation alone. According to

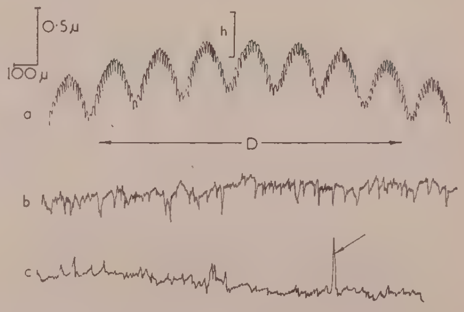

FIG. 5. Profiles of surfaces. (a) Model surface. (b) Unworn steel ring. (c) Worn steel ring.

---

[12] J. F. Archard and W. Hirst, Proc. Roy. Soc. (London) **A238**, 515 (1957).

[13] I am indebted to Dr. J. S. Halliday for the material used in this and the following section.

Halliday,[14,15] who has extended the original analysis of Blok,[16] the irregularities can be flattened without plastic flow if their maximum slope (θ) is given by

$$\tan\theta \leqslant \beta H(1-\nu^2)/E, \tag{8}$$

where H is the hardness of the specimens, ν and E are Poisson's ratio and Young's modulus, respectively, and β is a numerical constant (lying between 0.8 and 1.7) which depends upon the assumed shape of the irregularities. The theory therefore provides a simple method of assessing the smoothness of surfaces; if the slopes of the surface irregularities are less than that predicted by Eq. (8), plastic flow is most unlikely to occur.

Reflection electron microscopy is a method of surface examination particularly suited to the measurement of the slopes of surfaces irregularities.[14,17] The surface is illuminated by a beam of electrons incident at a shallow angle; this angle of illumination is reduced until the protuberances cast shadows upon the surface. In this work the major experimental difficulty is the formation of carbonaceous deposits upon the surface, caused by the interaction of the incident electrons with adsorbed oil molecules, and because of this some special precautions are required.[15,17]

Halliday has used the reflection electron microscope to test the validity of Eq. (8) in the following manner. Rough etched surfaces of the metal under test were pressed against an anvil of carefully polished hardened steel. (Subsidiary experiments showed that these steel surfaces were extremely smooth; most parts of the surfaces contained no irregularities with slopes greater than 0.1° but a few protuberances with slopes as high as 0.3° were revealed.) The loads used in the experiments were sufficient to cause large-scale flow of the metal under test (at least 50% reduction in length of the specimen) and it is clear that the protuberances on the etched surface must also undergo plastic deformation. With the removal of the load these protuberances will relax elastically and they should then assume a form which can just be pressed flat without plastic flow. Thus these surfaces should conform to the theory of Eq. (8).

TABLE II. Smoothness of soft metal pressed against flat chrome-bearing steel anvil.

Metal	E 10^3 kg/mm²	ν	H kg/mm²	Slopes (deg) Theoret. θ_t	Exptl. θ_e
Aluminium	6.8	0.32	40	0.34	0.45±0.1
Zinc	9.6	0.26	58	0.40	0.35±0.05
Lead	1.6	0.45	14	0.40	0.60±0.1
Copper	12.7	0.31	118	0.63	0.60±0.1
Duralumin	7.3	0.25	83	0.68	0.60±0.05
Magnesium	4.2	0.25	55	0.70	0.70±0.05
Iron	20.4	0.27	201	0.84	0.70±0.1
Nickel	21.1	0.31	228	0.90	0.65±0.1
60/40 leaded brass	9.8	0.37	160	1.0	0.75±0.1
60/40 brass	9.8	0.37	209	1.3	0.8 ±0.1

TABLE III. Similar metal disks rolled together.

Metal	E 10^3 kg/mm²	ν	H kg/mm²	Slopes (deg) Theoret. θ_t	Exptl. θ_e
Mild steel	22.4	0.28	180	0.4	0.40±0.05
Mild steel	22.4	0.28	226	0.5	0.50±0.1
Copper	12.7	0.31	144	0.5	0.60±0.1
Duralumin	7.3	0.25	143	0.9	0.40±0.1

Table II shows the results obtained with 10 different metals. The final column shows values of θ_e, the slopes of the surface irregularities obtained experimentally. The penultimate column shows corresponding values of θ_t, the theoretical value of the slope derived from Eq. (8). The values of E, ν, and H used in the derivation of θ_t are shown in the earlier columns. The values of H were obtained from microhardness indentations taken after the experiment; thus work-hardening of the surfaces has been taken into account. It will be seen that in six of the ten examples given in Table II the values of θ_e and θ_t agree within the limits of experimental error; in the other instances the values of θ_e follow the trend of the theoretical values.

In another series of experiments disks of the same material about 3 in. in diameter were rolled together without sliding under loads sufficient to cause bulk plastic flow. Once again the results, shown in Table III, show reasonable agreement between theory and experiment. It is clear that the measurement of the surface slopes using reflection electron microscopy provides a suitable method for assessing whether the surface protuberances will bear their loads by elastic or plastic deformation.

VIII. EXAMINATION OF RUBBED AND WORN SURFACES

In explaining the variation of friction with load obtained with polished and run-in brass crossed cylinders [Fig. 4(c)] it was argued that at light loads the local protuberances relaxed elastically, causing multiple-contact conditions. If this argument is correct, the slopes of these protuberances should conform to Eq. (8). The theoretical value θ_t for two brass surfaces is 0.42°. Reflection electron micrographs of the surfaces showed that load-bearing regions on the cylinders were smoother than 0.4°. Thus reflection electron microscopy confirms the deductions made from the friction experiments.

A more surprising result was obtained in the examination of brass specimens rubbed against tool steel surfaces in unlubricated wear experiments. The wear of

---

[14] J. S. Halliday, Proc. Inst. Mech. Engrs. (London) **169**, 777 (1955).

[15] J. S. Halliday, Proc. Inst. Mech. Engrs. (London) Conference on Lubrication and Wear, 647 and 868 (1957).

[16] H. Blok, Proc. Roy. Soc. (London) **A212**, 480 (1952).

[17] M. E. Haine and W. Hirst, Brit. J. Appl. Phys. **4**, 239 (1953).

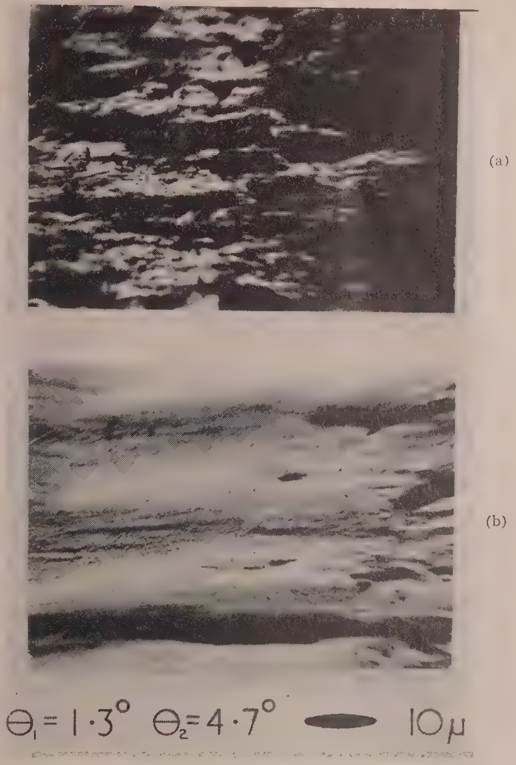

FIG. 6. Micrographs of worn 60/40 brass.

this combination has been examined in some detail,[6,18–20] and it has been shown that wear occurs by welding of the brass to the steel surface and its subsequent detachment. Despite the severity of the wear process the value of *K* (Table I) is only 6×10^{-4}. Two contrasting micrographs of the brass surface are shown in Fig. 6. Parts of the surface [Fig. 6(a)] are very rough and will be plastically deformed under the applied load, but a considerable proportion of the surface [Fig. 6(b)] is smooth. Parts of the surface had slopes as low as 0.4° and would thus bear their part of the load without plastic flow. This suggests that even under these severe wear conditions, the low value of *K* is due, at least in part, to the existence of elastic rather than plastic deformation at asperity encounters.

The onset of elastic deformation is not the only reason for low values of *K*. Two unlubricated specimens of mild steel were subjected to severe wear; there was much welding and the value of *K* was 3.5×10^{-3}. Examination of the surfaces in the reflection electron microscope showed no smooth portions and therefore the low value of *K* must be attributed to some other factor, such as transfer of material to and fro between the surfaces without the production of loose debris.

IX. INTERPRETATION OF *K*

When brass rubs against steel under conditions of severe wear, *K* has a definite value, of the order of 10^{-3}, and this is taken to imply that, roughly, only one in every thousand contacts contributes to the wear. Two interpretations of this statement appear possible. It can be argued that wear is the result of an accident, for example, that wear occurs when the conditions at the contact are sufficiently severe. As a very simple form of this interpretation one might suggest that plastic flow occurs at one contact in every thousand and that the remainder involve only elastic deformation. An important part of this interpretation of *K* is that it involves the operation of the laws of chance. Alternatively it can be suggested that it is necessary, on an average, to rub each protuberance a thousand times before it becomes liable to damage and that the thousand encounters are an essential prerequisite for the production of a worn particle.

Some recent work by Hirst and Lancaster[20] throws some light on this important question. Their work suggests that when brass rubs on steel, the production of a worn particle is the final result of a succession of asperity encounters. In each of these encounters, under the combined influence of both normal and tangential forces, the elastic limit is exceeded only by the small amounts necessary to account for the gradual development of a strain pattern beneath the surface. It is the weakening of the underlying material by these subsurface strains rather than the formation of a strong weld which leads to a transferred or worn particle.

X. CONCLUSIONS

The study of wear profoundly affects our view of the nature of solid friction. It becomes clear that damage and welding occur very infrequently and that the more typical event in rubbing is an encounter between elastically deformed protuberances which separate without apparent damage. This type of event has received little attention in friction studies but it is this, and not welding, which largely determines the magnitude of the friction.

AKNOWLEDGMENTS

The author is indebted to Dr. W. Hirst for his interest, encouragement, and advice in the preparation of this paper and to his colleagues for many discussions of the work described. Thanks are due to Dr. T. E. Allibone, C.B.E., F.R.S., Director of the Laboratory, for permission to publish.

---

[18] M. Kerridge and J. K. Lancaster, Proc. Roy. Soc. (London) **A236**, 250 (1956).

[19] J. K. Lancaster, Proc. Phys. Soc. London **B70**, 112 (1957).

[20] W. Hirst and J. K. Lancaster, Proc. Roy. Soc. (London) **A259**, 228 (1960).

JOURNAL OF APPLIED PHYSICS VOLUME 32, NUMBER 8 AUGUST, 1961

Rolling Friction of Polymeric Materials. II. Thermoplastics

D. G. Flom*
General Electric Research Laboratory, Schenectady, New York

The results of rolling friction studies of several thermoplastics provide additional evidence for the correlation of such friction with dynamic mechanical losses in polymeric materials. Among the polymers discussed are polymethyl methacrylate, polytetrafluoroethylene, polyethylene, nylon, polyvinyl chloride, polyvinyl acetate, and polystyrene. The effects of spin and other deviations from pure rolling are demonstrated for polymethyl methacrylate, polytetrafluoroethylene, and nylon by varing the experimental parameters. In essentially pure rolling, the dependence of friction on temperature illustrates the importance of the extent of crystallinity in polytetrafluoroethylene, the amount of branching in polyethylene, and the concentration of plasticizer in polyvinyl chloride. In the latter effect, it is found that the temperature at which the rolling friction goes through a maximum varies linearly with plasticizer content.

INTRODUCTION

THE theory of rolling friction for a sphere on a plane has been the subject of previous publications.[1,2] Experimental corroboration of this theory for the case of elastomers has also been presented.[3] Briefly stated, this theory relates the frictional force in pure rolling to the dynamic mechanical losses within the materials in contact. As a consequence, one can predict how rolling friction will vary as a function of load, modulus, ball size, temperature, and rolling speed. Conversely, if these relationships are known for a given material, one can use measurements of rolling friction to determine dynamic mechanical losses for that material.

In the present work on thermoplastics, additional evidence for the correlation between rolling friction and dynamic losses is presented. New features include the demonstration of spin and surface effects owing to the experimental arrangement in which spheres are made to travel in a circular path rather than a straight line. These effects, then, represent deviations from pure rolling. As shown for nylon, this dependence on geometry affords a means of separating surface interactions from bulk effects.

The effect of plasticizer on rolling friction is demonstrated for polyvinyl chloride. It is found that the addition of plasticizer lowers the temperature at which the rolling friction peak occurs and also broadens this peak. A similar effect owing to the addition of plasticizer has been reported by others for mechanical, and also electrical, losses in polyvinyl chloride.[4–6]

MATERIALS

Polytetrafluoroethylene (Teflon) was obtained in sheet form ($\frac{1}{4}$ in. thick) from the Ethylene Chemical Corporation. This material was estimated by means of x-ray diffraction to be approximately 50% crystalline in the "as-received" condition. Disks $4\frac{1}{2}$ in. in diameter were cut from these sheets.

Polymethyl methacrylate was obtained both in rigid sheet form and as molding powder from the Rohm and Haas Company. The first of these was designated as Plexiglas II with a reported molecular weight of about 3 000 000. The second was designated as Plexiglas Y with a molecular weight of about 250 000. Both were reported to be unplasticized methyl methacrylate polymers containing less than 1% additives. Disks $\frac{1}{2}$ in. thick and $4\frac{1}{2}$ in. in diameter were prepared from these materials. Unless stated otherwise, this was the size of disks used for all of the polymers in this study.

Linear polyethylene was obtained as Marlex 50 from the Phillips Chemical Company. Branched polyethylene was obtained as Alathon 10 from E. I. du Pont de Nemours and Company. Both polyethylenes were in the form of pellets from which disks could be molded.

Nylon 66 (polyhexamethylene adipamide) was obtained in disk form (Polypenco FM-10001) from the Cadillac Plastic and Chemical Company.

Two kinds of polyvinyl chloride (PVC) were used. The first (to be designated as I) consisted of a disk of Bakelite rigid vinyl VSA 3300. This material was reported to contain 2–3% lead stabilizer and 8% titanium dioxide as colorant and filler. It was reported to contain no plasticizer. The second kind of PVC (to be designated as II) consisted of disks prepared from Geon 101 molding powder manufactured by the B. F. Goodrich Company.

Polyvinyl acetate disks were prepared from Gelva V-100 molding powder obtained from the Shawinigan Resins Corporation.

Polystyrene was obtained in rigid sheet form and disks were cut from this material.

Balls of Teflon, Plexiglas, Alathon, linear polyethylene, and nylon were obtained in four sizes from the Ace Plastic Company and the Orange Products Company. Steel balls (52100) of the type contained in conventional bearings were also used. The grooved disk in the apparatus, now to be discussed, was made of cold-rolled steel.

---

* Present address: Space Sciences Laboratory, General Electric Missile and Space Vehicle Department, Philadelphia, Pennsylvania.

[1] A. M. Bueche and D. G. Flom, Wear **2**, 168 (1959).

[2] D. G. Flom and A. M. Bueche, J. Appl. Phys. **30**, 1725 (1959).

[3] D. G. Flom, J. Appl. Phys. **31**, 306 (1960).

[4] L. E. Nielsen, R. Buchdahl, and R. Levreault, J. Appl. Phys. **21**, 607 (1950).

[5] B. Maxwell, Princeton Plastics Lab. Tech. Rept. 46C (August 15, 1957).

[6] K. Schmieder and K. Wolf, Kolloid Z. **127**, 65 (1952).

EXPERIMENTAL

The apparatus for measuring rolling friction has been described previously.[3] Briefly, it consists of two concentric disks between which balls are made to roll in a circular path in the manner of a thrust bearing (Fig. 1). One disk, ordinarily the lower one, is of steel and contains a shallow, circumferential groove for keeping the balls in a circular path. The second disk is either of steel or of polymer backed with steel and has a plane surface. The balls may be either steel or polymer.

The torque exerted on the upper disk when the lower is made to rotate is measured by deflection of a phosphor bronze spring to which strain gauges are attached. While the absolute friction may be low, the precision of measurement is high. Also, the measurement is relatively insensitive to surface and atmospheric effects indicating that bulk properties predominate.

With this apparatus only three balls are needed for optimum stability and distribution of load. This may be shown by utilizing the fact that the rolling friction for *Teflon* balls between steel disks is much greater than for *steel* balls between steel disks (Fig. 2). To obtain the curve in Fig. 2, the friction was first measured with three steel balls between the two disks. A Teflon ball of the same size was then substituted for one of the steel balls and the friction measurement was repeated. Two Teflon balls were then substituted, and so on, until three balls of Teflon only were in the apparatus. As shown by the curve, the friction was directly proportional to the number of Teflon balls substituted for the steel ones. Introduction of additional Teflon balls (beyond three) did not increase the friction appreciably. This proves that at any one time only three balls carry the entire load, even though the load might shift periodically from ball to ball. The slight increase in friction for five and six balls probably results from momentary sliding as each ball is called upon to carry its share of the load.

A furnace surrounding the main body of the apparatus is used for measurements at elevated temperatures. The temperature is measured with a boot-type thermocouple inserted through the backing plate and into the plastic disk. There is probably a small, consistent difference between this temperature and that at the ball-disk interface as indicated by the fact that the ambient temperature within the furnace is usually found to be several degrees higher than that measured within the plastic.

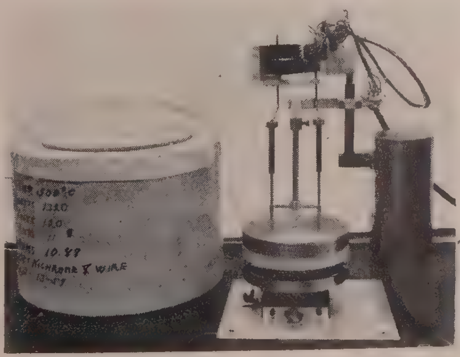

FIG. 1. Rolling friction apparatus.

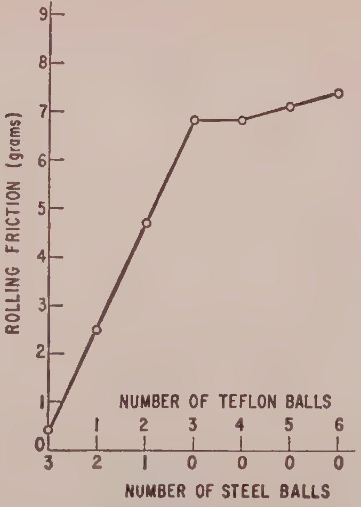

FIG. 2. Rolling friction of mixed balls between steel disks. Total load = 1255 g; speed = 17 cm/sec.

To prevent permanent flow of the plastic, during heating, at the points of contact with the balls, the disk is raised between friction measurements. Prior to each measurement, the balls are positioned by rotating the lower disk and arresting the balls at the ends of retractable tubes (not shown in Fig. 1) connected to the house vacuum line.

SPIN AND OTHER DEVIATIONS FROM PURE ROLLING

The process of rolling in the present apparatus is admittedly an approximation to that of a ball rolling in a straight line between flat surfaces. For example, it is apparent that forcing balls to rotate in a circular path imparts a certain amount of spin, however minute, to the balls. The result is an increase in friction if, as is usually the case, the coefficient of sliding friction is greater than the coefficient of rolling friction. To evaluate the importance of spin, three balls were rolled between flat disks at various track radii. It was found that if the balls were initially positioned so as to touch each other and rotation of the lower disk was then started, the balls would slowly creep outwards in an ever-increasing spiral until they eventually reached the outer edge. This effect has been studied in some detail by Johnson.[7]

If rotation of the lower disk was stopped periodically

---

[7] K. L. Johnson, J. Appl. Mech. 25, 332 (1958).

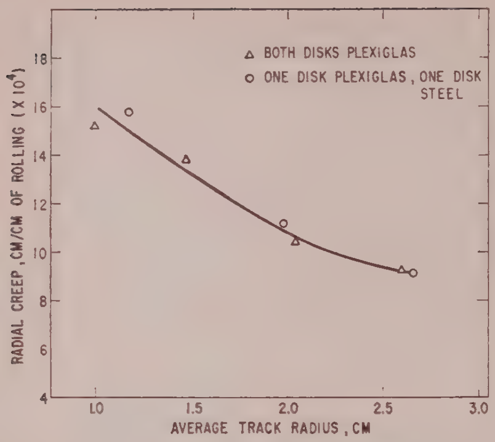

FIG. 3. Radial creep of steel balls ($\frac{1}{2}$-in. diam) rolling between two flat disks at low speed (2 rpm). Load = 1222 g/3 balls.

and the ball positions relative to the central axis were determined, it was found that radial creep per disk rotation gradually increased. This can be explained by the fact that with each succeeding rotation of the disk the track radius became greater and the number of ball revolutions increased. However, the radial creep per unit distance of travel *decreased*, indicating that spin became less important as the balls moved outward. The results are shown in Fig. 3. It is apparent that the extent of creep was essentially the same whether both disks were steel or whether one was Plexiglas and the other was steel. In the experiment involving Plexiglas, the coefficient of friction λ was measured at the beginning and at the end of rotation, correction being made for the different torque arms in the two cases. It was found that λ decreased from 0.011 at the beginning to 0.0073 at the end, again showing that the contribution of spin was markedly lower for the larger track radius.

Additional experiments using $\frac{1}{8}$-in. balls in place of $\frac{1}{2}$-in. balls revealed an even greater decrease in λ as the track radius increased. Also, the radial creep per unit distance traveled was greater for the smaller balls than for the larger ones, indicating that the controlling factor was the number of ball revolutions which had to be made within a given distance.

These results show then that spin effects, representing deviations from pure rolling, can be minimized by using sufficiently small balls and large track radii. Based on these considerations, and on calculations using Johnson's equations,[7] large track radii ($1\frac{1}{2}$- to 2-in. radius) were chosen for subsequent experiments.

That surface effects had been made negligible for the steel-Plexiglas combination was proven by the fact that use of lubricants such as graphite, MoS_2, oleic acid in cetane, and petroleum oil did not decrease the rolling friction measured. For nylon, on the other hand, the effects of lubrication were different and surface effects persisted even for relatively small balls. This will be discussed in more detail in later paragraphs.

With the present apparatus, centrifugal forces can exert an undue effect unless rolling speeds are kept sufficiently low. For this reason, peripheral disk speeds of less than 30 cm/sec have been used ordinarily. In the case of Plexiglas it was desirable to extend this range somewhat, and the coefficient of friction was measured over more than three decades of speed. The results (Fig. 4) are in good agreement with the effect of speed on friction at 25°C observed previously for the lubricated sliding of steel on Plexiglas.[1] It should be noted, however, that the absolute values for the coefficients were much lower in rolling than in sliding.

Because of the time consumed in measuring λ as a function of speed, particularly at low speeds, this relationship was not pursued further. Brief measurements at elevated temperatures, however, indicated that the slope of the friction-vs-speed curve would become positive, at some higher temperature, as had been found also for lubricated sliding.

EFFECT OF LOAD

In any of these experiments in which rolling is started on a fresh polymer surface (e.g., a disk) previously unstressed, it is found that the friction decreases markedly during the first few disk revolutions. In the case of Teflon, this decrease may be as much as 30%. At the same time, a groove (small for Plexiglas, and similar materials, but appreciable for Teflon) forms in the polymer surface indicating that some plastic deformation takes place. The extent of the grooving and the decrease in friction are, as one would expect, dependent on the load. This effect has been observed previously for metals by Tabor and Eldredge.[8] After this initial stage of deformation, the groove remains constant in size and the friction levels off at a nearly constant value. From then on the deformation

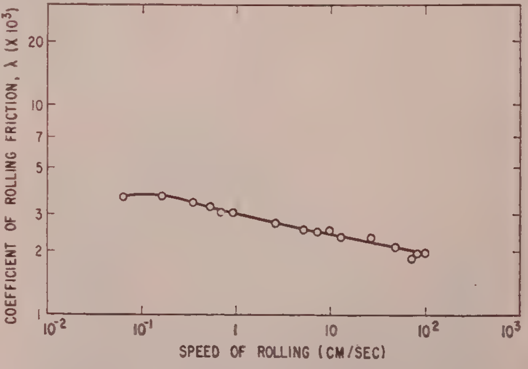

FIG. 4. Dependence of friction on speed for steel balls ($\frac{1}{8}$-in. diam) rolling on Plexiglas II. Load = 989 g/3 balls; temperature = 25°C.

---

[8] D. Tabor, Phil. Mag. **43**, 1055 (1952); K. R. Eldredge and D. Tabor, Proc. Roy. Soc. (London) **A229**, 181 (1955).

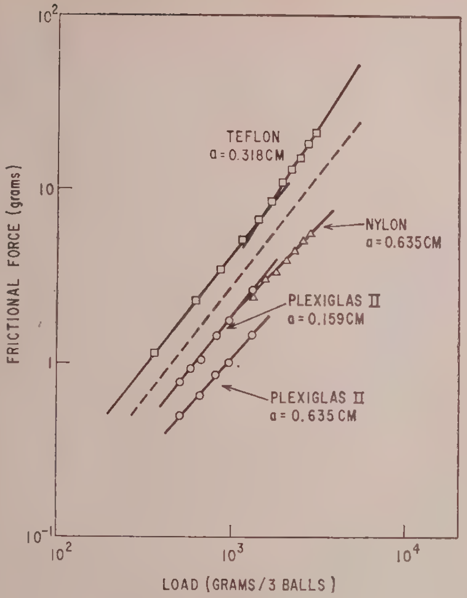

FIG. 5. Load dependence for rolling friction of steel balls on Plexiglas and Teflon and for nylon balls on steel. Speed = 9 cm/sec; slope of theoretical line (dashed) = 1.3.

is elastic and the rolling friction is proportional to elastic losses. Unless otherwise stated, the experiments described in this paper were made on surfaces which had already undergone a "rolling-in" period, and in this respect were "prestressed."

The variation of frictional force with load over a narrow range for a Plexiglas disk is shown in Fig. 5. Two sizes of balls were used, $\frac{1}{8}$ in. (a=0.159 cm) and $\frac{1}{2}$ in. (a=0.635 cm). The track radius in the lower steel disk was 1 in. and the machined groove radius was $\frac{3}{8}$ in. It will be noted from Fig. 5 that the slopes of the straight lines agree well with the slope of 1.3 which would be predicted by the theoretical relation

$$\lambda = K(W/Ga^2)^{\frac{1}{3}} \tag{1}$$

derived for a material exhibiting appreciable mechanical losses.[2] In this equation the losses (to be referred to as tanδ) appear in the factor K. W is the load, G is the shear modulus, and a is the ball radius.

The slope of the friction-vs-load curve for "prestressed" Teflon changes from 1.3 to 1.6 at a load of about 1500 g (Fig. 5). It is possible that this behavior is the result of increased strain in a manner similar to that found by Tabor for metals.[9] Preliminary calculations, not presented here, indicate this to be the case.

For nylon the slope of the friction-vs-load curve (Fig. 5) is appreciably less than the 1.3 which would be expected on the basis of Eq. (1). An explanation for this will be given presently.

EFFECT OF BALL SIZE

If the functional relationships in Eq. (1) were rigidly obeyed, one would expect the coefficient of friction to vary inversely as $a^{\frac{2}{3}}$. The extent to which this holds for some of the polymer balls of this study is shown in Fig. 6. It should be noted that the friction in this case is twice as great as for steel balls on a polymer disk because the area of contact between steel and polymer balls is twice that of the reverse combination. Except for the extreme ball sizes in the case of Alathon 10, the agreement of the observed slopes with the theoretical is quite satisfactory. For Marlex 50 and Plexiglas, which exhibit the lowest rolling friction, there appears to be an added friction component for the largest ball size. A partial explanation of this is that this radius of ball approaches that of the groove in the steel disk; hence, a sliding component is introduced. This effect can be readily verified by deliberately matching the ball radius to the groove radius and observing the increased friction. In addition to this, however, a surface effect is introduced if the ball radius becomes a significant fraction of the track radius, as discussed earlier.

It may be noted that the slope for the Teflon curve in Fig. 6 comes quite close to obeying the theoretical slope. If, however, the load is increased from 1255 g to 3974 g, the slope is changed from −0.74 to −0.95. This is the trend expected if loss becomes dependent on strain at higher loads. A calculation similar to that of Tabor's[9] yields the result that, if loss is directly

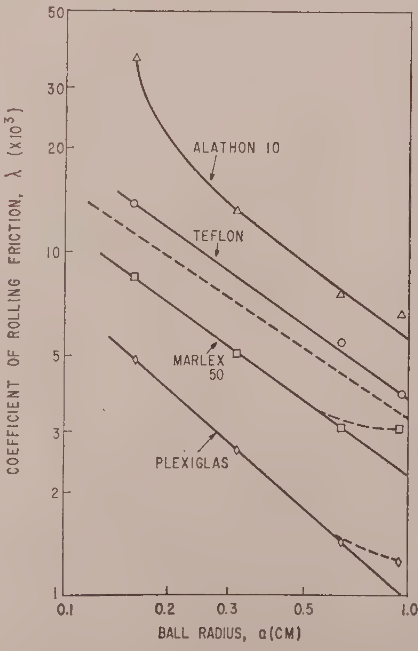

FIG. 6. Rolling friction of polymer balls between steel disks. Load = 1255 g/3 balls; slope of theoretical line (dashed) = −2/3.

---

[9] D. Tabor, Proc. Roy. Soc. (London) A229, 198 (1955).

proportional to strain, λ is then inversely proportional to $a^{\frac{4}{3}}$ rather than to $a^{\frac{2}{3}}$.

NYLON SURFACE EFFECTS

Because of the interesting dependence of friction on ball size found for nylon, the data for that polymer are shown separately (Fig. 7). It may be noted from the solid curve that the friction dependence is not uniform when steel balls are rolled on a nylon disk. Even more interesting are the results for a combination of nylon *balls* and metal *disks*, plotted as the dashed curve. This relationship is typical of a large number obtained using different balls, loads, and disks. The results are the same whether the nylon balls are rolled between steel disks or between one Dural disk and one steel disk.

It appears that a fairly simple explanation can be given for the shape of the dashed curve in Fig. 7 as well as for the slope of the nylon friction-vs-load curve in Fig. 5. This explanation hinges on the fact that surface effects, if present in addition to bulk effects, can give rise to the observed behavior. One needs only to assume that the surface part of the friction is proportional to contact area and that the latter is determined by elastic deformation. In other words

$$F_s = K_s A = K_s \pi l^2, \tag{2}$$

where F_s is the frictional force arising from surface interactions and A is the contact area of which l is the radius. K_s is a surface constant which may be left unspecified for the moment. As will be seen shortly, it can be thought of as a shear strength multiplied by the fraction of the contact area actually involved in sliding.

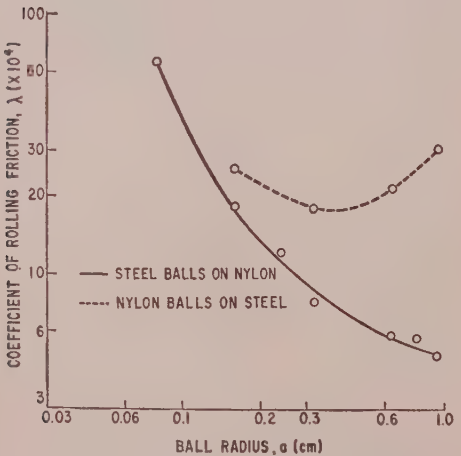

FIG. 7. Effect of ball size on rolling friction of nylon vs steel. Load = 1491 g/3 steel balls and 1255 g/3 nylon balls.

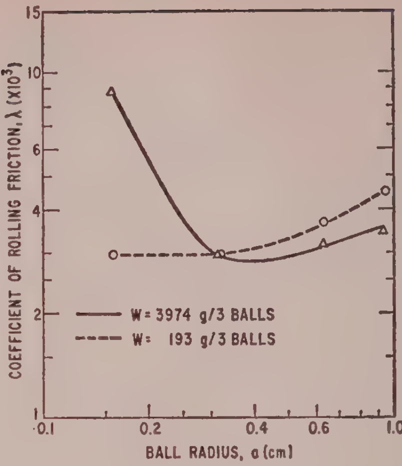

FIG. 8. Load effect on ball size–friction relationship for nylon.

The radius l in Eq. (2) can be eliminated by means of the Hertz expression for elastic deformation; namely,

$$l^3 = \tfrac{3}{8}(Wa/G)[(1-\sigma^2)/(1+\sigma)], \tag{3}$$

where σ is Poisson's ratio. In this equation we assume that deformation of the metal is negligible compared to that of the nylon. From Eqs. (2) and (3) we obtain

$$F_s = C_s(Wa/G)^{\frac{2}{3}}, \tag{4}$$

where C_s is given by

$$C_s = K_s\pi\{\tfrac{3}{8}[(1-\sigma^2)/(1+\sigma)]\}^{\frac{2}{3}}. \tag{5}$$

On rewriting Eq. (1) so that K may be expressed as the product of a bulk constant, K_b, and a mechanical loss, $\tan\delta$, we have

$$\lambda_b = K_b \tan\delta (W/Ga^2)^{\frac{1}{3}}. \tag{6}$$

A combination of bulk and surface effects therefore leads to the expression

$$\lambda = \lambda_{\text{bulk}} + \lambda_{\text{surf}} = K_b \tan\delta (W/Ga^2)^{\frac{1}{3}} + C_s(a^2/WG^2)^{\frac{1}{3}}. \tag{7}$$

If the two terms in Eq. (7) for a particular case are of comparable magnitude, one may expect that for high loads and small balls, λ will be proportional to $(a^{\frac{2}{3}})^{-1}$. Conversely, for low loads and large balls, λ will be proportional to $a^{\frac{2}{3}}$. The results of measurements made for two extremes in load are plotted in Fig. 8; these show that the expected relationships are indeed approached in the case of nylon.

Again, for Eq. (7) to apply, the variation of friction F with load ought to fall within the limits of $F \alpha W^{\frac{4}{3}}$ and $F \alpha W^{\frac{2}{3}}$. That this occurs for nylon balls, at least within a narrow load range, is shown by the slope of the friction-load relationship in Fig. 5.

By rearranging Eq. (7), after multiplying each term by 2 because of the doubled area of contact for plastic balls, one then obtains

$$\frac{\lambda}{(W/a^2)^{\frac{1}{3}}} = \frac{2K_b \tan\delta}{G^{\frac{1}{3}}} + \frac{2C_s}{G^{\frac{2}{3}}}\left(\frac{a^4}{W^2}\right)^{\frac{1}{3}}. \tag{8}$$

A plot of $[\lambda/(W/a^2)^{\frac{1}{3}}]$ vs $(a^4/W^2)^{\frac{1}{3}}$ should give a straight line. That this is satisfied in a general way, despite a wide scatter of points, is shown by Fig. 9. From the slope and intercept of this line, drawn according to the method of least squares, it is possible to evaluate the extent of sliding as well as the mechanical losses involved in rolling. For the first calculation we assume a Poisson ratio of 0.3 and a dynamic modulus for nylon of 9×10^9 d/cm².[10] From the slope, equal to $2C_s/G^{\frac{2}{3}}$, and the use of Eq. (5), we then obtain a value for K_s of 217 g/cm². If now we postulate that the surface effects involved consist of shearing of junctions over a fraction of the contact area, we may calculate this fractional area by comparing the value of K_s with the shear strength of nylon. Shooter and Tabor[11] report the latter to be 6×10^5 g/cm². This means that in the present case the area involved in shear is only 1/3000 of that calculated by means of the Hertz equation. This order of magnitude is in line with the amount of sliding to be expected from minute spin as discussed earlier for Plexiglas. Johnson has shown, for example, that when rolling is accompanied by spin the region of slip is confined to a thin region at the trailing edge of the contact area.[7,12]

An estimate of mechanical losses involved in rolling can be obtained from the intercept of the straight line in Fig. 9. According to Eq. (8) this should equal $2K_b\tan\delta/G^{\frac{1}{3}}$. For K_b we may use the value of 0.12 which results from the analysis of Greenwood and Tabor[13] and also Drutowski.[14] The resulting calculation leads to a value of 0.08 for $\tan\delta$. While somewhat greater than the $\tan\delta$ obtained from loss data at 25–30°C,[10,15] the agreement is still within a factor of 2 and may be considered satisfactory in view of the many approximations involved in the calculation.

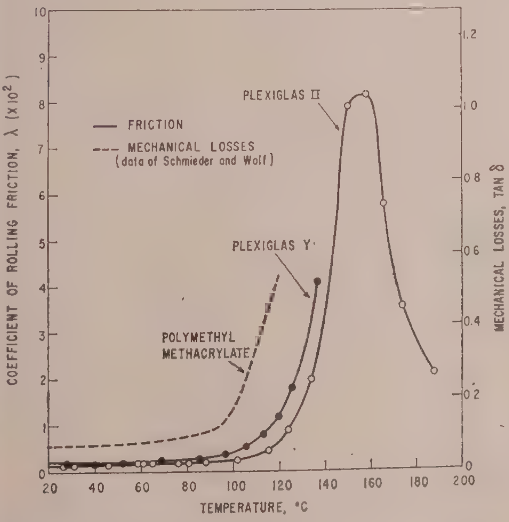

FIG. 9. Rolling friction of nylon balls between metal disks. Ball radius a=0.159, 0.317, 0.635, and 0.952 cm.

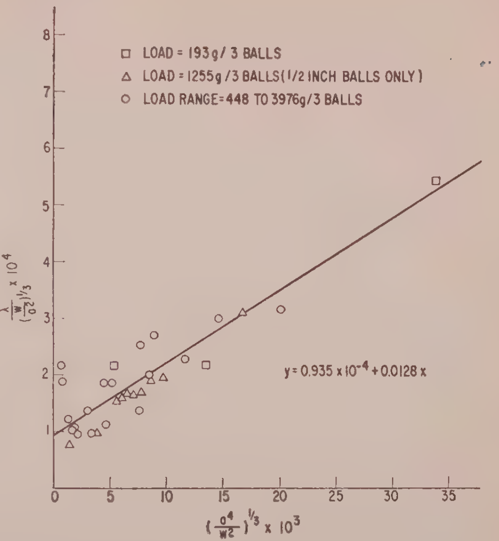

FIG. 10. Comparison of rolling friction of steel balls on polymethyl methacrylate with mechanical losses in that polymer. Load=1443 g/3 balls.

A final consideration in the rolling of nylon balls between metal disks is the effect of lubrication. The use of either graphite or petroleum oil does *not* lower the friction but may actually *raise* it as much as 20–30%. The use of aqueous sodium stearate, on the other hand, *lowers* the rolling friction (at a load of 3974 g) by nearly 50% for the larger balls. The reason for these grossly divergent effects is not yet clear. It should be noted, however, that one may not conclude from the sodium stearate results that only surface effects are involved. Nylon is known to be extremely sensitive, even in bulk properties, to moisture and to polar materials.

EFFECT OF TEMPERATURE

The main aspect of this study is determination of the extent of correlation between rolling friction and dynamic mechanical losses. One way to do this is to measure λ as a function of rolling speed and to compare this with values of $\tan\delta$ as a function of stress frequency. Such a procedure could be followed with the present apparatus but, as stated earlier, it would be

---

[10] K. Schmieder and K. Wolf, Kolloid Z. **134**, 149 (1953).

[11] K. V. Shooter and D. Tabor, Proc. Phys. Soc. (London) **B65**, 661 (1952).

[12] K. L. Johnson, Paper 24, Proc. Conf. Lubrication and Wear, London, 620 (1957).

[13] J. A. Greenwood and D. Tabor, Proc. Phys. Soc. (London) **71**, 989 (1958).

[14] R. C. Drutowski, Annual Meeting ASME, New York, November 30–December 5, 1958.

[15] C. W. Deeley, A. E. Woodward, and J. A. Sauer, J. Appl. Phys. **28**, 1124 (1957).

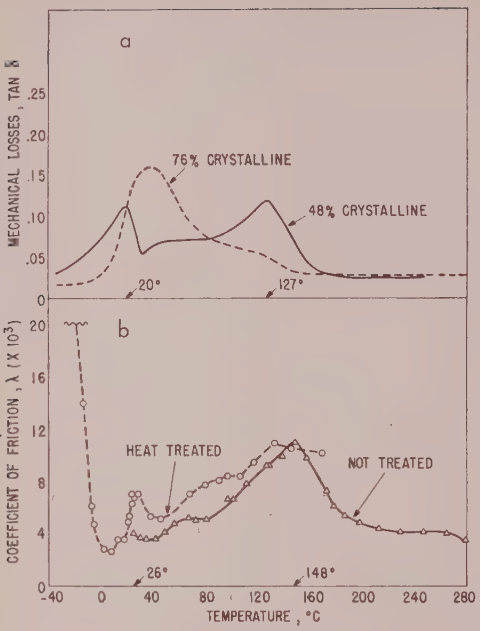

FIG. 11. Comparison of (a) mechanical losses in Teflon (data of McCrum) with (b) rolling friction of steel balls on Teflon. Load = 1510 g/3 balls.

time consuming, particularly since the range covered would need to be great (i.e., a logarithmic relationship is involved rather than a linear one). A more convenient way of comparing λ with tanδ is to study the variation of each with changing temperature. This has been done for the polymers in the present study. Unless stated otherwise, the steel balls used were $\frac{1}{4}$ in. in diameter and the rolling speed was 9 cm/sec.

Plexiglas

Figure 10 shows the dependence of rolling friction on temperature for steel balls on disks of Plexiglas II and Plexiglas Y. These curves are compared with dynamic mechanical losses in polymethyl methacrylate, the curve for the latter being obtained from the data of Schmieder and Wolf.[6] Their measurements were made with a torsion pendulum at low frequencies (1–60 cps). Since the frequencies in rolling were considerably higher (about 280 cps), the loss peak would be expected to occur at a lower temperature than the rolling friction peak. As shown by Fig. 10, this is the behavior observed. In addition to this, thermal gradients in the present furnace could account for part of the difference in temperatures noted.

There can be little doubt but that the loss and friction peaks in Fig. 10 correspond to the glass transition associated with motion of the polymer chain backbone. In an attempt to find evidence for transitions involving side groups in the chain, rolling experiments on Plexiglas Y were extended to −40°C. A slight secondary inflection was obtained between −10° and 20°C. However, the indication was not strong enough to allow a definite assignment to a specific transition. As shown by the work of Schmieder and Wolf, such a peak would be observed only at relatively low frequencies within the present temperature range.[6]

Teflon

The correlation between rolling friction and dynamic losses can be studied conveniently for Teflon because it exhibits several loss peaks within a temperature range of a few hundred degrees [Fig. 11(a)]. As shown in Fig. 11(b), these peaks and inflections also show up in rolling friction. It appears that these peaks are intimately related to the extent of crystallinity in Teflon. According to the work of McCrum,[16] the loss peaks may be attributed to amorphous relaxations at −97°C and 327°C. His measurements were made with a torsion pendulum at frequencies in the vicinity of 1 cps. Taking into account the higher frequency of stress in rolling (∼100 cps), it appears then that the friction peak at 148°C in our present work can be attributed to an amorphous relaxation. Similarly, the inflection between 20° and 30° is probably the result of the well-known crystalline transition at that temperature. The latter, incidentally, can account at least partially for the sharp change in *sliding* friction observed in the vicinity of 20°C by Flom and Porile.[17]

The Teflon sample represented by the solid curve in Fig. 11(b) was used in the "as-received" condition. As explained earlier, this sample was approximately 50%

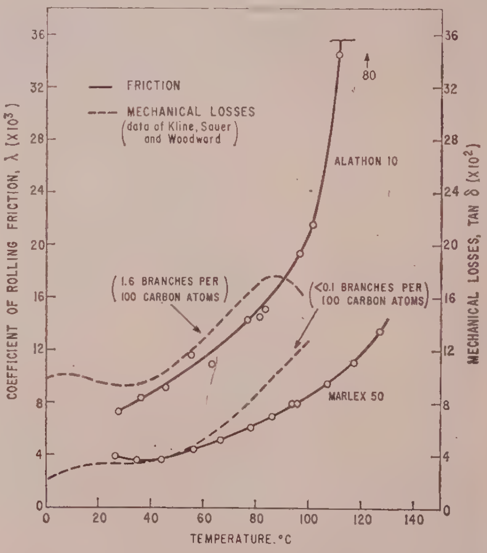

FIG. 12. Comparison of rolling friction of steel balls on polyethylene with mechanical losses in polyethylene. Load = 1570 g/3 balls.

---

[16] N. G. McCrum, J. Polymer Sci **34**, 355 (1959).

[17] D. G. Flom and N. T. Porile, J. Appl. Phys. **26**, 1088 (1955).

crystalline. In an attempt to produce Teflon with higher crystallinity for comparison with McCrum's data, a disk of the material was heated to 380°C for 1 hr and then cooled slowly to room temperature ($\frac{1}{2}$ to $1\frac{1}{2}$°C/min). X-ray diffraction patterns showed no detectable change in structure as a result of the heat treatment and cooling. Rolling friction measurements, however, indicated that some crystallinity had been introduced. This is shown by comparison of the dashed curve in Fig. 11(b) with the loss curve for the more crystalline Teflon in Fig. 11(a). The sharp upswing in the friction curve at low temperatures is somewhat unexpected, but may be possibly a remnant of the −97°C amorphous peak.

From these results it is evident that rolling friction measurements can be used to indicate the extent of crystallinity in a Teflon sample. Such a method can be quite sensitive in view of the high precision with which the friction can be measured.

Polyethylene

In the rolling of steel balls on polyethylene the marked effect of branching on friction is evident (Fig. 12). The coefficient of friction for Alathon 10 (branched polyethylene) is about twice that for Marlex 50 (linear polyethylene) up to 100°C. According to the data of Kline, Sauer, and Woodward, plotted as dashed curves in Fig. 12, a similar but slightly larger ratio is observed for the dynamic mechanical losses of branched and unbranched polyethylene.[18] As proposed by Kline *et al.*, the mechanical losses probably arise from the motion of branched chains within the amorphous regions of the polymer. Since decreased branching is accompanied by increased crystallinity, the mechanical losses are also lowered thereby.

While differing considerably in magnitude, the friction results in rolling for Alathon and Marlex are reminiscent of the friction results in sliding observed earlier for the same polymers.[1] A part of the difference in friction for the two materials, in rolling as well as sliding, would stem from the lower dynamic modulus of Alathon as opposed to that of Marlex. While the modulus was not determined in the present study, the apparatus has been modified subsequently to provide for such measurement.[19]

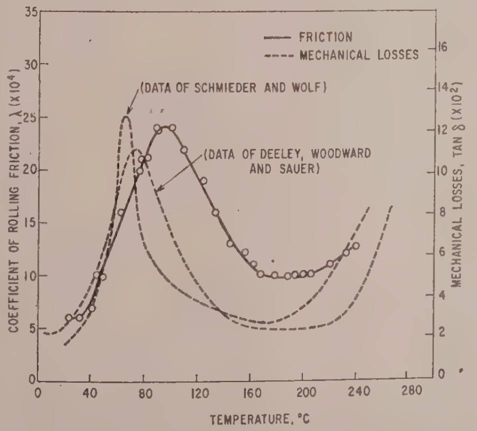

FIG. 13. Comparison of rolling friction of steel balls ($\frac{1}{2}$-in. diam) on nylon with mechanical losses in nylon. Load = 1516 g/3 balls.

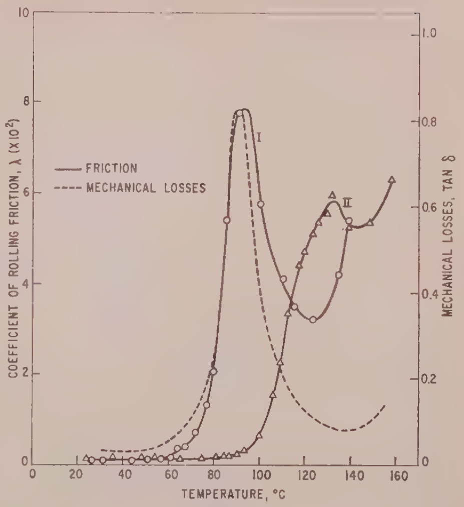

FIG. 14. Comparison of rolling friction of steel balls ($\frac{1}{4}$ in. in diameter) on polyvinyl chloride with mechanical losses in polyvinyl chloride. Load (I) = 1538 g/3 balls and load (II) = 1625 g/3 balls.

Nylon

The effect of temperature on rolling friction for nylon is shown in Fig. 13. The data were obtained with steel balls of $\frac{1}{2}$-in. diameter prior to discovery of the surface effects described earlier. Hence, the friction includes a small component owing to spin as indicated by the solid curve of Fig. 7 and as just discussed for nylon balls. In spite of the probable surface component, the general agreement of the friction results with the loss data of Schmieder and Wolf[10] and of Deeley, Woodward, and Sauer[15] is good. It is more difficult in this case to correlate the temperatures of the peaks on the basis of stress frequencies (140 cps in rolling, 3 cps in the work of Schmieder and Wolf, 100–1000 cps in the work of Deeley *et al.*). This may result not only from surface effects but also from the known sensitivity of nylon bulk properties to past thermal and mechanical history.

Polyvinyl Chloride

The results of friction-vs-temperature measurements for both kinds of PVC are shown in Fig. 14. For comparison with dynamic mechanical losses the data of

---

[18] D. E. Kline, J. A. Sauer, and A. E. Woodward, J. Polymer Sci. **22**, 455 (1956).

[19] D. G. Flom, Anal. Chem. **32**, 1550 (1960).

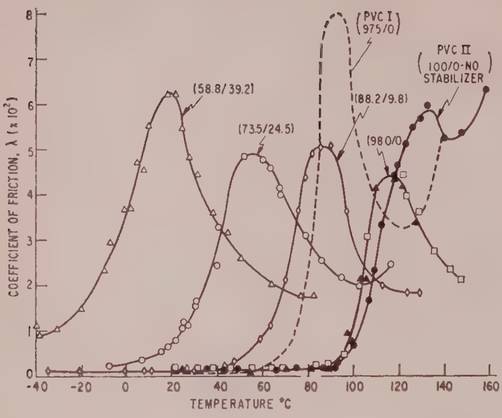

FIG. 15. Rolling friction of steel balls on polyvinyl chloride containing varying amounts of dioctyl phthalate (DOP) plasticizer and dibasic lead phosphite (Dyphos) stabilizer. Ratios given are PVC/DOP. Load = 1540 to 1625 g/3 balls.

Wolf and Schmieder, obtained by torsion pendulum techniques, are shown as the dashed curve.[20] It would appear that the results for PVC I agree more closely with the torsion pendulum study than do those for PVC II. However, it should be noted that because of the higher stress frequency in rolling one would expect the friction peak to occur at a higher temperature than the loss peak. Also, the somewhat excessive broadening of the peak for PVC II was probably not a true characteristic of that material but was rather the result of chemical degradation during heating owing to the lack of stabilizer in that material. That sample was observed to be almost completely disintegrated at the end of the series of friction measurements extending to 160°C.

The effect of the addition of dioctyl phthalate plasticizer (DOP) to PVC II is shown in Fig. 15. Except for the one case noted, and discussed above, each of the samples contained 2% dibasic lead phosphite stabilizer (trade name "Dyphos"). It is apparent from Fig. 15 that the principal effect of the plasticizer was to broaden the friction peak and also lower the temperature at which the peak occurred. The same effect has been shown for dynamic mechanical losses. An example is given in Fig. 16, in which data of Schmieder and Wolf are plotted showing the losses for PVC containing varying amounts of dibutyl phthalate.[6] The same authors have presented curves for diethyl hexyl succinate plasticizer which resemble the friction curves of Fig. 15 even more closely than the dibutyl phthalate curves.

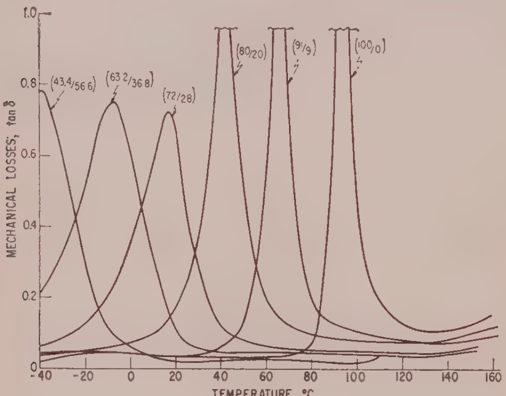

FIG. 16. Dynamic mechanical losses of polyvinyl chloride with different polymer/plasticizer ratios. Plasticizer was dibutyl phthalate. Data of Schmieder and Wolf.[6]

Within the range of concentrations used, the shift of the friction peak temperature is directly proportional to plasticizer concentration (Fig. 17). It is significant that the temperature shift, namely, 2.4°C/1% plasticizer, is close to the temperature shift for loss peaks given by Schmieder and Wolf for the dibutyl and dioctyl phthalate plasticizers, namely, 2.7°C/1%. An important consequence of this result is the fact that for polyvinyl chloride and similar materials one can "build in," within certain limits, any desired frictional characteristics merely by suitable choice of plasticizer concentration. An even further extension of this principle to the field of wear is indicated by the results of James, in which the type of wear debris formed during sliding is found to be related to temperature and to plasticizer content.[21]

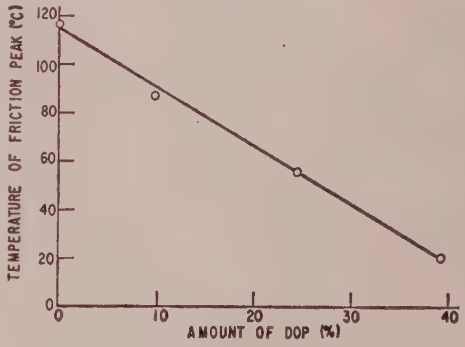

FIG. 17. Effect of DOP plasticizer on temperature of rolling friction peak for polyvinyl chloride.

In addition to concentration, the particular *kind* of plasticizer is also important in the effectiveness to lower and broaden the rolling friction peaks. Again, this is in accord with mechanical loss results as shown in Fig. 18, where comparison is made of dioctyl phthalate and tricresyl phosphate (TCP) plasticizers. The comparisons are for roughly equal concentrations by volume (46%) of DOP and TCP. The dashed curves are taken from the paper of Buchdahl and Nielsen[22] and show the temperature dependence of the coefficient *n* in the Nutting equation, a number which has been shown to be closely related to the damping coefficient as obtained from dynamic mechanical measurements.

---

[20] K. Wolf and K. Schmieder, *International Symposium on Macromolecular Chemistry, Torino, Italy, September 26–October 2, 1954* (International Union of Pure and Applied Chemistry, 1956), p. 732.

[21] D. I. James, Wear 2, 183 (1959).

[22] R. Buchdahl and L. E. Nielsen, J. Appl. Phys. 22, 1344 (1951).

A more detailed study of the relationship between plasticizer and friction peak *heights* would involve close control over the time and temperature of heating as well as aging of the samples studied. Thermal history has been found by Fuoss[23] to be important in electrical losses in PVC. Similar influence would be expected in mechanical losses and in rolling friction. The effect of aging on mechanical losses and other mechanical properties in plasticized PVC has been demonstrated by Wolf and Schmieder[6] and by Gruntfest, Young, and Kooch.[24] In the present study measurements were made between one and 26 days after preparation of the samples, but since some samples were reheated an accurate evaluation of aging could not be made.

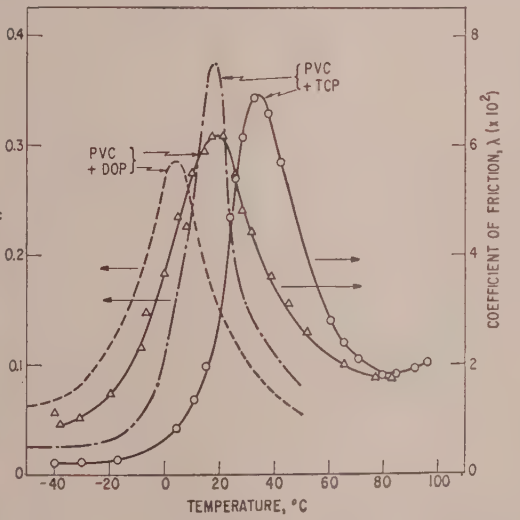

Fig. 18. Effect of two plasticizers (DOP and TCP) on rolling friction coefficient and on Nutting exponent *n* (α tanδ) for PVC.

Polyvinyl Acetate

None of the polymers included in this study exhibit as high rolling friction in the vicinity of a transition temperature as polyvinyl acetate (Fig. 19). A coefficient of 0.2 at the peak is three orders of magnitude greater than the coefficient of rolling friction for a hard metal. In line with these friction results, none of the other polymers in our study exhibits as high mechanical losses as polyvinyl acetate (dashed curve, Fig. 19), again determined by torsion pendulum methods.[20] Two solid curves are shown in Fig. 19, representing successive friction-temperature runs on the same material. The increase in peak height and broadening of the peak in the second run may be the result of the previous thermal history. However, the difference may not be significant since experimental difficulties incurred in supporting the polymer disk lowered the precision of the data at temperatures greater than that of the transition.

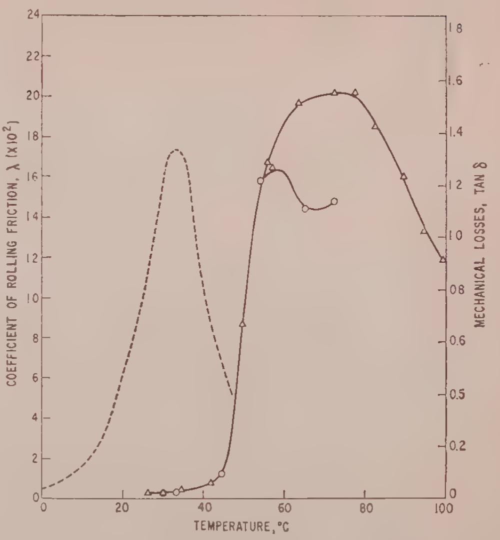

Fig. 19. Comparison of rolling friction of steel balls (¼ in. in diameter) on polyvinyl acetate with mechanical losses in polyvinyl acetate. Load = 1635 g/3 balls. Circles denote friction run 1; triangles, friction run 2. Dotted line indicates mechanical losses (data of Wolf and Schmieder[20]).

Polystyrene

For polystyrene the temperature characteristics in both rolling and in mechanical losses are rather flat up

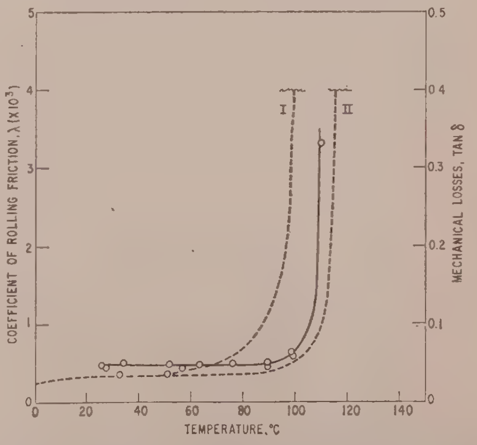

Fig. 20. Comparison of (solid line) rolling friction of steel balls (½ in. in diameter) on polystyrene with (dotted line) mechanical losses in polystyrene, data of Schmieder and Wolf.[10] Load = 1440 g/3 balls.

---

[23] R. M. Fuoss, J. Am. Chem. Soc. 61, 2329 (1939).

[24] I. J. Gruntfest, E. M. Young, Jr., and W. Kooch, J. Appl. Phys. 28, 1106 (1957).

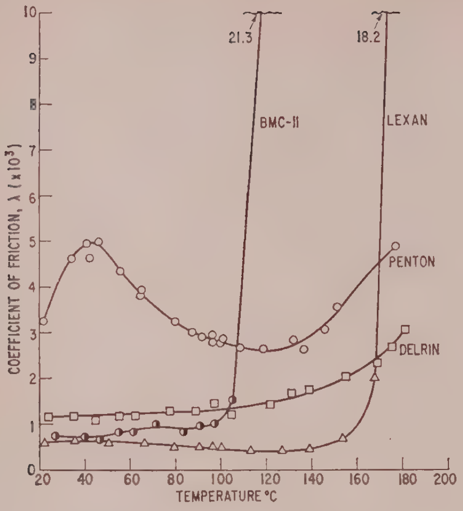

Fig. 21. Rolling friction of steel balls ($\frac{1}{4}$ in. in diameter) on four commercial plastics. Load = 1565 to 1642 g/3 balls.

to the glass temperature (Fig. 20). The data of Schmieder and Wolf, represented by dashed curves I and II, show that this temperature varies with the particular sample of polystyrene.[10] They reported the "osmotic" molecular weight of product I to be 80 000, whereas that of product II was 120 000. On the other hand, the "sedimentation" molecular weight of I was 170 000, whereas that of II was 150 000. Thus, product I was more polydisperse than product II. As Schmieder and Wolf point out, however, one should not draw conclusions about the shift of tanδ with molecular weight in this case because the softening temperature of I was about 16° below that of II, owing to the presence in I of about 1% monomer, dimer, and trimer.

The molecular weight of the polystyrene in the present work was determined by intrinsic viscosity measurements to be 170 000. Hence, this material was probably most similar to product I of Schmieder and Wolf's work. On this basis one would expect, because of the difference in stress frequencies, that the friction peak would occur at a higher temperature than the loss peak for product I. That this is the experimental result is shown by Fig. 20.

Other Polymers

Four commercial plastics were included in this study, although dynamic loss data for these materials were not available for comparison with rolling friction measurements. The four were Lexan, an aromatic polycarbonate; BMC-11, an acrylonitrile-styrene copolymer; Delrin, a polyacetal resin; and Penton, a chlorinated polyether. Friction results for the four are shown in Fig. 21. By comparison of the rolling friction coefficients with those of the other polymers reported here, it is apparent that below their transition temperatures all four of the plastics in Fig. 21 exhibit very low friction characteristics. This result was anticipated in the case of Lexan by preliminary rebound measurements of plastic balls against a steel surface. In those measurements, tanδ losses for Lexan were 0.05 as opposed to 0.06 for Plexiglas and 0.07 for nylon.

SUMMARY

The results presented here lend further support to the thesis that dynamic mechanical losses are predominant in the friction of a pure rolling contact. When deviations from pure rolling occur, surface effects become significant. By suitable choice of experimental parameters, these effects can be separated from the bulk effects and, if desired, can be minimized.

Structural features of thermoplastics are reflected in the rolling frictional behavior of these materials. This is well illustrated by the effects of crystallinity on friction for Teflon and for polyethylene and by the effect of plasticizer content on friction for polyvinyl chloride.

ACKNOWLEDGMENT

The author gratefully acknowledges helpful discussions with Dr. A. M. Beuche during the course of this work.

JOURNAL OF APPLIED PHYSICS VOLUME 32, NUMBER 8 AUGUST, 1961

Friction of Metals in Reciprocating Sliding

YASUKATSU TAMAI
Aeronautical Research Institute, Meguro, Tokyo, Japan

A number of experiments were conducted on the metallic friction in reciprocating sliding with a pendulum. It was shown that the reciprocating sliding gives quite different results from those of single-traverse or unidirectional repeated sliding, which were emphasized in both the coefficient of friction and the electric contact resistance, surface damage due to sliding, and the low friction phenomenon.

INTRODUCTION

FRICTION in reciprocating sliding has been studied far less than that in single-traverse or in unidirectional repeated sliding, with the exception of study of so-called fretting corrosion. The present study was planned to get further information on the friction of metals in this mode of reciprocating sliding.

For this purpose a friction pendulum was used which is identical in principle with that of Kyropoulos and Shobert.[1] Generally speaking, use of a pendulum is not favorable because the sliding velocity varies with its amplitude. However, when the speed is not of primary importance, the pendulum has the advantage of its mechanical simplicity.

EXPERIMENTS

The friction couple consisted of one rotating journal of the pendulum (2 mm in diameter) and four supporting cylindrical bearings (5 mm in diameter) which were arranged in the form of crossed cylinders as shown in Fig. 1. The load at each contact was 100 g. The sliding speed, which varied during the swing, had a maximum value of 3 mm/sec. The period of the pendulum was 0.5 sec. The automatic record of the damping motion of the pendulum was made by means of a variable electric condenser. Typical records are illustrated in Fig. 2. The coefficient of friction can be found from the envelope of the curve. Curve A shows uniform damping. The irregularities in curve B result from stick-slip sliding at one contact. When stick-slip occurs, only an approximate value of the coefficient of friction μ can be found.

Simultaneously with measurement of μ, the electric contact resistance R was measured by a dc potential method. The current was kept constant—30 ma for R less than 1 ohm and 3 ma for greater R. The measurable range was between 10^{-2} and 10^{2} ohm. Typical resistance-vs-sliding time curves are shown in Fig. 3. (The letters a, b, and c indicate corresponding positions in Fig. 2.) Curve A is smooth during the oscillation of the pendulum, even when the reversals of sliding direction occur. Curve B shows noticeably the fluctuation in resistance, and in the region from b to c, the average value of R could be obtained with a precision of only one figure.

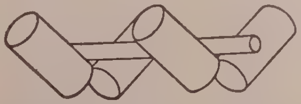

FIG. 1. Arrangement of specimens.

In addition to friction and resistance, microhardness measurement, H kg/mm², and observation with an optical microscope were made. Wear scars could be classified into two groups: those severely damaged, suggesting the occurrence of local welding, and those abraded mildly. Almost all of the experiments were carried out at room temperature and in the ordinary laboratory atmosphere.

RESULTS AND DISCUSSION

Metals examined were commercially pure gold, silver, copper, platinum, nickel, aluminum, and tin, as well as alloys of 18-8 stainless steel, high- and low-carbon steels, brass, and white metal. The specimens were degreased very carefully before each measurement.

Friction and resistance were measured repeatedly more than 20 times without any change in the specimens and their arrangement throughout a single experiment. μ and R were not always steady but often varied

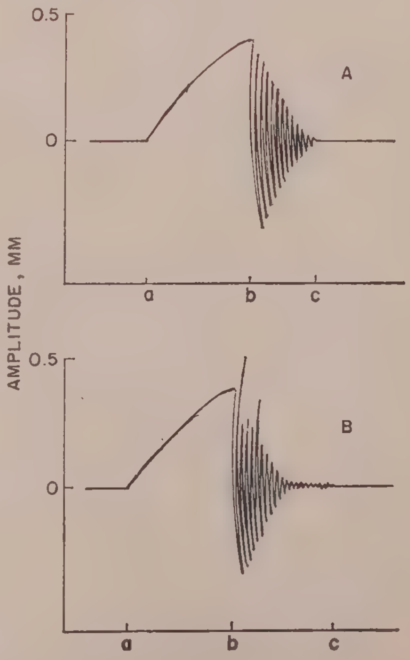

FIG. 2. Typical records of damping motion.

---

[1] S. Kyropoulos and E. I. Shobert, Rev. Sci. Instr. 8, 151 (1937).

Table I. Friction, resistance, microhardness, and other characteristics.

Substance	$\bar{\mu}_1$	$\bar{\mu}_\infty$	$\Delta\mu_{av}$	$\bar{R}_1$	$\bar{R}_\infty$	ΔR_{av}	H	Stick-slip	Scar damage	R fluct.
Gold	0.53	0.53	0.09	0	0.2	0.08	80	+	+	−
Silver	0.53	0.46	0.11	0	0.02	0.01	80	+	+	−
Copper	0.22	0.40	0.08	0.2	0.3	0.08	90	+	+	−
Platinum	0.50	0.50	0.10	0.15	0.15	0.04	120	+	+	−
Nickel	0.60	0.85	0.11	0.1	0.2	0.08	270	+	+	−
Aluminum	0.76	0.58	0.11	0.3	0.3	0.0	60	+	+	−
Tin	0.53	0.53	0.04	1.2	1.5	0.24	8	+	+	+
Stainless steel	0.44	0.42	0.03	0.4	0.6	0.16	360	+	±	−
High-carbon steel	0.50	0.53	0.01	0.4	1.1	0.20	900	−	−	+
Low-carbon steel	0.40	0.41	0.02	0.35	0.7	0.30	120	−	−	+
Brass	0.50	0.46	0.02	0.2	0.2	0.08	200	−	−	−

on measurement, and in some cases increased or decreased gradually to an equilibrium value after repeated measurements. The original data were divided into successive groups of five readings. Each group was characterized by median values of the coefficient of friction and electric resistance, $\bar{\mu}$ and $\bar{R}$, respectively. The ranges of μ and R for each group are denoted by $\Delta\mu$ and ΔR. An indication of the magnitude of irregularities in μ and R is given by $\Delta\mu_{av}$ and ΔR_{av}, the values of $\Delta\mu$ and ΔR averaged over all groups.

The results of experiments are summarized in Table I. From Table I it is readily seen that stick-slip is always accompanied by large values of $\Delta\mu$, and wear scar is evidence of pronounced damage. The larger the resistance, the larger becomes the range of resistance.

Comparison of Reciprocating Sliding with Single Traverse

Figures 4 and 5 give the comparison of μ and R of the present results with those of single-traverse studies, respectively. Friction data are quoted from 13 published sources. The wide scattering of the data may be due to the wide varieties of applied load and sliding speed, which indicates that the surface conditions at the sliding contact are very much different from each other. Therefore the comparison may seem meaningless. Nevertheless, it is easily seen from Fig. 4 that for soft metals μ tends to be somewhat lower in reciprocating sliding. For harder metals it is about the same for both modes of sliding.

Resistance values are those from four published sources. Resistance in reciprocating sliding is much higher than in single traverse, and very near to that of static contact. The higher resistance is usually attributed to the surface oxide. The high resistance in reciprocating sliding may also be related to the surface oxide. The high value for gold and platinum after repeated measurements is, however, hard to explain at this stage of the investigation. Recently reported organic deposits on the sliding contact of gold and platinum might have some relation to these results.[2]

Significance of Fluctuating Resistance

As shown in Fig. 3, there are two kinds of resistance traces. For examples, steel causes a fluctuating trace and copper a smooth one. With steel, at the beginning

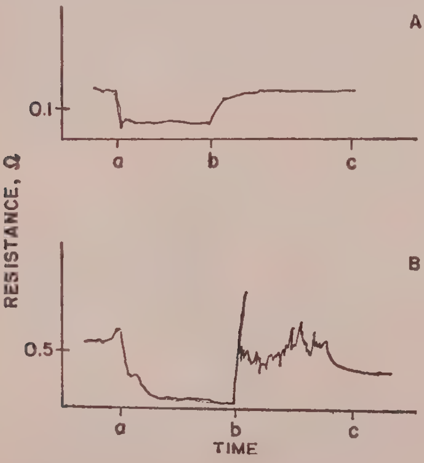

Fig. 3. Typical records of contact resistance.

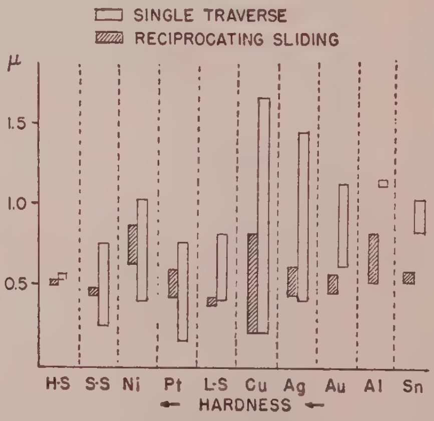

Fig. 4. Comparison of friction ($H-S$, $S-S$, $L-S$: high-carbon, stainless, and low-carbon steel, respectively).

---

[2] H. W. Hermance and T. F. Egan, Bell System Tech. J. 37, 739 (1958).

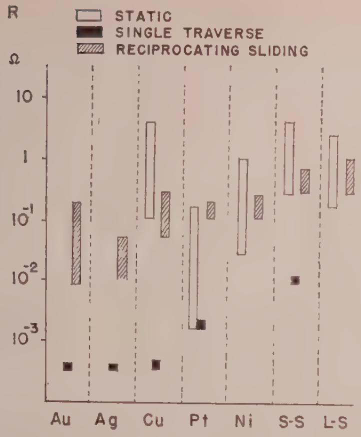

FIG. 5. Comparison of contact resistance.

of the measurement when the journal specimen was placed on the bearing specimens, R was usually between 0.5 and 1.0 ohm, indicating oxide-oxide contact. As the pendulum began to swing to the starting position, R decreased to a value of 10^{-2} ohm or less. This has already been noticed by many investigators, and is considered due to breakdown of the oxide layer.[3] As soon as the pendulum was allowed to swing freely, R increased suddenly and fluctuated violently over a considerable range of 0.5–1.2 ohm. When the pendulum stopped, R settled to a lesser value, but not necessarily to 10^{-2} ohm, and in fact was usually somewhat greater. However, R again decreased to 10^{-2} ohm in the period of unidirectional slow sliding; i.e., from *a* to *b* in Fig. 3, in the following measurement. It is probable that the large and fluctuating resistance during sliding may arise from loose oxide debris generating between the specimens.[4] The resistance at rest may result from the debris still remaining, and the slow unidirectional sliding squeezes out the intervening debris.

In contrast to steel, the resistance of copper during swing was actually greater than during unidirectional sliding, but did not fluctuate. To get further information, both steel and copper specimens were heated to high temperature to get a surface oxide layer of 10^3-A thickness. With steel it was found that μ decreased from 0.50 to 0.45 and R increased very much from 0.8 to 1.8 ohm or higher, still fluctuating violently. With copper there appeared a marked and definite change in the characteristics of resistance; that is, it fluctuated during swing together with the increase from 0.3 to 0.6 ohm.

It may be concluded, therefore, that the fine oxide debris makes the resistance trace smooth. According to Barwell *et al.*,[5] the wear debris of steel is fairly large but

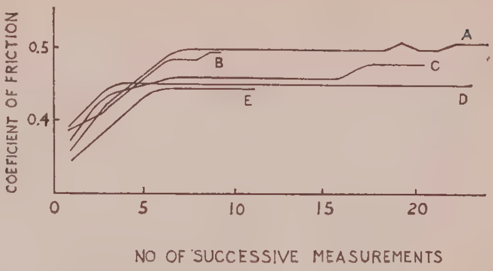

FIG. 6. Effect of surface oxide of steel on friction.

that of copper is considerably smaller. When heated, the surface oxide layer became thicker and crystalline, which resulted in the larger oxide debris. Larger debris between sliding surfaces causes more readily the fluctuation of resistance.

In reciprocating sliding the resistance has little relation to the friction, which is a marked difference from single traverse. Thus the resistance of low-carbon steel increased from 0.35 to 0.7 ohm, while the friction was constant throughout the measurements.

Surface Breakdown in Reciprocating Sliding

Friction was measured with several specimens of high-carbon steel which had surface oxide layers of different thickness: natural (A); 500 A (B); 700 A (C); 1000 A (D); and 10^3 A (E). Figure 6 shows the results in which μ increased gradually to a steady value as the reciprocating sliding was repeated. This indicates that the breakdown of the oxide film occurred despite the fact that the load was kept constant and less than the critical value sufficient to break the oxide film in single traverse. Reciprocating sliding seems to cause more severe wear than unidirectional sliding.

Combination of Dissimilar Metals

Table II gives some of the results with dissimilar couples which are of special interest because of the marked contrast in their friction and resistance characteristics. The friction characteristics are almost the same as those of steel. On the other hand, the resistance characteristics are those of silver or white metal. There is neither stick-slip nor resistance fluctuation. With these dissimilar couples metallic welding may not occur and the wear of steel does not take place to form large wear debris.

TABLE II. Dissimilar combinations.

Combination	$\langle\mu_\infty\rangle_{av}$	$\langle\Delta\mu\rangle_{av}$	$\langle R_\infty\rangle_{av}$	$\langle\Delta R\rangle_{av}$	Stick-slip	Scar damage	R fluct.
Silver-silver	0.46	0.11	0.02	0.01	+	+	−
Steel-silver	0.41	0.02	0.08	0.0	−	−	−
Steel-steel	0.41	0.02	0.7	0.3	−	−	+
Steel–white metal	0.41	0.03	0.12	0.0	−	−	−

---

[3] R. W. Wilson, Proc. Phys. Soc. (London) **B68**, 625 (1955).

[4] J. S. Halliday and W. Hirst, Proc. Roy. Soc. (London) **A236**, 411 (1956).

[5] F. T. Barwell, L. Grunberg, A. A. Milne, and K. H. R. Wright, World Petrol. Congr., Proc. 4th Congr. **VI**, C-3 (1955).

Low Friction in Reciprocating Sliding

It was found quite unexpectedly that with some metals, very low friction less than 0.10 was observed. Table III lists the metals that show low friction, and some other metals for comparison.

Table III. Low friction.

Combination	Occurrence
Gold-gold	+
Silver-silver	+
Copper-copper	+
Platinum-platinum	+
Nickel-nickel	−
Aluminum-aluminum	−
Brass-brass	−
Steel-steel	−
Oxid. copper–oxid. copper	−
Steel-silver	−
Gold plat.–gold plat.	− →+

Gold, silver, copper, and platinum exhibit low friction. However, surface-oxidized copper did not. Gold behaved the same at 200°C as at room temperature. A gold-plated steel specimen showed low friction at the beginning but as soon as the gold was rubbed off by repeated sliding, it did not. A dissimilar friction couple of silver and steel did not give the low friction.

The low friction appears when the amplitude of swing becomes more or less narrow; for gold it starts at 500 μ, for silver 170 μ, for platinum 60 μ, and for copper 50 μ. Except for gold, these metals show low friction occasionally: 0.9 of the time for silver, 0.6 for platinum, and 0.4 for copper, in the same order as with the amplitude.

Halliday and Hirst[4] have found the lowering of friction with mild steel, aluminum, copper, and nickel at small amplitude of fretting. However, further investigation should be required to see any relation between their finding and the present one or to explain this phenomenon more perfectly.

JOURNAL OF APPLIED PHYSICS VOLUME 32, NUMBER 8 AUGUST, 1961

Influence of Surface Energy on Friction and Wear Phenomena

E. Rabinowicz
Surface Laboratory, Department of Mechanical Engineering, Massachusetts Institute of Technology, Cambridge, Massachusetts

A number of friction and wear phenomena are explicable in terms of the surface energy of adhesion of the contacting materials. In the friction field, it is found qualitatively that high friction coefficients are found for sliding materials with high surface energy/hardness ratios and conversely. Unfortunately, it is not easy to test this relationship quantitatively because the derived expression contains parameters which cannot be independently controlled. However, in the wear field, it has been found possible to derive an expression for the size of loose wear particles which can be readily tested; namely, that the average size of loose wear particles is proportional to the surface energy/hardness ratio, the nondimensional constant of proportionality being 60 000. Experiments with 15 different materials show the validity of this expression. Another phenomenon, adhesion, which also seems to be governed by surface energy considerations, is discussed in qualitative terms.

INTRODUCTION

THE theory of the friction process in recent years has been dominated by the equation

$$f=s/p, \tag{1}$$

which denotes the fact that the friction coefficient represents the ratio of the shear strength s to the hardness p of the softer of two contacting materials. This equation has helped explain many frictional phenomena; however, it has failed to make much of a contribution to two of the main frictional problems; namely, that of describing the scale on which phenomena occur, and that of selecting frictional materials suitable for practical use. Indeed, taken at its face value, Eq. (1) suggests that almost any material will give essentially the same frictional behavior as any other, since s and p have essentially a constant ratio for all but a very few materials. However, it is known that friction coefficients do vary over a fair range, with friction coefficients of metals, sliding in air, varying from 2.0 for indium to 0.5 for titanium; also, that the appearance of surfaces after sliding varies from very rough to quite smooth. Hence, it seems clear that we must modify Eq. (1) in some way so as to bring to bear additional properties of the sliding materials. It is my contention that this may be done by considering the work of adhesion W_{ab} of the contacting materials. The quantity W_{ab} is defined by the equation

$$W_{ab}=\gamma_a+\gamma_b-\gamma_{ab}, \tag{2}$$

where γ_a and γ_b are the surface free energies of materials a and b, and γ_{ab} the interface free energy, all per unit area.

VALUES FOR THE WORK OF ADHESION OF SOLIDS

It must be stated at the outset that reliable data for the work of adhesion of solids are not generally available.

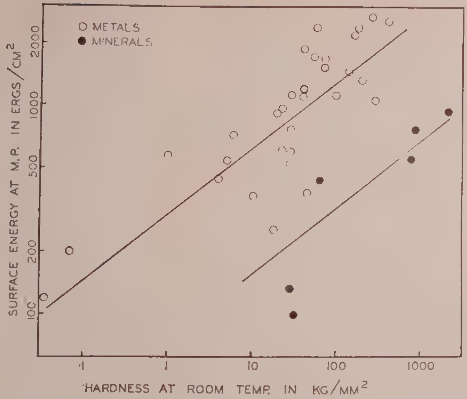

FIG. 1. Plot of surface tension as a function of hardness for the metals tabulated by Bondi[1] and Taylor,[2] also a few nonmetals. The surface tensions increase as a low power (between $\frac{1}{3}$ and $\frac{1}{4}$) of the hardness.

What is available, to a fairly high degree of accuracy, are values of the surface energies γ_a and γ_b of the materials in the liquid state and, in a few cases, values for the interfacial energy γ_{ab} when the lower melting material is a liquid and the other is a solid. Tabulations of the data are given, for example, in Bondi[1] and in Taylor.[2]

Additionally, some values are available of the surface energies of a few solids and the interfacial energies of a few pairs of solids at temperatures fairly close to their melting point. These data are tabulated by McLean,[3] who shows that values of γ_{ab} are of the order of $\frac{1}{2}$ to $\frac{1}{4}$ of $(\gamma_a+\gamma_b)$. It seems that the surface energies of solids are not very temperature dependent, being at the melting point nearly the same as those of the corresponding liquids and increasing by about 0.5 erg/cm² for every 1°C reduction in temperature from that point on. If this variation is maintained down to room temperature, it suggests that the surface energies of most metals are about twice as great at room temperature as at the melting point.

These values apply only when the surfaces are investigated in a vacuum. When tests are carried out in an atmosphere such as nitrogen, the surface energies are lower by factors of the order of 2; thus, since we are ordinarily interested in the work of adhesion of solids in air at or near room temperature, we may assume that the two factors of 2 cancel out.

The surface energies of metals appear to be quite well correlated with their hardness. Thus, if we plot the surface energies of all the metals tabulated by Bondi[1] and Taylor[2] against their hardnesses as given by Tabor,[4] we find that a straight line of slope $\frac{1}{4}$ fits the data quite well (Fig. 1). This suggests that the ratio W_{ab}/p, which we shall later encounter, varies approximately as $p^{-\frac{3}{4}}$, being smaller for the harder metals. Figure 1 also shows some values for a few nonmetals; these seem to fall on a line parallel to that for the metals, but lower (i.e., with smaller values of surface energy for the same value of hardness).

TABLE I. Data of Machlin and Yankee (1954).

Sliding combination	W_{ab}	W_{aa} (softer material)	Static friction (inert atmosphere)
Ag on Cu	2330 erg/cm²	2260	0.75
Cu on Fe	2675	2260	0.72
Ag on Fe	712	1780	0.48
Cu on SiO_2	325	2260	0.10

ATTEMPTS TO EXPLAIN FRICTION PHENOMENA IN TERMS OF SURFACE ENERGIES

The earliest paper in which friction phenomena are discussed in terms of W_{ab} appears to be that of Machlin and Yankee.[5] These authors compared the work of adhesion W_{ab} of the sliding combination with the work of cohesion W_{aa} of the weaker material, and postulated that welding during sliding would not occur if $W_{ab}<W_{aa}$. Their experimental work supported this postulate, though in a limited way, since very limited data on W_{ab} were available (see Table I).

It is of interest to note that Machlin and Yankee felt that the work of adhesion concept could also be applied in a different way, for they state: "Perhaps a more representative criterion would be the quotient of the work of adhesion and the strength of the weaker component."

Next, there is a paper by Coffin,[6] who notes that nickel has a very low work of adhesion against aluminum oxide and that, consequently, nickel should be a good material to slide against alumina (see Table II). Experiments show that nickel does have low friction and surface damage when slid against aluminum oxide in an inert atmosphere. Coffin's method of selecting nickel as the most promising material to slide against alumina is seen to depend on quite small differences in the work of adhesion.

TABLE II. Data of Coffin (1958).

Combination	Work of adhesion (in H_2)
Si on Al_2O_3	670 erg/cm²
Ni on Al_2O_3	480
Fe on Al_2O_3	695

Coming to my own work, I showed some years ago[7]

---

[1] A. Bondi, Chem. Revs. **52**, 417 (1953).

[2] J. W. Taylor, Metallurgia **50**, 161 (1954).

[3] D. McLean, *Grain Boundaries in Metals* (Oxford University Press, New York, 1957), p. 78.

[4] D. Tabor, *The Hardness of Metals* (Oxford University Press, New York, 1951).

[5] E. S. Machlin and W. R. Yankee, J. Appl. Phys. **25**, 576 (1954).

[6] L. F. Coffin, ASLE Trans. **1**, 108 (1958).

[7] E. Rabinowicz, ASLE Trans. **1**, 96 (1958).

Table III. Data for clean metals.

Material	Work of adhesion (erg/cm²)	Hardness (d/cm²)	W_{aa}/p (cm)	Friction coefficient
lead on lead	900	4.10^8	2.2×10^{-6} cm	1.2
low-carbon steel on low-carbon steel	2500	2.10^{10}	1.2×10^{-7} cm	0.6

that Eq. (1) was not a complete expression for the friction coefficient of sliding surfaces, if the work of adhesion was considered. If we take a cone of angle θ pressed into a flat surface which deforms plastically (Fig. 2), we may write the total energy E in the form

$$E=x\cdot\Delta L-\int\pi r^2p\cdot dx+\pi r^2W_{ab}. \tag{3}$$

Substituting $r=x\cot\theta$ and noting that equilibrium is obtained when $dE/dx=0$, we have

$$\Delta L=\pi r^2p-2\pi rW_{ab}\cot\theta. \tag{4}$$

The friction force ΔF is assumed to equal πr^2s. Hence, if r and θ are the same for all junctions,

$$f=\frac{\sum\Delta F}{\sum\Delta L}=\frac{s}{p-2W_{ab}(\cot\theta)/r}. \tag{5}$$

This last expression may be written in the series expansion

$$f=(s/p)[1+2W_{ab}(\cot\theta)/pr$$
$$+4W_{ab}^2(\cot\theta)^2/(pr)^2+\cdots]. \tag{6}$$

It will be seen that as a result of surface energy, the friction coefficient has been increased, and consideration of Eq. (5) shows that this increase becomes great without limit if

$$W_{ab}/p=r/2\cot\theta. \tag{7}$$

This mathematical description of the friction process seems to give a good account of the high friction coefficients given by soft metals. For simplicity, we may consider the case of metals sliding on themselves, and for this case assume that γ_{aa} is zero, which is not strictly correct, but will not influence our results unduly. We may then compare W_{aa}/p ratios for a typical soft and a typical hard metal, as has been done in Table III.

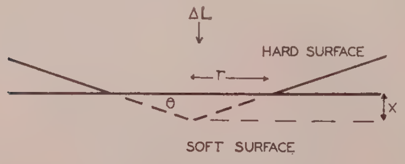

Fig. 2. Schematic representation of a conical asperity pressed into a flat surface.

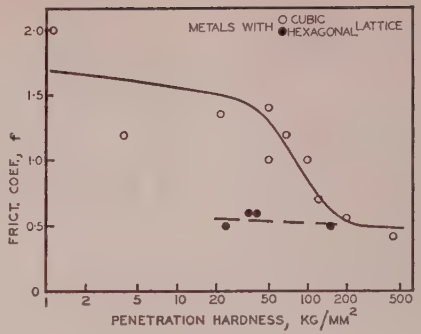

Fig. 3. Plot of friction coefficient as a function of hardness for uncontaminated metals sliding in air.

Soft metals have much higher W_{aa}/p ratios. They also have higher friction coefficients (see Fig. 3). An interesting effect is that metals with hexagonal structure give lower friction coefficients than metals with cubic structure, and it is possible that the extra slip planes of the cubic metals allows them to deform in such a way as to minimize the interfacial energy γ_{aa}, while the hexagonal metals have higher values of γ_{aa} and thus lower W_{aa}/p ratios. A study of friction coefficients as outlined above does not lend itself well to detailed experimental verification of the energy of adhesion concept since two of the terms in Eqs. (3) to (7), namely the junction radius and the surface roughness, are generated during sliding and not imposed externally. Hence they cannot be purposely varied, or even controlled.

EFFECT OF SURFACE ENERGY ON THE SIZE OF LOOSE WEAR PARTICLES

However, another surface phenomenon does exist which is governed by surface energy and which can be specified completely in terms of known parameters. This phenomenon is the formation of loose wear particles accompanying the sliding of smooth surfaces. In a recent paper,[8] we have suggested that for a particle to come off loose, the elastic energy stored in the particle while it was being formed must equal or exceed the energy of adhesion which binds it to its substrate. In most cases, when a wear particle is made up by the aggregation of smaller fragments, the particle will come off loose as soon as its elastic energy becomes as large as its adhesive energy. For a hemispherical particle, we have (Fig. 4),

$$\tfrac{1}{2}\cdot(\sigma_r^2/E)\cdot(\pi d^3/12)=W_{ab}\cdot\pi d^2/4, \tag{8}$$

where σ_r is the residual stress in the fragment and E its Young's modulus. If, as is obtained using many models,

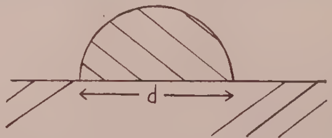

Fig. 4. Schematic representation of a hemispherical fragment on a flat surface.

---

[8] E. Rabinowicz, Wear 2, 4 (1958).

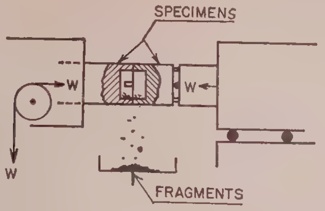

FIG. 5. Apparatus for producing loose wear particles.

we put

$$\sigma_r^2/\sigma_{yp}^2=\nu^2=\tfrac{1}{10}, \tag{9}$$

where σ_{yp} is the yield stress of the material in compression and ν its Poisson's ratio, we find

$$d=60EW_{ab}/\sigma_{yp}^2. \tag{10}$$

It has been found that σ_{yp} is about $\frac{1}{3}$ the hardness p, and moreover, that σ_{yp}/E is about 3.10^{-3} for many materials. Hence we may write

$$d=60\,000W_{ab}/p. \tag{11}$$

This, then, is a relation between a measurable quantity (the diameter of loose wear particles) and W_{ab} which involves no unknown quantities, and may thus be checked experimentally.

Equation (11) is unusual in that the nondimensional constant which appears in it is surprisingly large. The 1/60 000 with which d must be multiplied to obtain W_{ab}/p is made up of a factor of $\frac{1}{10}$ representing ν^2; a factor of $\frac{1}{2}$ for the energy expression, a factor of $\frac{1}{3}$ being the shape factor for a hemispherical particle; another factor of $\frac{1}{3}$ corresponding to the σ_{yp}/p ratio; and, finally, a factor of 1/333 representing the maximum elastic strain. Owing to the successive multiplications, the small W_{ab}/p distance is amplified into a quantity, namely, the wear particle diameter, which takes on considerable size.

It should be noted that the quantity W_{ab}/p has entered both into Eq. (6) and into Eq. (11). It is my belief that this quantity is an important parameter which governs a number of frictional phenomena. It, therefore, deserves close study.

EXPERIMENTAL VERIFICATION OF THE LOOSE WEAR FORMULA

In my earlier paper on the size of loose wear particles, I gave some data on the variations of the wear particle size produced by varying the mechanical properties of zinc as a result of heating it close to its melting point. It seemed worthwhile to confirm Eq. (11) more definitely by carrying out a comprehensive series of tests, and for these we used a wear tester in which a fixed annular specimen is pressed against another annular specimen which is mounted in the chuck of a lathe (Fig. 5). Wear fragments fall out of the sliding zone through slots in the annular specimens and are collected for later examination.

The first problem which arose was that of deriving from each collection of wear particles a typical particle diameter, which could be substituted in Eq. (11). It was found most expedient in the case of most of the collections of wear particles to sort out the particles in a set of sieves, and to define an average particle as that particle which has all the particles heavier than it equal in weight to all those particles lighter than it. The "diameter" of the particle is assumed to be the opening of a sieve which would just let the particle through. In most cases, repeat wear tests give values of the average particle diameter as defined above which differ by 10% or less from previously obtained values.

In the case of the smallest particles, the average particle size had to be determined by inspection of the fragments in a microscope, but this method is of inherently smaller accuracy.

RESULTS OF LOOSE WEAR PARTICLE EXPERIMENTS

After satisfying ourselves that the average wear particle diameters were reproducible and substantially independent of load and speed of sliding, we carried out tests on a wide variety of metals and a few nonmetals. The results are shown in Fig. 6, which plots the observed average fragment diameter against the W/p ratio. The straight line has been drawn to fit Eq. (11) and seems to fit the data quite satisfactorily. It may be noted that the average wear rate was found not to be a simple function of hardness, and some soft metal combinations gave very low wear rates. However, each wear particle was then very large.

It might be argued that it is more satisfactory to use Eq. (10) than Eq. (11), which is based on it, and constitutes a fairly severe approximation. However, Eq. (11) is so much more convenient to use, since the hardness can be readily measured while the elastic limit in compression cannot, that we have decided to use it wherever possible.

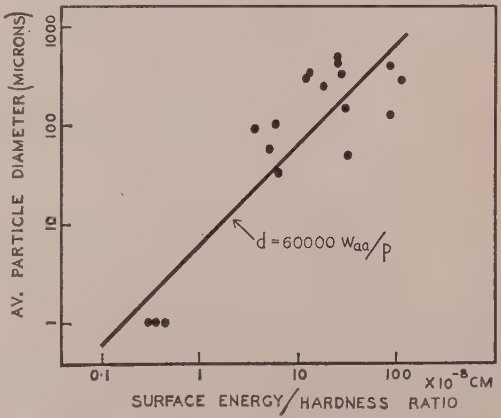

FIG. 6. Plot of average wear particle diameter against W_{aa}/p ratio for metallic and nonmetallic particles. Load 2000 g, speed 11 cm/sec.

A peculiar situation was observed with some metals, of which low-carbon steel was typical. During sliding, there were intervals, often lasting for several hours, when most of the wear debris was in the form of steel fragments of an average diameter $60\,\mu$, and then periods of several hours during which oxide particles of diameter $1\,\mu$ were formed. The same behavior was observed with aluminum. Apparently, Eq. (11) applies to the oxide and to the metal, in each case for values of W_{aa} and p characteristic of the material making up the wear debris. There is evidence to suggest that the metal/oxide ratio is determined partly by chance (random effects), partly by moisture content of the air, and partly by the load and speed.

When a lubricant is used, the fragments observed are much smaller in size than for the unlubricated metals, suggesting that W_{aa} is also smaller.

All the observations discussed above were obtained with like sliding combinations. When unlike metals are slid together, the wear particles are smaller. For example, when copper is slid on mild steel, the average wear particle size of the copper is $100\,\mu$, as against $240\,\mu$ for copper on copper. This suggests that W_{ab} is smaller in about the same ratio.

This experiment in which copper is run against a low-carbon steel allows us to make a comparison of the sizes of loose and of adherent wear particles, since the size distribution of adherent copper fragments on a low carbon steel surface has been previously published.[9] The adherent fragments, average diameter $45\,\mu$, are smaller in diameter by a factor of about 2, and hence smaller in volume by a factor of about 8. This suggests that a number of adherent copper fragments form on top of each other, before a fragment is formed which is sufficiently large to be removed. Direct observations of such particle accumulation have been described by Kerridge and Lancaster[10] and by Cocks.[11]

DISCUSSION

In this paper, we have proposed that the work of adhesion W_{ab} is an important characteristic of surfaces in sliding contact, and that it usually enters quantitatively into friction and wear expressions as the ratio W_{ab}/p or some equivalent formulation. Illustrations of the utility of this ratio have been drawn from the fields of friction and of wear.

It is of interest to note that the concept of work of adhesion has a long and successful history in the theory of lubrication. As early as 1925, Bachman and Brieger[12] postulated that the lubricant with the largest work of adhesion against a metal surface made the most effective lubricant. This was later interpreted to mean that a large work of adhesion implied strong lubricant-to-surface bonds, and thus good resistance to the removal of the lubricants by shear during sliding. However, our hypothesis would regard a high work of adhesion of a lubricant against a surface as being important in that it leads to a low work of adhesion when two lubricated surfaces are placed in contact.

Besides friction, wear, and lubrication, the work of adhesion concept would seem to be applicable to studies of adhesion. Indium and, to a lesser extent, lead adhere at room temperature; these are, of the metals stable in air, the ones with the highest W_{aa}/p ratios. Other metals must be heated till they soften before they adhere well,[13] and this suggests again that a minimum W/p ratio is required. Recently, Rarety and Tabor[14] have shown that the strength of adhesion of various organic materials against ice correlates positively with their work of adhesion. One of the reasons these authors give for dismissing this relationship is that the strength of adhesion and the work of adhesion do not vary in direct proportion. However, Eq. (5) in this paper shows that this kind of behavior may readily arise.

Finally, we must draw attention to one complicating factor; namely, the so-called size effect, whereby specimens of small volume appear to be stronger—often much stronger—than specimens of normal size. This effect has been ascribed to the low probability of finding enough dislocations in the small specimens. As far as surface energy effects are concerned, this means that relations such as Eq. (10) should be written in the form

$$d=60EW_{ab}/\sigma_{yp}(d). \qquad (12)$$

Depending on the way the yield strength varies with fragment size, this equation may have solutions over a wide range of fragment diameters. This effect helps to explain the range of sizes of wear particles observed during one experiment.

ACKNOWLEDGMENTS

I am indebted to the Office of Ordnance Research, U. S. Army, for sponsorship of this work under project DA-19-020-ORD-4706. My thanks are also due to Laurence Dunn and James U. Purdy, who carried out much of the experimental work on the size distribution of wear particles.

---

[9] E. Rabinowicz, Proc. Phys. Soc. (London) **66**, 929 (1953).

[10] M. Kerridge and J. K. Lancaster, Proc. Roy. Soc. (London) **A236**, 250 (1956).

[11] M. Cocks, J. Appl. Phys. **29**, 1609 (1958).

[12] W. Bachmann and C. Brieger, Kolloid-Z., spec. No., 142 (1925).

[13] F. P. Bowden and G. W. Rowe, Proc. Roy. Soc. (London) **233**, 429 (1956).

[14] L. E. Rarety and D. Tabor, Proc. Roy. Soc. (London) **A245**, 184 (1958).

JOURNAL OF APPLIED PHYSICS VOLUME 32, NUMBER 8 AUGUST, 1961

Lubrication of Polymers

C. RUBENSTEIN*
The British Cotton Industry Research Association, Shirley Institute, Manchester, England

Previous work on the lubrication of polymers is reviewed and the explanations which have been advanced are examined and are shown to be inadequate. An alternative mechanism of polymer lubrication is proposed which is based on the hypothesis that when a lubricant is applied to a polymer it is possible for the lubricant molecules to penetrate the polymer and alter its mechanical properties. An investigation into the lubrication behavior of textile polymers is described and an explanation of the results of this and other investigations is offered in terms of the proposed mechanism.

INTRODUCTION

In contrast to the numerous investigations into the mechanism of the boundary lubrication of metals[1–5] there has been relatively little work done to elucidate the mechanism of the boundary lubrication of polymers. Moss[6] and Röder[7] have applied different lubricants to yarns and fibers and, more recently, Lyne[8] has investigated the effect of varying the amount and the viscosity of white oils applied to cellulose acetate yarn. Pascoe[9] (quoted by Tabor[10]) has investigated the lubrication of nylon and polythene by fatty acids and finds only a slight reduction in friction. This agrees with the results obtained by Zisman *et al.*[11] who concluded that nylon was difficult to lubricate efficiently as compared with metals.

The mechanism of the boundary lubrication of metals may be summarized by the equation

$$F=A\{\alpha S_0+(1-\alpha)S_L\},$$

where F is the frictional force, A is the true area of contact, α is the fraction of the true area at which intermetallic contact occurs, S_0 is the shear strength of the intermetallic contacts, and S_L is the shear strength of the lubricant film. Thus the effective shear strength

$$S_E=\alpha S_0+(1-\alpha)S_L. \qquad (1)$$

Now the area of contact is related to the normal load L by the equation

$$L=p_0A,$$

where p_0 is the hardness pressure and therefore

$$\mu=F/L=\alpha S_0/p_0+(1-\alpha)S_L/p_0. \qquad (2)$$

An effective lubricant is one which can maintain α as low as possible and for which the shear strength S_L is low. Hence, in order that α shall be low, the lubricant molecules should be firmly attached to the underlying surface and the molecules should have strong lateral adhesion. In order that S_L, and hence S_E, should be as small as possible the lubricant should be easily sheared.

Attempts have been made to explain the behavior of lubricated polymers by applying these ideas. Thus, Pascoe accounts for the difference between polymers and metals as follows: The low friction occurring when metals are lubricated by fatty acids arises from the fact that the shear strength of the lubricant film is considerably less than that of the metal; with polymers, however, the lubricant layer consists of long chain molecules which are similar to those of the underlying polymer. Hence, even if the lubricant is present as a strongly adsorbed film, its shear strength will not be very different from that of the underlying polymer. In terms of Eq. (2) Pascoe's suggestion is that while for metals $S_L<S_0$, for polymers $S_L\simeq S_0$ and therefore for these latter materials

$$\mu\simeq S_L/p_0\simeq S_0/p_0.$$

Pascoe's suggestion overlooks the fact that while for most metals (save possibly the very softest) $S_0>S_L$, it is only with reactive metals that fatty acids are effective lubricants. Thus, effective lubrication is not simply a consequence of the inequality $S_0>S_L$ as implied by Pascoe.

An alternative suggestion advanced by Zisman *et al.*[11] to account for the difficulty of lubricating nylon efficiently is that with nylon there are relatively few adsorption sites available, so that it is not possible for a lubricant film to be adsorbed which is sufficiently condensed to prevent polymer-polymer contact, whence there results only a comparatively slight reduction in friction. Zisman *et al.* suggest that when steel slides on nylon it is possible for a condensed film of lubricant to be adsorbed on the metal surface so that more effective lubrication is possible. In support, Zisman *et al.* showed that the static coefficient of friction of steel on nylon was always lower than that of nylon on nylon when each of 16 lubricants was applied. This evidence is inadequate, however, for even in the absence of lubricant the static coefficient of friction of steel on nylon

---

* Present address: Jackson Brothers (of Knottingley) Ltd., Headland Glassworks, Knottingley, Yorkshire, England.

[1] F. P. Bowden, J. N. Gregory, and D. Tabor, Nature **156**, 97 (1945).

[2] F. P. Bowden, and D. Tabor, *The Friction and Lubrication of Solids* (Oxford University Press, New York, 1950).

[3] E. B. Greenhill, Trans. Faraday Soc. **45**, 631 (1949).

[4] E. D. Tingle, Trans. Faraday Soc. **46**, 93 (1950).

[5] R. L. Cottington, E. G. Shafrin, and W. A. Zisman, J. Phys. Chem. **62**, 513 (1958).

[6] E. Moss, Brit. J. Appl. Phys. Suppl. No. 1, **2**, 19 (1951).

[7] H. L. Röder, J. Textile Inst. Trans. **44**, 256 (1953).

[8] D. G. Lyne, J. Textile Inst. Proc. **46**, 112 (1955).

[9] M. W. Pascoe, Ph.D. dissertation, Cambridge, England, 1954.

[10] D. Tabor, Wear **1**, 5 (1957).

[11] R. C. Bowers, W. C. Clinton, and W. A. Zisman, Ind. Eng. Chem. **46**, 2416 (1954).

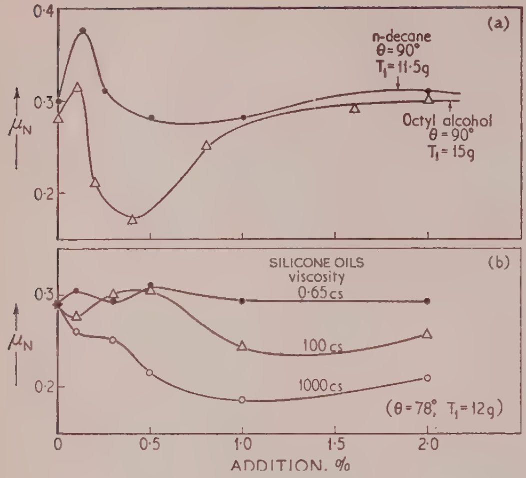

FIG. 1. Friction-addition curves for 15-denier nylon monofilament yarn lubricated with *n*-decane, octyl alcohol, and silicone oil—viscosities 0.65, 100, 1000 centistokes. For explanation of μ_N, θ, T_1 see reference 28.

was less than that of nylon on nylon. A further point in this proposed mechanism is the implication that lubricant molecules are adsorbed on nylon exclusively via hydrogen bonding, for Zisman *et al.* only consider the amide groups in the nylon molecule as adsorption sites, ignoring the possibility of adsorption by nonpolar van der Waals forces at the ethylene groups in the nylon molecule. There can be little doubt, however, that in some instances at least, adsorption by nonpolar van der Waals forces occurs (e.g., Finch[12]). From this it appears that the relatively wide separation of the amide radicals in the nylon molecule does not, in itself, obviate the possibility of a close-packed lubricant film occurring on the surface of nylon.

Thus it is obvious that previously proposed mechanisms of polymer lubrication are far from satisfactory, and the purpose of the present work is to offer an alternative suggestion more in accordance with the facts.

CRUCIAL EXPERIMENTAL DATA

There are two experimental observations which any theory of polymer lubrication must explain. First, the application of a "lubricant" can increase the coefficient of friction of a polymer. This has been reported by Zisman *et al.*[11] who quote the data given in Table I for nylon. This observation has been confirmed by the present author with nylon lubricated with *n*-decane, octyl alcohol, and a low-viscosity silicone oil (Fig. 1).

TABLE I. Data for nylon.

Lubricant	μ
None	0.46
Water	0.52
Ethylene glycol	0.58
Perfluorolube oil	0.58

Second, the application of a "lubricant" can increase the wear of a polymer. Thus, when a nylon yarn lubricated with up to 1% by weight of octyl alcohol was drawn round a smooth glass cylinder there was a pronounced squeak audible and an opaque layer of white material was deposited on the rod. This layer was firmly attached to the rod and proved to be insoluble in common organic solvents (which were capable of dissolving octyl alcohol) but it was soluble in meta-cresol, a solvent for nylon 66. Although the coefficient of friction of unlubricated nylon was only slightly lower, there was no deposition of material in this case. Similarly, with Terylene lubricated with a series of fatty alcohols a visible layer was deposited on the glass rod.

THE HYPOTHESIS

These results are in marked contrast to those obtained with metals and it is hardly surprising to find that the mechanism advanced to account for the boundary lubrication of metals cannot account for these results. With a view to explaining these phenomena, it will be instructive to consider what assumptions are made when, as in previously proposed explanations, it is suggested that the mechanism of the boundary lubrication of metals is applicable to polymers. These may be listed conveniently as follows:

(1) The frictional resistance in both cases arises from adhesion at those regions in intimate contact. The work of Shooter and Tabor[13] justifies this assumption being applied to polymers.

(2) Boundary lubrication in both cases is effected by an adsorbed layer of lubricant molecules. The work of Zisman and co-workers[11,14] justifies this assumption being applied to polymers.

(3) The mechanical properties of the underlying materials are unaffected by the lubricant. This is a reasonable assumption in the case of metals but is unjustified in the case of polymers for the following reasons. First, it has been shown that when, in particular instances, polymers are immersed in solutions, preferential sorption of solute occurs via a diffusion process[15–18] (which is the mechanism of the direct

---

[12] G. I. Finch, J. Chem. Soc. **1938**, 1137.

[13] K. V. Shooter and D. Tabor, Proc. Phys. Soc. (London) **B65**, 661 (1952).

[14] A. H. Ellison and W. A. Zisman, J. Phys. Chem. **58**, 260 (1954).

[15] S. M. Neale, J. Text. Inst. Trans. **20**, 373 (1929).

[16] R. J. B. Marsden and A. R. Urquhart, J. Text. Inst. Trans. **33**, 105 (1942).

[17] M. V. Forward and H. J. Palmer, J. Text. Inst. Trans. **45**, 510 (1954).

[18] W. J. Roff, J. Text. Inst. Trans. **50**, 353 (1959).

dyeing process with textile polymers[19–22]). Again, pure liquids have been shown to penetrate and swell polymers.[23–26] When this happens, the polymer becomes "plasticized." For these reasons it is intended to explore the potentialities of a hypothesis which makes, in place of assumption (3), the assumption that when a lubricant is applied to the surface of a polymer it is possible for the lubricant molecules to penetrate the amorphous regions of the polymer and, by weakening the interchain forces, the bulk properties of the polymer may be altered. In particular, it is suggested, *the application of a lubricant can reduce the hardness p_0 and the shear strength S_0 of the polymer.*

DEDUCTIONS FROM THE HYPOTHESIS

Assuming the validity of the hypothesis we see, immediately, that the distinction in behavior after lubrication exists not between polymers and metals, specifically, but between permeable and impermeable materials. With impermeable materials the application of a lubricant will reduce the shear strength of the contacting regions by ensuring that α and S_L are as small as possible, but the hardness of the load-bearing regions of the sliding members (and hence, the area of contact) will be unaffected. Thus the reduction in the shear strength from S_0 to S_E [Eq. (1)] produces a reduction in the coefficient of friction.

With a material which is capable of being penetrated and softened by a lubricant (e.g., a polymer) the situation is different. In the unlubricated state its shear strength will be S_0 and its hardness p_0. If, due to lubricant penetration, the polymer softens, then S_0 is reduced to S, p_0 is reduced to p and the coefficient of friction of the lubricated polymer will be

$$\mu=\alpha S/p+(1-\alpha)S_L/p.$$

Since S and p are interrelated strength properties, it may well be that S/p is not very different from S_0/p_0, but S_L/p will increase as p decreases due to softening. Thus any reduction in friction which may occur as a consequence of a reduction in S_E will be offset by an increase in friction resulting from softening. Hence, the lubrication of polymers will tend to be relatively ineffective, in agreement with the experimental observations of Pascoe and of Zisman *et al.*

It follows immediately that it is possible for the increase in friction resulting from softening (the softening effect) to outweigh the reduction in friction produced by the lowering of the shear strength (the lubricating effect). If this happens, then the coefficient of friction of the lubricated polymer will exceed that of the unlubricated polymer and, as we have seen, this phenomenon has been observed experimentally. Again, the hypothesis suggests that the reduction in the strength properties attendant on softening should tend to produce behavior similar to that of soft, ductile metals and in this connection the wear phenomena reported above are reminiscent of the transfer wear characteristic of, for example, indium or lead.

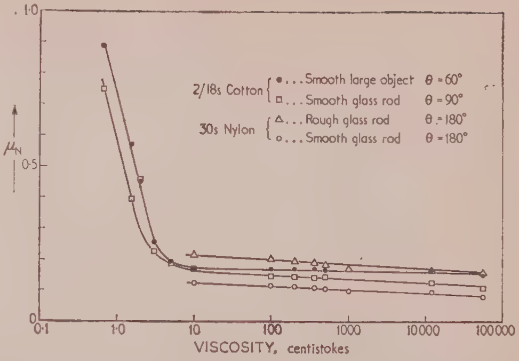

FIG. 2. The variation of the coefficient of friction of 2/18s cotton and 30s spun nylon yarns (lubricated with 2% of a series of silicone oils), with lubricant viscosity.

It can be seen that the hypothesis is capable of explaining the two sets of results which are considered crucial to any theory of polymer lubrication. In the following it will be shown that it enables a plausible explanation of the effects of lubricant chain length and of lubricant addition to be offered.

INFLUENCE OF LUBRICANT CHAIN LENGTH

Generally, high frictional resistance and severe surface damage occur when sliding surfaces come into contact with each other and if the separation of the surfaces can be increased by the interposition of an easily sheared layer, then it may be expected that the friction and surface damage will be reduced. One way of increasing the separation of the surface is to increase the chain length of the lubricant molecules.

Investigations into the lubrication of impervious materials[2,27] have revealed that increasing the lubricant chain length (by progression through a homologous series) produces a reduction both in the coefficient of friction and in the surface damage over a limited range of chain lengths. Further increase in chain length beyond a particular point (which depends on the lubricant and the sliding surface material) effects no further benefit. Although this has been observed with impervious materials, there is no reason, provided the lubricant molecules form an orientated surface layer,

---

[19] S. M. Neale and W. A. Stringfellow, Trans. Faraday Soc. **29**, 1167 (1933).

[20] J. Boulton and T. H. Morton, J. Soc. Dyers Colourists **56**, 145 (1940).

[21] H. A. Standing, Trans. Faraday Soc. **41**, 410 (1945).

[22] T. Vickerstaff, *The Physical Chemistry of Dyeing* (Oliver and Boyd, London and Edinburgh, 1950).

[23] H. Staudinger, Trans. Faraday Soc. **32**, 323 (1936).

[24] A. J. Stamm and H. Tarkow, J. Phys. Chem. **54**, 745 (1950).

[25] H. J. Palmer, J. Text. Inst. Trans. **45**, 539 (1954).

[26] P. H. Hermans, *Physics and Chemistry of Cellulose Fibers* (Elsevier Publishing Company, Inc., New York, 1949).

[27] W. A. Zisman, *Friction and Wear*, edited by R. Davies (Elsevier Publishing Company, Inc., New York, 1959), p. 110.

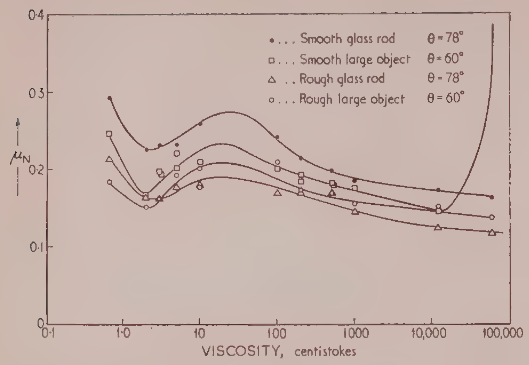

FIG. 3. The variation of the coefficient of friction of 15-denier nylon monofilament yarn (lubricated with 1% of a series of silicone oils) with lubricant viscosity.

why this effect should not occur with materials which are permeable to lubricants. With these materials, however, a second effect, dependent on lubricant chain length can be expected to occur, viz., as the chain length increases it should become progressively more difficult for the lubricant molecules to penetrate the polymer. Hence, any softening produced by the application of a homologous series should tend to decrease as the chain length increases. These effects supplement each other so that with polymers, as with impervious solids, progression through a homologous series of chemical compounds should result in a decrease in the coefficient of friction. Generally this has been confirmed; for example, Fig. 2 shows the monotonic reduction in the nominal coefficient of friction[28] μ_N of cotton and nylon lubricated with 2% of a series of silicone oils[29] as the viscosity increases. For these oils, Barry[30] has shown that the logarithm of the viscosity varies linearly with the square root of the chain length for oils of viscosity greater than 40 centistokes so that Fig. 2 is, effectively, a μ_N-chain length characteristic. While this is a typical example of the variation of μ_N with chain length obtained with spun yarns, quite a different characteristic was obtained with nylon monofilament lubricated with 1% of a series of silicone oils (Fig. 3). Here μ_N first decreases then increases and finally decreases as the chain length of the lubricant increases. It seems unlikely that these curves arise from any complexity in the lubricating effect; on the other hand, there exists experimental evidence from which it may be inferred that the softening effect could be complex. It has been assumed that as lubricant penetration and plasticization increases so also does softening and swelling of the polymer so that the filament diameter may be regarded as an index of the amount of softening. Hence, any complexity in, for example, the diameter-addition curve should be reflected in the μ_N-addition curve; this has been observed experimentally [Fig. 4(a), (b)]. For these reasons, the diameters of samples of the yarns used to obtain Fig. 3 were measured with a microscope and the results show that the diameter first increases and then decreases as the viscosity (i.e., chain length) increases (Fig. 5). If, in the light of Fig. 4, it be assumed that the softening effect varies with viscosity in a similar way, then it follows that the μ_N-viscosity relation of Fig. 3 results from a combination of characteristics similar to those idealized in Fig. 6. Depending on the relative importance of each of these factors, a variety of μ_N-viscosity curves could result from such a combination, one obvious shape being that shown in Fig. 3.

So far consideration of the effects of lubricant chain length has been restricted to cases where the amount of lubricant present on the yarn has remained fixed. In the remainder of this section the result of changing also the amount of lubricant on the yarn will be considered. In producing specimens from which these friction-addition curves were obtained, all the yarns were immersed in solutions of the lubricants for approximately the same period of time and to apply more lubricant to the yarn the strength of the solution was increased. Since lubricant penetration must take place by a diffusion process, it may be expected that, generally, as more lubricant is applied to the yarn the amount of lubricant which has penetrated a given distance and, consequently, the degree of softening will increase which, in turn, can be expected to tend to

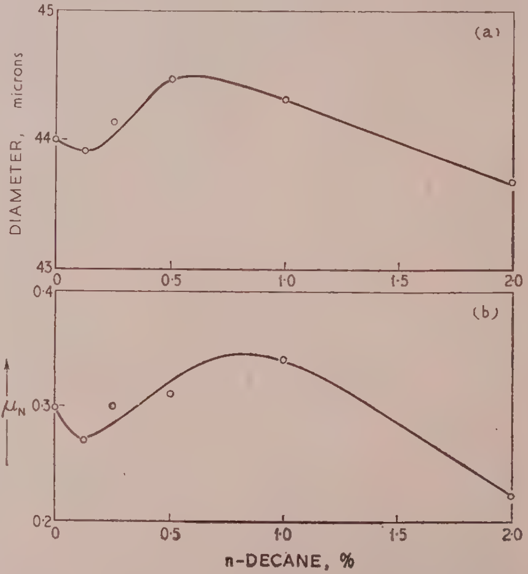

FIG. 4. (a) The variation in the diameter and (b) the variation in the friction of aged specimens of 15-denier nylon monofilament yarn lubricated with *n*-decane.

---

[28] μ_N is calculated from the equation $T_2/T_1 = e^{\mu_N \theta}$, where T_1, T_2, are the on-going and off-going tensions, respectively, in a string which traverses transversely a cylindrical bollard for an angle of lap θ.

[29] These silicone oils are polydimethylsiloxanes.

[30] A. J. Barry, J. Appl. Phys. **17**, 1020 (1946).

produce an increase in the coefficient of friction. At the same time an increase in the amount of lubricant on the surface should reduce the coefficient of friction by virtue of the "lubricating" effect. Once again, therefore, the effect is a composite one being compounded of two mutually opposed factors.

The friction-addition curves obtained with nylon monofilament yarn lubricated with *n*-decane and with octyl alcohol are shown in Fig. 1; it is suggested that the undulatory nature of the curves is due to a corresponding variation in the softening effect with lubricant addition. Figure 1 also shows μ_N-addition curves for nylon monofilament yarn lubricated with three different silicone oils and the change in shape as the chain length of the oil is increased can readily be seen.

A particular feature of the curves shown in Fig. 1 worth mentioning is the ultimate increase in the coefficient of friction with increase in addition. It has already been suggested that after the percentage addition has reached a certain value, further addition will not add to the lubricating effect. If, at this stage, the softening effect has not reached its maximum, then further increase in addition will increase the coefficient of friction on this account. Provided the lubricant is not a solvent for the material, it follows that softening cannot proceed indefinitely and, consequently, the rise in the friction-addition curve will ultimately cease. To verify this, samples of nylon monofilament yarn were lubricated with 4% and 8% of octyl alcohol when it was found that the coefficient of friction remained constant at 0.30 (the value obtained with 2% addition).

Supplementary Evidence. The Friction Index *n*

Elsewhere,[31] a power-law relation between the fictional force F and the normal load L, viz., $F=CL^\beta$, has been derived. In this it was assumed that the stress (σ)-strain (ϵ) curve of the material in compression could be expressed as $\sigma=b\epsilon^x$, where b is the stress-strain modulus and x is the stress-strain index. For a material which obeys the friction law $F=CL^\beta$, the relation between the on-going tension T_1, and the off-going tension T_2 in a string of the material traversing a cylindrical bollard of radius ρ for an angle of lap θ is

$$T_2^{1-n}-T_1^{1-n}=K(1-n)\rho^{1-n}\theta,$$

where the parameter K depends, *inter alia*, on the shear strength of the contacting material and on the roughness of the contact while the index n depends primarily on x. Now if a highly cross-linked polymer is subjected to a stress, then, provided the interchain bonds are not ruptured, the deformation of the material will be largely elastic, the stress-strain index will tend to be high and n correspondingly low. If, on the other hand, the cross-linkage is greatly reduced, e.g., because of penetration by a lubricant, then the application of a stress will cause the chainlike molecules to slip past each other, giving rise to delayed elastic and viscous deformation, i.e., the stress-strain index will decrease and, therefore, n will increase.

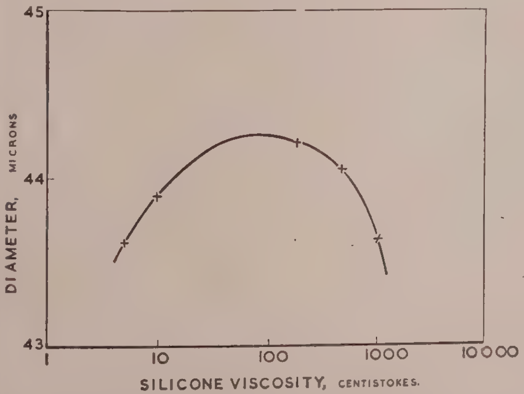

FIG. 5. The diameter of 15-denier nylon monofilament yarn lubricated with 1% silicone oil (applied from solution in carbon tetrachloride), plotted against silicone viscosity.

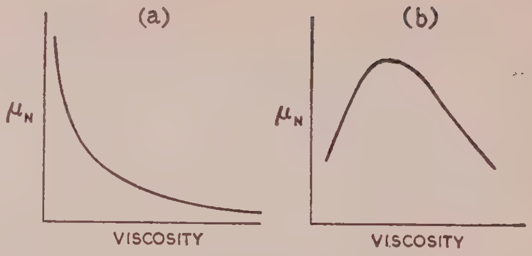

FIG. 6. Idealized friction-viscosity characteristics for (a) the lubricating effect; (b) the softening effect.

Thus, it follows, *ex hypothesi*, that the application of a lubricant which is capable of penetrating a polymer should produce an increase in the friction index of the polymer, the size of the increase depending on the ability of the lubricant to penetrate and "plasticize" the polymer. Now previously,[32] with nylon monofilament yarn lubricated with the normal production finish and running against smooth glass at 32 cm/sec the value of $n=0.76$ was obtained. In the present work the following values of n were obtained for similar yarn lubricated with (1) oleic acid, $n=0.90$, and (2) silicone oils, $n=0.83$. Since the value of n depends on the value of the stress-strain index,[33] the fact that n varies according to which lubricant is applied indicates that the application of a lubricant can change the deformation properties of the polymer and, as such, these results are evidence in support of the hypothesis.

CONCLUSION

The softening hypothesis advanced in this paper has been shown to account for the increased friction and wear which may occur when a lubricant is applied to a polymer. Where the softening effect supplements the lubricating effect (i.e., with cotton and, to a lesser extent, with spun nylon) the behavior is similar to that of impervious materials and can be explained without invoking the softening, or any other, mechanism. Such, however, is not the case with nylon monofilament, the behavior of which cannot be accounted for in terms of the lubricating effect acting alone. At this stage, it is desirable that this hypothesis be regarded as no more than a plausible, working hypothesis which enables us to offer an explanation of boundary lubrication embracing the behavior of metals, impervious nonmetals and polymers.

---

[31] C. Rubenstein, Proc. Phys. Soc. (London) **B69**, 921 (1956).

[32] C. Rubenstein, J. Text. Inst. Trans. **49**, 181 (1958).

[33] C. Rubenstein, J. Text. Inst. Trans. **49**, 13 (1958).

JOURNAL OF APPLIED PHYSICS VOLUME 32, NUMBER 8 AUGUST, 1961

Frictional Behavior of a Simple Rheological Material

R. T. Spurr
Ferodo Limited, Chapel-en-le-Frith, Stockport, England

Simple experiments made on a hard bitumen support the adhesion theory of friction. The static friction of the bitumen depends upon its rheological properties, and for hemispherical specimens, μ_s is determined by the shear strength and flow pressure of the bitumen, the latter being obtained from identation measurements. For nominally flat specimens, the time and temperature dependence of μ_s can be determined from indentation measurements. At low sliding speeds the dynamic friction can be related to the static friction, and to the rheological properties of the bitumen; at higher speeds frictional heating complicates interpretation of results.

INTRODUCTION

ONE of the ultimate aims of work on friction is to relate quantitatively the frictional behavior of a material with its physical properties and the sliding conditions. There are two obvious methods of approach to this problem—the friction and the relevant physical properties of a wide range of materials can be measured and a search made for relationships, or alternatively one material can be used and the variation of its frictional with its other properties studied over as wide a range of conditions as practicable. The μ of a hard bitumen (Mexphalte H80/90) depends markedly upon the conditions of testing (values obtained range from 0.1 to 32), varying with load, velocity, temperature, and surface condition, and is therefore a very suitable material to permit the second method to be used. The frictional behavior of this bitumen, together with its rheological behavior, has therefore been studied.

ADHESION THEORY OF FRICTION

The basic assumption of the adhesion theory of friction is that the relationship $F=SA$ applies, where F is the force of friction, A the true area of contact, and S the "shear strength" of the adhesive junctions formed between the two surfaces at the real areas of contact. This relationship can be verified by using different contaminants on the surface of a flat specimen when S can be altered without at the same time changing A, which depends upon load alone provided no junction growth occurs. Consequently, if F is measured at various loads with different contaminants and F plotted against L on a log-log scale, a series of parallel curves should be obtained, one for each of the contaminants used. This experiment was done with the bitumen, the static friction being measured on a clean and on a contaminated plate. Provided the contaminant film remained intact, the curves were parallel.

If a bitumen specimen is left in contact with a clean metal plate, adhesion occurs. The longer the specimen is loaded against the plate the greater the adhesion becomes, the areas of contact growing through creep. Flat specimens were loaded under various loads against a polished metal plate for 30 sec and the friction measured with the load still applied (to obtain "μ_{on}") and with the load removed (to obtain "μ_{off}"). The normal adhesion was also measured. It was found that $\mu_{\text{off}}=K\sigma$, where σ is the ratio of adhesion to load and that $\mu_{\text{on}}>\mu_{\text{off}}$. The difference between μ_{on} and μ_{off} was due to elastic recovery occurring at the surface when the normal load was removed, this recovery tending to break the junctions. Thus, if the adhesive forces were made small compared with the elastic forces $\mu_{\text{on}}\gg\mu_{\text{off}}$ and, indeed, if the surface was sufficiently contaminated, $\mu_{\text{off}}=0$. In Fig. 1 μ_{off} is plotted against μ_{on} for varying amounts of plate contamination. Conversely, if the adhesive forces were made large compared with the elastic forces, for example, by permitting creep to occur for longer periods, μ_{off} approached μ_{on}. It appears, therefore, that the friction between the bitumen specimen and the metal plate is due to adhesion, and that when the normal load is removed the adhesion is in general reduced by elastic recovery, and if the surface is sufficiently contaminated the adhesion falls to zero.

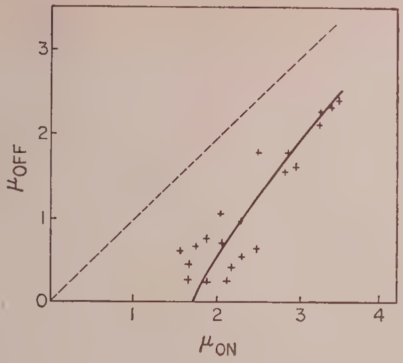

FIG. 1. μ_{off} plotted against μ_{on} for varying amounts of plate contamination.

With surfaces in general, the elastic recovery occurring on removing the load is sufficient to completely overcome the adhesion.

STATIC COEFFICIENT OF FRICTION

Not only does the static coefficient of friction μ_s of the bitumen depend upon the time the surfaces are in contact, but it also depends upon the normal load L. Over the experimental range of loads (100 to 4000 g) and times (5 to 1000 sec) used, μ_s is very well represented by the equation $\mu_s = KL^{-p}t^m$, where K, p, and m are constants, K and m depending upon the temperature of the specimen. Consequently $\mu_s = KL^{-p}t^m = SA/L$. The problems, therefore, are to measure, if possible, S and A and to predict the value of the constants K, p, and m.

In general it is very difficult to measure the real area of contact A directly, but in the case of hemispherical specimens an estimate of A can be made. When a soft hemisphere is loaded against a flat glass surface the apparent area of contact is given by the equation $A' = L/P$ (where P is the Meyer hardness) and can be measured microscopically. The real area of contact is, however, much smaller than the apparent area, but when a tangential load is applied in addition to the normal load, the real areas under certain conditions grow in magnitude until the real and apparent contact areas are approximately equal when the specimen slides bodily over the surface.[1] Therefore, it would be expected that the limiting static coefficient of friction $\mu_s = SA/L$, where S is the shear strength of the specimen. Bitumen hemispheres ($\frac{3}{8}$ in. in diameter) were loaded against glass plates for various times and under various loads and the apparent areas of contact measured. The frictions were also measured. It was found that $\mu_s = KL^{-0.27}t^{0.25}$ and that $A/L = K'L^{-0.27}t^{0.25}$, that is, the indices in both sets of measurements were the same within the experimental error. The value of S was calculated from the equation $F = SA'$ and found to be about 0.15 kg/mm² whereas the measured value of the shear strength was 0.10 kg/mm² at 20°C.

The area of contact between a single hemisphere and flat surface is, in general, given by an equation of the form $A = KL^N$, with N ranging between $\frac{2}{3}$ for an elastic to 1 for a plastic material. Archard[2] has shown that if a surface is covered with an array of such hemispheres and each hemisphere is covered in turn by smaller hemispheres, then the total area of contact $A = K'L^N$ and $N \rightarrow 1$ as the surface becomes more and more complex. When $N = 1$, μ is independent of load. If a nominally flat surface of bitumen is considered covered by such hemispheres then μ_s should be proportional to L^{-p}, where p can have values from $\frac{1}{3}$ to 0 depending upon the complexity of the hemispherical arrays.

The variation of the static coefficient of friction of the bitumen with load was measured. There was considerable scatter and variation in the results; this is not surprising, for relaxation of the asperities occurred between measurements and the surface roughness of the specimen was not always the same. Surfaces run in at high speeds and temperatures so that they had a smooth highly flowed appearance generally acquired a curvature on relaxing and for such surfaces the index p was about $-\frac{1}{3}$. The μ of flat surfaces roughened by previous measurements, however, was independent of load. The apparent area of contact changed in the same way. On the run-in surfaces, contact occurred over one main contact zone which increased in area with increasing load, and the total area A was proportional to $L^{0.7}$, whereas with a suitably roughened specimen contact occurred at numerous sites and A was proportional to $L^{0.95}$ over the experimental range of loads. The dynamic friction was, in general, less load-dependent than the static friction. Measurements were also made on a very large specimen 10 sq cm in area made very flat and smooth by loading it while warm against a flat highly polished plate; for this specimen μ_s again was independent of load. The μ_s was dependent upon the time the surfaces were in contact; μ_s was proportional to t^m and the index m was about 0.2 at room temperature.

It appears, therefore, that the frictional behavior of flat specimens might be related to the indentation hardness of the bitumen and so the latter was examined in some detail. For convenience the penetration h of steel balls into bitumen surfaces was measured and not vice versa (though the stress distribution in the indented bitumen surface is not necessarily the same as that when a bitumen hemisphere deforms against a flat rigid surface).

For a constant time of loading the areas of contact of hemispheres of different diameter D ($\frac{1}{8}$ to 1 in.) were given, over the experimental range of loads 100–4000 g, by the Meyer formula $4L/\pi d^2 = K(d/D)^{n-2}$, where d is the diameter of the indentation. In the following, $4L/\pi d^2 = L/\pi Dh$ will be referred to as the flow pressure

---

[1] R. C. Parker and D. Hatch, Proc. Phys. Soc. (London) **B63**, 185 (1950).

[2] J. F. Archard, Proc. Roy. Soc. (London) **A243**, 190 (1957).

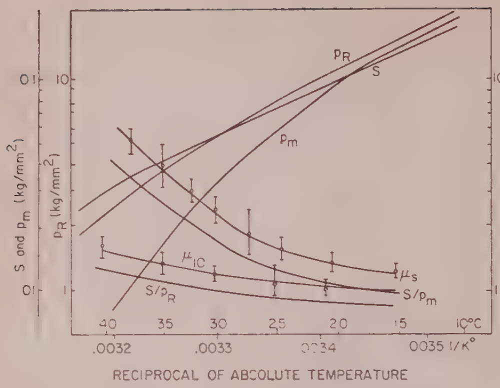

FIG. 2. Logarithm of friction, shear strength, and hardness plotted against reciprocal of the absolute temperature.

p_m. For the bitumen used $n=2.70$ (compared with 3 for an elastic material), so that $L=Eh^{1.35}D^{0.65}$, where E was about 10^8 dynes/cm^2 at room temperature. n did not alter appreciably with temperatures over the experimental range 0–40°C.

For all balls, h, and, therefore, the area of contact, was proportional to t^m, where t was the time for which the ball was applied (5 to 1000 sec). The index m was about 0.25 at room temperature, increasing to 0.40 at 35°C. The variation of penetration with temperature was measured over the temperature range $-30°$ to 40°C and E found to decrease markedly over this range.

Indentation measurements were also made for very short times of loading by dropping steel balls on to a bitumen slab lightly dusted with powder and measuring the diameter of the impression made. The rebound flow pressure p_R was calculated[3] from the equation $mgH=p_RV$, where V is the volume of the indentation formed by dropping a ball of mass m g from a height of H cm. p_R was 11.5 kg/mm^2 at 20°C when a $\frac{1}{4}$-in. ball weighing 1 g was dropped from 200 cm, whereas p_m (20-sec loading) was 0.10 kg/mm^2 at 20°C. The total time of impact, deduced[3] from the same equation, was 10^{-4} sec. The measured time of impact was of the same order, and was determined by dropping the balls on to fine wires with their ends just apart resting on the slab, one wire being connected directly to a cathode-ray oscilloscope, the other connected through an oscillator to the oscilloscope.

The relationship between the variations of μ_s with temperature and of penetration with temperature was investigated in more detail. μ_s was measured over the temperature range 15°–35°C using a load of 200 g applied for 20 sec, about a hundred measurements being made in all. Lower temperatures could not be used because of condensation on the specimen. The penetration of a $\frac{3}{8}$-in. ball into the bitumen specimen was measured for the same load, time, and temperatures, and the variation of shear strength of the bitumen measured in a simple grab over the same temperature range. In Fig. 2, logμ_s, logp_m, log$S$, and logS/p_m are plotted against the reciprocal of the absolute temperature K. The slopes of the various lines represent, in effect, the activation energies for the various deformations and it can be seen that the logμ_s and the logS/p_m curves are parallel. The time to shear the cylinders in the grab was much the same as that for shearing the junctions during a frictional measurement.

It can be seen that a good indication of the variation of μ_s with time and temperature can be obtained from indentation measurements made on the specimen and that the variation of μ with load can be plausibly accounted for.

DYNAMIC FRICTION

So far only the static friction of the bitumen has been discussed.

The transition from static to dynamic conditions is in general abrupt. If an increasing tangential force F is applied to a stationary specimen, sliding begins when F becomes greater than SA, but as the original junctions become progressively sheared the total area of contact becomes less as the new junctions formed have not the time to grow to the same area as the original ones. Consequently $F \gg SA$ and the specimen accelerates. If the surface over which the bitumen slid was perfectly smooth and flat and the bitumen did not wear, the original set of contact areas should persist and $\mu=\mu_s$, provided the shear strength was independent of the velocity. When, however, an actual specimen once sliding is made to slide at lower and lower speeds, μ progressively decreases and appears to tend to μ_s.

Examination of a well-bedded-in specimen shows that only a few centimeters of sliding are necessary for a large proportion of its surface to become covered with very fine scratches so that the contact areas must change very rapidly. It is reasonable to assume, therefore, that the life of an individual contact is inversely proportional to the velocity, although under some

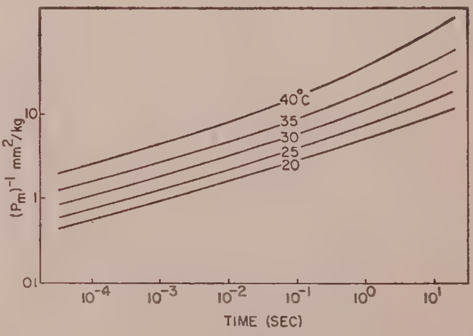

FIG. 3. Variation of log $(p_m)^{-1}$ with log time at various temperatures.

---

[3] D. Tabor, *The Hardness of Metals* (Oxford University Press, New York, 1951).

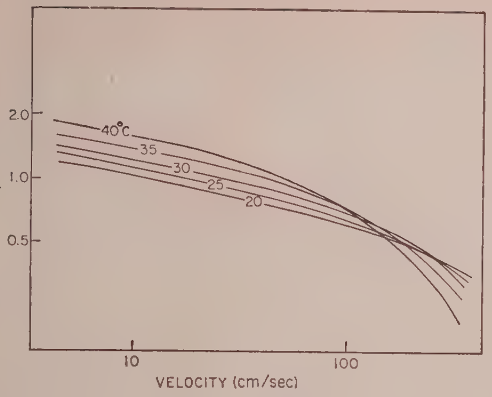

FIG. 4. Variation of log μ with log velocity at various temperatures.

conditions the life might depend upon the rpm of the disk or even the wear rate of the specimen.

At low sliding speeds $\mu=Kv^{-m}$, where m is about 0.20–0.25 but in the static case $\mu_s=Kt^m$, where m is again 0.25, which suggests that the only difference between μ_s and μ is that in the latter case the junctions have less time in which to grow. The value of μ for a 200-g load and a sliding speed of 10 cm/sec falls on the $\log\mu_s$ vs $\log t$ curve extrapolated to very small times at a time of 4×10^{-2} sec.

The equality of the indices suggests that the equation $p_m=p_0t^{-m}$ extends over many decades of time. The rheological behavior of the bitumen over a range of times and temperatures is shown qualitatively in Fig. 3, values of $(p_m)^{-1}$ for times of more than a few seconds being obtained by creep measurements, the variation of $(p_m)^{-1}$ with temperature for very small times by rebound measurements and for intermediate times by the superposition principle.[4] The curves shown, however, are only approximate owing to the times not being accurately known for the rebound measurements and to the difficulty of making creep and rebound measurements under equivalent loads, but they are in reasonable agreement with published data.[5] The curves suggest that at a given velocity the index m should be the same for all temperatures provided the velocity is high enough, and that the shear strength S is not dependent upon velocity.

The μ/v variation of the bitumen was therefore measured at various temperatures, the plate being heated electrically and the specimen left in contact with it until the required temperature was reached. It can be seen (Fig. 4) that at low speeds the slopes of the $\log\mu$ vs $\log v$ lines do not depend upon the temperature of the specimen. The variation of μ with temperature after the $\log\mu$ vs $\log v$ curves have become parallel should be similar to that of S/p_R, where p_R is the rebound hardness. Log (S/p_R) is shown plotted against the reciprocal of the absolute temperature in Fig. 2 and it can be seen that the curve obtained is parallel to the experimental $\log\mu$ curve. p_R was obtained by dropping a $\frac{1}{4}$-in. steel ball from a height of 200 cm.

At speeds above 50 cm/sec or so frictional heating of the specimen becomes important. Temperatures reached during sliding were measured using a small thermocouple inserted in the surface of the specimen. The temperature rise of the bitumen was approximately proportional to μv, but varied very slowly with normal load, presumably increasing the load, though it increased the rate of working μLv, also increased the real area of contact in such a way that the rate of working per unit area of contact was not altered. Bitumen has a very low thermal conductivity and consequently frictional heating produces a temperature gradient and a corresponding variation in physical properties at the rubbing face.

Frictional heating, provided no high-temperature gradients exist near the surface, should increase μ and so reduce the apparent μ-velocity variation, but if a temperature gradient is present the shear strength should be reduced more rapidly than the contact area is increased, and so μ should fall at high speeds and it can be seen (Fig. 4) that such is the case. The drop in shear strength can be demonstrated by loading a cold specimen against the rotating disk heated to relatively high temperatures, e.g., 80°C when the specimen wears rapidly, softened bitumen forming a lip at the trailing edge, and the μ is very low.

ACKNOWLEDGMENTS

The author wishes to thank T. P. Newcomb for his collaboration, and the Directors of Ferodo Ltd. for permission to publish.

---

[4] A. V. Tobolsky, in *Rheology*, edited by F. R. Eirich (Academic Press, Inc., New York, 1958), Vol. II, p. 63.

[5] C. Van der Poel, *Proceedings of the Second International Congress of Rheology*, edited by V. G. W. Harrison (Butterworths Scientific Publications, London, 1954), p. 331.

JOURNAL OF APPLIED PHYSICS VOLUME 32, NUMBER 8 AUGUST, 1961

Use of Graphite Whiskers in a Study of the Atmosphere Dependence of Graphite Friction*

F. R. Rollins, Jr.
Midwest Research Institute, Kansas City, Missouri

Several physical properties of graphite whiskers have been measured in ultra-high vacuum and other controlled atmospheres. The properties which have been studied include elasticity, electrical resistance, and cohesion between whiskers. The atmosphere dependence of these properties suggests that surface adsorption of contaminants is the most important factor in producing changes in graphite friction. There is some evidence that the adsorbed gases reduce surface roughness on an atomic scale. This ability of the adsorbed film to smooth out surface asperities may be used to explain some of the friction and wear characteristics of graphite.

I. INTRODUCTION

THE atmosphere dependence of graphite friction and wear has been established by a number of workers.[1-3] It has been conclusively shown that the high friction and wear exhibited by graphite in vacuum or dry nitrogen can be reduced by the introduction of oxygen, water vapor, or certain other gases. The exact mechanism by which these gases reduce graphite friction and wear has not been firmly established. Adsorption of gas molecules onto the graphite surface is most often used to explain this phenomenon.

In addition to the adsorption theory, there have been suggestions that the gases may penetrate the graphite lattice, perhaps even forming molecular compounds with graphite. The presence of the molecules or atoms in the lattice might then alter the physical properties of graphite. Evidence suggestive of such changes may be found in the atmosphere dependence of the transverse bend strength of graphite,[4] and in the way certain gases facilitate the orientation of graphite during the sliding process.[5]

The work reported here is aimed at a better understanding of the atmosphere dependence of graphite friction. Emphasis is placed on determining whether the dependence is strictly a result of surface adsorption or whether some volume diffusion and consequent physical change occurs. Evaluation of the latter effect would be difficult in a polycrystalline sample. Graphite whiskers, although not perfect single crystals, have a unique structure which facilitates the measurement of certain single crystal properties. The whisker properties which were considered are: (a) surface properties such as tensile and shear strength of cohesive bonds formed between two whiskers, and (b) volume properties such as elastic moduli and electrical resistance. This paper describes how these properties vary with the surrounding atmosphere.

II. GRAPHITE WHISKERS

The whiskers used in this investigation were grown by the methods of Bacon and Bowman.[6] Whiskers of this type have been studied by several workers,[7-9] and they are known to possess rather unique structural properties. Generally, the whiskers consist of graphite sheets rolled up like a scroll. While their cross section is not always circular, in this study only whiskers which did have a nearly circular cross section were used. In addition to their desirable geometry, these whiskers normally have a very smooth surface. Figure 1 shows an electron micrograph of the surface of a specially selected whisker. In addition to being very smooth, the whisker surface is everywhere tangent to the graphite basal plane. If two whiskers are placed in contact at right angles, intimate contact of the two basal planes may occur. The nature of these small contacts and certain other whisker properties have been studied during this investigation.

III. VACUUM SYSTEMS

Two different vacuum systems have been used during this study. One system utilizes an oil diffusion pump with a nitrogen cold-trap between the pump and the vacuum chamber. The ultimate vacuum obtained was about 10^{-6} mm Hg.

The second vacuum system utilizes a getter-type[10] pump with a pumping speed of 5 liters/sec. Figure 2 is a photograph of this system with one of the experimental chambers attached. The system has a total volume of less than 1 liter, and pressures of 10^{-9} mm Hg are attained after suitable bakeout. An adsorption pump[11] located under the table in Fig. 2 lowers the chamber pressure to the $20\,\mu$ Hg required to start the getter. The use of organic pump oils is thus completely

---

* This work was supported by the Office of Ordnance Research, U. S. Army.

[1] R. H. Savage, J. Appl. Phys. **19**, 1 (1948).

[2] W. E. Campbell and R. Kozak, Trans. ASME **70**, 491 (1948).

[3] F. P. Bowden, and J. E. Young, Proc. Roy. Soc. (London) **A208**, 444 (1951).

[4] R. J. Diefendorf, *Proceedings of the 4th Conference on Carbon* (Pergamon Press, New York, 1960), p. 489.

[5] R. O. Jenkins, Phil. Mag. **17**, 457 (1934).

[6] R. Bacon and J. C. Bowman, Bull. Am. Phys. Soc. **2**, 131 (1957).

[7] R. Bacon in *Growth and Perfection of Crystals*, edited by R. H. Doremus, B. W. Roberts, and D. Turnbull (John Wiley & Sons, Inc., New York, 1948), p. 197.

[8] R. Bacon, J. Appl. Phys. **31**, 283 (1960).

[9] P. J. Bryant, T. B. Daniel, and F. R. Rollins, Jr., J. Appl. Phys. **30**, 1839 (1951); P. J. Bryant, WADD Tech. Rept. 60-529 October, 1960.

[10] Varian Vac-ion.

[11] Varian Vac-sorb.

eliminated in the system and whisker contamination is held to a minimum. Gases are introduced into this system through a Granville-Phillips-type valve which can also be used as a controlled leak to establish pressures between 10^{-9} and 10^{-4} mm Hg.

IV. VOLUME PROPERTIES

A. Elastic Properties

The elastic properties of graphite whiskers were studied by two different methods. In both techniques, emphasis was placed on detection of moduli changes that might be caused by diffusion of gas molecules into the graphite lattice. Figure 3 illustrates one of the techniques used. A graphite whisker is shown cemented to a wire with the free end deflected downward by the weight of several small beads of diphenyl carbazide. In later tests, the diphenyl carbazide was replaced by small beads of silver paint so the whiskers could be outgassed at higher temperatures.

The nonhomogeneous anisotropic character of the graphite whiskers makes it difficult to relate the whisker deflection to single-crystal elastic constants. However, if the weight on the whisker and the temperature remain constant, a change in the free-end deflection would indicate a change in the "effective" elastic properties. This technique was only sensitive to deflection changes greater than $1\frac{1}{2}\%$. With this method, no significant change in whisker deflection was observed between conditions of high vacuum, saturated water vapor, or 1 atm of oxygen.

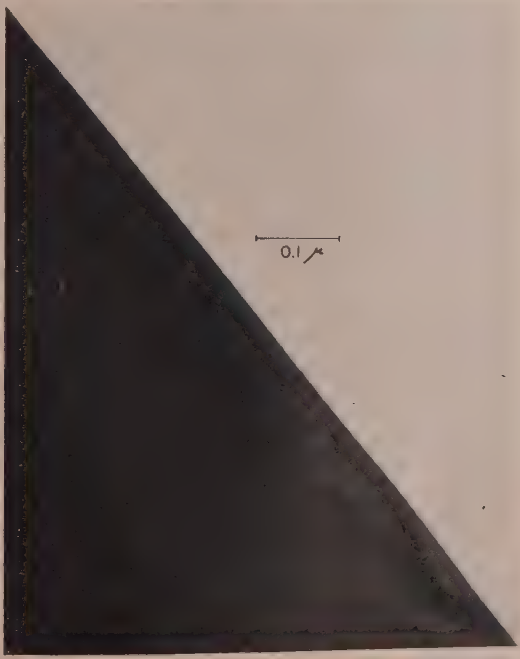

FIG. 1. Electron micrograph of graphite whisker surface.

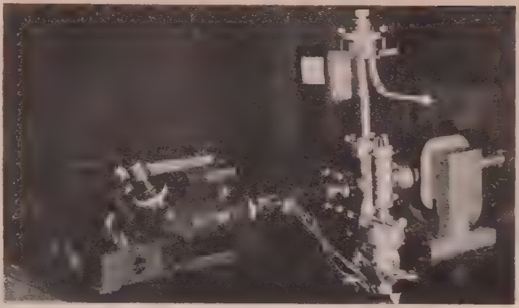

FIG. 2. Vac-ion vacuum system.

Although the whisker deflection was apparently unaffected by changes in the surrounding atmosphere, it did increase when the temperature was raised. An increase in deflection would be caused by an increase in whisker length, a decrease in the radius, or a decrease in whisker "stiffness." Our apparatus was not set up for accurate measurement of the whisker length, but a rough measurement indicated that the change in length was too small to account for the increased deflection. It is impossible to observe changes in whisker radius without the aid of an electron microscope, but the radius would be expected to increase rather than decrease at higher temperatures. It does appear likely then that part of the increased deflection is due to a decrease in the whisker stiffness. It is interesting to note that Young's modulus in polycrystalline graphite has been reported[12] to increase at high temperatures. The behavior of graphite whiskers suggests that the effects observed in polycrystalline graphite may be due to changes in particle-particle binding. For example, the low value of Young's modulus at room temperature may be due to the existence of adsorbed gases between the particles, these gases being desorbed at higher temperatures.

A much more sensitive technique for observing changes in whisker stiffness was based on the resonant frequency of a vibrating whisker. Figure 4 schematically illustrates this technique. The whisker was excited to resonant vibration by using the sine-wave output of a Hewlett Packard audio oscillator (model 0-10/APA -6x). Use of a diode in parallel with the load resistance produced a dc bias in the sine-wave voltage across the

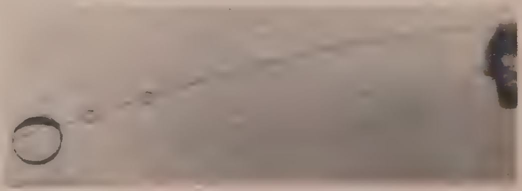

FIG. 3. Graphite whisker mounted for study of elastic properties.

---

[12] C. Malmstrom, R. Keen, and L. Green, Jr., J. Appl. Phys. **22**, 593 (1951); F. E. Farris, L. Green, Jr., and C. A. Smith, *ibid.* **23**, 89 (1952).

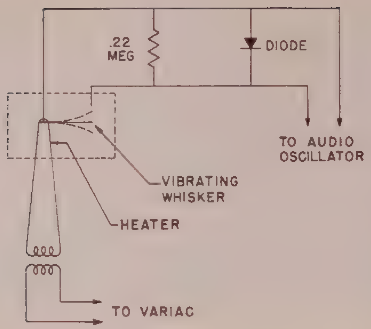

Fig. 4. Schematic diagram of apparatus for transverse vibration of graphite whiskers.

resistor just equal to one-half the peak-to-peak voltage. This prevented the frequency doubling usually encountered in this method. The frequency was determined by a Berkley Universal Counter and Timer model 5500. The whisker was mounted on a tungsten wire which could be heated by current passage. This facilitated outgassing the whisker in high vacuum.

Resonance for the three whiskers studied occurred at frequencies between 900 and 1000 cps. The resonant frequency was reproducible to about 0.2 cps or 0.02%.

The vibrating-whisker technique of studying the whisker stiffness produced a temperature variation similar to that observed using the first method above. The resonant frequency of the whiskers decreased as the temperature was increased. This behavior would be expected if the stiffness decreased. In both of the experiments concerned with the temperature dependence of the elastic properties, 400°C was the highest temperature used. Additional study of this phenomenon is planned at higher temperatures, using an apparatus which will permit more accurate measurement of the whisker length.

After the vibrating whiskers were heated in high vacuum, the temperature was quickly lowered but the resonant frequency did not immediately return to its preheat value. It was normally 0.2–0.3% low, but the initial value was finally reached after approximately 2–3 days. The recovery time was not appreciably affected by the pressure or the residual gas in the chamber. It was initially believed that this effect was caused by the slow annealing of defects introduced when the whiskers were rapidly cooled. However, a much slower cooling cycle produced similar results. The long recovery time plus the exponential nature of the recovery suggests the effect may be a result of gas molecules diffusing into the graphite lattice. Further study is required to completely identify the origin of this effect.

B. Electrical Resistance

The electrical resistance was studied by the current-potential method. Graphite whiskers were "welded" to the test specimen for potential probes and the potential drop between the probes was measured with a Leeds and Northrup type K potentiometer. Measurements were made immediately after outgassing in high vacuum and subsequently in atmospheres of oxygen, nitrogen, and water vapor. No detectable change in the whisker resistance was observed. The sensitivity of the apparatus and the reproducibility of results indicate that if a change did occur, it was less than 0.1%.

The resistivity along the whisker length was only slightly higher than the *a*-axis resistivity[13] of flake graphite. If diffusion of gases into the graphite lattice does occur, it does not appreciably affect the high electrical conductivity along the graphite basal plane. Since one would expect the gas atoms or molecules to primarily exist between basal planes, it would be more appropriate to measure the *c*-axis conductivity in various atmospheres. This measurement cannot be performed on graphite whiskers; however, the magnetoresistance can be measured and this property is dependent on the anisotropy of electrical resistance. An investigation of the magnetoresistance of graphite whiskers is planned for the near future.

V. SURFACE PROPERTIES

The nature of the cohesive bond formed when two crossed whiskers touch has been studied in vacuum and in various atmospheres. Figure 5 shows a sketch of one instrument used for this type of work. This particular chamber was attached to the Vac-ion system and was used to study the tensile strength of the cohesive bonds formed when whisker *A* and whisker *B* were brought together.

The whiskers were manipulated by bimetal strips which could be independently heated. Whisker *A* was attached only at one end and could be moved in the horizontal plane. Whisker *B* was attached at both ends, its axis was in the horizontal plane, and for small deflections, it moved in a nearly vertical direction. The whiskers were attached to the small tungsten wires with Wesgo silver paint and then fired in an inert atmosphere to 1100°F leaving the silver embedded in a matrix of low melting point glass. The resulting bonds were electrically conductive. The whiskers were heated to incandesence in high vacuum by passing current through them. This heating cleaned the surface for further studies. The current to heat whisker *A* must be passed through the junction between *A* and *B*. As the relatively large current would probably disturb the contact surfaces, the heating contacts were made away from the surfaces where tests were planned.

With the bimetal strips at room temperature, whisker *B* rested approximately 1 mm above the end of whisker *A*, which was observed with a 75× microscope. In a typical measurement, whisker *B* was lowered until contact was made with whisker *A*. Positive loads could be applied if desired by depressing *A* below its rest position. Whisker *B* was then slowly retracted and the upward deflection of whisker *A* just prior to bond rupture was used to indicate the strength of the bond. The force-vs-deflection sensitivity of each whisker was not accurately determined since we were primarily interested in relative changes. However, calculations based on the elastic modulus given by Bacon[8] indicated that forces of 10^{-5} d should be detectable when the whisker deflections were observed at 75×.

---

[13] D. E. Soule, Phys. Rev. **112**, 698 (1958).

The apparatus described above was primarily used to observe changes in the tensile strength of the cohesive bonds. The shear strength of the bonds was investigated using an apparatus similar to that shown in Fig. 5, except that direct mechanical coupling was used to manipulate the whiskers.

In studying the nature of the contacts formed between whiskers, the effect of stray charges was reduced by connecting both whiskers to ground. Alternating-current pickup by the leads was eliminated by shielding all leads and reducing the amount of the ac equipment in the vicinity of the test apparatus.

The experimentally determined energy of cohesion between graphite basal planes[14] is 260 erg/cm^2. By making some simple assumptions about the way the graphite whiskers separate, the energy of cohesion can give an estimate of the area of contact. Calculations of this type yielded an area of approximately 10^{-12} cm^2.

The cohesive bond tests do not give much quantitative information, but they do provide some knowledge of the character of the junction between the two whiskers. It should be emphasized that the area of contact between the whiskers is so small that contact at the same point on two successive tests is very unlikely. Unless the surfaces were atomically smooth and both whiskers completely circular in cross section, this variation in the point of contact would be expected to produce some scatter in the results. This scatter required each measurement to be repeated many times in order to obtain usable values. The deviation in results made it difficult to observe bond strength changes of less than a factor of 2. Reproducible changes of this magnitude were not observed, even between the conditions of high vacuum and saturated water vapor. However, if we compare the energy of cohesion between graphite layers (260 erg/cm^2) and the cohesion between water films[15] (140 erg/cm^2), we see that large changes would not necessarily be expected.

Some qualitative observations can be made from the data on the tensile strengths of bonds. The scatter in the measurements taken in high vacuum was definitely greater than when oxygen or water vapor was admitted to the system. This was especially noticeable after the whiskers had been heated to incandescence at 10^{-9} mm Hg. This variation is believed to be primarily due to roughness on the whisker surface. When the surface is clean a slight roughness, such as steps at terminating basal planes, would reduce the area of intimate contact between whiskers. Germer *et al.*[16] have shown how gas molecules or atoms condense on nickel in a very regular crystalline manner. It appears plausible that the gas molecules which condense on the graphite whiskers have a tendency to first fill out incomplete basal planes. As subsequent layers of the adsorbate are laid down, the surface would perhaps become smoother and more uniform than the original surface.

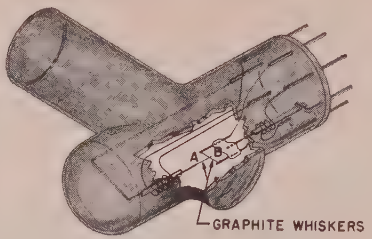

FIG. 5. Apparatus for studying the cohesion between two graphite whiskers.

The effect of contaminants on the shear strength of the bonds is less subtle. A definite decrease in shear strength of the bonds was observed when water vapor or oxygen was admitted. Most of the strength was recovered when the chamber was re-evacuated, indicating that the most important part of the contaminant film was physically adsorbed rather than chemisorbed. When pure dry nitrogen was admitted to the chamber, there was a small but perceptible increase in the bond shear strength which is not yet explained. However, when water vapor was subsequently admitted, the bond strength decreased as if the water had been introduced first. In the shear strength measurements, the oxygen and water vapor again reduced the scatter in results, thus indicating a more uniform surface.

The electrical contact resistance between two whiskers was measured using the R X 1000 scale of a Triplet multimeter. The small current drawn by this meter did not seriously affect the strength of cohesive bonds, provided the meter was disconnected and the whiskers regrounded prior to measuring the bond strength. After making contact between two whiskers, the total resistance as indicated by the meter was usually in the range of 5000–30 000 ohm. Most of this was contact resistance since the whisker resistance alone is between 100 and 300 ohm. No significant correlation was found between contact resistance and bond strength unless welding of the whiskers was produced by first passing a larger current through the whisker-whisker contact. The measured contact resistance did not change appreciably until the welding current was increased to about 10^{-5} amp. Currents greater than 10^{-5} amp produced an apparent welding of the whiskers which re-

---

[14] L. A. Girifalco and R. A. Lad, J. Chem. Phys. **25**, 693 (1956).

[15] See p. 9 of reference 1.

[16] L. H. Germer, E. J. Scheibner, and C. D. Hartman, Phil. Mag. **5**, 222 (1960).

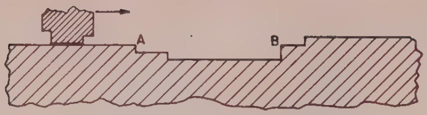

SINGLE CONTACT BETWEEN CLEAN GRAPHITE SURFACES

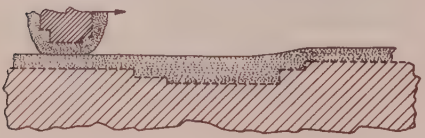

SAME AREAS AFTER SURFACE CONTAMINATION

FIG. 6. Idealized contacts between clean and contaminated graphite.

sulted in much lower contact resistance and increased bond strength. This welding occurred if the current was passed with the whiskers either in high vacuum or in air. Taking the previously calculated contact area of 10^{-12} cm², it is interesting to note that a current density of 10^7 amp/cm² is required at the contact before apparent damage occurs. This value is in substantial agreement with the calculated[1] current density which flows across the real area of contact in graphite brushes.

VI. CONCLUSIONS

The examination of several whisker properties in various atmospheres indicates that surface properties, particularly the shear strength of the cohesive bonds, are more affected than internal properties. There is little evidence to indicate that the atmosphere dependence of graphite friction is due to anything other than changes in graphite surface properties. The lamellar structure of graphite facilitates the establishment of smooth surfaces between sliding contacts, and the presence of adsorbed gases may further improve the quality of these surfaces. The improvement of surface smoothness on an atomic scale may be a significant part of the atmosphere dependence of graphite friction. Imagine an extremely small contact with a shearing force on it, as shown in Fig. 6. When such a contact is first made, energy is given up to the surrounding graphite lattice. Subsequently the energy of cohesion of the contact area must be expended whether the contact is broken in tension or in shear. If the surface surrounding the contact is atomically smooth, then the area of contact may be slipped without creating additional surface. The force required to move the contact along clean graphite may be low because of dislocations at the contact interface. When the contact reaches the incomplete basal planes at A, additional surface is created and external energy must be supplied. As the contact moves further and reaches B, it is obvious that shearing or ploughing must occur. The lower part of Fig. 6 gives an idealized picture of the same surface after adsorption of a contaminant gas. In addition to perhaps lowering the shear strength of the contact region, we see that the contact may now pass across A without breaking and forming additional surface. The difficult task of getting over the stepup at B may also be made easier by gas molecules forming a type of fillet. The ability of the contaminant to prevent graphite-graphite contact at B should reduce wear greatly. This may be the mechanism by which the contaminants reduce dusting and wear more than friction.

It is interesting to note that graphite friction should be velocity dependent if the "make" and "break" of contacts play a significant role. Bisson[17] has reported that graphite friction does indeed increase with surface speed.

ACKNOWLEDGMENTS

The author wishes to thank Dr. S. L. Levy and G. E. Gross for their encouragement and advice and many other members of the Institute staff for technical assistance and helpful discussions. Special thanks are also extended to Dr. Roger Bacon of the National Carbon Company for supplying the graphite whiskers used in this investigation.

---

[17] E. E. Bisson, Lubrication Eng. **9**, 75 (1953).

JOURNAL OF APPLIED PHYSICS VOLUME 32, NUMBER 8 AUGUST, 1961

Regular Articles

Electron Spin Resonance in Neutron-Irradiated Quartz*

ROBERT H. SILSBEE†
Laboratory of Atomic and Solid State Physics and Department of Physics, Cornell University, Ithaca, New York

(Received March 10, 1961)

The electron spin resonance of one of the defects produced by fast neutron irradiation of crystalline quartz is analyzed. The g tensor and hyperfine tensors deduced from these results imply that the defect electron is in a nonbonding tetrahedral hybrid orbital on a silicon. It is suggested that the instability of the lattice at high doses results in part from the presence of these defects.

INTRODUCTION

IRRADIATION of crystalline quartz by fast neutrons produces a number of paramagnetic defects which have been studied both by resonance and by optical absorption techniques.[1–3] Very heavy irradiation results in a complete breakdown of the crystal structure, subsequent annealing returning the crystal to a polycrystalline material rather than to the original single crystal.[4] It was hoped that a detailed knowledge of the structure of some of the irradiation-produced defects might give a clue to the mechanism responsible for the breakdown of the crystal. The spectrum of one of the resonances, characterized by narrow lines at room temperature and a negative g shift (the E_1' center of Nelson and Weeks[2,3]) has been analyzed in detail. Although certain implications as to the nature of the defect are discussed, no specific model has been constructed which is considered to be satisfactory.

EXPERIMENTAL RESULTS

The crystal used for this investigation was a fast neutron-irradiated synthetic crystal grown by the General Electric Company of England. The irradiation and subsequent measurements were done at room temperature. The optical rotation and etch patterns[5,6] indicated that the crystal was left-handed quartz. The sign of the piezoelectric effect and the nature of the etch patterns gave the positive sense of the x axis and the x-ray results of de Vries[7] were used to determine which of the enantiomorphic crystal structures was appropriate to use in trying to fit possible defect models into the quartz unit cell.

The resonance results were obtained with a conventional microwave spectrometer operating at x band and using balanced bolometer detection.[8] The crystal was mounted on a turntable in the microwave cavity and the magnet could be rotated about an axis perpendicular to the axis of crystal rotation, thus giving two degrees of freedom and allowing any desired orientation of the static field relative to the crystallographic axes.

The simplest spectrum appears with the static field parallel to the c axis of the crystal. There is a strong central line with a number of pairs of weak satellites with full splittings of 400, 9, 8, 0.7, (and perhaps 0.4[9]) gauss. The only nuclear isotope with a nuclear moment of appreciable concentration is the 4.7% abundant Si^{29} with spin of $\frac{1}{2}$. The suggested interpretation is an electron concentrated primarily on one silicon (giving the 400-gauss splitting) and interacting weakly with two more silicons (the 9- and 8-gauss lines). The smaller splittings arise from more distant silicons and will not be considered further. The predicted intensity of each of the weak lines (defects with a Si^{29} in the appropriate one of the sites leading to resolvable hyperfine structure) relative to the strong line (no Si^{29} in any of these sites) is about 2.5%, in reasonable agreement with the observed relative intensities.

As the static field is moved away from the c axis, each of these lines breaks up into six and these lines

TABLE I. Parameters describing the g tensor and hyperfine tensors of the resonance discussed in the text. The estimated accuracies: all directions to $\pm 2°$ except the weak hyperfine interaction which is $\pm 4°$; relative g values to $\pm 5\times 10^{-5}$ and absolute g values to $\pm 2\times 10^{-4}$ assuming a g value of 2.0036 for powdered diphenyl picryl hydrazyl[10]; strong hyperfine components to $\pm 2\times 10^{-4}$ cm^{-1} and weak hyperfine components to $\pm 0.05\times 10^{-4}$ cm^{-1}.

	Principal values of g and B tensors·Principal directions–polar angles (θ,ϕ)			Isotropic part of hyperfine tensor
g value	2.00176 (66°, −10°)	2.00049 (52°,99°)	2.00029 (45°, −126°)	
strong hfs	40×10^{-4} cm^{-1} (67°, −10°)	-20×10^{-4} cm^{-1} Axially symmetric		384×10^{-4} cm^{-1}
weak hfs	1.21×10^{-4} cm^{-1} (39°,46°)	-0.60×10^{-4} cm^{-1} Axially symmetric		7.94×10^{-4} cm^{-1}
weak hfs	1.15×10^{-4} cm^{-1} (55°, −157°)	-0.57×10^{-4} cm^{-1} Axially symmetric		7.46×10^{-4} cm^{-1}

---

* This work was supported jointly by the Atomic Energy Commission and by the Alfred P. Sloan Foundation.

† Alfred P. Sloan Fellow.

[1] R. A. Weeks, J. Appl. Phys. **27**, 1376 (1956).

[2] C. M. Nelson and R. A. Weeks, J. Am. Ceram. Soc. **43**, 396 (1960).

[3] R. A. Weeks and C. M. Nelson, J. Am. Ceram. Soc. **43**, 399 (1960).

[4] M. C. Wittels, Phil. Mag. **2**, 1445 (1957).

[5] G. W. Willard, Bell System Tech. J. **23**, 11 (1944).

[6] W. L. Bond, Z. Krist. **99**, 488 (1938).

[7] A. de Vries, Nature **181**, 1193 (1958).

[8] G. Feher, Bell System Tech. J. **36**, 449 (1957).

[9] R. A. Weeks (private communication).

[10] L. S. Singer and C. Kikuchi, J. Chem. Phys. **23**, 1738 (1955).

can be followed as a function of crystal orientation. Because of the symmetry of the quartz structure (the c axis is a threefold screw axis and the x axis is a twofold axis), both the g tensor and the hyperfine tensors can be derived from data taken with the magnetic field in the plane perpendicular to the twofold axis, where the lines break up into three instead of six components. Knowledge of the crystal symmetry allows the calculation of the g tensor and hyperfine tensors of any of the six equivalent sites within the unit cell once they are known for any one of the sites. The principal directions for these tensors for one of the sites are given in Table I in terms of the polar angles (θ,ϕ). θ is measured from the c axis, ϕ clockwise from the x axis (10.0) The angles for the other sites will be $(\theta,\phi\pm120°)$, $(180°-\theta, -\phi)$, and $(180°-\theta, -\phi\pm120°)$. The directions for a right-handed crystal would be obtained from these by reversing the sign of ϕ.

The results are summarized in Table I where the principal values and principal axes of the g tensor and the three hyperfine tensors are given. The Hamiltonian of the system is assumed to be of the form

$$\mathcal{H}=\beta\mathbf{S}\cdot\mathbf{g}\cdot\mathbf{H}+\sum_{i=1}^{3}(A_i\mathbf{I}_i\cdot\mathbf{S}+\mathbf{I}_i\cdot\mathbf{B}_i\cdot\mathbf{S}).$$

The index i refers to the three silicon sites near the electron and the term of index i in the sum will appear only if that site is occupied by a Si^{29} nucleus. The hyperfine interaction is written as the sum of an isotropic part and anisotropic part, the latter described by the tensor of zero trace $\mathbf{B}$. The value of S is taken to be $\frac{1}{2}$, appropriate to a defect with a single free spin.

Two assumptions in the interpretation above need further justification. The first is the assumption that the weak lines are indeed to be interpreted as hyperfine components and not as arising from an unrelated defect. The relative intensities suggested their interpretation as hyperfine components. For the two pairs with about 8- and 9-gauss full splitting, it is easy to see from the data that these break up into a number of pairs as the crystal is rotated, each pair being centered on one of the strong central lines. One can verify this also for the pair with 400-gauss separation, though here the second-order hyperfine correction must be calculated in computing the center of gravity of the pairs. A final piece of evidence is that one can also observe very weak ($\sim$0.6% of the central line) satellites with 8- and 9-gauss full splitting on either side of the 400-gauss satellites, corresponding to two of the silicon sites being occupied by Si^{29}.

The second assumption above is that of a center of spin $\frac{1}{2}$. The possibility of an electronic spin greater than $\frac{1}{2}$ can be ruled out on the basis of the simplicity of the hyperfine structure. For electronic spin equal to one, there will be second-order hyperfine splittings of the 400-gauss satellites equal to $(A^2/2g\beta H)\sim25$ gauss and there will be comparable splittings for larger S. The absence of such splittings assures that the center does indeed have $S=\frac{1}{2}$.

INTERPRETATION

In an optimistic frame of mind one would assume that a cursory comparison of the principal directions of these tensors with various bond directions in the quartz structure would immediately suggest a suitable model for this defect. Such has not been the case. The evidence that the unpaired spin is in a nonbonding sp hybrid on a silicon is strong, but it is by no means apparent how this silicon is situated in the crystal.

The association of the spin with the sp hybrid is based on a comparison of the strong hyperfine interaction with that expected for an atomic $3s$ and $3p$ electron. Kohn and Luttinger[11] estimate the isotropic hyperfine interaction for the 3s electron to be

$$A(\text{atomic }3s) = (8\pi/3)g_e\beta_e g_n\beta_n|\psi_{3s}(0)|^2\sim1600\cdot10^{-4}\text{cm}^{-1}.$$

Barnes and Smith[12] estimate $\langle1/r^3\rangle$ for a $3p$ electron on silicon from the observed fine structure splittings. This gives for the major principal value of the anisotropic hyperfine interaction of an atomic $3p$ electron on silicon,

$$B_{||}(\text{atomic }3p) =\tfrac{4}{5}g_e\beta_e g_n\beta_n\langle1/r^3\rangle_{3p}\sim64\cdot10^{-4}\text{ cm}^{-1}.$$

Comparison with the experimental results for the strong hyperfine interaction suggests the unpaired electron is in an orbit of 24% atomic $3s$ character and 63% atomic $3p$ character. In view of the uncertainties in the estimates of the free atom interaction constants, these results are in good accord with the model of an electron in a tetrahedral sp hybrid orbital.

The ratio of the isotropic to anisotropic parts of the strong hyperfine interaction are nearly the same as for the A center described by Watkins and Corbett[13] (9.6 in the present work, 8.5 for the A center). The magnitude of the interaction in the $\mathrm{SiO_2}$ center is 2.6 relative to that in the A center indicating that the electron is more strongly associated with a single silicon. This same result is of course implied by the estimate above that the electron spends 87% of its time on a single silicon.

The gross features of the g tensor ($\delta g_{||}\sim0, \delta g_{\perp}\sim-0.002$, with the major axis parallel to the hyperfine major axis) are also in reasonable accord with the model of an electron in a free (nonbonding) sp hybrid on a silicon, with the remaining hybrids used in normal covalent bonding. In a first approximation, the g shift results from the admixture, by spin-orbit coupling, of states involving both the excitation of the electrons in the normal covalent bonds to the nonbonding orbital (giving a positive g shift), and the excitation of the unpaired electron to antibonding orbitals (giving a negative g shift). In this approximation, the g shift for the magnetic field parallel to the sp hybrid will be zero and for the field perpendicular will be less than or of the order of the ratio of the spin orbit coupling constant to the energy of the SiO bond or $\delta g_\perp \lesssim 0.0075$. As indicated above, there are both a positive and a negative term in the calculation of $\delta g_\perp$ and the partial cancellation of these terms results in the value of $\delta g_\perp$ roughly one-third the estimate. The dominance of the negative term may result from the difference in the energy of excitation for the two types of terms but is more naturally explained in terms of the difference in the matrix elements for the two terms. The partially ionic character of the Si-O bond implies that in the bonding orbital the electron spends more of its time on the oxygen; the antibonding orbital then contains a correspondingly larger fraction of silicon wave function. The result in the g calculation is to make the matrix element for the excitation of the unpaired electron to the antibonding orbital larger than the matrix element leading to the positive term in the g shift. In view of the uncertainties in the energies of excitation, more detailed considerations would not be significant.

---

[11] W. Kohn and J. M. Luttinger, Phys. Rev. **97**, 883 (1955).

[12] R. G. Barnes and W. V. Smith, Phys. Rev. **93**, 95 (1954).

[13] G. D. Watkins and J. W. Corbett, Phys. Rev. **121**, 1001 (1961).

The departure of $g_{||}$ from the free electron value and the departure of the g tensor from axial symmetry do not follow from this simple picture and presumably an explanation of these results would require a more detailed model for the center.

The presence of weak hyperfine interaction with at least two other silicons gives further information about the center. The orientation of the weak hyperfine tensors is interpreted as a rough measure of the positions of the next two silicons relative to the silicon associated directly with the defect. The anisotropy in this interaction may be caused by a number of mechanisms, namely direct dipolar interaction, some p character in the overlap of the electron wave function onto the silicons, or a superexchange mechanism through an oxygen which is bound both to the defect silicon and that giving the weak interaction. Only in the case of the direct dipolar interaction does the orientation of the hyperfine tensor determine the relative position of the electron and the "weak silicon". The large s contribution to the weak hyperfine interaction implies that one of the other mechanisms must also be involved, thus giving some ambiguity in the interpretation.

As indicated above, the resonance data is interpreted rather naturally in terms of an electron occupying a tetrahedral hybrid orbital on a silicon in which the remaining three orbitals are used in normal covalent bond formation, the electron interacting weakly with more distant silicons to give the additional hyperfine lines. This model does *not* fit into the structure of crystalline quartz in any natural way and it has not been possible to construct a satisfactory microscopic picture of the defect. Although one can find SiO bonds which, when broken by removal of the oxygen, would leave an empty hybrid in roughly the orientation required by the g and strong hyperfine tensors, the weak hyperfine interaction is not predicted from the location of neighboring silicons. It is the fitting of the details of the weak hyperfine interaction that has proved to be the stumbling block in understanding this resonance. The model for the E_1 center proposed by Weeks and Nelson does not seem to be satisfactory since it fails to explain the presence of the strong hyperfine interaction.

The trouble may be in the conclusions drawn above, e.g., perhaps the orbital in question is a trigonal hybrid and the silicon has normal covalent bonding with only two oxygens. The weak interaction could then be via a superexchange-type mechanism with silicons beyond those two oxygens. However, one would expect larger g shifts for such a model, as a result of coupling to the remaining p orbital which lies perpendicular to the plane defined by the trigonal orbitals.

Another possibility is that the local distortion near the defect is so large that the principal directions of the various tensor are not related in any simple way to the bond directions in the undistorted material.

Although no detailed model is proposed for this defect, the existence of the unpaired electron in a nonbonding orbital suggests the source of the instability of the quartz lattice upon irradiation. Upon heavy irradiation ($>3.10^{19}$ centers/cm^3), the concentration of paramagnetic centers saturates with further irradiation[14] and it is at this stage in the irradiation that the density shows an accelerated decrease and the x-ray diffraction lines begin to show a marked broadening. At somewhat higher doses the material becomes amorphous and anneals to a polycrystal instead of a single crystal upon heating.[4] It is suggested that the crystal can support only a small concentration ($\sim 10^{-3}$) of nonbonding electrons (or free radicals). Upon further irradiation, the normal quartz structure is broken down in favor of a more random, glasslike, network (also a more open network according to the work of Wittels[4]) which can incorporate more of the defect electrons into the covalent bonding.

CONCLUSION

Neutron irradiation of crystalline quartz results, at low doses, in the production of several types of defects, and at high doses, in the complete breakdown of the crystalline structure. The analysis of the electron spin resonance of one of the defects produced at low irradiation indicates the existence of an unpaired electron in a nonbonding orbital on a silicon (a "dangling bond" or "free radical"). Such an unpaired electron is chemically active and the instability of the quartz at high irradiation may result from the presence of the high concentration of this defect.

---

[14] D. K. Stevens, W. J. Sturm, and R. H. Silsbee, J. Appl. Phys. **29**, 66 (1958).

ACKNOWLEDGMENTS

The author should like to thank Dr. R. A. Weeks and Dr. J. H. Crawford for many discussions concerning irradiation damage of quartz. This work was an extension of the detailed study of this resonance carried on by Dr. Weeks, and the crystal used in this study was kindly provided by him.

JOURNAL OF APPLIED PHYSICS VOLUME 32, NUMBER 8 AUGUST, 196

Grain-Boundary Diffusion*

A. E. Austin and N. A. Richard
Battelle Memorial Institute, Columbus, Ohio

(Received February 23, 1961)

The diffusion of nickel into grain boundaries of various tilt angles in copper bicrystals was studied. The concentration contours from the grain boundary and the lateral lattice diffusion were measured by means of electron-probe microanalysis. The product of grain-boundary width and diffusion coefficient were calculated, and comparisons were made with theoretical solutions. The grain-boundary coefficient is concentration dependent above 3% nickel in a 45° tilt boundary. With lower tilt angles, the coefficient is concentration dependent above 0.5% nickel.

INTRODUCTION

THE diffusion of a solute into a polycrystalline solvent proceeds through the lattice and along grain boundaries. Many experiments have shown that, at low temperatures, the diffusion rates in the grain boundaries may be several orders of magnitude greater than lattice diffusion.[1–4] Some studies have indicated a variation of grain-boundary diffusion with the degree of misalignment of the grains[3–5] and also with the orientation of the diffusion direction. Thus, according to the dislocation model, in the high-angle ($\theta \approx 45$ deg) boundaries the dislocations interact to form incoherent boundaries with narrow regions of misfit. The low-angle boundaries contain separated dislocations which may act as pipes with high diffusion rates.[6,7]

The present mathematical solutions[8,9] of grain-boundary diffusion are based on a model of a grain boundary as a narrow region having a high diffusion rate relative to the adjacent grain. The lattice and grain-boundary diffusion rates are assumed to be independent of concentration. These solutions predict concentration contours resulting from lattice diffusion away from the boundary. Such concentration contours have been shown qualitatively by differential etching and autoradiography.

Quantitative data have been lacking to evaluate the extent of lateral lattice diffusion and of possible concentration dependence in the grain boundary. The recent development of electron-probe microanalysis techniques has provided a means of determining such concentration contours and of calculating the grain-boundary concentrations. The present investigation involves the study of grain-boundary and lateral-lattice diffusion of nickel into copper bicrystals. The concentration gradients were determined by electron-probe microanalysis of sections cut parallel to the diffusion direction.

EXPERIMENTAL DETAILS

It was recognized initially that the nature of the experiments, as well as the materials and analytical methods to be applied, would require careful surface preparation. The main considerations were the avoidance of excessive strain in the single-crystal material and cold working of the prepared surfaces. All cutting was done with a No. 9 jeweler's saw using a water-soluble cutting fluid for lubrication. The cut surfaces were then ground under water on 400- and 600-grit carborundum paper, depending upon the amount of material to be removed, and lapped on 600-grit alumina paper. The surfaces were subsequently electropolished, using an electrolyte of 376 cc concentrated phosphoric acid in 634 cc of water, to remove any worked material from the surfaces.

---

* This research was supported in whole or in part by the Aeronautical Research Laboratory, an element of the Air Force Research Division, located at Wright-Patterson Air Force Base, Ohio.

[1] A. D. LeClaire, Progr. in Metal Phys. **4**, 265 (1953).

[2] D. McLean, *Grain Boundaries in Metals* (Oxford University Press, New York, 1957).

[3] S. Yukawa and M. J. Sinnott, Trans. AIME **203**, 996 (1955).

[4] W. R. Upthegrove and M. J. Sinnott, Trans. Am. Soc. Metals **50**, 1031 (1955).

[5] R. E. Hoffman, Acta Met. **4**, 97 (1956).

[6] C. Leymonie, D. LaCombe, and C. Libante, Compt. rend. **246**, 1209 (1955).

[7] D. Turnbull and R. E. Hoffman, Acta Met. **2**, 419 (1954).

[8] J. C. Fisher, J. Appl. Phys. **22**, 74 (1951).

[9] R. T. P. Whipple, Phil. Mag. **45**, 1225 (1954).

The seed crystals, from which the bicrystals were to be grown, were made by cutting a single crystal normal to the (001) planes at an angle $\theta/2$ with the (100) planes, where θ was the desired tilt angle. The orientations were determined from back-reflection Laue x-ray diffraction photographs. A second seed crystal was prepared in a similar manner but of opposite hand. It was found necessary to trim the remaining portions of the two crystals to provide a degree of symmetry of mass to assure that neither crystal would predominate in the nucleation of growth of the bicrystal.

The two seed crystals were then mechanically joined together in such a manner that the [001] axes of the crystals were parallel with the surfaces, describing an angle $\theta/2$ with the (100) planes, in contact. At this point another Laue photograph was made normal to the common (001) planes and in such a manner that both crystals were sampled simultaneously to provide a direct measure of θ, the angle between the (100) planes of the two crystals, and, in addition, to provide a quality check of the crystal surfaces; i.e., the degree of cold work, if any.

The seed crystal assembly was arranged in the crystal pulling apparatus with the common [001] axes parallel to the proposed growth direction. It was rotated at 6 rpm as the bicrystal was grown in purified helium from an inductively heated source of molten copper, contained in an AVC (National Carbon Company) graphite crucible. With a growth rate of 2.5 cm/hr, bicrystals up to 10 cm in length could be grown conveniently. The temperature of the molten copper was adjusted to provide a cylindrical bicrystal approximately 2 cm in diameter. A semiquantitative spectrographic analysis of the copper from which the bicrystals were grown showed the following impurities: silicon, 0.005%; iron, 0.003%; zinc, 0.002%; silver, <0.0001% (N.D.); cobalt, 0.0001%; and trace quantities of magnesium, lead, and vanadium. Bicrystals were grown with boundaries having tilt angles of 45, 30, 22, and 8 deg. Figure 1 shows schematically the seed assembly and the bicrystal orientations as well as the methods of couple preparation.

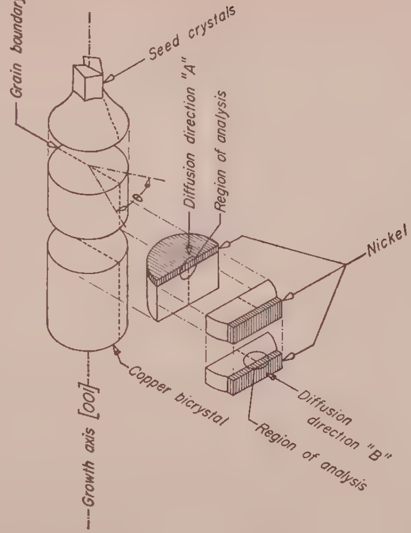

FIG. 1. Schematic diagram of bicrystal ingot showing sectioning relative to crystal orientations and growth axis.

Sections approximately 4 mm thick were cut from the bicrystal ingot, normal to the growth direction. The surfaces of the sections were ground and lapped through 600-grit alumina paper and lightly etched with 10:1 nitric acid to reveal the grain boundary. From a Laue photograph the orientation of the two crystals and the relative position of the grain boundary were determined. In all specimens the grain boundary approximately bisected the bicrystal ingot. However, in some cases, there was a tendency for the plane of the grain boundary to deviate from the plane bisecting the tilt angle between the (100) planes of the two crystals. The deviation was generally limited to a region near the edges of the bicrystal. Consequently, it was always possible to choose an appropriate section of the grain boundary in preparing the diffusion couples. The individual sections were then cut approximately in half, with the plane of the cut mutually perpendicular to both the section surface [common (001) plane] and the plane of the grain boundary as shown in Fig. 1. Both of these surfaces were lapped through 600-grit alumina paper and electropolished. A strip of stopoff lacquer about 4 mm wide was applied to the section surface adjacent to the normal surface and to all other surfaces not to be electroplated.

Nickel was electrodeposited onto the appropriate surfaces to a thickness of approximately 125 μ. The plating was done from a solution composed of $NiSO_4 \cdot 7H_2O$, 350 g/liter; $NiCl_2 \cdot 6H_2O$, 50 g/liter; H_3BO_3, 45 g/liter. The pH of the solution was maintained at 2.5–4.0 through the addition of $NiCO_3$. The plating was performed in the agitated solution at 55°C. The rate of deposition was about 40 μ/hr, with a current density of 2 amp/cm^2 at 4 v.

After plating, the stopoff lacquer was removed and the couples were washed in methyl-ethyl ketone and warm tap water and dried with warm air. The couples were then placed in individual Vycor capsules and vacuum degassed for 3 hr at 250°C, at which time the capsules were sealed under a vacuum of about 3×10^{-6} mm Hg.

The couples were given diffusion anneals at 750±2°C for periods of 10, 40, 80, 160, and 240 hr. The capsules were inserted into the furnace at temperature and were air quenched upon withdrawal.

The annealed couples were sectioned normal to the plated surfaces (parallel to the diffusion directions) and mounted in standard metallurgical mounts for surface

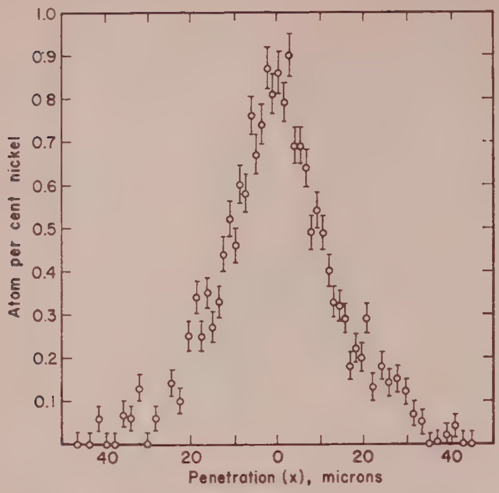

FIG. 2. Nickel concentration profile across 45-deg boundary at 100 μ from the Matano interface after 160 hr at 750°C.

preparation. The surfaces to be examined were normal to the grain boundary and also to the original couple interface, and individually represented diffusion directions both normal and parallel to the growth axis of the bicrystal.

The surfaces to be analyzed were prepared initially by grinding and lapping through 600-grit alumina paper. The surfaces were further lapped on wax laps run at 300 rpm using Linde "A" (Linde Air Products Company) abrasive suspended in distilled water. When the lapped surfaces were relatively scratch free, the specimens were lightly etched with a 3:1 dilution of a reagent prepared by the addition of 1 cc HCl/liter to a saturated solution of $FeCl_3$ in water. This etch reveals imperfections in the bicrystal without excessively attacking the grain boundary or the diffusion alloyed regions of the couples. With the grain boundary thus made visible, several microhardness indentations were placed at about 10 μ on either side of the grain boundary to bracket its location and to provide reference marks for future measurements. The specimens were then lapped further with Linde "A" abrasive to remove the effects of the etching and finally with Linde "B" abrasive to limit the size of any residual scratches. Some porosity was observed in the grain boundaries of the couples with longer diffusion times. The porosity occurred in the grain boundary adjacent to the original interface, the incidence of the porosity being greatest for the high-angle, 45°, boundary. These pores were evidently the result of a grain-boundary Kirkendall effect.

The concentration gradients in the vicinity of the grain boundary were determined by electron-probe microanalysis.[10,11] This is a quantitative method of instrument analysis which is accomplished through the measurement of characteristic x rays generated from the specimen by a focused beam, or probe of electrons ($\approx 1\ \mu$ in diameter). Electron scattering in the specimen enlarges the local region being analyzed to a diameter of 3–4 μ. An analysis of any individual region on the surface of the specimen consists, then, in determining the absolute x-ray intensities of the elements present in a curved crystal focusing x-ray spectrometer[10] and relating these experimental intensities to the intensities of similar x rays generated in the same manner from the elements in their pure form. Concentration gradients were determined by making a series of such analyses at small increments across a region of interest. A small carbonaceous deposit is formed on the specimen surface at the point of impact of the electron probe. It is theorized that the source of this contamination is a reaction between the residual oil vapor in the vacuum system and the electron beam. The quantity of this contamination deposited on the specimen surface is not sufficient to cause attenuation of the x rays but does, fortuitously, provide an exact record of where the analyses were obtained.

The instrument, which was employed in this study, provides a means for moving the specimen in increments as small as 0.3 μ. The specific method of determining the concentration gradients in this study was to make a series of individual analyses along a chosen direction (a traverse) at increments of either 0.635 or 1.27 μ, depending upon the gradient. First, a traverse was made normal to the copper-nickel interface at an arbitrary point, remote from the grain boundary. From the data of this traverse, the lattice diffusion coefficients of copper and nickel were computed and the position of the Matano interface was located on the specimen surface. The concentration-vs-penetration data of this traverse were also used to aid in locating the positions of subsequent traverses made across the grain boundary within the region of lattice diffusion. A series of parallel

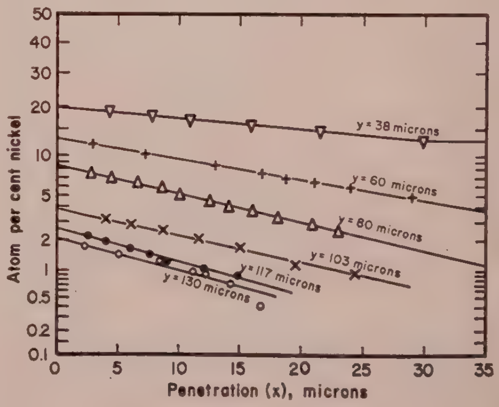

FIG. 3. Probability plot of nickel concentration gradients away from the 22-deg grain boundary at successive distances from the Matano interface after 240 hr at 750°C.

---

[10] R. Castaing, J. Philibert, and C. Crussard, J. Inst. Metals 9, 389 (1957).

[11] H. A. Liebhafsky, E. H. Winslow, and H. Pfeiffer, Anal. Chem. 32, 240 (1960).

traverses was then made normal to the grain boundary, to determine the maximum concentration of nickel at the grain boundary at various points along the boundary and to determine the concentration gradients along the boundary. Figure 2 shows the data of a typical traverse in the X direction normal to the grain boundary. Since the maximum resolution of the microanalyzer is about 3–4 μ and the width of the grain boundary is only a few angstroms, it is impossible to directly measure the concentration of nickel at the boundary itself. The maximum or peak concentration at the boundary was, therefore, extrapolated from an arithmatic probability plot of the concentration gradients away from the boundary. This is illustrated in Fig. 3, which shows a probability plot of the lateral concentration gradients at various distances y from the original interface, along a 22° tilt boundary in a couple annealed for 240 hr. The slopes, representing data taken at 38 and 60 μ from the original interface, were within the region which was also affected by lattice diffusion. At $y=38$ μ the contribution from lattice diffusion was 4% while at $y=60$ μ, the contribution was about 0.3%. The data of Fig. 3 also show the general increase in the concentration gradient away from the grain boundary with increasing distance from the original couple interface.

A measure of the mass flow of nickel along the grain boundary, $\int Cdx$, was obtained by measuring with a planimeter the area of the concentration profile plots, Fig. 2, and expressing the area in terms of μ% nickel.

The accuracy of the analysis is, of course, dependent upon the statistical accuracy with which the absolute x-ray intensities may be determined, as measured with a Geiger tube detector and scaler. The total number of counts produced in a standard interval of time were recorded for both copper and nickel at each increment of the traverse. The intensities, after suitable corrections had been applied for detector dead-time and background, were related to the standard intensities of the pure elements to arrive at the weight ratios of the two elements. The counting intervals used were 20±0.01 sec for intensities corresponding to concentrations greater than 10% and 50±0.01 sec for those less than 10%. The statistical accuracy of the analysis in terms of concentrations is shown in Fig. 4.

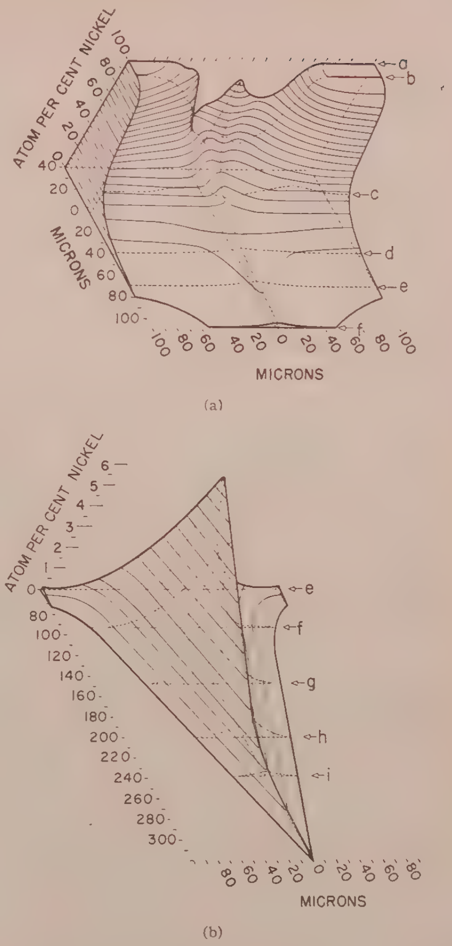

(a)

(b)

FIG. 5. Nickel isoconcentration contours, resulting from diffusion into 45-deg copper bicrystal annealed 240 hr at 750°C. (a). Isoconcentration contours at 5% nickel intervals within range of lattice diffusion from original interface. (b). Isoconcentration contours at 0, 0.1, 0.3, 0.5, 1.0, 1.5, 2.0, 2.5, 3.0, 3.5, 4.0, 4.5, and 5.0% nickel from grain-boundary and lateral lattice diffusion.

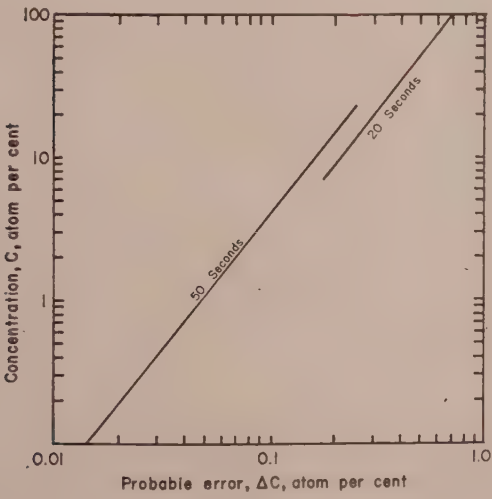

FIG. 4. Variation of the probable error ΔC in nickel concentration vs composition.

EXPERIMENTAL RESULTS

The maximum grain-boundary diffusion was observed in the couple containing a 45-deg tilt boundary annealed 240 hr at 750°C. Figures 5(a) and 5(b) show the nickel concentration gradients resulting from diffusion

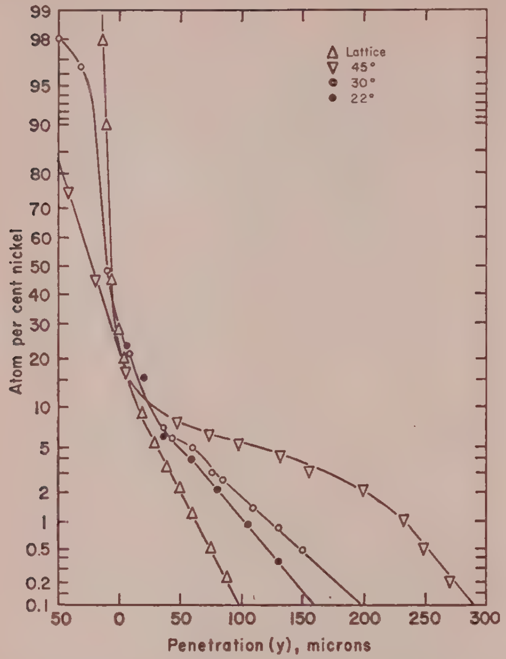

[Fig. 6. Grain-boundary nickel concentration-penetration curves for 240 hr at 750°C of 45, 30, and 22-deg copper bicrystals.

in a section cut parallel with the common [001] tilt axis and normal to the original plated interface of this couple. The horizontal space coordinates x and y are referenced respectively to the grain boundary and to the Matano interface of lattice diffusion into single crystal copper. The solid horizontal contour lines denote equiconcentration levels and the dashed lines, as indicated by lettered arrows a through i, mark concentration gradients across the grain boundary as measured by traverses with the microanalyzer. There is a broad minimum in the nickel electroplate with a peak opposite the grain boundary. Beyond the Matano interface, about 5 μ into the bicrystal, a shallow minimum forms at the grain boundary with a broad maximum on either side, as shown in traverse section c. At a point between the 10 and 15% contours, the nickel concentration in the grain boundary becomes greater than in the adjacent copper crystals. This is about the beginning of visible copper color in the crystals. Beyond this point, the concentration contours reveal the rapid grain-boundary penetration and lateral diffusion of the nickel.

The concentration contours of the other 45-deg bicrystal couples with shorter diffusion times were similar to those of Fig. 5(a) and 5(b). The 30-deg bicrystal couples had nickel concentration contours similar to those of the 45-deg tilt boundary but with less grain-boundary penetration. The 240-hr couple of the 30-deg bicrystal also showed a minimum of nickel concentration in the grain boundary with maxima in the copper bicrystal just beyond the Matano interface. This minimum was not evident for the shorter diffusion times and for the 40-hr couples a maximum was found at the grain boundary within 10 μ of the Matano interface. Thus, there appears to be a change, with longer diffusion times, from a maximum to a minimum of nickel concentration in the grain boundary near to the Matano interface.

Figure 6 is a probability plot of the grain-boundary concentrations for the 240-hr couples and of the concentrations due to lattice diffusion into single crystal copper. It illustrates the decrease in nickel penetration along the grain boundary with a decreasing tilt angle of the bicrystals. There is an inflection in the boundary concentration curves between 10 and 15% nickel, indicating a change in the diffusion coefficient. In the 8-deg bicrystal couples there was no grain-boundary concentration detectable above that from lattice diffusion. No difference was discerned for diffusion parallel or perpendicular to the common [001] tilt axis. Observations on the 22-deg bicrystal, for the two diffusion directions, gave the same grain-boundary penetration within 10 μ, down to 0.5% nickel.

Figures 7, 8, 9, and 10 are log plots of the grain-boundary concentrations C_p and of the integral $\int Cdx$ vs boundary penetration y for the various diffusion times of the 45- and 30-deg bicrystals, respectively. The integral values are given only for those traverses beyond the range of lattice diffusion. There is a decrease in the slopes, at the lower concentrations, with increasing

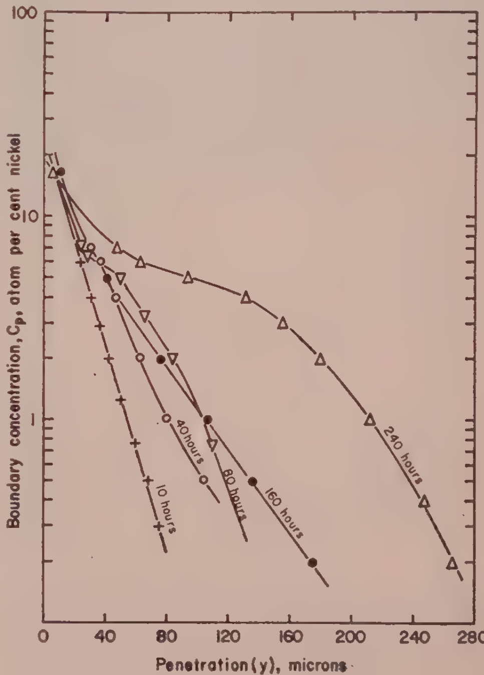

Fig. 7. Grain-boundary nickel concentration-penetration curves of 45-deg bicrystals annealed 10–240 hr at 750°C.

TABLE I. Lattice diffusion coefficients of nickel-copper at 750°C.

Composition, at.% Ni	$D_v \times 10^{-13}$ cm²/sec
0.5	70
1.0	52
2	51
5	43
10	33
20	16
30	9
40	5
60	3
80	2
90	1.7
95	1.7

time. The data for the 240-hr anneal are nonlinear, with the slope decreasing with decreasing concentration. It should be noted that the grain-boundary penetrations are nearly constant, from 40 to 240 hr in the region from 30–10% nickel, as compared to the lattice penetrations which, as shown in Fig. 11, exhibit the expected increase with time. This may indicate a change in the grain-boundary diffusion at concentrations above 10% nickel with increasing time. The nearly linear log plots, at concentrations below 5%, of the 10- and 40-hr data are approximately in agreement with the solutions of Fisher[8] and Whipple.[9] However, with increased time there is an increasing downward curvature which is the reverse of that predicted according to Whipple and Fisher.

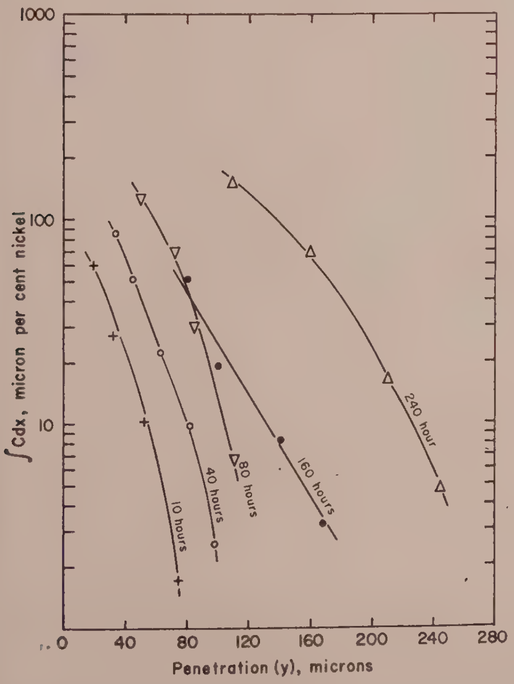

FIG. 8. Plot of the integrated concentration from grain-boundary diffusion of 45-deg bicrystals annealed 10–240 hr at 750°C.

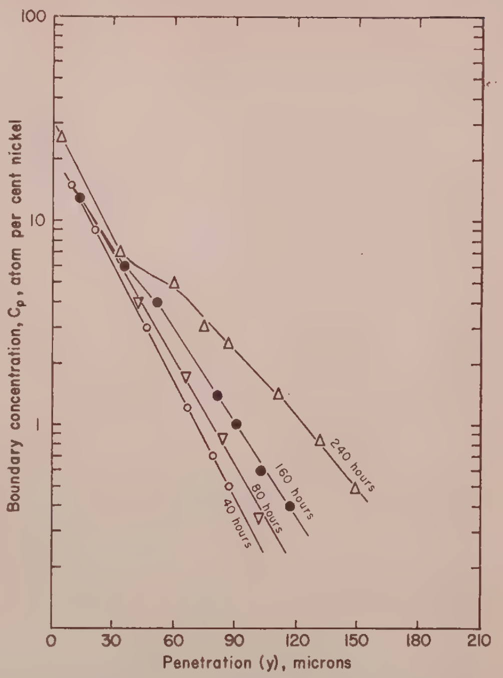

FIG. 9. Grain-boundary nickel concentration-penetration curves of 30-deg bicrystals annealed 40–240 hr at 750°C.

The nickel concentration gradients resulting from lattice diffusion were measured in the various couples. The lattice diffusion coefficients D_v were calculated from the concentration-vs-penetration curves, using the Matano method.[12] The data, averaged for the 240- and 160-hr couples, are given in Table I. A fluctuation in copper content up to 0.5% was detected in the nickel plate out to the free surface. This was due to grain-boundary diffusion in the polycrystalline nickel. The results for low nickel concentrations about 50 to 70×10^{-13} cm²/sec are comparable to values obtained from radioactive tracer experiments. Ikushima[13] obtained 33.6×10^{-13} cm²/sec at 785°C, while 22×10^{-13} cm²/sec was calculated from Mackliett's[14] data. A log-log plot of D_v vs concentration gives about 80×10^{-13} cm²/sec for copper self-diffusion, while tracer data[15,16] range from 70 to 180×10^{-13} cm²/sec.

COMPARISON WITH THEORY

Values of $D_{gb}w$, the product of grain-boundary diffusion coefficient D_{gb} and width w, were calculated from Fisher's[8] and Whipple's[9] solutions. The steepest-descents approximation of Whipple was used. Separate

---

[12] C. Matano, Japan. J. Phys. **8**, 109 (1932–1933).

[13] A. Ikushima, J. Phys. Soc. Japan **14**, 1636 (1959).

[14] C. A. Mackliett, Phys. Rev. **109**, 1964 (1955).

[15] A. Kuper, H. Letaw, L. Slifkin, E. Sonder, and C. Tomizaka, Phys. Rev. **96**, 1224 (1954).

[16] J. Steigman, W. Shockley, and F. C. Nix, Phys. Rev. **56**, 13 (1939).

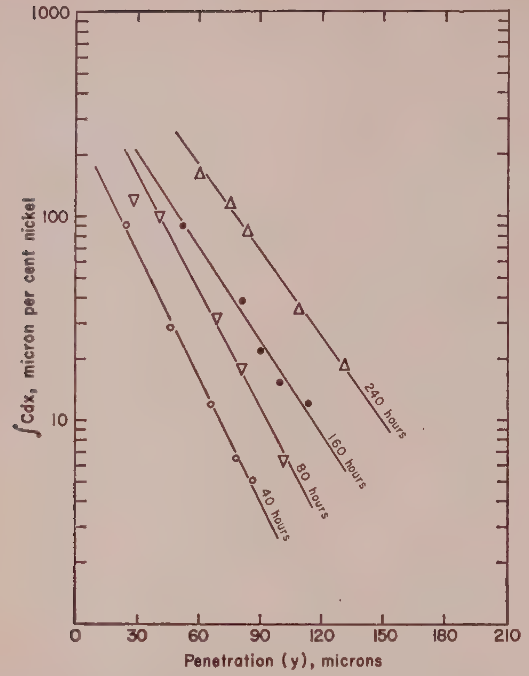

FIG. 10. Plot of the integrated concentration from grain-boundary diffusion of 30-deg bicrystals annealed 40–240 hr at 750°C.

solutions were obtained from the slope dy/dx of the lateral concentration contours at the grain boundary, from the boundary concentrations, and from the integrated concentrations $\int Cdx$.

The approximate equation of Fisher is

$$C_{x,y}=\exp\left[-\frac{\sqrt{2}y}{w^{\frac{1}{2}}(\pi D_vt)^{\frac{1}{4}}(D_{gb}/D_v)^{\frac{1}{2}}}\right]\operatorname{erf}\frac{x}{2D_vt}, \qquad (1)$$

where the exponential term gives the grain-boundary concentration. According to this, the slope of the log plots of boundary concentration and of $\int Cdx$ should be the same. This is implicit in Fisher's assumptions, that the grain-boundary diffusion is very rapid and that the concentration gradient from lateral lattice diffusion was about the same as would be produced with a constant grain-boundary concentration. The slope of the lateral concentration contour at the boundary is

$$\frac{dy}{dx}=\frac{w^{\frac{1}{2}}}{\sqrt{2}(\pi D_vt)^{\frac{1}{4}}}\left(\frac{D_{gb}}{D_v}\right)^{\frac{1}{2}}. \qquad (2)$$

Whipple's exact solution is

$$C_{x,y}=\operatorname{erf}\frac{\eta}{2}+\frac{\eta}{(\pi)^{\frac{1}{2}}}\int_0^1\exp\left(\frac{-\eta^2\tau^2}{4}\right)\operatorname{erf}\frac{1}{2}\left(\frac{1}{\tau^2\beta}-\frac{1}{\beta}+\xi\right)d\tau, \qquad (3)$$

where $\eta=y/(D_vt)^{\frac{1}{2}}$, $\xi=(x-a)/(D_vt)^{\frac{1}{2}}$, a = half-width of the boundary, and $\beta=[(D_{gb}/D_v)-1]\cdot a/(D_vt)^{\frac{1}{2}}$. The first term is the normal lattice diffusion and the second term is the contribution from boundary diffusion. The steepest-descents approximation of the second term is

$$C_{x,y}=1.159\beta^{\frac{1}{3}}\eta^{-\frac{2}{3}}\exp-[0.473\beta^{-\frac{2}{3}}\eta^{\frac{4}{3}}-0.396\beta^{-\frac{1}{3}}\eta^{\frac{2}{3}}(1-\beta\xi)]; \qquad (4)$$

then the integral concentration $\int Cdx$ at a given η is

$$\int Cd\xi=5.824\beta^{\frac{2}{3}}\eta^{-\frac{4}{3}}\exp-[0.473\beta^{-\frac{2}{3}}\eta^{\frac{4}{3}}-0.396\beta^{-\frac{1}{3}}\eta^{\frac{2}{3}}]. \qquad (5)$$

The limiting slope of the concentration contour at the boundary is

$$dy/dx=d\eta/d\xi=-0.63\eta^{\frac{1}{3}}\beta^{\frac{1}{3}}[1-0.421(\eta\beta)^{-\frac{2}{3}}]. \qquad (6)$$

This equation is quite similar to that from Fisher's approximation, varying mainly in the dependence on

TABLE II. Slopes of concentration contours of 45° bicrystal.

Concentration, at.% Ni	Slope dy/dx at grain boundary for 10 hr	40 hr	80 hr	160 hr	240 hr
0.2	3.4	4.4	2.4	3.2	3.2
0.5	4.1	4.2	2.4	3.3	3.5
1.0	3.9	4.0	2.5	2.6	3.9
2.0	3.8	3.6	2.6	3.0	4.4
3.0	3.5	3.8	2.5	...	5.5
4.0	3.4	...	2.3	...	5.5
5.0	...	...	...	...	5.5

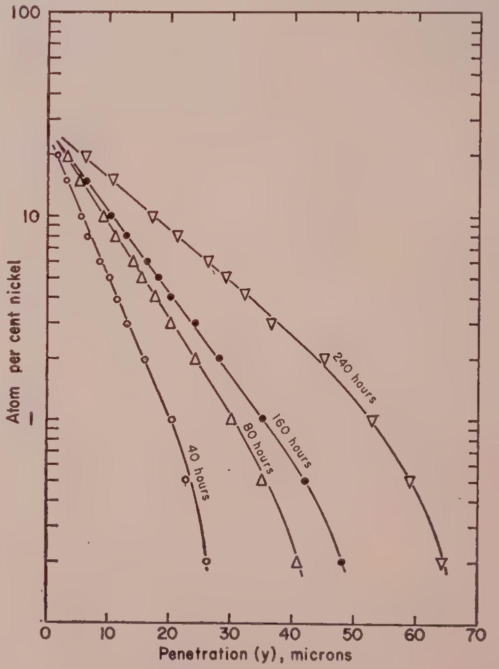

FIG. 11. Nickel concentration-penetration curves from lattice diffusion into single copper crystals for 40–240 hr at 750°C.

TABLE III. Slopes of concentration contours of 30° bicrystal.

Concentration, at.% Ni	Slope dy/dx at grain boundary for 40 hr	80 hr	160 hr	240 hr
0.2	4.0	2.7	2.8	2.4
0.5	4.2	2.2	2.2	2.5
1.0	3.5	2.0	1.6	2.4
2.0	2.9	1.6	1.5	1.5
3.0	2.8	...	1.5	1.3
4.0	...	...	...	1.3
5.0	...	...	...	0.70

the $\frac{1}{3}$ power of D_{gb}/D_v rather than the $\frac{1}{2}$ power. Thus, rewriting in terms of y and x and assuming that $(D_{qb}/D_v)\cdot[a/(D_vt)^{\frac{1}{2}}]$ is equivalent to β, then

$$\frac{dy}{dx}=\frac{-0.63y^{\frac{1}{3}}a^{\frac{1}{3}}}{(D_vt)^{\frac{1}{3}}}\left(\frac{D_{gb}}{D_v}\right)^{\frac{1}{3}}+\frac{0.266y^{-\frac{1}{3}}a^{\frac{1}{3}}}{(D_vt)^{-\frac{1}{3}}}\left(\frac{D_{gb}}{D_v}\right)^{-\frac{1}{3}}. \quad (7)$$

The second term of the equation may be neglected when D_{gb}/D_v is large.

Tables II–VI give the data on the slopes of the concentration contours and the values of $D_{gb}w$, calculated from Fisher's and Whipple's solutions, Eqs. (2) and (6). At boundary concentrations above 3% nickel there is some contribution by lattice diffusion from the original interface. The values of $D_{gb}w$ are essentially the same by both solutions. The 45-deg bicrystal has a constant slope from 0.2 to 3% nickel and, accordingly, a constant $D_{gb}w$. However, there is an increase with the longer diffusion times.

The 30- and 22-deg bicrystals exhibited decreasing slopes with increasing nickel concentrations. Thus, $D_{gb}w$ decreased by a factor of 10 for the 22-deg bicrystal and 30 for the 30-deg bicrystal, over the concentration range of 0.2–5% nickel. The value of 4×10^{-13} cm^3/sec for the 22-deg bicrystal at 0.2% nickel was about $\frac{2}{3}$ that of the 30-deg bicrystal. The data from both bicrystals indicate that $D_{gb}w$ is the same at concentrations above 2% nickel and much less than that of the 45-deg bicrystal.

TABLE IV. Values of $D_{gb}w$ calculated from the slopes of concentration contours of 45° bicrystal.

Concentration at.% Ni	10 hr	40 hr	80 hr	160 hr	240 hr
A. $D_{gb}w\times10^{13}$ cm^3/sec from Fisher's solution.					
0.2	2.7	8.6	3.5	8.8	11
0.5	3.5	7.2	3.2	8.9	12
1.0	2.8	5.8	3.1	5.0	14
2.0	1.4	2.9	2.8	4.0	14
3.0	1.2	2.9	2.1	...	17
4.0	...	...	...	...	17
5.0	...	...	...	...	17
B. $D_{gb}w\times10^{13}$ cm^3/sec from Whipple's solution.					
0.2	2.9	8.8	2.9	9.0	9
0.5	5.4	8.0	2.9	11	11
1.0	5.1	7.2	2.9	7.0	19
2.0	2.7	4.2	3.2	8.0	22
3.0	1.2	4.6	2.6	...	33
4.0	...	...	...	...	44
5.0	...	...	...	...	40

TABLE V. Values of $D_{gb}w$ calculated from the slope of concentration contours of 30° bicrystal.

Concentration at.% Ni	40 hr	80 hr	160 hr	240 hr
A. $D_{gb}w\times10^{13}$ cm^3/sec from Fisher's solution.				
0.2	6.8	4.4	6.6	6.0
0.5	7.4	2.9	4.1	6.3
1.0	4.5	2.0	1.9	5.5
2.0	2.5	1.1	1.3	1.7
3.0	1.9	...	1.2	1.0
4.0	...	...	...	1.0
5.0	...	...	...	0.2
B. $D_{gb}w\times10^{13}$ cm^3/sec from Whipple's solution.				
0.2	7.6	4.4	8.2	7.0
0.5	9.0	3.0	5.0	7.8
1.0	6.0	2.2	2.1	6.6
2.0	3.5	1.1	1.6	1.9
3.0	2.8	...	1.4	1.4
4.0	...	...	...	1.3
5.0	...	...	...	0.2

Table VII lists values of $D_{gb}w$ calculated from the mean slopes of grain-boundary concentration C_p and of the integrated concentration $\int Cdx$. The results according to Fisher's equation are 2–3 times less than those from Whipple's for the 45- and 30-deg bicrystals. For short diffusion times, the slopes of C_p and $\int Cdx$ were the same and, accordingly, Fisher's solution gave the same value of $D_{gb}w$. However, for the longer diffusion times of the 45- and 30-deg bicrystals, the two slopes were different and the integrated concentration data gave lower values of $D_{gb}w$ for Fisher's solution. Whipple's equation gave the same results for both boundary concentration and integrated concentration, but the values were less than those obtained from the concentration contour slopes.

For the 30-deg bicrystal, the solutions by Whipple's equations were in agreement at 2–3% nickel and for the 22-deg bicrystal, at 5% nickel. Calculations were not possible for the 45-deg bicrystal annealed for 240 hr since the log plots of the boundary concentrations and the integrated concentrations were nonlinear and had a downward curvature which is the reverse of that predicted by Whipple's equation for a constant D_{gb}.

TABLE VI. Slopes of concentration contours and calculated values of $D_{gb}w$ of the 22° bicrystal for 240 hr.

Concentration, at.% Ni	Slope dy/dx	$D_{gb}w\times10^{13}$ cm^3/sec Fisher	Whipple
0.2	1.95	4	4
0.5	1.90	3.8	4.3
1.0	1.70	2.6	3.0
1.5	1.50	1.8	2.2
2.0	1.40	1.4	1.6
3.0	1.30	1.0	1.3
5.0	0.95	0.3	0.4

TABLE VII. Values of $D_{gb}w$ calculated from grain-boundary concentrations and from integrated concentrations.

	$D_{gb}w \times 10^{13}$ cm³/sec			
	Fisher's solution for		Whipple's solution for	
Diffusion time, hr	C_p	$\int Cdx$	C_p	$\int Cdx$
A. 45° bicrystal.				
10	0.56	0.56	1.0	2.0
40	0.77	0.29	0.9	1.0
80	0.52	0.20	1.4	1.4
160	0.9	0.46	1.2	1.2
B. 30° bicrystal.				
40	0.42	0.42	0.8	1.0
80	0.52	0.53	0.8	0.8
160	0.54	0.51	1.4	1.4
240	0.58	0.35	1.5	2.0
C. 22° bicrystal.				
240	0.30	0.22	0.2	0.2

However, a decrease in D_{gb} with increasing nickel would produce the observed curvature.

Fisher's solution gives a $t^{\frac{1}{4}}$ dependence of the boundary penetration to equal concentrations. This is approximated for the shorter times at concentrations below 3% nickel. However, the penetration is greater than that predicted for the 240 hour couples. This is shown in Fig. 12, the plot of penetration to 1% nickel vs $t^{\frac{1}{4}}$ for the 45- and 30-deg bicrystals. The penetration curves vs $t^{\frac{1}{4}}$ are comparable for the range 0.5–3% nickel. Yukawa and Sinnott[3] observed the same effect in their radiographic study. The penetration to equal values of $\int Cdx$ varies with $t^{\frac{1}{2}}$ as illustrated in Fig. 13. The penetration with time decreases at concentrations greater than 5% nickel and becomes about constant at concentrations above 10% nickel.

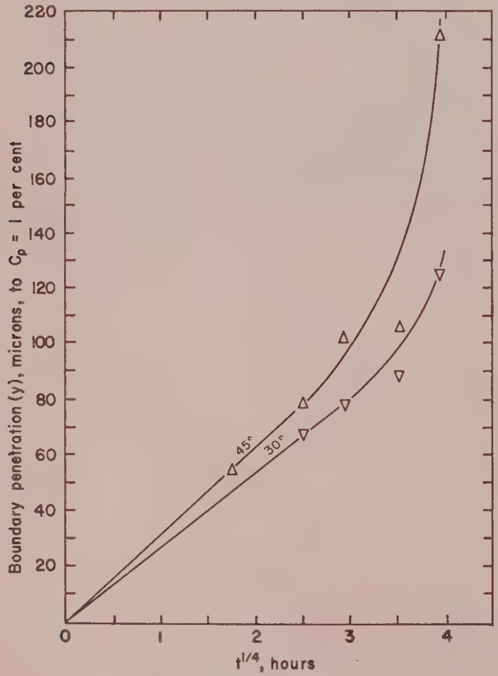

FIG. 12. Plot of grain-boundary penetration to 1% nickel vs $t^{\frac{1}{4}}$ for 45-deg and 30-deg bicrystals.

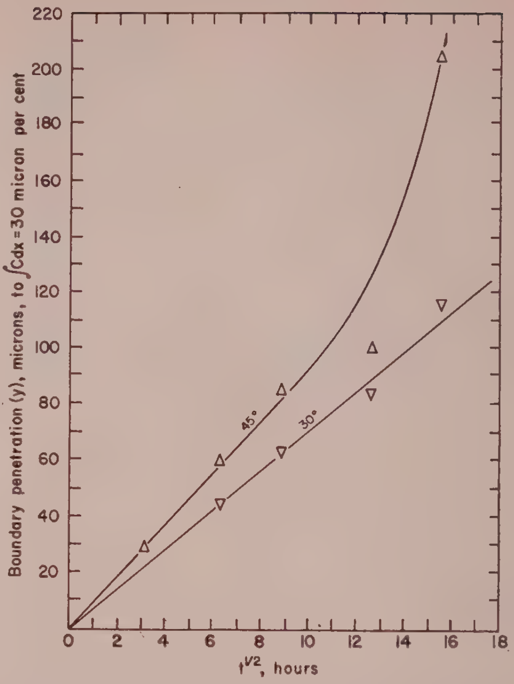

FIG. 13. Plot of the grain-boundary penetration to equal values of integrated concentration of 30 μ% nickel vs $t^{\frac{1}{2}}$ for the 45-deg and 30-deg bicrystals.

Turnbull and Hoffman[7] expressed the coefficient of grain-boundary diffusion D_{gb} in terms of diffusion along dislocations D_p as $\sin\theta/2$, where θ is the tilt angle and lattice spacing λ for a boundary of line dislocations of effective diameter l. Thus,

$$D_{gb}w = 2D_p(l^2/\lambda)\sin\theta/2 \qquad (8)$$

by assuming

$$w \cong l \cong \lambda \cong 5 \times 10^{-8} \text{ cm},$$

then Eq. (8) can be written as

$$D_p = D_{gb}/\sin\theta/2. \qquad (9)$$

Using the values of $D_{gb}w$ for 0.5% nickel, calculated from the slopes of the concentration contours of the 240-hr couples, one obtains values of $D_p = 26$, 25, and 22×10^{-6} cm²/sec for the 45-, 30-, and 22-deg couples, respectively. The ratio D_p/D_v is about 2.1×10^6. Thus, the data at low concentrations agree, within the errors of determination, with this model of a grain boundary. However, at higher concentrations, the grain-boundary diffusion coefficient decreases more rapidly with the lower angles of tilt than for the 45-deg boundary, and estimates of D_p do not agree.

For $w=5\times 10^{-8}$ cm, values of D_{gb} calculated from data of Tables IV, V, and VI for 0.5% nickel were 2×10^{-5}, 1.5×10^{-5}, and 0.8×10^{-5} cm²/sec for 45, 30, and 22 deg, respectively. The corresponding ratios of D_{gb}/D_v were 3.1×10^6, 2.1×10^6, and 1.1×10^6. These values of D_{gb} and of D_{gb}/D_v are about 100 times greater than those reported by Yukawa and Sinnott[3] from radiographic measurements. The latter calculated their values from penetration measurements to an estimated concentration of 0.005% nickel, using Fisher's solution. The calculations of the present data from the slopes of the grain-boundary concentrations gave values of D_{gb} of 1.8×10^{-6}, 1.1×10^{-6}, and 0.6×10^{-6} cm²/sec for 45, 30, and 22 deg, respectively. These coefficients are greater than those of Yukawa and Sinnott by about 30 times. The differences may be due to the type of couples used since Yukawa and Sinnott used a thin nickel plate 1–2 μ thick, as compared to the present work using couples with 125 μ of nickel. Their assumption of a constant concentration of nickel at the interface, therefore, does not appear to be valid.

Hubner and Shockley[17] have derived an equation relating the vertex angle 2φ of the isoconcentration contour with velocity of advance ν as

$$(\nu \tan\varphi)^{-1}=(w_d \sin^2\varphi-w_0)/2D_v, \qquad (10)$$

where w_0 is the thickness of normal material containing impurities equal to those in the grain boundary and w_d is effective diffusion thickness which formally is identical to $D_{gb}w/D_v$. This equation requires a linear plot of $\nu \tan\varphi$ vs $\sin 2\varphi$. The data of the present experiment do not satisfy this relation. The velocity appears to vary with time, and $\tan\theta$ does not increase proportionately with time.

DISCUSSION AND CONCLUSIONS

The grain-boundary diffusion coefficient of nickel into copper grain boundaries is concentration dependent. At low concentrations, below 3% nickel, the coefficient is essentially constant for high-angle, 45-deg boundaries. However, for lower tilt angles, such as 30 and 22 deg, the grain-boundary coefficient decreases for concentrations greater than 0.5% nickel. The coefficients at/or less than 0.5% nickel vary with respect to $\sin\theta/2$ or according to the line dislocation model of a grain boundary. Grain-boundary diffusion decreases rapidly at nickel concentrations above 5%. However, the diffusion coefficient D_{gb} is not calculable at higher nickel concentrations because the present solutions do not allow for the concentration dependence both of grain-boundary and of lattice diffusion. At nickel concentrations above 10%, there is a negligible increase in penetration with time from 10–240 hr as compared to the $t^{\frac{1}{2}}$ dependence of lattice diffusion. This would indicate an initial rapid diffusion which decreases with concentration and with time.

The observation of a minimum at the grain boundary and a maximum in the adjacent grains, for the longer diffusion times, is interpreted as the result of depletion of an initial boundary maximum. Thus, the short diffusion times produce a grain-boundary maximum with increased concentration in the adjoining grains caused by lateral lattice diffusion. The rate of grain-boundary diffusion at the same region decreases with the increased concentration, finally becoming equal to that of lattice diffusion at the same concentration. Thus, the source effectively moves from the original interface into the boundary. However, enhanced diffusion continues along the extended grain boundary beyond this region and tends to deplete it with respect to the adjacent copper crystals.

The disparity in the various solutions of Fisher's equations indicates that the assumptions used are not valid even for short diffusion times and low concentrations. The solutions by Whipple's equations are preferable, but the range of validity of the steepest-descents solution is not defined. This work indicates a need for derivation of the boundary diffusion equations for the conditions where the grain boundary and/or lattice diffusion coefficients are concentration dependent.

ACKNOWLEDGMENTS

The authors were assisted in this work by R. Kinney in electron-probe microanalysis, W. Wolfe in preparation of Laue photographs, and J. Mock in crystal growth.

---

[17] K. Hubner and W. Shockley, *Structure and Properties of Thin Films* (John Wiley & Sons, Inc., New York, 1959), p. 306.

JOURNAL OF APPLIED PHYSICS VOLUME 32, NUMBER 8 AUGUST, 1961

Operation of the Field Ion Microscope with a Dynamic Gas Supply*

B. J. Waclawski and E. W. Müller
Field Emission Laboratory, Pennsylvania State University, University Park, Pennsylvania

(Received February 27, 1961)

The brightness level of the field ion microscope has been increased two orders of magnitude with little loss of resolution by the addition of a dynamic gas supply system. Space charge at the emitter is not a limiting factor. Cathode sputtering by the imaging helium ions may release negative ions which are accelerated toward the tip. These ions gain sufficient kinetic energy so that irrespective of subsequent multiple ionization in the high field region near the tip they are capable of striking the tip surface and cause damage to the tip lattice. This effect can be eliminated by proper electrode design.

I. INTRODUCTION

ONE of the difficulties encountered with the operation of a field ion microscope (FIM) has been the relatively low image brightness. If a statistical supply of polarized neutral gas molecules to the emitter tip is considered, and full ionization under the conditions of best image details is assumed, the image-forming ion current can be calculated[1,2] to be approximately

$$i=\frac{0.1e\alpha}{m^{\frac{1}{2}}k^{\frac{3}{2}}T^{\frac{3}{2}}}pV^2 \text{ (amps)}, \tag{1}$$

where $e=1.6\times10^{-19}$ coul, α=polarizability in cm^3, m=mass of molecule in grams, k=Boltzmann constant, T=gas temperature, p=gas pressure in d/cm^2, and V is the applied voltage in esu. Since the efficiency of the phosphorescent screen is approximately independent of voltage in the range used, the image brightness I for a given gas and temperature becomes proportional to the beam power, that is,

$$I=CpV^3. \tag{2}$$

The voltage V for best image details is very closely determined by the given tip radius, and only relatively little dependent upon the cone angle of the tip or the distance between tip and accelerating electrode. In practical field ion microscopy, tips are used which have radii between 100 and 3000 A, and the corresponding voltages for operation with helium ions vary between 4 and 50 kv.

The admissible gas pressure is limited by the condition that no noticeable scattering should occur when the imaging ions travel through the gas from tip to screen. The length of this path is a compromise among magnification, resolution, and screen brightness. Raising the tip-to-screen distance increases the magnification, but places an upper limit to the gas pressure above which resolution is impaired by ion scattering. If the tip-to-screen distance is lowered, higher gas pressures can be employed, increasing the image brightness, but then details of the image are lost in the phosphor graininess and by the limited resolution of the photographic material. In the conventional FIM a balance has been chosen with about 10 cm for both the tip-to-screen distance and the screen diameter.

A helium gas pressure of 2 μ presents the optimum in brightness without noticeable loss of resolution resulting from scattering. If the microscope is operated with neon or hydrogen, which is often desirable because of the lower field strength required for ionization, then the optimum pressure is below 1 μ because of the much larger small-angle scattering cross section of these gases. Under practical working conditions with a silver-activated zinc silicate screen, and use of an $f/1$ objective and Kodak 103*ag* film, the typical photographic exposure times can be approximately expressed by

$$t=A/pV^3 \text{ (sec)}. \tag{3}$$

With gas pressure p expressed in microns, and V in kilovolts, the exposure constants are $A_{\mathrm{He}}=100\,000$, $A_{\mathrm{Ne}}=1\,200\,000$, and $A_{\mathrm{H_2}}=33\,000$. Good images are obtained, for instance, from a 1000-A tip with 2 μ of helium at 15 kv and 15-sec exposure time, while for a very fine tip of 100 A, at the same pressure and 4 kv, the exposure time will be about 15 min.

II. DYNAMIC GAS SUPPLY

In the new system a novel means is employed to increase the gas supply to the tip and still eliminate loss of resolution resulting from scattering (Fig. 1). The tip resides in a high-pressure region separated by an aperture from the main volume of the microscope which is pumped continuously.[1–3] As the path in the high-pressure region can easily be reduced from the original 100 mm to about 1 mm without requiring too stringent conditions for centering the emitter tip above the 1-mm diameter aperture, it appears possible to increase the pressure correspondingly by a factor of 50 without noticeable loss of resolution resulting from gas scattering.

The gas is fed into the cooling mantle through the liquid hydrogen filled cold finger. Precooling in a liquid

---

* Supported by the Office of Naval Research.

[1] E. W. Müller, "Field ionization and field ion microscopy" in *Advances in Electronics and Electron Physics*, edited by L. Marton (Academic Press, Inc., New York, 1960), Vol. 13, p. 83.

[2] B. J. Waclawski, "Field ion microscope with dynamic gas supply," Master's thesis, Pennsylvanis State University, University Park, Pennsylvania, 1961.

[3] B. J. Waclawski and E. W. Müller, 7th Field Emission Symposium, McMinnville, Oregon, 1960.

nitrogen trap is employed, and the supply is regulated by a needle valve and monitored by a thermocouple gauge. The main volume of the microscope is evacuated by a two-stage 20-liters/sec oil-diffusion pump to less than 1 μ. A liquid nitrogen cooled baffle is provided in the entrance side of this pump. In the preliminary experiments this pump was used to circulate the helium back into the supply volume. However, it was found that too much contaminating gas, most likely a decomposition product of the pump oil, got into the gas supply in constantly increasing amounts and reduced the image contrast. Although the gas could probably have been cleaned by adsorption on charcoal, it was found to be more convenient to discard the used helium gas.

Two difficulties would be expected when the gas pressure in the tip region is raised to about 100 μ. A gaseous discharge might ignite between the tip electrode and the cooling mantle at the higher voltages and a loss of resolution might occur resulting from the positive space charge near the emitter tip. Both disturbing effects proved to be nonexistent up to pressures of 60 μ. It is known from experiments[4] that space charge effects in field electron emission become noticeable only above a current density of 10^7 amp/cm^2. For the same geometry and accelerating voltage, the corresponding critical current density for ion emission should be lower by a factor of $(m/M)^{\frac{1}{2}}$, where M is the ion mass, and m is the mass of the electron. For helium, the critical current density is above 10^5 amp/cm^2, two orders of magnitude higher than those actually encountered in ion emission at 100-μ pressure. The ion-ion interaction near the emitter tip can also be estimated to be negligible by considering the average time interval and spacing between successively emitted ions. The enormously high field of 500 Mv/cm removes each ion from its origin so quickly that the average distance to the next one is approximately 10^{-5}cm, and the interaction correspondingly small.

Ion current and screen brightness measurements as functions of gas pressure were carried out to confirm proportionality with p. For this experiment, a probe line from a McLeod manometer was connected directly to the cooling mantle volume in order to eliminate the pressure drop in the supply line. Ion currents were measured to be 2×10^{-7} amp at 20 kv and 60-μ pressure. True ion currents, without disturbance from secondary electrons, were measured by making a connection to the conductive coating of the microscope tube while the cooling mantle was kept at -30 v dc.

Photographs obtained at high dynamic pressures confirmed the expectations: for the same tip specimen there is apparently no difference in resolution between a photograph taken under static conditions at 2-μ pressures, and with a dynamic gas supply of 60-μ effective pressure at the tip location. A photograph of a 9.4-kv tungsten image taken at $f/1$ and 1 sec, and a helium pressure of 50 μ, revealed the 2.74-A spacing of the 112 planes.

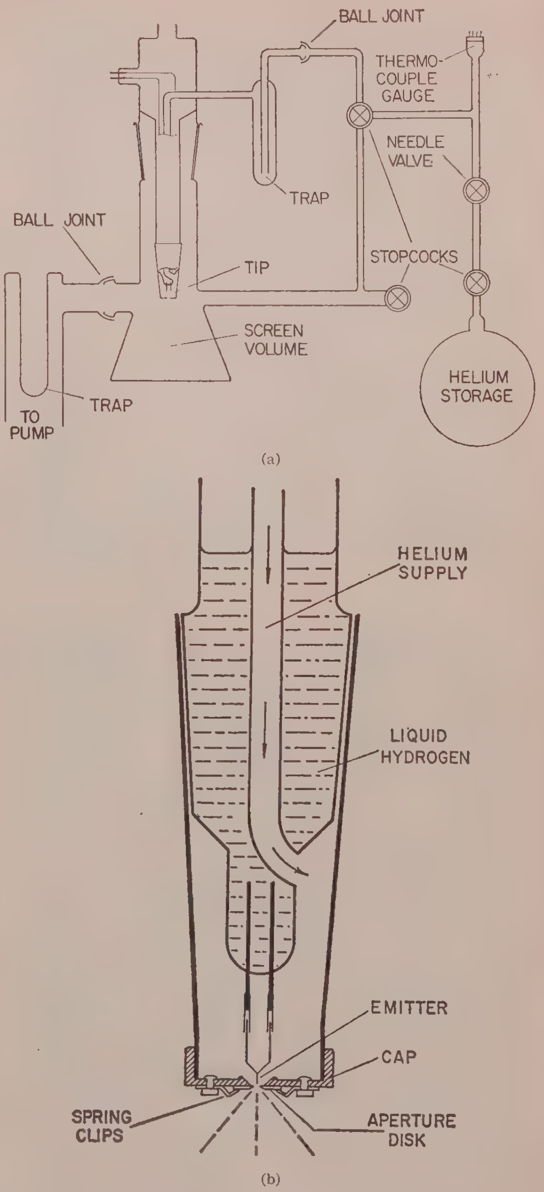

FIG. 1. (a) Schematic diagram of the field ion microscope with the external gas supply system. (b) High-pressure tip region indicating relative positioning of tungsten emitter and aperture.

III. DAMAGE TO THE TIP BY IMPINGING FAST PARTICLES

One of the unique features of the FIM when operated with helium or neon at 20°K is that the surface of the tip specimen stays absolutely clean. Surfaces that have been produced by exposing the interior of the tip crystal

---

[4] J. P. Barbour, W. W. Dolan, J. K. Trolan, E. E. Martin, and W. P. Dyke, Phys. Rev. 92, 45 (1953).

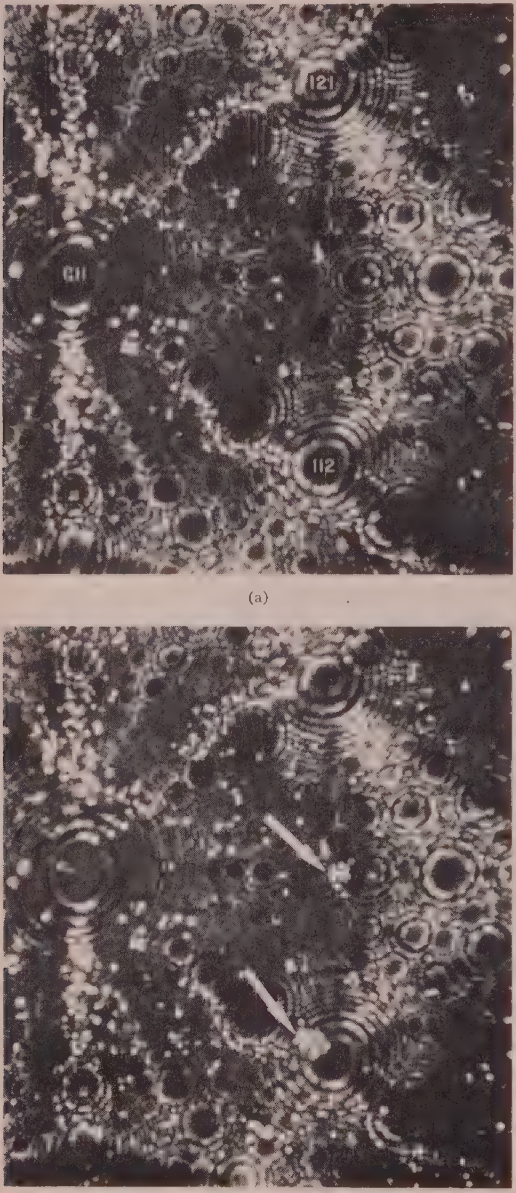

(a)

(b)

Fig. 2. (a) 20 kv tungsten crystal photographed 20 sec after cleaning surface by field evaporation. (b) Same crystal surface photographed 1 min after 2(a). Prominent impact areas are indicated by arrows.

by low-temperature field evaporation are not contaminated by even one foreign atom during an observation time of many hours. This is true also for relatively high contamination gas pressures of the order of 10^{-6} torr as they occur in the conventional unbaked FIM tube with greased joints. Contaminating gas molecules simply cannot reach the tip surface because they have a much lower ionization potential than helium or neon. When they approach the emitter with, essentially, thermal velocity they will be ionized by electron tunneling in a region well above the tip surface where the field is about 200–300 Mv/cm, while the helium or neon atoms can reach the surface where the field is held at 450 or 350 Mv/cm, respectively.

It was then somewhat surprising in the early stages of this work with a dynamic gas supply to find that the emitter surface sometimes was changed considerably during the observation. Bright clusters and other damage to the crystal structure appeared [Figs. 2 (a) and (b)] resembling the effects of cathode sputtering described elsewhere,[5] or the damage caused by alpha-particle bombardment.[6] The observed damage may be explained as being caused by the release of negative ions from the surface of the accelerating electrode when it is bombarded by the imaging helium ions. A negative ion so released would be accelerated toward the tip, gaining almost the full energy corresponding to the accelerating voltage of the microscope. When the particle approaches the tip into the high-field region, it will first be neutralized by electron tunneling and still continue traveling toward the tip. In the immediate vicinity of the tip surface it will probably be ionized once more to become a positive ion. However, as a result of its inertia, it may still continue against the field and strike the surface, thereby causing damage to the lattice.

This sputtering effect was found to be profuse when the accelerating electrode material surrounding the aperture was either aluminum or stainless steel, both known to possess heavy oxide surface layers, and to yield many negative ions. The effect was eliminated by using a gold-plated accelerator electrode, and by carefully centering the tip above the aperture so that very little of the helium ion beam could strike this electrode. It would also be helpful to shape the accelerating electrode in such a way that the negatively charged particles which are released would not be focused toward the tip. The further study of the emission of negative particles on aluminum and stainless steel might be of interest for the better understanding of high-voltage breakdown in accelerator tubes which often are constructed with these materials.

IV. CONCLUSIONS

With the elimination of the negative ion sputtering effect, the FIM with a dynamic gas supply, because of its enhanced brightness, promises to become useful for the study of transient atomic events on the surface of metal crystals such as field evaporation, motion of dislocations and slip bands, appearance at the surface of interstitials during low temperature annealing, and effects of irradiation by individual particles *in situ*. All these effects have been observed with the conventional FIM mostly visually so far, since photographs, even with sensitive films, required exposure times of minutes.

---

[5] E. W. Müller, Report 20th Annual Conference on Physical Electronics, Massachusetts Institute of Technology, Cambridge, Massachusetts, March, 1960.

[6] E. W. Müller, in *Structure and Properties of Thin Films*, edited by C. A. Neugebauer, J. B. Newkirk, and D. A. Vermilyea (John Wiley & Sons, Inc., New York, 1959), p. 476.

Further improvement appears possible by combining the FIM with an image amplifier, which would then permit recording the above-mentioned events with standard-speed motion picture equipment for more detailed examination.

JOURNAL OF APPLIED PHYSICS VOLUME 32, NUMBER 8 AUGUST, 1961

Shock Wave Compression of Hardened and Annealed 2024 Aluminum*

G. R. Fowles
Poulter Laboratories, Stanford Research Institute, Menlo Park, California

(Received December 27, 1960)

Measurements of the Hugoniot equations of state of hardened and annealed 2024 aluminum at pressures below 50 kbar are presented. The major aim of the experiments was to determine the validity of elastic-plastic theory, which predicts that, at a given compression, the stress normal to the shock front is larger than the hydrostatic pressure necessary to produce the same compression by an amount equal to two-thirds the yield strength in simple tension. Oblique shock geometry was employed. Shock and free-surface velocities were recorded with a streak camera by means of a light-reflection technique employing the principle of the optical level. This technique provides continuous recording of free-surface motion with time, an essential requirement because of the existence of a double shock system. The observed elastic wave amplitudes (5.4±0.2 kbar and 0.9±0.2 kbar for hardened and annealed material, respectively) agree within experimental precision with values predicted from static tensile specimen data. The shock wave data, in the range 25–50 kbar, yield one-dimensional strain isotherms which, while significantly different for the two different hardness conditions, agree within experimental precision with semitheoretical curves based on Bridgman's hydrostatic data to 30 kbar and on simple tension stress-strain data. No significant strain rate effects are evident. It is concluded that elastic-plastic theory is valid for the description of plane shock waves in this material.

I. INTRODUCTION

THE determination of equations of state of solids by the use of shock waves induced by high explosive is now a well established technique. Since publication of the first experiments by Walsh and Christian[1] a large number of materials have been investigated,[2,3] and the pressure range has been widely extended.[4,5]

Most existing measurements have been made at pressures of 100 kbar or more, a pressure where effects due to material rigidity can be safely neglected. In this paper experiments on 2024 aluminum designed to observe small differences in Hugoniot equations of state due to differences in strength of the material are described.

In all dynamic equation-of-state measurements the experimental method for determining pressure-density states is indirect in that the observed quantities are the shock velocity and, usually, the free-surface velocity produced upon normal reflection of the shock from a free boundary. Pressure (strictly, stress normal to the wave front) and corresponding density are computed from these measurements by means of the Rankine-Hugoniot conservation relations, together with an expression relating free-surface velocity to particle velocity prior to reflection. An x-ray method has also been used to determine density directly.[6,7]

More explicitly, the assumptions invoked in converting the measured velocities to pressure-density states are that:

(a) Shock waves with steady state profiles (in the compressive portion of the wave) are obtained. This allows application of the jump conditions expressing conservation of mass and momentum.

(b) Equilibrium is attained in times short compared to the time of measurement.

In addition, it has usually been assumed that:

(c) The stress is sufficiently isotropic that an ordinary fluid-type equation of state is valid. Thus, effects due to material rigidity are assumed negligible.

(d) The material is relieved from the shocked state along an isentrope from that state.

That these assumptions are adequate for pressures of the order of 100 kbar or more is evident from the reason-

---

* Work materially supported by Directorate of Solid State Sciences, U. S. Air Force Office of Scientific Research, ARDC, Washington, D. C., under contract.

[1] J. M. Walsh and R. H. Christian, Phys. Rev. **97**, 1544 (1955).

[2] J. M. Walsh, M. H. Rice, R. G. McQueen, and F. L. Yarger, Phys. Rev. **108**, 196 (1957).

[3] M. H. Rice, J. M. Walsh, and R. G. McQueen in *Solid State Physics*, edited by F. Seitz and D. Turnbull (Academic Press, Inc., New York, 1958), Vol. 6.

[4] R. G. McQueen and S. D. Marsh, J. Appl. Phys. **31**, 1253 (1960).

[5] L. V. Al'tshuler, K. K. Krupnikov, B. N. Ledenev, V. I. Zhuchikhin, and M. I. Brazhnik, Soviet Phys.—JETP **34**, 606 (1958); L. V. Al'tshuler, K. K. Krupnikov, and M. I. Brazhnik, *ibid.* **34**, 614 (1958).

[6] R. Schall, Explosivstoffe **6**, 120 (1958).

[7] J. Dapoigny, J. Kieffer, and B. Vodar, Compt. rend. **245**, 1502 (1957).

able agreement obtained with extrapolation of hydrostatic data.

The neglect of material rigidity, which leads to assumption (c), and to some extent assumption (d), is justified on the basis that most materials are capable of withstanding stress differences of only a few kilobars. Hence, where the stress normal to the front (the experimentally determined quantity), is 100 kbar or more this stress can be taken equal to the mean stress, or pressure, to an approximation within experimental error.

This assumption, however, is clearly not necessarily valid for shock pressures comparable to the yield strength of the material. Application of elastic-plastic theory to the case of one-dimensional strain (corresponding to the strain configuration of a plane shock) shows that for this case the stress in the direction of compression is larger than the hydrostatic stress necessary to produce the same density by an amount equal to two-thirds the yield strength in simple tension.[8,9]

In this paper, shock wave equation-of-state experiments designed to observe, at a given density, the offset in stress between hardened and annealed 2024 aluminum are described. The motivation was to examine the validity of the elastic-plastic model of shock propagation at least for this material. Determination of the validity of this model is important not only for the description of the transition region between elastic and "hydrodynamic" wave propagation, but also in that it would provide a firmer theoretical basis for the higher-pressure data. Aluminum was chosen for these experiments mainly because of the availability of hydrostatic data, and the 2024 alloy primarily because of its relatively high yield strength.

It should be noted that it is not entirely obvious that the simple elastic-plastic model should be correct for shock waves in metals, primarily because of possible strain-rate effects. In shock waves, strain rates are larger than the rates of deformation for which plasticity theory is known to apply by factors of 10^6 or more. At high strain rates, increases in yield strength have in fact been observed in a number of metals.[10] Johnson *et al.*[11] have reported a 20% increase in yield strength for annealed 2S aluminum. Bell,[12] however, in a different experimental arrangement, has observed no strain-rate effects in aluminum. Whiffin[10] has reported a 50–150% increase in yield strength for Duralumin of approximately the same composition and static yield strength as the material of the present experiments.

Normally attainable precision in shock wave equation-of-state experiments is approximately 2% in pressure at a given compression. Hence, in order for the predicted offset in stress (approximately 1.2 kbar between hardened and annealed aluminum) to be experimentally significant it is necessary that measurements be made on shock waves whose amplitudes lie below about 50 kbar.

Theory shows that at these pressures in aluminum a single shock front is unstable and splits into two fronts.[3] The first travels with elastic dilatational velocity and has stress amplitude equal to the elastic limit appropriate to the case of one-dimensional strain. This front is followed by a slower plastic shock wave which carries the material to the final pressure. The region between the two waves is substantially a constant state. (It is strictly constant only for nonwork-hardening material.) Since the jump conditions cannot be applied across the entire wave system, it is necessary to observe the amplitudes of both waves individually. In effect, this requires a method for recording free-surface motion continuously with time.

The experimental requirements of low shock pressure were met by use of wedge geometry, as described previously by Katz *et al.*[13] and by Doran *et al.*[14] Continuous recording of free-surface motion was accomplished by a light-reflection technique employing the principle of the optical lever in conjunction with a rotating mirror streak camera. This technique is similar to one described earlier by Allen and McCrary.[15]

II. THEORY

Application of elastic-plastic theory to the case of one-dimensional strain leads to a stress-strain relation in terms of the stress-strain relation obtained from ordinary simple tension (one-dimensional stress) experiments, and the isothermal, hydrostatic equation of state. The isothermal, one-dimensional strain equation of state so derived corresponds closely to the relation expected to obtain in plane shock wave experiments; i.e., the Hugoniot equation of state. The correspondence is not exact because of the temperature increase in the shock caused by adiabatic heating, plastic work, and other irreversible processes occurring within the shock front. Since, for purposes of comparison of theory and experiment, it is possible to adjust the dynamic data to isothermal conditions, temperature effects are not directly considered in the elastic-plastic theory.

The following derivation[16] is a straightforward application of fundamental relations as given, for example, by Hill.[17] Similar derivations have been given earlier.[8,9,18]

---

[8] L. W. Morland, Phil. Trans. Roy. Soc. London **A251**, 341 (1959).

[9] D. S. Wood, J. Appl. Mech. **19**, 521 (1952).

[10] G. I. Taylor and A. C. Whiffin, Proc. Roy. Soc. (London) **A194**, 289 (1948).

[11] J. E. Johnson, D. S. Wood, and D. S. Clark, J. Appl. Mech. **20**, 523 (1953).

[12] J. F. Bell, J. Appl. Phys. **31**, 277 (1960).

[13] S. Katz, D. G. Doran, and D. R. Curran, J. Appl. Phys. **30**, 568 (1959).

[14] D. G. Doran, G. R. Fowles, and G. A. Peterson, Phys. Rev. Letters **1**, 1–2 (1958).

[15] W. Allen and C. L. McCrary, Rev. Sci. Instr. **24**, 165 (1952).

[16] The author is indebted to Dr. J. E. Neimark for suggesting a similar derivation.

[17] R. Hill, *The Mathematical Theory of Plasticity* (Oxford University Press, London, 1950).

[18] J. M. Walsh (unpublished).

These have generally treated work hardening somewhat less explicitly, however.

A. Fundamental Relations

In tensor notation, Hooke's Law, expressing linearity between stress increments $d\sigma_{ij}$ and elastic (natural) strain increments $d\epsilon_{ij}^e$, can be written

$$d\epsilon_{ij}^e=(d\sigma_{ij}'/2\mu)+[(1-2\nu)/E]\delta_{ij}d\sigma, \tag{1}$$

where $d\sigma_{ij}'$ is the deviatoric stress increment acting in the i direction on a plane perpendicular to the j direction. The subscripts i and j refer to Cartesian coordinates; δ_{ij} is the Kroneker delta ($\delta=0$, $i\neq j$; $\delta=1$, $i=j$); and the summation convention for repeated subscripts applies. The symbols μ, ν, and E denote the shear modulus, Poisson's ratio, and Young's modulus, respectively. The deviatoric stress increment $d\sigma_{ij}'$ is defined by $d\sigma_{ij}'=d\sigma_{ij}-d\sigma$, where $d\sigma=\frac{1}{3}d\sigma_{ii}$. Throughout this section, compressive stresses and strains are taken positive.

The von Mises yield criterion is

$$Y(W_p)=(\tfrac{3}{2})^{\frac{1}{2}}(\sigma_{ij}'\sigma_{ij}')^{\frac{1}{2}}, \tag{2}$$

where Y is the yield stress in simple tension. Work hardening is included by means of the assumption that Y is a function of the plastic work W_p.

The incremental plastic work is defined by

$$dW_p=\sigma_{ij}d\epsilon_{ij}^p, \tag{3}$$

where $d\epsilon_{ij}^p$ is the plastic, or irrecoverable, component of the strain:

$$d\epsilon_{ij}^p=d\epsilon_{ij}-d\epsilon_{ij}^e,$$

and $d\epsilon_{ij}$ is total strain.

A further assumption is that no volume changes result from the plastic components of strain, i.e.,

$$d\epsilon_{ii}^p\equiv 0. \tag{4}$$

Equations (1)–(4) can be specialized to the cases of one-dimensional stress (simple tension) and of one-dimensional strain. This leads to a relation between the stress-strain curves of the two configurations, and thereby allows the difference between hydrostatic and one-dimensional strain equations of state to be determined from ordinary tensile specimen data.

For both configurations two regimes are to be distinguished, depending on whether the yield criterion, Eq. (2), is satisfied. These are specified as the elastic and plastic regions.

B. One-Dimensional Stress

By denoting the direction of applied stress as the s direction, Eq. (1) for this case becomes:

$$\begin{aligned} d\epsilon_s^e&=(d\sigma_s'/2\mu)+[(1-2\nu)/E](d\sigma_s/3)\\ &=d\sigma_s/E. \end{aligned} \tag{5}$$

The yield criterion, Eq. (2), is simply

$$\sigma_s=Y(W_p). \tag{6}$$

The incremental plastic work, Eq. (3), is then

$$\begin{aligned} dW_p&=Yd\epsilon_s^p\\ &=Y[d\epsilon_s-(d\sigma_s/E)]\\ &=Y[d\epsilon_s-(dY/E)]. \end{aligned} \tag{7}$$

C. One-Dimensional Strain

By denoting the direction of net total strain (direction of shock propagation) as the x direction, Eq. (1) becomes:

$$\begin{aligned} d\epsilon_x^e&=E^{-1}(d\sigma_x-\nu d\sigma_y-\nu d\sigma_z)\\ &=E^{-1}(d\sigma_x-2\nu d\sigma_y). \end{aligned} \tag{8}$$

Similarly,

$$d\epsilon_y^e=E^{-1}(d\sigma_y-\nu d\sigma_y-\nu d\sigma_z)=d\epsilon_z^e. \tag{9}$$

Since y and z components must be equal from symmetry, Eq. (2) is:

$$\sigma_x-\sigma_y=Y(W_p) \tag{10}$$

and Eq. (4) is:

$$d\epsilon_x^p+2d\epsilon_y^p=0. \tag{11}$$

Since the total strain in the lateral directions must be zero, the elastic and plastic components of strain must cancel. Hence,

$$d\epsilon_y^e=-d\epsilon_y^p$$

and, therefore,

$$d\epsilon_x=d\epsilon_x^e+2d\epsilon_y^e. \tag{12}$$

The incremental plastic work, Eq. (3), is:

$$\begin{aligned} dW_p&=\sigma_x d\epsilon_x^p+2\sigma_y d\epsilon_y^p\\ &=(\sigma_x-\sigma_y)d\epsilon_x^p. \end{aligned}$$

On substituting for $\sigma_x-\sigma_y$ from Eq. (10),

$$dW_p=Y(W_p)d\epsilon_x^p, \tag{13}$$

which is the same as for the case of one-dimensional stress.

The plastic strain increment in Eq. (13) can be related to the total strain increment. Since

$$d\epsilon_x^p=d\epsilon_x-d\epsilon_x^e,$$

we have, from Eq. (1),

$$d\epsilon_x^p=d\epsilon_x-\frac{d\sigma_x'}{2\mu}-[(1-2\nu)/E]d\sigma. \tag{14}$$

Also, from Eqs. (1) and (4),

$$\begin{aligned} d\epsilon_{ii}&=d\epsilon_{ii}^p+(d\sigma_{ii}'/2\mu)+[3(1-2\nu)/E]d\sigma\\ &=[3(1-2\nu)/E]d\sigma\\ &=d\epsilon_x. \end{aligned} \tag{15}$$

Further,

$$\begin{aligned} d\sigma_x'&=d\sigma_x-\tfrac{1}{3}(d\sigma_x+2d\sigma_y)\\ &=\tfrac{2}{3}(d\sigma_x-d\sigma_y)\\ &=\tfrac{2}{3}dY. \end{aligned} \tag{16}$$

Hence, combining Eqs. (14), (15), and (16),

$$d\epsilon_x{}^p=\tfrac{2}{3}[d\epsilon_x-(dY/2\mu)],$$

and Eq. (13) can be written:

$$dW_p=\tfrac{2}{3}Y[d\epsilon_x-(dY/2\mu)]. \qquad (17)$$

The relation between stress increment $d\sigma_x$ and total strain increment $d\epsilon_x$ is obtained as follows.

Equation (12) states:

$$d\epsilon_x=d\epsilon_x{}^e+2d\epsilon_y{}^e.$$

Substituting from Eq. (1),

$$\begin{aligned}d\epsilon_x&=[(1-2\nu)/E](d\sigma_x+2d\sigma_y)\\&=[3(1-2\nu)/E](d\sigma_x-\tfrac{2}{3}dY)\end{aligned}$$

or

$$d\sigma_x=Kd\epsilon_x+\tfrac{2}{3}dY, \qquad (18)$$

where K is the isothermal bulk modulus. Since the mean stress $d\sigma$ is given by

$$d\sigma=Kd\epsilon=Kd\epsilon_x,$$

Eq. (18) can be written

$$d\sigma_x-d\sigma=\tfrac{2}{3}dY, \qquad (19)$$

which integrates directly to give $\sigma_x-\sigma=\frac{2}{3}Y$. It is evident that in the plastic range the stress is larger than the corresponding hydrostatic stress for the same strain by an amount $\frac{2}{3}Y$. Thus, the difference between one-dimensional strain and hydrostatic stress-strain curves depends only on the yield stress as a function of strain. This relation can be obtained from standard tensile specimen data provided the comparison is made at appropriate corresponding values of strain, i.e., strains for which the plastic work is the same. The relation between the total strains is obtained as follows.

From Eqs. (7) and (17) it is apparent that for the same values of W_p and dW_p we have

$$\tfrac{2}{3}[d\epsilon_x-(dY/2\mu)]=d\epsilon_s-(dY/E).$$

By simplifying,

$$d\epsilon_x=\tfrac{3}{2}d\epsilon_s-(dY/6K), \qquad (20)$$

which is the desired relation.

To a good approximation the variation in K with mean stress can be neglected, and Eq. (20) can be integrated immediately to give:

$$\epsilon_x-\epsilon_x{}^0\cong\tfrac{3}{2}(\epsilon_s-\epsilon_s{}^0)-[(Y-Y^0)/6K], \qquad (21)$$

where superscripts "0" refer to the initial yield point.

Since

$$\epsilon_x{}^0=[(1+\nu)/E]Y^0$$

and

$$\epsilon_s{}^0=Y^0/E,$$

Eq. (21) reduces to

$$\epsilon_x\cong\tfrac{3}{2}\epsilon_s-(Y/6K). \qquad (22)$$

The procedure is therefore to determine Y as function of ϵ_s from standard tensile specimen data, and to determine corresponding values of ϵ_x from Eq. (22) and $\sigma_x-\sigma$ from Eq. (19).

The results are summarized for convenience in the following.

Elastic Region

In this region integration of the equations is immediate since the coefficients are constants, and stress and strain go to zero simultaneously. Hence, the differential notation is simply dropped. We then have:

$$\begin{aligned}\epsilon_z=\epsilon_y&=0\\ \sigma_x&=[E(1-\nu)/(1+\nu)(1-2\nu)]\epsilon_x\\ \sigma_y&=[\nu/(1-\nu)]\sigma_x\\ \sigma_x-\sigma_y&=[(1-2\nu)/(1-\nu)]\sigma_x\\ p=\sigma&=[(1+\nu)/3(1-\nu)]\sigma_x=K\epsilon_x\\ \sigma_x-p&=\tfrac{2}{3}[(1-2\nu)/(1-\nu)]\sigma_x=\tfrac{4}{3}\mu\epsilon_x\\ &=\tfrac{2}{3}(\sigma_x-\sigma_y).\end{aligned} \qquad (23)$$

At the yield point, therefore,

$$\sigma_x=[(1-\nu)/(1-2\nu)]Y^0 \qquad (24)$$

and

$$\begin{aligned}\sigma_x-p&=\tfrac{2}{3}Y^0\\ \epsilon_x{}^0&=[(1+\nu)/E]Y^0;\quad \epsilon_s{}^0=Y^0/E.\end{aligned}$$

Plastic Region

$$\begin{aligned}d\sigma_x&=Kd\epsilon_x+\tfrac{2}{3}dY\\ dp&=Kd\epsilon_x\\ dW_p&=\tfrac{2}{3}Y[d\epsilon_x-(dY/2\mu)]\\ d\epsilon_x{}^p&=\tfrac{2}{3}[d\epsilon_x-(dY/2\mu)]=-2d\epsilon_y{}^p\\ d\epsilon_x{}^e&=\tfrac{1}{3}d\epsilon_x+(dY/3\mu)\\ d\epsilon_y{}^e&=\tfrac{1}{3}d\epsilon_x-(dY/6\mu)\\ \sigma_x-p&=\tfrac{2}{3}Y\\ \epsilon_x&\cong\tfrac{3}{2}\epsilon_s-(Y/6K).\end{aligned} \qquad (25)$$

The relation between relative volume V/V_0 and natural strain ϵ_x is:

$$V/V_0=\exp(-\epsilon_x).$$

Engineering strain e is related to ϵ and V by

$$e=1-(V/V_0)=1-\exp(-\epsilon_x).$$

From the three relations between strain increments in Eqs. (25) it is apparent that, except for the (small) increment in dY, the elastic strain increments in the plastic region are isotropic. Further, of the total strain increment in the x direction, two-thirds is plastic and one-third elastic.

These results are depicted qualitatively in Fig. 1. In one-dimensional strain the material first strains elastically until the yield criterion is satisfied at $\sigma_x{}^0$.

Additional strain is then approximately two-thirds plastic and one-third elastic. The offset in stress with respect to the hydrostatic curve is equal to two-thirds the yield strength for the same value of plastic strain.

If after loading the material to, say, point C the stress is relieved one-dimensionally, the strain is initially again elastic (CD in Fig. 1) until the yield criterion is again satisfied. The stress difference between points C and D is approximately $2\sigma_x^0$, (neglecting Bauschinger effect and changes in the elastic constants with pressure).

Upon further relief of stress, path DE is followed, again offset from the hydrostatic curve by $\frac{2}{3}Y$. It will be noted that at $\sigma_x=0$ the material is left with a net strain. This is due to an elastic stress parallel to the boundary which is not relieved in this process and which maintains the material at the yield point. This lateral stress can be relieved only by lateral expansion which, in this idealized case, is not permitted.

III. EXPERIMENTAL METHOD

As mentioned in Sec. I, the dynamic method for determining stress and corresponding compression requires simultaneous measurement of the shock velocity and associated free-surface velocity, produced upon reflection of the wave at a free boundary. These velocities, together with a relation between free-surface velocity and particle velocity prior to reflection, give stress and corresponding compression by means of the Rankine-Hugoniot jump conditions expressing conservation of mass, momentum, and energy.[19] These are

$$V_2/V_1=1-\frac{u_2-u_1}{U_2-u_1} \quad \text{conservation of mass}$$

$$\sigma_2-\sigma_1=\rho_1(U_2-u_1)(u_2-u_1) \quad \text{conservation of momentum} \tag{26}$$

$$E_2-E_1=\frac{\sigma_2+\sigma_1}{2}(V_1-V_2) \quad \text{conservation of energy,}$$

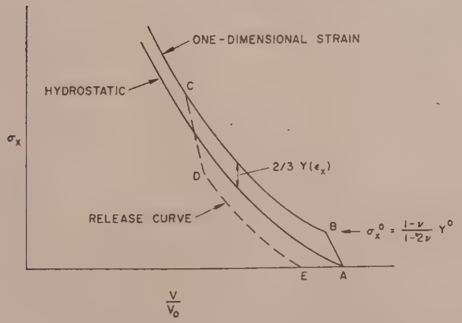

FIG. 1. Qualitative stress-strain paths.

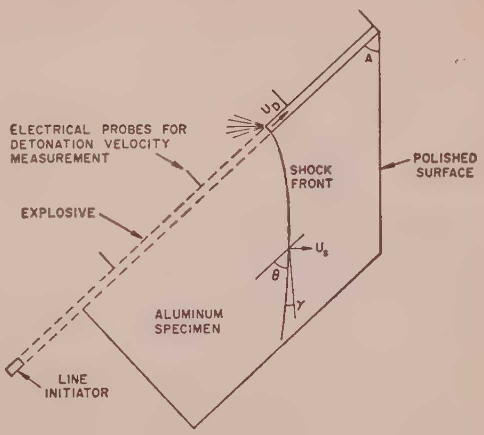

FIG. 2. Side view of experimental arrangement.

where U is shock velocity (laboratory coordinates), u is particle velocity, V is specific volume, σ is stress normal to the wave front, and E is specific internal energy. Subscripts 1 refer to the state ahead of the wave front and subscripts 2 refer to the state immediately behind the front.

The experimental arrangement for determining shock velocities and corresponding free-surface velocities is shown schematically in Fig. 2. This geometry was chosen because it provides continuous data over a range of stress from a single shot, and because the necessary low shock stresses are easily obtained. Use of this geometry with a different recording method was first reported by Katz *et al.*[13]

The explosive slab is initiated at the rear with a flying-plate line initiator. As the detonation progresses with constant velocity, a shock wave is induced into the specimen which decays with distance from the explosive. When the detonation wave has traveled far enough, the shock wave will be steady in time; i.e., the point of intersection of the shock with any horizontal plane will travel with an apparent velocity equal to detonation velocity. Under these conditions it is apparent from the figure that shock velocity U_s at any point is given by

$$U_s=U_D \sin\theta=U_a \sin\gamma, \tag{27}$$

where U_D is detonation velocity and U_a is the apparent velocity with which the shock intersects a plane parallel to the wedge face.

Moreover, since

$$\theta+\gamma=A$$
$$\sin\theta=(U_a/U_D)\sin(A-\theta),$$

from which

$$\cot\theta=\cot A+(U_D/U_a \sin A). \tag{28}$$

Thus, if U_a, U_D, and A are measured, U_s can be calculated from Eqs. (27) and (28). This velocity, together

---

[19] R. Courant and K. O. Friedrichs, *Supersonic Flow and Shock Waves* (Interscience Publishers, Inc., New York, 1948).

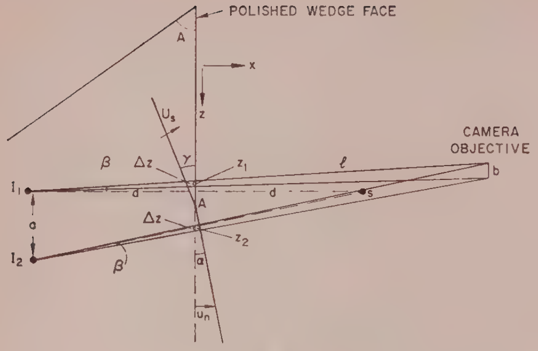

FIG. 3. Diagram of recording method.

with a simultaneous measurement of free-surface velocity at each point on the wedge face, constitute the desired experimental quantities.

Detonation velocity is determined by recording the arrival times of the detonation front at a series of electrical contactor pins of known spacing.

The apparent velocity U_a, together with the normal component of free-surface velocity u_n, are measured with a streak camera by the observation of images of point light sources reflected in the polished specimen surface.

A sketch of the recording method is shown in Fig. 3. The wedge face is polished to a mirror surface and light sources represented by S are placed a (normal) distance d away from the surface. The camera is focused on the virtual image of S represented in the undisturbed face by I_1. The wedge face is deliberately cut so that the wave to be observed is inclined at a small angle γ to the surface. The point of intersection is designated as "A" in the figure. As the wave arrives, it turns the free surface through an angle α which, for α small, is related to the free-surface and apparent velocities by

$$\alpha \cong u_n / U_a,$$

where u_n is the component of free-surface velocity normal to the original surface.

In the turned surface the light source S has a second virtual image I_2 displaced from I_1 by a distance a, given by

$$a \cong 2d\alpha.$$

Thus measurement of d and a determines α. It will be noted that the magnification can be simply varied by changing the distance d. Moreover, the displacement of the images is directly proportional to the free-surface velocity.

Apparent velocity U_a is measured by the time required for point A to travel from z_2 to z_1. As point A moves along the wedge face, the images I_1 and I_2 remain stationary. Further, I_1 can be seen only through the undisturbed mirror surface which acts as an aperture, i.e., above a plane determined by a line from I_1 to A. Similarly, I_2 can be seen only in the region below a plane determined by a line from I_2 to A. The figure is drawn for the case where both images are visible in the camera simultaneously. Image I_1 will disappear, however, as A crosses the distance Δz at $z = z_1$.

The resolution of the system depends upon several factors. Maximum resolving power is determined by the characteristics of the smear camera, for which the time resolution is approximately 0.01 μsec and the space resolution is approximately 180 lines per mm on the film. This resolution is not achieved in practice, however, because of the fact that the light from a given image is reflected from an area of the wedge face (Δz in Fig. 3). If this area is not substantially plane, a broadened image results. The position of the center of this image is determined by some average of the deflection angle taken over the interval Δz. In general, therefore, the structure of an incident wave cannot be distinguished within a distance, measured in the direction of the normal to the wave front, equal to $\Delta z \sin\gamma$. In the present experiments Δz amounted to approximately 1 mm and γ to 10–20°. Hence, the space resolution is approximately 0.2–0.4 mm. For a wave velocity of 6 mm/μsec this is equivalent to a time resolution of 0.03–0.07 μsec. It is apparent that this resolution depends on the angle γ and improves with decreasing angle.

For a given curvature of the surface, image broadening is reduced and resolution improved by decreasing the angle β. In most cases this can be accomplished only by reducing the camera aperture b, since the distances l and d are fixed by other considerations. Even given sufficient light intensity, however, b cannot be reduced indefinitely because of diffraction around b. In the present experiments the aperture was chosen, somewhat arbitrarily, such that the central maximum in the diffraction pattern appeared to be approximately twice as wide as the image width (~0.1 mm).

In practice, the light source consisted of a grid of narrow lines on the face of an explosive argon candle. The lines were oriented perpendicular to the slit direction so that the camera effectively viewed only a row of point light sources. In the experiments, approximately six lines per inch on the wedge face were employed.

In the above description it has been assumed for simplicity that the state behind the incident wave is steady, i.e., U_a and u_n are independent of z. While this is substantially correct for the elastic wave it is not true for the decaying shock. In this case the free-surface velocity can be deduced from the record as follows:

Denoting displacement in the direction normal to the wedge face by x, and considering the free-surface velocity u_n as a function of time t and position z, we have

$$x(z,t) = \int_{t_0(z)}^{t} u_n(z,t)dt,$$

where t is the time of measurement and $t_0(z)$ is time of arrival of the wave at the surface at point z.

Let

$$\tau(z,t)=t-t_0(z);$$

then

$$x(z,\tau)=\int_0^{\tau(z,t)} u_n(z,\tau)d\tau.$$

Hence

$$\alpha=\left(\frac{\partial x}{\partial z}\right)_t=\int_0^{\tau}\frac{\partial u_n}{\partial z}d\tau+u_n(z,\tau)\left(\frac{\partial \tau}{\partial z}\right)_t;$$

but

$$\frac{\partial\tau(z,t)}{\partial z}=\frac{\partial\tau}{\partial t_0}\frac{dt_0}{dz}=-\frac{dt_0}{dz}=-\frac{1}{U_a(z)}.$$

Hence

$$\alpha(z,\tau)=-\frac{u_n(z,\tau)}{U_a(z)}+\int_0^{\tau}\frac{\partial u_n}{\partial z}d\tau. \qquad (29)$$

The second term on the right is the correction to the measurement resulting from the gradient in u_n. It is reasonable to assume that u_n is constant with time, however, once equilibrium is established, i.e., after the rise time of the shock. Assuming u_n to be a function of z only gives:

$$\alpha(z,\tau)=-[u_n(z)/U_a(z)]+(\partial u_n/\partial z)\tau. \qquad (30)$$

Since α is measured as a function of τ at constant z in the experiments, Eq. (30) suggests a slope-intercept graphical type of analysis in which, for fixed z, α is plotted as function of τ. The slope is then $\partial u_n/\partial z$ and the intercept $-u_n/U_a$. In practice the second term of Eq. (30) amounts to 5–10% of the first term. Hence, the correction is not a large one.

The normal component of free-surface velocity determined by the above analysis must be related to the particle velocity behind the front prior to reflection in order to compute stress-density states.

For the elastic wave, elasticity theory may be applied.[20] The direction of particle motion with respect to the normal is given by

$$\cos\delta=1-[(2\nu-1)/(\nu-1)]\sin^2\gamma, \qquad (31)$$

where δ is the angle between the normal and the direction of particle motion, ν is Poisson's ratio, and γ is the angle of incidence of the wave on the boundary. Free-surface velocity u_f is then

$$u_f=u_n\sec\delta, \qquad (32)$$

and particle velocity is related to free-surface velocity by

$$u=u_f\left[\frac{\sin\delta\cos\gamma+\cos\delta\sin(\gamma-\delta)}{\sin 2\gamma}\right]. \qquad (33)$$

The angle of incidence is known from Eq. (28); hence u can be calculated from the observed quantities, α and U_a, by means of Eqs. (30)–(33).

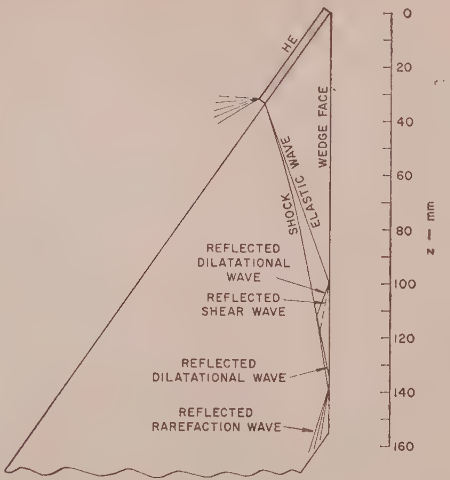

FIG. 4. Wave diagram (to scale).

For the shock the situation is somewhat more complicated. The initial elastic wave reflects from the free surface as both a dilatational and a shear wave. These relieve the stress normal to the boundary but do not entirely relieve the compressive stress parallel to the boundary. The reflected waves in turn interact with the shock with the result that a second elastic compressional wave precedes the shock which, because of the residual lateral stress, is slightly larger in amplitude than the initial elastic wave. In effect, elastic waves reverberate between free surface and shock front. A drawing of the wave pattern as it appears at one particular instant of time is shown in Fig. 4.

The details of the interaction are in general very complicated even for the case of normal incidence where shear waves are not generated. Walsh[18] has shown, however, that for the case of normal incidence the final free-surface velocity is given simply by:

$$u_f=\int_0^{e_x}\left(\frac{1}{\rho_0}\frac{d\sigma_x}{de_x}\right)^{\frac{1}{2}}de_x+u_s, \qquad (34)$$

where u_s is the shock particle velocity and e_x is engineering strain.

The integral in Eq. (34) (the Riemann integral) is to be evaluated along the stress-strain path corresponding to rarefaction (path CDE of Fig. 1). Its value in general depends upon the equation of state, which is not known in advance. It can be evaluated approximately, however, without specific knowledge of the equation of state above the elastic limit, by assuming the values of $d\sigma_x/de_x$ to be constant for each of paths CD and DE. It is further assumed that for the elastic portion (CD) the value is the same as for the initial elastic wave and that the difference in strain from C to

---

[20] W. M. Ewing, W. S. Jardetzky, and F. Press, *Elastic Waves in Layered Media* (McGraw-Hill Book Company, Inc., New York, 1957), p. 27.

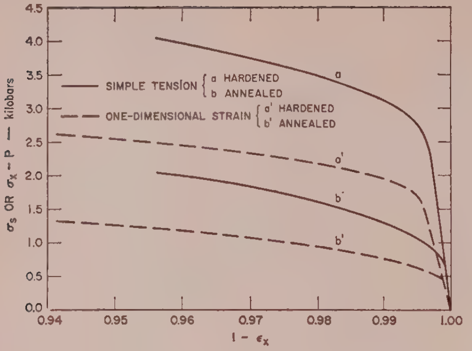

FIG. 5. Static stress-strain curves (true stress and natural strain).

D is twice the initial elastic strain to σ_x^0. Since the curvature in the plastic portion DE is small, an average value of $d\sigma_x/de_x$ can be assumed. With these assumptions, Eq. (34) can be written:

$$u_s = u_f - 2u_e - \bar{c}_p(e_x - 2e_x^e - e_x^*), \tag{35}$$

where e_x^* is the residual strain after relief of stress (EA in Fig. 1), and $\bar{c}_p$ is an average value of $[(1/\rho_0)\times(d\sigma_x/de_x)]^{\frac{1}{2}}$ for the plastic portion of the relief (DE). The quantities $\bar{c}_p$ and e_x can be written in terms of shock velocity U_s and particle velocity u_s by means of the jump conditions [Eq. (26)]. These give:

$$e_x = e_x^e + \frac{u_s - u_e}{U_s - u_e} - \frac{e_x^e(u_s - u_e)}{U_s - u_e},$$

where u_e is the particle velocity of the elastic wave. Also,

$$\bar{c}_p = \bar{U}_s(1 - e_x^e)^{\frac{1}{2}},$$

where $\bar{U}_s$ is a suitable average value of shock velocity over the pressure range of interest. Substitution of the above in Eq. (32) and simplification gives:

$$u_s = \frac{u_f - 2u_e + u_e(1-e_x^e)^{\frac{1}{2}} + [\bar{U}_s/(1-e_x^e)^{\frac{1}{2}}](e_x^e + e_x^*)}{1 + (1-e_x^e)^{\frac{1}{2}}}$$

or, approximately,

$$u_s = \frac{u_f}{2} + \frac{\bar{U}_s(e_x^e + e_x^*) - u_e}{2}. \tag{36}$$

Although the assumptions employed in deriving Eq. (36) are rather broad, the correction to the usual relation $u_s = u_f/2$, valid for fluids, is not large. The maximum value of the second term on the right of Eq. (36) amounts to some 6% of the first term. Since the equation of state is relatively insensitive to errors in particle velocity, this approximation is considered to be satisfactory.

Except for the elastic wave, the direction of particle motion is assumed to be normal to the free surface. This approximation is valid where the turning angle α is small and where the amplitude of the reflected shear wave can be neglected. Experimental verification of this approximation for strong shocks in metals has been obtained by Allison and Watson.[21]

The measured wave velocities and the particle velocities obtained from the free-surface velocities by Eqs. (33) and (36) are employed in the Rankine-Hugoniot jump conditions to calculate the stress normal to each front and the corresponding strain [Eq. (26)]. In the present experiments these relations were applied successively across each of the two waves to determine the final state.

It will be noted that in the analysis of the data it is assumed that the strains are purely one-dimensional. In the experiments, however, the elastic and shock fronts are not parallel so that the net strain in the elastic wave is not in the same direction as the net strain in the shock. The angular difference is about 10°. Neglect of this difference leads to an error in final shock stress of the order of $Y(1-\cos 10°)$, which is well within experimental precision.

IV. EXPERIMENTS

The material used in the experiments was commercial 2024-T4 aluminum.[22] There were several reasons for this choice of material for the experiments. Because of the low density, relatively high free-surface velocities are obtained at low pressures and this facilitates the measurements. Hydrostatic data are also available for pure aluminum so that, except for possible differences in compressibility due to the presence of the alloying elements, a direct comparison of dynamic and static results is possible.[23] Moreover, this material has relatively high yield strength as supplied, and is available in large samples.

A total of six wedges were fired. Of these, four were cut from the same bar of stock material. Three were fired with hardened material as supplied; the other three were annealed by heating to 800°F for 2 hr followed by cooling at the approximate rate of 50°F per hour. Tensile specimens of these materials gave the stress-strain curves (reduced to true stress and natural strain) shown in Fig. 5. Yield strengths at 0.2% offset strain were 42 100 psi and 14 500 psi for the material as supplied and annealed, respectively.

The dimensions of each specimen are given in Table I. The explosive in each case was Composition B, $\frac{1}{8}$ in. thick. It covered the entire upper surface of the specimen, with an additional overlap at the rear to minimize any effects due to initiation.

---

[21] F. E. Allison and R. W. Watson, J. Appl. Phys. 31, 842 (1960).

[22] Nominal composition: 93.4% Al, 4.5% Cu, 1.5% Mg, and 0.16% Mn, by weight.

[23] Calculation of the initial slopes of the pressure-volume curves for commercially pure aluminum and Dural (17S), based on measured acoustic velocities and initial densities, shows a difference of less than 0.1% [*Americal Institute of Physics Handbook*, edited by D. Gray (McGraw-Hill Book Company, Inc., New York, 1957), pp. 3–77 to 3–80].

TABLE I. Summary of experimental data.[a]

			Elastic wave								Shock wave			
Shot No. and condition	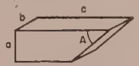 Specimen dimensions	Detonation velocity (mm/μsec)	Elastic wave velocity (mm/μsec)	Initial free-surface velocity (m/sec)	Stress (kbar)	Strain (%)	Calculated yield strength (kbar)	Final free-surface velocity (m/sec)	Stress (kbar)	Strain (%)	Shock velocity (mm/μsec)	Free-surface velocity (m/sec)	Stress (kbar)	Relative volume (V/V_0)
5711 (as supplied)	A=45°05′ a=2½ in. b=3½ in. c=9 in.	7.88	6.41	60.8	5.44	0.474	2.81							
5843 (as supplied)[b]	A=35°0′ a=2½ in. b=3½ in. c=9 in.	7.87	6.46	57.8	5.22	0.447	2.70	80.0	7.10	0.63	5.801	609	50.9	0.94704
											5.771	591	49.3	0.94836
											5.745	572	47.5	0.94981
											5.723	542	45.0	0.95225
											5.704	520	43.1	0.95405
											5.685	496	41.1	0.95603
											5.669	472	39.1	0.95804
											5.658	447	37.1	0.96018
											5.647	421	34.9	0.96242
6237 (as supplied)[b]	A=34°59′ a=3½ in. b=3½ in. c=9½ in.	7.88	6.40	61.4	5.49	0.480	2.84	80.8	7.12	0.64	5.721	535	44.5	0.95275
											5.702	515	42.8	0.95428
											5.683	493	40.9	0.95609
											5.664	471	39.1	0.95791
											5.643	449	37.2	0.95973
											5.624	426	35.4	0.96157
											5.603	403	33.4	0.96359
											5.582	379	31.4	0.96563
											5.559	354	29.5	0.96767
											5.535	329	27.4	0.96991
											5.510	302	25.3	0.97216
6054 (annealed)[b]	A=35°03′ a=3½ in. b=3½ in. c=9½ in.	7.84	6.42	8.0	0.7	0.06	0.4	16.2	1.4	0.13	5.671	573	45.5	0.94967
											5.639	530	41.9	0.95312
											5.617	502	39.6	0.95544
											5.597	474	37.2	0.95778
											5.558	444	34.6	0.96020
											5.543	414	32.2	0.96280
6382 (annealed)[b]	A=35°02′ a=3½ in. b=3½ in. c=7¾+1½ in.	7.88	6.41	7.6	0.7	0.06	0.4	18.2	1.6	0.15				
6926 (annealed)	A=35°00′	7.78	6.39	14.5	1.3	0.11	0.7	25.3	2.2	0.20	5.676	559	44.8	0.95061
	a=3½ in.										5.659	546	43.7	0.95161
	b=3½ in.					Observed yield strengths (kbar)					5.642	530	42.3	0.95289
	c=12 in.					(tensile specimens)					5.626	513	40.8	0.95427
							Prop. limit	0.2% offset			5.611	495	39.3	0.95576
						Hard	2.40	2.90			5.595	480	38.0	0.95697
						Annealed	0.70	1.0			5.581	462	36.5	0.95849
											5.567	443	35.0	0.96010
											5.552	426	33.6	0.96152

---

[a] Elastic wave velocity measured ultrasonically (9.0 Mc), $U^e=6.30$ mm/μsec. Hydrostatic curve, fitted to Bridgman's data to 30 kbar, $P=712.25(\Delta V/V_0)+2621.63(\Delta V/V_0)^2$ (kbar). Various constants used in the analysis were: elastic constants (zero pressure), $E=760.0$ kbar, $K=728.0$ kbar, $\mu=286.6$ kbar, $\nu=0.326$; initial density, $\rho_0=2.794$ g/cm³; Gruneisen's ratio (zero pressure), $\gamma_0=2.13$; heat capacity, $C_V=9.25\times10^6$ erg/g °C; $(\partial P/\partial T)_V=0.055$ kbar/°C.

[b] Cut from same bar of stock material.

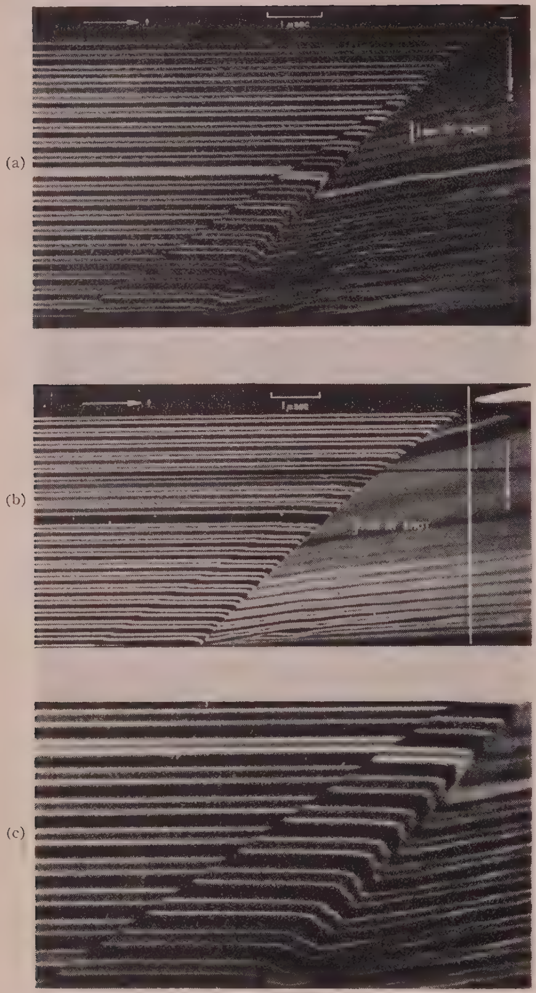

FIG. 6. Smear camera photographs: (a) hardened, shot No. 6237; (b) annealed, shot No. 6926; (c) enlargement of portion of (a).

Photographs of the records obtained in two of the shots are shown in Fig. 6. Figure 6(a) is for a hardened specimen; Fig. 6(b) is for an annealed specimen in which all other experimental conditions were essentially the same. Figure 6(c) is an enlargement of a portion of Fig. 6(a) to show the detail of the wave structure.

The double-wave system is clearly evident in the photographs. The amplitude of the elastic wave is seen to be substantially smaller in the annealed material.

In the hardened material an arrival due to one reverberation of the elastic wave between free surface and shock front is also visible [Fig. 6(c)]. This wave was generally slightly larger in amplitude than the initial elastic wave. In part this is due to work hardening and in part because this wave propagates into previously stressed material. As mentioned in Sec. III, the reflection of the first elastic wave from the free surface does not entirely relieve the compressive stress parallel to the boundary. It will be noted that behind the first elastic wave the deflection angle α slowly increases. This is assumed to be due to a simple, nonsteady compression wave, due to work hardening, between the elastic and shock fronts. This increase was treated approximately by assuming the jump conditions to apply, with an effective wave velocity equal to the average of observed shock and elastic wave velocities.

A more detailed treatment is possible in principle. However, because this increase is small and the experimental precision correspondingly low, a more refined analysis does not appear warranted. Limits to the possible error introduced by this approximate treatment amount to less than $\pm 2\%$ in stress at a given density.

The traces behind the shock wave are obscured in the upper half to two-thirds of each record because of image broadening resulting from curvature of the surface. These data could be recorded also, but at the expense of either a reduction in magnification or a larger angle of incidence of the waves on the free surface. Either of these would reduce the precision of the low-pressure data. Since the elastic wave amplitudes and low-pressure shock data are of primary interest, no attempt was made to record this information. Moreover, data from the lowermost traces are not reliable because of interference from the elastic waves reflected from the bottom surface of the specimens. Only the data considered most reliable are reported.

Although it appears that the rise time of the shock is recorded in Fig. 6(a), this rise time is an apparent one resulting from reverberation of the elastic wave between shock and free surface. The competition between the two terms in Eq. (25) in determining α behind the shock is evident. The initial downward jump is described by the first term, and the slow climb upward is described by the increasing contribution of the second term.

The experimental results are given in Table I. Shock wave data are given for only four of the six experiments. In shot 5711 these data were not obtained because of too high magnification. In shot 6382 the specimen consisted of two pieces butted together to increase the length to that of the other specimens. The cut was not expected to give any difficulty but the reproducibility with the other annealed shots lies outside expected experimental precision. It appears that steady state was not obtained in the shock.

V. EXPERIMENTAL RESULTS

The experimental pressure-volume points are plotted in Fig. 7, together with Bridgman's hydrostatic isothermal data for pure aluminum. It is evident that the points for hard aluminum lie above those for annealed material, and that both sets lie above Bridgman for pressures less than about 30 kbar.

Figure 8 is a plot of shock velocity (laboratory coordinates) as function of final free-surface velocity. The reproducibility for separate shots of the same material is seen to be excellent. The difference between the sets of points for hardened and annealed material is at about the expected limit of experimental precision, which is estimated to be $\pm 1\%$ in shock velocity and $\pm 5\%$ in free-surface velocity in a single experiment. The difference between each group of points and a single line drawn halfway between them is therefore about the estimated probable error and hence is not considered significant. Thus, the reproducibility between different shots of the same material appears to be somewhat fortuitous. (Since some data smoothing is done in the analysis procedure, each set of points necessarily lies on a reasonably smooth curve.)

It should be noted in this regard that differences in Hugoniot equation of state do not depend solely on differences in these data, because of differences in elastic wave amplitudes.

Three bases for comparison of theory and experiment exist. These are: (a) comparison of observed and predicted elastic wave amplitudes, (b) comparison of the difference in Hugoniot equations of state for hardened and annealed material with the difference predicted from simple tension stress-strain data, and (c) comparison of dynamic stress-volume data, adjusted to isothermal conditions, with semitheoretical curves based on isothermal, hydrostatic data and on simple tension stress-strain curves.

Of these, the latter effectively includes the other two but cannot be performed as rigorously because hydrostatic data exists only for pure aluminum and not for the 2024 alloy. Moreover, some uncertainty arises from the temperature correction applied to the Hugoniot points to adjust them to isothermal conditions. Nevertheless, at least approximate agreement on this basis would be expected.

The comparison of elastic wave amplitudes is shown in Table I. Calculated yield strengths are obtained from the observed elastic wave amplitudes by means of the relation $Y=(1-2\nu/1-\nu)\sigma_x$ (Sec. II). Two values of observed yield strength from simple tension experiments are also reported. These are the proportional limit and the value at 0.2% offset strain. The values calculated from the observed wave amplitudes are seen to fall between these two values for hardened material, for which the experimental precision is reasonably good ($\pm 3\%$). The calculated values for annealed material are generally lower than observed values, but the precision of these measurements ($\pm 20\%$) is poor because of the small free-surface velocities. Such disagreement as exists is not considered experimentally significant.

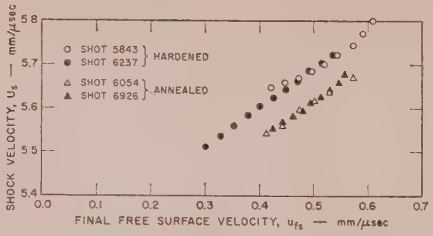

Fig. 8. Shock velocity (laboratory coordinates) as function of final free-surface velocity.

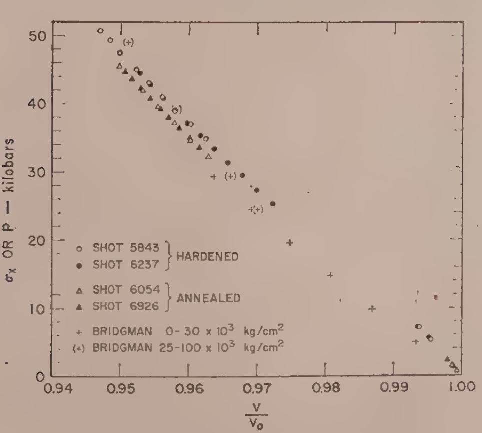

Fig. 7. Experimental Hugoniot points.

A direct comparison of the dynamic stress-volume points with those predicted on the basis of hydrostatic, isothermal compression data and simple tension stress-strain curves requires, of course, that the hydrostatic curve be known with a precision at least equivalent to that of the dynamic measurements. In Bridgman's account of his hydrostatic experiments he states that his initial experiments to 30 kbar, performed by the method of linear compressibility, give considerably more precise data than the later runs from 25 to 100 kbar.[24] Moreover, a substantial lack of reproducibility was noted in separate runs to 100 kbar. Because of this uncertainty above 30 kbar, the course adopted in this paper has been to fit a parabola by the method of least squares to Bridgman's initial data to 30 kbar, and to use this fit for extrapolation to 50 kbar. This procedure is, of course, subject to criticism and makes any comparison above 30 kbar somewhat suspect. However, since some dynamic data are available below 30 kbar, and since the conclusions are not based solely on the agreement with hydrostatic data, this procedure in no way affects the final conclusion as to the validity of elastic-plastic theory.

In order to compare dynamic and static results it is also required that a temperature correction be applied to the dynamic data to reduce them to isothermal conditions. This has been done by computing temperatures along the Hugoniots by a method due to Walsh and Christian,[1] in which various thermodynamic parameters are assumed constant. This method necessarily assumes

---

[24] P. W. Bridgman, Proc. Am. Acad. Arts Sci. **74**, 21 (1940); **76**, 55 (1948).

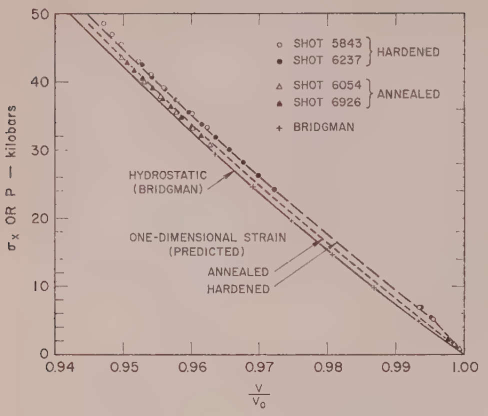

FIG. 9. Isothermal equations of state.

the existence of a fluid-type P, V, E, equation of state, where P denotes mean pressure. Such an assumption is not valid where the elastic strains are anisotropic. However, in the present case the additional internal energy at a given pressure and volume due to anisotropy of the elastic strains is sufficiently small to be negligible.

The jump conditions give σ_x, V, and E. Determination of P requires knowledge of the lateral stresses associated with σ_x. These are not determined experimentally, so that in order to perform the temperature adjustment some assumption as to their magnitude must be made. In the present case P was assumed given, in accord with elastic-plastic theory, by:

$$P=\sigma_x-\tfrac{2}{3}[(1-2\nu)/(1-\nu)]\sigma_x^e,$$

where σ_x^e is the observed elastic wave amplitude. Although work hardening is thereby neglected, this procedure avoids any reference to tensile specimen data with which it is desired to eventually compare the results.

The procedure, outlined below, is to determine temperatures along the P, V, E curve, or "reduced" Hugoniot obtained from the dynamic data by the above relation.

Since

$$TdS=dE+PdV,$$

along the "reduced" Hugoniot

$$T(dS/dV)_H=(dE/dV)_H+P, \qquad (37)$$

where the subscript H means differentiation along the Hugoniot. But

$$(dS/dV)_H=(\partial S/\partial V)_T+(\partial S/\partial T)_V(dT/dV)_H.$$

Further,

$$(\partial S/\partial V)_T=(\partial P/\partial T)_V$$

and

$$(\partial S/\partial T)_V=C_V/T.$$

Hence, substituting for $(dS/dV)_H$ in Eq. (37),

$$T(\partial P/\partial T)_V+C_v(dT/dV)_H=(dE/dV)_H+P.$$

Assuming the parameters $(\partial P/\partial T)_V$, C_v, and the ratio[25] γ/V to be constant, this equation can be integrated to give:

$$T=\frac{1}{C_V}e^{-\gamma_0(1-e)}\int_0^e\left[\left(\frac{dE}{de}\right)_H-V_0P\right]e^{\gamma_0(1-e)}de+T_0e^{\gamma_0 e}, \qquad (38)$$

where e is engineering strain $[e=1-(V/V_0)]$, γ_0 is Gruneisen's ratio at zero pressure, and C_V is heat capacity at constant volume.

Pressure differences between the Hugoniots and isotherms are then calculated from:

$$\Delta P=(\partial P/\partial T)_V(T-T_0),$$

where $(\partial P/\partial T)_V$ is taken equal to the zero pressure value.

In the present experiments the thermal pressure ΔP amounted to some 2–4% of the total pressure.

In Fig. 9 the dynamic stress-volume points reduced to isothermal conditions are compared with semitheoretical curves based on Bridgman's data and simple tension stress-strain data. The agreement is seen to be quite satisfactory.[26]

The agreement is shown on a more expanded scale in Fig. 10, in which only differences with respect to Bridgman's hydrostatic curve are plotted. Also shown are precision limits amounting to ±2% in stress at a given volume, which is the expected accuracy. In general, the points agree with the predicted curves within experimental precision. Since some uncertainty also arises from possible errors in the hydrostatic curve and from the temperature calculation, the disagreement is not considered experimentally significant.

The differences between the Hugoniot equations of state of hardened and annealed material are very nearly the same as the differences in the isothermal equations of state shown in Fig. 10. The difference in Hugoniots is slightly larger (~0.1 kbar) than the difference in isotherms because of the larger amount of plastic work and resultant heating in the hardened material.

VI. DISCUSSION

The agreement between the dynamic measurements and the stress-volume curves predicted by means of elastic-plastic theory leads to the conclusion that the theory is substantially valid for this material at the strain rates involved in the experiments. A lower limit to the strain rate, $\dot{e}$, can be estimated from the time resolution of the measurements. This gives, for the elastic waves, $\dot{e}>10^5$ sec^{-1}; and, for the shock waves,

---

[25] D. G. Doran, doctoral dissertation, Washington State University, Pullman, Washington (1960, unpublished).

[26] *Note added in proof.* Recent measurements by C. D. Lundergan on 6061-T6 aluminum using electrical contactor pins to record free-surface motion show the Hugoniot to lie above Bridgman's hydrostatic curve by approximately 2 kbar in the pressure range 6.5 to 26 kbar (private communication).

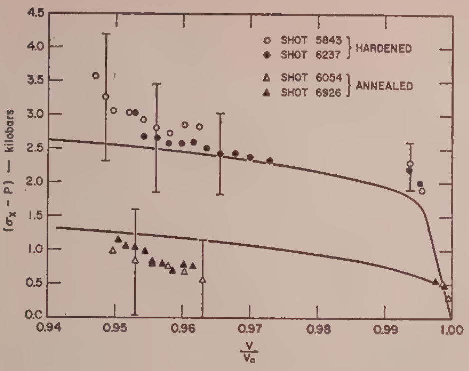

FIG. 10. Difference in isothermal equations of state.

$\dot{e} > 10^6$ sec^{-1}. Since strain rate is not considered in the theory, and since the static and dynamic data which form the basis for the comparison are obtained at strain rates differing by at least six or seven orders of magnitude, it is concluded that no appreciable strain rate effects occur under the conditions of the dynamic experiments. Further, the influence of the relatively high mean stresses on the yield strength must also be small.

Although no significant strain rate effects are observed, the possibility of some increase in yield strength cannot be ruled out because of the finite precision of the measurements.

The estimated probable error is such that an increase in yield strength immediately behind the elastic wave front of up to 10% for hardened and 20% for annealed material would not be considered experimentally significant. This is substantially less than the increase reported by Whiffin[10] for Dural (17S), amounting to 50% and 150% for hardened and annealed material, respectively.

The precision of the measurement of yield strength decreases with mean stress, and behind the shock fronts increases in yield strength of up to 50% for both hardened and annealed material could occur unresolved.

The only measurement which may differ significantly from the predicted value is that of the state immediately ahead of the shock front in hardened material. Here the discrepancy is slightly greater than estimated precision, and may indicate a higher rate of work hardening under dynamic loading conditions. Further experimentation is required, however, to establish whether such a conclusion is valid.

ACKNOWLEDGMENT

The author wishes to thank particularly Dr. G. E. Duvall for suggesting this problem and for invaluable suggestions and encouragement. He also wishes to thank Dr. J. M. Walsh for making available a copy of his (unpublished) manuscript dealing with the theory of elastic-plastic waves, and Dr. D. G. Doran and Dr. D. R. Curran for many helpful discussions.

JOURNAL OF APPLIED PHYSICS VOLUME 32, NUMBER 8 AUGUST, 1961

Scattering of Plane Waves by a Rigid Ribbon in a Solid

K. Harumi*
Department of Physics, Tohoku University, Sendai, Japan

(Received February 10, 1961)

The scattering of plane compressional and shearing waves by an infinitely long rigid ribbon with width a in an elastic medium is computed by the use of the Mathieu functions. The diffraction patterns for $ka/2=1, 2,$ and 4 are calculated numerically; the distributions-in-angle of the elastic waves bears no resemblance to that of the sound except for the normally incident compressional wave. The expressions for the scattering field and cross section, in powers of $ka=h$, are obtained in the Rayleigh case. In this case the scattering cross section is of the order of the wavelength, as it is in the case of the scattering of the sound by an absorbing ribbon. Some new expansions of the Mathieu functions in powers of h are listed in the Appendix.

I. INTRODUCTION

The scattering of sound or electromagnetic waves by an infinitely long ribbon or a slit has been widely studied.[1] The scattering of an elastic wave in a solid by any obstacle has been studied only for some kinds of obstacles, as far as the author is aware. Ying and Truell[2] studied the scattering of a plane compressional wave when the obstacle is a sphere, mainly in the case of Rayleigh scattering; Einspruch and Truell[3] treated the case of the liquid-filled sphere; Einspruch, Witterholt, and Truell[4] treated the case of an incident shearing wave. Kato[5] considered the scattering of a compressional wave by a cylindrical cavity when the obstacle is a cylinder; White[6] studied the scattering of a plane compressional or shearing wave obliquely incident on a cylindrical obstacle and obtained the distributions in angle for the empty or liquid-filled cylinder. Sezawa[7] treated the scattering of a normally incident compressional wave by a spherical or cylindrical obstacle, and he referred to the scattering by a rigid or empty ribbon discontinuity, substituting the cylindrical functions for the Mathieu functions, as the details of the Mathieu functions had not been known. In this paper we shall consider the scattering of both compressional and shearing waves obliquely incident on a rigid ribbon. Using the expansion of the Mathieu function by $\sin\eta$ and $\cos\eta$, we obtained the exact solutions. The distributions-in-angle for normally incident waves and the scattering cross sections are obtained. The Rayleigh case is considered.

Several expansions of the Mathieu functions are obtained in the Appendix; these are used in the Rayleigh approximation.

II. FUNDAMENTAL EQUATION AND SOLUTIONS

The equation of motion for an isotropic elastic solid may be written, using the displacement vector $\mathbf{u}$;

$$\rho(\partial^2\mathbf{u}/\partial t^2)=(\lambda+2\mu)\,\mathrm{grad}\,\mathrm{div}\mathbf{u}-\mu\,\mathrm{rot}\,\mathrm{rot}\mathbf{u}, \qquad (1)$$

where ρ is the density of the solid, and λ and μ are Lamé's constants. We shall assume that the displacement has a harmonic time dependence $\exp(i\omega t)$, and it may be omitted throughout. The general solutions of Eq. (1) in the circular, elliptic, and parabolic cylindrical coordinates are expressed as the sum of the vectors $\mathbf{L}$, $\mathbf{M}$, and $\mathbf{N}$[8]:

$$\mathbf{u}=\mathbf{L}+\mathbf{M}+\mathbf{N}, \qquad (2)$$

$$\mathbf{L}=\mathrm{grad}\Phi, \qquad (3)$$

$$\mathbf{M}=\mathrm{rot}(\hat{a}_z\Psi)=\mathrm{grad}\Psi\times\hat{a}_z, \qquad (4)$$

$$\mathbf{N}=\frac{1}{k_s}\,\mathrm{rot}\,\mathrm{rot}(\hat{a}_z\chi)=k_s\hat{a}_z\chi+\frac{1}{k_s}\,\mathrm{grad}\left(\frac{\partial\chi}{\partial z}\right), \qquad (5)$$

where the vector $\mathbf{L}$ is the compressional part of the displacement, and is derived from the scalar potential Φ; $\mathbf{M}$ is the shearing part whose displacement is tangential to the xy plane, and $\mathbf{N}$ is the other shearing part. These shearing parts are derived from the vector potentials $\hat{a}_z\Psi$ and $\hat{a}_z\chi$. Each of the potential functions Φ, Ψ, and χ is the solution of the scalar wave equation

$$\nabla^2\Phi+k_c^2\Phi=0, \qquad (6)$$

$$\nabla^2\Psi+k_s^2\Psi=0, \quad \nabla^2\chi+k_s^2\chi=0, \qquad (7)$$

where $\hat{a}_z$ is a z unit vector, and

$$k_c^2=\frac{\rho\omega^2}{\lambda+2\mu}=\frac{\omega^2}{v_c^2}, \qquad (8)$$

$$k_s^2=\frac{\rho\omega^2}{\mu}=\frac{\omega^2}{v_s^2}, \qquad (9)$$

where v_c is the velocity of the compressional wave, and v_s is the velocity of the shearing wave.

---

* Now at Department of Applied Science, Tohoku University, Sendai, Japan.

[1] P. M. Morse and P. J. Rubenstein, Phys. Rev. **54**, 895 (1938); R. Müller and K. Westpfahl, Z. Physik **134**, 245 (1953); C. J. Bouwkamp, Repts. Progr. in Phys. **17**, 35 (1954); Y. Nomura and S. Katsura, J. Phys. Soc. Japan **12**, 190 (1957).

[2] C. F. Ying and R. Truell, J. Appl. Phys. **27**, 1086 (1956).

[3] N. G. Einspruch and R. Truell, J. Acoust. Soc. Am. **32**, 214 (1960).

[4] N. G. Einspruch, E. J. Witterholt, and R. Truell, J. Appl. Phys. **31**, 806 (1960).

[5] K. Kato, Mem. Inst. Soc. Ind. Research Osaka Univ. **9**, 16 (1952).

[6] R. M. White, J. Acoust. Soc. Am. **30**, 771 (1958).

[7] K. Sezawa, Bull. Earthquake Research Inst. Tokyo Univ. **3**, 19 (1927); **4**, 59 (1928).

[8] P. M. Morse and H. Feshbach, *Methods of Theoretical Physics* (McGraw-Hill Book Company, Inc., New York, 1953), Vol. 2, p. 1764.

III. ELLIPTIC COORDINATE AND MATHIEU FUNCTIONS

Let us consider the scattering of a plane wave obliquely incident on an infinitely long rigid ribbon with width a in a solid, as is shown in Fig. 1.

It may be preferable to take the elliptic coordinate with the foci at $x=\pm a/2$ and $y=0$. We can obtain this elliptic coordinate from the xy coordinate by the transformation

$$x=(a/2)\cosh\xi\cos\eta,\quad y=(a/2)\sinh\xi\sin\eta. \tag{10}$$

The scalar wave equation in the elliptic cylindrical coordinate is

$$\nabla^2\Phi+k_j^2\Phi=\frac{1}{h_1^2}\left(\frac{\partial^2\Phi}{\partial\xi^2}+\frac{\partial^2\Phi}{\partial\eta^2}\right)+\frac{\partial^2\Phi}{\partial z^2}+k_j^2\Phi=0, \tag{11}$$

where the scale factor

$$h_1=\left[\left(\frac{\partial x}{\partial\xi}\right)^2+\left(\frac{\partial y}{\partial\xi}\right)^2\right]^{\frac{1}{2}}=\left(\frac{a}{2}\right)(\sinh^2\xi+\sin^2\eta)^{\frac{1}{2}}.$$

We may take

$$\Phi=S(s_j,\eta)Z(s_j,\xi)\exp(-ikz), \tag{12}$$

assuming that it has a harmonic part of z; then the Mathieu function S and the radial Mathieu function Z in Eq. (12) satisfy

$$(d^2S/d\eta^2)+(b-s_j\cos^2\eta)S=0, \tag{13}$$

$$(d^2Z/d\xi^2)-(b-s_j\cosh^2\xi)Z=0, \tag{14}$$

where the subscript $j=c$ for the compressional wave, and $j=s$ for the shearing wave; b is the separation constant, and

$$s_j=h_j^2=\left(\frac{k_j'a}{2}\right)^2=\left(\frac{\pi a}{\lambda_j'}\right)^2,$$

$$k_j'^2=k_j^2-k^2,$$

where k_j' is the wave number in the $\xi\eta$ plane.

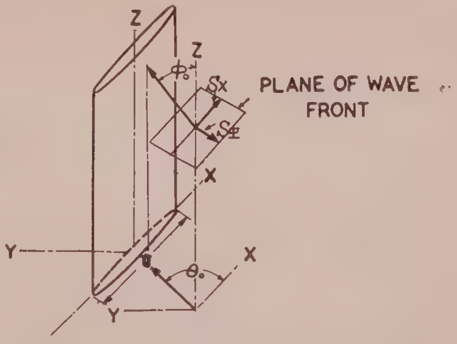

FIG. 1. Direction of the incident wave and the rigid ribbon of width a fixed on $\xi=0$: The displacement of the incident C wave and S_Ψ wave lies in the propagating direction and in xy plane normal to the propagating direction, respectively, and the displacement of the incident S_X wave is normal to those of the C wave and the S_Ψ wave.

The Mathieu function S can be expanded into a series in $\cos n\eta$ and $\sin n\eta$, and separates into $Se_m(s,\eta)$, the even function of η, and $So_m(s,\eta)$, the odd function of η:

$$Se_{2m}(s,\eta)=\sum_{n=0}^{\infty}De_{2n}^{(2m)}\cos 2n\eta,\quad Se_{2m+1}(s,\eta)=\sum_{n=0}^{\infty}De_{2n+1}^{(2m+1)}\cos(2n+1)\eta, \tag{16}$$

$$So_{2m}(s,\eta)=\sum_{n=1}^{\infty}Do_{2n}^{(2m)}\sin 2n\eta,\quad So_{2m+1}(s,\eta)=\sum_{n=0}^{\infty}Do_{2n+1}^{(2m+1)}\sin(2n+1)\eta. \tag{17}$$

These functions are normalized by[9]

$$Se_m(s,0)=1,\quad (d/d\eta)So_m(s,0)=So_m'(s,0)=1. \tag{18}$$

The radial Mathieu function Z can be expanded into a series in the Bessel functions, and separate into $Ze_m(s,\xi)$ or $Zo_m(s,\xi)$, each corresponding to the Mathieu function $Se_m(s,\eta)$ or $So_m(s,\eta)$,

$$Ze_{2m}(s,\xi)=\left(\frac{\pi}{2}\right)^{\frac{1}{2}}(-1)^m\sum_{n=0}^{\infty}(-1)^nDe_{2n}^{(2m)}Z_{2n}(h\cosh\xi),$$
$$Ze_{2m+1}(s,\xi)=\left(\frac{\pi}{2}\right)^{\frac{1}{2}}(-1)^m\sum_{n=0}^{\infty}(-1)^nDe_{2n+1}^{(2m+1)}Z_{2n+1}(h\cosh\xi), \tag{19}$$

$$Zo_{2m}(s,\xi)=\left(\frac{\pi}{2}\right)^{\frac{1}{2}}(-1)^m\tanh\xi\sum_{n=1}^{\infty}(-1)^nDo_{2n}^{(2m)}(2n)Z_{2n}(h\cosh\xi),$$
$$Zo_{2m+1}(s,\xi)=\left(\frac{\pi}{2}\right)^{\frac{1}{2}}(-1)^m\tanh\xi\sum_{n=0}^{\infty}(-1)^nDo_{2n+1}^{(2m+1)}(2n+1)Z_{2n+1}(h\cosh\xi), \tag{20}$$

---

[9] The notations and the normalization of the Mathieu functions in this paper are from *Tables Relating to Mathieu Functions* (Columbia University Press, New York, 1951).

where $Z_n(h\cosh\xi)$ are the Bessel function of order n and argument $h\cosh\xi$.

IV. INCIDENT WAVES

Let us consider the compressional and shearing plane waves obliquely incident on an infinitely long rigid ribbon, as is shown in Fig. 1.

The angle between the propagating direction and the positive z axis is denoted by φ_0, and the angle between the propagating direction projected on $\xi\eta$ plane and the positive x axis is denoted by θ_0. We may take the incident waves with unit displacement, and three types of displacement are considered. One type is the compressional wave: (1) Incident C wave is the compressional wave whose displacement is derived by gradΦ_0 from the scalar potential

$$\Phi_0=\frac{i}{k_c}\exp[-ik_c\{z\cos\phi_0+(x\cos\theta_0+y\sin\theta_0)\sin\phi_0\}]. \tag{21}$$

Two types of displacements are the shearing waves: (2) Incident S_Ψ wave has the displacement which lies in the $\xi\eta$ plane and is derived by rot$(\hat{a}_z\Psi_0)$ from the vector potential $\hat{a}_z\Psi_0$, where

$$\Psi_0=\frac{i}{k_s}\exp[-ik_s\{z\cos\phi_0+(x\cos\theta_0+y\sin\theta_0)\sin\phi_0\}]. \tag{22}$$

(3) Incident S_χ wave has the displacement which is derived by $(k_s)^{-1}$ rot rot$(\hat{a}_z\chi_0)$, which lies in the plane perpendicular to the propagating direction and perpendicular to the direction of the displacement of S_Ψ wave, and whose vector potential is $\hat{a}_z\chi_0$, where

$$\chi_0=\frac{1}{k_s}\exp[-ik_s\{z\cos\phi_0+(x\cos\theta_0+y\sin\theta_0)\sin\phi_0\}]. \tag{23}$$

The plane wave of these potentials may be expanded into the series of the Mathieu function[10]:

$$\exp[-ik_j\{z\cos\phi_0+(x\cos\theta_0+y\sin\theta_0)\sin\phi_0\}]=\exp(-ikz)(8\pi)^{\frac{1}{2}}\sum_{m=0}^{\infty}(-i)^m[(N_m)^{-1}Se_m(s_j,\theta_0)Se_m(s_j,\eta)Je_m(s_j,\xi)$$
$$+(N_m')^{-1}So_m(s_j,\theta_0)So_m(s_j,\eta)Jo_m(s_j,\xi)], \tag{24}$$

where $Je_m(s_j,\xi)$ and $Jo_m(s_j,\xi)$ are the radial Mathieu functions with the Bessel functions of the first kind in Eqs. (19) and (20), and $k=k_j\cos\phi_0$, $j=c$ for compressional waves, and $j=s$ for shearing waves, and

$$N_m=\int_0^{2\pi}Se_m^2(s,\eta)d\eta,\quad N_m'=\int_0^{2\pi}So_m^2(s,\eta)d\eta. \tag{25}$$

Any displacement may be expressed by a linear combination of these three independent waves. In the particular case of $\phi_0=\pi/2$, that is, $k=0$, the wave which has the displacement of the z component, is only the S_χ wave; in this case the scattered wave is the same as that of the sound wave scattered by the perfectly absorbing long ribbon, and the distributions-in-angle have been obtained.[11]

V. SCATTERED WAVES

Scattered waves may also be expressed by the linear combination of the compressional wave **L**, and shearing waves **M** and **N**, each of which is derived from the potential function Φ, Ψ, and χ. Because the scattered waves must take the outgoing like $(k_j'r)^{-\frac{1}{2}}\exp(-ik_j'r)$ for large values of $k_j'r$, we must take the Hankel function of the second kind in Eqs. (19) and (20), and the potential functions of scattered waves are

$$\Phi=\exp(-ikz)\sum_{m=0}^{\infty}[B_mSe_m(s_c,\eta)He_m^{(2)}(s_c,\xi)$$
$$+C_mSo_m(s_c,\eta)Ho_m^{(2)}(s_c,\xi)], \tag{26}$$

$$\Psi=\exp(-ikz)\sum_{m=0}^{\infty}[D_mSe_m(s_s,\eta)He_m^{(2)}(s_s,\xi)$$
$$+E_mSo_m(s_s,\eta)Ho_m^{(2)}(s_s,\xi)], \tag{27}$$

$$\chi=\exp(-ikz)\sum_{m=0}^{\infty}[F_mSe_m(s_s,\eta)He_m^{(2)}(s_s,\xi)$$
$$+G_mSo_m(s_s,\eta)Ho_m^{(2)}(s_s,\xi)], \tag{28}$$

where B_m, C_m, D_m, E_m, F_m, and G_m are the coefficients to be determined by the boundary conditions. The wave number k of the z component must be the same as that of the incident wave in order that the boundary conditions are to be satisfied.[12] Therefore the scattered wave number k of the z component must be $k=k_c\cos\phi_0$ for the incident compressional wave, and $k=k_s\cos\phi_0$ for the incident shearing wave. The wave numbers are related by $k_s>k_c$, and in case of the incident shearing waves, as the incident angle ϕ_0 decreases, it may happen $k>k_c$. We postpone this case, because it offers some difficulty,[13] and treat the case $k<k_c$. The latter is the case in which the angle does not exceed the critical angle.

Substituting the potential functions (26), (27), and (28) into Eqs. (3), (4), and (5), we obtain the component of displacement for the scattered waves:

---

[10] Reference 8, Vol. 2, p. 1422.

[11] Reference 1.

[12] A. E. Love, *The Mathematical Theory of Elasticity* (Cambridge University Press, New York, 1952), p. 287.

[13] J. N. Goodier and R. E. D. Bishop, J. Appl. Phys. **23**, 124 (1952).

$$u_\xi=(h_1)^{-1}\exp(-ikz)\sum_{m=0}^{\infty}\Big[B_mSe_m(s_c,\eta)He_m^{(2)\prime}(s_c,\xi)+C_mSo_m(s_c,\eta)Ho_m^{(2)\prime}(s_c,\xi)+D_mSe_m'(s_s,\eta)He_m^{(2)}(s_s,\xi)$$
$$+E_mSo_m'(s_s,\eta)He_m^{(2)}(s_s,\xi)-\frac{ik}{k_s}\{F_mSe_m(s_s,\eta)He_m^{(2)\prime}(s_s,\xi)+G_mSo_m(s_s,\eta)Ho_m^{(2)\prime}(s_s,\xi)\}\Big],\tag{29}$$

$$u_\eta=(h_1)^{-1}\exp(-ikz)\sum_{m=0}^{\infty}\Big[B_mSe_m'(s_c,\eta)He_m^{(2)}(s_c,\xi)+C_mSo_m'(s_c,\eta)Ho_m^{(2)}(s_c,\xi)-\{D_mSe_m(s_s,\eta)He_m^{(2)\prime}(s_s,\xi)$$
$$+E_mSo_m(s_s,\eta)Ho_m^{(2)}(s_s,\xi)\}-\frac{ik}{k_s}\{F_mSe_m'(s_s,\eta)He_m^{(2)}(s_s,\xi)+G_mSo_m'(s_s,\eta)Ho_m^{(2)}(s_s,\xi)\}\Big],\tag{30}$$

$$u_z=\exp(-ikz)\sum_{m=0}^{\infty}\Big[-ik\{B_mSe_m(s_c,\eta)He_m^{(2)}(s_c,\xi)+C_mSo_m(s_c,\eta)Ho_m^{(2)}(s_c,\xi)\}$$
$$+\frac{k_s^2-k^2}{k_s^2}\{F_mSe_m(s_s,\eta)He_m^{(2)}(s_s,\xi)+G_mSo_m(s_s,\eta)Ho_m^{(2)}(s_s,\xi)\}\Big],\tag{31}$$

where

$$Se_m'(s,\eta)=(\partial/\partial\eta)Se_m(s,\eta),$$

and

$$He_m^{(2)\prime}(s,\xi)=(\partial/\partial\xi)He_m^{(2)}(s,\xi),$$

and h_1 is the scale factor which is given in Eq. (11).

VI. BOUNDARY CONDITIONS AND DETERMINATION OF COEFFICIENTS

The boundary conditions for the rigid ribbon with width a in a solid is the vanishing of the displacement u on the ribbon surface, that is,

$$u_{i,\text{scatter}}+u_{i,\text{inc}}=0\quad\text{at}\quad\xi=0,\tag{32}$$

where $i=\xi$, η, and z, and $u_{i,\text{scatter}}$ are given in Eqs. (29), (30), and (31), and $u_{i,\text{inc}}$ has an expression similar to $u_{i,\text{scatter}}$, except that the radial parts $He_m^{(2)}(s,\xi)$ and $Ho_m^{(2)}(s,\xi)$ in $u_{i,\text{scatter}}$ are replaced by $Je_m(s,\xi)$ and $Jo_m(s,\xi)$.

In determining the coefficients, as $Se_m'(s,\eta)$ and $So_m'(s,\eta)$ are contained in the displacement u_i of Eqs. (29) and (30), it is preferable to use the orthogonality of $\sin n\eta$ and $\cos n\eta$ in Eqs. (16) and (17), rather than to use the orthogonality of the Mathieu functions.

Omitting the factor $(h_1)^{-1}\exp(-ikz)$ in the equations for u_ξ and u_η of Eq. (32), and excluding the factor $\exp(-ikz)$ in the equation for u_z, we obtain the equations for the boundary condition by using the orthogonality of $\sin n\eta$ and $\cos n\eta$:

$$\begin{aligned}
&\sum_{m=0}^{\infty} b_{mn}^{(\xi)}B_m+e_{mn}^{(\xi)}E_m+f_{mn}^{(\xi)}F_m=U_{n,\xi}\\
&\sum_{m=0}^{\infty} b_{mn}^{(\eta)}B_m+e_{mn}^{(\eta)}E_m+f_{mn}^{(\eta)}F_m=U_{n,\eta}\\
&\sum_{m=0}^{\infty} b_{mn}^{(z)}B_m\qquad\qquad\;\;+f_{mn}^{(z)}F_m=U_{n,z},
\end{aligned}\tag{34}$$

$$\begin{aligned}
&\sum_{m=0}^{\infty} c_{mn}^{(\xi)}C_m+d_{mn}^{(\xi)}D_m+g_{mn}^{(\xi)}G_m=\bar{U}_{n,\xi}\\
&\sum_{m=0}^{\infty} c_{mn}^{(\eta)}C_m+d_{mn}^{(\eta)}D_m+g_{mn}^{(\eta)}G_m=\bar{U}_{n,\eta}\\
&\sum_{m=0}^{\infty} c_{mn}^{(z)}C_m\qquad\qquad\;\;+g_{mn}^{(z)}G_m=\bar{U}_{n,z},
\end{aligned}\tag{35}$$

where $n=0,1,2,\cdots$ and

$$\begin{aligned}
b_{mn}^{(\xi)}&=De_n^{(m)}He_m^{(2)\prime}(s_c,0)\\
b_{mn}^{(\eta)}&=-nDe_n^{(m)}He_m^{(2)}(s_c,0)\\
b_{mn}^{(z)}&=-ikDe_n^{(m)}He_m^{(2)}(s_c,0),\\
e_{mn}^{(\xi)}&=nDo_n^{(m)}Ho_m^{(2)}(s_s,0)\\
e_{mn}^{(\eta)}&=-Do_n^{(m)}Ho_m^{(2)\prime}(s_s,0)\\
f_{mn}^{(\xi)}&=\frac{-ik}{k_s}De_n^{(m)}He_m^{(2)\prime}(s_s,0),\\
f_{mn}^{(\eta)}&=\frac{ik}{k_s}nDe_n^{(m)}He_m^{(2)}(s_s,0)\\
f_{mn}^{(z)}&=\frac{k_s^2-k^2}{k_s}De_n^{(m)}He_m^{(2)}(s_s,0),
\end{aligned}\tag{36}$$

$$\begin{aligned}
c_{mn}^{(\xi)}&=Do_n^{(m)}Ho_m^{(2)\prime}(s_c,0)\\
c_{mn}^{(\eta)}&=nDo_n^{(m)}Ho_m^{(2)}(s_c,0)\\
c_{mn}^{(z)}&=-ikDo_n^{(m)}Ho_m^{(2)}(s_c,0),\\
d_{mn}^{(\xi)}&=-nDe_n^{(m)}He_m^{(2)}(s_s,0)\\
d_{mn}^{(\eta)}&=-De_n^{(m)}He_m^{(2)\prime}(s_s,0),\\
g_{mn}^{(\xi)}&=-\frac{ik}{k_s}Do_n^{(m)}Ho_m^{(2)\prime}(s_s,0)\\
g_{mn}^{(\eta)}&=-\frac{ik}{k_s}nDo_n^{(m)}Ho_m^{(2)}(s_s,0)\\
g_{mn}^{(z)}&=\frac{k_s^2-k^2}{k_s}Do_n^{(m)}Ho_m^{(2)}(s_s,0),
\end{aligned}\tag{37}$$

U, and $\bar{U}$ are given as follows for different kind of incident waves;

(1) Incident C wave

$$U_{n,\eta}=-\frac{(8\pi)^{\frac{1}{2}}}{k_c}\sum_{m=0}^{\infty}(-i)^{m+1}(N_m)^{-1}Se_m(s_c,\theta_0)\times nDe_n{}^{(m)}Je_m(s_c,0)\tag{38}$$

$$U_{n,z}=-(8\pi)^{\frac{1}{2}}\frac{k}{k_c}\sum_{m=0}^{\infty}(-i)^{m}(N_m)^{-1}Se_m(s_c,\theta_0)\times De_n{}^{(m)}Je_m(s_c,0),$$

$$\bar{U}_{n,\xi}=\frac{(8\pi)^{\frac{1}{2}}}{k_c}\sum_{m=0}^{\infty}(-i)^{m+1}(N_m')^{-1}So_m(s_c,\theta_0)\times Do_n{}^{(m)}Jo_m'(s_c,0)\tag{39}$$

$$U_{n,\xi}=\bar{U}_{n,\eta}=\bar{U}_{n,z}=0,$$

where we use the relation $Jo_m(s,0)=0$ and $Je_m'(s,0)=0$.

(2) Incident S_Ψ wave

$$U_{n,\eta}=-\frac{(8\pi)^{\frac{1}{2}}}{k_s}\sum_{m=1}^{\infty}(-i)^{m+1}(N_m')^{-1}So_m(s_s,\theta_0)\times Do_n{}^{(m)}Jo_m'(s_s,0),\tag{40}$$

$$\bar{U}_{n,\xi}=-\frac{(8\pi)^{\frac{1}{2}}}{k_s}\sum_{m=0}^{\infty}(-i)^{m+1}(N_m)^{-1}Se_m(s_s,\theta_0)\times nDe_n{}^{(m)}Je_m(s_s,0)\tag{41}$$

$$U_{n,\xi}=U_{n,z}=\bar{U}_{n,\eta}=\bar{U}_{n,z}=0.$$

(3) Incident S_χ wave

$$U_{n,\eta}=(8\pi)^{\frac{1}{2}}\frac{ik}{k_s^2}\sum_{m=0}^{\infty}(-i)^{m+1}(N_m)^{-1}Se_m(s_s,\theta_0)\times nDe_n{}^{(m)}Je_m(s_s,0)\tag{42}$$

$$U_{n,z}=-(8\pi)^{\frac{1}{2}}\frac{i(k_s^2-k^2)}{k_s^2}\sum_{m=0}^{\infty}(-i)^{m}(N_m)^{-1}Se_m(s_s,\theta_0)\times De_n{}^{(m)}Je_m(s_s,0),$$

$$\bar{U}_{n,\xi}=-(8\pi)^{\frac{1}{2}}\frac{ik}{k_s^2}\sum_{m=1}^{\infty}(-i)^{m+1}(N_m')^{-1}So_m(s_s,\theta_0)\times Do_n{}^{(m)}Jo_m'(s_s,0)\tag{43}$$

$$U_{n,z}=\bar{U}_{n,\eta}=\bar{U}_{n,z}=0.$$

Simultaneous linear equations (34) and (35) determine the coefficients B_m, C_m, D_m, E_m, F_m, and G_m.

When the parameter s_j is small ($s_j\cos^2\theta_0<4$), the following series are obtained from

$$\exp[-ik_j(x\cos\theta_0+y\sin\theta_0)],$$

differentiating by ξ and η and substituting $\xi=0$:

(1) Incident C wave

$$\begin{aligned}U_{n,\eta}&=+\cos\theta_0S_n(s_c),\\ \bar{U}_{n,\xi}&=-\sin\theta_0S_n(s_c),\\ U_{n,z}&=(k/k_c)T_n(s_c),\end{aligned}\tag{38'}$$

where

$$S_n(s_j)=\frac{a}{2}\sum_{r=n-1}^{\infty}{}'\left[\frac{-i(s_j)^{\frac{1}{2}}\cos\theta_0}{2}\right]^r\times\frac{n}{[\frac{1}{2}(r+n+1)!][\frac{1}{2}(r-n+1)!]},\tag{44}$$

$$T_n(s_j)=(2)_n\sum_{r=0}^{\infty}\left(\frac{-i(s_j)^{\frac{1}{2}}\cos\theta_0}{4}\right)^{n+2r}\frac{1}{[(n+r)!]r!}.\tag{45}$$

In Eq. (44) $\sum'$ implies to take odd r for even n, and even r for odd n.

(2) Incident S_Ψ wave

$$\begin{aligned}U_{n,\eta}&=\sin\theta_0S_n(s_s),\\ \bar{U}_{n,\xi}&=+\cos\theta_0S_n(s_s).\end{aligned}\tag{40'}$$

(3) Incident S_χ wave

$$\begin{aligned}U_{n,\eta}&=-(k/k_s)\cos\theta_0S_n(s_s),\\ \bar{U}_{n,\xi}&=+(k/k_s)\sin\theta_0S_n(s_s),\\ U_{n,z}&=+[(k_s^2-k^2)/k_s^2]T_n(s_s).\end{aligned}\tag{42'}$$

VII. SCATTERING CROSS SECTIONS FOR NORMALLY INCIDENT WAVE

The scattering cross section of a scatterer is defined as the ratio of the total energy scattered per unit time to the energy per unit area carried per unit time by the incident wave, the unit area being normal to the direction of propagation of the incident wave. The energy flow P, passing through a surface Ω, may be written[14]

$$P=\frac{\partial\bar{W}}{\partial t}=\int_\Omega\frac{\partial\mathbf{u}}{\partial t}\cdot\mathbf{T}\cdot d\mathbf{A},\tag{46}$$

where **u** is the displacement, and **T** is the stress tensor which is derived from the scalar potential and the displacement as follows:

$$\begin{aligned}T_{\xi\xi}&=-\lambda k_c^2\Phi+\frac{2\mu}{h_1}\left(\frac{\partial u_\xi}{\partial\xi}+\frac{1}{h_1^2}\frac{\partial h_1}{\partial\eta}u_\eta\right),\\ T_{\eta\eta}&=-\lambda k_c^2\Phi+\frac{2\mu}{h_1}\left(\frac{\partial u_\eta}{\partial\eta}+\frac{1}{h_1^2}\frac{\partial h_1}{\partial\xi}u_\xi\right),\\ T_{\xi\eta}&=u\left[\frac{\partial}{\partial\xi}\left(\frac{u_\eta}{h_1}\right)+\frac{\partial}{\partial\eta}\left(\frac{u_\xi}{h_1}\right)\right].\end{aligned}\tag{47}$$

---

[14] Reference 8, Vol. 1, p. 151.

We consider the incident compressional wave with unit displacement. Then the energy flow of the incident wave passing through the unit area is

$$P_{\text{inc}}=\rho\omega^3/k_c. \tag{48}$$

As the energy loss in the elastic medium is zero, we may take the cylindrical surface with an infinitely large radius, and calculate the scattering energy flow through the surface. We consider the scattered energy flow per unit length of ribbon, then the cylindrical surface Ω with infinitely large ξ becomes

$$\int_\Omega dA=\int_0^1\int_0^{2\pi}\frac{a}{2}\sinh\xi d\eta dz\rightarrow\int_0^{2\pi}rd\eta, \tag{49}$$

and Eq. (46) is given as follows when we take the energy as real.

$$P_{\text{scatter}}=\frac{-i\omega}{2}\int_0^{2\pi}[u_\xi\bar{T}_{\xi\xi}+u_\eta\bar{T}_{\xi\eta}-\bar{u}_\xi T_{\xi\xi}-\bar{u}_\eta T_{\xi\eta}]rd\eta, \tag{50}$$

where $\bar{u}$ and $\bar{T}$ are the complex conjugate of u and T. Substituting Eqs. (29), (30), (31), and (47) into Eq. (50), and using the orthogonality relations of Eq. (25) and the following expressions for very large value of ξ,

$$h_1\rightarrow r,\quad \frac{\partial h_1}{\partial\xi}\rightarrow r,\quad \frac{\partial h_1}{\partial\eta}\rightarrow\frac{a^2}{4r}\sin\eta\cos\eta, \tag{51}$$

$$\begin{aligned}He_m^{(2)}(s,\xi)&\rightarrow(kr)^{-\frac{1}{2}}\exp[-i\{kr-\tfrac{1}{2}\pi(2m+\tfrac{1}{2})\}],\\ \partial He_m^{(2)}/\partial\xi&\rightarrow -i(kr)^{\frac{1}{2}}\exp[-i\{kr-\tfrac{1}{2}\pi(2m+\tfrac{1}{2})\}],\\ \partial^2He_m^{(2)}/\partial\xi^2&\rightarrow -(kr)^{\frac{3}{2}}\exp[-i\{kr-\tfrac{1}{2}\pi(2m+\tfrac{1}{2})\}],\end{aligned} \tag{52}$$

we obtain the two kinds of scattered energy flow per unit length of the ribbon

$$P_c=\rho\omega^3\sum_{m=0}^{\infty}[|B_m|^2N_m+|C_m|^2N_m'], \tag{53}$$

$$P_s=\rho\omega^3\sum_{m=0}^{\infty}[|D_m|^2N_m+|E_m|^2N_m'], \tag{54}$$

where P_c is the energy flow of the compressional scattered wave, and P_s is that of the shearing scattered wave, and N_m and N_m' are given in Eq. (25). From Eqs. (48), (53), and (54), we obtain the scattering cross section for the incident compressional wave with unit amplitude:

$$Q_{cc}=P_c/P_{\text{inc}}=k_c\sum_{m=0}^{\infty}[|B_m|^2N_m+|C_m|^2N_m'], \tag{55}$$

$$Q_{cs}=P_s/P_{\text{inc}}=k_c\sum_{m=0}^{\infty}[|D_m|^2N_m+|E_m|^2N_m']. \tag{56}$$

In a similar way we obtain the scattering cross sections for the incident shearing wave as follows:

$$Q_{sc}=P_c/P_{\text{inc}}=k_s\sum_{m=0}^{\infty}[|B_m|^2N_m+|C_m|^2N_m'], \tag{57}$$

$$Q_{ss}=P_s/P_{\text{inc}}=k_s\sum_{m=0}^{\infty}[|D_m|^2N_m+|E_m|^2N_m']. \tag{58}$$

VIII. CASE OF $h_c=k_c'a/2$, $h_s=k_s'a/2\ll 1$

In the case of the Rayleigh approximation, when the wavelength is considerably longer than the width of the ribbon, we may obtain the expression in terms of $h_c=(\pi a/\lambda_c')$ and $h_s=(\pi a/\lambda_s')$ for normally incident waves ($\phi_0=\pi/2$). In this case, it may be preferable to calculate rigorously by substituting the expansion of the Mathieu functions in Eqs. (34), and (35). Some corrected expansions of the Mathieu functions in Morse and Feshbach[15] and several other expansions are given in the Appendix. Expanding the element of Eqs. (34) and (35) in terms of h_c and h_s, we may obtain the coefficients B_m, C_m, D_m, and E_m with use of the successive approximation by neglecting the higher order of h_c and h_s. Some of the coefficients are given as follows:

$$\begin{aligned}|B_0|&=[\tfrac{3}{16}h_c^3\cos^2\theta_0+O(h^5)]Y,\\ |B_1|&=[h_c\cos\theta_0+O(h^3)]X,\\ |B_2|&=[\tfrac{3}{16}h_c^3\cos^2\theta_0+O(h^5)]Y,\end{aligned} \tag{60}$$

$$\begin{aligned}|C_1|&=[h_c\sin\theta_0+O(h^3)]X\\ |C_2|&=[\tfrac{3}{8}h_c^3\sin\theta_0+O(h^5)]Y,\end{aligned} \tag{61}$$

$$\begin{aligned}|D_0|&=[\tfrac{3}{16}h_ch_s^2\sin\theta_0\cos\theta_0+O(h^5)]Y,\\ |D_1|&=[h_s\sin\theta_0+O(h^3)]X,\\ |D_2|&=[\tfrac{3}{16}h_ch_s^2\sin\theta_0\cos\theta_0+O(h^5)]Y,\end{aligned} \tag{62}$$

$$\begin{aligned}|E_1|&=[h_s\cos\theta_0+O(h^3)]X,\\ |E_2|&=[\tfrac{3}{8}h_ch_s^2\cos^2\theta_0+O(h^5)]Y,\end{aligned} \tag{63}$$

where

$$\begin{aligned}X&=(a/2)(2\pi)^{\frac{1}{2}}[h_c^2\log h_c+h_s^2\log h_s+O(h^2)]^{-1},\\ Y&=(a/2)(2\pi)^{\frac{1}{2}}[h_c^2+h_s^2+O(h^4)]^{-1},\end{aligned} \tag{64}$$

and $O(h^2)$ is Landau's symbol, and it is assumed that h_c and h_s are small quantities of the same order and it is denoted by h in $O(h^2)$. Likewise for the incident S_Ψ waves we obtain similar expressions, but we omit these expressions here.

From these coefficients and Eqs. (55)–(58), it follows that in the case of Rayleigh scattering, the scattering cross sections are given, Neglecting the higher order

---

[15] Reference 8, Vol. 2, p. 1413.

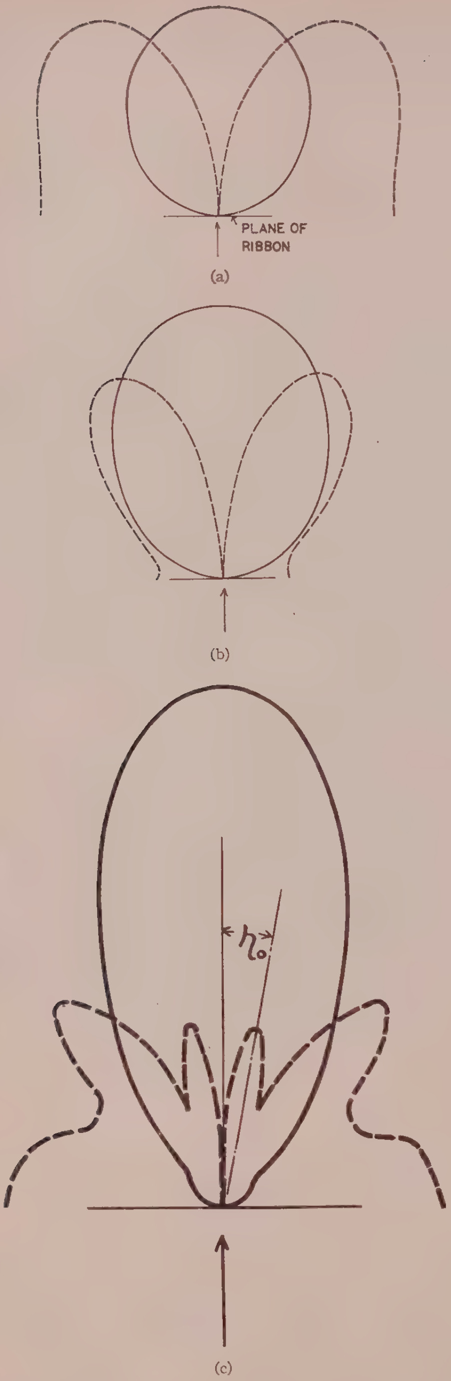

FIG. 2. Distributions-in-angle of the scattered wave for incident C wave with the incident angle in $\xi\eta$ plane $\theta_0=\pi/2$ The cases for $h_c=1$, 2, and 4 are given in (a), (b), and (c); $h_s=2h_c$. The angle η_0 in (c) is the angle between the positive y axis and the first maxima of the scattered shearing wave, which is given by $\sin\eta_0=\pi/(2h_s)$; The solid curve is for compressional wave and the dashed curve is for shearing wave.

of h,

$$Q_{cc}=\frac{a}{2}\cdot\frac{2\pi}{h_c}\left(\frac{h_c^2}{h_c^2\log h_c+h_s^2\log h_s}\right)^2+\cdots$$

$$=\lambda_c\left(\frac{h_c^2}{h_c^2\log h_c+h_s^2\log h_s}\right)^2+\cdots,\qquad(65)$$

$$Q_{cs}=\frac{a}{2}\cdot\frac{2\pi h_c}{h_s^2}\left(\frac{h_s^2}{h_c^2\log h_c+h_s^2\log h_s}\right)^2+\cdots$$

$$=\frac{\lambda_s^2}{\lambda_c}\left(\frac{h_s^2}{h_c^2\log h_c+h_s^2\log h_s}\right)^2+\cdots,\qquad(66)$$

$$Q_{sc}=\frac{a}{2}\cdot\frac{2\pi h_s}{h_c^2}\left(\frac{h_c^2}{h_c^2\log h_c+h_s^2\log h_s}\right)^2+\cdots$$

$$=\frac{\lambda_c^2}{\lambda_s}\left(\frac{h_c^2}{h_c^2\log h_c+h_s^2\log h_s}\right)^2+\cdots,\qquad(67)$$

$$Q_{ss}=\frac{a}{2}\cdot\frac{2\pi}{h_s}\left(\frac{h_s^2}{h_c^2\log h_c+h_s^2\log h_s}\right)^2+\cdots$$

$$=\lambda_s\left(\frac{h_s^2}{h_c^2\log h_c+h_s^2\log h_s}\right)^2+\cdots.\qquad(68)$$

These equations show that the scattering cross sections are of the order of the wavelength in the case of Rayleigh scattering, as in the case of the scattering of sound by the perfectly absorbing ribbon.[16] The above scattering cross sections by the rigid ribbon agree with the scattering cross section by the rigid cylinder with diameter a in the sense of neglecting the higher order of h_c and h_s, but we shall omit the details here.

IX. NUMERICAL CALCULATION

In the case of scattering of sound by an infinitely long ribbon, the distributions of intensity in angle are calculated by Morse and Rubenstein[1,17] for $h=(\pi a/\lambda)=1$, 2, and 4, and for $\theta_0=90°$, 60°, and 30°, where θ_0 is the angle between the propagating direction and the positive x axis, and for $\phi_0=\pi/2$. We computed the normally incident ($\phi_0=\pi/2$) compressional and shearing waves, and obtained the distributions of displacement in angle. The calculations assume that Poisson's ratio σ is $\frac{1}{3}$ (i.e., $\lambda=2\mu$), thus making $h_s=2hc$ as in the case of aluminum, and they are carried out for h_c equal to 1, 2, and 4. In computing Eqs. (34) and (35), these infinite equations are approximated by a finite number of linear equations having up to 20 unknowns and are computed on electronic computers NEAC-2203 and SENAC-1; the values of constants in Eqs. (36) and

---

[16] Reference 8, Vol. 2, p. 1430.

[17] See reference 1; M. W. McLachlan, *Theory and Application of Mathieu Functions* (Clarendon Press, Oxford, 1951), p. 363.

(37) are taken from the "Tables relating to Mathieu functions."[18]

Computed far-zone distributions of displacement in angle $f(\eta)$ of scattered compressional waves, and $g(\eta)$ of scattered shearing waves are given as

$$u_\xi = -i(r)^{-\frac{1}{2}} \exp(-ikz - ik_c'r) f(\eta)$$

$$u_\eta = i(r)^{-\frac{1}{2}} \exp(-ikz - ik_s'r) g(\eta),$$

where

$$f(\eta) = (k_c')^{\frac{1}{2}} \sum_{m=0}^{\infty} (i)^m [B_m Se_m(s_c,\eta) + C_m So_m(s_c,\eta)]$$

$$g(\eta) = (k_s')^{\frac{1}{2}} \sum_{m=0}^{\infty} (i)^m [D_m Se_m(s_s,\eta) + E_m So_m(s_s,\eta)].$$

The computed distributions-in-angle are shown in Figs. 2, 3, 4, and 5, for various wavelengths and incident angles θ_0. In these figures the solid curves represent the distributions-in-angle of the scattered compressional waves $|f(\eta)|$, and the dashed curves represent those of the scattered shearing waves $|g(\eta)|$.

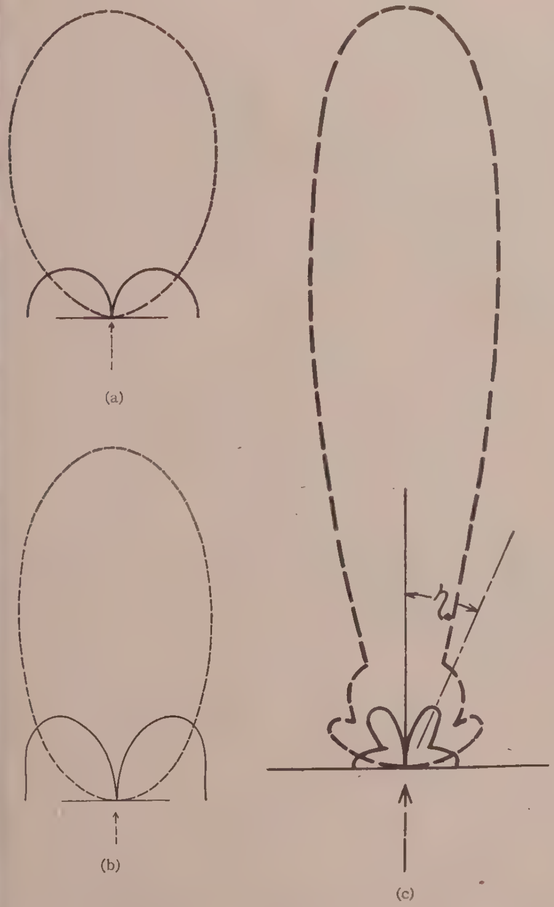

FIG. 3. Distributions-in-angle of the scattered wave for normally incident S_Ψ wave with the incident angle $\theta_0 = \pi/2$. The cases for $h_s = 2$, 4, and 8 are given in (a), (b), and (c). The angle η_0 in (c) shows the first maxima of the scattered compressional wave, which is given by $\sin\eta_0 = \pi/(2h_c)$.

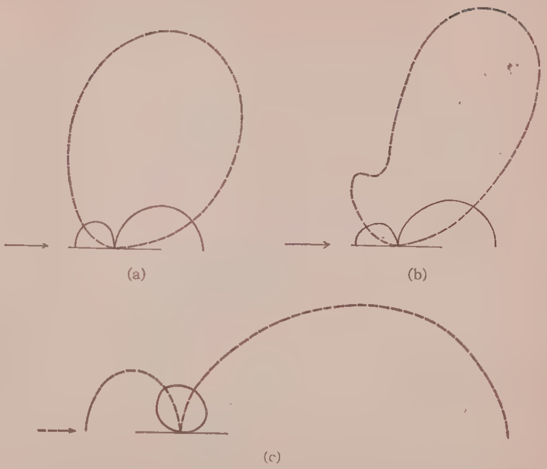

FIG. 4. Distributions-in-angle of the scattered wave for the incident wave propagating to the positive x axis, that is, $\theta_0 = 0$. The cases for the incident C wave with $h_c = 1$ and $h_c = 2$ are given in (a) and (b); the case for the incident S_Ψ wave with $h_s = 2$ is given in (c).

From these patterns it may be concluded that: (1) When the incident angle $\theta_0 = \pi/2$, it is the scattered compressional wave from an incident compressional wave (Fig. 2) rather than the scattered shear wave from an incident shear wave (Fig. 3) which has a distribution in angle similar to that of the sound scattered by the ribbon.

(2) When the wavelengths become shorter than the width of ribbon, and when the incident angle $\theta_0 = \pi/2$, the scattered shearing wave for the incident compressional wave in Fig. 2(c) and the scattered compressional wave for the incident shearing wave in Fig. 3(c) may be expected to show the sharp angular dependency which is evaluated from Huygens' principle. That is, the angle η_0 which shows the first maxima from the y axis may be evaluated from the equation

$$\sin\eta_0 = \lambda_j / 2a = \pi / 2h_j.$$

The computed scattering cross sections per unit length of the ribbon for the incident waves are obtained as follows:

(1) Incident C wave

(a) Incident angle $\theta_0 = \pi/2$

$h_c = 1$:	$Q_{cc}/a = 0.7993$	$Q_{cs}/a = 0.7614$
$h_c = 2$:	$= 1.234$	$= 0.4594$
$h_c = 4$:	$= 1.671$	$= 0.4570$

(b) Incident angle $\theta_0 = 0$

$h_c = 1$:	$Q_{cc}/a = 0.1451$	$Q_{cs}/a = 0.5625$
$h_c = 2$:	$= 0.1604$	$= 0.5421$

---

[18] Reference 9.

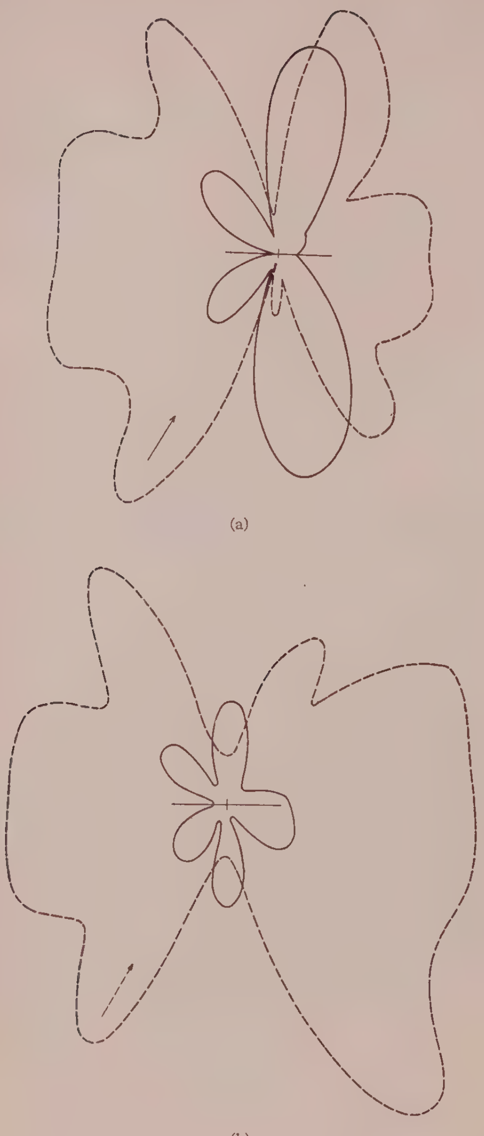

(a)

(b)

FIG. 5. Distributions in angle for the scattered wave with the incident angle $\theta_0=60°$. (a) and (b) show the case for the normally incident C wave and S_Ψ wave with the wavelength $h_c=4$ and $h_s=8$. The amplitudes of these figures must be enlarged by twice the present length.

(2) Incident S_Ψ wave

(a) Incident angle $\theta_0=\pi/2$

$h_s=2$: $Q_{ss}/a=1.283$ $Q_{sc}/a=0.3356$
$h_s=4$: $=1.419$ $=0.1634$
$h_s=8$: $=1.809$ $=0.1164$

(b) Incident angle $\theta_0=0$

$h_s=2$: $Q_{ss}/a=1.424$ $Q_{sc}/a=0.1427$.

X. CONCLUSION

The scattering of the elastic wave by any obstacles in a solid is quite complicated, and the evaluation may be impossible even for an obstacle with a simple shape.

In order to obtain some properties of the scattering in a solid, the case of the rigid ribbon has been treated. For the distributions-in-angle, it is found that a similarity exists between the scattered compressional elastic wave and the scattered sound wave by the rigid ribbon when the incident wave is the compressional wave, and only in the case that the incident wave propagates in the direction normal to the ribbon. This fact suggests that if one of the boundary conditions is similar to the boundary condition of the scattering of sound, as is shown in Sec. IX, the above similarity may exist. This fact may be exemplified by the case where the discontinuity is a cavity, which will be reported in a forthcoming paper (part II).

For the scattering cross section in the Rayleigh case, it may be concluded that the scattering cross sections are of the order of the wavelength, just as in the case of sound by the perfectly absorbing ribbon.

When the wavelength becomes shorter than the width of the ribbon, sharp angular dependency of the scattered waves may be expected from the Huygens' principle, judging from the condition shown in Figs. 2(c) and 3(c).

There is difficulty in solving Eqs. (34) and (35), but the electronic computer has facilitated the solution of these equations.

ACKNOWLEDGMENT

The author expresses his hearty gratitude to Professor Y. Nomura for advice and support during this work.

APPENDIX. SOME EXPANSIONS OF THE MATHIEU FUNCTION

In order to get the expressions for the Rayleigh case, we obtained the expansions of the Mathieu functions in terms of $h_c=(k_ca)/2=(\pi a)/\lambda_c$ and h_s. The expansions of the radial Mathieu function are obtained in Morse and Feshbach.[19] We obtained some corrected expansions of them, and added some expansions.

$$Je_2(s,0)=\frac{h^2}{16}\left(\frac{\pi}{2}\right)^{\frac{1}{2}}\left[1+\frac{h^2}{12}+\cdots\right],$$

$$Jo_3'(s,0)=\frac{h^3}{64}\left(\frac{\pi}{2}\right)^{\frac{1}{2}}\left[1-\frac{h^2}{64}+\cdots\right],$$

$$Je_3(s,0)=\frac{h^3}{192}\left(\frac{\pi}{2}\right)^{\frac{1}{2}}\left[1+\frac{h^2}{64}+\cdots\right],$$

$$No_1'(s,0)=\frac{2}{h}\left(\frac{2}{\pi}\right)^{\frac{1}{2}}\left[1+\frac{h^2}{4}\log\frac{\gamma h}{4}-\frac{5}{32}h^2+\cdots\right],$$

---

[19] Reference 15.

$$Ne_1(s,0)=\frac{2}{h}\left(\frac{2}{\pi}\right)^{\frac{1}{2}}\left[1-\frac{h^2}{4}\log\frac{\gamma h}{4}+\frac{h^2}{32}+\cdots\right],$$

$$Ne_2(s,0)=-\frac{8}{h^2}\left(\frac{2}{\pi}\right)^{\frac{1}{2}}\left[1+\frac{h^2}{24}+\cdots\right],$$

$$Ne_2'(s,0)=\frac{16}{h^2}\left(\frac{2}{\pi}\right)^{\frac{1}{2}}\left[1-\frac{h^2}{24}+\cdots\right],$$

$$Ne_3(s,0)=-\frac{64}{h^3}\left(\frac{2}{\pi}\right)^{\frac{1}{2}}\left[1-\frac{h^2}{64}+\cdots\right],$$

$$Ne_3'(s,0)=\frac{192}{h^3}\left(\frac{2}{\pi}\right)^{\frac{1}{2}}\left[1-\frac{h^2}{64}+\cdots\right],$$

$$No_3(s,0)=-\frac{64}{h^3}\left(\frac{2}{\pi}\right)^{\frac{1}{2}}\left[1+\frac{h^2}{64}+\cdots\right],$$

$$No_3'(s,0)=\frac{192}{h^3}\left(\frac{2}{\pi}\right)^{\frac{1}{2}}\left[1-\frac{h^2}{64}+\cdots\right],$$

where $\gamma=1.781$.

JOURNAL OF APPLIED PHYSICS VOLUME 32, NUMBER 8 AUGUST, 1961

Surface Kinetics and Physics Investigation of the Reaction between Single-Crystal Germanium and Iodine

W. J. Heinecke* and S. Ing, Jr.†
Semiconductor Division, Raytheon Company, Newton, Massachusetts

(Received December 12, 1960)

A study of the kinetics of the reaction between iodine and single-crystal germanium and the resulting electrical surface has been undertaken. An activation energy of 18.5 kcal/mol has been found for the reaction of each of the three crystallographic planes studies. However, frequency factors were found to differ with orientation. An aging effect of the surface was found through field-effect surface measurements. A surface acceptorlike trap having an energy level (E_t-E_v) of 0.44 ev was found and investigated. The density of the trap was found to be 1.4×10^{12} cm^{-2}.

INTRODUCTION

Vapor phase etching of single-crystal germanium could be of merit in processing semiconductor devices. However, a detailed knowledge of the reaction and the resulting surfaces is necessary. The purpose of this work was to investigate the kinetics and the mechanism of germanium and iodine vapor reaction, and the electrical properties of the germanium surface resulting from vapor etching.

There is little information available on the thermodynamics of the reactions

$$\mathrm{Ge(s)+I_2(g)\rightleftarrows GeI_2(g)}, \tag{1}$$

$$\mathrm{Ge(s)+2I_2(g)\rightleftarrows GeI_4(g)}. \tag{2}$$

By using the very approximate values of the free energies and the heats of formation of the reactions given by Quill,[1] the equilibrium constants were calculated for reactions (1) and (2) up to a temperature of 800°K. The results indicate that the above reactions proceed essentially to completion in the forward direction within the stated temperature range.

The di-iodide and the tetra-iodide would establish an equilibrium with each other through the disproportionation reaction

$$\mathrm{2GeI_2(g)\rightleftarrows Ge(s)+GeI_4(g)}. \tag{3}$$

Sirrine[2] and Jolly and Latimer[3] studied the equilibrium of the above reaction independently. The standard free energy change was found by Sirrine to be $\Delta F^0=-30\,900+44T$ cal/gmol of GeI_4 formed, and was found by Jolly and Latimer to be $\Delta F^0=-27\,500+8T\ln T-22.6T$ cal/gmol of GeI_4 formed. The two results differ by a wide margin. According to Sirrine, GeI_2 was the predominant product above 700°K, but Jolly's free energy equation indicated that a significant amount of GeI_4 existed in equilibrium with GeI_2 at these temperatures. No attempt was made to ascertain the validity of either finding in this study. The extent of reactions (1) and (2) in the forward direction was investigated. Jolly's data was arbitrarily considered to give the correct equilibrium molar ratio of GeI_2 to GeI_4 in the vapor phase.

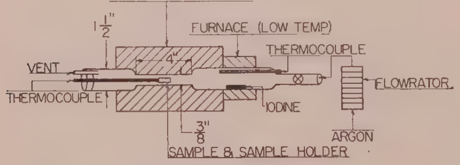

Fig. 1. Atmospheric pressure flow reactor.

The reaction rate studies were carried out in an atmospheric pressure and a low-pressure flow reactor (see Figs. 1 and 2). In using these two different systems, it became possible to investigate the reaction under a great variety of etching conditions.

In evaluating the electrical properties of the etched surfaces, both ac and pulsed field-effect measurements were made. Rupprecht's method of analysis was followed for the pulsed field-effect data.[4,5] The expres-

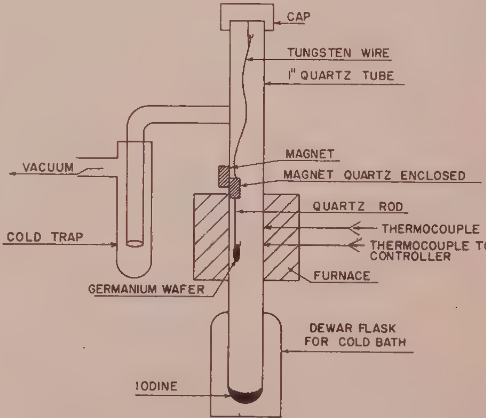

Fig. 2. Low-pressure reactor.

---

* Present address: Transitron Electronic Corporation, Wakefield, Massachusetts.

† Present address: General Electric Company, Advance Semiconductor Laboratory, Syracuse, New York.

[1] L. L. Quill, *The Chemistry and Metallurgy of Miscellaneous Materials* (McGraw-Hill Book Company, Inc., New York, 1950).

[2] R. C. Sirrine, Gen. Elec. Rept. TIS, R58E-GP14 (1958).

[3] W. L. Jolly and W. M. Latimer, J. Am. Chem. Soc. **74**, 5754 (1952).

[4] G. Rupprecht, Phys. Rev. **111**, 75 (1958).

[5] G. Rupprecht, Tech. Memo No. T-198, Research Division, Raytheon Company, Waltham, Massachusetts.

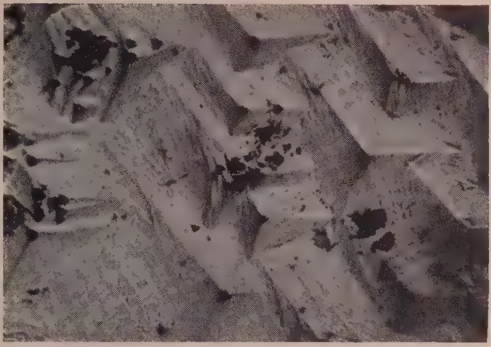

FIG. 3. (1,1,1) surface which was etched in atmospheric pressure flow reactor at 550°C. 150×.

FIG. 4. (1,1,0) surface which was etched in the atmospheric pressure flow reactor at 540°C. 150×.

sion which describes the transient behavior of the pulsed measurements is

$$(dn_t/dt)=r_n n_s(N_t-n_t)-g_n n_t(N_c-n_s), \tag{4}$$

where n_t=number of trapped electrons, n_s=number of free electrons in the surface region, N_t=number of surface traps, N_c=number of states in the conduction band, r_n,g_n are recombination and generation rate constants of electrons, respectively. A similar equation can be written to describe the interaction of holes with the valence band.

In those experimental cases reported herein, the initial slopes and the time constants describing the relaxation were found to be independent of the applied field voltage when a positive field pulse was used. Since the effect of the pulse is to increase n_s, the first term of Eq. (4) can not be instrumental in describing the transient behavior. A similar argument applies in the case of holes, except that for the n-type surface, the hole concentration is small. Therefore the corresponding first term for the holes is negligible.

Assuming the relations $N_c \gg n_s$ and $N_v \gg p_s$, Eq. (4) and its analog describing hole behavior reduce to

$$dn_t/dt=-g_n n_t N_c, \tag{5}$$

$$dp_t/dt=-g_p p_t N_v, \tag{6}$$

where p_t is the number of trapped holes and g_p the generation rate constant of holes.

Further, it had been shown that in the case where certain energy configurations had been established, a plot of the log of the time constant characterizing the surface pulse decay vs the reciprocal of the absolute temperature can be used to establish the energy level.[4] However, if one considers the capture cross section and the density of valence band states as functions of temperature, an expression is obtained which is of the form

$$\sigma \exp(-\Delta E/kt)=F/\tau T^2, \tag{7}$$

where F is a constant which depends upon the semiconductor material. ΔE refers to the trap energy level at 0°K, σ is the apparent capture cross section, and τ is the experimental time constant of the conductivity decay. Therefore, a plot of log $(F/\tau T^2)$ vs $1/T$ should give rise to a straight line whose slope is related to the energy level while the intercept is related to the cross section shown in this paper.

EXPERIMENTS AND RESULTS

Atmospheric Pressure Flow Reactor

The reactor consisted of a quartz tube which was placed in a two-zone furnace. Solid iodine was located in the low-temperature reservoir. Germanium wafers were situated in the high-temperature zone where the etching reaction took place. Pure argon, used as the carrier gas, was passed through the iodine reservoir to become saturated with iodine vapor before entering the reaction zone. Gaseous reaction products and the carrier gas were vented to the atmosphere after emerging from the high-temperature area. The iodine partial pressure and the reaction temperature were regulated through the temperature controllers of the furnace.

Germanium wafers (10–20 mils thick) CP-4 etched and oriented in the (1,1,1), and (1,0,0) directions were used in the etching. The surfaces were lined up parallel to the gas flow. Etching rates were obtained by measuring the germanium weight loss, the reaction time, and the apparent surface area. Variables investigated were the gas flowrate, the iodine partial pressure, and the reaction temperature, whose ranges were:

Average gas linear flow rate	0.2–6 cm/sec
I_2 partial pressure	0.004–0.02 atm
Reaction temperature	300°–550°C.

Reaction times of 5–20 min were employed.

The results indicated that at high gas velocities, the reaction rate was limited by the diffusion of the reactant and products in the gas phase. Observations leading to this conclusion were:

(a) The reaction temperature exerted little influence on the rate.

TABLE I. Rates of formation of germanium iodides during experimental runs.

Run No.	Argon flow rate (cc/min) at STP	P_{I_2} (atm) in reservoir	T_{Ge}(°C)	Rate of I_2 supplied (gmol/min)	Calc rate of GeI_2 formed (gmol/min)	Calc rate of GeI_4 formed (gmol/min)	Calc rate of I_2 consumed (gmol/min)
46	4.2	0.0057	312	0.98×10^{-6}	1.05×10^{-6}	$0.05\ \times10^{-6}$	1.15×10^{-6}
47	6.6	0.0086	311	2.32×10^{-6}	1.55×10^{-6}	$0.38\ \times10^{-6}$	2.31×10^{-6}
48	8.0	0.0042	433	1.38×10^{-6}	1.45×10^{-6}	0.023×10^{-6}	$1.5\ \times10^{-6}$
49	14.4	0.0042	503	2.48×10^{-6}	2.55×10^{-6}	$0.02\ \times10^{-6}$	2.59×10^{-6}
50	14.8	0.01	507	6.06×10^{-6}	6.25×10^{-6}	$0.1\ \times10^{-6}$	6.45×10^{-6}
51	19.0	0.0057	489	4.43×10^{-6}	3.70×10^{-6}	$0.1\ \times10^{-6}$	$3.0\ \times10^{-6}$
52	15.0	0.01	518	6.13×10^{-6}	$5.5\ \times10^{-6}$	$0.17\ \times10^{-6}$	5.84×10^{-6}
54	7.2	0.01	555	2.94×10^{-6}	2.90×10^{-6}	$0.07\ \times10^{-6}$	3.04×10^{-6}
55	14.8	0.01	556	6.05×10^{-6}	$5.1\ \times10^{-6}$	$0.16\ \times10^{-6}$	5.42×10^{-6}

(b) The etching rate was directly proportional to the iodine partial pressure.

(c) The gas flowrate affected the reaction rate in an erratic manner.

Results obtained at low gas flow suggested that the forward reactions proceeded essentially to completion within the temperature range employed, which is in accord with the estimations obtained from the data mentioned previously. The relevant low gas flow rate etching data are presented in Table I. In deriving the tabulated data, GeI_4 and GeI_2 were assumed to exist in equilibrium molar ratios calculated from Jolly's data.[3] Their rates of formation were calculated based on the rates of loss of germanium.

It is seen from Table I that the iodine supply rates are approximately equal to the consumption rates at the operating temperatures. Most of the discrepancies between the two rates are within the experimental error.

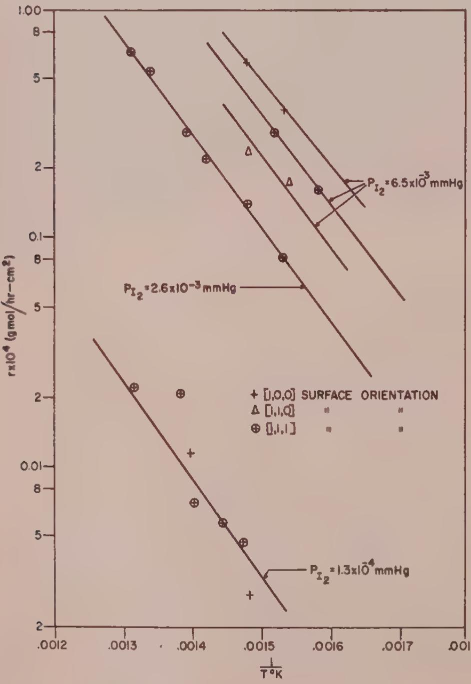

FIG. 5. Plot of reaction rate vs $1/T$.

The visual surface conditions after the etching were closely observed. It was found that at an etching temperature below 450°C, the surface was generally quite pitted without any characteristic patterns for the various orientations. However, as the temperature was raised above 450°C, the surface appearance improved. Under high magnification, various surface structures were observed for different orientations; on the (1,1,1) oriented surfaces, pyramidal formations resulted; on (1,0,0) orientations, undulatory surfaces were obtained, while the (1,1,0) surface was flat in general with patches of streak marks. Figures 3 and 4 show the typical surfaces obtained for (1,1,1) and (1,1,0) orientations. The peripheral areas, particularly around the leading edges, were always eroded to a greater extent and exhibited no characteristic patterns.

Low-Pressure Reactor

A quartz tube reactor was again employed. The reaction zone was externally heated and was directly exposed to an iodine source (see Fig. 2). The system was evacuated to a background gas pressure below 10^{-5} mm Hg. Several slush baths were used to maintain reservoir temperature in order to control the iodine vapor pressure. The germanium wafer was hung at the end of a quartz rod and could be easily pulled out or inserted into the heated zone. The system was first allowed to reach equilibrium and then the germanium wafer was introduced into the reaction zone. The rate was again determined by the weight change of the germanium wafer per unit time and apparent area.

Runs were made at three different iodine pressures: 1.3×10^{-4}, 2.6×10^{-3}, and 6.5×10^{-3} mm Hg. Wafers with (1,1,1) surface orientation were used for most runs. At iodine vapor pressures of 1.3×10^{-4} and 6.5×10^{-3} mm Hg (1,0,0) surface orientation was also employed, while (1,1,0) oriented wafers were only used at 6.5×10^{-3} mm Hg iodine vapor pressure. The temperature range employed was 358–491°C.

The logarithm of the reaction rates in units of gmol germanium removed per hour per square centimeter were plotted vs $1/T$°K for each pressure, as presented in Fig. 5. Straight lines were then drawn through the data points. Deviations of the points from the lines were within experimental error. It is to be noted that the straight lines are quite parallel to each other. An activation energy of the over-all reaction was calculated from the slope of the lines to be 18.4 kcal/gmol of reacted germanium. As can be seen from the data points taken at an iodine pressure of 6.5×10^{-3} mm Hg, the etching rates vary somewhat between various surface orientations. However, the slopes of log rate vs $1/T$ lines are about the same for various surface orientations.

The etched surface structures can be seen in Figs. 6 and 7. No etch pits were observed on the etched surfaces except at the lowest temperature employed; i.e., 358°C.

Alternating Current and Pulsed Field Effect Measurements

Samples of (1, 1, 1) orientation were prepared from 20 to 26 ohm-cm n-type material. Bars of approximately 3 by 10 by 0.25 mm had gold antimony leads pulsed bonded to the ends. The excess lead was removed and the sample pre-etched in CP-4 without Br_2. A layer of gold was evaporated across their ends and made contact with the bonded area. These films were alloyed by heating to a temperature above that of eutectic formation, but below that causing rapid thermal conversion.

Etching was accomplished in the low-pressure reactor already described. To prevent the migration of gold, the reaction temperatures were maintained at the lower end of the range which gave planar etching. Immediately after etching, the sample was removed, mounted in the field-effect apparatus, and the measurements were made.

Alternating current field effect patterns have consistently shown the surface to be n type. This result is in contrast to the case of Cl_2 adsorbed on a germanium surface having an intervening oxide layer.[6] In all cases the freshly treated surfaces had accumulated enough charge so that it was not possible to find the conductance minimum.

After the sample had been exposed to dry nitrogen or vacuum for several hours, there was decided shift both in the minimum of the curve and the field induced conductance change. Qualitatively, these amounted to a reduction in traps and in trapped charge, and consequently in the surface potential. Figure 8 illustrates the conductance change which is being discussed here, while Fig. 9 shows the change in trap population before and after aging.

Surfaces freshly etched with I_2 displayed decays with time constants which were considerably smaller than the limiting instrumental time constant of approximately 15 μsec. For this reason, pulsed field-effect measurements were made on the "aged" surfaces. In each case, upon application of a positive pulse, there was an initial increase in conductance with a subsequent decay.

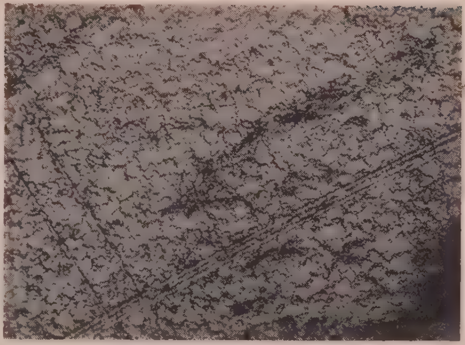

FIG. 6. (1,1,1) surface which was etched in the low-pressure reactor at 538°C. Approximately 3 μ have been removed. 150×.

The logarithm of the measured time constants vs the reciprocal of the absolute temperatures are plotted in Fig. 10. It is seen that a straight line results over a wide range of values. The activation energy resulting from this line is 0.55±0.01 ev.

A plot of log $(F/\tau T^2)$ vs reciprocal temperature has also been made (Fig. 11). The slope of the resulting straight line renders an activation energy of 0.47 ev. The apparent capture cross section (σ) seems to be independent of the temperature within the experimental range.

Derived data is presented in Table II.

DISCUSSION OF RESULTS

The controlling gas phase diffusion process found in the atmospheric pressure reactor made that system unsuitable for the chemical kinetic study of the germanium iodine reaction. However, the system did give some indication of the equilibrium and the relative stability of various surface orientations. Table I shows the forward reactions of Eqs. (1) and (2) to be favored within the temperature range employed. Etching

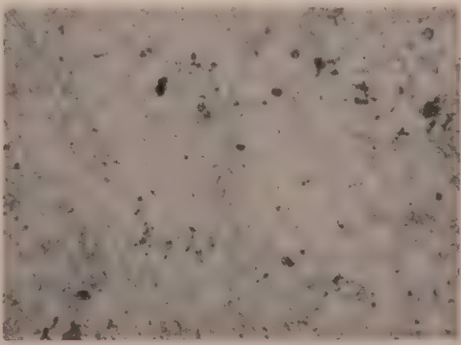

FIG. 7. (1,0,0) surface which was etched in the low-pressure reactor at 403°C. Approximately 1.5 μ have been removed. 200×.

---

[6] R. H. Kingston, J. Appl. Phys. 27, 101 (1956).

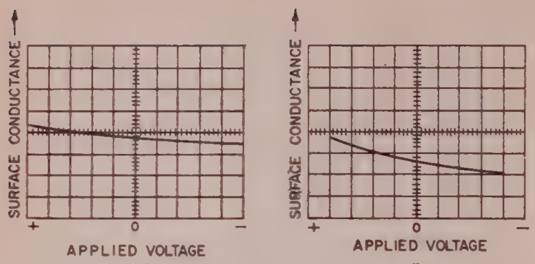

(a) (b)

FIG. 8. (a) Typical curve of conductivity vs applied field voltage on a surface immediately after etching. As indicated, a positive applied voltage to the field plate corresponds to a horizontal displacement to the left. (b) Curve of surface conductivity vs applied field voltage on the same surface after it has aged several hours in dry nitrogen. The coordinates for this curve have the same scales as those in (a).

processes seemed to take place preferentially on the (1,1,1) surfaces with the stable (1,1,1) plane showing after the reaction. The same was true for the (1,0,0) surfaces, where the more stable (1,1,1) planes showed as the edge planes of the resulting wavy pattern. (1,1,0) surfaces exhibited large flat areas, which would indicate that the plane was stable under the etching condition. Streak marks which appeared on the etched (1,1,0) surfaces were probably etch pits that were formed during the reaction process. In general, surface patterns resulting from iodine etching closely resembled some of the epitaxially grown germanium surfaces (as obtained by Sirrine[2]), who used the disproportionation reaction of germanium di-iodide.

The low-pressure reactor, which greatly facilitated the diffusion of products, yielded true kinetic data with the characteristic high temperature dependence of the reaction rate. This data is presented on the straight-line plots of rate vs reciprocal temperature obtained for the various surface orientations (Fig. 5). The rate was then plotted against the pressure of iodine at two temperatures (Fig. 12). Parallel straight lines were obtained yielding an order of the over-all reaction of 1.18. The rate expression is then:

$$r = A\exp(-18\,400/RT)P_{\mathrm{I}_2}{}^{1.18},$$

where r is the specific rate and A is a frequency factor which is dependent on the surface orientation. With "P_{I_2}" in the atmospheric pressure units, the frequency factors for the (1,1,1), (1,1,0), and (1,0,0) surface orientations were calculated to be 3.54×10^7, 2.4×10^7, and 5.2×10^7, respectively. Their relative stability seemed to substantiate the results obtained from the atmosphere pressure flow reactor.

TABLE II. Surface trap data. Calculations from room-temperature data.

Activation energy (ev)	0.55±0.01; 0.47±0.01
Cross section (cm^2)	1.14×10^{-13}
Density of states (cm^{-2})	1.4×10^{12}

The reaction mechanism could be visualized as comprised of the following steps: (1) adsorption and formation of a bond between the iodine and a surface germanium atom, (2) formation of another single bond with another iodine atom, (3) breaking of the covalent bonds with neighboring germanium atoms, (4) desorption of germanium di-iodide. Either step (2) or (3) could be the rate-limiting steps. However, in view of the seemingly constant activation energy between the differently orientated surfaces where the number of covalent bonds are not the same, step (2) is postulated as the controlling mechanism. It is conceivable that in step (2) the electron would have to cross a high potential barrier to form the bond with the second iodine atom. Hence, high energy would be required in forming such a transition complex on the surface.

Carasso and Stelzer[7] had studied the etching reaction of chlorine vapor on germanium. Within the pressure and temperature range employed (1.51–11.62 cm Hg pressure, 175°–258°C), the kinetics was found to be of zero order, and showed no evidence of retardation by products, thus indicating full surface coverage. Only (111) surface orientation was used. The reaction mechanism proposed involved successive stages of localization of a hole and adsorption of a chlorine atom, with a progressively higher energy barrier on account of electrostatic repulsive force. Hence the mechanisms of the chlorine etch and the iodine etch of germanium are seemingly of the same nature. The high iodine pressure dependence as found in this work suggests that at the pressure and the temperature range employed, the surface coverage of iodine is not complete.

The frequency factors of the three differently orientated surfaces seem to vary inversely with the surface densities of the atoms on the germanium crystals.

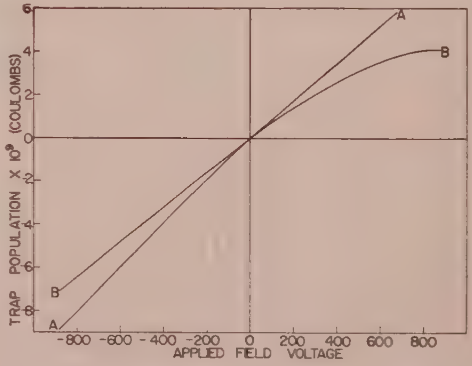

FIG. 9. Curves of the change of surface trap population from the zero applied field condition vs applied field plate voltage. The sample is the same as that used in obtaining Fig. 8. Curve A-A corresponds to the freshly etched surface. Curve B-B portrays the population after aging.

---

[7] J. I. Carasso and I. Stelzer, J. Chem. Soc. **1960**, 1797.

Handler[8] gives the surface densities as 6.3×10^{14}, 7.2×10^{14}, and 9.0×10^{14} atoms/cm^2 for the (1,0,0) (1,1,1), and (1,1,0) orientations, respectively. The relative magnitude of frequency factors could be explained from the point of view of the high affinity between the iodine and the surface germanium atoms, causing the surface to be largely covered with iodine atoms. Most of the bonds would arise from simple chemisorption of one germanium to one iodine atom. Because of the larger size of the iodine atoms it would be difficult, from space considerations alone, to have a germanium atom acquiring two iodine atoms. The degree of difficulty would be dependent upon the density of the adsorpted atoms, and hence the surface density of the germanium atoms.

Gualtieri *et al.*[9] had studied some of the mechanisms of etching germanium with gaseous halogens using a light reflectrogram technique. Generally, it was observed that the (1,1,0) zone between (1,1,0) and (1,1,1) planes appeared after etching, and in all cases the (1,1,1) plane appeared. Thus, this part of the (1,1,0) zone is, usually, more resistant to attack than the other planes or zones. The reason given was that the above-mentioned zone contained only these planes that are composed of atoms which had just one electron available for bonding. In addition, the remainder of the zone, between (0,0,1) and (1,1,1), was made up of atoms which were bonded to only two neighboring atoms, thereby forming the additional bonds. However, in the case of iodine vapor etching, the (0,0,1) plane was attacked slowly and appeared in the light figure pattern. This appearance of the (0,0,1) plane was attributed to the insufficient space available for the relatively large iodine atoms to form bonds that were tetrahedrally oriented about the germanium atoms.

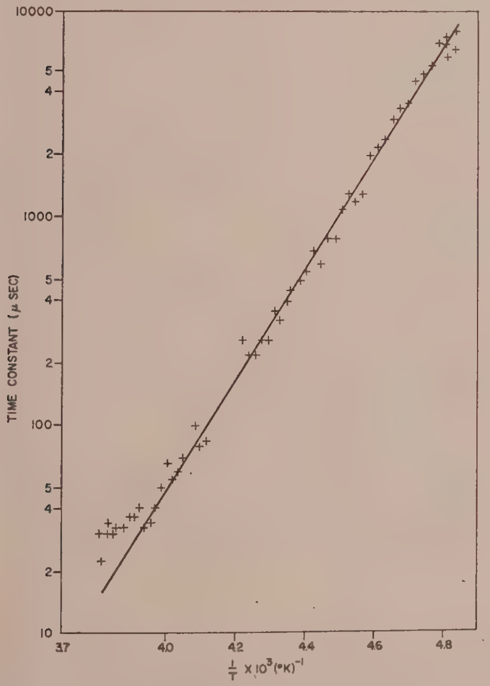

FIG. 10. Logarithm of the time constant of the pulsed field effect decay vs $1/T$.

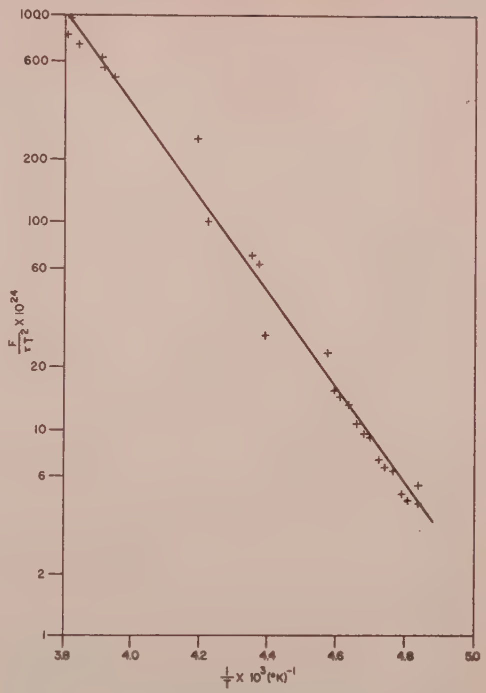

FIG. 11. Plot of logarithm of $F/\tau T^2$ vs $1/T$.

The relative stability of various surface orientations was not explicitly determined for this particular system.

The lack of etch pits for all etched samples, except on the one prepared in the low-pressure reactor, at the lowest temperature, suggested that under the high-temperature conditions the difference in the activities between the dislocation centers and the normal lattice sites on the surface was minimized.

Alternating current and pulse field effect observations of the trap population, conduction, and minima shifts of the surface indicated that something was being removed rather than deposited during the aging process. To further substantiate this, a dc field was coupled to the aged surface in an effort to find a change in slow state population. Long-term change in the surface conductance for periods up to 10 min was not detected. Whether the substance is physically adsorbed iodine, a germanium iodide, or a chemically adsorbed layer of iodine which has continued to produce an iodide at room temperature has not been ascertained.

---

[8] P. Handler in *Semiconductor Surface Physics*, edited by R. H. Kingston (University of Pennsylvania Press, Philadelphia, Pennsylvania, 1957), p. 25.

[9] J. G. Gualtieri, M. J. Katz, and G. A. Wolff, Z. Krist. **114**, 9 (1960).

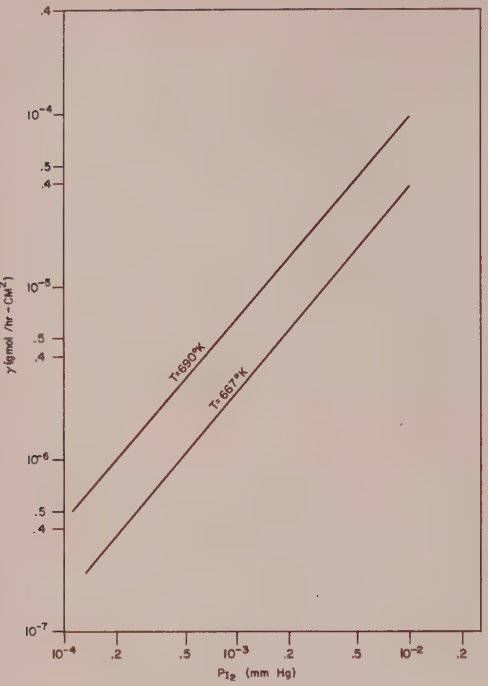

FIG. 12. Logarithm of the etching rate r of the (1,1,1) surface vs the pressure of I_2 in mm Hg.

In order to get a time constant which was independent of the surface charge, only positive pulses of from 100–1100 v were used. That is, the number of electrons at the surface was increased by the pulse. This allows one to eliminate Eq. (5) as a description of the process, since an increase in the number of electrons does not cause a generation of the electrons from the traps. Further, increasing the number of electrons would decrease the number of holes. Therefore, the previous arguments surrounding Eq. (6) are still valid. It is then seen that only the interaction of trapped holes and the valence band was measured.

For this reason, the activation energy which was obtained is $(E_T - E_V)$. Comparison of these results with those reported elsewhere in the literature where electron capture has been studied give values for $(E_C - E_T)$ of approximately 0.22 ev.[10,11] The sum of this value and the value of $(E_T - E_V)$ obtained here is 0.77 ev. This compares well with known values of the energy gap.

While this may be fortuitious, there is the possibility that the same trap that others have found was also observed in this work. In other studies, however, the surfaces have been prepared by etches of the HF-HNO_3 type. In this case, a completely different type of system has led to the same result. This is in keeping with the suggestion that this trap may be due to something inherent in the material interface rather than to the surface treatment. It is to be noted that the density of states found in this study is higher than those reported elsewhere.

Because of the definite n-type character of the I_2 etched surface, and the p-type layer that is formed upon adsorption of Cl_2 on normally etched samples, the surfaces are seen to be of fundamentally different natures. This may arise from the electronic distribution when the iodine octet is completed by forming an ionic bond with a surface Ge atom; in this case a discrete dipole perpendicular to the surface is established with the first layer of Ge atoms assuming a net positive charge. Immediately under this layer, a space-charge layer enriched in electrons would then exist, which accounts for the n-type layer. Further, such a model would explain the differences between the clean-surface[12] and the etched-surface behavior.

An alternative explanation, suggested by Carasso and Stelzer,[13] depends upon the formation of a positive iodine ion chemisorbed on the surface. Extension of the field effect work to other halogen germanium systems should provide a test for the proposed mechanism. There may also be other possible explanations based upon the formation of more complex chemical surface species.

ACKNOWLEDGMENTS

The authors express their appreciation to Dr. G. Rupprecht for his helpful discussions, to R. Sweeney, who prepared many of the samples, and to Mrs. B. A. Cochrane for her help in preparing the manuscript.

---

[10] H. Statz, G. A. deMars, L. Davis, and A. Adams, Phys. Rev. **101**, 1272 (1956).

[11] A. Many and D. Gerlich, Phys. Rev. **107**, 404 (1957).

[12] W. B. Pearson and G. A. Wolff, Discussions Faraday Soc. **28**, 142 (1959).

[13] J. I. Carasso and I. Stelzer, J. Chem. Soc. **1956**, 3726.

JOURNAL OF APPLIED PHYSICS VOLUME 32, NUMBER 8 AUGUST, 1961

Back Scattering of Electrons

G. D. Archard
Electron Physics Section, Associated Electrical Industries, Ltd., Research Laboratory, Aldermaston, Berkshire, England

(Received February 23, 1961)

The behavior of a stream of electrons penetrating a solid target is studied with a view to determining the proportion which return to the surface and pass back into space. Two existing theories (diffusion and large-angle single elastic scattering) are adapted to this end. These theories predominate for high and low atomic numbers, respectively. A combination of the two theories agrees well with experiment.

I. INTRODUCTION

WHEN a steam of electrons is directed against a solid target most of the electrons penetrate into the target, but some come out again. A few of these may be the products of collisions and are classed as secondary electrons; they are generally slow, having an energy less than 50 ev. Most of the returning electrons, however, are members of the original beam which have penetrated to a greater or lesser extent into the target, suffered elastic or inelastic collisions or both, and returned to escape from the surface.

The behavior of the electrons in the target before escaping is of particular importance in connection with calculations of x-ray yield, and it is therefore desirable to set up a theory capable of explaining the experimental back-scattering results of such workers as Schonland, Palluel, Sternglass, Holliday and Sternglass, Kanter, Matskevich, and Mulvey and Doe[1] on the basis of some reasonable form of electron path inside the target.

According to one approach,[2] electrons are supposed to travel straight into the target up to a certain specified distance, after which they diffuse evenly in all directions. This theory acknowledges the fact that owing to multiple collisions an electron's progress eventually becomes random, but it ignores the possibility of electrons' undergoing large single elastic reflections somewhere between the surface and the "depth of complete diffusion."

According to a more recent approach[3] electrons are supposed to travel straight into the target, suffering retardation in accordance with the Thomson-Whiddington law,[4] but also undergoing elastic collisions in accordance with Rutherford's law of scattering. This theory acknowledges the presence of electrons elastically scattered through large angles, but ignores the diffusing effect of multiple collisions; for example, all electrons not turned through more than a right angle are assumed not to have been turned at all.

In reality there is little doubt that the processes emphasized by each of these theories occur together, and the possibility of uniting them will be the subject of the following theory.

It should be mentioned, of course, that inelastic collisions also make an appreciable contribution to the electron distribution for low energies of the incident electrons. However, for present purposes in which the range of incident energies envisaged does not fall below 5 kev, these may fairly be neglected.

II. DIFFUSION THEORY

Bethe *et al.*[2] define the "depth of complete diffusion" as the depth at which the average cosine between the actual direction of motion and the direction of the primary beam becomes $1/e$ (i.e., the directions differ by an angle of 68.4°). This corresponds to a critical energy E_d, where

$$\int_{E_d}^{E_0} \frac{dE}{\lambda|dE/dx|}=\frac{1}{2} \tag{1}$$

and

$$\frac{1}{\lambda}=\frac{\pi Ne^4Z^2}{2E^2}\ln\frac{2a_Hm(2E/m)^{\frac{1}{2}}}{\hbar Z^{\frac{1}{3}}}; \tag{2}$$

N = number of atoms/cc, e = electronic charge, m = electronic mass, $\hbar$ = Planck's reduced constant, Z = atomic number, a_H = Bohr hydrogen radius, and E_0 = initial energy.

The ratio dE/dx may be determined from Bethe's[5] original theory, of which the Thomson-Whiddington law constitutes an approximation.[6] In its precise form this law is given by:

$$dE/dx=2\pi Ne^4Z\ln(2E/J)/E, \tag{3}$$

where

$$J=11.5Z \text{ ev.}$$

Substitution of the quantities defined in Eqs. (2) and (3) into Eq. (1) yields

$$\int_{V_d}^{V_0} \frac{Z}{4V}\frac{\ln(0.54V^{\frac{1}{2}}Z^{-\frac{1}{3}})}{\ln(0.174VZ^{-1})}dV=\frac{1}{2}, \tag{4}$$

---

[1] B. F. J. Schonland, Proc. Roy. Soc. (London) **A104**, 235 (1923); **A108**, 187 (1925); P. C. R. Palluel, Compt. rend. **224**, 1492, 1551 (1947); E. J. Sternglass, Phys. Rev. **95**, 345 (1954); J. E. Holliday and E. J. Sternglass, J. Appl. Phys. **28**, 1189 (1957); H. Kanter, Ann. Physik **20**, 144 (1957); T. L. Matskevich, Soviet Phys.–Tech. Phys. **2**, 255 (1957); T. Mulvey and N. Doe (private communication, 1960).

[2] H. A. Bethe, Ann. Physik **5**, 325 (1940).

[3] T. E. Everhart, J. Appl. Phys. **31**, 1483 (1960).

[4] J. J. Thomson, *Conduction of Electricity Through Gases* (Cambridge University Press, Cambridge, England, 1906).

[5] H. A. Bethe, M. E. Rose, and L. P. Smith, Proc. Am. Phil. Soc. **78**, 573 (1938).

[6] See, for example, C. R. Worthington and S. G. Tomlin, Proc. Phys. Soc. (London) **A69**, 401 (1956).

where $V=E/e$ now represents the energy measured in volts, so that eV_d is the energy at the depth of complete diffusion.

For elements $Z=10$ to $Z=80$, the ratio of the logarithms changes very little between 5000 v and 50 000 v, and still less in the range of integration V_0 to V_d. It is therefore reasonable to assign this ratio a constant value and to take it outside the integral. The mean value for initial voltage 10 kv and $Z=10$ to 80 is 0.70. Thus the condition for complete diffusion becomes

$$Z\ln(V_0/V_d)=20/7. \tag{5}$$

The depth of penetration x_d corresponding to the state of complete diffusion may now be found by integrating Eq. (3). This gives

$$\rho x_d=4.24\times 10^{-10}ZA[f(V_0)-f(V_d)], \tag{6}$$

where

$$f(V)=\langle Ei\rangle[2\ln(0.174V/Z)]. \tag{7}$$

The function $\langle Ei\rangle$ is tabulated by Jahnke and Emde.[7] For arguments considerably greater than unity it is conveniently represented by the semiconvergent series

$$\langle Ei\rangle(y)=(e^y/y)(1+1/y+2!/y^2+\cdots). \tag{8}$$

Behavior of this series over the range useful in practice is shown in Fig. 1.

From Eq. (6), the ratio of the depth of complete diffusion to the full range x_r is given by

$$x_d/x_r=[f(V_0)-f(V)]/f(V_0) \tag{9}$$

and when $f(V)$ is expanded by means of Eqs. (7) and (8), this becomes

$$\frac{x_d}{x_r}=1-\left(\frac{V_d}{V_0}\right)^2\frac{\ln(0.174V_0/Z)(1+1/y_d+\cdots)}{\ln(0.174V_d/Z)(1+1/y_0+\cdots)}. \tag{10}$$

The ratio of the logarithms and of the series is in general very near unity, so that there is not much error in writing

$$x_d/x_r=1-(V_d/V_0)^2. \tag{11}$$

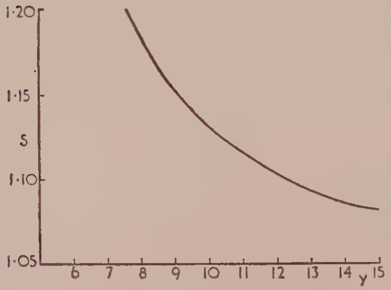

FIG. 1. Values of the semiconvergent series. $S=1+1/y+2!/y^2+\cdots$.

Equations (5) and (10) give the ratio x_d/x_r in terms of atomic number (the dependence on V_0 turns out to be very slight). For approximate purposes, however, V_0-V_d may be regarded as small compared with V_0 and Eqs. (5) and (10) reduced to

$$x_d/x_r=40/7Z. \tag{12}$$

Suppose now that electrons move equally in all directions from the depth of complete diffusion in such a way that their over-all paths equal the full range. Their distribution may then be represented by a sphere (Fig. 2) of which the conical sector projecting above the target surface contains the back-scattered electrons which would be detected in experiments. This model is reminiscent of the photographs of electron glow published by Ehrenberg and Franks.[8] Only the electrons contained in the solid angle 2θ escape from the target. The ratio of this solid angle to the complete sphere into which electrons are diffused is

$$\frac{1}{4\pi}\int_0^\theta 2\pi\sin\theta d\theta,$$

where

$$\cos\theta=x_d/(x_r-x_d).$$

Thus the back-scattering coefficient R becomes

$$R=\tfrac{1}{2}[(1-2x_d/x_r)/(1-x_d/x_r)]. \tag{13}$$

Together with Eq. (12), Eq. (13) gives

$$R=(7Z-80)/(14Z-80) \tag{14}$$

and, although this result is subject to the rather coarse approximation involved in the derivation of Eq. (12), it gives values of R differing by only a few percent from those obtained by using in full the more exact Eqs. (5) and (10).

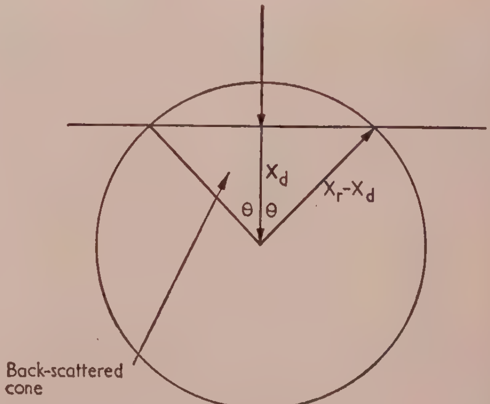

FIG. 2. Illustrating motion of back-scattered electrons.

---

[7] E. Jahnke and F. Emde, *Tables of Functions* (Dover Publications, New York, 1945).

[8] W. Ehrenberg and J. Franks, Proc. Phys. Soc. (London) **B66**, 1057 (1953).

Figures 3 and 4 give the values of x_d/x_r and R as functions of V_0/Z for several varieties of target material. Note that the theory predicts zero R for atomic numbers lower than 12, as is indeed immediately obvious from the approximate equation (14) (negative values of course have no significance).

Values of R for high incident voltage are plotted against Z in Fig. 5 (curve A) together with various experimental results. The theoretical curve agrees broadly with experiment for high values of Z, but its sharp cutoff at $Z=11$ is not borne out by experiment. This is not really surprising, since the value of x_d/x_r rises as Z falls; hence, in targets of low Z the electrons traverse a large part of their range before diffusion sets in, so that other forms of back scattering, such as large-angle single elastic collisions, have a chance to occur. These will be considered in the next section.

III. LARGE SINGLE ELASTIC SCATTERING THEORY

According to Everhart,[3] electrons are retarded in accordance with the Thomson-Whiddington law [Eq. (3) with a constant mean value for the logarithm]. The law provides an expression for the electron velocity at various depths of penetration, and when this is put into the Rutherford single elastic scattering formula, there results an angular distribution of elastically scattered electrons. Only those reaching the surface before fulfilling their total range escape from the target. Everhart deduces a back scattering coefficient

$$R_E=(a-1+0.5^a)/(a+1), \qquad (15)$$

where

$$a=\pi Z^2e^4N_A/m^2cA; \qquad (16)$$

N_A=Avogadro's number, c=constant, and the remainder of symbols are as before.

The constant c comes from the Thomson-Whiddington law written in the form

$$v^4=v_0^4-c\rho x \qquad (17)$$

(v=velocity), and is thus more explicitly given as

$$c=(16\pi N_Ae^4Z/m^2A)\ln(2E/J), \qquad (18)$$

where J is as in Eq. (3), so that

$$a=Z/16\ln(0.174V_0/Z). \qquad (19)$$

The single elastic back-scattering coefficient R_E is thus given as a function of V_0 and Z by Eqs. (15) and (19).

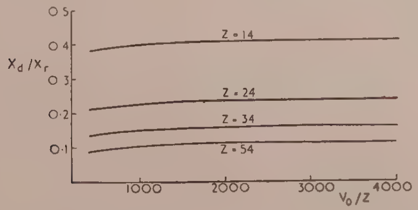

FIG. 3. Values of x_d/x_r for targets of atomic numbers 14, 24, 34, 54.

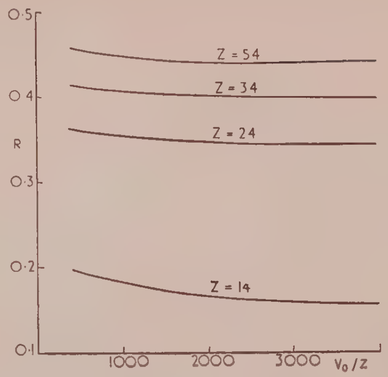

FIG. 4. Values of R for targets of atomic numbers 14, 24, 34, 54.

With the value of a given by Eq. (19) for a moderate voltage (10 kev) the R_E-Z curve falls far below the experimental points in Fig. 5. Everhart acknowledged this, and empirically adjusted the value of a, obtaining curve B in the figure. This agrees well with all but the top group of points, but is of necessity a little incomplete without justification of the empirical adjustment. Such justification will now be sought.

Everhart gives the number of electrons incident on a plane at relative depth η in the target as

$$n_0(\eta)=n_0-\int_0^\eta\int_0^{\pi/2}dn(\eta,\theta), \qquad (20)$$

where $dn(\eta,\theta)$ is obtained from the Rutherford scat-

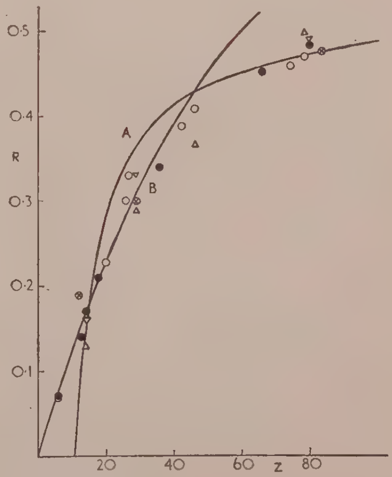

FIG. 5. Back scattering vs atomic number. Curve A, diffusion; curve B, elastic collisions. Experimental points: ○ Palluel (1947, 16 kv); △ Schonland (1923, 100 kv); ▽ Kanter (1923, 100 kv); ⊗ Mulvey and Doe (1960, 23 kv); ● Holliday and Sternglass (1957, 20 kv).

tering formula and depends on θ by virtue of the factor

$$\sin\theta d\theta / \cos^4(\theta/2).$$

The limits imposed on the θ integration imply that electrons deflected through less than a right angle are not deflected at all. Clearly, there will in fact be many electrons which suffer deflections between 0° and 90°, and an improved theory should result when these are allowed for. Consider an electron initially deflected at 45°. In order to get back into its original direction and so accord with Everhart's analysis, it must suffer a second deflection of 45° in the opposite sense. But it might equally well be deflected by 45° in the *same* sense, so acquiring a total deflection of 90° and becoming lost to subsequent layers in the target. If then Everhart's theory constitutes a first approximation to the true state of affairs, a very fair second approximation may be gained by supposing that *half* the electrons deflected between 0° and 90° are lost to subsequent layers. Thus, the θ integration in Eq. (20) will be

$$\int_0^{\pi/2} \frac{\sin\theta d\theta}{\cos^4(\theta/2)} + \frac{1}{2}\int_{\pi/2}^{3\pi/4} \frac{\sin\theta d\theta}{\cos^4\theta/2},$$

the second term constituting the correction. The effect of this is to raise the value of a/Z from 0.012 to 0.041, which is very nearly the empirical value 0.045 used by Everhart for curve B in Fig. 5.

IV. COMBINED THEORY

The diffusion and large single elastic scattering theories invoke different mechanisms and must be regarded as complementary rather than contradictory. It would be naive simply to take the mean of curves A and B in Fig. 5, since in targets of low Z the ratio x_d/x_r is greater than in targets of high Z, and there is therefore a greater relative distance in which single elastic collisions can take place before the onset of diffusion. It would thus constitute a more reasonable approximation to assign weight x_d to curve B and $x_r - x_d$ to curve A, but at best this is only a guess; it is perhaps preferable rather to present both curves together, indicating the range in which each appears to be dominant, and considering which way each would move if further corrections were taken into consideration.

First, then, consider diffusion for low Z. An electron which has penetrated to a depth x_d cannot reach the surface until it has traversed at least another distance x_d. Thus, when x_d/x_r is of the order of $\frac{1}{2}$, very few electrons will reach the surface by way of diffusion. This is of course reflected in the sharp cutoff of curve A at $Z=11$. But the relatively large value of x_d/x_r affords plenty of opportunity for single elastic collisions, and in this region it therefore appears that only curve B should be considered. In Fig. 6, therefore, curve A is shown only in the region of medium and high Z.

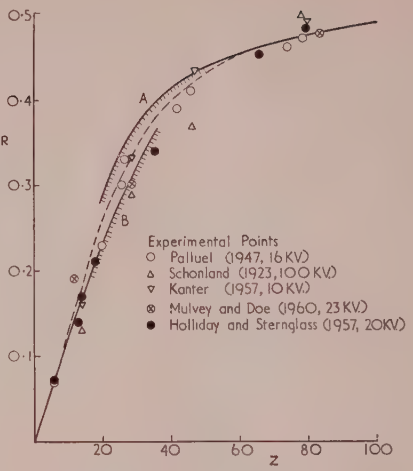

FIG. 6. Back scattering vs atomic number (composite theory). Curve A, diffusion; curve B, elastic collisions. Experimental points as in Fig. 5.

Now as Z rises, the ratio x_d/x_r falls, and many more electrons diffuse back through the surface. But the model of Fig. 2 has been rather oversimplified in that it assumes that electrons which just get back to the surface at the end of their range necessarily escape from it with an energy sufficient to distinguish them from secondary electrons (generally regarded as having energies <50 ev and excluded from experimental measurements by biasing). Plainly there will be a few genuinely back-scattered electrons which will be lost in this way. In the region of medium and high Z, therefore, curve A constitutes a slight overestimate, and the shading shows which way it should move in order to allow for this.

In regions of high Z the ratio x_d/x_r is very small; electrons become diffused almost immediately and there is little chance of large single elastic scattering. Curve B is therefore discontinued in this region, where almost all back scattering may safely be ascribed to diffusion. In regions of medium and low Z, curve B probably still constitutes an overestimate, since the correction for electrons scattered between 0° and 90° gave 0.041 as the value of a/Z, whereas curve B uses Everhart's empirical value 0.045. This tendency is also indicated by shading.

There now remain three regions: one in which the diffusion theory predominates, one in which the large single elastic scattering theory predominates, and a central region in which, due note being taken of the shading, the two curves fall very close together, so that, whatever system of weighting were used, the mean of the two theories would not alter a great deal. Moreover, the experimental points agree well with the theoretical curves in all regions. It is therefore simple to conceive a composite curve, taking in the full line curves where they stand alone, and their mean where they run together. Such a curve, shown dotted in Fig. 6, completely agrees with experiment.

The author's attention has been drawn to further work of Bothe[9] in which a slightly different criterion, involving a combination of scattering and absorption mean free paths, is used to determine a depth at which forward- and backward-moving electrons may be separated. This yields a back-scattering curve of the same general nature as that shown dotted in Fig. 6, but situated rather higher.

ACKNOWLEDGMENTS

The author wishes to thank Mr. D. P. R. Petrie, Dr. J. S. Halliday, and Mr. T. Mulvey for helpful comment, and Dr. T. E. Allibone, C.B.E., F.R.S., Director of the Laboratory, for permission to publish this paper.

---

[9] W. Bothe, Ann. Phys. 6, 44 (1949).

JOURNAL OF APPLIED PHYSICS VOLUME 32, NUMBER 8 AUGUST, 1961

Low-Angle X-Ray Diffraction of Crystalline Nonoriented Polyethylene and Its Relation to Crystallization Mechanisms[*][†]

L. Mandelkern, A. S. Posner, A. F. Diorio, and D. E. Roberts
National Bureau of Standards, Washington 25, D. C.

(Received February 23, 1961)

X-ray diffraction maxima at low angles have been observed in crystalline but nonoriented linear polyethylene, the crystallization process being conducted from the melt of the pure undiluted polymer. Several orders of diffraction are observed in favorable cases, and the spacings corresponding to the first-order reflections range from 150–850 A. The values of the maxima depend on the mode of crystallization. Previous assertions that in such systems the maxima are limited to 100–200 A are shown to be very restrictive and typical only of crystallization processes conducted at very large undercooling. Major attention is focused on the properties of specimens crystallized isothermally at relatively low values of the undercooling. The spacings are very sensitive to the crystallization temperature in this range. The highest values are observed at low undercooling, and substantial decreases occur as the temperature is lowered. Concomitantly, the density observed after isothermal crystallization significantly decreases with a lowering of the crystallization temperature.

The fact that a periodicity can be developed in such systems, the magnitude of the maxima, and their dependence on the crystallization temperature, is explicable by the application of nucleation theory. It is assumed that subsequent to the formation of critical-size nuclei from a bundle of polymer chains, crystal growth along the chain direction is severely retarded, while in the transverse direction essentially unimpeded crystallization occurs. From the observed temperature coefficient of the low-angle spacings, the ratio of the excess free energy (resulting from the junction of crystalline and amorphous regions at the crystallite ends) to the bulk enthalpy of fusion is found to be 2.6. The magnitude of this ratio receives confirmation from another type of experiment.

INTRODUCTION

X-RAY diffraction studies at low angles have been a useful tool in studying the morphology of crystalline polymers at levels above that of the unit cell. Major attention has heretofore been restricted primarily to two areas of investigation. The intensity maxima of highly axially ordered crystalline polymers have been investigated as well as maxima from polymers crystallized from very dilute solution. Only slight attention, with very little systematic study, has been given to an analysis of low-angle x-ray diffraction maxima of polymers crystallized in the bulk in the absence of any external orienting influence on the resulting crystalline regions.[1–3]

For many of the fibrous proteins[4–7] and for well-oriented synthetic polymers, several orders of well-defined meridionally directed diffraction maxima have been observed.[8–12] Although it had been assumed that for synthetic polymers the values of the long spacings are limited to the range 100–200 A,[13,14] recent work has shown that this is not the case.[9,11,12] In particular, in the case of polyethylene fibers it has been shown[12] that the observed values of the spacings depend on the orientation and thermal treatment of the specimens. Several orders of a prime spacing of 510 A have already been

---

[*] Presented in part at the 133rd Meeting of the American Chemical Society, Boston, Massachusetts, April, 1959.

[†] This investigation was supported in part by a U. S. Public Health Service research grant.

[1] R. Eppe, E. W. Fischer, and H. A. Stuart, J. Polymer Sci. 34, 721 (1959).

[2] H. A. Stuart, Ann. N. Y. Acad. Sci. 83, 3 (1959).

[3] C. Sella, Compt. rend. 248, 1819 (1959). Abstract of paper presented before the International Symposium on Macromolecules, Wiesbaden, Germany, 1959.

[4] R. S. Bear, J. Am. Chem. Soc. 66, 1297 (1944).

[5] R. S. Bear, Advances in Protein Chem. 7, 69 (1959).

[6] R. S. Bear and H. S. Rugo, Ann. N. Y. Acad. Sci. 53, 627 (1951).

[7] R. S. Bear, J. Cellular Comp. Physiol. 49, Suppl. 1, 303 (1957).

[8] H. Kiessig, Kolloid-Z. 152, 62 (1957).

[9] W. O. Statton, J. Polymer Sci. 28, 423 (1958); 41, 143 (1959).

[10] B. Belbeoch and A. Guinier, Compt. rend. 247, 310 (1958); Makromol. Chem. 31, 1 (1959).

[11] L. Mandelkern, C. R. Worthington, and A. S. Posner, Science 127, 1052 (1958).

[12] A. S. Posner, L. Mandelkern, C. R. Worthington, and A. F. Diorio, J. Appl. Phys. 31, 536 (1960).

[13] H. A. Stuart, Kolloid-Z. 165, 3 (1959).

[14] A. Keller, Kolloid-Z. 165, 34 (1959).

achieved in such fibrous systems. The wide range in the magnitude and nature of the diffraction maxima that can be observed makes clear that a morphological description of the crystalline or partially crystalline state of oriented fibers based solely on the premise of maxima limited to 200 A is incorrect.[13,14]

When crystallized from extremely dilute solutions, plate-like single crystals are the usual morphological form of the crystallized polymer.[15–18] Under the electron microscope, step heights of about 100 A are observed which represent the thickness of the platelets. Selected area electron diffraction observations indicate that the polymer chain direction is normal to the wide surface of the crystals. With the periodicity of 100 A, it has been inferred that the polymer chain must successively fold back on itself in a regular periodic fashion.[16,17] The periodicity observed in the electron microscope is substantiated by low-angle x-ray diffraction studies. Several orders of diffraction from a prime spacing of 100 A are obtained, which varies slightly with crystallization conditions.[16,19] The relationship between this mode of crystallization and its associated periodicity and the morphology of either fibrous polymers or unoriented polymers crystallized in the bulk has been a matter of conjecture and of extensive speculation.[2,18,20]

Since periodicities at low angles can be obtained from crystalline but unoriented specimens,[12] it is of interest to investigate the dependence of these spacings on crystallization conditions. Previous reports by Eppe, Fischer, and Stuart[1] and Stuart[2,13] indicate spacings limited to the range of 50–200 A. These observations, together with those from polymers crystallized from dilute solution, has engendered the concept that, when crystallized from the melt, polymer chains assume a pleated conformation in the crystal.[2,20] Consideration of the crystallization mechanism from the melt,[21] however, leads to the general conclusion that the resulting morphology of crystalline polymers must be highly dependent on the crystallization conditions. When the crystallization process is carried out isothermally, a strong influence of the crystallization temperature can be anticipated. In view of these considerations, we report the results of a low-angle x-ray diffraction study of highly crystalline but unoriented linear polyethylene, crystallized under controlled conditions over a wide temperature interval. Particular emphasis is placed on isothermal crystallization at temperatures close to the melting point. Following a preliminary report of these results,[22] which emphasized that large spacings are obtained when polyethylene is crystallized at temperatures near the melting point, Flory and co-workers[23] have succeeded in crystallizing a well-defined molecular weight sample of linear polyethylene which possesses a diffraction maximum corresponding to a spacing of 1100 A.

EXPERIMENTAL

Materials and Crystallization Procedures

The polymer used in this study was an unfractionated linear polyethylene manufactured by the Phillips Petroleum Company under the name of Marlex-50. Specimens for the density and most of the low-angle diffraction studies were 1.0 mm thick and prepared by compression molding. For certain selected diffraction experiments, thinner specimens prepared by the same method were also utilized. Isothermal crystallization at temperatures above 125°C were carried out in sealed evacuated tubes. The samples were first heated at 165–185°C for about 10 min to ensure melting and immediately transferred to thermostats set at the predetermined temperatures. The samples were held at these temperatures for specified lengths of time. For isothermal crystallization at temperatures below 125°C, the specimens were wrapped in gold foil, rendered molten as described, and directly immersed in silicon oil baths at the desired temperatures. Samples that were subjected to long-time annealing were placed in evacuated tubes after the initial crystallization and were then maintained at the desired temperatures. The temperatures of the thermostats in which the crystallization occurred were maintained constant to within ±0.05°C.

The times allowed for crystallization to ensue at a given fixed temperature are listed in Table I. In these experiments it was necessary to ensure that no significant further crystallization occurred at room temperature, the temperature at which the densities were measured and the x-ray diffraction measurements performed.[21] The half-time $\tau_{\frac{1}{2}}$ for each temperature is given in the third column of the table. This quantity represents the time in which half the crystallinity has developed before the onset of the very slow final process in the crystallization isotherm.[21] Comparison of columns two and three in Table I indicates that an adequate amount of time has been allowed for the crystallization process at each temperature so that crystallization sufficiently complete for present purposes has been developed. It should be noted that extremely long periods of time are required at the higher crystallization temperatures to develop the required crystallinity.

Densities of the samples were determined by the

---

[15] P. H. Till, J. Polymer Sci. **17**, 447 (1957).

[16] A. Keller, Phil. Mag. **2**, 1171 (1957); Discussions Faraday Soc. **25**, 114 (1958).

[17] E. W. Fischer, Z. Naturforsch. **12a**, 753 (1957).

[18] P. Geil, J. Polymer Sci. **34**, 449 (1960).

[19] B. G. Ränby, F. F. Morehead, and N. M. Walter, J. Polymer Sci. **34**, 349 (1960).

[20] A. Keller, in *Growth and Perfection of Crystals*, edited by R. H. Doremus, B. W. Roberts, and D. Turnbull (John Wiley & Sons, Inc., New York, 1958), p. 498.

[21] L. Mandelkern in *Growth and Perfection of Crystals*, edited by R. H. Doremus, B. W. Roberts, and D. Turnbull (John Wiley & Sons, Inc., New York, 1958), p. 467.

[22] See asterisk reference.

[23] R. Chiang, S. S. Pollock, W. H. Robinson, and P. J. Flory (to be published).

TABLE I. Conditions for isothermal crystallization.

Temp °C	Time allowed for crystallization (days)	$\tau_{\frac{1}{2}}$[21] (min)
131	62	. . .
130	40	19 000
129	11	3300
128	10	580
127	10	190
125	1	26
123	1	12.5
120	1	~5
118	1	
115	1	
110	1	
105	1	
75	1	
50	1	
25	1	
0	1	

method of hydrostatic weighings[24] utilizing water as the flotation fluid.

X-Ray Diffraction

The low-angle camera has already been described in detail.[25] It was designed with a slit-type collimating system, and in the absence of central scatter, it is capable of resolving diffraction maxima up to 800 A. Nickel-filtered Cu K_α radiation was utilized, and the specimen-to-film distance was 22.5 cm. Typical exposure times ranged from 36–48 hr. All x-ray diffraction patterns were taken at room temperature.

RESULTS

Isothermal Crystallization

Specific Volume

The specific volumes of the specimens at 25°C are plotted in Fig. 1 as a function of the crystallization temperature. It is apparent that, for a crystallization process carried out in the prescribed manner, the specific volumes attained are strongly dependent on the crystallization temperature. For crystallizations at temperatures below 100°C, the specific volumes vary from 1.06–1.04, within the range of values usually reported for this polymer.[26] However, as the crystallization temperature is further increased, a rather sharp decrease occurs in the specific volume achieved. The specific volumes are now much more sensitive to small variations in the crystallization temperature. For crystallization temperatures close to the melting temperature, much lower specific volumes are obtained than have been hitherto reported for this polymer. For example, after crystallization at 130° for 40 days, a specific volume of 1.0182 is observed. After isothermal crystallization at the same temperature for 130 days, the specific volume is 1.0175 while, after crystallization for 400 days at this temperature, the specific volume is further reduced to a value of 1.0155. Concomitant with the changes in the density of the specimens at room temperature, the level of crystallinity must also be varying. Estimates of the degree of crystallinity at 25°C, 1−λ, can be obtained by utilizing the simple relation

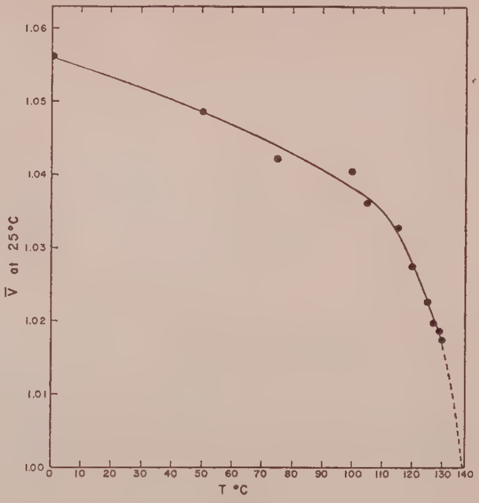

FIG. 1. Plot of specific volumes at 25°C for unfractionated linear polyethylene (Marlex 50) against temperature of crystallization. Times of crystallization for each temperature are given in Table I.

$$1-\lambda=(\bar{V}_a-\bar{V})/(\bar{V}_a-\bar{V}_c), \qquad (1)$$

where $\bar{V}_a$ and $\bar{V}_c$ are the specific volumes of the liquid and crystalline polymers, respectively. By taking $\bar{V}_a$ to be 1.174[27] and $\bar{V}_c$ to be 1.000,[28] the degree of crystallinity at 25°C is found to vary from 65–90%. The higher levels of crystallinity are observed only after crystallization at elevated temperatures for extremely long periods of time.

Low-Angle X-Ray Diffraction

Well-defined diffraction maxima are observed at low angles for all the specimens that were crystallized in the manner set forth above. The nature of the resulting patterns is very similar to that previously reported[29] for completely shrunken fibrous polyethylene. In contrast to the reflections observed for highly oriented specimens, which are restricted to the meridian, these patterns exhibit a circular-shaped maximum at low angles. This is indicative of a random arrangement of the diffracting elements and is consistent with the mode

---

[24] L. A. Wood, N. Bekkedahl, and F. L. Roth, J. Research Natl. Bur. Standards 29, 391 (1942).

[25] C. R. Worthington, J. Sci. Instr. 33, 66 (1956).

[26] F. A. Quinn, Jr., and L. Mandelkern, J. Am. Chem. Soc. 80, 3178 (1958).

[27] R. Chiang and P. J. Flory, J. Am. Chem. Soc. (to be published).

[28] C. W. Bunn, Trans. Faraday Soc. 35, 483 (1939).

[29] See Fig. 2(e) of reference 12.

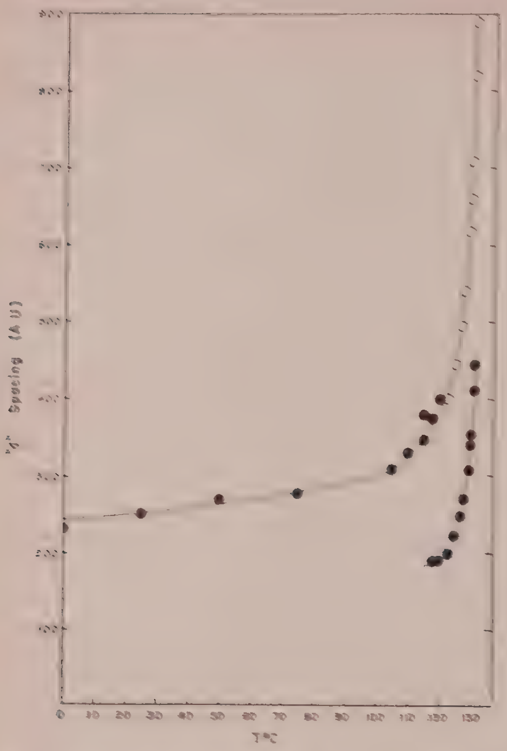

FIG. 2. Plot of low-angle diffraction spacings (in A) against temperature of crystallization for specimens of unfractionated linear polyethylene, Marlex 50, 1.0 mm thick. ● Diffraction maxima actually observed. ○ Calculated first-order reflections.

of crystallization since no restraints favoring crystallite orientation are imposed. This is confirmed by the wide-angle diffraction patterns from which it can be deduced that the crystallites are randomly arranged relative to one another. Besides the maxima that are developed, intense diffuse scattering off the central beam is also observed. This situation prevents the resolution of maxima greater than about 400–450 A by the photographic method employed.

As a matter of convenience, the spacings corresponding to the maxima are reported in Angstroms, as calculated from Bragg's Law. The results of the x-ray investigation for the isothermal crystallization of specimens 1.0 mm thick are summarized in Fig. 2, wherein the "*d*" spacings are plotted against the crystallization temperature. The solid circles represent the intensity maxima which are actually observed on the photographic film. For several of the crystallization temperatures, two orders of a well-defined maximum can be resolved, in agreement with the recent report by Sella.[3] The open circles represent the first-order reflections for those samples for which only the second order could be resolved. The justification for adopting this procedure will be discussed subsequently.

The most significant result of these diffraction experiments are the spacings observed and their very strong dependence on the crystallization temperature. For crystallization at temperatures below about 100°C the diffraction maxima correspond to spacings of about 250 A and are not very sensitive to the crystallization temperature. This is consistent with the oft quoted statement that polymers crystallized in the bulk possess long spacings in the vicinity of 100–200 A.[2,13,14] The fact that this point of view is of extremely limited validity is clearly discernible from Fig. 2. As the crystallization temperature is raised above 100°, a sharp increase in the magnitude of the spacings occurs, and values up to 850 A are observed. This value is obtained after isothermal crystallization at 131°C.

An experimental assessment of the influence of sample thickness was also undertaken by studying the diffraction patterns obtained from thinner specimens. For such specimens, the cooling rate from the melt to the thermostat temperature should be much greater and the heat of crystallization more easily dissipated. If these factors have an appreciable effect on the crystallization process, then the values of the diffraction maxima observed should be altered. The adoption of this procedure does have the disadvantage that when specimens thinner than 1.0 mm are employed individual samples must be packed together to provide the optimum thickness for diffraction of the radiation employed. The intensity maxima in the resulting diffraction pattern can be expected to be less clearly defined. Despite this anticipated difficulty, crystallization experiments were conducted following the same procedures, but utilizing film 0.1 and 0.5 mm thick, to test the aforementioned hypothesis.

The results given in Table II demonstrated that for the same crystallization temperature the thinner specimens yield significantly lower values of the diffraction maxima than their thicker counterparts. The effect of sample thickness can be related to the difficulties of attaining isothermal crystallization at large values of undercooling for a polymer whose crystallization rate is relatively rapid.

It is clear that in order to adequately discuss low-angle diffraction maxima, a detailed specification of

TABLE II. Comparison of first-order reflections at low angles for polyethylene specimens of varying thickness.

Crystallization temperature °C	"*d*" spacings 1.0 mm	0.5 mm	0.1 mm
0	230		150
105	306		238
110	330		256
115	345,380	277	257
118	375		277
120	380,400		270
[illegible]	400		[illegible]
[illegible]	[illegible]		[illegible]

TABLE III. Specific volume and low-angle diffraction maxima of samples initially crystallized at 0°C then annealed at indicated temperatures for specified time.[a]

	Time of annealing								Results of isothermal crystallization[c]	
	6 days		36 days		66 days		96 days			
T,[b] °C	$\bar{V}$	"d"	$\bar{V}$	"d"	$\bar{V}$	"d"	$\bar{V}$	"d"	$\bar{V}$	"d"
120	1.0308	322	1.0287	[illegible]	1.0274	[illegible]	1.0277	[illegible]	1.0276	[illegible]
125	1.0282	370, 182	1.0253	380, 180	1.0248	405, 180	1.0239	364, 173	1.0227	446, 223
130	1.0249	460, 198	1.0222	480, 220	1.0207	430, 215	1.0210	440, 206	1.0182	710, 355

[a] Initially $\bar{V}$ = 1.0562, "d" = 150 A. [b] Temperature of annealing. [c] Taken from data of Figs. 1 and 2.

crystallization conditions must be made. The variation of spacings with crystallization temperature accompanies the change in density observed. These two types of apparently diverse observations must be intimately connected with the crystallization mechanisms and their influence on the resulting morphology.

Nonisothermal Crystallization

In addition to the experiments in which the crystallization took place from the melt at a series of fixed temperatures, observations were also made on specimens crystallized at one temperature and then annealed at an elevated temperature for specified time periods. A systematic study was made on samples initially crystallized at 0°C, with the individual samples held at 120, 125, and 130°C, respectively. The specific volume and "d" spacings resulting from these experiments are given in Table III, together, for comparative purposes, with the results obtained after isothermal crystallization at the specified temperature.

At each temperature, both the specific volume and "d" spacings reach an almost constant value after 36 days. There is an initial large decrease of the specific volume (from that observed after crystallization at 0°C), and an asymptotic levelling off occurs with time. Concomitantly, the "d" spacings increase significantly after the initial annealing and then also approach an asymptotic limit. The final values of $\bar{V}$ and "d" achieved by the annealed specimens are characteristic of the annealing temperature, and these quantities assume higher values as the annealing temperature is increased. Comparison between the annealed specimens with those obtained after isothermal crystallization at the corresponding temperatures indicates that $\bar{V}$ and "d" are approaching the values characteristic of the isothermal crystallization. However, except for the specific volumes at 120°, the annealed specimens do not yield densities and "d" spacings as large as those obtained isothermally.

The spacings of 446 and 710 A given in Table III for the specimens isothermally crystallized at 125° and 130°C are those of the upper curve in Fig. 2. These are considered to be first-order reflections of the maxima that are actually resolved at 223 and 355 A, respectively. This conclusion is supported by a variety of observations. After isothermal crystallization in the vicinity of 120°, as is indicated in Fig. 2, two intensity maxima are actually observed which are numerically equivalent to first- and second-order reflections. The upper curve of Fig. 2 is smooth and continuous when it is assumed that above 123°C the observed reflections are second order. In addition, Sella[3] has reported that after the "slow crystallization" of a linear polyethylene from the melt, several orders of a prime spacing of 420 A are detected by his technique. From the crystallization rates indicated in the last column of Table I, his procedure would correspond to crystallization occurring in the range 120–125°C. His observations are therefore in agreement with the above interpretation. The data obtained in the present work after annealing also lead to the conclusion that at the higher crystallization temperatures first-order reflections are not observed. This difficulty occurs because of the intense diffuse scatter observed off the central beam at low angles, so that diffraction maxima greater than 400–450 A cannot be resolved by the photographic method utilized. Recognition of this fact allows for a consistent interpretation of the order of the observed diffraction maxima, an interpretation which is in agreement with the recent report of an 1100-A spacing being observed in linear polyethylene.[22]

DISCUSSION

Specific Volume Measurements

The equilibrium requirements for a crystalline homopolymer demand not only that high levels of crystallinity be developed but that it remain invariant with temperature, except in the melting range.[30] The data in Fig. 1 indicate that these conditions are not usually attained; the level of crystallinity observed is strongly dependent on the crystallization temperature. The equilibrium condition is approached only under the most stringent conditions which require crystallization from the melt at high temperatures for long periods of time. These procedures are rarely employed so that, if significance is to be placed on the level of crystallinity, careful specification of the mode of crystallization must be made. The demonstration of the wide range of densities that can be observed at 25°C for the same homopolymer makes the adoption of this procedure mandatory.

---

[30] P. J. Flory, J. Chem. Phys. 17, 223 (1949).

Because of the difficulty, previously discussed, in attaining isothermal crystallization conditions for specimens 1.0 mm thick, the specific volumes observed in the range 0–120° may not be characteristic of the thermostat temperature but of a higher temperature. However, at temperatures greater than 125° the crystallization rates are sufficiently retarded so that isothermal crystallization at the ambient temperature can be assumed to occur. It is in this temperature range that densities significantly higher than heretofore reported are observed. A one- or two-degree variation of the temperature in this range significantly alters the final density values. This strongly suggests that the level of crystallinity is controlled by nucleation processes, a conclusion which is in accord with the general mechanism proposed for the crystallization of polymer systems.

An extrapolation of the specific volume-crystallization temperature plot of Fig. 1, as indicated by the dashed curve, portends the strong possibility that at still higher crystallization temperatures the achievement of even lower densities can be anticipated. Experimental confirmation of this extrapolation would involve crystallization for intolerably long periods of time. For the hypothetical experiment of conducting the crystallization process, from the completely molten state, within a degree or two of the equilibrium melting temperature, the data of Fig. 1 indicate that a specific volume of about 1.00 would be observed. This corresponds to the density of the completely crystalline polymer as deduced by Bunn[28] from the x-ray determination of the crystal structure of polyethylene. It implies the formation of a nearly perfect macroscopic single crystal. This conclusion is in accord with the prediction of the statistical thermodynamic theory of the crystalline state in polymers.[30] It is further enhanced by the direct experimental evidence of the increased sharpness of the fusion process for polymers initially crystalized at elevated temperatures (low undercooling).[27,31] It can be concluded, therefore, that the specimens crystallized at the higher temperatures represent a significant advance in the approach to equilibrium conditions.

The results of the annealing experiments at the selected temperatures, after crystallization at 0°C, are in accord with previous dilatometric studies of the fusion process. It has been found for a variety of polymers[31] that when slowly heated, partial melting and recrystallization occurs. Thus, the less perfect crystallites formed at the lower temperatures preferentially melt, and more perfect stabler structures are formed. However, this type of annealing process does not yield the abundance of the more perfect crystallites, as indicated by the density, that are obtained by direct isothermal crystallization at temperatures close to the melting temperature. Consequently, the fusion curves of specimens initially crystallized in the vicinity of 130–131°C and then slowly cooled to room temperature are extremely sharp and do not display the phenomena of partial melting and recrystallization upon heating.[27]

Low-Angle Diffraction

A description of the texture and morphology of bulk-crystallized polymers must now be consistent with the first-order reflections reported and their marked dependence on temperature. Assertions have been made[2,13,14] that the spacings in such systems result from the regular, successive folding of polymer chains in the crystalline state. Thus, the morphology in bulk polymers has been identified with the platelet-type structure which is observed to form from dilute solution under certain conditions of crystallization. For the latter case, it has been presumed that completely pleated polymer chains comprise the single crystals formed. The lamellar structures observed by electron microscopy on fracture surfaces of polymers have been offered as supporting evidence of this thesis.[1,2,13,17,18] However, lamellar structures do not necessarily have to be equated with pleated chains. A consideration of the molecular-weight distribution[32,33] of the polymer studied here makes it extremely difficult to reconcile the level of crystallinity and the first-order reflections observed with the concept that the crystallites are composed of pleated chains. For example, for a spacing of 1000 A and the trivial case of only one fold per molecule, about 30–40% of the system by weight could not participate in the crystallization. For the same spacing, in order to participate in as little as five consecutive folds, a molecule must have a minimum molecular weight of at least 67 200. This requirement permits a weight fraction of only 0.35 to participate in the crystallization unless the highly improbable statistical situation[30] of chain ends meeting in juxtaposition within the crystallites occurs.

If one allows for imperfect matching of molecular ends in forming crystals of pleated chains, the defects developed should be more numerous for the larger spacings. In other words, the larger the spacing, the more imperfect the crystal must be. This conclusion is not compatible with the experimental fact that both the higher and the sharper melting temperatures are observed for crystals formed at lower degrees of undercooling. The sharpest melting reported to date for polyethylene is obtained after crystallization at 131.3°C. Thus, once the concept that diffraction maxima are limited to 100–200 A is removed, it is extremely difficult to conclude that in bulk systems crystallites are composed of pleated polymer chains. The above considerations do not preclude the possibility of backlooping or partial folding of an individual chain so that different crystalline sequences from the same molecule could occur in nonadjoining positions within a given crystallite.

---

[31] L. Mandelkern, Rubber Chem. and Technol. 32, 1392 (1959).

[32] L. H. Tung, J. Polymer Sci. 24, 333 (1957).

[33] H. S. Kaufman and E. K. Walsh, J. Polymer Sci. 26, 124 (1957).

The strong negative temperature dependence of the diffraction maxima is again suggestive that they are controlled, at least in part, by nucleation processes. Having rejected the possibility of polymer chains being in a pleated conformation in bulk-crystallized material, we consider the problem of the formation of crystallites from a bundle of polymer chains. In common with the similar process for monomeric substances, the crystallization of polymers involves a primary nucleation step and the subsequent growth of the stable nuclei thus formed.[21] Quantitative studies of the rate of growth of spherulites in bulk homopolymers show that this is also a nucleation-controlled process.[22,34–38]

The free energy change in homogeneously forming a primary nucleus of critical size, comprised of a bundle of polymer chains, can be written as [21,39,40]

$$\Delta F^* = 8\pi\sigma_u^2\sigma_e/\Delta F_u^2. \tag{2}$$

The number of chains comprising such a nucleus is

$$\rho^* = 4\pi(\sigma_u/\Delta F_u)^2, \tag{3}$$

while ζ^*, the number of chain-repeating units along the length of the nucleus, is

$$\zeta^* = 4\sigma_e/\Delta F_u. \tag{4}$$

In the foregoing expressions, ΔF_u represents the free energy of fusion per mole of repeating units, σ_u the lateral surface free energy per mole of unit, and σ_e the excess free energy resulting from the joining of the crystallite ends with the contiguous amorphous regions. If the usual approximation is made that $\Delta F_u = \Delta H_u \Delta T/T_m$, where ΔH_u is the enthalpy of fusion per mole of repeating units, T_m the equilibrium melting temperature, and ΔT, termed the undercooling, is the difference between the melting temperature and the crystallization temperature, then

$$\Delta F^* = 8\pi\sigma_u^2\sigma_e T_m^2/(\Delta H_u \Delta T)^2 \tag{2'}$$

$$\rho^* = 4\pi\sigma_u^2 T_m/(\Delta H_u \Delta T)^2 \tag{3'}$$

$$\zeta^* = 4\sigma_e T_m/\Delta H_u \Delta T. \tag{4'}$$

The dimensions of the critical-sized nucleus are strongly dependent on the crystallization temperature and increase as the undercooling is decreased. The rate of decrease of ζ^* and ρ^* with crystallization temperature depend, in this formulation, solely on the ratios of the quantities $(\sigma_e/\Delta H_u)$ and $(\sigma_u/\Delta H_u)$.[41]

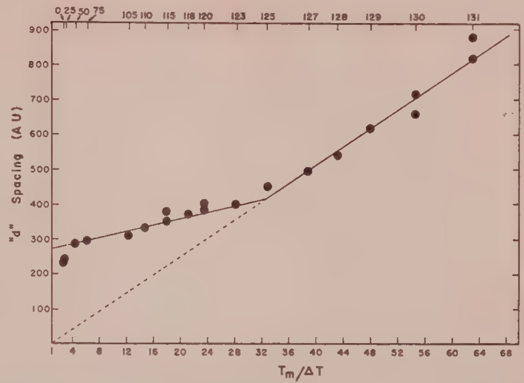

FIG. 3. Plot of low-angle diffraction maxima (in A) against temperature function $(T_m/\Delta T)$. Upper scale indicates crystallization temperatures in centigrade degrees.

The observation of the strong negative temperature dependence in the low-angle diffraction maxima suggests that they may arise from a characteristic dimension related to that of the critical-size nuclei. This suggestion as to the origin of the low-angle diffraction maxima in polymers has been previously offered by Flory and McIntyre.[34] Thus, if in at least one direction nuclei do not grow significantly beyond critical size, a well-developed periodicity in crystallite dimensions will evolve which will be very dependent on the crystallization temperature. In accordance with this hypothesis, the experimentally observed first-order "*d*" spacings for specimens 1.0 mm thick are plotted against the temperature variable $T_m/\Delta T$ in Fig. 3.

In this figure, the horizontal axis is nonlinear in temperature so that for convenience the crystallization temperatures are indicated. The higher temperatures of crystallization are disproportionately spread out in this plot, while temperatures corresponding to very large undercooling are restricted to a region in the vicinity of the origin. The lowest value that the function $(T_m/\Delta T)$ can assume is unity. When plotted in this manner, the data for the higher crystallization temperatures obey a linear relation, which extrapolates to very small "*d*" spacings at very large undercoolings. For crystallization conducted below about 125°C, however, significant deviations from this straight line occur. The data can still be represented by a straight line, but one of much reduced slope. In this region the diffraction maxima undergo only a relatively small change in magnitude over a wide temperature interval.

---

[34] P. J. Flory and A. D. McIntyre, J. Polymer Sci. **18**, 592 (1955).

[35] B. B. Burnet and W. F. McDevit, J. Appl. Phys. **28**, 1101 (1957).

[36] M. Takayanagi and T. Yamashita, J. Polymer Sci. **22**, 552 (1956); M. Takayanagi, Mem. Fac. Eng. Kyushu Univ. **16**, No. 3, 111 (1957).

[37] B. Kahle, Z. Electrochem. **61**, 1318 (1957).

[38] F. P. Price, Ann. N. Y. Acad. Sci. **83**, 20 (1959).

[39] L. Mandelkern, F. A. Quinn, Jr., and P. J. Flory, J. Appl. Phys. **25**, 830 (1954).

[40] L. Mandelkern, J. Appl. Phys. **26**, 443 (1955).

[41] The expressions for ΔF^*, ζ^*, and ρ^* in the foregoing have been calculated on the basis of a simplifying assumption that the free energy of forming a nucleus is independent of the level of crystallinity present in the system.[39,40] More specifically, in the case of a pure homopolymer, the influence of already present crystallites on the formation of new nuclei has been neglected, as have been any changes that might occur in the constitution of the molten phase as the transformation progresses. However, these necessary modifications of nucleation theory as applied to polymeric systems should leave unimpaired the temperature dependence of the dimensions of a critical-sized nucleus.

We consider first the data obtained at the higher range of temperatures and its linear representation. Since the times allowed for crystallization at each temperature were chosen so as to ensure that no significant further development of crystallinity would occur, the same considerations must also apply to the hypothetical data represented by the extrapolated portion of the straight line. On this basis, therefore, at very large undercoolings with a relatively high level of crystallinity being developed, the long spacings are predicted to be very small, falling in the range 0–50 A. This is a strong argument that the dimensions of the critical-sized nucleus control the relation between the spacings and morphology of samples crystallized at elevated temperatures. These dimensions are not only very sensitive to the crystallization temperature in the manner observed, but they are also expected to become exceedingly small in samples crystallized at large undercoolings.

The data in Fig. 3 indicate that the low-angle diffraction maxima for specimens crystallized at the lower temperatures apparently do not obey the same linear relations just discussed. Since these conditions represent very large departures from equilibrium, it is possible that the morphology and the arrangement of chains within the crystallite have now been altered and are not very sensitive to the crystallization temperature. As has been discussed previously, however, the distinct possibility exists that in this region the ambient temperature and the temperature at which the major portion of the crystallization occurs are not identical, the latter temperature being higher. This explanation is in qualitative accord with experiment, spacings being observed which are of greater magnitude than expected from the indicated temperature.

The results obtained with the thinner specimen, which are given in Table II, strongly support the latter possibility. The spacings fall on the dashed line of Fig. 3 for crystallization temperatures as low as 115°C. At still lower crystallization temperatures, though deviations from linearity occur, they are not as marked as with the thicker specimens. It is indicated, therefore, that if isothermal crystallization could be achieved, the straight line which extrapolates to the origin would represent the temperature dependence of the diffraction maxima over the complete range. Relatively small values of the spacings would then be expected for crystallization conducted at low temperatures.[42]

From these considerations it is postulated that at low undercooling the development of a nucleus significantly beyond critical size in at least one direction is severely restricted and that the periodicity observed arises from this cause. We further assume that growth along the chain direction or c axis of the crystal is that which is retarded, while the lateral development of crystallinity is essentially uninhibited. An analogous assumption yields an explanation of the dependence of the melting temperature of natural rubber, utilizing fast-heating rates, on the crystallization temperature.[43] If the spacings in this temperature interval are now identified with the length of a critical-size nucleus, then from Eq. (4′) the slope of the straight line is equal to $4\sigma_e/\Delta H_u$. The ratio of $(\sigma_e/\Delta H_u)$ is then found to be equal to 2.6. For ΔH_u equal to 960 cal per mole of units,[26] σ_e is equal to 2500 cal per mole of units. From the known dimensions of the unit cell[28] this latter quantity can also be expressed as 95 ergs/cm^2. This value of σ_e should be considered an upper limit since the simplifying assumption has been made that the crystallite length can be identified exactly with that of a critical-size nucleus.

The ratio $\sigma_e/\Delta H_u$ thus deduced appears to be exceptionally high and larger than previously anticipated.[39] Confirmatory evidence for the magnitude of this ratio is clearly required. This quantity is also involved in the detailed description of the equilibrium melting of copolymers.[44] This results from restrictions being imposed on the longitudinal development of crystallites because of compositional differences among the chain units. The restrictions in this instance are a consequence of equilibrium rather than kinetic considerations. According to Richardson and Flory,[45] an analysis of the fusion of ethylene/propylene copolymers according to previously developed theory[44] yields a value of $\sigma_e/\Delta H_u$ slightly greater than four. Though the reason for the different values obtained by the two methods must eventually be resolved, this matter is of secondary importance for present purposes. The significant deduction, however, is the fact that it is now necessary to assign a relatively large value to the quantity σ_e. From the point of view of nucleation theory, this quantity can be formally treated as a surface free-energy characteristic of the surface bounding the crystallite ends. However, since the change in order between the crystallite and the pure melt cannot occur over the interval of one unit, it actually represents the sum of excess free energies for the sequence of units of a given chain which traverse the region of perfect crystallinity to that of complete liquid disorder. A high value of σ_e could then result if the intermediate region was one of high enthalpy and low entropy. The acceptance of the deduced value of the ratio $\sigma_e/\Delta H_u$ then allows for a simple interpretation of the origin of the low-angle diffraction maxima in samples prepared at the higher crystallization temperatures.

---

[42] In the foregoing discussion of the origin of the diffraction maxima, the periodicity has been assumed to arise solely from the crystalline regions, the contribution of the linear dimension encompassed by the amorphous regions being neglected. When the level of crystallinity is about 90%, at the low undercoolings this effect will be small. When the crystallinity is reduced to about 70%, as is indicated by the lower densities observed at the lower crystallization temperatures, the dimensions of the crystalline regions under consideration will be somewhat reduced from the observed "d" spacing.

[43] L. Mandelkern, J. Polymer Sci. **47**, 494 (1960).

[44] P. J. Flory, Trans. Faraday Soc. **51**, 848 (1955).

[45] M. Richardson and P. J. Flory (private communication).

At large values of undercooling, the temperature function $T_m/\Delta T$ is essentially independent of the melting temperature and hence would assume the same value for different polymers. If wide divergences in the ratio of $\sigma_e/\Delta H_u$ do not exist among the different polymers, then spacings of the order of 100 A or less would be universally expected for crystallizations conducted at the large undercoolings. The results of Eppe *et al.*[1] for a polyurethane sample crystallized from the glassy state at temperatures well removed from the melting temperature, confirm this expectation, since diffraction maxima ranging between 50 and 150 A have been observed. It is possible that the misconception that diffraction maxima in polymers are limited to this range is a result of the widespread study of specimens crystallized under conditions far removed from equilibrium.

In harmony with the density observations, specimens annealed at temperatures above the crystallization temperature display increases in the diffraction maxima when held at these temperatures for periods of days. A slow recrystallization process is evidenced, with the values of the maxima approaching, but not reaching, those obtained when crystallized from the melt isothermally. Insofar as the density and low-angle diffraction maxima can be utilized in describing the perfection and extent of the crystallinity developed, it can be concluded that a more perfect state is obtained by isothermal crystallization at low undercooling, in contrast even to very slow annealing processes at elevated temperatures subsequent to low-temperature crystallization. This conclusion is supported by a comparison of the sharpness of the fusion curves of specimens prepared by both procedures.[27,31]

Statton and Geil have reported[46] that if after crystallizing polyethylene from dilute solution, the crystals formed are separated from the mother liquor and heated in the vicinity of 125–130°, the characteristic spacing of 100 A is increased to 300–400 A. Strong evidence has been given that the melting temperature of crystals prepared from dilute solution is much less than that of bulk-crystallized polymer.[47] Therefore, in the above experiments the temperature range of interest is such that melting or partial melting must occur, followed by recrystallization, the recrystallization process now occurring from the pure polymer melt. The low-angle diffraction maxima should now display characteristics typical of the latter process. Based on the experimental observations reported in this paper, the magnitude of the spacings reported by Statton and Geil is in accord with this concept. Their results can then be interpreted as a change of the conformation of the chains within the crystallite as a result of the heat treatment, with the morphology characteristic of crystallization from pure polymer being approached.

CONCLUSION

The observation of well-defined periodicities, which range from several hundred to a thousand Angstroms, depending on the crystallization conditions, can receive explanation from consideration of the role played by nucleation processes during the liquid-to-crystal transformation. The morphology deduced at this level of organization is thus consistent with conclusions in regard to mechanisms of crystallization derived from studies of the kinetics of the process, wherein in bulk systems stable nuclei comprised of bundles of polymer segments are formed. This interpretation requires the assignment of relatively large values of the ratio $\sigma_e/\Delta H_u$, a fact which receives support from studies of the equilibrium fusion of copolymers. If, for example, $\sigma_e/\Delta H_u$ is equal to 2.5 for polyethylene, then for crystallization at 100° ($\Delta T=37.5$) there will be required 110 methylene units to form the length of a critical-size nucleus. If the undercooling is lowered to $\Delta T=7.5°$, then 550 chain units will be required. The required selection from a polymer chain of such large numbers of consecutive units in order to form a critical-size nucleus will result, if the process is random, in the isolation of sequences of crystallizable units which cannot participate in the nucleation act. As the transformation progresses, this must result in a retardation of the crystallization rate and a deterrent to achieving the high levels of crystallinity required by equilibrium considerations. These latter factors are common experimental observations in studies of crystallization kinetics from the melt[21] and can thus be given qualitative explanation.

ACKNOWLEDGMENT

The authors wish to acknowledge very helpful discussions with Dr. P. J. Flory in regard to the basis for the high values of $\sigma_e/\Delta H_u$, and to thank him for making available before publication the low-angle diffraction results and copolymer melting studies obtained by him and his collaborators.

---

[46] W. O. Statton and P. Geil, J. Appl. Polymer Sci. 3, 357 (1960).

[47] R. Chiang and P. J. Flory, Abstract of paper presented before Division of Polymer Chemistry, 138th Meeting of the American Chemical Society, New York, September, 1960.

JOURNAL OF APPLIED PHYSICS VOLUME 32, NUMBER 8 AUGUST, 1961

An Approximate Solution of Fick's Diffusion Equation

T. Tsang
Solid State Science Division, Argonne National Laboratory, Argonne, Illinois

(Received January 30, 1961)

An approximate method of solving Fick's diffusion equation (or the heat conduction equation) with variable diffusion coefficients is discussed. Simple solutions may be obtained. In one example, the result appears to be in good agreement with the more elaborate numerical calculations by Crank.

ANALYTICAL solutions of equations for transient-state heat conduction in solids and for diffusion (in systems where Fick's law of diffusion is obeyed) are well known when the thermal conductivities, volume heat capacities, and diffusion coefficients are constant. The situation is, however, extremely complicated in the case of variable properties (for example, concentration-dependent diffusion coefficients). A number of solutions have been recently reviewed by Crank.[1] The advantages of analytical solutions over numerical and computer solutions appear to be dubious; unfortunately, the latter, although preferrable in many cases, often cannot be readily interpreted.

A new approximate solution of these nonlinear equations will be given here. The discussion will be limited to the simple case of a one-dimensional diffusion problem with Dirichlet-type boundary conditions. Generalizations to other types of boundaries (for example, cylinders and spheres) and to heat conduction problems are, however, straightforward and involve little difficulty. Methods of generalization have been previously discussed.[2]

Let us consider a slab of thickness L and infinite area, with initial uniform solute concentration C_1 and in perfect contact with an environment with solute concentration C_0. The diffusion coefficient D in the slab is assumed to be concentration dependent. The concentration is then given by:

$$\frac{\partial C}{\partial \tau}=\frac{\partial}{\partial x}\left(D\frac{\partial C}{\partial x}\right), \tag{1}$$

where x and τ are distance and time variables. Defining $D(C_0)=D_0$, and introducing dimensionless variables $t=D_0L^{-2}\pi^2\tau$, $z=\pi x/L$, $\phi=(C-C_0)/(C_1-C_0)$, and $\alpha=D/D_0$, then (1) may be written as

$$\frac{\partial \phi}{\partial t}=\frac{\partial}{\partial z}\left(\alpha\frac{\partial \phi}{\partial z}\right). \tag{2}$$

The initial and boundary conditions are

$$\text{At } t=0: \qquad \phi=1, \tag{3}$$

$$\text{At } t=\infty: \qquad \phi=0, \tag{4}$$

$$\text{At } z=0 \text{ and } \pi: \quad \phi=0. \tag{5}$$

The set of functions $(2/\pi)^{\frac{1}{2}}\sin nz$ satisfies (5) and is complete and orthonormal in the interval $0\leqq z\leqq\pi$:

$$(2/\pi)\int_0^\pi \sin nz\,\sin kz dz=\delta_{nk}. \tag{6}$$

Therefore, the function $\phi(t,z)$ may be expanded as follows:

$$\phi(t,z)=\sum_{n=1}^{\infty} f_n(t)(2/\pi)^{\frac{1}{2}}\sin nz. \tag{7}$$

The f_n's are functions of t only. Such an expansion is always possible; a general proof of this has been given.[3] Symmetry requires that all even n terms drop out. Substitution of (7) into (2) gives

$$\sum_{n=1,3,5\cdots}^{\infty} (2/\pi)^{\frac{1}{2}}[(df_n/dt)\sin nz+n^2\alpha f_n\sin nz \\ -n(\partial\alpha/\partial z)f_n\cos nz]=0. \tag{8}$$

Using the orthonormal property, multiplication of (8) by $(2/\pi)^{\frac{1}{2}}\sin kz$ and integration from $z=0$ to π gives

$$[df_k(t)/dt]=\sum_{n=1,3,5\cdots}^{\infty}[\alpha_{kn}(t)+\beta_{kn}(t)]f_n(t), \tag{9}$$

where

$$\alpha_{kn}(t)=(-2n^2/\pi)\int_0^\pi \alpha\sin kz\,\sin nz dz, \tag{10}$$

$$\beta_{kn}(t)=(2n/\pi)\int_0^\pi (\partial\alpha/\partial z)\sin kz\,\cos nz dz. \tag{11}$$

On using (3), the initial conditions are

$$f_k(0)=(8/\pi k^2)^{\frac{1}{2}} \quad \text{for} \quad k=1,3,5,\cdots. \tag{12}$$

Equation (9) with $k=1, 3, 5, \cdots$ may be regarded as an infinite matrix equation and cannot be readily solved. All the matrix elements are time dependent. However, if α varies slowly with z, then it can be shown that all f_n terms for $n>k$ in (9) may be neglected without introducing serious errors. Thus, (9) may be approximated by

$$[df_k(t)/dt]=\sum_{n=1,3,\cdots,k}[\alpha_{kn}(t)+\beta_{kn}(t)]f_n(t). \tag{13}$$

---

[1] J. Crank, *Mathematics of Diffusion* (Oxford University Press, New York, 1956), Chaps. 9 and 12.

[2] T. Tsang, Ind. Eng. Chem. **52**, 707 (1960).

[3] P. O. Lowdin, Advances in Chem. Phys. **2**, 260 (1959).

In order for (13) to hold, we must show that the effect of neglecting $n>k$ terms is indeed small. The proof can be easily carried out for a special example using an order of magnitude argument. Let us consider the interaction between f_1 and f_N where $N\gg 1$. (That is, the effect of the nondiagonal elements α_{1N}, α_{N1}, β_{1N}, β_{N1} on the functions f_1 and f_N will be studied.) α may be Fourier analyzed to give

$$\begin{gathered}\alpha=\alpha^{(0)}(t)+\alpha^{(1)}(t)\sin z+\cdots,\\ \alpha^{(0)}(t)=0(1),\quad \alpha^{(1)}(t)=0(1).\end{gathered}\tag{14}$$

To study the typical behavior, inclusion of the first two terms in (14) will suffice. Consider the case $k=N$. On performing the integration, (9) can be written as (only $n=1$ and N terms are included)

$$[df_N(t)/dt]=-0(N^2)f_N(t)-0(N^{-1})f_1(t).\tag{15}$$

Notice that the first term on the right side of (15) comes from both $\alpha^{(0)}$ and $\alpha^{(1)}$. If the nondiagonal terms are neglected, then from (9), by setting $k=1$, we get

$$f_1(t)=0(1)e^{-t}.\tag{16}$$

On using (12) and (16), the solution of (15) is

$$f_N(t)=0(N^{-1})\exp[-0(N^2)t]-0(N^{-3})f_1.\tag{17}$$

Therefore, for $k=1$, (9) can be written as (including $k=1$ and N terms only)

$$\begin{aligned}df_1/dt=(\alpha_{11}+\beta_{11})f_1+0(N^{-2})f_1&\\ +0(1)\exp[-0(N^2)t].&\end{aligned}\tag{18}$$

The correction to f_1 caused by the nondiagonal interaction between 1 and N is clearly small. A more general proof including all terms is exactly analogous except for more complicated notations. Hence, (13) is indeed a good approximation.

A further simplification may be made by replacing f_k's for $k\neq 1$ by $f_k(0)\exp[-k^2t]$ without introducing serious errors since the higher harmonics quickly become unimportant compared to the fundamental harmonic as t increases. Also, $f_k(0)\exp[-k^2t]$ and $f_k(t)$ are identical at $t=0$ and have the same asymptotic behavior as t approaches infinity.

As an example, let us consider the case where D is a linear function of C. Then α may be written as

$$\alpha=1+\lambda\phi=1+(2/\pi)^{\frac{1}{2}}\lambda f_1(t)\sin z+\cdots.\tag{19}$$

By replacing α in (10) and (11) by the first two terms on the right side of (19), (13) (for $k=1$) may be written as

$$\begin{aligned}df_1/dt&=f_1\biggl[-1+\lambda f_1(8/\pi^3)^{\frac{1}{2}}\\ &\qquad\times\biggl(\int_0^\pi\cos^2z\sin z\,dz-\int_0^\pi\sin^3z\,dz\biggr)\biggr]\\ &=-f_1[1+(4\lambda/3\pi)(2/\pi)^{\frac{1}{2}}f_1].\end{aligned}\tag{20}$$

TABLE I. ϕ_{av} as a function of $2t^{\frac{1}{2}}\pi$ and λ, from (24) and Crank.[4]

			ϕ_{av}					
			$\lambda=2.5$		$\lambda=4.8$		$\lambda=10.0$	
$2t^{\frac{1}{2}}\pi$	t	$\lambda=0$	(24)	Crank	(24)	Crank	(24)	Crank
0.1	0.0247	0.886	0.860	0.846	0.838	0.815	0.792	0.763
0.2	0.0987	0.774	0.691	0.692	0.629	0.629	0.531	0.538
0.3	0.222	0.660	0.523	0.542	0.439	0.475	0.324	0.340
0.4	0.395	0.548	0.381	0.408	0.310	0.351	0.200	0.217
0.5	0.617	0.435	0.267	0.287	0.206	0.242	0.123	0.138
0.6	0.888	0.332	0.184	0.202	0.133	0.160	0.078	0.084
0.8	1.579	0.165	0.079	0.087	0.053	0.063	0.030	0.031

By using (12), (20) may be integrated to give

$$f_1(t)=\left(\frac{8}{\pi}\right)^{\frac{1}{2}}\frac{3\pi^2e^{-t}}{3\pi^2+16\lambda-16\lambda e^{-t}}.\tag{21}$$

Define $\phi^{(0)}$ as the solution of (2) with $\alpha\equiv 1$ which satisfies (3), (4), and (5):

$$\phi^{(0)}(t,z)=\sum_{n=1,3,5\cdots}^{\infty}\frac{4}{n\pi}\exp[-n^2t]\sin nz.\tag{22}$$

Then ϕ may be written as

$$\phi=\phi^{(0)}-\left(\frac{64\lambda}{\pi}\right)\frac{e^{-t}-e^{-2t}}{3\pi^2+16\lambda-16\lambda e^{-t}}\sin z.\tag{23}$$

The average values of ϕ over distance ($\phi_{\mathrm{av}}=\int_0^\pi\phi dz/\pi$) have been evaluated by Crank[4] using numerical methods as a function of t and λ. This corresponds to the weight loss during desorption from an infinite slab, the diffusion coefficient varying linearly with respect to concentration. From (23), we have

$$\phi_{\mathrm{av}}=\phi_{\mathrm{av}}{}^{(0)}-\left(\frac{128\lambda}{\pi^2}\right)\frac{e^{-t}-e^{-2t}}{3\pi^2+16\lambda-16\lambda e^{-t}},\tag{24}$$

where

$$\phi_{\mathrm{av}}{}^{(0)}=\frac{8}{\pi^2}\sum_{n=1,3,5\cdots}^{\infty}\frac{1}{n^2}\exp[-n^2t].\tag{25}$$

ϕ_{av} from Crank by numerical methods and from (24) are compared in Table I. The agreement may be regarded as quite satisfactory considering the crudeness of the approximations made in arriving at (24).

In a previous publication,[2] the diffusion equation was solved by a time-dependent perturbation method. If the method was applied to our example above, and only the first correction term is kept, then the solution is

$$\phi=\phi^{(0)}-\frac{64\lambda}{\pi(3\pi^2+16\lambda)}(e^{-t}-e^{-2t})\sin z.\tag{26}$$

When λ is small, (23) and (26) give essentially identical results. By comparison with Crank's numerical results on desorption weight losses, however, it can be shown that (26) fails when λ is much above unity.

---

[4] J. Crank, *Mathematics of Diffusion* (Oxford University Press, New York, 1956), p. 278, Fig. 12. 16.

The results of this paper and a previous publication[2] indicate that certain approximate methods may be used to solve the transient-state heat conduction and diffusion equation with variable coefficients, and the simple solutions thus obtained are in quite satisfactory agreement with the more elaborate calculations. The results are, however, only preliminary, and further investigations seem to be worthwhile. Some of the conclusions reached in this paper (for example, the higher harmonics decay very rapidly with time as compared to the fundamental harmonic) should be studied more carefully.

It is a pleasure to thank Dr. Donald E. O'Reilly of the Argonne National Laboratory for several very interesting discussions.

JOURNAL OF APPLIED PHYSICS VOLUME 32, NUMBER 8 AUGUST, 1961

Etch Pits in Electroluminescent Zinc Sulfide Crystallites*

Paul Goldberg
General Telephone and Electronics Laboratories, Inc., Bayside, New York

(Received February 23, 1961)

Through suitable etching techniques, triangular etch pits are developed on the surfaces of electroluminescent ZnS:Cu,Cl powder crystallites at densities in the range 10^6–10^8/cm^2. These pits, seen by means of the electron microscope, are essentially absent in similarly etched nonelectroluminescent ZnS:Cu,Cl crystallites. Also present on the electroluminescent particles are surface striations. The etch pits appear physically related to the striations in that the pits form only on those faces bearing the striations. All triangular pits on a given face point in the same direction, which is normal to the striation direction. This direction is one of the crystallographic polar axes in sphalerite and the *c* axis in wurtzite. The pits have also been found in other electroluminescent compositions such as ZnS:Cu,Al; ZnS:Cu,Cl-Pb; and ZnS:Cu,Cl-Mn. The possible interpretations of the pits and striations are discussed in terms of defect structures (e.g., dislocations and stacking faults) which may be of importance to the nature of the barriers believed to reside within the volume of electroluminescent particles. Some experiments with large crystal specimens are reported.

INTRODUCTION

THE barrier theory is successful in providing a basis for understanding several of the important characteristics of electroluminesence in zinc sulfide. Among them are the highly localized emission of light within an emitting crystal and the ability of luminescent centers to be excited at a field strength well below that of electrical breakdown of the lattice.[1,2] In spite of this success the detailed nature of the barrier itself has remained an elusive problem. The proposed concept of the barrier as a conductive surface phase of the activator does not appear satisfactory.[3] We may expect that progress will be made in understanding the nature of the barrier and the mechanism of electroluminescence when chemical or physical differences can be demonstrated in electroluminescent phosphors which are absent in nonelectroluminescent ones. Recent chemical studies have specified the ranges of activator and coactivator compositions in which electroluminescence can appear in copper-activated ZnS.[4] It has not been possible thus far, however, to reveal any significant chemical differences between electroluminescent and nonelectroluminescent forms.

The present report describes a characteristic which appears to differentiate electroluminescent copper-activated zinc sulfide phosphors from their nonelectroluminescent counterparts. This characteristic is a lattice defect which exists primarily in the electroluminescent powders and whose presence is revealed by the formation of etch pits on the crystallite surfaces. In the following sections, detailed descriptions will be given of the conditions under which the pits occur, their relation to the sulfide lattice, and their possible significance for the mechanism of electroluminescence.

Surface striations are another feature which distinguishes electroluminescent from nonelectroluminescent phosphors.[3] The relationship of the pits and striations will be discussed.

MATERIALS AND EXPERIMENTAL TECHNIQUES

The phosphors employed were mainly of the ZnS:Cu, Cl type with Cu activator concentrations in the range 0.03–0.08% by weight. They were made according to the method described by Solomon and Goldberg.[4] This method is particularly suitable for the present work in that the electroluminescent phosphors are synthesized from previously crystallized nonelectroluminescent powders without further particle growth and with little or no detectable change in activator content. This provides substances for experiment which are similar in gross chemical composition and particle size but yet possess levels of electroluminescence which are orders of magnitude apart. Both hexagonal and cubic structures may be obtained in this way.

---

* Presented at the Meeting on Color Centers and Crystal Luminescence, Turin, Italy, September 8–12, 1960.

[1] D. Curie, J. phys. radium **13**, 317 (1952).

[2] W. W. Piper and F. E. Williams, Phys. Rev. **87**, 151 (1952).

[3] P. Goldberg and S. Faria, J. Electrochem. Soc. **107**, 521 (1960).

[4] A. L. Solomon and P. Goldberg, Abstr. Electrochem. Soc. Electronics Div. **9**, 105 (1960).

The powders were etched with aqueous hydrogen peroxide solutions both before and after the thermal treatment which rendered them electroluminescent. The pits were readily developed with H_2O_2 solutions at concentrations of 7.5% to 30%. Etching times were 10 min, to 1 hr at temperatures in the range 60°–80°C. After etching, the powders were thoroughly washed with KCN solution, water, acetic acid, and water again and dried at 100°C. Electron micrographs were taken of at least 10 particles in each sample. Direct carbon replicas with platinum metal preshadowing were employed. Although etch patterns varied from particle to particle, the etch characteristics were reasonably consistent within a group of photographs representing a single specimen. In a few cases etch pit densities were counted.

The etching proceeded by two reactions:

$$ZnS+4H_2O_2 \rightarrow ZnSO_4+4H_2O,$$
$$ZnS+H_2O_2 \rightarrow ZnO+S+H_2O.$$

Both sulfate and ZnO were found after etching, the former by precipitation with Ba^{++} and the latter by the observation of hexagonal rodlets in the micrographs of unwashed powders.

While the following discussion applies in detail to ZnS:Cu, Cl, phosphors, the same general characteristics have also been found in these material types: ZnS:Cu, Al,[5] ZnS:Cu, Cl-Pb,[6] and ZnS:Cu, Cl-Mn.

DESCRIPTION OF ETCHED SURFACES

Figure 1 shows the surface of a representative particle etched with 15% H_2O_2 solution for 10 min at 60°–80°C. This particle is from an electroluminescent sample showing mainly cubic structure by powder x-ray methods. The triangular etch pits and the surface striations[7] are the most prominent features. The pits are found only on faces which bear surface striations. All the pits on a given face are commonly oriented and point normal to the striations. This directional property indicates that the individual particles are largely single crystals.

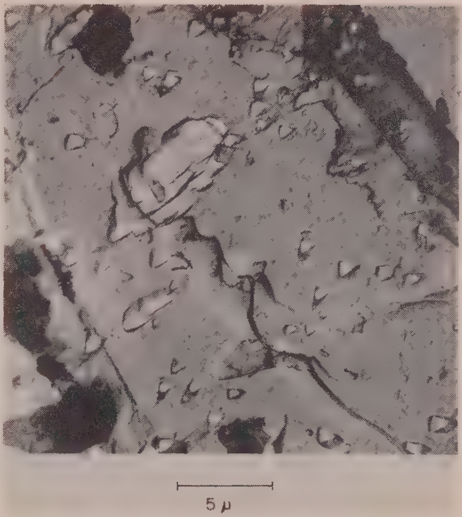

FIG. 1. Representative particle from a cubic electroluminescent phosphor. Etched with 15% H_2O_2, 10 min. Triangular pits are uniformly oriented perpendicular to striations.

Figure 2 shows the surface of an etched particle selected from an hexagonal electroluminescent powder. Here again the striations and the directional properties of the pits relative to the striations are evident. In this photograph a sequence of eight pits can be seen which lies parallel to the striation direction.[8] This direction is indicated by the line drawn in the figure. A physical relation between the striations and the defects associated with the pits is suggested by the parallelism of the line of pits and the striation direction.

In both Figs. 1 and 2, pits and striations occur at rather high densities. It has been found that in some phosphors of weak electroluminescent intensity, the pits and striations develop to a lesser extent. Figure 3 shows a specimen selected from such a powder, with hexagonal structure. Figure 3 is further evidence in favor of the

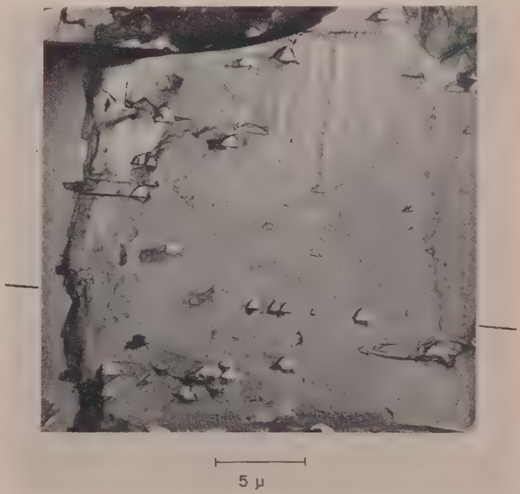

FIG. 2. Particle selected from hexagonal electroluminescent phosphor showing row of pits colinear with striation direction (heavy line). Etched with 30% H_2O_2, 1 hr. The nearly vertical striations in the upper part of the figure are probably cleavage markings.

---

[5] H. Froelich, J. Electrochem. Soc. **100**, 496 (1953).

[6] H. H. Homer, R. W. Rulon, and K. H. Butler, J. Electrochem. Soc. **100**, 566 (1953).

[7] The striations can be seen without etching.

[8] *Note added in proof.* Two of the eight pits are too small to be easily seen in Fig. 2.

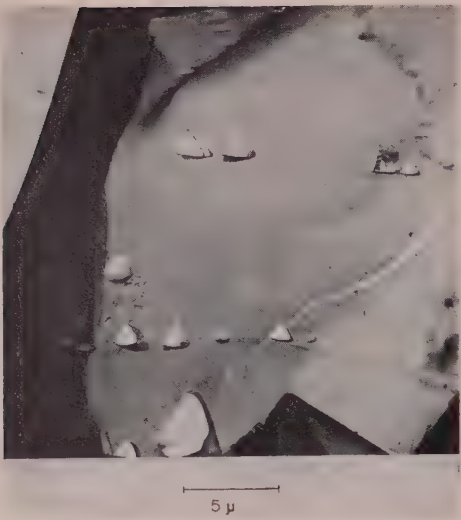

Fig. 3. Particle selected from weakly electroluminescent hexagonal powder. Pits and striations are located in the same narrowly defined areas. Etched with 30% H_2O_2, 15 min.

physical relation of pits and striations in that they both occur only in the same narrowly defined regions. Figure 4 shows in detail some particularly well formed pits at higher magnification for a particle also selected from a weakly electroluminescent powder.

Other characteristics which appear occasionally in the electroluminescent crystallites can be seen in Fig. 1. Among these are (a) pencil-like grooves which do not follow any obvious low-index planes and (b) elongated craters running parallel to the striation direction which appear to be composites of many pits.

Figure 5 shows a representative particle selected from a nonelectroluminescent phosphor of similar chemical composition and etching history to that of Fig. 2. Very few striated or pitted particles are found in this class of material. This point will be discussed quantitatively in a later section.

CRYSTALLOGRAPHIC ASPECTS OF ETCH CHARACTERISTICS

The sphalerite and wurtzite lattices possess, as a consequence of their crystal classes, uni-terminal symmetry axes. In the particular case of ZnS, stacking faults can occur and these have been shown to lie with the plane of the fault perpendicular to the polar symmetry axes; i.e., the c axis in wurtzite and one of the $\langle 111\rangle$ axes in sphalerite.[9] The surface striations in Figs. 1–4 are probably to be identified as stacking faults for the following reasons: As previously mentioned, the surface striations appear in electroluminescent phosphors but not in the nonelectroluminescent ones. In the same phosphor specimens, x-ray data indicate that stacking faults are present in the electroluminescent ones and are not detectable in nonelectroluminescent ones.[10] Also, striation densities, as determined directly from electron micrographs of electroluminescent phosphors, are consistent with stacking fault densities as determined from x-ray studies in the same specimens.[10] By both techniques the fraction of faulted planes is the order of 1%.

From the discussion in the preceding section it may be said that a physical relation exists between the stacking faults and the defects associated with the pits. Also, this defect appears physically governed by the polar axis because (a) the pits occur together with, and are related to, the stacking faults which lie normal to the polar axis, and (b) the pits possess a collective uni-terminal orientation such that one apex always points parallel to the polar axis.

No x-ray data are available for indexing the faces bearing the pits. It is possible, though, that they lie on the cleavage faces which are of the (110) and $(\bar{1}2\bar{1}0)$ types for the cubic and hexagonal forms, respectively.

PHOSPHOR HISTORY AND ETCH PIT FORMATION

It must be emphasized that no measurement of electroluminescence performance and etching characteristics have as yet been made on one and the same phosphor particle. The connection between the ability of the phospher to develop pits and the ability to electroluminesce can, however, be seen in the following experiment. A nonelectroluminescent hexagonal phosphor containing 0.012% Cu showed no detectable etch pit formation after etching with peroxide solution (i.e., the pit density was less than $10^5/\text{cm}^2$). Another portion of

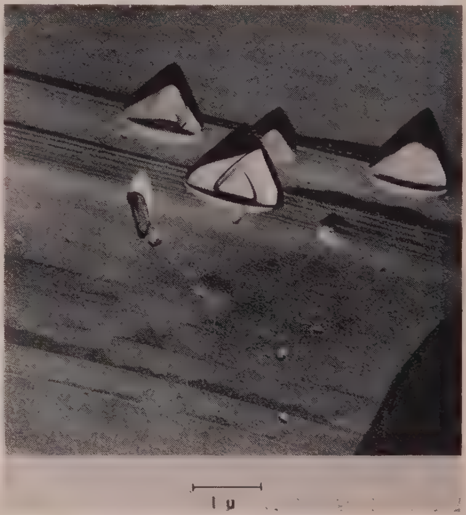

Fig. 4. Detail at high magnification of pits and striations. Particle is from weakly electroluminescent hexagonal powder. Etched with 30% H_2O_2, 15 min.

---

[9] W. J. Merz in *Solid State Physics in Electronics and Telecommunications, Brussels Conference* (Academic Press, Inc., New York, 1960), Vol. 2, Part 2, p. 811.

[10] V. Brophy, J. Singer, and P. Goldberg (unpublished).

this nonelectroluminescent material was blended in a SPEX Industries Mixer/Mill with additional Cu activator (10 g of sample in 2-oz. glass jar with two plastic, 5-mm balls). It was then annealed at 700°C and developed strong blue electroluminescence. After etching this material showed significant pitting at densities falling in the range of 10^7 to $10^8/\mathrm{cm}^2$. A sample of the original nonelectroluminescent phosphor was mechanically and thermally treated as above, but with *no* additional Cu activator. No electroluminescence developed and no pits were detected following etching. This phospher did, however, show striations (stacking faults) undoubtedly introduced by the mechanical and thermal treatment.

The significance of the above experiment is that it shows the pits are a measure of the electroluminescence capability of the crystallites, and not of any mechanical deformation in the phosphor history.

Etch pit densities depend somewhat on phosphor history; most materials exhibit values in the range 10^6–$10^8/\mathrm{cm}^2$.

ETCHING EXPERIMENTS WITH LARGE CRYSTAL SPECIMENS

Etch pits much like those in powder particles have been found in larger synthetic crystals and natural sphalerite. Figure 6 shows a cleaved specimen of natural sphalerite etched with hot 30% H_2O_2 solution for about 1 hr. Distinct arrays of triangular pits may be seen which trace out the striation lines. The directional properties of the pits are the same as found in the powder samples. Actually, a two-dimensional ordering of pits is seen in Fig. 6, one along the striations and the other at an angle to the striations. This angle was measured as 71° 58′, which is close to the octahedral angle of 70° 32′ between, for example, (111) and $(\bar{1}\bar{1}1)$ planes intersecting the $(0\bar{1}1)$ face in an fcc lattice.

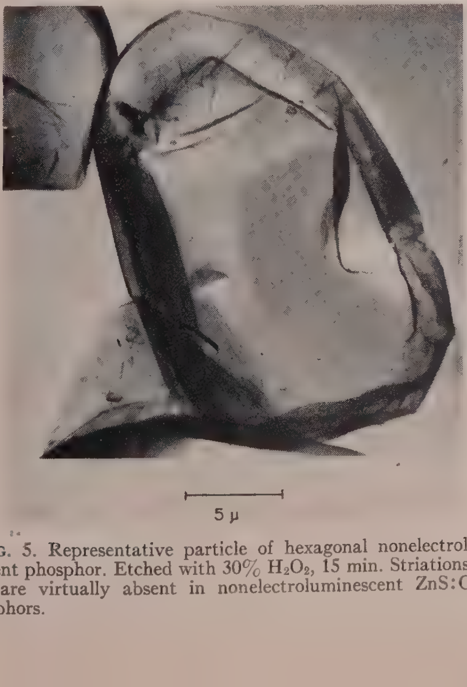

FIG. 5. Representative particle of hexagonal nonelectroluminescent phosphor. Etched with 30% H_2O_2, 15 min. Striations and pits are virtually absent in nonelectroluminescent ZnS:Cu,Cl phosphors.

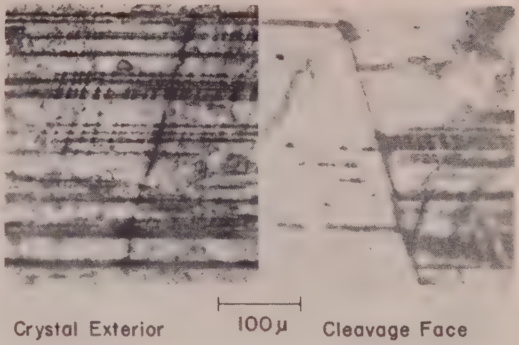

FIG. 6. Natural sphalerite viewed on opposite faces of cleaved fragment after etching with hot 30% H_2O_2, about 1 hr. The two parts of this figure are *not* from corresponding points on the opposite sides of the fragment.

The appearance in natural sphalerite of etch pits bearing a strong resemblance to those in electroluminescent crystallites does not in itself diminish the pertinence of the pits and their associated defects to electroluminescence. It does mean, however, that the presence of such defects may be a necessary but not a sufficient requirement for electroluminescence to occur.

The natural sphalerite crystals are useful for establishing the reproducibility of the etchant for pit development and for elucidation of the nature of the defects associated with the pits. For example, a crystal may be cleaved and etched on the matching cleavage faces. If arrays of pits on the matching faces are mirror images of each other, then the reproducibility of the etchant is established. Furthermore, this mirror symmetry would be strong evidence for interpretation of the etch pits as the emergence points of dislocations.[11] Figures 7(a) and (b) show optical micrographs of the patterns which were developed on the matching surfaces of freshly cleaved natural spalerite after etching with 30% H_2O_2 for 1 hr at 70°–80°C. The mirror symmetry is easily seen, and provides support for a dislocation model for the pit-forming defects. Further evidence of dislocation character is found in Fig. 7(b). A row of pits can be seen, each one of which is associated with a dark streak running to the right penetrating into the body of the crystal. This feature suggests decorated dislocations.[12]

DISCUSSION

The etch pits found in the electroluminescent phosphor grains are suggestive of certain types of defects.

---

[11] J. J. Gilman and W. G. Johnston, J. Appl. Phys. **27**, 1018 (1956).

[12] W. C. Dash in *Properties of Elemental and Compound Semiconductors*, edited by H. C. Gatos (Interscience Publishers, Inc., New York, 1960), p. 195; cf. discussion of this paper by J. Patel, *ibid.*, p. 209.

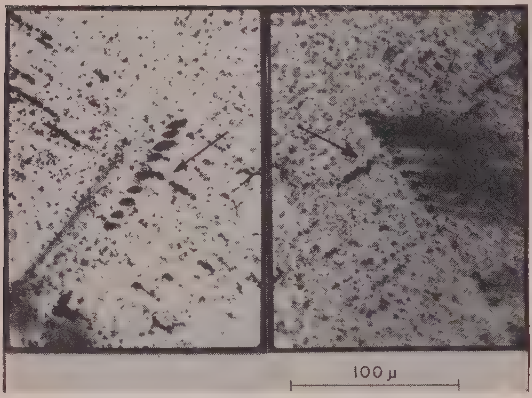

(a) (b)

FIG. 7. Matching cleavage faces of natural sphalerite crystal etched in 30% H_2O_2 for 1 hr, 70°–80°C. Note mirror symmetry of pit arrays, e.g., the areas indicated by the arrows. Photographed with optical microscope using transmitted light.

First, they may represent deposits of impurities *not* associated with dislocations. Dash has reported etch-pit formation without attendant dislocations.[12]

Second, the pits may be the emergence points of dislocations. If dislocations prove to be the correct interpretation, then their spatial coincidence with the stacking faults must be explained. One answer may be that, since stacking faults and dislocations are both regions of higher energy than perfect regions, the total energy of the lattice may be lowered through their mutual interaction. Another possibility is that the dislocations are *partial dislocations*. Partial dislocations are defined as line defects which arise when stacking faults terminate within a crystal.[13,14]

The following properties attributable to dislocations make them an attractive focus of speculation:

(a) Dislocations act as sites where impurities can segregate.
(b) Dislocations have been suggested as sites where avalanche breakdown may be initiated and where microplasmas may occur in reverse-biased junctions.[15] Both factors can be of importance for the mechanism of electroluminescence.

While the dislocation interpretation is attractive, it must be emphasized that no independent experiments have as yet been performed on electroluminescent specimens (such as x-ray studies, mechanical deformation experiments, etc.) which demonstrate that these pits represent dislocations. The cleavage experiments were not performed with electroluminescent crystals but with natural sphalerite. The equivalent work in electroluminescent ZnS has yet to be done. It is therefore premature to discuss in any greater detail the contribution of dislocations to electroluminescence.

SUMMARY

Through etching ZnS phosphor powder crystallites with hydrogen peroxide solutions, a defect is revealed which is associated with electroluminescence capability. The defect is shown in the form of triangular etch pits and occurs on faces which show surface striations. The striations are attributed to stacking faults. All triangular pits on a given crystal face are commonly oriented with one apex pointing normal to the striation direction. The planes on which the pits develop are probably of the (110) and $(\bar{1}2\bar{1}0)$ families in cubic and hexagonal ZnS, respectively.

Etch-pit densities fall in the range 10^6–$10^8/\text{cm}^2$ for electroluminescent phosphors. Little or no pit formation occurs in nonelectroluminescent phosphors, which means, from the technique of measurements, that pit densities in nonelectroluminescent crystallites are $<10^5/\text{cm}^2$.

From the arrangement of pits in some particles it appears that a physical connection exists between the defects associated with the pits and the stacking faults. The pits may be a consequence of impurity aggregates located at the stacking faults. Alternatively they may be due to partial dislocations or dislocations residing at stacking faults. The defects may form part of the site at which field intensification occurs.

ACKNOWLEDGMENTS

The author wishes to express his gratitude to Dr. D. H. Baird and Dr. R. N. Summergrad for many helpful discussions, and to C. F. Tufts for the electron micrographs without which this work would not have been possible. The aid of S. Faria and J. T. Ragusin in various aspects of phosphor preparation and etching procedures is gratefully acknowledged. Mr. Faria first suggested the use of H_2O_2 as an etchant for these phosphors.

---

[13] W. T. Read, Jr., *Dislocations in Crystals* (McGraw-Hill Book Company, Inc., New York, 1953), p. 92.

[14] B. Chalmers, *Physical Metallurgy* (John Wiley & Sons, Inc., 1959), p. 103.

[15] A. G. Chynoweth and G. L. Pearson, J. Appl. Phys. **29**, 1103 (1958).

JOURNAL OF APPLIED PHYSICS VOLUME 32, NUMBER 8 AUGUST, 1961

Nonlinear Damping Losses in YIG

Robert L. Conger*
U. S. Naval Ordnance Laboratory, Corona, California

(Received November 11, 1961)

High-power ferromagnetic resonance in a flat plate has a small component of the precession parallel to the applied dc field. This component causes frequency doubling and also coherent amplification of some scattered spin waves. These spin waves then cause a linear damping of the parallel component of the precession, which in turn causes a nonlinear damping of the principal component of the precession. The nonlinear damping causes the microwave susceptibility to decrease with increasing power and to become approximately inversely proportional to the rf field at high power levels.

I. INTRODUCTION

A SET of theoretical curves of the imaginary part of the ferromagnetic resonance susceptibility as a function of rf power with the ratio of intrinsic to scattering spin wave generation as a parameter has been presented by Suhl.[1] Experimental data determined by Weiss[2] fit the Suhl curves for a large scattering-to-intrinsic ratio. This indicates that the decrease in susceptibility at high power levels is caused largely by spin wave scattering. Schlömann *et al.*[3] have studied the decrease in susceptibility resulting from spin wave scattering.

High-power resonance can result in the production of microwave power at twice the frequency of the input. If the dc field of the ferromagnetic resonance experiment is tangential to the surface of a thin plate or disk, the demagnetizing field will cause the precession of the magnetization vector to be constrained largely to the plane of the disk so that the precession is largely an oscillation in this plane. If total magnetization is constant, the oscillation of the magnetization vector in this plane has two components; one at right angles to the dc field at the uniform precession frequency, and the other parallel to the dc field at twice the precession frequency.

The component of the precession parallel to the dc field that produces frequency doubling also causes coherent amplification of spin waves. The spin waves cause a linear damping of this parallel component which in turn results in a nonlinear damping of the principal component of the precession. The nonlinear damping then causes the susceptibility to decrease with increasing power and to be inversely proportional to h_{rf} at high power levels.

II. THEORY

All garnets, ferrites, etc. contain many defects in the form of holes, inclusions, etc. These defects act as scattering centers for spin waves. In this section we consider the spin wave which would be generated when a long wavelength wave strikes such a scattering point. The scattered wave starts out as a spike or impulse function and then spreads out with time until it occupies the entire sample.

The equation of motion without damping is:

$$\partial\mathbf{M}/\partial t=\gamma(\mathbf{M}\times\mathbf{H}_{\text{eff}}), \qquad (1)$$

where $\mathbf{M}$ is the magnetization and γ is the gyromagnetic ratio.

Let the thin plate of ferrite or yttrium iron garnet (YIG) be in the $x-z$ plane. The dc field H_0 will be in the z direction. For this geometry,

$$\mathbf{H}_{\text{eff}}=-\mathbf{j}4\pi M_y+\mathbf{k}H_0+(2A/M_0^2)\nabla^2\mathbf{M},$$

where $\mathbf{H}_0$ is the applied dc field, $\mathbf{j}$ and $\mathbf{k}$ are unit vectors, and A is the exchange constant. For spin waves progressing in the z direction,

$$\nabla^2=\partial^2/\partial z^2 \quad \text{and} \quad \nabla^2 M_z=0.$$

For small precession angles $M_z\cong M_0$, and the x and y components of Eq. (1) become

$$\dot{M}_x=[-(2\gamma A/M_0)(\partial^2/\partial z^2)+\gamma(H_0+4\pi M_0)]M_y \qquad (2)$$

$$\dot{M}_y=[(2\gamma A/M_0)(\partial^2/\partial z^2)-\gamma H_0]M_x. \qquad (3)$$

From Eqs. (2) and (3),

$$\frac{\partial^2 M_x}{\partial t^2}=-\left[\left(\frac{2\gamma A}{M_0}\right)^2\frac{\partial^4 M_x}{\partial z^4}-\gamma(2H_0+4\pi M_0)\frac{2\gamma A}{M_0}\frac{\partial^2 M_x}{\partial z^2}+\omega_0^2 M_x\right], \qquad (4)$$

where ω_0 is the uniform precession frequency:

$$\omega_0=\gamma[H_0(H_0+4\pi M_0)]^{\frac{1}{2}}. \qquad (5)$$

The first two terms of the binomial expansion of Eq. (5) give

$$\omega_0\cong\gamma(H_0+2\pi M_0); \qquad (6)$$

so for H_0 much larger than $4\pi M_0$, Eq. (4) takes the form

$$\frac{\partial^2 M_x}{\partial t^2}=-\left[\left(\frac{2\gamma A}{M_0}\right)^2\frac{\partial^4 M_x}{\partial z^4}-2\omega_0\left(\frac{2\gamma A}{M_0}\right)\frac{\partial^2 M_x}{\partial z^2}+\omega_0^2 M_x\right]. \qquad (7)$$

---

* Work supported by the Bureau of Weapons, U. S. Navy.

[1] H. Suhl, J. Appl. Phys. **30**, 1961 (1959).

[2] M. T. Weiss, J. Appl. Phys. **31**, 103S (1960).

[3] E. Schlömann, J. J. Green, and U. Milano, J. Appl. Phys. **31**, 386S (1960).

For YIG, $4\pi M_0 = 1.7\times 10^3$ gauss and $H_0 = 2.5\times 10^3$ gauss for resonance at X band in a flat plate. For these values of H_0 and $4\pi M_0$, ω_0 as determined from Eq. (5) is 0.97 of ω_0 as determined from Eq. (6), and therefore Eq. (7) is an almost exact equation for the scattered spin waves. Consider the case where $M_x = 0$ at $t = t_0$ except for a spike at $z = z_0$. A solution of Eq. (7) with this initial condition is

$$M_x = C(t-t_0)^{-\frac{1}{2}} \cos\left[\frac{M_0(z-z_0)^2}{8\gamma A(t-t_0)} - \omega_0 t\right]. \tag{8}$$

Equation (8) represents a wave of constant amplitude in which the wavelengths become progressively shorter as z moves away from z_0. But a spin wave shorter than one lattice constant can not be supported and so the wave must decrease in amplitude for wavelengths shorter than some limiting value. At $t = t_0$, only the central spike is possible. As time advances from $t = t_0$, the wave pattern spreads out and also decreases in amplitude as $(t-t_0)^{-\frac{1}{2}}$. The scattered spin waves represented by Eq. (8) will spread out until they strike boundaries, holes, or other obstacles. An equation identical to Eq. (7) applies to M_y and so an equation of the same form as Eq. (8) must apply to M_y also. Equations (2) and (3) show that M_y has a phase shift of $\pi/2$ with respect to M_x, and that where the spin-wavelength is long enough for the terms involving $\partial^2/\partial z^2$ to be smaller than the terms involving H_0, M_y is smaller than M_x. This is a result of the demagnetizing field of a flat plate.

At high rf power levels there is a mechanism for coupling energy from the uniform precession mode to these waves. Since the demagnetizing field restrains the uniform precession magnetization vector to approximately the plane of the YIG plate, the x, z plane, for this vector

$$M_z \cong (M_0^2 - M_x^2)^{\frac{1}{2}}, \tag{9}$$

and since M_x is $\ll M_0$ at low and medium power levels,

$$M_z \cong M_0[1 - \tfrac{1}{2}(M_x/M_0)^2] \tag{10}$$

by expansion. If the uniform precession in the $x-z$ plane is represented by a sinusoidal variation of M_x, then

$$M_z \cong M_0[1 - (A^2/4) + (A^2/4)\cos 2\omega_0 t], \tag{11}$$

where A and ω_0 are the amplitude and frequency of the uniform precession. Equation (11) shows that the M_z variation at $2\omega_0$ is proportional to the square of the amplitude of the uniform precession. Frequency doubling experiments show this second power dependence on the input power.

At higher power levels this variation of M_z at $2\omega_0$ serves as a pump to increase the amplitude of the nonuniform spin waves excited by defect scattering as represented by Eq. (8).

A pumping term $P\cos 2\omega_0 t$ will be added to Eq. (8) to give

$$\frac{\partial^2 M_x}{\partial t^2} = -(\omega_0^2 + P\cos 2\omega_0 t)M_x - \left[\left(\frac{2\gamma A}{M_0}\right)^2 \frac{\partial^4 M_x}{\partial z^4} - 2\omega_0\left(\frac{2\gamma A}{M_0}\right)\frac{\partial^2 M_x}{\partial z^2}\right]. \tag{12}$$

For $P \ll \omega_0^2$, an approximate solution of Eq. (12) is

$$M_x = Ee^{(P/4\omega_0)(t-t_0)}(\sin\omega_0 t - \cos\omega_0 t) + Ge^{(P/4\omega_0)(t-t_0)}(\sin 3\omega_0 t - \cos 3\omega_0 t), \tag{13}$$

where $G = (P/16\omega_0^2)E$ and E is

$$C(t-t_0)^{-\frac{1}{2}} \cos\left[\frac{M_0(z-z_0)^2}{8\gamma A(t-t_0)}\right].$$

The exponential increase in amplitude in Eq. (13) shows the effect of the pumping action. Damping action not included in Eq. (12) will limit M_x to some finite value.

The amplified spin waves are coherent and can react back on the z component of the uniform precession. This back reaction will be considered as a damping proportional to $\dot{M}_z$ for the uniform precession. Since the precession is largely an oscillation in the plane of the YIG plate, an equation of motion can be written as

$$(\partial^2 M_x/\partial t^2) + kM_0\dot{M}_z + r\dot{M}_x + \omega_0^2 M_x = A\cos\omega_0 t, \tag{14}$$

where k is a damping constant for spin wave damping, r a linear damping constant proportional to the damping constant α in the Landau-Lifshitz equation, and A is proportional to the rf driving field. From Eq. (10) at low power levels,

$$\dot{M}_z = M_x\dot{M}_x/M_0. \tag{15}$$

Substitution of Eq. (15) into Eq. (14) gives the nonlinear equation to be solved:

$$(\partial^2 M_x/\partial t^2) + (k|M_x| + r)\dot{M}_x + \omega_0^2 M_x = A\cos\omega_0 t. \tag{16}$$

The nonlinear damping will depend only on the absolute value of M_x. For single-crystal YIG, the damping constant k would be expected to be small. For k smaller than ω_0 and A not too large, an approximate solution of Eq. (16) can be obtained in the following way. Let

$$M_x = a\sin\omega_0 t + b\cos 3\omega_0 t + c\cos 5\omega_0 t; \tag{17}$$

b and c will be small. The term $|M_x|$ will be taken as the Fourier series expansion for the rectified sine wave. To three terms,

$$|M_x| = a[(2/\pi) - (4/3\pi)\cos 2\omega_0 t - (4/15\pi)\cos 4\omega_0 t]. \tag{18}$$

Equations (17) and (18) are substituted into Eq. (16). Since k, b, and c are small, terms involving kb and kc are dropped. The resulting equation is solved for a, b, and c.

The result is

$$a=-(3\pi/8k)\{r-[r^2+(16Ak/3\pi\omega_0)]^{\frac{1}{2}}\}, \quad (19a)$$

$$b=-(ka^2/10\pi\omega_0), \quad (19b)$$

$$c=-(ka^2/180\pi\omega_0). \quad (19c)$$

At low power levels where A is small, Eq. (19a) reduces to $A/\omega_0 r$. For this case the amplitude of the uniform precession is proportional to the rf driving field and the susceptibility χ'' is independent of rf power. At higher power levels where A is larger, the coefficient a changes smoothly over to $(3\pi A/4k\omega_0)^{\frac{1}{2}}$. For this second case, the amplitude of the uniform precession is proportional to the driving field to the $\frac{1}{2}$ power and the susceptibility χ'' is inversely proportional to the rf field to the $\frac{1}{2}$ power.

At high power levels, $\dot{M}_z$ must be determined from Eq. (9) rather than Eq. (10), and Eq. (16) takes the form:

$$\frac{\partial^2 M_x}{\partial t^2}+\frac{k|M_x|\dot{M}_x}{[1-(M_x/M_0)^2]^{\frac{1}{2}}}+rM_x+\omega_0{}^2\dot{M}_x=A\cos\omega_0 t. \quad (20)$$

The second term can be expanded to give

$$(\partial^2 M_x/\partial t^2)+k|M_x|\dot{M}_x[1+\tfrac{1}{2}(M_x/M_0)^2+\cdots]$$
$$+r\dot{M}_x+\omega_0{}^2M_x=A\cos\omega_0 t. \quad (21)$$

Equations (8) and (13) are based on the assumption of small amplitudes for spin waves. At high power levels an additional correction must be made in Eq. (21) to account for large amplitude spin waves.

The effects of increased damping resulting from increased spin wave amplitude and from increased precession angle can be approximated simultaneously by replacing M_0 in Eq. (21) by a term smaller than M_0 and proportional to the maximum spin wave amplitude.

Solutions of Eq. (21) were determined by the use of an analog computer. For these calculations, the term M_0 was set equal to ω. At low power levels, $A\ll\omega$; computer solutions verified Eqs. (17)–(19). As the power level was increased, M_x changed from a sine wave to a round scallop-wave form. As long as M_x was smaller than ω the amplitude of M_x was proportional to the square root of the driving field A. At high power levels where M_x became greater than ω, M_x was proportional to the fourth root of A.

In this region the susceptibility is inversely proportional to the rf field to the $\frac{3}{4}$ power. At still higher power levels, higher-powered terms become important in the second term of Eq. (21) and the damping increases very rapidly with increasing drive. The damping term eventually becomes so large that no appreciable further increase in the magnitude of M_x takes place. This is the region where the susceptibility approaches a $1/h_{\mathrm{rf}}$ dependence.

Increasing the damping constant k had the same effect as increasing the driving field.

A curve of microwave susceptibility of polycrystalline yttrium iron garnet as a function of $1/h_{\mathrm{rf}}$ was presented by Seiden and Shaw.[4] Their Fig. 1 shows clearly an initial region of decrease in susceptibility where the susceptibility is approximately proportional to $(1/h_{\mathrm{rf}})^{\frac{1}{2}}$, followed at higher power levels by a region where the susceptibility becomes proportional to $1/h_{\mathrm{rf}}$.

The large third harmonic in M_x at high power levels suggests frequency tripling experiments. The maximum amplitude of the third harmonic is about $\frac{1}{6}$ the amplitude of the fundamental. The triple frequency output would be in the same plane as the input.

III. CONCLUSIONS

The decrease in the imaginary part of the rf susceptibility that is observed in YIG high-power resonance experiments can be interpreted as the result of nonlinear damping of the uniform precession resulting from spin wave generation. The spin waves are produced by scattering from crystal defects, surface roughness, and other centers in the YIG crystal, and are enhanced coherently by the same variation in the z component of magnetization that produces frequency doubling. With this damping mechanism, damping at low power levels is very small, and so any linear damping that is present will predominate at low power levels. At high power levels, the amplitude of the uniform precession is proportional to the square root of the applied rf field and microwave susceptibility is inversely proportional to the square root of the applied field. At still higher power levels the susceptibility becomes almost inversely proportional to the rf field.

ACKNOWLEDGMENT

The author wishes to acknowledge the work of Erwin Hoffer on computer solutions of the nonlinear differential equations involved in this paper.

---

[4] P. E. Seiden and A. J. Shaw, J. Appl. Phys. **31**, 225S (1960).

JOURNAL OF APPLIED PHYSICS VOLUME 32, NUMBER 8 AUGUST, 1961

Experimental Study of Arc Stability. II. An Investigation of Mercury Arc Stability

G. A. FARRALL AND G. H. REILING*
General Electric Research Laboratory, Schenectady, New York

(Received March 6, 1961)

The duration of an arc struck on a mercury pool has been studied under a variety of arc currents and vapor pressures. It is shown that at temperatures greater than −38°C the distribution of arc lifetimes follows an exponential decay law over the entire current range studied, whereas a distinct departure from this distribution occurs between −57° and −195°C. Over the current range 0.02–2.0 amp the mean arc lifetime varies from a few microseconds to 0.1 sec on a mercury cathode at 23.5°C. This study extends previous work and establishes that there is a sudden change in arc stability at the melting point. The data demonstrate, contrary to experience with liquid mercury, that an arc can be struck for very low currents in the case of solid mercury and, once struck, will burn for a finite length of time given by $\tau=\tau_0+KI$, where τ_0 is a residual lifetime for almost zero current. It is shown, however, that as the current is reduced, the probability of drawing an arc becomes diminishingly small.

INTRODUCTION

PREVIOUSLY, it has been established that under frequently encountered conditions a dc arc with a mercury cathode, once struck, will burn a finite length of time and then spontaneously extinguish.[1] Earlier work shows that although this period of time varies for given experimental conditions, the average burning time or arc lifetime, for a large number of successive trials, is a reproducible number. For instance, Copeland and Sparing[2] and Kesaev[3] showed the average life at room temperature is an exponential function of arc current and dependent upon circuit and tube parameters such as circuit reactance and the area of the cathode pool. The former authors[2] also considered briefly the effect of a change in ambient mercury vapor pressure. The work reported here substantially extends these earlier measurements of arc lifetime as a function of current and vapor pressure and reports stability data obtained for the mercury arc on a frozen cathode and for the mercury-rubidium arc at room temperature.

At present, no guiding theory is available for the study of these arcs. Visually, the cathode emission is obtained from one or more bright spots moving randomly on the pool surface. The spot is normally bright blue-white and appears to have a sharp boundary separating the visible light from the low-luminosity plasma of the arc. In the immediate vicinity of the spot, considerable mercury is evaporated, sprayed, and ejected from the spot. The current density in the emission zone is very high and it is estimated to be about 10^4–10^5 amp/cm^2.[4] Our study further extends the data on the cathode emission on cold metals in the hope that it will clarify the nature of the cathode spot.

EXPERIMENTAL TECHNIQUE

According to a previously adopted convention, a total number of 40 trials was considered adequate to determine an average arc lifetime for a given temperature, current, and experimental circuit.[1] This number of trials is expected to yield a probable relative error of 10.3% If the number of trials were doubled, the probable relative error is reduced only 3%. Therefore, unless stated to the contrary, each point in the reported data is the average of 40 successive trials.

The arcs studied in this work were drawn in the tube shown in Fig. 1. A molybdenum anode 1.9 cm in diameter was mounted on a stainless steel bellows so that the anode could be moved into contact with the pool below. Electrical connection to the pool was provided by a 0.2-cm molybdenum rod extending through the glass at the bottom of the pool. The tube was carefully outgassed to 10^{-8} mm Hg by heating to 400°C and

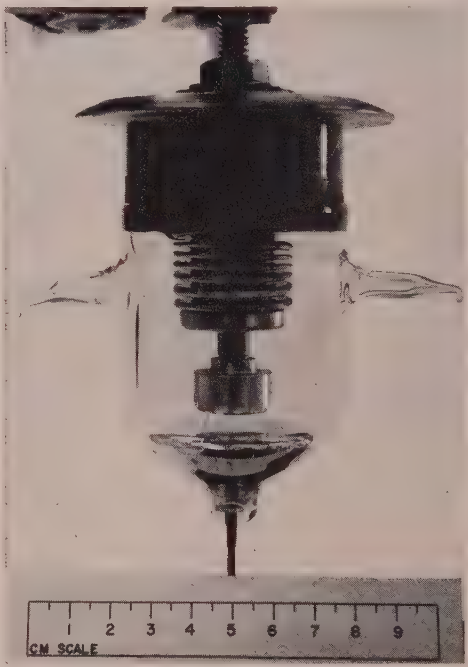

FIG. 1. An experimental mercury arc tube for measuring arc stability.

---

* Present address: General Electric Company, Photo Lamp Department, Nela Park, Cleveland 12, Ohio.

[1] J. D. Cobine and G. A. Farrall, J. Appl. Phys. 31, 2296 (1960).

[2] P. Copeland and W. H. Sparing, J. Appl. Phys. 16, 302 (1945).

[3] I. G. Kesaev, Soviet Phys.—Tech. Phys. 4, No. 12, 1351 (1960).

[4] J. D. Cobine and C. J. Gallagher, Phys. Rev. 74, 1924 (1958).

following conventional degassing procedures. An ampoule of mercury, previously distilled, was redistilled into the tube while the tube was on exhaust. Following seal-off, the mercury surface had a bright metallic appearance, indicating a high degree of purity.

After voltage was applied to this tube, arcs were initiated by moving the anode into contact with the pool using a mechanical lever. The lever operated against a spring which was adjusted to give a static gap length of 0.5 cm. The arc was drawn by separating the electrodes initially in contact. In order to control the mercury vapor density, it was necessary to immerse this tube in a bath held at a suitable temperature. For vapor densities corresponding to room temperature and higher, the bath consisted of approximately six gallons of silicon oil whose temperature was controlled by resistance heaters. The bath was vigorously stirred by a motor-driven propeller. At ambient temperatures below 20°C, a smaller bath was used which consisted of either liquid nitrogen or a slurry of dry ice in Dowanol.

An equivalent circuit of the power source and connection to the tube in which the dc arcs were measured, is shown in Fig. 2. Current was supplied through a series variable resistor by a 40-kw dc motor-generator set. The leads from the generator were relatively long and had a distributed inductance and capacitance of 27 μh and 0.02 mf, respectively. The inductance of the current limiting resistor was determined by the value of the resistance used and therefore varied with current. For arc currents below 5 amp, the inductance was 0.67 I^{-1} mh, and above 5 amp, 2.6 I^{-1} mh, where I is the current in amperes. The capacitance across the gap of the mercury pool tube was measured to be the order of 10 mmf. In order to determine accurately the burning time of the arc, a 5-turn coil of wire 5 cm in diameter was placed in the vicinity of the mercury tube. The signal induced in this coil by the arc noise was observed visually on a type 535 Tektronix oscilloscope with a persistent phosphor screen. Previously,[1] it has been found that added shunt capacitance alters arc lifetime and thus this coil has the advantage of no direct connection of cables to the mercury tube.

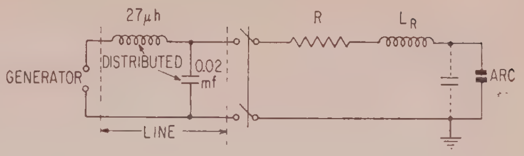

FIG. 2. Equivalent circuit used in arc stability measurements.

RESULTS

Data taken at room temperature for a mercury arc are shown in Fig. 3 together with measurements of Kesaev[3] and extrapolated results of Copeland and Sparing.[2] As mentioned earlier, each data point in this study represents the average of 40 consecutive arcs. Copeland and Sparing worked at currents greater than 2.5 amp and used a glass tube at a mercury vapor pressure of 1.2×10^{-3} mm Hg. An ignitor was used to strike the arc. The source voltage was approximately 105 v. Kesaev operated at the same vapor pressure using a 90-v source. In spite of the differences in the circuit, tube geometry, and operating conditions, the agreement appears satisfactory. In Fig. 3 it may be noted that the experimental curve appears to have two lower current limits at which the arc becomes extremely unstable, one at 0.02 amp and the other at 0.05 amp. When the data were initially taken, the lower limit of 0.02 amp was established. After extensive arcing, the lower limit was found to occur at 0.05 amp. The higher current range of this curve however was consistently reproducible. Similarly, observations at an operating temperature of 90°C showed the same effect with the shift occurring from 0.05 to 0.14 amp. However, at 141° and 192°C, no lifetimes were measurable at a current less than 0.190 amp. Subsequent measurement at 50°C showed that no lifetimes were measurable again at currents less than 0.19 amp. It is known that films on cold metal surfaces increase the stability of arcs. Therefore, a plausible explanation of the effect is that during periods of disuse there is a gradual accumulation of a surface film of products evolved from previous arcing on the mercury pool. Subsequent prolonged use at high temperature may have removed the film, thereby decreasing stability.

Figure 4 demonstrates the effect of vapor density on mercury arc stability. The ambient temperature was varied from 50° to 192°C. As seen from Fig. 5, these ambient temperatures correspond to mercury vapor densities of 4.5×10^{14} atoms/cm^3 and 2×10^{17} atoms/cm^3, respectively.[5] The variation of stability with tem-

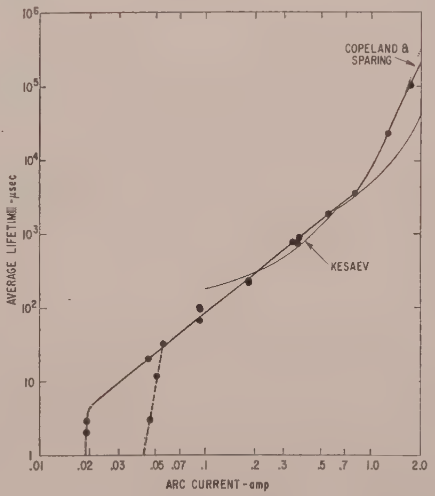

FIG. 3. Mean arc lifetime as a function of cathode arc current for mercury pool at 23.5°C.

---

[5] Data plotted from R. E. Honig, RCA Rev. 18, 195 (1957).

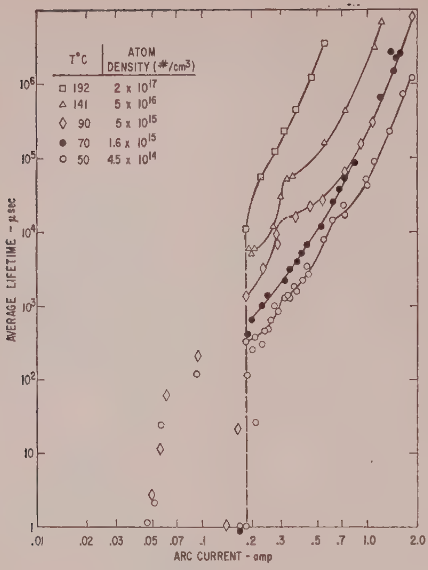

FIG. 4. Mean arc lifetime vs arc current for various mercury vapor densities.

perature stresses the need for a constant ambient temperature in measuring arc stability. If appreciable heat is generated in the period of time in which 40 successive arcs are drawn the resulting change in vapor density will alter the measured arc duration. In order to estimate the magnitude of this effect, consider a 1 amp arc with a 15-v arc drop in the case of simple radial heat flow across the glass wall of the tube.[6] If arcs with a mean lifetime of 1 sec are drawn at 2-sec intervals, the temperature drop across the glass would be no more than 3°C. This rise will not affect the experimental results significantly. However, for higher currents and longer lifetimes, the increase in internal temperature would be observed as an increase in lifetime for each successive arc. In Fig. 4, the very longest lifetimes are estimated to be 50% too long as a result of this condition in spite of the constant temperature bath. Under extreme conditions it is possible for this "self-enhancement" of vapor density of a single arc to produce a condition wherein the longer it burns the more likely it is to continue. Thus the arc lifetime may become independent of bath temperature.

All of the inflection points in the data of Fig. 4 are reproducible and suggest that at the corresponding current, cathode spot splitting may occur. Thus, for currents higher than 0.3 amp, for instance, two spots instead of one may exist.

As shown in Fig. 4, there is an abrupt change in stability at 0.19 amp which suggests this as an appropriate current at which to show the relationship between arc lifetime and ambient atom density. This result is given in Fig. 6 which implies that at low vapor densities, arc duration tends to become independent of the ambient vapor surrounding the arc. Furthermore, near the melting point at which the ambient vapor density is three orders of magnitude lower than that at room temperature, the average arc lifetime at 0.19 amp on liquid mercury was 0.12 msec. This also suggests a small dependence of arc lifetime on ambient vapor at low vapor densities. Data for higher currents plotted in a similar fashion do not generally lie on a smooth curve. This may be the result of a more complicated behavior of the arc at higher currents.

The mean free path within the experimental tube becomes comparable with tube dimensions at a vapor density of 10^{14} atoms/cm^3. It would follow that at this density the average arc lifetime should become independent of ambient atom concentration and approach as a limit a lifetime which is determined by the vapor supplied from the cathode spot itself. This appears to be verified in Fig. 6.

During the measurements made at 70°C and at room temperature, the polarity of the voltage applied to the tube was reversed, making the molybdenum electrode the cathode. By this time, the tube had undergone extended arcing. The molybdenum electrode, therefore, had been thoroughly wet by the mercury and was covered with a thin coating. Results obtained of arc lifetime measurements under these conditions were not detectably different from those obtained when the mercury pool was the cathode. Previous arc lifetime measurements[1] have shown that an arc on pure molybdenum is substantially less stable than mercury. One

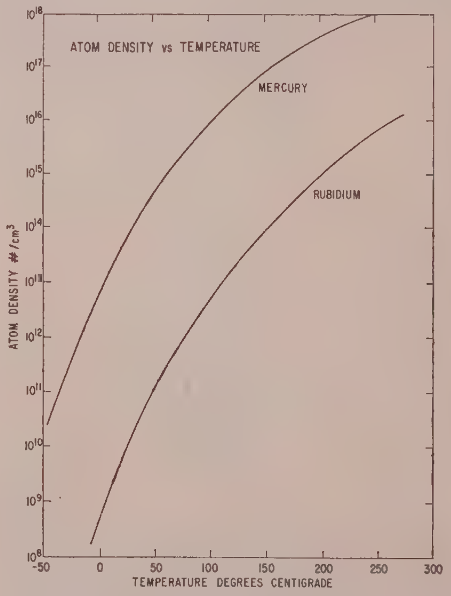

FIG. 5. Mercury and rubidium vapor density vs temperature for vapors in equilibrium with pure liquid or solid.

---

[6] L. R. Ingersoll, O. J. Zobel, and A. C. Ingersoll, *Heat Conduction* (University of Wisconsin Press, Madison, Wisconsin, 1954).

might conclude from this experiment on reversed polarity that only a very thin layer of metal is required to determine the stability characteristics of an arc. When using the molybdenum electrode as a cathode, frequently at high currents an arc would be drawn which was unusually stable. This was attributed to a mercury droplet adhering to the molybdenum surface when the arc was drawn. Then, the authors feel, the cathode spot or spots anchored on the concave meniscus at the wetted molybdenum-mercury junction. Anchored spots are known to be many times more stable than free spots.

An extension of the present study was made to include the measurement of stability of an arc drawn, at room temperature, on a mercury pool cathode to which had been added 1% by weight of rubidium. Although the concentration of rubidium is small and its vapor pressure is about three orders of magnitude below that of mercury, the rubidium ionization potential is 6.3 ev lower than that of mercury. Assuming that the vapor pressure of the solution follows Raoult's law, the mercury atom concentration will be depressed only 2.3% in this tube. In a pure mercury tube, this same change in concentration can be produced by a change in temperature of only 0.005°C, well below the limit of temperature control in these measurements. The solubility of rubidium in mercury at 25°C is 1.3% by weight.[7] Thus, the addition of 1% by weight rubidium should not significantly alter the metal vapor density of the tube. Figure 7 shows the stability data of the mercury-rubidium pool at room temperature, where the ambient concentration is expected to have only a small effect on the stability of the arc because of the long mean free path. When the arc burns, however, the evaporated vapor density in the vicinity of the cathode spot must be greater by several orders of magnitude.

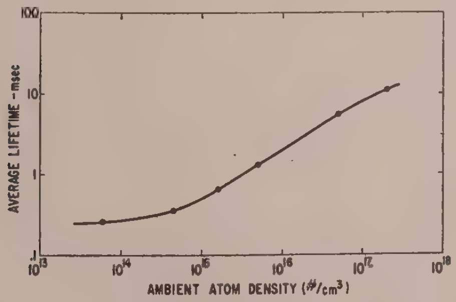

FIG. 6. The average arc lifetime vs vapor density for a current of 0.2 amp.

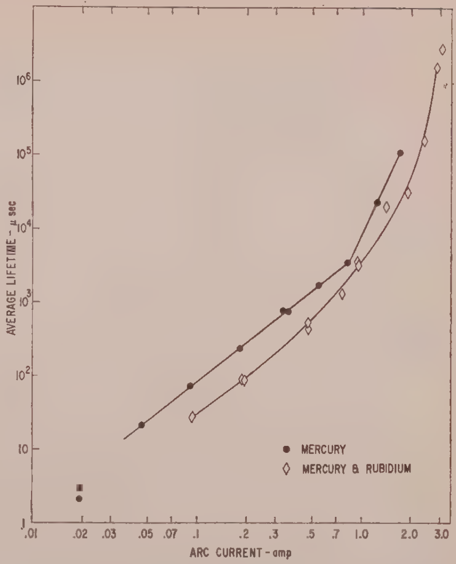

FIG. 7. Mean arc lifetime as a function of cathode current for a mercury-rubidium electrode at 24°C compared with that of a mercury cathode.

Now examining Fig. 7, the stability of the mercury-rubidium arc is seen to be detectably lower than that of pure mercury. A reasonable interpretation of this result is that the arc stability decreases because less material is being evaporated from the cathode spot. Of possible explanations, this could either be the result of deviation from Raoult's law (that is, a lower evaporated vapor density than predicted by Raoult's law) or the arc spot burning primarily in the vicinity of rubidium atoms. This may occur because of the lower ionization potential and the lower work function of rubidium requiring less energy for electron emission. If the latter case is correct, the arc burns as if the mercury were largely absent. In either case, the decrease in arc stability is probably caused by the lower vapor density in the vicinity of the cathode spot.

Stability at the mercury melting point was studied by immersing the experimental tube in a slush of dry ice and Dowanol. With the bath initially at a temperature of −57°C, the tube was removed from the bath and allowed to warm slowly in air. The arc current had been adjusted to 1.23 amp and stability measurements made as the cathode changed from solid to liquid. The burning lifetime of each arc drawn is indicated as a single point in Fig. 8. Between the 26th and 33rd arcs an unmistakable transition occurred which was tentatively identified as the change in phase from solid to liquid. This was confirmed by replacing the tube in the cold bath and measuring arc lifetimes for various currents at bath temperatures slightly above and below the freezing point of mercury. Although the exact temperature adjacent to the cathode spot could not be precisely controlled, Fig. 8 demonstrates there is a sudden change of arc stability with a change in phase of the cathode. Observations of a similar nature have been briefly reported by Kesaev and Levshenkova for mercury, bismuth, lead, and tin in the liquid and solid phase.[8] Thermodynamically, melting is a first-order phase transition in which the temperature and pressure remain constant but in which entropy and volume change.

---

[7] M. Hansen and K. Anderko, *Constitution of Binary Alloys* (McGraw-Hill Book Company, Inc., New York, 1958).

[8] I. G. Kesaev and L. A. Levshenkova, Soviet Phys.–Tech. Phys. 5, 767 (1961).

The determination of arc lifetimes on a mercury cathode immersed in liquid nitrogen produced results which were not expected in the view of experiments on the liquid pool. It will be recalled that at higher temperatures an arc could not be drawn below a current of 0.19 amp. For the solid mercury cathode arcs drawn at currents below this limit burned for relatively long periods, but as the current was made smaller it became increasingly more difficult to draw an arc. Either the arc would burn for a relatively long period or it could not be initiated. When we say an arc is not initiated, we imply that it either did not ignite or burned for a time less than a minimum measurable value. Arc lifetimes on solid mercury were measured by a Tektronix type 555 dual-beam oscilloscope with one beam operating at a slow sweep speed to determine the duration of the drawn arc. The other beam was operated at a fast sweep speed to determine the minimum measurable time limit in the event that the arc was not initiated. In general, this lower limit was about 10 μsec. A transient signal generated in the pickup coil by the separation of the electrodes was of this duration and obscured measurements for times less than this. The appearance of the transient, however, indicated good initial contact between anode and cathode. Ignoring for the moment the actual burning time of the arc, Fig. 9 shows the relative number of times an arc was struck in a series of 40 attempts vs the current flowing if an arc were drawn. The probability of obtaining an arc at a given current can be represented by an empirical equation

$$P(I)=\frac{1}{1+e^{-\alpha(I-I_0)}}, \tag{1}$$

where I_0 is that current for which an arc is obtained 50% of the time and has the value 0.135 amp. The constant α is 38.2 amp^{-1}.

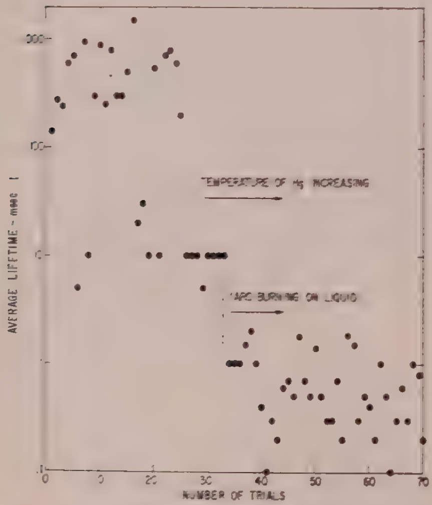

FIG. 8. Arc lifetime for single arcs vs successive arcs as the mercury cathode changed from solid to liquid.

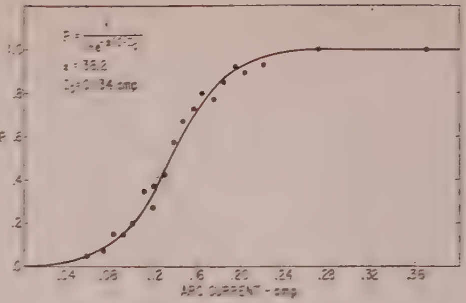

FIG. 9. The probability of striking an arc in 40 successive trials as a function of current.

The average arc lifetime for solid mercury is compared with that obtained at room temperature in Fig. 10, and can be approximately represented above 0.19 amp by the relation

$$\tau=\tau_0+KI, \tag{2}$$

where τ_0 and K are constants and τ is the lifetime at current I. There is considerable scatter in the results especially at the lower currents. This is the result, in part, of the fewer number of successfully drawn arcs involved in determining an average at low currents.

It has previously been shown that in the case of mercury at room temperature the probability that an arc will burn longer than a given time t at a constant current is given by

$$P=e^{-\lambda t}, \tag{3}$$

where λ is the reciprocal of the average arc lifetime and depends upon current, vapor pressure, and circuit constants.[1,2] In the present study this relation was found to hold for all measurements made on liquid mercury above the melting point. However, below the melting point this is not the case. Figure 11, curves (a), (b), and (c) shows the relative number of arcs N/N_0 (equal to P) that will last longer than time t for various temperatures. Figure 11(a) shows the distribution obtained for liquid mercury near the freezing point; 11(b) the distribution for solid mercury near the freezing point; and 11(c) the distribution for solid mercury at liquid nitrogen temperature. It is seen that curve 11(b), although substantially exponential, has developed a flat top in the time interval 30–175 msec. Curve 11(c) cannot be considered exponential. There is no great difference in the average lifetime vs current curves for solid mercury near its freezing point and at liquid nitrogen temperature. [In Figs. 11 (b) and (c), the average lifetime for curve (b) is 323 msec, whereas the average for curve (c) is 228.7 msec. As Fig. 11 demonstrates, however, there is a significant difference in the statistical distribution of points which determine

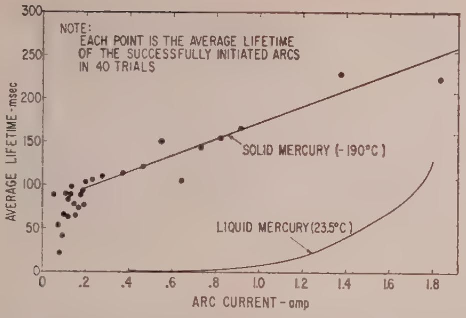

FIG. 10. Mean arc lifetime for a mercury cathode at liquid nitrogen temperature (−190°C) and room temperature.

the average lifetimes for these two cases.] Empirically, it is found for the solid mercury cathode that the distribution of arc lifetimes for any current is well represented by

$$P=\frac{1}{1+\exp\{\alpha[\tau/(1+I)-\beta]\}}\qquad \begin{matrix}\alpha=109\\ \beta=0.08.\end{matrix}\qquad (4)$$

It may be noted that for a constant probability, this equation reduces to the form of τ vs I given earlier in Eq. (2).

DISCUSSION

As shown in Fig. 3, Kesaev's data which were taken with a static gap length of 2 cm and Copeland and Sparing's data taken with a gap length of at least 30 cm agree with the data reported here. It therefore appears that the experimental results presented here are substantially representative of an arc occurring between stationary electrodes although measurements were made on a drawn arc.

Perhaps the most striking observation in these experiments is the abrupt change in arc duration as the cathode changes between the liquid and the solid state. Various physical properties such as specific heat, resistivity, and latent heat do undergo discontinuous changes at the melting point and these may in part account for the experimental results. The properties of liquid and solid surfaces may also influence arc duration. It has been observed that at high currents where arc lifetime is relatively long, the continuous random motion of cathode spots on a liquid pool agitates the entire cathode surface. The random excursions of the spots on a solid cathode, on the other hand, are visually observed to be far less violent with, of course, the surface being undisturbed. It is felt that the local agitation of the liquid surface by the motion of cathode spots further increases the tendency for the spots to move, leading to a higher spot mobility on the liquid than on the solid. Ultimately, the emission for maintaining the arc must come from the power input to the cathode surface. Greater stability for the solid mercury is therefore expected as a result of the relatively slow movement of the cathode spots and the more efficient utilization of the power input at the emission sites. In previous work, Copeland and Sparing have determined that a reduction of cathode pool area results in a marked increase in arc stability. Kesaev has reported that an axial magnetic field produces an increase in arc stability. There is evidence that anchoring of the cathode spots results in an enhancement of stability as well as a reduction in the mercury spray from the emission zone. All of these factors may be viewed as further evidence that confining the random excursions of the cathode spots results in an increase in arc stability.

Since the emission mechanism of the cathode spot remains undetermined, it is impossible at this point to relate stability to physical processes of emission. However, certain statements can be made from experimental observations on the mercury arc.

(1) The distribution of arc lifetimes for the mercury cathode at liquid nitrogen temperature cannot be represented by the simple survival law previously determined for a liquid mercury cathode and other solids.

(2) For a solid mercury cathode, the arc can be drawn at very small currents and once struck will burn for a period of time substantially longer than that observed for the liquid pool. However, as the current is reduced, the probability of drawing the arc becomes diminishingly small.

(3) Although vapor pressure and residual gas density play a significant part in arc stability, the fact that arc lifetime changes discontinuously at the melting point by several orders of magnitude shows that other undetermined parameters are equally important. The violent motion of the cathode spot may in itself contribute to the extinction of the arc.

(4) As the mean free path in the residual vapor becomes the order of the tube dimensions, the arc life-

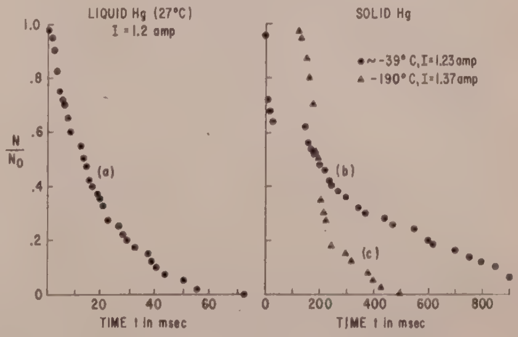

FIG. 11. Distributions of arc lifetimes for liquid and solid mercury cathodes.

time becomes largely independent of the residual vapor density.

(5) In spite of a small percentage of rubidium in the mercury-rubidium cathode, the average arc lifetime was shorter than that normally observed for the pure mercury arc. This strongly indicates that the arc burned preferentially at the easily ionized rubidium atom sites and that the arc lifetime was primarily determined by the lower vapor pressure of the rubidium.

ACKNOWLEDGMENTS

The authors are indebted to Dr. J. D. Cobine for reading the manuscript. They wish to acknowledge the assistance of R. H. Johnston in conducting the experiment.

JOURNAL OF APPLIED PHYSICS VOLUME 32, NUMBER 8 AUGUST, 1961

Orientation-Dependent Dissolution of Lithium Fluoride

M. B. Ives*
Metals Research Laboratory, Carnegie Institute of Technology, Pittsburgh, Pennsylvania

(Received February 27, 1961)

It is shown that the etch rate of lithium fluoride crystals in both a modified CP-4 etchant and a dilute aqueous solution of ferric fluoride is a function only of crystallographic orientation. This conclusion is reached by comparing experimental observations with the results of a recent topographical theory of crystal dissolution.

THE topographical theory of orientation-dependent dissolution of single crystals developed by Frank[1] has been usefully applied to the case of dissolution of germanium in a hydrogen peroxide-hydrofluoric acid etchant by Frank and Ives[2] by demonstrating that the theory could successfully predict dissolution shapes if the etch rate were known as a function of crystallographic orientation. Following the success of this application, and in order to further test the applicability of the Frank[1] theorems, the dissolution of lithium fluoride in the etchants developed by Gilman and Johnston[3] was studied.

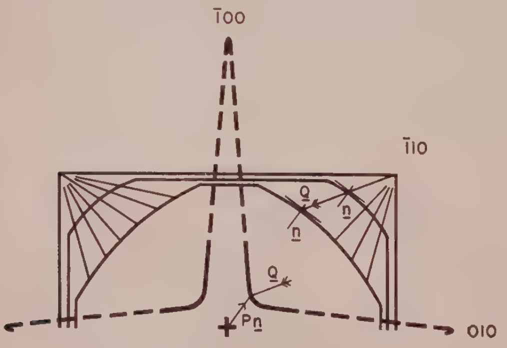

FIG. 1. Section of a square prism of lithium fluoride dissolved in "A" etchant, showing straight line trajectories Q and the deduced reluctance diagram.

The first orientation-dependent theorem (theorem I) states that if the rate of dissolution of a crystal surface is a function only of orientation (or depends on time only through orientation independent factors) then the locus in space of a particular orientation of crystal surface on dissolution is a straight line. If the dissolution rate is defined as measured normal to the actual crystal surface (rather than normal to a particular crystallographic plane) and the polar diagram of the reciprocal of this dissolution rate as a function of orientation is constructed, a second theorem (theorem II) shows that the trajectory of a point of given orientation on the crystal surface is parallel to the normal to the polar diagram at the point of corresponding orientation.

In the previous application[2] the theorems were used to predict dissolution shapes using known etch rate values. The converse—the deduction of dissolution data from observed dissolution shapes—is possible, once straight line trajectories are known to be applicable to the particular dissolution system. Figure 1 shows that

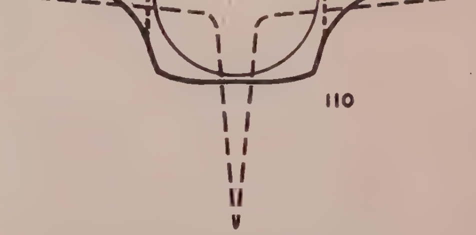

FIG. 2. Sketchwise deduction of the dissolution of a cylindrical groove in lithium fluoride, corresponding to the reluctance diagram of Fig. 1.

---

* Present address: Department of Metallurgy and Metallurgical Engineering, McMaster University, Hamilton, Ontario, Canada.

[1] F. C. Frank, *Growth and Perfection of Crystals* (John Wiley and Sons, Inc., New York, 1958), p. 411.

[2] F. C. Frank and M. B. Ives, J. Appl. Phys. **31**, 1996 (1960).

[3] J. J. Gilman and W. G. Johnston, *Dislocations and Mechanical Properties of Crystals* (John Wiley and Sons, Inc., New York, 1957), p. 116.

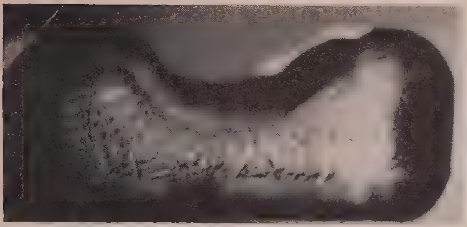

FIG. 3. Specimen of lithium fluoride with cylindrical groove, after 190-hr "A" etching. 10×.

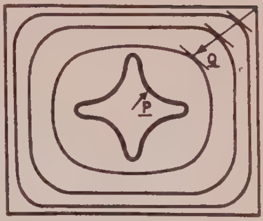

FIG. 4. Dissolution of a rectangular prism in "W" etch, and the reluctance diagram thereby deduced.

straight trajectories are indeed produced by the dissolution of lithium fluoride in "A" etchant.[3] Here, superposed dissolution profiles of a half-section of an originally square prism of lithium fluoride do allow straight lines drawn from the original crystal corners to be loci of individual crystallographic orientations.

The two-dimensional form of the Frank theory[1] may be used for the profile on a plane of cross section of a crystal which is simultaneously a symmetry plane for the crystal structure and for the initial form of the specimen. Therefore, using theorem II, it is possible to deduce the form of the polar diagram of reciprocal normal dissolution rate (the "reluctance diagram") once the directions of the trajectories are known for each of the orientations represented in the dissolution figures. A reversal of the procedure described by Frank and Ives[2] for germanium produces that part of the reluctance diagram which is drawn unbroken in Fig. 1. Only the orientations present in the innermost figure (produced after 40 hr-"A" etch) can be thus deduced, but measurement of the ratio of etch rates in the ⟨100⟩ and ⟨110⟩ directions gives the ratio of **P**, the reluctance vector, for these two directions. The remainder of the diagram may then be constructed assuming a reasonable linearity of line in the interpolated regions. The reluctance diagram for the dissolution of a {100} section of lithium fluoride in "A" etchant is seen to display considerable anisotropy of etch rate.

With the reluctance diagram for the dissolution system now known, it is possible to predict dissolution shapes for other symmetry sections, and this has been done in Fig. 2 for the case of a cylindrical groove in a {100} surface of lithium fluoride. The principal feature of the predicted shape is the edge at ⟨110⟩. (Due to the intersection of the converging trajectories brought about by the considerable curvature of the reluctance diagram in this region.) In Fig. 2 the broken line takes no account of dissolution from the sides of the groove, while the continuous profile allows for it. Figure 3 shows the 190-hr "A"-etchant shape of a lithium fluoride crystal initially machined with a cylindrical groove in its upper face. The predicted features are certainly qualitatively achieved.

Dissolution of a prism of lithium fluoride in "W" etchant[3] allows for similar treatment, and the results are depicted in Fig. 4. Again, straight trajectories **Q** are applicable, but the deduced reluctance diagram (the innermost figure) shows considerably less anisotropy of dissolution than was observed for the "A" etchant.

The present experiments therefore well demonstrate that the dissolution of lithium fluoride in both the aqueous and acidic etchants of Gilman and Johnston[3] is only orientation-dependent since straight line trajectories are obtained. Further, the construction of polar reluctance diagrams for the two cases by means of the Frank theory, shows that the acidic etchant is much more anisotropic in action than the aqueous. This is consistent with the author's etch rate studies[4] on parallel-sided crystal plates of known orientation which have given the "A" etch rates as 5 A/sec for "(100)"[5] and 34 A/sec for (110), and those of Gilman, Johnston, and Sears[6] on tumbled spheres, which give the "W" etch rates as 91 A/sec for "(100)" and 109 A/sec for (110).

---

[4] M. B. Ives, Ph.D. thesis, The University of Bristol, England, 1959.

[5] The etch rate for the close-packed surface of a perfect crystal should be zero. Real crystals record a finite rate due to the formation of etch pits. The measured etch rates are therefore more correctly a measure of the rate of retreat of the pit sides which, supposing they are inclined at 10° to the close-packed surface, would give the measured rate, $R_{\text{“(100)”}}=R_{10^\circ \text{ from } (100)}\cdot\cos 10^\circ$.

[6] J. J. Gilman, W. G. Johnston, and G. W. Sears, J. Appl. Phys. 29, 747 (1958).

JOURNAL OF APPLIED PHYSICS VOLUME 32, NUMBER 8 AUGUST, 1961

Lattice Parameter Determinations with an X-Ray Spectrogoniometer by the Debye-Scherrer Method and the Effect of Specimen Condition

HENRY M. OTTE
RIAS, Baltimore, Maryland

(Received March 3, 1961)

It is shown that the Debye-Scherrer method can be used successfully on an x-ray spectrogoniometer by removing the bisecting mechanism. Complete profiles of the diffraction lines have been recorded and the center of gravity (CG) determined with an accuracy of $\pm 0.005°2\theta$. Monochromated Cu$K\alpha_1$ radiation was employed and the complete x-ray unit housed in a room maintained at constant temperature to within ±1°C. The lattice constant was calculated from each reflection and plotted against the Nelson-Riley function; a straight line could be drawn through all the points. The limiting factors in the accuracy of the lattice constant determination are the uncertainties in the correction for vertical divergence, monochromatization, and tail effects in measuring the CG (and in the x-ray wavelength). Solid rods as well as compacts made of filings were examined after annealing and after deformation. The lattice constant of pure Al was found to be unaffected (within ±0.00005 A) by the condition in which it was examined, contrary to observations by certain other investigators. However, the lattice constants of single-phase alloys are in general quite sensitive to their state of preparation. The influence of short-range ordering, stacking faults, solute clustering, quenching stresses, etc., are discussed and their relative importance assessed.

I. INTRODUCTION

SPECTROGONIOMETER (SPG) techniques even in their early stages[1] were based on flat or curved sample geometry using parafocusing methods, and very little has been done with arrangements corresponding to the Debye-Scherrer (D-S) method. An important deciding factor was the volume of sample that could be irradiated and consequently the intensity of the diffracted beam. With the greatly increased efficiency of modern counter tubes and also of the amplification of signals, diffracted beams of comparatively low intensity (50 cps) can be detected quite easily; hence, it seemed worthwhile to examine further the use of the D-S method on the SPG.

In measuring accurate lattice parameters the D-S method (and variations of it) using a film and camera is most frequently employed because an external calibration standard is not required, and because the 2θ-zero alignment of the instrument is not critical since it can be easily determined and the readings corrected. However, many deformed metals and alloys show considerable line broadening accompanied generally by an appreciable deterioration of peak-to-background ratio to such an extent that photographic techniques become entirely unsuitable. Attempts to measure changes of lattice parameter under these conditions have nevertheless been made[2] by selecting only one diffraction line for study, usually in the back reflection region, and photographing it at a sufficiently large distance from the specimen to give the desired precision in the lattice parameter. This approach has been carried over, with modifications to the SPG technique.[3,4] Changes in lattice parameter deduced by such methods become unreliable when complicating effects from, for instance, stacking faults, introduced by deformation or heat treatment, are present, since these may produce in fcc metals line shifts that depend on the reflection.[5]

Furthermore, standard tensile test specimens with a circular cross section must generally be replaced by a specimen with rectangular cross section when x-ray work is to be performed simultaneously. A definite advantage is therefore to be gained in exploring the D-S method on the SPG.

II. EXPERIMENTAL ARRANGEMENT

A General Electric SPG was employed with the bisecting mechanism removed, so that the main protractor was free to swing through a complete 360° when clear of the x-ray tube. The original scatter shields had to be replaced by a direct beam stop and other shields that did not interfere with the diffracted rays. The arm of the bisecting mechanism attached to the sample holder platform was not removed, but fixed instead to a bracket, to prevent the platform from swinging freely.

A specially constructed spinner was used in preference to the one available commercially. It contained an interchangeable synchronous motor with a direct drive through a flexible shaft to the specimen stage. A motor speed of 150 rpm was found most expedient, and this also was the speed of rotation of the specimens, which were 25–45 mm long and varied in diameter from $\frac{1}{2}$ to 3 mm.

A range of Bragg angle from $-139°$ to $165°\ 2\theta$ was utilized, though this depended on where and how the x-ray tube was placed with respect to the SPG. The

---

[1] See, for example, D. P. LeGalley, Rev. Sci. Instr. **6**, 279 (1935); R. Lindemann and A. Trost, Z. Physik **115**, 456 (1940); W. P. Davey, F. R. Smith, and S. W. Harding, Rev. Sci. Instr. **15**, 37 (1944).

[2] See, for example, W. A. Wood, Proc. Roy. Soc. (London) **172A**, 231 (1939); J. H. Auld and G. B. Greenough, Acta Met. **2**, 209 (1954).

[3] A. L. Christenson and E. S. Rowland, Trans. Am. Soc. Metals **45**, 638 (1953).

[4] D. P. Koistinen and R. E. Marburger, Trans. Am. Soc. Metals **51**, 537 (1959).

[5] M. S. Paterson, J. Appl. Phys. **23**, 805 (1952).

TABLE I. Effect of scanning speed and alignment, Cu−6.6 at. % Si (1.2 at. % Mn), 3.1 mm diam, annealed 2 hr at 700°C.[a] Proportional counter (tube No. 1).

	Alignment *A*. SPG speed, 10 min/deg 2θ; chart speed, 60 in./hr.				Alignment *B*. SPG speed, 25 min/deg 2θ; chart speed, 24 in./hr.				
Line Σh^2	$2\theta_-$ $\pm 0.005°$	$2\theta_+$ $\pm 0.005°$	$\frac{1}{2}\Delta 2\theta$[b]	$\langle 2\theta \rangle$ $\pm 0.005°$	$2\theta_-$ $\pm 0.005°$	$2\theta_+$ $\pm 0.005°$	$\frac{1}{2}\Delta 2\theta$[b]	$\langle 2\theta \rangle$ $\pm 0.005°$	a_0, A $\lambda(\mathrm{Cu}K\alpha_1)=1.54050$ A
3	44.12_5	44.30_5	−0.09	44.21_5	44.30	44.11	$+0.09_5$	44.20_5	3.5449, 3.5456 ±0.0004
4	51.18	51.36	−0.09	51.27	51.36	51.18	+0.09	51.27	3.5608 $\pm 0.0003_5$
8	74.61	74.82	-0.10_5	74.71_5	74.80_5	74.62_5	+0.09	74.71_5	3.5903 ±0.0002
11	90.20	90.44	−0.12	90.32	90.38	90.26	+0.06	90.32	3.6028 $\pm 0.0001_5$
12	95.34_5	95.59_5	-0.12_5	95.47	95.53	95.41	+0.06	95.47	3.6056 $\pm 0.0001_5$
16	116.74	117.03	−0.14	116.89	...	116.85	(+0.04)[c]	116.89	3.6156 ±0.0001
19	...	136.18	(−0.16)[c]	136.02_5	...	135.99_5	(+0.03)[c]	136.02_5	3.6208 $\pm 0.0000_5$
20	...	144.12_5	(-0.16_5)[c]	143.96	...	143.93_5	$(+0.02_5)$[c]	143.96	$3.6223_5 \pm 0.0000_5$

[a] Radiation, Cu$K\alpha_1$; KVP, 50; ma, 16; beam slit, none; detector slit, 0.2°; Soller slit, none; spinner speed, 150 rpm; temperature, 24±1°C; time constant 22.8 sec. 2θ determined from CG (cf. Table II).
[b] $\Delta 2\theta = 2\theta_- - 2\theta_+$.
[c] By extrapolation.

range quoted applies to an arrangement using a Siemens curved quartz crystal monochromator (Johansson focusing) bent elastically to a radius of 25 cm, and a beam slit at the focus to cut off the $K\alpha_2$ component. The monochromator was attached to the x-ray tube to facilitate alignment, though greater flexibility[6] could have been obtained by placing the monochromator between the specimen and counter tube.

III. RECORDING OF THE DATA

Certain experimental conditions that influence the shape and position of the recorded line profile were examined in order to determine their effect, if any, on the mean position of the line. X rays generated by 50 KVP were used throughout.

A. Direction of Scanning

This is, as it should be, immaterial, provided of course that the direction for any particular run is always the same. Due to the finite scanning rate and time constant of the recording circuit, there is a slight displacement from the true peak position, but this is canceled out when taking the average of the "positive" and "negative" readings, provided both are obtained with the detector moving in the same direction (clockwise or counterclockwise).

B. Rate of Scanning

This is also immaterial within certain limits that are difficult to define, but depend on (a) the grain size of the specimen, (b) the speed of rotation of the specimen, and (c) the time response of the recording instrument. Virtually identical line profiles were obtained with scanning speeds of 10 min and 25 min per deg 2θ, when the specimen was rotated at 150 rpm. The average diameter of the grains in the specimen was 0.15 mm (and ranged from 0.1 to 0.55 mm). Table I shows that the averaged or corrected line positions remain unaffected. When the scanning speed was increased to 0.5 min/$2\theta°$, a noticeable loss in peak intensity was observed. A reduction in the spinning speed of the specimen to 100 rpm resulted in poor line profiles for an aluminum wire with grains 2–3 mm in diameter.

C. Slit Arrangement

Normally, any of the available beam and receiving slits can be used; their choice will be dictated by a compromise between resolution and recorded intensity. With the monochromator, only the 0.2° receiving slit was employed in order to have a reasonable working intensity. This ranged from a minimum of 40 cps up to about 1200 cps (including a background of 5–10 cps), the latter value corresponding to the most intense diffraction peak from the largest specimen, using a No. 2 proportional counter tube. When no great resolution is required, as with simple single-phase cubic metals and alloys for which all the diffraction peaks are well separated, the 0.2° receiving slit is perfectly adequate.

Soller slits limit both the vertical and horizontal divergence of the x-ray beam, and in the low-angle region this can have a significant effect on the line position, as Table II illustrates. The effect of vertical divergence is the only one that cannot be eliminated by the standard extrapolation techniques[7] and has been treated theoretically by a number of investigators, the most detailed and recent being by Pike.[8] He showed that for the case of one set of Soller slits approaching zero aperture ($q=0$ in Pike's notation), the correction for vertical divergence becomes simply $(h^2/6R^2)\cot 2\theta$, where R is the SPG radius and h is the height of the beam, assumed constant from source to receiving slit. Now with a monochromator this condition could be met

---

[6] Such as the examination of specimens that fluoresce with the chosen radiation (though frequently the effect of the fluorescent radiation can be suppressed with a pulse-height analyzer).

[7] W. Parrish and A. J. C. Wilson, *International Tables for X-Ray Crystallography*, edited by J. S. Kasper and K. Lonsdale (Kynoch Press, Birmingham, England, 1959), Vol. 2, p. 216.

[8] E. R. Pike, J. Sci. Instr. **34**, 355 (1957); **36**, 52 (1959).

TABLE II. Effect of Soller slits on line position and line symmetry. Alignment A. SPG speed, 10 min/deg 2θ; aluminum and CuSi(Mn) specimens, 3 mm in diameter. Other data as in Table I.

A. Principal measurements.			Center of gravity				Peak position			
		Line	$2\theta_-$	$2\theta_+$	$\frac{1}{2}\Delta 2\theta$	$\langle 2\theta \rangle$	$2\theta_-$	$2\theta_+$	$\frac{1}{2}\Delta\theta$	$\langle 2\theta \rangle$
Without Soller slit (WOS)	Al	3	39.37	39.60	-0.11_5	39.48_5	39.42_5	39.62	-0.10	39.52
		4	45.60	45.83	-0.11_5	45.71_5	45.64	45.84	-0.10	45.74
	Cu−6.6 Si	20	···	144.11_5	···	···	···	144.11_5	···	···
With MR Soller slit (WS) in front of detector slit	Al	3	39.45	39.67	-0.11	39.56	39.48_5	39.66_5	-0.09	39.57_5
		4	45.66_5	45.88_5	-0.11	45.77_5	45.69	45.88_5	-0.10	45.79
	Cu−6.6 Si	20	···	(144.10)[b]	···	···	···	144.10	···	···

B. Difference values from part A.

	$2\theta_{\mathrm{WOS}}-2\theta_{\mathrm{WS}}$		$2\theta_{\mathrm{CG}}-2\theta_{\mathrm{PP}}$	
2θ	CG	PP	WOS	WS
39.5	-0.07_5	-0.05_5	-0.03_5	-0.01_5
45.7	-0.06	-0.05	-0.02_5	-0.01_5
144	(0.01_5)	$+0.01_5$	0.00[a]	···

[a] Also zero for line 8 (74°) and higher. [b] Estimated: complete line not recorded.

to a certain extent, since introduction of the HR (high resolution) Soller slit between the specimen and the monochromator did not affect the position of the center of gravity (CG) of the line profiles, thus indicating that the monochromator gave an almost, if not actually, parallel beam. Hence, in principle Pike's equation for $q=0$ could be used to correct for the vertical divergence between the specimen and receiving slit. Since no simple independent experimental verification of this equation could be obtained, illustrative data given here were not corrected for vertical divergence.

D. Effect of SPG Alignment

This is illustrated in Table I, where data are presented for two alignments, A and B; the SPG was moved a small distance in changing alignment from A to B. The 2θ zero correction ($\frac{1}{2}\Delta 2\theta$ column) is different for the two alignments, but the corrected 2θ is the same in both cases. The alignment, therefore, is not critical.

The correction factor $\frac{1}{2}\Delta 2\theta$ is not necessarily constant, and may vary linearly with 2θ. (The slope of the line for $\frac{1}{2}\Delta 2\theta$ vs 2θ is the same for both sets of values A and B in Table I, though the actual corrections, $\frac{1}{2}\Delta 2\theta$, are not.) This variation is probably due to a nonuniform intensity distribution across the width of the crystal monochromated beam, accentuated by absorption in the specimen.

E. Effect of Counter Tube

Two counter tubes with different quenching media were tried, and both gave the same results. According to the manufacturer's data, tube No. 2 (krypton at 650 mm Hg) is only slightly more efficient (77% vs 69%) than tube No. 1 (argon at 650 mm Hg) at the Cu$K\alpha_1$ wavelength, but appreciably more efficient (85% vs 19%) at $\frac{1}{2}\lambda$Cu$K\alpha_1$. At $\frac{1}{4}\lambda$Cu$K\alpha_1$, the efficiency of tube No. 2 is also greater (27% vs 4–15%). Though the monochromated beam contained these (and other) harmonics, the same line position (CG) was obtained with either counter tube. If the harmonics were present to any large extent this would not be expected necessarily, since the observed line position depends to a certain extent on absorption in the specimen, and this in turn is a function of the wavelength.

IV. EVALUATION OF THE LATTICE PARAMETER

The important factor here is the measurement of the line position from the recorded profile, and two alternative criteria are available for determining this position. One is to measure the peak of the line profile and the other is to measure its CG. The former is easier and quicker, but the latter is a more tractable quantity in theoretical calculations.[7] When the line profile is symmetrical, the two criteria naturally yield the same value for the line position. This is generally the case when 2θ is 70° or more. Table II shows the difference in values for two low-angle lines which are rendered asymmetrical by absorption, and the geometry of the x-ray paths. The difference between the peak position and CG is decreased by reducing the vertical divergence, an expected consequence of the attendant greater line symmetry.

A frequently troublesome feature in measuring the CG of unsymmetrical line profiles is the sensitivity of the measurements to the tails of the profiles, especially if these tails are long. With the exception of the data in Fig. 3, all the results presented in this paper were obtained from specimens yielding comparatively sharp lines, which normally have short tails and permit determination of the CG to within $\pm 0.005°2\theta$.

In the data given below as examples, the CG has been measured, because the value of a_0 obtained from it gave a straight line in the plot of a_0 vs the Nelson-Riley function (NRF).[9] Values of a_0 obtained from the peak position gave a straight line only for the points from the higher angles; for the low angles the values of a_0 fell below the line.

---

[9] J. B. Nelson and D. P. Riley, Proc. Phys. Soc. (London) **57**, 160 (1945).

V. ILLUSTRATIVE RESULTS

Several materials were examined using the Cu$K\alpha_1$ radiation ($\lambda = 1.54050$ A) and specimens ranging in diameter from $\frac{1}{2}$ to 3 mm. The width and height of the beam, as viewed on a fluorescent screen at the specimen location, were about $3\frac{1}{4}$ mm and 15 mm, respectively. The effective diameter of the SPG is 291.1 mm (11.46 in.; circumference 36.00 in.). The temperature of the whole room was maintained continuously (24 hr a day) at 24 ± 1°C.

In all cases the complete line profile was recorded on a chart and simultaneously counts were also recorded at preset intervals on a digital printer. Except for the low intensity and/or very broad lines, the CG was determined to $\pm 0.005° \; 2\theta$ directly from the charts. (This is well within the manufacturer's stated accuracy for the SPG of $0.002° 2\theta$.) The only correction applied prior to plotting a_0 against the NRF was one arising from a small but measurable misalignment of the specimen and SPG axis.

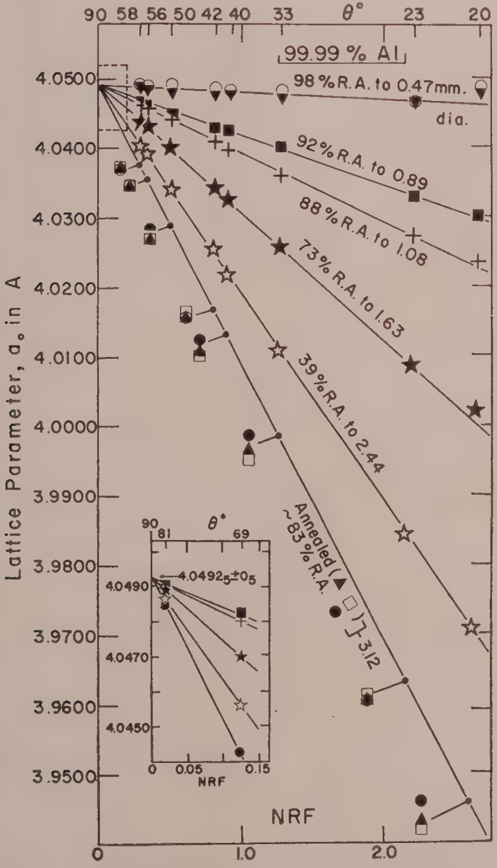

FIG. 1. Effect of specimen diameter and deformation on the extrapolated lattice parameter for aluminum (99.99% pure). Inset is a 5X enlargement of the region (indicated by a set of broken lines) at the extrapolation point. R.A. = Reduction in Area of wire by drawing through a die at room temperature. NRF $= \frac{1}{2}[(\cos^2\theta/\sin\theta) + (\cos^2\theta/\theta)]$.

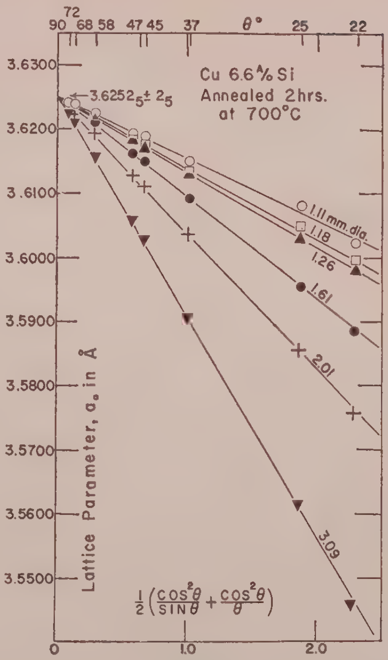

FIG. 2. Effect of specimen diameter on the extrapolated lattice parameter for a commercial Cu−6.6 at. % Si (1.2 at. % Mn) alloy. All specimens annealed 2 hr at 700°C and air cooled in evacuated capsule.

Figure 1 shows a set of lines for aluminum specimens of different diameter and different amounts of deformation (given at room temperature). All lines extrapolate to the same value (4.0492_5 A) within $\pm 0.0000_5$ A. For the smallest-diameter (0.47 mm) specimen, the intensity of all reflections was rather low (less than 100 cps), and a noticeable scatter of the points was obtained. Extrapolation is unreliable, but a straight line drawn through all the points extrapolated reasonably close to the others. Aluminum filings (both annealed and as cold worked) compacted with Duco cement into rods 2 mm in diameter gave an extrapolated value of $a_0 = 4.0492 \pm 0.0000_5$ A, in good agreement with that obtained from the solid specimens, Fig. 1.

Similar data for a commercial Cu−6.6 at. % Si alloy (containing 1.2 at. % Mn) are shown in Fig. 2. Though all specimens were given the same annealing treatment (in evacuated Vycor tubes of equal size) agreement between the extrapolated lattice parameter for various diameters was only within $\pm 0.0002_5$ A, not as good as for the aluminum. No clear trend with specimen size could be detected, though it might have possibly existed. The apparently larger scatter for the

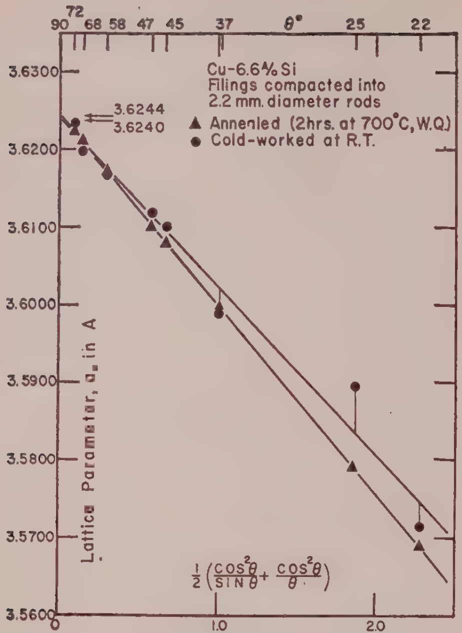

FIG. 3. Lattice parameters for filings before annealing (as "cold worked") and after annealing for a commercial Cu−6.6 at. % Si (1.2 at. % Mn) alloy. WQ=water quenched.

alloy could be due to the fact that the closest experimental points are not as near to the extrapolation point as for the aluminum, or it may be a real effect in this material. The latter possibility was examined further by measuring filings before and after annealing as for the aluminum. Figure 3 discloses that deforming (at room temperature) causes an appreciable "scatter" of the points due to the formation of stacking faults, but that even after annealing, the extrapolated lattice parameter (3.6244 A) is still appreciably lower than for the solid samples, in marked contrast to the observations on aluminum. Similar discrepancies obtained for a number of other alloys are given in Table III.

VI. DISCUSSION

Consideration will first be given to the precision and accuracy of the present data. Possible reasons for the variations in lattice constant of the alloys will then be discussed. One of the main conclusions to be reached is that differences in solute clustering, arising presumably from differences in cooling rate, may be the most important variable affecting the lattice constant of single-phase alloys.

A. Precision and Accuracy of Measurement

The extent to which the extrapolation method affects the value of a_0 depends to a certain degree on how close the last measured point falls to the extrapolated value, on the slope of the extrapolation line, and on the particular extrapolation function employed. As may be seen from Figs. 1 and 2, the widely used NRF is satisfactory in the present circumstances since a

TABLE III. Extrapolated lattice parameter a_0 (in A) at 24±1°C ($\lambda=1.54050$ A).

	Solid specimens			Filings[l]	
Material[a]	Heat treatment[e]	Diameter (mm)	a_0, A[g]	Heat treatment[e]	a_0, A[g]
Al (99.99%)	65.5 hr at 250°C, AC +31 hr at 300°C, AC	3.12	$4.0492_5\pm0_5$[h]	30 min at 600°C, WQ	4.0492
Cu (*OF HC*)	1 hr at 700°C, AC	2.07	$3.6150_5\pm1$	1 hr at 700°C, AC	3.6149_5
Cu−6.6 Si (1.2 Mn)[b]	2 hr at 700°C, AC	3.09 (largest)	$3.6252_5\pm2_5$[i]	2 hr at 700°C, WQ	3.6244
	406 hr at 900°C+19.5 hr at 700°C, AC	2.67	$3.6252_5\pm1$		
Cu−15 Al	2 hr at 750°C, WQ	2.90	$3.6535\pm0_5$	2 hr at 750°C, WQ	3.6534
	2 hr at 750°C, cooled at 11°C/hr[f]	1.63 to 1.82	$3.6536_5\pm0_5$[j]		
Cu−30 Zn[b]	1 hr at 700°C, AC	3.14	3.6827 ± 1	1 hr at 700°C, AC	3.6822
	406 hr at 900°C+19.5 hr at 700°C, AC	3.13 and 2.20	3.6826 ± 2[k]	10 min at 300°C, AC	3.6824
Cu−35 Zn[b]	2 hr at 450°C, WQ	2.55	$3.6948\pm0_5$	2 hr at 450°C, WQ	3.6940
Ag−25 Zn[c]	1 hr at 700°C, WQ	2.95	$4.0393\pm1_5$	1 hr at 700°C, WQ	4.0401
Al−1.8 Mg[d]	1 hr at 450°C, WQ	2.70	$4.05865\pm0_5$	1 hr at 450°C WQ	4.0576_5
Al−1.7 Zn[d]	1 hr at 450°C, WQ	2.69	$4.0485\pm0_5$	1 hr at 450°C, WQ	4.0485

[a] Composition in at. %.
[b] Commercial alloys.
[c] Specimens from T. B. Massalski, Mellon Institute.
[d] Specimens from M. E. Fine's group, Northwestern University.
[e] All specimens heat treated in evacuated and sealed Vycor capsules (4 mm i.d., 6–10 cm long) and not removed from capsule until room temperature was reached (vacuum better than 10^{-3} mm Hg). AC, air cooled; WQ, water quenched.
[f] Heat treatment by M. S. Wechsler, Oak Ridge National Laboratory, from whom other specimens were also obtained.
[g] Except where indicated otherwise, only one specimen measured; given any one specimen, extrapolated value is within $\pm0.0000_5$ A for filings and up to ±0.0002 A for solid specimens, depending on degree of preferred orientation in the specimen.
[h] Cf. Fig. 1.
[i] Six specimens; cf. Fig. 2.
[j] Four specimens; all four showed evidence of marked preferred orientation.
[k] Preferred orientation quite severe.
[l] Filings compacted (with Duco cement) into rods 2.2 mm in diameter after heat treatment.

straight line may be drawn through all the points, and all the lines meet at NRF=0.

The slope of the a_0-NRF graph is principally a function of the absorption of the x-ray beam by the specimen, and this in turn is directly related to specimen diameter. The slope is also proportional to a_0; to compare data from different materials, the slopes should therefore all be reduced to the same a_0. The effect of doing this in Fig. 4 is to reduce the spread of the lines. Figure 4 shows that when the slope of the graph is plotted against the specimen diameter, not only for Al and the Cu-Si-Mn alloy studied, but for other materials that have been examined, the resulting line does not pass through the origin.[10] This may be partly a consequence of employing x rays generated by 50 KVP, and thus containing several harmonics that are not eliminated by the monochromator. Correcting for vertical divergence raises all the lines in Fig. 4 and thus causes them to pass nearer the origin. The correction required to make all lines pass exactly through the origin is considerably greater than would appear reasonable, and further investigation of this effect seems desirable. However, Fig. 4 stresses that considerable caution must be exercised in determining the lattice constant by extrapolating to zero diameter from plots of a_0 (calculated from a chosen reflection) vs the specimen diameter, as suggested by Pines and Kaluzhinova.[11]

A precision in the extrapolated value of a_0 is frequently claimed[12] for film techniques which is higher than quoted here. This is in general to be questioned. One necessary condition stipulated in the film techniques is that measurements be confined only to samples which give very sharp diffraction lines, so that errors in placing the hairline visually over the diffraction profile on the film are minimized. Not only is this a restricting condition, but it is furthermore uncertain what particular property of the profile is measured in this way.[13] Though the peak position can in practice be measured more precisely than the CG, it is unfortunately sensitive to the intensity distribution in the primary beam.

In order to obtain absolute values of the lattice parameters, proper corrections must be made for the vertical divergence and for refractive index. Both of these corrections are positive, and when applied would make the values of a_0 reported here larger possibly by as much as two or three parts in 10^5, with the major contribution coming from the correction for vertical divergence. Consequently the value of a_0 for aluminum reported here is, as expected, on the low side when compared with published values.[14] However, it has also been pointed out[15] that Johansson focusing monochromators always distort the wavelength distribution of the incident characteristic radiation. The effect may be large enough to cause an error of several parts in 10^4 in the value of a_0, and depends principally on the exact position of the crystal on the focusing circle and on the perfection of the crystal itself. Nevertheless the value of a_0 (not corrected for refraction) for aluminum differs from the accepted value, $4.0493_5 \pm 1$ a.u. at 24°C[14] by less than 0.01%, the limit of agreement found between different investigators in an international project.[16] Similarly for copper, agreement with the accepted value of $3.6149_5 \pm 1$ A at 24°C[15] is good.

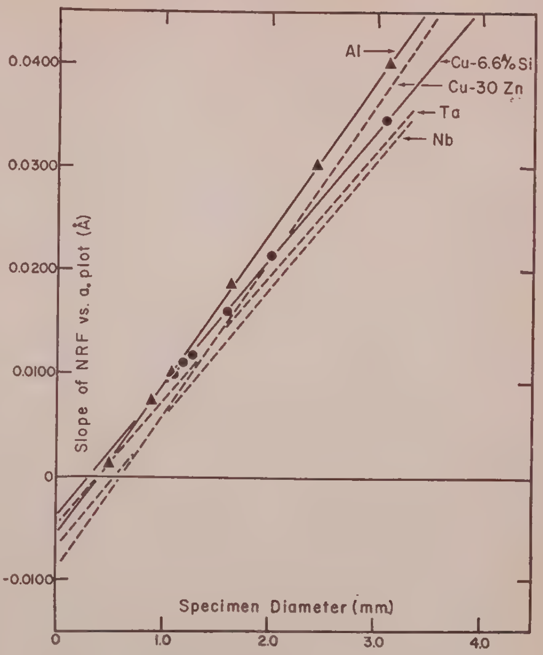

FIG. 4. Effect of specimen diameter on the slope of the straight line in the Nelson-Riley plot.

B. Effect of Plastic Deformation

Contrary to the recent work of Straumanis,[17–19] the lattice parameter of pure aluminum was found to be independent not only of the specimen diameter, but also of its physical condition. Metallographic examination showed that the aluminum used in the present work recrystallized between 250°–300°C, and thus was measured in the deformed state as indicated in Fig. 1.

---

[10] In some early data on the Cu-Si-Mn alloy, the line did pass through the origin and was a little steeper, though the extrapolated a_0 values were virtually the same as in Fig. 2. No explanation for the discrepancy has been found.

[11] B. Ya. Pines and N. V. Kaluzhinova, Zhur. Tekh. Fiz. 24, 320 (1954).

[12] M. E. Straumanis and A. Ievins, *The Precision Determination of Lattice Constants by the Asymmetric Method* (Julius Springer, Berlin, 1940). Translation of part by K. E. Beu (Goodyear Atomic Corporation, Portsmouth, Ohio, 1959), Tech. Springer Verlag, Publ. GAT-T-643.

[13] E. R. Pike and A. J. C. Wilson, Proc. Phys. Soc. (London) 72, 908 (1958).

[14] W. B. Pearson, *Handbook of Lattice Spacings and Structures of Metals and Alloys* (Pergamon Press, New York, 1958), p. 312.

[15] J. Cermak, Czechoslov. J. Phys. Prague **B10**, 215 (1960); Acta Cryst. **13**, 832 (1960).

[16] W. Parrish, Acta Cryst. **13**, 838 (1960).

[17] M. E. Straumanis, J. Appl. Phys. **30**, 1965 (1960).

[18] M. E. Straumanis and T. Ejima, Acta Met. **8**, 56 (1960).

[19] M. E. Straumanis, Acta Cryst. **13**, 818 (1960).

For cold-drawn (amount not reported) aluminum wires, of the same purity as in the present work, Straumanis[17] obtained values for a_0 of 4.0480 A and 4.0489 A,[20] depending on whether measurements were perpendicular or parallel to the axis of the wire, respectively. Both these values are on the low side, even when corrected for temperature,[20] and as in this investigation were not obtained by linear extrapolation. In Straumanis' other paper,[18] the values of a_0 (given for 25°C) are closer to those generally quoted in the literature,[14] but no extrapolation curves were presented.

Figure 3 shows that plastic deformation may affect the lattice parameter under certain conditition, principally in alloys where ordering and stacking faults play an important role.

C. Effect of Residual Stresses

Whereas in filings, a change in a_0 may be attributed directly to the effect of imperfections introduced by plastic deformation (Fig. 3, for example), in the case of solid specimens the possibility of macroscopic residual elastic strains must also be considered.

The results on the aluminum showed no evidence that residual elastic strains in the deformed bulk specimens were affecting the lattice parameter. This is contrary to observations summarized by Greenough[21] and made by other investigators who did, in general, find changes in lattice parameters of cold-rolled aluminum sheets. The x-ray techniques were based on back-reflection Laue methods for which the results are difficult to interpret because of the highly selective conditions whereby grains contribute to a reflection.

D. Effect of Quenching Stresses

The difference between a_0 for the filings and for the solid specimens, found in most of the alloys (Table III), might be attributed possibly to quenching stresses. The quenching process as generally visualized[22,23] in a bulk cylindrical sample would be expected to give rise to radial tensile stresses (in addition to the longitudinal compressive stresses) which are zero at the free surface, but reach a maximum at the axis of the cylinder. Due to the finite penetration of the x-rays, and since the present method would be principally sensitive to the radial strain component, with possibly a small contribution from the tangential component, it follows that a_0 for the solid specimen should be larger than for filings in which quenching stresses are supposed to be negligible.[24]

Though this explanation may appear valid for the Cu-Si-Mn and Cu-Zn alloys, it cannot explain the observation of the reverse effect in the Ag-Zn alloy, or the very small effect in the Cu-Al alloy (Table III).

In addition, the lattice parameters of specimens from both the Cu-Si-Mn and the Cu-Zn alloys were remeasured after 0.2 to 0.5 mm had been removed from the surface by electrolytic polishing. No change in a_0 could be detected at any stage. If quenching strains had been present, they would have been reduced in the remaining portion of the specimen after polishing, and a decrease in a_0 should have been noted.

An explanation in terms of quenching stresses (respectively quenching strains) is thus not tenable, though observations reported in the literature of similar effects in Al-Cu and Al-Mg alloys, for example,[25,26] cannot always be dismissed as readily. Frequently the possibility of alloying losses during heat treatment is present,[25,26] and in some of the older literature it is difficult to eliminate as an alternative cause of lattice parameter variation. This aspect in the present work will be considered next.

E. Effect of Alloying Losses

All the observations in Table III might conceivably be interpreted as due to a larger quantity of alloying losses in the filings than in the bulk specimens. It will be shown that this is not possible. Losses through oxidation would have to be due to the small amount of oxygen present at a pressure below 10^{-3} mm Hg, in a volume less than 1 cc. Assuming the formation of the most stable oxides and allowing for some occluded oxygen in the case of filings, it is a simple matter to calculate that the alloying losses for any of the cases in Table III could not exceed 0.01% to a depth of 2×10^{-5} cm for the solid specimens, neglecting diffusion from the interior, tending to compensate the loss. For filings this would probably be less due to the considerably larger surface area. In the most extreme case this would correspond to a change in a_0 of about 0.0000_5 A, the limit of accuracy, provided the penetration of the x-ray beam does not exceed the depth of 2×10^{-5} cm. Since the effective penetration of the x-ray beam is at least an order of magnitude greater, it follows that possible alloying losses are too small to account for the data in Table III.

For the Cu-Zn alloy a batch of (cold-worked) filings was split into two parts which were given heat treatments, as indicated in Table III. Both the high (700°C) and the low (300°C) temperature heat treatment yielded nearly the same a_0 (Table III). Also, the small affect in the Cu-Al alloy shows that interpretation of the difference in a_0 between the filings and the solid specimens in terms of alloying losses is a sufficiently remote possibility in the present cases as to be considered unlikely.

---

[20] Temperature not stated, but presumably 20°C, as for the measurements on wolfram reported in the same paper.

[21] G. B. Greenough, Progr. in Metal Phys. **3**, 176 (1952).

[22] B. H. Kear and P. L. Pratt, Acta Met. **6**, 457 (1958).

[23] W. M. Baldwin, Jr., Proc. ASTM **49**, 1 (1949).

[24] Alternately, a larger a_0 for the solid specimens may be expected on the basis that the radial strain near the free surface will be increased due to the compressive longitudinal and tangential stresses.

[25] A. Phillips and R. M. Brick, Trans. AIME **111**, 94 (1934).

[26] R. M. Brick, A. Phillips, and A. J. Smith, Trans. AIME **117**, 102 (1935).

F. Effect of Particle Size

When the predominant size of the particles is below 10^3 A, line broadening becomes apparent and differences in cell dimensions from those of larger particles have been reported.[15] However, in the present work no broadening due to this effect has been observed in the spectrum from the filings. Furthermore, optical inspection showed that the particle sizes not only varied considerably but in all cases were larger than 5 μ in diameter.

G. Effect of Stacking Faults and Degree of Short-Range Order

Stacking faults may occur in pure metals as well as in alloys. Their precise effect on the lattice parameter has not as yet been investigated. Figure 3 shows that stacking faults may possibly have a small effect on the lattice parameter. Since, in fcc metals, stacking faults cause line shifts (as well as line broadening), the interpretation is not straightforward. In bcc and hcp materials stacking faults do not produce line shifts,[27] and the effect could be studied more directly in those cases. It is therefore not possible to say whether the scatter in extrapolated lattice parameters of the Cu-Si-Mn alloy (Fig. 2) might be associated with stacking faults either incompletely removed on annealing the cold-drawn rods, or perhaps formed in small quantity during cooling. The total faulted area would in any case be reduced to below that detectable by the x-ray method, and it is questionable whether stacking faults could be responsible for the differences in a_0 between filings and the solid specimens.

Increase in short-range order would lead to a decrease in a_0,[28] and this could conceivably be the interpretation for the Ag-Zn alloy, since the solid specimen would be expected to cool less rapidly in the capsule than the filings and thus have more short-range order. However, the reverse effect in the Cu-Zn alloy could not be explained. Furthermore, in the Cu-Zn alloy, up to several hours at temperatures between 125°–190°C are required to detect any appreciable change in a_0 due to changes in degree of short-range order.[29] For the Cu-Si-Mn alloy an interpretation in terms of short-range order would not be likely.

H. Solute Segregation

No evidence for solute segregation was obtained. The possibility of having nonuniform distribution of alloying elements in the solid specimens was checked in two ways. Material from the surface was removed by electrolytic polishing, and a_0 was redetermined. The lattice parameter was also measured after a long-term anneal (Table III). In neither case was any change in a_0 detected.

I. Effect of Lattice Defects

The dilatation due to dislocations in any reasonable number is extremely small and almost certainly too small for measurement with x rays with the present precision.[30] Thus the differences in a_0 of Table III are not likely to be caused by even large variations in the number of quenched-in dislocation loops.[31]

Point defects may affect the lattice parameter[30,32,33]; estimates indicate, however, that in the case of vacancies to produce even 0.0001 A difference in a_0, unreasonably large differences in vacancy concentration between the filings and the solid specimens would have to be postulated. Furthermore, the same effect should be observed for all the alloys, irrespective of whether the solute atom increases or decreases the lattice parameter of the solvent atom lattice.

J. Solute Clustering

Although none of the alloys examined (Table III) are supersaturated at room temperature according to the accepted phase diagrams,[34] estimates based on the approximate extrapolation to room temperature of the appropriate phase boundary, place all the alloys close to such a boundary. Pre-precipitation phenomena, or solute clustering, may possibly therefore occur in these alloys. The present accumulation of evidence for solute clustering is based largely on studies of the decomposition of supersaturated solid solutions of binary aluminum alloys.[35–38] Solute clustering is thought to occur subsequent to and even during quenching from high temperatures and to be strongly dependent on the vacancy concentration; it is hence strongly dependent on the cooling rate and to some extent dependent on the alloy composition and quenching temperature.

---

[27] B. E. Warren, Progr. in Metal Phys. **8**, 147 (1959).

[28] G. J. Dienes, Acta Met. **6**, 278 (1958).

[29] R. Feder, A. S. Nowick, and D. B. Rosenblatt, J. Appl. Phys. **29**, 984 (1958).

[30] R. O. Simmons and R. W. Balluffi, J. Appl. Phys. **30**, 1249 (1959).

[31] See, for example, D. Kuhlmann-Wilsdorf & H. G. F. Wilsdorf, J. Appl. Phys. **31**, 516 (1960).

[32] J. D. Eshelby, Solid State Phys. **3**, 79 (1956).

[33] R. W. Balluffi and R. O. Simmons, J. Appl. Phys. **31**, 2284 (1960).

[34] M. Hansen, *Constitution of Binary Alloys* (McGraw-Hill Book Company, Inc., New York, 1958).

[35] J. Dash and M. E. Fine, Acta Met. **9**, 149 (1961).

[36] R. B. Nicholson, G. Thomas, and J. Nutting, J. Inst. Metals **87**, 429 (1959).

[37] C. Panseri and T. Federighi, Acta Met. **8**, 217 (1960).

[38] D. Turnbull, H. S. Rosenbaum, and H. N. Treaftis, Acta Met. **8**, 277 (1960).

TABLE IV. Additional number of clustered solute atoms in filings compared with solid specimen, calculated from difference in lattice parameter.

Alloy	Change, in a_0 per unit at. % element, A[a]	Difference[b] $(a_0)_s-(a_0)_f$ (A) (from Table III)	Corresponding change Δc in composition at. %	Number of atoms per cc in clusters corresponding to Δc
Cu Si Mn	0.0006_8 Si	0.0008	1.25	1.07×10^{21}
	0.0036_7 Mn		0.2_2	1.85×10^{20}
Cu Al	0.0025_5 Al	0.0001	0.0_4	3.3×10^{19}
		0.0002_5	0.1_0	8.2×10^{19}
Cu Zn (30)	0.0022_7 Zn	0.0005	0.2_2	1.76×10^{20}
Cu Zn (35)	0.0022_7 Zn	0.0008	0.3_5	2.77×10^{20}
Ag Zn	-0.0018_5 Zn	-0.0008	0.4_2	2.54×10^{20}
Al Mg	0.0039 Mg	0.0010	0.2_6	1.53×10^{20}
Al Zn	-0.0007 Zn	0.0000	0.0	?

[a] Calculated from reference 14.

[b] $(a_0)_s$ and $(a_0)_f$ are the a_0 values for the solid specimen and filings, respectively, as given in Table III.

Of interest in the present case is principally the dependence of clustering on cooling rate. Increasing the quenching rate increases the concentration of vacancies retained in solution at low temperatures and in turn increases the clustering rate as the vacancies anneal out or precipitate. In using these ideas to interpret the results of Table III, it is supposed that in sealed Vycor tubes cooled under similar conditions, filings will reach the ambient temperature before a solid specimen will, so that the amount of clustering (during quenching and during the period prior to making the x-ray measurements) may be greater in filings than in bulk samples. This would be reflected in a change of lattice parameter corresponding to the loss of solute atoms to the clusters, provided the clusters make an insignificant contribution to the change in a_0.[39]

The data of Table III have been examined in the light of the preceding possibility. The additional number of clustered solute atoms in the filings compared with the solid specimen were calculated from the difference in lattice parameter as in Table IV. If Δc=the difference in concentration (expressed as an atom fraction) of solute atoms deduced from the difference in a_0 between the solid and the filings, then the number of solute atoms in clusters per cc is given (for the fcc structure) by the expression

$$4\times10^{24}\Delta c/(a_0)^3,$$

where a_0 (in A) may be taken as the value for the solid specimen. The last column in Table IV gives the extra number of clustered solute atoms per cc in the filings. The value for Si in the Cu-Si-Mn alloy is rather high, and suggests that the effect is principally due to the clustering of Mn. If the average cluster contains between 10 and 10^3 solute atoms, then the number of clusters is between 10^{16} and 10^{19} per cc. For Al alloys the density has been estimated to be between 10^{17} and 10^{18} per cc.[36]

This interpretation would also suggest that a definite trend in the value of a_0 with specimen diameter should really exist for the Cu-Si-Mn alloy. The failure to detect such a trend (Fig. 2) may be due to the fact that under the given conditions the difference in cooling rate between a 1-mm diam and a 3-mm diam rod is of the same order of magnitude as the differences in the reproducibility of the cooling rate. With the cooling rate more rigidly controlled, the effect of specimen diameter on a_0 may well be detectable.

The interpretation of the present data (Table III) in terms of solute clustering has to be examined with regard to the belief that short-range ordering occurs in these alloys,[29,40–42] since in solute clustering the number of like bonds is considered to be greater than in a random solution, whereas in short-range ordering the reverse is the case (i.e., the number of unlike bonds is greater than in a random solution). Theories incorporating the possibility that both phenomena can occur, but under different conditions, have been proposed.[43] However, for none of the alloys examined is there any good direct evidence for the occurrence of short-range order. In Cu−30Zn, short-range order was looked for with neutron diffraction,[44] but the results were quite inconclusive. For the Cu−15Al alloy, solute clustering was indicated by a theoretical analysis of relaxation effects,[41] and also by some observations of x-ray low-angle scattering[45]; yet x-ray diffuse scattering was attributed to short-range order.[46] Relaxation effects for Ag−(10–30%)Zn alloys showed considerable discrepancies when interpreted in terms of short-range order.[41] Evidence that short-range ordering occurs in the alloys studied here is thus not at all well established. However, a possibility worth exploring further is the formation in certain cases of clusters that consist of regions in which the degree of short-range order is high and where even an appreciable amount of long-range order exists, because the composition is locally stoichometric (perhaps AB rather than A_3B). This situation might prevail where the tendency to ordering becomes strong only at relatively low temperatures. If the tendency to ordering is already pronounced at higher temperatures where the atomic mobility is greater, then the degree of ordering obtained by the speculated clustering mechanism would be considerably less than that possible by a slow cool. The fact that ordering can occur by more than one mechanism has been clearly demonstrated for the AuCu alloy by Smith and Bowles.[47] For the remainder of the discussion, however, no specific assumptions will be made about the constitution of the clusters.

---

[39] On the basis of a simple elastic-sphere-in-hole model,[32,33] a small effect from the clusters might be expected, analogous to that obtained from vacancies as mentioned in Sec. I. If the solute atom is larger than the solvent atom, then association of vacancies and solute atoms in the clusters could be accommodated with negligible strain. However, if the substitutional solute atom is smaller, then the clusters will in general produce a dilatation in the same sense as that resulting from the matrix solute depletion (to the clusters). When all the change in a_0 is now attributed solely to the loss of solute atoms to the clusters, this loss will appear larger than it actually is.

[40] B. G. Childs and A. D. Le Claire, Acta Met. **2**, 718 (1954).

[41] A. D. Le Claire and W. M. Lomer, Acta Met. **2**, 731 (1954).

[42] L. M. Clarebrough, M. E. Hargreaves, and M. H. Loretto, Proc. Roy. Soc. (London) **A257**, 326, 338, 363 (1960).

[43] R. R. Hasiguti, J. Japanese Inst. Metals **19**, 103 (1955).

[44] D. T. Keating, Acta Met. **2**, 885 (1954).

[45] R. W. Cahn and R. G. Davies, Phil. Mag. **5**, 1119 (1960).

If the lattice parameter decreases with increasing solute element, as for Ag-Zn, then changing the cooling rate will not distinguish between ordering and clustering. However, if the reverse is the case, as for the Cu alloys examined here, then it should be true that for

ordering: Δa is negative,
clustering: Δa is positive,

where $\Delta a = a_0$ (slow cool)$-a_0$ (fast cool). The present data (Table III) are consistent with such a condition and suggest that it may be quite general.[48] Thus in a solid solution system for which there is good evidence that ordering occurs over a certain composition range, it may be possible to detect a reversal of sign in Δa as the composition is changed. A system which satisfies the requirements for observing the proposed effect is the Ni-rich Ni-Fe system. The existence of ordering in the composition range 20–25 at. % Fe, about Ni_3Fe, is well established,[34] and in addition a_0 increases with increasing Fe content. Fortunately also reliable data[14,49] are available for the effect of cooling rate on a_0. Comparison of a_0 for filings water quenched from 900°C and filings cooled from 900°C to room temperature in 3 days does indeed show that up to about 17 at. % Fe, Δa is positive, indicative of clustering and from 17–50 at. % Fe, Δa is negative, consistent with ordering, though the actual magnitude of Δa shows appreciable fluctuations. The investigators[49] noted that the effect of quenching temperature in the range 700°–900°C was comparatively unimportant, but that the cooling rate was of vital importance. In the absence of any suitable explanation they suggested that the way in which the alloy cooled through the Curie point (350°–600°C for the various alloys) may be a controlling factor. The reversal of Δa at about 17 at. % Fe is clearly difficult to explain on such a basis, since the curve of Curie temperature vs composition shows a temperature maximum at about 34 at. % Fe but no other inflections or discontinuities. A Ni−10% Al alloy, which lies close to the limit of the primary solid solution and has a considerably lower Curie temperature (about 100°C) also shows a positive Δa,[14,50] indicative of clustering. More extensive comparison is not possible since considerable confusion exists about the ordering of the Ni_3Al phase.[14]

VII. CONCLUSIONS

For certain types of problems the accurate determination of lattice parameters by the Debye-Scherrer film technique becomes virtually impossible. This is particularly true when extremely broad diffraction lines from deformed metals are encountered or when measurements on thick wire specimens (as used for resistivity work or mechanical testing) are desired. It has been demonstrated here that the Debye-Scherrer method can be used successfully on an SPG to determine lattice constants accurately in such cases.

Measurements were made on several materials in the form of solids up to 3 mm in diameter and in the form of filings compacted into rods 2 mm in diameter. In the case of pure metals, particularly aluminum, the lattice constant was the same in whatever state the metal was examined. For alloys, however, the method of preparation is of considerable importance. Homogenizing for long periods at high temperatures is of itself insufficient if the cooling rate is not controlled. Evidence discussed in this paper suggests that the influence on the observed lattice constant of cooling rate and solute clustering (and short-range ordering) is of greater importance than such factors as quenching stresses, if they exist.

For highly pure and perfect crystals the lattice constant can be determined with an accuracy comparable to that with which x-ray wavelengths are determined.[51] This should also be possible for alloys if prepared under specified and controlled conditions.

---

[46] C. R. Houska and B. L. Averback, J. Appl. Phys. **30**, 1525 (1959).

[47] R. Smith and J. S. Bowles, Acta Met. **8**, 405 (1960).

[48] *Note added in proof.* The results in Table III on two aluminum alloys were obtained since this paper was completed and accepted for publication, and are essentially in agreement with the other data. For the Al−1.8 Mg alloy, the variation of lattice parameter with solute concentration is sufficiently large to yield a difference in a_0 between quenched filings and quenched solid samples (Table III) that can be interpreted in terms of solute clustering (Table IV). On the other hand, zinc, per at. %, does not change the lattice parameter of aluminum sufficiently to give a measurable effect.

[49] A. J. Bradley, A. H. Jay, and A. Taylor, Phil. Mag. **23**, 545 (1937).

[50] A. J. Bradley and A. Taylor, Proc. Roy. Soc. (London) **A159**, 56 (1937).

[51] W. L. Bond, Acta Cryst. **13**, 814 (1960).

ACKNOWLEDGMENTS

Many useful suggestions on the experimental arrangement as well as comments on an early version of this paper by H. W. Pickett were greatly appreciated. Discussions with M. S. Wechsler during various stages of this work were found to be most valuable and extremely helpful. I am also indebted to the following for their interest in this work: R. W. Cahn, J. B. Cohen, J. Dash, L. F. Vassamillet, and V. E. Buhrke; and in particular to R. W. Balluffi for comments on a final version of this paper.

The encouragement received from W. W. Bender has made this work possible and is gratefully acknowledged here; the unfailing assistance of W. G. Montague is also appreciated.

OURNAL OF APPLIED PHYSICS VOLUME 32, NUMBER 8 AUGUST, 1961

Temperature-Compensated Debye Temperature of Carbonyl Iron

CHARLES P. GAZZARA AND RAYMOND M. MIDDLETON*
Watertown Arsenal Laboratory, Watertown Arsenal, Watertown, Massachusetts

(Received October 27, 1960; in final form, April 7, 1961)

The explicit temperature function τ which relates the Debye temperature to a change in temperature has been found to be 4.1 for annealed carbonyl iron from x-ray diffraction integrated intensity measurements. The corresponding Debye temperature, corrected for temperature diffuse scattering, was calculated to be 435°K at temperature 310°K.

NOMENCLATURE

Θ = Debye characteristic temperature
Θ_1 = Debye characteristic temperature at $T_1 = 98°\mathrm{K}$ (note: subscript 1 on any symbol refers to temperature T_1)
Θ_2 = Debye characteristic temperature at $T_2 = 310°\mathrm{K}$ (note: subscript 2 on any symbol refers to temperature T_2)
$\bar{\mu}_T^2$ = total mean-squared atomic displacement (Angstroms^2)
$\bar{\mu}_D^2$ = dynamic mean-squared atomic displacement (Angstroms^2)
$\sum h_i^2$ = summation of indices squared $(h^2+k^2+l^2)$
I_B = Bragg diffracted integrated intensity (TDS corrected total measured integrated intensity)
τ = explicit temperature-dependent function
λ = weighted Mo$k\alpha$ radiation wavelength
θ = Bragg angle
v = volume of unit cell
a = lattice constant
m = multiplicity factor
f = atomic scattering factor
h = Planck's constant
m_a = mass of iron atom
k = Boltzmann's constant
(L.P.) = Lorentz-Polarization factor
α = coefficient of volume expansion; 35.5×10^{-6} for iron
γ = Grüneisen's constant; 1.60 for iron[1]
K = constant

$$\Psi = \text{Debye function} = \left(\frac{T}{\Theta}\int_0^{\Theta/T}\frac{\xi d\xi}{e^{\xi}-1}\right)+\frac{\Theta}{4T}$$

INTRODUCTION

The determination of the Debye characteristic temperature and atomic displacements from measurements of integrated diffracted x-ray intensities is subject to several errors.

A study of temperature diffuse scattering (TDS)[2,3] showed that a contribution of diffracted intensity caused by TDS may be as much as 15% of the total diffracted intensity using a lead specimen. In the case of carbonyl iron, the TDS factor introduces a correction in Θ of approximately 4%.[4]

Since Θ is usually obtained from measurements of line intensities at two or more temperatures, in which the increase in separation increases the accuracy of fixing Θ, and further, since Θ is temperature dependent (implicitly dependent on temperature through a change in volume,[5] and explicitly temperature dependent), these temperature-related function corrections should be taken into consideration. The implicit temperature dependence has been taken into account in a Debye temperature study of carbonyl iron,[4] and a complete explicit temperature dependence was computed for aluminum[5] through the use of elastic constant data, and for β brass, aluminum, and lead,[6] by selection of a linear Θ vs temperature curve from empirically determined plots.

---

* The authors are employed by Watertown Arsenal Laboratory, Watertown, Massachusetts, as solid-state physicists.

[1] J. C. Slater, *Introduction to Chemical Physics* (McGraw-Hill Book Company, Inc., New York, 1939), p. 451.

[2] D. R. Chipman and A. Paskin, ASTIA Doc. No. 154006 (1958).

[3] D. R. Chipman and A. Paskin, ASTIA Doc. No. 154007 (1958).

[4] C. P. Gazzara, Watertown Arsenal Tech. Rept. 805.2/1 (1960).

[5] A. Paskin, ASTIA Doc. No. 203646 (1958).

The concept of an atomic distortion or displacement of solvent atoms in dilute solid solutions was treated theoretically, assuming isotropic, elastic behavior[7] and applied to a gold-copper system.[8] Further investigation of the separation of the static and dynamic mean atomic displacements obtained through x-ray diffraction technique was made on Cu_3Au, CoPt, NiAu, and LiMg[9] and this method was also applied to carbonyl iron.[4,10] Recently, the total mean atomic displacements were determined up to 1100°K from x-ray intensity measurements correcting for the implicit temperature dependence of the Debye temperature of silver.[11]

In this paper, the temperature function τ was determined from x-ray intensities taken at two ambient temperatures without a knowledge of elasticity data. The experiment was executed with pure iron powder, which was fully annealed with a minimum grain growth, so that the static atomic displacement vector could be assumed to be zero, thereby allowing τ to be computed.

Other sources of errors are taken into consideration, such as a change in those terms in the intensity equation [see Eq. (1)] which are a function of the Bragg angle θ, e.g., Lorentz polarization factors, the temperature gradient through the specimen, so that the true surface temperature could be obtained.

PROCEDURE

General

The equations necessary to calculate the mean atomic displacements and the Debye temperatures from integrated diffracted intensities have been developed[12,13] and are listed[4] as:

$$\bar{\mu}_{T1}^2 = -\frac{\lambda^2}{16\pi^2 \sin^2\theta_1} \ln \frac{I_{B1}v_1}{Kmf_1^2(\text{L.P.})_1}, \qquad (1)$$

$$\bar{\mu}_{D1}^2 = \left(\frac{h}{2\pi}\right)^2 \frac{3T_1\Psi_1}{m_a k \Theta_1^2}; \quad \bar{\mu}_{D2}^2 = \left(\frac{h}{2\pi}\right)^2 \frac{3T_2\Psi_2}{m_a k \Theta_2^2}, \qquad (2)$$

$$\Theta_1^2 = \Theta_2^2[1+\tau\gamma\alpha(T_2-T_1)]. \qquad (3)$$

If the iron powder is properly annealed, the only mean atomic displacement is that resulting from thermal vibrations. Thus, the static displacements may be assumed to be zero and $\bar{\mu}_{T1}^2=\bar{\mu}_{D1}^2$; $\bar{\mu}_{T2}^2=\bar{\mu}_{D2}^2$.

From the experimentally determined values of $\bar{\mu}_{D1}^2$ and $\bar{\mu}_{D2}^2$, Θ_1 and Θ_2 were calculated by equating (1) and (2), and τ in Eq. (3) establishes the explicit temperature dependency of Θ.[5]

Experimental Procedure

The diffracted integrated intensities of the iron powders were obtained from the peaks $\sum h_i^2=8$ ($hkl=220$), 14 ($hkl=321$), 26 ($hkl=510/431$), 34 ($hkl=530/433$), 38 ($hkl=611/532$), 54 ($hkl=721/633/552$), using filtered Mo$K\alpha$ radiation and a low-temperature specimen holder. These lattice planes diffracting in the high 2θ region were selected to minimize extinction effects. Also, the diffraction peaks diffracted from more than one plane were chosen to decrease the error in the integrated intensity measurements resulting from preferred orientation. The data were obtained at specimen temperatures of 98° and 310°K. The stability of the discrimination detection equipment was maintained within $\pm\frac{1}{2}\%$ throughout a series of measurements and the integrated intensity of a reference peak was measured between each background and peak scan count-time reading; all data being corrected with respect to the reference measurements.

The specimens consisted of a carbonyl iron powder specimen annealed in vacuum for 90 hr at 400°C, and an unannealed carbonyl iron powder specimen. Carbonyl iron, a product of the thermal decomposition of $Fe(CO)_5$, was selected because the carbonyl iron particles possessed a granular shape thereby further minimizing preferred orientation. However, the diffraction maxima of carbonyl iron, as received, are quite broad and the above annealing procedure was found necessary to effectively reduce the diffraction line broadening. Both specimens were kept in vacuum or inert gas from the time of preparation until after the x-ray measurements were completed. A 0.4° receiving slit and a 3° beam slit were employed and all other experimental conditions were similar to those described for the large receiving slit scanning procedure.[4]

Results

The experimental data are summarized in Fig. 1. The values of $\ln[vI/(\text{L.P.})mf^2]$ for each point were analyzed with an LGP-30 computer by a least squares approximation to give the best straight line fit. The lines drawn in Fig. 1 are not necessarily the computed linear relations used in the computations. The Debye temperatures $\Theta_1=446$°K and $\Theta_2=435$°K with a corresponding calculated value of $\tau=4.1$ were obtained for annealed carbonyl iron. The values of $\Theta_1=447$°K and $\Theta_2=436$°K at an assumed value of $\tau=4.1$ were obtained for the unannealed sample. These results and

---

[6] D. R. Chipman, Watertown Arsenal Materials Research Lab. Rept. No. 67, (1959).

[7] K. Huang, Proc. Roy. Soc. (London) **A190**, 102 (1947).

[8] R. A. Coyle and B. Gale, Acta Cryst. **8**, 105 (1955).

[9] F. H. Herbstein, B. S. Borie, and B. L. Averbach, Acta Cryst. **9**, 466 (1956).

[10] B. J. Wuensch, Watertown Arsenal Tech. Note 826/1 (1960).

[11] J. Spreadborough and J. W. Christian, Proc. Phys. Soc. (London) **74**, 609 (1959).

[12] P. J. W. Debye, *The Collected Papers of Peter J. W. Debye* (Interscience Publishers, Inc., New York, 1954), p. 28.

[13] R. W. James, *The Optical Principles of the Diffraction of X Rays* (G. Bell and Sons, London, England, 1954), Chap. 5.

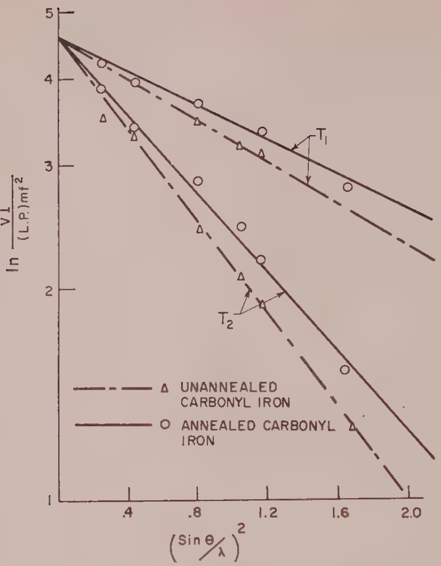

FIG. 1. A plot of the logarithm of $[vI/(\mathrm{L.P.})mf^2]$ versus $(\sin\theta/\lambda)^2$.

those tabulated in Fig. 1 have been corrected for TDS. The chemical analysis of the carbonyl iron was:

C	O_2	Si	Mn	S	P	Cu	Ni	Cr	Mo
0.006	···	0.01	0.006	···	0.005	0.003	0.005	0.003	0.003

Discussion

From a determination of the explicit temperature dependence of Θ for aluminum, β brass, and lead,[5,6] τ was determined as being equal to approximately twice the implicit temperature-dependent function[14] or equal to 4, in agreement with the calculated value of $\tau=4.1$. If pure iron is deformed or cold worked, $(\bar{\mu}_{T_2}{}^2)^{\frac{1}{2}}$ is increased from 0.067 to 0.0706 A and the assumption $\bar{\mu}_{T_1}{}^2=\bar{\mu}_{D_1}{}^2$ and $\bar{\mu}_{T_2}{}^2=\bar{\mu}_{D_2}{}^2$ is no longer justified. An interesting result to note is that the integrated intensities of carbonyl iron increased with annealing treatment but the Debye temperatures did not change. Despite the utilization of background measurements at greater angular separation from the peak positions, there was a loss in integrated intensity of the unannealed sample. This apparent loss is probably the result of the long tapered "tails" associated with diffracted peaks from cold worked materials overlapping the angular background positions.[15]

The absolute values of the Debye temperature are dependent on the accuracy of the values of the scattering factor.[6] In this work, recent values of the scattering factor for iron were used[16] with a Hönl dispersion correction for Mo$K\alpha$ radiation.[17] To minimize this error, the diffraction peaks at high $(\sin\theta/\lambda)$ values were examined by using a low λ radiation (Mo$K\alpha$) and $\sum h_i^2$ between 8 and 54.

An annealed sample of electrolytic iron was examined by the same procedure used on the carbonyl iron. The experimental error, using electrolytic iron, was high, as the result of preferred orientation in the sample and carbon contamination in the filing operation, and the results are not reported.

CONCLUSIONS

The explicit temperature dependency of the Debye temperature has been determined and used in calculating the Debye temperature at $T_1=98°\mathrm{K}$ and $T_2=310°\mathrm{K}$, corrected for TDS, change in Lorentz polarization factor and volume, for annealed carbonyl iron. The introduction of cold-work distortion has not been found to change the Debye temperature of iron.

ACKNOWLEDGMENTS

The authors are deeply indebted to R. Julian for making calculations and to Dr. A. Paskin, Dr. D. Chipman, and Dr. R. Weiss for helpful suggestions.

---

[14] At $\tau=2$, τ becomes the implicit Debye temperature-dependent function.[5]

[15] B. L. Averbach and B. E. Warren, J. Appl. Phys. **20**, 1066 (1949).

[16] A. J. Freeman and J. H. Wood, Acta Cryst. **12**, 27 (1959).

[17] C. H. Dauben and D. H. Templeton, Acta Cryst. **8**, 841 (1955).

JOURNAL OF APPLIED PHYSICS VOLUME 32, NUMBER 8 AUGUST, 1961

Acceleration of Rigid, Conducting, Diamagnetic Bodies by a Magnetic Field*

R. U. AYRES
The G. C. Dewey Corporation, New York, New York

(Received January 30, 1961)

A scheme is developed for treating very fast acceleration processes involving plasmoids. The plasmoid is assumed to move approximately as a rigid body during the acceleration. Two coupled nonlinear differential equations must be solved simultaneously. A power series development valid for short times is given. Two examples are treated which are reminiscent, respectively, of exploding wires in the one case, and certain propulsion devices in the other case. Apart from an analysis of the first two terms in the power series development, no numerical work is attempted. The result of the analysis is that the kinetic energy acquired by the plasmoid can quite generally be expressed as a function of distance traveled, in the form $\frac{1}{2}m\dot{x}^2(x)=C'[\frac{1}{2}(\partial L/\partial x)|_{x=0}]^{\frac{1}{2}}\{x^{\frac{3}{2}}+\frac{1}{3}[(\partial^2L/\partial x^2)/(\partial L/\partial x)|_{x=0}]x^{\frac{5}{2}}+\cdots\}$, where $L(x)$ is the inductance of the total circuit, depending on the location of the plasmoid and its shape, and C' is an experimentally determined constant depending on the circuit parameters and plasmoid mass prior to acceleration. The above expression is only valid for short distances (times).

I. INTRODUCTION

A LARGE segment of plasma physics research today is concerned with fast acceleration processes, in such applications as exploding wires, shock tubes, plasma injection, and plasma propulsion. The acceleration of the plasmoid as a function of time is obviously of interest in many connections. Where possible, of course, one would like to use a hydromagnetic approach such as Rosenbluth's "snowplow model."[1] However, in some applications this model is impractical to apply, due to geometrical complexity.

In order to attack fast acceleration problems, therefore, we begin by even further simplifying our model of the plasma. In fact, at the outset we ignore the "fluid" aspect of the plasma's behavior altogether and concentrate on gross electromagnetic features alone. Later, hydrodynamic behavior can be reintroduced, but at a cost of making the mathematics much more complicated.

A certain amount of experimental justification for this procedure can be adduced. In the first place, the plasma does have a tendency to cohere in a "blob" as it moves through a magnetic field. That is to say, it does *not* immediately fragment. Instabilities such as the Rayleigh-Taylor instability do indeed eventually cause this to happen, but the plasma resists for a short while. This is partly due to inertia, and partially to the fact that, since $\mathbf{E}+\mathbf{v}\times\mathbf{B}=0$ in the plasma, if two value elements of plasma begin to move away from a common center, with opposite values of $\mathbf{v}$, they also become polarized in opposite directions, resulting in an electrostatic attraction. This has a stabilizing effect which adds a further effective inertia to the system. Hence, a pinched discharge persists for as long as 1 or 2 μsec instead of breaking up in a few millimicroseconds.[2]

II. FORCE ON A BODY IN A MAGNETIC FIELD

Having argued that for discussing fast acceleration of a plasma it may not be too bad to assume that the plasmoid behaves like a rigid body, we can proceed from purely macroscopic considerations. Suppose we have a body of fixed shape and size in the field due to an external circuit (e.g., capacitors, a coil or loop, etc.). The plasma may be a direct part of the circuit, as in an exploding wire circuit, or a rail gun, or it may be linked to the circuit only by a mutual inductance. For the present our arguments are quite general. In mks units, the force on the body in a vacuum is conventionally given by:

$$\mathbf{F}=\frac{1}{\mu_0}\int_S[\mathbf{B}(\mathbf{B}\cdot\mathbf{n})-\tfrac{1}{2}B^2\mathbf{n}]dA$$

$$=\mu_0\int_S[\mathbf{H}(\mathbf{H}\cdot\mathbf{n})-\tfrac{1}{2}H^2\mathbf{n}]dA, \qquad (1)$$

where the integration is carried over the surface of the body (the plasmoid). The notation more familiar to plasma physicists is:

$$\mathbf{F}=\int_V \nabla p\,dV$$

$$=\frac{1}{\mu_0}\int_V[(\mathbf{B}\cdot\nabla)\mathbf{B}-\tfrac{1}{2}\nabla B^2]dV$$

$$=-\frac{1}{\mu_0}\int_V[(\nabla\cdot\mathbf{B})\mathbf{B}+\tfrac{1}{2}\nabla B^2]dV+\frac{1}{\mu_0}\int_S\mathbf{B}(\mathbf{B}\cdot\mathbf{n})dA, \qquad (2)$$

on using Gauss's theorem in an extended form. Now, using the fact that

$$\nabla\cdot\mathbf{B}=0, \qquad (3)$$

the vector integration theorems, Eq. (2) are equivalent to Eq. (1). The second term is usually called the "magnetic pressure" and the first term is frequently ignored. It is clear from Eq. (1) that the first term can never contribute to the pressure on a perfectly dia-

---

* This research was supported in part by Picatinny Arsenal under a U. S. Army Ordnance contract.

[1] M. Rosenbluth, Los Alamos Rept. LA 1850, Los Alamos, New Mexico (1954).

[2] There is ample experimental evidence for this persistence in exploding wire experiments and elsewhere. See, for example, *Exploding Wires*, edited by W. G. Chace and H. K. Moore (Plenum Press, Inc., New York, 1960).

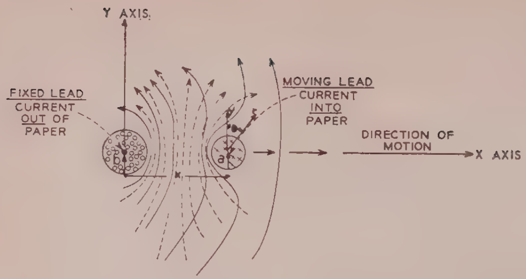

FIG. 1. Cylindrical configuration. Solid lines illustrate field configuration if only induced currents exist in moving lead. Dotted lines illustrate field for bifilar lead.

magnetic body. This is because the field is completely excluded from the inside of the body, and consequently must be everywhere tangential at the surface. However, if the diamagnetism is not perfect the $\mathbf{B}\cdot\mathbf{n}$ contribution may be quite large.

Now carry out a formal decomposition of the field $\mathbf{H}$ into "external" and "internal" parts:

$$\mathbf{H}=\mathbf{H}^{(e)}+\mathbf{H}^{(i)}. \tag{4}$$

The external component $\mathbf{H}^{(e)}$ arises from the external circuit; that is to say, all currents except currents in the plasmoid itself. The internal component arises from all currents in the plasmoid from whatever source. Now suppose the force $\mathbf{F}$ is being exerted in the x direction. Then

$$\begin{aligned}F_x=\mu_0\int_S\big[&H_x^{(e)}(\mathbf{H}^{(e)}\cdot\mathbf{n})-\tfrac{1}{2}(\mathbf{H}^{(e)}\cdot\mathbf{H}^{(e)})n_x\\&+H_x^{(i)}(\mathbf{H}^{(i)}\cdot\mathbf{n})-\tfrac{1}{2}(\mathbf{H}^{(i)}\cdot\mathbf{H}^{(i)})n_x\\&+H_x^{(e)}(\mathbf{H}^{(i)}\cdot\mathbf{n})+H_x^{(i)}(\mathbf{H}^{(e)}\cdot\mathbf{n})\\&-(\mathbf{H}^{(e)}\cdot\mathbf{H}^{(i)})n_x\big]dA.\end{aligned} \tag{5}$$

Now it is easily seen that the fields arising from external sources alone exert no force on the body since these terms exactly give the force acting on a body whose permeability is the same as that of a vacuum, $\mu=\mu_0$. Similarly, the fields arising from internal currents alone can exert no motive force on the body, only an inward pressure. Therefore, only cross terms contribute to linear acceleration:

$$\begin{aligned}F_x=\mu_0\int_S\big[&H_x^{(e)}(\mathbf{H}^{i}\cdot\mathbf{n})+H_x^{(i)}(\mathbf{H}^{(e)}\cdot\mathbf{n})\\&-(\mathbf{H}^{(e)}\cdot\mathbf{H}^{(i)})n_x\big]dA.\end{aligned} \tag{6}$$

There are many situations when Eq. (6) can be greatly simplified. Before specializing to particular cases one further remark of a general nature is in order. It is difficult or impossible to calculate $H^{(i)}$ exactly in the presence of a nonuniform external field; yet if the external field $H^{(e)}$ is uniform the body will experience no net force. In the following examples, therefore, we calculate $H^{(i)}$ in the presence of an external field which is *locally* uniform. In a uniform field, $H^{(i)}$ depends parametrically on $H^{(e)}$. Having obtained this parametric dependence on $H^{(e)}$, we now let $H^{(e)}$ be a slowly varying function of position.

Two specific examples are considered in the following: (a) a current-carrying bifilar lead in which one cylindrical wire is fixed and the other is allowed to move laterally away, maintaining its parallel orientation, and (b) a spheroid which is allowed to move along the axis of a conical coil. The case of a sphere moving along the axis of a single loop, considered by Brueckner and Klein,[3] is a specialization of case (b). The first example was chosen because it is obviously reminiscent of exploding wire circuits where it is desired to project the plasmas outward in some direction. The second example was chosen because of its similarity to various designs for plasma guns, plasma rocket motors, etc.

III. FORCE ACTING ON A BIFILAR LEAD

A cross-sectional view of the arrangement is given in Fig. 1.

We wish to calculate $H^{(i)}$, assuming a locally uniform external field $H^{(e)}$. This problem is solved in a number of standard tests,[4] with the result, in cylindrical coordinates,

$$H_r^{(i)}=[(k-1)/(k+1)](a^2/r^2)H_r^{(e)}, \tag{7}$$

$$H_\theta^{(i)}=(I'/2\pi r)+[(k-1)/(k+1)](a^2/r^2)H_\theta^{(e)}, \tag{8}$$

$$H_z^{(i)}=0, \tag{9}$$

where a is the radius of the moving cylindrical lead, $-I'$ is the current through the lead due to an externally applied electric field (if any), and k is the permeability of the material in the cylinder. If the cylinder is perfectly diamagnetic we have $k=0$. Now Eqs. (7) and (8) give the parametric dependence of $H^{(i)}$ upon the external field $H^{(e)}$, namely the field due to the current I flowing through the *fixed* lead. This is given by

$$H^{(e)}\cong\frac{I}{2\pi x}=\frac{I}{2\pi(x+a\sin\theta)}=H_y^{(e)}, \tag{10}$$

where x is the distance between the centers of the two cylinders and θ is the angle between the radius r and the y axis. The integral (6) becomes

$$\begin{aligned}F_x=\mu_0 2la\int_{-(\pi/2)}^{(\pi/2)}&(H_r^{(e)}H_r^{(i)}\sin\theta+H_r^{(e)}H_\theta^{(i)}\cos\theta\\&+H_r^{(i)}H_\theta^{(e)}\cos\theta-H_\theta^{(e)}H_\theta^{(i)}\sin\theta)d\theta,\end{aligned} \tag{11}$$

where l is the length of the lead. Equation (11) can be integrated easily by using Eqs. (7)–(10). The result is

---

[3] K. Brueckner and M. Klein, J. Appl. Phys. 31, 1437 (1960).

[4] See, for example, J. Stratton, *Electromagnetic Theory* (McGraw-Hill Book Company, Inc., New York, 1941), Chap. IV.

$$F_x(x)=\frac{\mu_0 l}{4\pi a}\left[-\left(\frac{k-1}{k+1}\right)I^2\frac{a^3}{(x^2-a^2)^{\frac{3}{2}}}+II'\frac{a}{(x^2-a^2)^{\frac{1}{2}}}\right]. \quad (12)$$

Of course, in general $I'=I$, but we have distinguished between the forces from two different causes. The first term on the right exists even if the moving cylinders are not a part of the main circuit; i.e., if only induced currents are present. This term is the diamagnetic term, and as expected, it drops off faster as a functions of distance than the direct term on the right. If $k<1$ the first term is positive, corresponding to a repulsion (diamagnetism); if $k>1$ it is negative and attractive (paramagnetism). The second term is positive if the current through the moving cylinders is opposite in sign to the current through the fixed cylinder. This is why we defined the current through the fixed cylinder as I and the current through the moving cylinder as $-I'$; thus I', I are both positive.

IV. FORCE ACTING ON A PROLATE SPHEROID ON THE AXIS OF A TRUNCATED CONICAL COIL

The arrangement being considered now is illustrated in Fig. 2. As before, we first calculate the induced field due to the presence of the spheroid as though the external field were locally uniform. As long as the spheroid is directed with its longest dimension (semiaxis α) along the x axis, and its shorter semiaxis β is small compared to the dimensions of the cone, this approximation is reasonable. The mouth of the cone has a radius R; the radius of the back end of the truncated cone is r. The magnetic field at this point becomes very large, but we will assume that the initial position of the center of the plasmoid x_0 is far enough from the truncated end to avoid any spurious divergence from this source. The next step is to compute the unperturbed magnetic field on the axis of the cone by summing (or integrating) over the contributions from a number of single loops.

The magnetic field outside a diamagnetic spheroid in a uniform external field is given in Stratton[4]:

$$\mathbf{H}=-\nabla\phi \quad (13)$$

where ϕ is the magnetic potential, given by

$$\phi=\lambda\phi^{(e)}\left[1+\frac{\alpha\beta^2}{2}(k-1)\int_0^{\xi}\frac{ds}{(s+\alpha^2)^{\frac{3}{2}}(s+\beta^2)}\right], \quad (14)$$

$$\lambda=\left[1+\frac{\alpha\beta^2}{2}(k-1)\int_0^{\infty}\frac{ds}{(s+\alpha^2)^{\frac{3}{2}}(s+\beta^2)}\right]^{-1}, \quad (15)$$

and ξ is a parameter which determines a family of confocal spheroids (equipotentials) around the given spheroid with semiaxes α, β. The potential $\phi^{(e)}$ is the magnetic potential which gives rise to the unperturbed external field which is locally uniform and has only an x component by assumption:

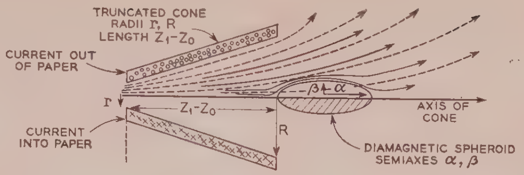

FIG. 2. Spheroidal configuration. Dotted lines represent unperturbed field due to coils alone; solid lines represent perturbed lines around spheroid.

$$\phi^{(e)}=-H^{(e)}x. \quad (16)$$

The integral which appears in λ is easily evaluated, giving

$$\lambda=\left[1+\frac{k-1}{2}\left(\frac{1-e^2}{e^2}\right)\left(\frac{1}{e}\log\left(\frac{1+e}{1-e}\right)-2\right)\right]^{-1}, \quad (17)$$

where e is the eccentricity of the spheroid, deafined s:

$$e=(1-\beta^2/\alpha^2)^{\frac{1}{2}}. \quad (18)$$

In evaluating the integral (6) we need the induced field at the surface of the spheroid, which corresponds to $\xi=0$. This means differentiating the integrals

$$\int_0^{\xi}\frac{ds}{(s+\alpha^2)^{\frac{3}{2}}(s+\beta^2)}$$

with respect to x, y, z, and evaluating at $\xi=0$. Notice that

$$\frac{\partial}{\partial q}\int_0^{\xi}\frac{ds}{(s+\alpha^2)^{\frac{3}{2}}(s+\beta^2)}\bigg|_{\xi=0}=\frac{1}{(\xi+\alpha^2)^{\frac{3}{2}}(\xi+\beta^2)}\frac{\partial\xi}{\partial q}\bigg|_{\xi=0}$$
$$=\frac{1}{\alpha^3\beta^2}\frac{\partial\xi}{\partial q}\bigg|_{\xi=0}. \quad (19)$$

Now ξ is found by solving the equation for a confocal ellipsoid:

$$[x^2/(\xi^2+\alpha^2)]+[(y^2+z^2)/(\xi^2+\beta^2)]=1. \quad (20)$$

Let $r^2+x^2+y^2+z^2$, and solve Eq. (20) for ξ:

$$\xi=\tfrac{1}{2}[r^2-(\alpha^2+\beta^2)]+\tfrac{1}{2}[(\alpha^2-\beta^2+r^2)^2-4x^2(\alpha^2-\beta^2)]^{\frac{1}{2}}$$
$$=\tfrac{1}{2}[r^2-\alpha^2(2-e^2)]+\tfrac{1}{2}[(\alpha^2e^2+r^2)^2-4\alpha^2e^2x^2]^{\frac{1}{2}}. \quad (21)$$

The condition that $\xi=0$ is found to be

$$r^2=\alpha^2-e^2(\alpha^2-x^2). \quad (22)$$

We can now carry out all the required differentiations, and by making use of the approximation discussed previously and assuming also that

$$H_y^{(e)}\cong H_z^{(e)}\cong 0,$$

we can obtain

$$H_x=\lambda H_x^{(e)}\times\left[1+\left(\frac{k-1}{2\alpha^2}\right)x^2\left(1+\frac{1}{2}\frac{\alpha^2(1-4e^2)+e^2x^2}{\alpha^2-e^2x^2}\right)\right]\hat{x}, \quad (23)$$

$$H_y=\lambda H_x^{(e)}\left(\frac{k-1}{2\alpha^2}\right)xy\left(1+\frac{1}{2}\frac{\alpha^2+e^2x^2}{\alpha^2-e^2x^2}\right)\hat{\mathbf{y}}, \tag{24}$$

$$H_z=\lambda H_x^{(e)}\left(\frac{k-1}{2\alpha^2}\right)xz\left(1+\frac{1}{2}\frac{\alpha^2+e^2x^2}{\alpha^2-e^2x^2}\right)\hat{\mathbf{z}}. \tag{25}$$

By the same token

$$H^{(e)}\cdot H^{(i)}\cong H_x^{(e)}H_x^{(i)}, \tag{26}$$

so that in the limit of perfect diamagnetism ($k=0$), the integral (6) reduces to

$$F_x\cong\mu_0\int_S(H_x^{(e)}H_x^{(i)})n_x dA. \tag{27}$$

If the plasmoid is *not* perfectly diamagnetic, then contributions from $H_y^{(i)}$ $H_z^{(i)}$ will also be needed, as Eq. (6) indicates. To the same approximation we find that

$$H_x^{(i)}(\mathbf{H}^{(e)}\cdot\mathbf{n})-(\mathbf{H}^{(e)}\cdot\mathbf{H}^{(i)})n_x\cong 0,$$

whence

$$F_x\cong\mu_0\int_S H_x^{(e)}(H_x^{(i)}n_x+H_y^{(i)}n_y+H_z^{(i)}n_z)dA. \tag{28}$$

For purposes of illustration we shall stick to the case of perfect diamagnetism, Eq. (27). The integral (27) is simplified by noticing that

$$n_x dA=2\pi\rho(x)[d\rho(x)/dx]dx=\pi d\rho^2(x), \tag{29}$$

where

$$\rho^2(x)=y^2+z^2=(1-e^2)(\alpha^2-x^2), \tag{30}$$

$$n_x dA=2\pi(1-e^2)x dx; \tag{31}$$

whence

$$\begin{aligned}F_x&=2\pi\mu_0(1-e^2)\int_{x-\alpha}^{x+\alpha}H_x^{(e)}H_x^{(i)}x'dx'\\&=2\pi\mu_0(1-e^2)\int_{x-\alpha}^{x+\alpha}H_x^{(e)}(H_x-H_x^{(e)})x'dx'\\&=2\pi\mu_0(1-e^2)\int_{x-\alpha}^{x+\alpha}H_x^{(e)}H_x^{(e)}\\&\quad\times\left[\lambda-1-\frac{\lambda}{2\alpha^2}x^2\left(1+\frac{1}{2}\frac{\alpha^2(1-4e^2)+e^2x^2}{\alpha^2e^2-e^2x^2}\right)\right]x'dx'.\end{aligned} \tag{32}$$

It remains to calculate $H_x^{(e)}$ as a function of x, along the axis of the truncated cone. This is done by integrating contributions from differential ring currents. Let the origin of the x axis be at the point where the truncated cone, if continued, would converge to a point, and let x be the coordinate of an infinitesimal test loop. Let z be the distance along the axis to a differential ring whose radius is $R(z)$. The field at x due to a single differential ring current at z is

$$\begin{aligned}\delta H_x^{(e)}(x,z)&=\frac{\delta I}{2}\frac{R^2(z)}{[R^2(z)+(x-z)^2]^{\frac{3}{2}}}\\&=\frac{I}{2l}\frac{R^2(z)dz}{[R^2(z)+(x-z)^2]^{\frac{3}{2}}}.\end{aligned} \tag{33}$$

Now $R(z)$ may have any form, but for a linear cone we choose

$$R(z)=Rz/z_1=\eta z \tag{34}$$

and integrate from $z=z_0$ to $z=z_1$, where z_1-z_0 is the length of the truncated cone and

$$r=Rz_0/z_1=\eta z_0=R\gamma. \tag{35}$$

Let

$$x/z_1=X,\quad z_0/z_1=\gamma,\quad R/z_1=\eta,\quad z/z_1=\xi. \tag{35}$$

Thus

$$\begin{aligned}H_x^{(e)}(X)&=\frac{I}{2(z_1-z_0)}\int_\gamma^1\frac{\zeta^2d\zeta}{[X^2-2X\zeta+(1+\eta^2)\zeta^2]^{\frac{3}{2}}}\\&=\frac{I}{2(z_1-z_0)}\left(\left(\frac{1-\eta^2}{1+\eta^2}\right)\left\{\frac{1}{(X^2-2X+1+\eta^2)^{\frac{1}{2}}}\right.\right.\\&\quad\left.-\frac{\gamma}{[X^2-2\gamma X+(1+\eta^2)\gamma^2]^{\frac{1}{2}}}\right\}-\frac{1}{(1+\eta^2)}\\&\quad\times\left\{\frac{X}{(X^2-2X+1+\eta^2)^{\frac{1}{2}}}\right.\\&\quad\left.-\frac{X}{[X^2-2\gamma X+(1+\eta^2)\gamma^2]^{\frac{1}{2}}}\right\}+\frac{\eta^2}{(1+\eta^2)^{\frac{3}{2}}}\\&\quad\times\left\{\sinh^{-1}\left(\frac{1+\eta^2-X}{\eta X}\right)\right.\\&\quad\left.\left.-\sinh^{-1}\left[\frac{(1+\eta^2)\gamma-X}{\eta X}\right]\right\}\right).\end{aligned} \tag{36}$$

Notice that when $X=0$ the field is finite, despite the apparent divergence:

$$H_x^{(e)}(0)=-\frac{I}{2(z_1-z_0)}\frac{\eta^2}{(1+\eta^2)^{\frac{3}{2}}}\ln\gamma. \tag{37}$$

In the limit of very large X a tedious expansion of Eq. (36) in powers of $1/X$ yields

$$H_x^{(e)}\approx\frac{I}{6(z_1-z_0)}\frac{\eta^2(1-\gamma^3)}{X^3}+\cdots 0\left(\frac{1}{X^4}\right), \tag{38}$$

which can be verified easily by expanding the integrand before integration.

An expansion in small X will not give the behavior of $H_x^{(e)}$ *inside* the cone because the point $X=0$ itself is not in the cone. Therefore we assume that the flux is approximately constant inside the cone, which leads immediately to a quadratic falloff:

$$H_X{}^{(e)}\cong\frac{H_x{}^{(e)}(1)}{X^2}=\frac{I}{2(z_1-z_0)}z_1{}^2\frac{g(\eta,\gamma)}{X^2},\qquad(39)$$

where $g(\eta,\gamma)$ is a geometrical factor obtained by evaluating Eq. (36) at $X=1$:

$$g(\eta,\gamma)=-\frac{\eta}{1+\eta^2}+\frac{1-(1-\eta^2)\gamma}{(1+\eta^2)(1-\gamma)^2+\eta^2\gamma^2}+\frac{\eta^2}{(1+\eta^2)^{\frac{3}{2}}}\times\left\{\sinh^{-1}\eta+\sinh^{-1}\left[\frac{1-(1+\eta^2)\gamma}{\eta}\right]\right\}.\qquad(40)$$

If the cone is not truncated $\gamma\rightarrow 0$ and

$$g(\eta)=\frac{1-\eta}{1+\eta^2}+\frac{\eta^2}{(1+\eta^2)^{\frac{3}{2}}}\left(\sinh^{-1}\eta+\sinh^{-1}\frac{1}{\eta}\right).$$

Now insert Eq. (39) in Eq. (32), and assume the dimensions of the cone are large compared to those of the plasmoid: $(z_1-z_0)\gg 2\alpha$. Then

$$F_x=-\frac{\pi}{2}\mu_0 I^2\frac{z_1{}^4}{(z_1-z_0)^2}g^2(\eta,\gamma)(1-e^2)\times\int_{x-\alpha}^{x+\alpha}\left\{\lambda-\frac{1-\lambda}{2\alpha^2}x'^2\left[1+\frac{\alpha^2(1-4e^2)+e^2x'^2}{\alpha^2-e^2x'^2}\right]\right\}\frac{dx'}{x'^3},$$

where x is the coordinate of the center of the plasmoid. Then, integrating,

$$F_x(x)=-\frac{\pi}{2}\mu_0 I^2\frac{z_1{}^4}{(z_1-z_0)^2\alpha^2}g^2(\eta,\gamma)(1-e^2)\times\left\{\frac{2(1-\lambda)\alpha^3x}{(x^2-\alpha^2)^2}+\left(e^2-\frac{3}{4}\right)\lambda\ln\left(\frac{x+\alpha}{x-\alpha}\right)-\left(e^2-\frac{1}{2}\right)\frac{\lambda}{2}\ln\left[\frac{\alpha^2-e^2(x+\alpha)^2}{\alpha^2-e^2(x-\alpha)^2}\right]\right\}.\qquad(41)$$

In the limit $e\rightarrow 1$ the spheroid degenerates into an infinite cylinder directed along the x axis, and $F_x=0$.

$$\lim_{e\rightarrow 1}F_x\rightarrow\frac{\pi}{8}\mu_0 I^2\frac{z_1{}^4}{(z_1-z_0)^2\alpha^2}g^2(\eta,\gamma)(1-e^2)\ln\left(\frac{x+\alpha}{x-\alpha}\right).\qquad(42a)$$

In the limit $e\rightarrow 0$ the spheroid degenerates into a sphere and

$$F_x=\frac{\pi}{2}\frac{\mu_0 I^2}{(z-z_0)^2}\frac{z_1{}^4}{\alpha^2}g^2(\eta,\gamma)\left[\frac{x\alpha^3}{(x^2-\alpha^2)^2}+\frac{9}{8}\ln\left(\frac{x+\alpha}{x-\alpha}\right)\right].\qquad(42b)$$

V. EQUATIONS OF MOTION FOR SHORT TIMES

Since the dimensions of the plasmoid are, by hypothesis, independent of time, there are two differential equations which must be solved simultaneously to find the motion of the plasmoid.

The first equation is simply [defining $f(x)$ as indicated]

$$F(x)=I^2f(x)=\dot{q}^2f(x)=m\ddot{x}\qquad(43)$$

where $F_x(x)$ is given by Eq. (12) or (41) for the two cases being considered. The second equation which must be solved in conjunction with Eq. (43), if the current is changing in time, is

$$(q_0{}^2-q^2)/2C=\tfrac{1}{2}L\dot{q}^2+\tfrac{1}{2}m\dot{x}^2+\int^t\dot{q}^2Rdt'\qquad(44)$$

or, differentiating once with respect to time,

$$-q\dot{q}/C=L\dot{q}\ddot{q}+\tfrac{1}{2}L\dot{q}^2+m\dot{x}\ddot{x}+\dot{q}^2R.\qquad(45)$$

The terms in Eq. (44) are easily identified as the stored energy in the capacitors, the stored energy in the magnetic field, the kinetic energy acquired by the plasmoid, and the energy lost to joule heating in the circuit. Since the inductance L depends on the position of the plasmoid it is an implicit function of time.

Short of solving the two equations exactly by analytic or numerical methods, there are two procedures which might be followed:

(1) We could assume that the current $\dot{q}$ changes very slowly, or very rapidly, during the time the plasmoid is being accelerated. If this is done Eq. (43) can be integrated formally to give the kinetic energy as a function of distance traveled if we replace $\dot{q}^2$ by a mean value $\langle\dot{q}^2\rangle$.

(2) We could assume, on the contrary, that the force and inductance terms change slowly during the time in which the capacitor is discharged. More precisely, suppose the plasmoid perturbs the field only slightly so that the current as a function of time can be calculated fairly accurately. Then the kinetic energy is given by Eq. (44) directly as a function of time.

The first procedure was followed by Brueckner and Klein[3] in their analytical estimate, but it does not seem to be very satisfactory for time scales which are usual in plasma problems. We follow the second procedure and develop a "short-time" approximation. By straightforward manipulation of Eqs. (43) and (45) we obtain

$$\ddot{q}+\left\{\frac{R+[\frac{1}{2}(\partial L/\partial x)+f(x)]\dot{x}}{L(x)}\right\}\dot{q}+\frac{q}{L(x)C}=0,\qquad(46)$$

which is similar to the equation of an oscillating damped LC circuit with an "effective resistance" due to the presence of the plasma. Suppose we replace the coefficients of $\dot{q}$ and q by mean values

$$\frac{R+[\frac{1}{2}(\partial L/\partial x)+f(x)]\dot{x}}{L(x)}\rightarrow\left\langle\frac{R+[\frac{1}{2}(\partial L/\partial x)+f(x)]\dot{x}}{L(x)}\right\rangle=\frac{R^*}{L_0}\qquad(47)$$

$$\frac{1}{L(x)C}\rightarrow\left\langle\frac{1}{LC}\right\rangle=\frac{1}{LC}.$$

Imposing the boundary conditions $q(0)=q_0$, $\dot{q}(0)=0$, and defining $\mu = R^*/2L_0$, $\omega = (1/LC - \mu^2)^{\frac{1}{2}}$, the solution of Eq. (46) is

$$q(t) = q_0[\cos\omega t + (\mu/\omega)\sin\omega t]e^{-\mu t}, \tag{48}$$

$$\dot{q}(t) = \omega q_0[1 + (\mu^2/\omega^2)]\sin\omega t e^{-\mu}, \tag{49}$$

and

$$\int_0^\tau \dot{q}^2(t)dt = \frac{q_0^2}{4\mu}(\mu^2+\omega^2)\left[1 - \left(1 + \frac{2\mu}{\omega}\sin\omega\tau\cos\omega\tau + \frac{2\mu^2}{\omega^2}\sin^2\omega\tau\right)e^{-2\mu\tau}\right]. \tag{50}$$

After a time τ has elasped,

$$\begin{aligned}\frac{1}{2}m\dot{x}^2(\tau) &= \frac{q_0^2 - q^2(\tau)}{2C} - \frac{1}{2}L\{x(\tau)\}\dot{q}^2(\tau) - R\int_0^\tau \dot{q}^2(t)dt \\ &= q_0^2\left[\frac{1}{2C} - \frac{R}{4\mu}(\mu^2+\omega^2) + \left(\frac{R}{4\mu}(\mu^2+\omega^2) - \frac{1}{2C}\cos^2\omega\tau\right.\right. \\ &\quad + [(R/2\omega)(\mu^2+\omega) - (\mu/\omega C)]\cos\omega\tau\sin\omega\tau \\ &\quad + \left[\frac{R\mu}{2\omega^2}(\mu^2+\omega^2) - \frac{L\{x(\tau)\}}{2\omega^2}(\mu^2+\omega^2)^2 - \frac{\mu^2}{2\omega^2 C}\right] \\ &\quad \left.\left.\times\sin^2\omega\tau\right)e^{-2\mu\tau}\right].\end{aligned} \tag{51}$$

Now if $R^* = R$ and $L = L_0$, then $\frac{1}{2}m\dot{x}^2(\tau) = 0$ for all τ, as expected since Eq. (51) must be satisfied with the lhs equal to zero. Now suppose τ is very small, so that $\mu\tau \ll 1$, $\omega\tau \ll 1$. Then we can expand in powers of τ, with the result

$$\tfrac{1}{2}m\dot{x}^2(\tau) = (q_0^2/3C^2)[(R^*/L_0L) - (R/L^2)]\tau^3 + \cdots. \tag{52}$$

Now by definition

$$\begin{aligned}\frac{1}{L} &= \left\langle\frac{1}{L(x)}\right\rangle, \\ \frac{R^*}{L_0} &= R\left\langle\frac{1}{L(x)}\right\rangle + \left\langle\frac{[\frac{1}{2}(\partial L/\partial x) + f(x)]\dot{x}}{L(x)}\right\rangle, \\ \frac{R^*}{L_0L} - \frac{R}{L^2} &= \frac{1}{L}\left(\frac{R^*}{L_0} - \frac{R}{L}\right) \\ &= \left\langle\frac{1}{L^{(x)}}\right\rangle\left\langle\frac{[\frac{1}{2}(\partial L/\partial x) + f(x)]\dot{x}}{L(x)}\right\rangle \\ &\approx (1/L_0^2)\langle[\tfrac{1}{2}(\partial L/\partial x) + f(x)]\dot{x}\rangle,\end{aligned} \tag{53}$$

keeping only first-order terms. The mean value is evaluated by making use of the relation between force and inductance.[5]

$$\begin{aligned}F_x &= \tfrac{1}{2}\dot{q}^2[\partial L(x)/\partial x] \\ f(x) &= \tfrac{1}{2}[\partial L(x)/\partial x],\end{aligned} \tag{54}$$

whence

$$\tfrac{1}{2}(\partial L/\partial x) + f(x) = \partial L/\partial x = 2f(x)$$

and, over the time interval τ:

$$\begin{aligned}\left\langle\frac{\partial L}{\partial x}\dot{x}\right\rangle_\tau &= \frac{1}{\tau}\int_0^\tau \frac{\partial L}{\partial x}\frac{\partial x}{\partial t}dt \\ &= \frac{1}{\tau}\int_{x(0)}^{x(\tau)} \frac{\partial L}{\partial x}dx = \frac{1}{\tau}[L\{x(\tau)\} - L\{x(0)\}] \\ &= \frac{1}{\tau}\Delta L\{x(\tau)\}.\end{aligned} \tag{55}$$

Therefore

$$\tfrac{1}{2}m\dot{x}^2(\tau) = \tfrac{1}{3}(q_0^2\tau^2/L_0^2C^2)\Delta L\{x(\tau)\} + \cdots. \tag{56}$$

We can solve L_0 in terms of the experimentally determined quantities ω, μ, to the required accuracy:

$$1/L_0C \approx \omega_0^2 + \mu_0^2.$$

Hence

$$\tfrac{1}{2}m\dot{x}^2(\tau) = \tfrac{1}{3}q_0^2\tau^2(\omega_0^2 + \mu_0^2)^2\Delta L\{x(\tau)\} + \cdots. \tag{57}$$

It would be possible, in principle, to calculate L_0 but this usually involves a considerable idealization of the circuitry and ignores external connections, switches, capacitors, etc. By taking the square root of both sides of Eq. (57), integrating, and solving for τ^2, we obtain an alternative expression:

$$\tfrac{1}{2}m\dot{x}^2(\tau) = \frac{2m^{\frac{1}{2}}}{3}q_0(\omega_0^2 + \mu_0^2)\Delta L\{x(\tau)\} \times\int_{x(0)}^{x(\tau)} \frac{dx}{[\Delta L(x)]^{\frac{1}{2}}} + \cdots, \tag{58}$$

which gives the kinetic energy as a function of position for very small times or very small displacements.

Now suppose $\Delta L(x)$ is expanded in a Taylor serie around the starting point x_0:

$$\begin{aligned}\Delta L(x) &= (x - x_0)\frac{\partial\Delta L(x)}{\partial x}\bigg|_{x=x_0} + \frac{(x-x_0)^2}{2}\frac{\partial^2\Delta L(x)}{\partial x^2}\bigg|_{x=x_0} \\ &\quad + \frac{(x-x_0)^3}{6}\frac{\partial^3\Delta L(x)}{\partial x^2}\bigg|_{x=x_0} + \cdots \\ &= 2(x-x_0)f(x_0) + (x-x_0)^2f'(x_0) \\ &\quad + [(x-x_0)^3/3]f''(x_0) + \cdots,\end{aligned} \tag{59}$$

making use of Eq. (54).

Dropping the third term as being very small whe $(X - X_0)$ is sufficiently small, we can evaluate th integral in Eq. (58):

---

[5] M. Abraham and R. Becker, *Classical Electricity and Magnetism* (Hafner Publishing Company, Inc., New York, 1933), pp. 162.

$$\int_{x_0}^{x(\tau)}[\Delta L(x)]^{-\frac{1}{2}}dx$$
$$\cong[-f'(x_0)]^{-\frac{1}{2}}\left\{\frac{\pi}{2}-\sin^{-1}\left[1+2\frac{f'(x_0)}{f(x_0)}(x-x_0)\right]\right\}. \quad (60)$$

Since $f(x)$ is decreasing, $f'(x_0)$ must be negative, and Eq. (60) is real. Now for very small values of $[2x_0f'(x_0)/f(x_0)](x-x_0)$ it can be shown that

$$\frac{\pi}{2}-\sin^{-1}\left[1+\frac{2f'(x_0)}{f(x_0)}(x-x_0)\right]$$
$$=2\left\{\left[-\frac{f'(x_0)}{f(x_0)}(x-x_0)\right]^{\frac{1}{2}}+\frac{1}{6}\left[-\frac{f'(x_0)}{f(x_0)}(x-x_0)\right]^{\frac{3}{2}}+\cdots\right\}. \quad (61)$$

The expansion (61) does not seem to be well known but it may be verified by taking the sine of both sides. Thus,

$$\int_{x_0}^{x(\tau)}[\Delta L(x)]^{-\frac{1}{2}}dx$$
$$=2[f(x_0)]^{-\frac{1}{2}}(x-x_0)^{\frac{1}{2}}\times\left\{1+\frac{1}{6}\left[-\frac{f'(x_0)}{f(x_0)}\right](x-x_0)+\cdots\right\}. \quad (62)$$

Combining with Eq. (59) and substituting into Eq. (58), we find that

$$\tfrac{1}{2}m\dot{x}^2=4(\tfrac{2}{3})^{\frac{1}{2}}q_0(\omega_0^2+\mu_0^2)[mf(x_0)]^{\frac{1}{2}}$$
$$\times\{(x-x_0)^{\frac{3}{2}}+\tfrac{1}{3}[f'(x_0)/f(x_0)](x-x_0)^{\frac{5}{2}}+\cdots\}. \quad (63)$$

Thus we find that initially the kinetic energy rises as the $\frac{3}{2}$ power of displacement and is proportional to the $\frac{1}{2}$ power of $f(x_0)$. Since the second term is negative the ultimate energy acquired will evidently be higher if the coefficient $f'(x_0)/f(x_0)$ is very small. In short, the maximum energy will be obtained if $f(x_0)$ is made very large and $f'(x_0)$ very small. This result is not very surprising. Lumping all circuit parameters together in a single term, we can write Eq. (63)

$$\tfrac{1}{2}m\dot{x}^2=C[f(x_0)]^{\frac{1}{2}}$$
$$\times\{(x-x_0)^{\frac{3}{2}}+\tfrac{1}{3}[f'(x_0)/f(x_0)](x-x_0)^{\frac{5}{2}}+\cdots\}. \quad (64)$$

VI. EXAMPLES

To obtain explicit numerical results from Eq. (64) in our two sample cases, (a) the moving cylinder and (b) the spheroid being ejected from a conical coil, it is only necessary to evaluate $f(x_0)$ and $f'(x_0)$ in the two cases and insert numerical values for the mass m, the initial charge on the condensers q_0, and the parameters ω_0, μ_0 which depend on L_0, C, and R_0, the inductance, capacitance, and resistance, respectively, of the unperturbed circuit. We shall rather arbitrarily assume that all these quantities are the same in the two cases in order to compare their relative efficiencies. Absolute efficiency, which is a ratio of the ultimate kinetic energy of the moving plasmoid to the initial stored energy, is somewhat harder to estimate in general and must rest on an extrapolation of the results for small $(x-x_0)$ to larger values where the expansions are not valid.

For the cylinder, we easily find from Eq. (12), assuming $k=0$,

$$[f(x_0)]_{\text{cyl}}=\frac{\mu_0l}{4\pi}\frac{x_0^2}{(x_0^2-a^2)^{\frac{3}{2}}}, \quad (65)$$

$$\left[\frac{x_0f'(x_0)}{f(x_0)}\right]_{\text{cyl}}=-\left(\frac{x_0^2+2a^2}{x_0^2-a^2}\right). \quad (66)$$

Now the coordinate x_0 of the starting point of a cylinder of radius a must be at least $a+a'$, where a' is the radius of the return conductor, or "backstrap." In a realistic experiment it is extremely unlikely that one can obtain x_0 smaller than $x_0=2a$, so we shall take this value, with $a=2$ mm and $l=2$ cm; then

$$[f(x_0)]_{\text{cyl}}\cong1.225\,\mu_0 \quad (67)$$

$$[x_0f'(x_0)/f(x_0)]_{\text{cyl}}\cong-2. \quad (68)$$

Now consider the spheroid being ejected from a cone. From Eq. (41)

$$f(x_0)=\Lambda\mu_0\left\{\frac{2(\lambda-1)\alpha^3x_0}{(x_0^2-\alpha^2)^2}-\left(e^2-\frac{3}{4}\right)\lambda\ln\left(\frac{x_0+\alpha}{x_0-\alpha}\right)+\left(e^2-\frac{1}{2}\right)\lambda\ln\left[\frac{e^2(x_0+\alpha)^2-\alpha^2}{e^2(x_0-\alpha)^2-\alpha^2}\right]\right\}, \quad (69)$$

$$\Lambda=(\pi/2)[z_1^4/(z_1-z_0)^2\alpha^2]g^2(\eta,\gamma)(1-e^2), \quad (70)$$

where z_0, z_1, α, $g(\eta,\gamma)$, e, and λ were defined in Sec. IV. Differentiating Eq. (69),

$$\left[\frac{x_0f'(x_0)}{f(x_0)}\right]_{\text{spheroid}}=-2(\lambda-1)\alpha^3x_0\frac{(3x_0^2+\alpha^2)}{(x_0^2-\alpha^2)^3}-2\left(e^2-\frac{3}{4}\right)\frac{\lambda\alpha}{(x_0^2-\alpha^2)}$$
$$\times\frac{-2(e^2-\frac{1}{2})\lambda e^2x_0(\{(x_0+\alpha)/[e^2(x_0+\alpha)^2-\alpha^2]\}-\{(x_0-\alpha)/[e^2(x_0-\alpha)^2-\alpha^2]\})}{[2(\lambda-1)\alpha^3x_0/(x_0^2-\alpha^2)^2]-(e^2-\frac{3}{4})\lambda\ln[(x_0+\alpha)/(x_0-\alpha)]+(e^2-\frac{1}{2})\lambda\ln\{[e^2(x_0+\alpha)^2-\alpha^2]/[e^2(x_0-\alpha)^2-\alpha^2]\}}. \quad (71)$$

For the spheroid we will try to maintain a rough parity with the above by making the volume approximately equal to the volume of the cylinder. Let us consider two subcases: an elongated prolate spheroid $\alpha=1$ cm, $\beta=2$ mm, and a sphere of radius $\alpha=3$ mm. The eccentricity $e=0.98$ for the spheroid and $e=0$ for the sphere. The parameter λ, defined by Eq. (17), is $\lambda=1.05$ for the spheroid and $\lambda=1.50$ for the sphere. The cone itself we take to be 18 cm in length, with smaller radius 1 cm and larger radius 4 cm so $z_0=0$ cm, $z_1=24$ cm, and $\eta=\frac{1}{6}$, $\gamma=\frac{1}{4}$, $g(\eta,\gamma)=1.78$. Finally, we assume that the plasma is injected at a point 6 cm from the smaller end of the cone and 12 cm from the larger end of the cone, so $x_0=12$ cm. The two subcases, $e=0.98$, $e=0$ are described pretty well by Eqs. (42a) and (42b), respectively. Using the simpler expression, we find on substituting into Eqs. (69), (70), and (71),

$$[f(x_0)]_{\text{spheroid}}=(0.042\Lambda\mu_0)_{\text{spheroid}} \tag{72}$$

$$[f(x_0)]_{\text{sphere}}=(0.188\Lambda\mu_0)_{\text{sphere}} \tag{73}$$

$$\Lambda_{\text{spheroid}}\cong 0.35 \tag{74}$$

$$\Lambda_{\text{sphere}}\cong 8.75 \tag{75}$$

$$\left.\frac{x_0 f'(x_0)}{f(x_0)}\right|_{\text{spheroid}}\cong\left.\frac{x_0 f'(x_0)}{f(x_0)}\right|_{\text{sphere}}\cong -1. \tag{76}$$

We now write Eq. (64) for all three cases:

$$(\tfrac{1}{2}m\dot{x}^2)_{\text{cyl}}=1.1\,\mu_0^{\frac{1}{2}}C[(x-x_0)^{\frac{3}{2}}-500(x-x_0)^{\frac{5}{2}}]; \tag{77}$$

$$(\tfrac{1}{2}m\dot{x}^2)_{\text{spheroid}}=0.12\,\mu_0^{\frac{1}{2}}C[(x-x_0)^{\frac{3}{2}}-8.3(x-x_0)^{\frac{5}{2}}]; \tag{78}$$

$$(\tfrac{1}{2}m\dot{x}^2)_{\text{sphere}}=1.28\,\mu_0^{\frac{1}{2}}C[(x-x_0)^{\frac{3}{2}}-8.3(x-x_0)^{\frac{5}{2}}]. \tag{79}$$

The salient differences between the three cases are fairly clear from Eqs. (77)–(79). In the first place, the most efficient of the three cases is the sphere. The energy picked up by the eccentric spheroid is considerably smaller, roughly by a factor of 10, due to the fact that there is less surface for the field to push on. However, the shape of the spheroid will not, in a practical situation, be subject to experimental modification; the plasma is not a rigid body and it will certainly be squeezed by the field into an eccentric prolate shape.

By examining the second term one can estimate in a crude way how far the expansion will remain valid. For the cylinder the convergence requirement is

$$500(x-x_0)\ll 1$$

$$x-x_0\ll 2\times 10^{-3}\text{ m}=2\text{ mm}.$$

Thus the series breaks down for very small displacements. In the case of the conical ejection, we have a much less restrictive condition:

$$8.3(x-x_0)\ll 1$$

$$x-x_0\ll 12\text{ cm}.$$

In this case the initial $\frac{3}{2}$ power behavior should hold approximately true while the plasma moves several times its own length. Hence, the power series development is quite useful in situations where the gradient of the force is small, but breaks down rapidly where this is not so.

JOURNAL OF APPLIED PHYSICS VOLUME 32, NUMBER 8 AUGUST, 1961

Single-Crystal Tin Films

RICHARD W. VOOK
International Business Machines Corporation, Yorktown Heights, New York

(Received February 20, 1961; and in final form, April 6, 1961)

High-purity tin films have been made in ultrahigh vacuum by evaporation on (001) faces of NaCl at liquid nitrogen temperature and 0°C. An evaporation rate of approximately 50 A/sec was used. Film thicknesses ranged from 1000 to 3600 A. The films were allowed to warm to room temperature before they were removed from the vacuum system and examined by the techniques of electron diffraction and electron microscopy. Single-crystal films were obtained when the substrates were at liquid nitrogen temperature and when cleaved surfaces and short successive evaporation times were used. If the substrates were at 0°C, or one continuous evaporation of more than about 10 sec was made, the resulting film was polycrystalline and (100) oriented. Grain growth in all the polycrystalline films could be produced by electron-beam bombardment in the electron microscope. Some of the factors influencing grain growth are discussed.

INTRODUCTION

THE experimental conditions under which evaporated films are made greatly influence their physical properties. In particular, their crystalline structure can be influenced by such things as the pressure during evaporation, the nature of the substrate surface, and the substrate temperature.[1–6] A technique has been developed for producing single-crystal tin films. The lateral dimensions of the single-crystal regions are larger than the film thickness by a factor of 10^4. The structure of these films has been investigated at room temperature by the techniques of transmission electron diffraction and electron microscopy.

EXPERIMENTAL TECHNIQUE

NaCl substrates were cleaved from a large Harshaw[7] single crystal along a (100) plane just prior to insertion in the evaporator. They were then mechanically clamped to a copper block which could be cooled to liquid nitrogen temperature. Tin was evaporated from two 0.020-in. diam tantalum[8] wire baskets which were previously outgassed in ultrahigh vacuum. A shutter between the substrate and evaporator was used to regulate the deposition time. Figure 1 is a photograph of the evaporator bulb.

In an attempt to obtain smooth films NaCl crystals were prepared by polishing the surface with a damp chamois. The crystals were then baked in an ultrahigh vacuum system for three to six hours at 375°C and sealed off in Pyrex tubes. Finally, they were baked in these tubes in another furnace at 500°C for about one hour. Examination of the resulting surface by reflection electron diffraction revealed diffuse Kikuchi lines, indicating a high crystal perfection in the first few atomic layers.

The ultrahigh vacuum conditions were obtained in an oil-free bakeable Pyrex glass system similar in principle to others previously reported.[9,10] Prior to evaporation, pressures in the low 10^{-9} or 10^{-10} torr region were achieved. During evaporation on 0°C substrates, the pressure rose to the low 10^{-7} torr range. For liquid-nitrogen-cooled substrates the pressure rose to the 10^{-9} to low 10^{-8} torr region.

The evaporant was high-purity tin.[11] It was outgassed prior to evaporation with the substrate considerably warmer than the liquid-nitrogen-cooled walls of the evaporator. The substrates were then carefully cooled to the desired temperature. The temperature rise of the substrate surface during evaporation was not measured, but there is evidence that it can be quite substantial.[12]

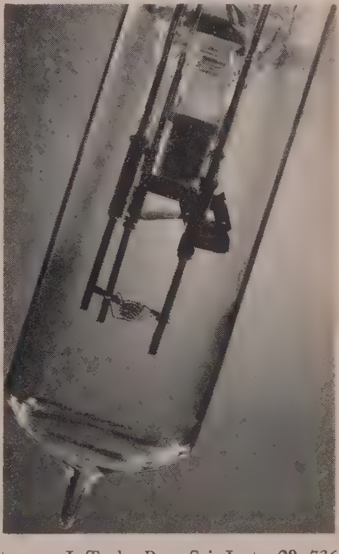

FIG. 1. Evaporator bulb.

---

[1] J. Priest, C. Chiou, and H. L. Caswell, J. Appl. Phys. (to be published).

[2] H. L. Caswell, J. Appl. Phys. **32**, 105 (1961).

[3] W. Buckel and R. Hilsch, Z. Physik **132**, 420 (1952); **138**, 109 (1954).

[4] H. D. Keith, Proc. Phys. Soc. (London) **B69**, 180 (1956).

[5] W. Buckel, Z. Physik **138**, 136 (1954).

[6] A. Segmuller, Z. Krist. **107**, 18 (1956).

[7] Harshaw Chemical Company, Cleveland, Ohio.

[8] National Research Corporation, Cambridge, Massachusetts.

[9] I. Ames, R. L. Christensen, J. Teale, Rev. Sci. Instr. **29**, 736 (1958).

[10] H. L. Caswell, *American Vacuum Symposium Transactions* (Pergamon Press, New York, 1959), p. 66.

[11] Vulcan Detinning Company, Sewaren, New Jersey, nominal purity was 99.999%. Spectrographic analysis showed the purity to be better than 99.994%.

[12] H. Wilman, Proc. Phys. Soc. (London) **B68**, 474 (1955).

For this reason, evaporation times were varied from short successive evaporations to longer single evaporations. Film thicknesses varied from 1000 to 3600 A.

The resulting films were always warmed to room temperature, taken out of the vacuum system, and prepared for electron optical examination. Transmission specimens were obtained by floating the film off the substrate and picking it up on a 200-mesh copper grid. A high-vacuum electron diffraction camera built under the author's direction was used to obtain reflection and transmission diffraction patterns. The films were also examined in a Phillips EM-100 electron microscope operating at 100 kv.

RESULTS

The electron diffraction experiments showed that both single-crystal and highly oriented fine-grained films were obtained. The grains in the single-crystal films covered areas of at least several square millimeters. These results contrast with those of Segmuller,[6] who, using high-vacuum techniques and similar sodium chloride substrates, did not obtain single-crystal tin films. Electron-microscope examination showed that the large grains contained many small-angle grain boundaries across which the lattice tilt (as determined by selected area diffraction) amounted to a few degrees. In some cases a single large grain contained a few small oriented polycrystalline regions.

Single-crystal tin films were always obtained under the following conditions: short successive evaporations of less than approximately 10 sec each, evaporation rates of about 50 A/sec, and cleaved NaCl substrates cooled to liquid-nitrogen temperature. Single-crystal films were not obtained when the substrates were cooled to 0°C or when the films were made with one long evaporation. Usually, single-crystal films could not be produced on polished and recrystallized NaCl substrates. Occasionally, however, a film that was about 50% single and the rest (200) oriented polycrystalline was obtained. Raether[13] studied the effects of polishing NaCl surfaces, their exposure to water vapor and subsequent heat treatment. Polished surfaces were polycrystalline and highly oriented. They were also much more hygroscopic than cleaved surfaces. Exposure to water vapor made (100) surfaces very flat and single crystals. Only after heat treatment at a temperature close to 500°C would a polished or water-treated surface become as perfect as a cleaved surface. Therefore the final bakeout in the ultrahigh vacuum system at 375°C probably was not adequate to remove surface imperfections in the NaCl substrates. Raether's work therefore explains the difficulties encountered in trying to obtain single-crystal films on polished NaCl surfaces.

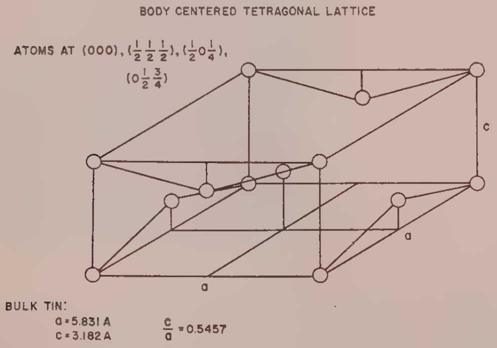
BODY CENTERED TETRAGONAL LATTICE
ATOMS AT (000), $(\frac{1}{2}\frac{1}{2}\frac{1}{2})$, $(\frac{1}{2}0\frac{1}{4})$, $(0\frac{1}{2}\frac{3}{4})$
c
a
a
BULK TIN:
a = 5.831 A
c = 3.182 A
$\frac{c}{a}$ = 0.5457

FIG. 2. White tin unit cell.

It was not possible to obtain a reflection electron diffraction pattern which could definitely be ascribed to the tin films and not to NaCl. The primary reason for this was that upon exposure to moist air, some of the NaCl substrate was dissolved and deposited on the top of the tin films by means of pin holes in the film. The orientation observed was (200). Analysis was complicated by the similar lattice parameters of NaCl, (5.63 A), and the *a* axis of tin, (5.831 A).[14] In reflection the resolution was insufficient to clearly distinguish between the two patterns. However, it was occasionally possible to get half of a true transmission single-crystal pattern on reflection. This pattern was observed when a small piece of film was lifted off a large cleavage step on the NaCl substrate by water vapor in the air just before it was placed in the diffraction camera. The angle between the small piece of film and the substrate approximated 90° so that the electron beam could pass straight through it.

White tin has a body centered tetragonal lattice Figure 2 shows the unit cell. The c/a ratio at 26°C is 0.5457.[14] Figure 3 shows a typical transmission electron diffraction pattern from one of the single crystal films. The c axis lies along the direction of the electron beam normal to the plane of the film. Using MgO "smoke" as a standard, it was possible to determine the a axis of an

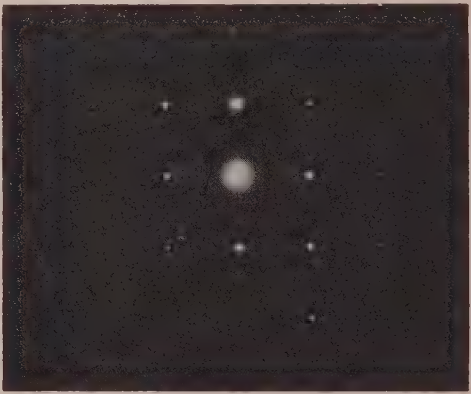

FIG. 3. Transmission electron-diffraction pattern of oriented single-crystal tin film.

---

[13] H. Raether, Optik 1, 296 (1946).

[14] H. E. Swanson and E. Tatge, Natl. Bur. Standards Circ. No. 539, 1, 24 (1953).

etched 3600 A film as 5.79±0.03 A. Bulk tin has an *a* axis of 5.831 A.[14] Figure 4 is an electron micrograph of a single-crystal film in which the *c* axis lies along the electron beam.

Figure 5 is the pattern from one of the oriented polycrystalline films. The orientation is (200) with additional orientation at 90° intervals around the *a* orientation axis. Such an orientation was found in all of the polycrystalline films studied. Only (0*kl*) reflections are allowed for a (200) orientation. The two most obviously missing reflections are the (220) and the (211). Figure 6 is an electron micrograph of an oriented polycrystalline film. The average grain size can be seen to be around 0.1 μ (i.e., approximately the film thickness). It does vary, however, about this value by a factor of approximately 5.

There are also a number of "extra" reflections. They all show variations of intensity along the rings indicating preferred orientation. Several weak reflections appear to belong to SnO, which is probably present on the film surface. Three prominent extra reflections located at positions corresponding to the (002), (022), and (042) reflections of tin can be seen in Fig. 5. They are normally forbidden by the white tin structure factor and do not appear in electron-diffraction patterns of unoriented tin films obtained by deposition on NaCl in poor vacua. X-ray transmission patterns also do not show the extra lines. They are not due to SnO, SnO_2, gray tin or NaCl. They can, however, be explained in terms of simultaneous diffraction events.[15] That is, two or more allowed reflections may be activated simultaneously. These reflections may add vectorially in reciprocal space to form the normally forbidden reflection. The possible combinations must be allowed both by the structure and also by the particular orientation of the crystallites in the film. In our case only (0*kl*) reflections are allowed. For example, the following (not unique) combinations may occur:

$$(1)\quad (013)+(0\bar{1}\bar{1}) \rightarrow (002)$$

$$(2)\quad (033)+(0\bar{1}\bar{1}) \rightarrow (022)$$

$$(3)\quad (053)+(0\bar{1}\bar{1}) \rightarrow (042).$$

The observed (002), (022), and (042) reflections have 4, 8, and 8 arcs in their rings, respectively. These numbers agree with the number of possible orientations of the respective planes for the orientation of the film inferred from the rings of the allowed reflections.

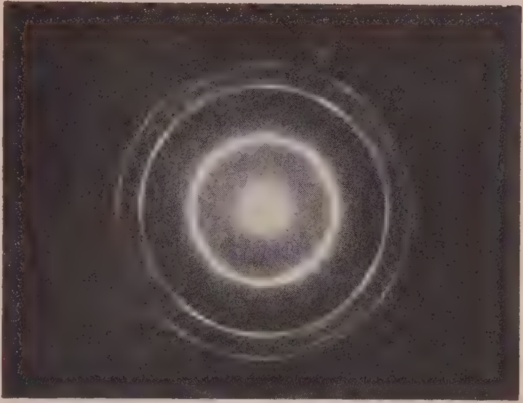

FIG. 5. Transmission electron diffraction pattern of *a* oriented polycrystalline tin film.

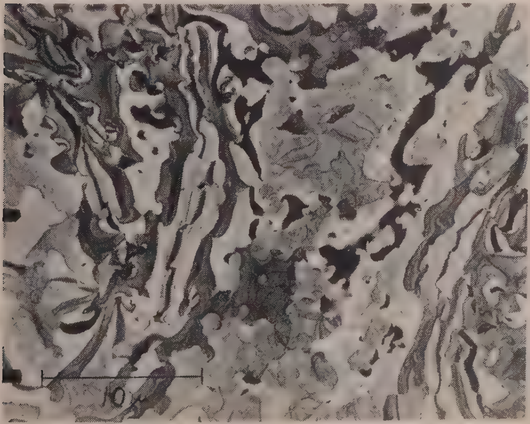

FIG. 4. Electron micrograph of single-crystal tin film. *c* axis approximately parallel to electron beam.

Several of the oriented polycrystalline films were heated in a high-temperature stage in the diffraction camera to approximately 220°C, at which temperature they melted. The pressure during the warmup was about 5×10^{-5} torr or less. No change in the transmission pattern was observed until the films melted, at which point a few very broad rings appeared.

With the oriented polycrystalline films, rapid grain growth could be made to occur by electron-beam bom-

FIG. 6. Electron micrograph of oriented polycrystalline film. *a* axis approximately parallel to electron beam.

---

[15] J. A. Darbyshire and E. R. Cooper, Proc. Roy. Soc. (London) **A152**, 104 (1935).

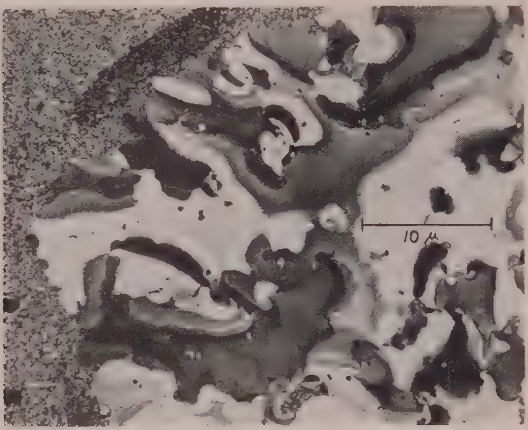

FIG. 7. Electron micrograph of oriented polycrystalline tin film in which grain growth occurred by electron beam bombardment.

bardment in the Phillips electron microscope but not in the diffraction camera. The latter had a much lower intensity electron beam. Consequently, heating effects were much less. Figure 7 shows a film containing a region in which grain growth occurred. The entire (001) oriented single crystal shown grew at a rate which visually appeared to be instantaneous. Such a growth rate was observed over regions as large as 10^{-5} cm². In all cases grain growth required an incubation period of from 2 to 7 min. In this time the film was being heated and strained, the strain being inferred from the motion of extinction contours. A general darkening also occurred, indicating the buildup of a contamination layer. Such a layer was not observed in the diffraction camera. It was further observed that when the beam was turned off for 10 to 15 min after grain growth had occurred and then turned on again, the required incubation period was cut to 20 to 30 sec. A similar reduction in the incubation period was observed for dislocation motion in the large *c* oriented grains. These effects seem to be correlated with the thickness of the contaminant film.

It might be pointed out that Figs. 4 and 7 show defects which often appear in the *c* oriented single crystals but never in the *a* oriented polycrystals. We do not yet know their origin or composition.

DISCUSSION

It is known that films laid down on liquid nitrogen cooled substrates contain a high concentration of defects.[1,3,5] As the films warm to room temperature these defects tend to anneal out. Moreover, the film is strained during warm-up by the greater thermal expansion of the NaCl substrate.[16,17] The highly strained state of the film prior to warmup and the further strain during warmup suggest that the single-crystal films are grown by a strain-anneal type mechanism. It is not yet known at what temperature the film becomes a single crystal. The following evidence suggests that the films are polycrystalline at liquid-nitrogen temperature. One tin film was laid down under conditions which would normally have given a single-crystal film. Then immediately after evaporation (with the substrate still at liquid-nitrogen temperature) gaseous oxygen at 10^{-4} torr was bled into the system for a few minutes. Thereafter, the normal procedures were followed. This film turned out to be (200) oriented polycrystalline with a grain size of approximately 0.1 μ. It was also approximately this thick. Keith[4] has shown that a monolayer of oxygen can severely inhibit grain growth in copper films deposited at liquid-nitrogen temperature and warmed to room temperature. If a tin film were a single crystal immediately after evaporation, it is difficult to imagine that oxygen would be able to convert it to a polycrystalline film during the warmup. On the other hand, if it were initially polycrystalline, an oxygen surface layer may reasonably have inhibited grain growth.

The rapid grain growth observed in the electron microscope may be the result of a structural similarity between the initial preferred orientation and the final single-crystal orientation. The latter crystal is oriented such that the *c* axis is normal to the plane of the film. The preferred orientation of the polycrystalline films consists of one of the *a* axes being normal to the plane of the film. Furthermore, there is preferred orientation about this *a* axis, as can be seen from Fig. 5. The inner ring is the (020) reflection of a (200) oriented film. It has four maxima spaced 90° apart. The projection of the unit cell on the plane of the film is a rectangle with sides *a* and *c*. c/a is approximately $\frac{1}{2}$. The diffraction pattern shown in Fig. 5 means that these rectangular projections are preferentially oriented at 90° intervals. The intensity variations around the (011) reflection bear this out. Hence, it is easily seen that this preferred orientation is structurally very similar to one in which the *a* axes are in the plane of the film and the *c* axis is normal to the film. Our single-crystal films have this latter orientation. The oriented polycrystalline films appear to be in a metastable state resulting from this structural similarity. Consequently, the transformation can occur rapidly by the addition of a small amount of energy in a particular manner to the atomic configuration. In our case this is done by electron-beam bombardment in the electron microscope. This bombardment results in local heating of the film and the formation of a contamination layer on the surface of the film. The former, as mentioned earlier, can be inferred from the motion of extinction contours while the latter results in increased electron-beam absorption and an observed darkening of the region being bombarded. Hirsch[18] has suggested that the surface contaminant film may play a major role in the formation of the stress required to unpin disloca-

---

[16] J. A. Rayne and B. S. Chandrasekhar, Phys. Rev. **120**, 1658 (1960).

[17] R. M. Buffington and W. M. Latimer, J. Am. Chem. Soc. **48**, 2306 (1926).

[18] P. B. Hirsch, J. Inst. Met. **87**, 406 (1958–59).

ions. Fourie, Weinberg, and Boswell[19] have similarly uggested that the surface film may be responsible for he stresses required to form deformation twins in hinned single-crystal tin foils. In view of the experiments on the incubation period for grain growth menioned earlier, it is believed that both processes are equired to transform a (200) oriented film to the (001) riented single crystal film.

---

[19] J. T. Fourie, F. Weinberg, and F. W. C. Boswell, Acta Met. 8, 851 (1960).

ACKNOWLEDGMENTS

The author wishes to express his appreciation to R. H. Jeppesen for his assistance in the preparation of the films, to C. Fisher for the glass blowing, to D. P. Cameron for the use of the electron microscope, to Dr. Henderson Cole and N. Stemple for helpful discussions concerning the analysis of the electron diffraction patterns and for doing the x-ray work, and to Dr. H. L. Caswell and Dr. W. B. Ittner, III, for reviewing the manuscript.

OURNAL OF APPLIED PHYSICS VOLUME 32, NUMBER 8 AUGUST, 1961

Ferromagnetic Nucleation Sources on Iron Whiskers

R. W. De Blois
General Electric Research Laboratory, Schenectady, New York

(Received March 2, 1961)

Previous experimental work has established that the near perfection of some selected iron whiskers brings the axial magnetic field required to nucleate the reversal of magnetization close to the theoretical coercive force limit of $2K/M_s$ (560 oe at 20°C). [R. W. De Blois and C. P. Bean, J. Appl. Phys. **30**, 225S (1959)]. Further experiments now show an approximately constant shift of the nucleation-field contour along an iron whisker with change in temperature, increases in nucleation field of several hundred oersteds along the lengths and at the tips of several iron whiskers following electropolishing, and a correlation between observed microscopic surface imperfections and regions of nucleation-field minima. These results support current ideas that abrupt surface contour variations are primarily responsible for reducing the observed nucleation fields for iron whiskers to below the ideal value.

INTRODUCTION

PREVIOUS experimental work has established that the near perfection of some selected iron whiskers brings the axial magnetic field required to nucleate the reversal of magnetization close to the theoretical coercive force limit of $2K/M_s$.[1] Here K is the first-order magnetocrystalline anisotropy constant and M_s the saturation magnetization. The maximum experimentally observed value[2] of 504 oe is 90% of the theoretical room temperature value of 560 oe and is about 10^4 times greater than the usual coercive-force value for pure bulk iron. These results, by bringing experiment close to ideal theory, resolved one contradiction in Brown's "paradox."[3]

The problems remained of introducing imperfections of a proper nature into the idealized theory of micromagnetics and of finding solutions for the resulting more realistic theory. Brown,[4] Aharoni and Abraham,[5] and Shtrikman and Treves[6] have been attempting to do this. At the request of Aharoni, who sought experimental confirmation of his present ideas on the importance to nucleation of surface imperfections, the author has carried out further work on ferromagnetic nucleation in iron whiskers.

APPARATUS

The modified experimental apparatus[1] consists of a five-turn field coil, $288\,\mu$ long, of $54\text{-}\mu$ diameter wire wound around a $505\text{-}\mu$ diameter capillary with an inside diameter of $45\,\mu$. A single-turn pickup coil is wound at one end of the field coil. The setting and biasing field is provided by a permanent magnet. The field is 22 oe for Figs. 1 and 4, and 40 oe for Figs. 2 and 3. The position of the iron whisker, resting inside the capillary, is measured with respect to the field coil by use of an eyepiece micrometer disk in an 80-power microscope. The iron whiskers used have [100] axial orientation and are about $15\,\mu$ in diameter.

In operation, an approximately $1\text{-}\mu$sec field pulse is applied to the region within the field coil in the reverse direction of the permanent-magnet axial field. The pulse, repetitive at about 70 cps, is critically adjusted in amplitude until reversal of magnetization occurs during most of the cycles. The magnetization reversal and the voltage amplitude across a standard resistance in series with

---

[1] R. W. De Blois and C. P. Bean, J. Appl. Phys. **30**, 225S (1959).

[2] A. Aharoni (private communication), by use of the paper by A. Aharoni and S. Shtrikman, Phys. Rev. **109**, 1522 (1958), has demonstrated theoretically that the demagnetizing field arising from reversal by curling is negligible for micron-thick iron whiskers. Thus the correction made in reference 1, decreasing 504 oe to 469 oe, is unnecessary.

[3] W. F. Brown, Jr., Revs. Modern Phys. **17**, 15 (1945); J. Appl. Phys. **30**, 62S (1959).

[4] W. F. Brown, Jr., J. phys. radium **20**, 101 (1959).

[5] A. Aharoni, J. Appl. Phys. **30**, 70S (1959); Phys. Rev. **119**, 127 (1960); C. Abraham and A. Aharoni, *ibid.* **120**, 1576 (1960).

[6] S. Shtrikman and D. Treves, J. Appl. Phys. **31**, 72S (1960).

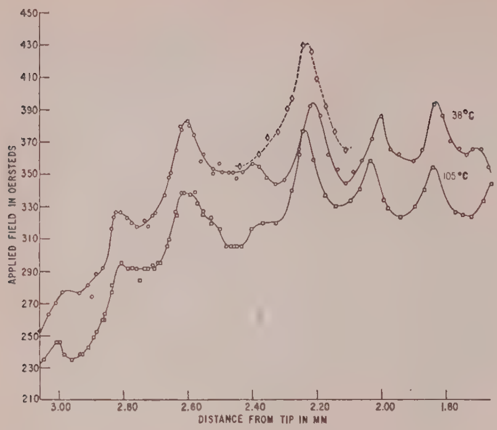

FIG. 1. Nucleation fields at 38°C (○) and 105°C (□) along a section of an iron whisker.

the field coil are conveniently observed on a dual-beam oscilloscope. The temperature is measured by using a copper-Constantan thermocouple placed close to the field coil.

EXPERIMENTAL RESULTS

Figure 1 shows the net nucleation fields at two different temperatures, 38° and 105°C, along a section of an iron whisker about 15 μ in diameter. The whisker is one that was previously tested 1.6 years ago and was found then to have a maximum nucleation field of 430 oe at room temperature. It had remained in a desiccator until the present experiments.

Evidence for deleterious corrosion exists in the region of 2.30 mm in Fig. 1. The data indicated by diamonds were taken near 38°C two days prior to the 105°C data and five days prior to the 38°C data. Elsewhere the diamond-point data match the 38°C data moderately well.

Further corrosion evidence resulted when the whisker, cooled to 195°K, collected moisture as it warmed overnight to room temperature and developed extensive visible corrosion on its surface. A region at 1.60 mm, nucleating before at 347 oe, was reduced in the morning to 164 oe, and 5 hr later to about 97 oe.

In accord with suggestions by Aharoni[7] and by Shtrikman and Treves[6] that etching might serve to raise whisker nucleation fields by smoothing out surface imperfections, the author carried out tests which proved successful when a CrO_3-glacial acetic acid electropolishing solution was used at about 3 v and at room temperature. Figure 2 shows the nucleation-field contour along a section of a whisker electropolished about 1 min. Originally, the nucleation field was nowhere higher than 100 oe. Data taken after a lapse of three days lie indistinguishably on the original curve, indicating that no corrosion occurred at room conditions during this period.

Figure 3 shows the development with electropolishing of the nucleation-field contour along a section of an originally 15-μ diameter whisker. Curve A shows the contour prior to electropolishing. Curve B shows the contour after 2 sec at 4.5 v. A further 2-sec electropolish produced a contour lying mostly below curve A. Curve C shows the contour after a total of 11 sec. An additional 10-sec electropolish reduced the maximum nucleation field to 208 oe.

Figure 4 shows the nucleation-field contour along a section of a whisker electropolished 4 sec. A search for surface imperfections was then made. All four sides were viewed and photographed at 1000 × in a Bausch & Lomb metallograph, and selected regions in a Zeiss interference microscope using a thallium light source ($\lambda = 0.54\mu$). A major surface defect is visible at the field minimum at 1.68 mm, where the whisker is 10 μ wide. It is a nearly flat valley 2 μ wide, 7 μ long, and 0.5 μ deep, running from one edge of the whisker perpendicular to its long axis. The sides are too steep to follow the fringes to the valley bottom, where there is a shift of about an integral number. Focusing at 1000 × with the Bausch & Lomb metallograph showed that the number must be two, giving the 0.5-μ depth. Other minor irregularities, with more gradually shifting fringes, are visible nearby at 1.65 mm (0.15 μ deep, 3μ wide), 1.96 mm (0.20 μ deep, 3 μ wide), and 2.35 mm (0.20 μ deep, 9 μ wide). Numerous imperfections are visible beyond 2.35 mm. Near 0.95 mm the photographs show several minute edge gaps, about $\frac{1}{3}\,\mu$ deep and 1 μ wide. Because the whisker had undergone extensive damage while being photographed, several attempts to raise the nucleation fields at 0.95 and 1.65 mm by further electropolishing yielded minimal results. At 0.97 mm, however, the nucleation field did increase by 13 oe over the value in Fig. 4 after 20 sec of electropolishing.

Electropolishing the ends of several cut sections of iron whiskers has raised the nucleation fields at the tips of three of them to 307, 322, and 400 oe. The last one,

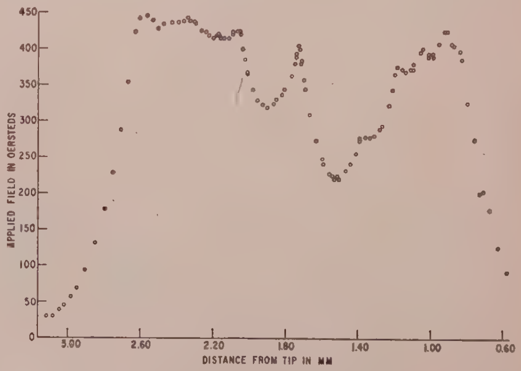

FIG. 2. Nucleation fields along a section of an electropolished iron whisker.

---

[7] A. Aharoni (private communication).

examined in the metallograph, appeared to taper gradually to about 1 μ at the tip.

CONCLUSIONS

That the contours in Fig. 1 are roughly parallel constitutes evidence that the major imperfections are irregularities such as pits or valleys on the surface or, possibly, voids or inclusions within the whisker. For, as a rough approximation, the demagnetizing field arising from an imperfection causing a local divergence in the magnetization adds to the applied field to equal the theoretical coercive force of $2K/M_s$. Since the demagnetizing field, proportional to M_s, would vary but little in the above temperature range, the change in applied field should approximate the change in $2K/M_s$, which for the above temperature change is about 50 oe.

The electropolishing results shown in Figs. 2 and 3 clearly support the assumption that surface imperfections are at least largely responsible for the reduction of the coercive force of iron whiskers to below the theoretical value.

The initial attempt to correlate the nucleation-field contour of Fig. 4 with the whisker surface condition indicates that abrupt surface discontinuities, even though minute, constitute favorable nucleation sites and gives hope that future detailed investigations will yield the quantitative data needed to check the more realistic theories of micromagnetics now being developed.

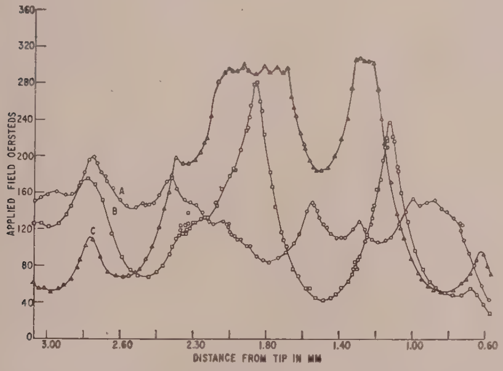

FIG. 3. Variation with electropolishing time of the nucleation fields along a section of an iron whisker. (Curve A, $t=0$; Curve B, $t=2$ sec; Curve C, $t=11$ sec).

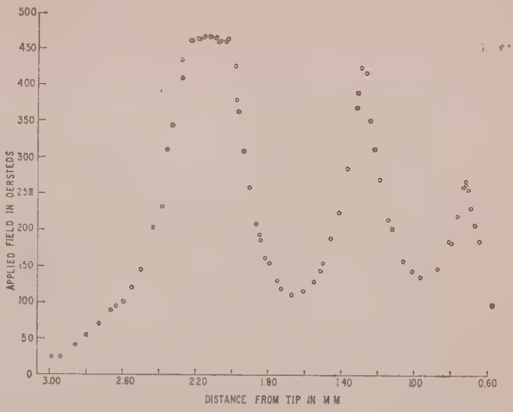

FIG. 4. Nucleation fields along a section of an electropolished iron whisker.

The high nucleation fields observed at the tips of three electropolished whiskers are of special significance with respect to the work of Shtrikman and Treves[6] and Fowler *et al.*,[8] on nucleation at the tips of square-ended whiskers. For sharp-cornered iron whiskers they find reverse domains persisting up to at least 6000 oe. In accord with their speculations, experiment now shows that reverse domains do not exist in smoothly tapered iron whisker tips until reverse fields approaching the theoretical limit of $2K/M_s$ are applied.

ACKNOWLEDGMENTS

The author wishes to thank A. Aharoni for his suggestion to reopen the experimental work on nucleation and thanks him, S. Shtrikman, and D. Treves for much stimulating correspondence. Thanks are also due to R. R. Russell and D. R. Ochar for extensive help in examining and photographing one iron whisker at high magnification.

---

[8] C. A. Fowler, Jr., E. M. Fryer, and D. Treves, J. Appl. Phys. **31**, 2267 (1960).

JOURNAL OF APPLIED PHYSICS VOLUME 32, NUMBER 8 AUGUST, 1961

Optimization of Emission-Limited Thermionic Generators*

ALFRED SCHOCK
Republic Aviation Corporation, Farmingdale, New York

(Received February 20, 1961)

Equations are derived describing the performance of space-charge neutralized thermionic converters with negligible transport effects. For a given anode work function and cathode temperature, optimization of the other system parameters leads to an expression for the maximum attainable conversion efficiency, in terms of the fundamental physical constants e, m, c, and k. The calculated results, presented graphically, suggest several distinct modes of high-efficiency operation, and lead to a number of interesting conclusions about converters with cesium coated cathodes. With electrodes having a thermal emissivity equal to that of hot tungsten, efficiencies in excess of 30% are shown to be possible.

INTRODUCTION

A NUMBER of excellent parametric studies of thermionic generators have appeared in the recent literature.[1–4] As will be seen, the present analysis approaches the problem from a somewhat novel point of view, while making a minimum of assumptions about the physical quantities involved. Moreover, the results of the optimization study are expressed in terms of fundamental physical constants, and are depicted graphically in a manner which, it is hoped, will provide the reader with new insight into the interrelationship of the basic variables of the conversion system.

The report confines its attention to the case of the emission-limited diode, whose current density is given by the Richardson-Dushman equation. In other words, we assume that space-charge effects, magnetic field effects, and transport effects may all be neglected. Let us briefly examine to what extent these assumptions may be realized in practice.

The assumption of complete space-charge cancellation by positive ions is borne out by a recent report[5] which states that the current produced by an experimental converter remained essentially constant over a range of cesium pressures from 10^{-3} mm to 1 mm Hg ($100°\mathrm{C} < T_{\mathrm{Cs}} < 250°\mathrm{C}$). This evidence suggests that complete space charge cancellation should be attainable, except possibly at very high current densities.

The second assumption, that the effect of self-induced magnetic fields can be reduced to a negligible level, appears to be achievable either by the application of a longitudinal magnetic field[6] or by operation at a high cesium density.[5]

The assumption of negligible internal plasma resistance is more questionable, since the performance of high-density cesium diodes is frequently poorer than that predicted by simple theory. However, recent reports[7,8] indicate that these devices are very sensitive to electrode spacing, and that at very close spacings (e.g., 3 mils) their performance approaches theoretical values. It therefore appears that the internal resistance of the plasma can be made negligibly small either by reducing the cesium pressure or by closing the electrode gap.

In any event, the results of this analysis are of interest since they represent an upper limit for the attainable efficiency.

ANALYSIS

The efficiency η of a thermionic converter is defined as the ratio of the electric power produced (current density J times load voltage V) to the total heat input rate (electron cooling q_e plus radiative heat loss q_r plus the conductive heat loss q_c through the lead wires) per unit area of electrode[9]:

$$\eta = JV/(q_e + q_r + q_c). \tag{1}$$

Before proceeding, we must distinguish two possible cases, depending on the relative magnitudes of the cathode work function ϕ_c, anode work function ϕ_a, load voltage V, and lead wire voltage drop V_w.[10] Let us first examine the case when

$$0 < V < \phi_c - \phi_a - V_w. \tag{2}$$

Assuming an anode temperature T_a low enough so that back emission may be neglected, the net current density with the cathode at temperature T_c is given by

$$J = \mathcal{A} T_c^2 \exp(-e\phi_c/kT_c). \tag{3}$$

Here the Richardson constant $\mathcal{A}$ (120 amp/cm² K^2) is defined by

$$\mathcal{A} \equiv 4\pi emk^2/h^3, \tag{4}$$

where e and m represent the charge and mass of an

---

[*] Work supported by U. S. Office of Naval Research.

[1] G. N. Hatsopolous and J. Kaye, Proc. I.R.E. **46**, 1574 (1958).

[2] J. M. Houston, J. Appl. Phys. **30**, 481 (1959).

[3] N. S. Rasor, J. Appl. Phys. **31**, 163 (1960).

[4] L. N. Dobretsov, Soviet Phys.–Tech. Phys. **5**, 343 (1960).

[5] V. C. Wilson, "Cesium converter studies," presented at the ARS Space Power Systems Conference, September, 1960.

[6] A. Schock, J. Appl. Phys. **31**, 1978 (1960).

[7] R. L. Hirsch, J. Appl. Phys. **31**, 2064 (1960).

[8] W. A. Ranken, G. M. Grover, and E. W. Salmi, J. Appl. Phys. **31**, 2140 (1960).

[9] Except where otherwise noted, mks units are used throughout this report.

[10] The work functions referred to in this report are *effective* work functions, as defined by E. B. Hensley, J. Appl. Phys. **32**, 301 (1961).

electron, and k and h denote Boltzmann's and Planck's constants, respectively.

In addition to overcoming the energy barrier $e\phi_c$, escaping electrons have an average kinetic energy $2kT_c$. Consequently, the electron cooling rate q_e is given by

$$q_e = J(\phi_c + 2kT_c/e). \tag{5}$$

Since $T_a^4 \ll T_c^4$, radiation from the anode may be neglected, so that the radiative cooling rate q_r is given by

$$q_r = \sigma\bar{\epsilon}T_c^4. \tag{6}$$

Here, the effective emissivity $\bar{\epsilon}$, which takes account of multiple reflections between the electrodes, can be expressed in terms of the cathode and anode emissivities ϵ_c and ϵ_a (at the appropriate temperatures[1]),

$$\bar{\epsilon} = [1/\epsilon_c(T_c) + 1/\epsilon_a(T_a^{\frac{1}{2}}T_c^{\frac{1}{2}}) - 1]^{-1}, \tag{7}$$

and the Stephan-Boltzmann constant σ is defined by

$$\sigma = 2\pi^5k^4/15c^2h^3, \tag{8}$$

where c denotes the velocity of light.

In computing the conductive heat loss q_c, previous analyses ignored the temperature dependence of the lead wire's thermal conductivity κ and electrical resistivity ρ. As will be seen, these approximations need not be made. Consider a lead wire of cross-sectional area A_w, connected to a cathode of area A_c. At any position x along the wire, its temperature gradient dT/dx is related to the heat flow rate Q through the wire by

$$dT/dx = -Q/\kappa A_w; \tag{9}$$

while the heat flow gradient dQ/dx is a function of ohmic heating by the current JA_c passing through the wire:

$$dQ/dx = (JA_c)^2\rho/A_w. \tag{10}$$

Therefore,

$$\frac{dQ}{dT} = \frac{dQ/dx}{dT/dx} = -\frac{J^2A_c^2\rho\kappa}{Q}. \tag{11}$$

The electrical and thermal conductivities of a metal at temperature T are related by the Wiedemann-Franz law:

$$\rho\kappa/T = \pi^2k^2/3e^2. \tag{12}$$

Inserting this into Eq. (11), we obtain the separable differential equation

$$dQ/dT = -[\pi kJA_c/\sqrt{3}e]^2(T/Q). \tag{13}$$

To integrate Eq. (13) between the cathode at temperature T_c and the load at temperature T_0, we note that the heat flow to the load is the sum of the cathode heat loss A_cq_c plus the heat A_cJV_w generated within the lead wire:

$$\int_{A_cq_c}^{A_c(q_c+JV_w)} QdQ = -\frac{\pi^2k^2J^2A_c^2}{3e^2}\int_{T_c}^{T_0} TdT. \tag{14}$$

Solving for q_c, and noting that $T_0^2 \ll T_c^2$, we finally obtain:

$$q_c = J\left[\frac{\pi^2k^2T_c^2}{6e^2V_w} - \frac{V_w}{2}\right]. \tag{15}$$

As would be expected from the principle of superposition, the first term in the square bracket is the conductive heat loss in the absence of heat generation, while the second term represents half of the heat generated within the lead wire. Note that neither area A_c nor A_w appears in Eq. (15).

Combining Eqs. (1), (3), (5), (6), and (15), we obtain the general equation for the efficiency η in terms of the system variables ϕ_c, ϕ_a, T_c, V, V_w, and $\bar{\epsilon}$:

$$\frac{V}{\eta} = \phi_c + \frac{2kT_c}{e} - \frac{V_w}{2} + \frac{\pi^2k^2T_c^2}{6e^2V_w} + \frac{\sigma\bar{\epsilon}T_c^2}{\mathcal{A}}\exp\left(\frac{e\phi_c}{kT_c}\right). \tag{16}$$

Differentiating with respect to the load voltage V, we obtain

$$d\eta/dV = \eta/V. \tag{17}$$

The above equations apply to the range $0 < V \leq \phi_c - \phi_a - V_w$. Equation (17) shows that η increases monotonically with V. Hence, the maximum efficiency must occur at a load voltage not less than $\phi_c - \phi_a - V_w$.

Let us now examine the special case when

$$V = \phi_c - \phi_a - V_w. \tag{18}$$

Although previous reports have demonstrated that this is the load voltage which maximizes the power density, we shall show that this is not necessarily the condition for maximum efficiency. To compute η', the efficiency corresponding to this load voltage, we insert Eq. (18) into (16):

$$\phi_c\left(\frac{1-\eta'}{\eta'}\right) - \frac{\phi_a}{\eta'} - \frac{2kT_c}{e} - \left(\frac{2-\eta'}{2\eta'}\right)V_w - \frac{\pi^2k^2T_c^2}{6e^2V_w} = \frac{\sigma\bar{\epsilon}T_c^2}{\mathcal{A}}\exp\left(\frac{e\phi_c}{kT_c}\right). \tag{19}$$

Next, we differentiate with respect to V_w and set $\partial\eta'/\partial V_w = 0$, obtaining an expression for the optimum lead wire voltage drop:

$$(V_w)_{\text{opt}} = \left(\frac{\pi kT_c}{e}\right)\left(\frac{\eta'}{6-3\eta'}\right)^{\frac{1}{2}}. \tag{20}$$

Insertion of Eq. (20) into Eq. (19) gives an explicit expression for η'', the efficiency attained by optimizing the lead wire resistance:

$$\eta'' = \frac{\xi\psi + 1 - (1 + 2\xi\psi - \xi^2)^{\frac{1}{2}}}{\psi^2 + 1}, \tag{21}$$

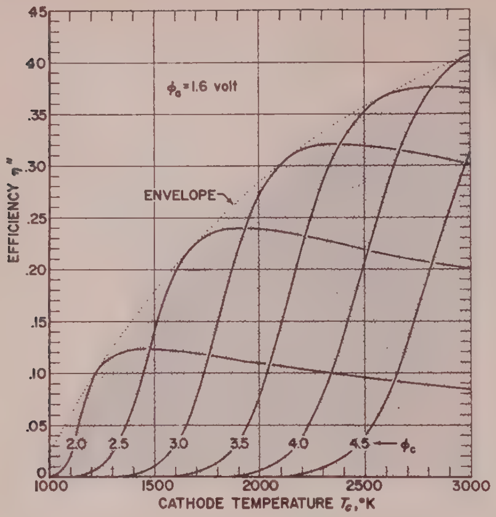

FIG. 1. Solution of Eq. (21) for various values of cathode work function and temperature (with $\phi_a=1.6$).

where

$$\xi\equiv\frac{\sqrt{3}}{\pi}\left(\frac{e\phi_c}{kT_c}-\frac{e\phi_a}{kT_c}\right),$$

$$\psi\equiv\frac{\sqrt{3}}{\pi}\left(\frac{e\phi_c}{kT_c}+2+\alpha\right),$$

and

$$\alpha\equiv\frac{e\sigma\bar{\epsilon}T_c}{\mathcal{A}k}\exp\left(\frac{e\phi_c}{kT_c}\right).$$

Finally, insertion of Eqs. (4) and (8) for $\mathcal{A}$ and σ gives

$$\alpha=\frac{\pi^4\bar{\epsilon}kT_c}{30mc^2}\exp\left(\frac{e\phi_c}{kT_c}\right). \qquad (22)$$

The system of Eqs. (21) and (22) is in terms of the fundamental physical constants e, m, c, and k. The only additional data required to study the dependence of η'' on ϕ_c, ϕ_c, and T_c are the electrode emissivities ϵ_c and ϵ_a.[11] To illustrate the various relationships, we shall take the cathode to be tungsten (W), and make the conservative assumption that the emissivity of the anode equals that of the cathode at temperature T_c. With the effective emissivity $\bar{\epsilon}$ thus taken as

$$\bar{\epsilon}=[2/\epsilon_W(T_c)-1]^{-1}, \qquad (23)$$

the variation of η'' was computed for the case where the anode is coated with a monatomic layer of cesium ($\phi_a=1.6$ v). The results of these computations are depicted by Fig. 1. Clearly, the family of curves has a common envelope, with the shaded area below that envelope representing the range of all possible solutions. To determine the equation of this envelope, we rewrite Eq. (21) in the form

$$\psi\eta''-\xi=-[(2-\eta'')\eta'']^{\frac{1}{2}}, \qquad (24)$$

differentiate with respect to ϕ_c, and set $\partial\eta''/\partial\phi_c=0$, obtaining

$$1/\eta''=1+\alpha. \qquad (25)$$

Combining Eqs. (24) and (25) with the definitions of α, ξ, and ψ, we can eliminate ϕ_c and obtain an equation for the maximum efficiency η^*:

$$(e\phi_a/kT_c)+\pi[\tfrac{1}{3}\eta^*(2-\eta^*)]^{\frac{1}{2}}+1+\eta^*$$
$$=(1-\eta^*)\ln[30mc^2(1-\eta^*)/\pi^4\bar{\epsilon}kT_c\eta^*]. \qquad (26)$$

Equation (26) defines the envelope for any given value of ϕ_a. At each cathode temperature T_c, the envelope is tangent to a curve of constant cathode work function, which we shall designate as ϕ_c^*. To find the equation for ϕ_c^*, we eliminate η'' from Eqs. (24) and (25), and insert the definitions of ξ and ψ. This gives

$$(\alpha^*+1)\frac{e\phi_a}{kT_c}+\pi(\tfrac{2}{3}\alpha^*+\tfrac{1}{3})^{\frac{1}{2}}-\alpha^*\frac{e\phi_c^*}{kT_c}+\alpha^*+2=0, \qquad (27)$$

where

$$\alpha^*=\frac{\pi^4\bar{\epsilon}kT_c}{30mc^2}\exp\left(\frac{e\phi_c^*}{kT_c}\right).$$

DISCUSSION

Let us now examine the physical significance of the quantities defined by Eqs. (21), (26), and (27). It will

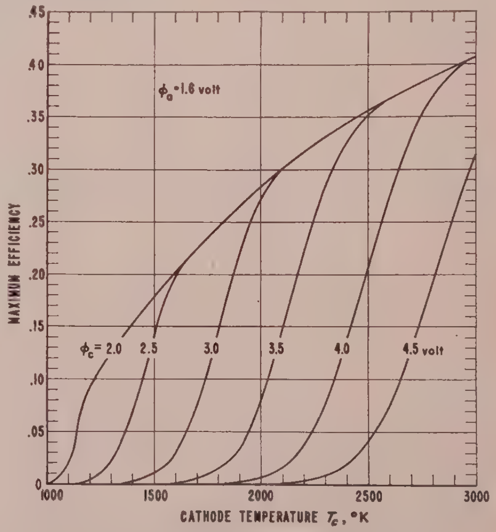

FIG. 2. Effect of cathode work function and temperature on maximum efficiency (with $\phi_a=1.6$ v).

---

[11] Actually, the maximum efficiency is not very sensitive to the assumed emissivities, because (under optimized conditions) the radiative cooling q_r is generally small in comparison to the electron cooling q_e (see Table I).

be recalled that these equations were derived for the case when $V=\phi_c-\phi_a-V_w$. If the load voltage were raised to some higher value

$$V=(\phi_c-\phi_a-V_w)+\Delta V, \tag{2a}$$

then the current density J would be reduced to

$$J=\mathcal{A}T_c^2\exp[-(e/kT_c)(\phi_c+\Delta V)], \tag{3a}$$

and the electron cooling rate q_e would change to

$$q_e=J(\phi_c+\Delta V+2kT_c/e). \tag{5a}$$

Since all other terms remain unchanged, it is easily shown that the efficiency η'' for this case is also given by Eq. (21), provided the cathode work function ϕ_c is replaced by an effective work function $(\phi_c+\Delta V)$.

We now inquire under what condition the efficiency is maximized when $V=\phi_c-\phi_a-V_w$, and under what condition a maximum occurs at some higher load voltage. This question can be answered by inspection of Fig. 1. Each curve, representing a specific cathode work function ϕ_c, is tangent to the envelope at one point. At cathode temperatures below that point of tangency, raising the cathode work function from ϕ_c to $\phi_c+\Delta V$ will clearly lower the efficiency. Therefore, at lower temperatures the optimum load voltage is $\phi_c-\phi_a-V_w$, and the maximum attainable efficiency η'' is given by Eq. (21).

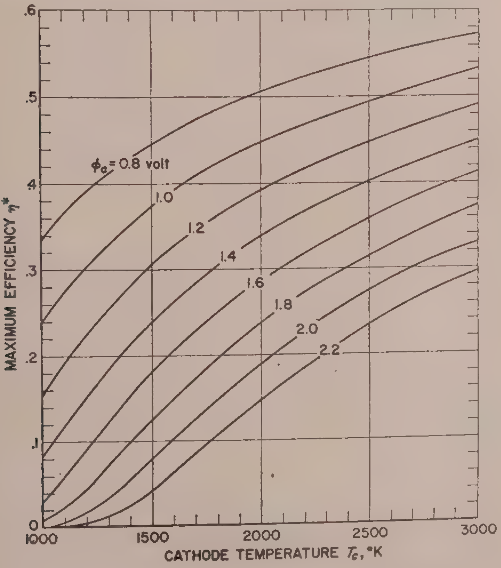

FIG. 3. Effect of anode work function and cathode temperature on maximum attainable efficiency, provided the cathode work function does not exceed the value shown by Fig. 4 [solution of Eq. (26)].

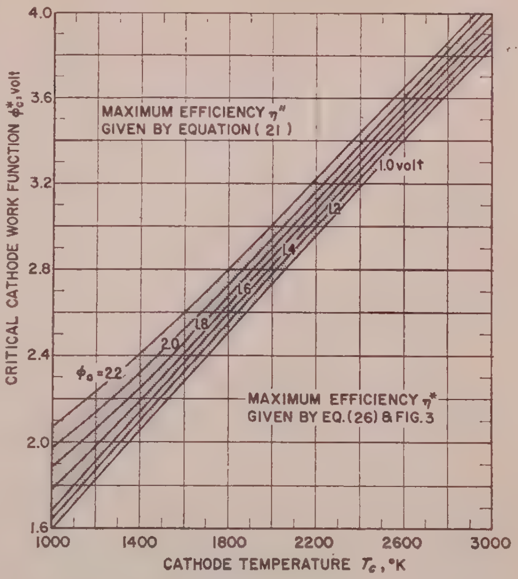

FIG. 4. Maximum allowable cathode work function for achieving the efficiency shown in Fig. 3 [solution of Eq. (27)].

At cathode temperatures above the point of tangency, Fig. 1 shows that the efficiency can in fact be improved by operating with an effective cathode work function greater than ϕ_c, which is achieved by operating with a load voltage greater than $\phi_c-\phi_a-V_w$. By optimizing the load voltage, the efficiency can be raised from η'' to η^*, the level of the envelope. To compute the load voltage required to achieve this optimization, we combine Eqs. (18), (20), (25), and (27). After eliminating ϕ_c and α, we obtain

$$V_{\text{opt}}=\left(\frac{\eta^*}{1-\eta^*}\right)\phi_a+\left[\left(\frac{\pi}{1-\eta^*}\right)\left(\frac{\eta^*}{6-3\eta^*}\right)^{\frac{1}{2}}+\left(\frac{1+\eta^*}{1-\eta^*}\right)\right]\frac{kT_c}{e}, \tag{28}$$

where η^* is given by Eq. (26).

A somewhat more rigorous proof of the above argument can be presented by substituting ϕ_a+V+V_w for ϕ_c in Eq. (16), and solving for the maximum attainable efficiency by optimizing V and V_w. The result obtained is identical to Eq. (26). Therefore, for a given anode work function ϕ_a and cathode temperature T_c, Eq. (26) defines the greatest possible efficiency in terms of the fundamental physical constants e, m, c, and k.

We can now prescribe a definite procedure for computing the maximum attainable efficiency for given values of ϕ_a, ϕ_c, T_c, and $\bar{\epsilon}$. First, we use Eq. (27) to compute the critical cathode work function ϕ_c^*. Then, if $\phi_c^*\leq\phi_c$, the maximum efficiency is given by Eq. (21); If $\phi_c<\phi_c^*$, the maximum efficiency is given by Eq. (26).

RESULTS AND CONCLUSIONS

For an anode work function of 1.6 v, Fig. 2 illustrates the effect of cathode work function and temperature

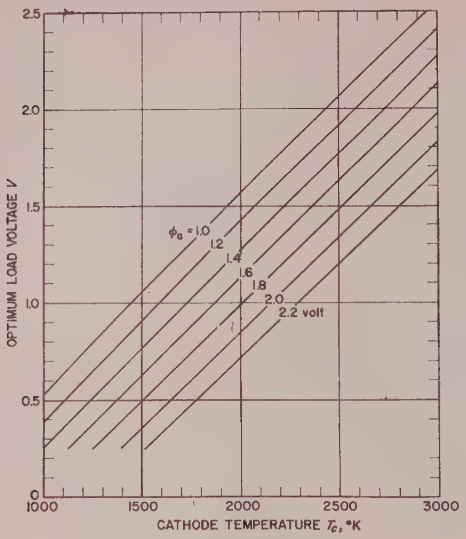

Fig. 5. Optimum load voltage, provided the cathode work function does not exceed the value shown in Fig. 4.

on maximum attainable efficiency.[12] As can be seen, the maximum efficiency increases with decreasing cathode work function and increasing temperature. However, at a given temperature T_c, there is no advantage in reducing the cathode work function below its critical value ϕ_c^*.

The effect of anode work function and cathode temperature on the maximum possible efficiency is shown in Fig. 3. This efficiency can only be achieved if the cathode work function does not exceed its critical value ϕ_c^*. As expected, η^* increases with decreasing ϕ_a and increasing T_c, at least over the range of practical interest.

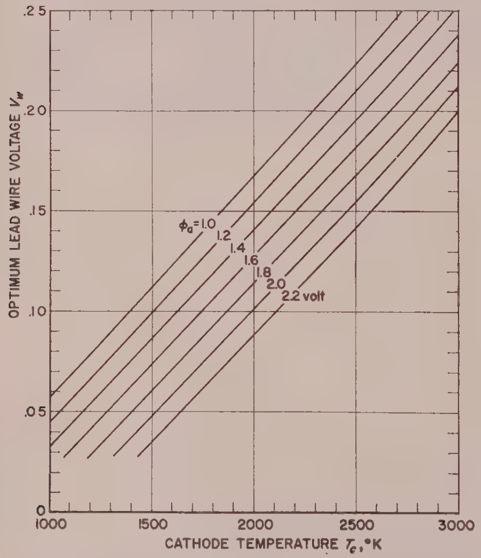

Fig. 6. Optimum lead wire voltage V_w, provided the cathode work function does not exceed the value shown in Fig. 4.

The variation of critical cathode work function with ϕ_a and T_c is depicted in Fig. 4. Each curve represents a given value of ϕ_a. The maximum efficiency is given by Eq. (21) for points above that curve, and by Eq. (26) in the region below the curve.

Once the maximum efficiency η^* has been determined, it is simple to compute the optimum load voltage [Eq. (28)] and lead wire voltage [Eq. (20)]. The results are shown by Figs. 5 and 6, respectively. Note that, as a rough rule of thumb, the optimum lead wire voltage is about one-tenth the optimum load voltage.

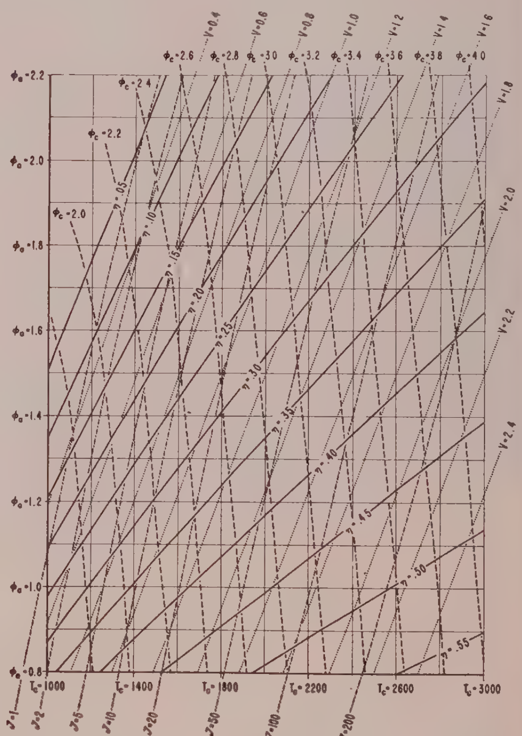

Fig. 7. Optimization of converter having anode work function ϕ_a and cathode temperature T_c, showing the maximum efficiency η^*, the critical cathode work function ϕ_c^*, the optimum load voltage V, and current density J (amp/cm²).

All results are combined in Fig. 7, which shows the interrelationship of the system variables ϕ_a, T_c, η^*, V, ϕ_c^*, and J for optimized operation.

Let us now examine which regions of Fig. 7 may be of practical significance and which are merely of theoretical interest. First, we eliminate the region $\phi_a<1.1$, since it is doubtful whether lower work functions can be achieved at present.

---

[12] All computations used the effective emissivity $\bar{\epsilon}$ defined by Eq. (23).

Next, we note that at low cathode temperatures there is insufficient ionization of incident cesium atoms for complete space-charge cancellation.[13] It is difficult to assign an exact lower temperature limit for the cathode, but certainly the domain $T_c < 1300$°K should be excluded.

We shall not eliminate the region in which the cathode work function is less than the ionization potential of cesium; first, because the cathode surface may be patchy, with enough high-work-function area to create the required number of positive ions, and also because processes other than resonance ionization at the cathode may serve to produce the cesium ions.

Although the melting point of tungsten is 3643°K, we shall exclude the region $T_c > 2800$°K. At that temperature tungsten evaporates at the rate of 2 mm per year,[14] and it is felt that higher cathode temperatures would result in too short a lifetime for most applications.

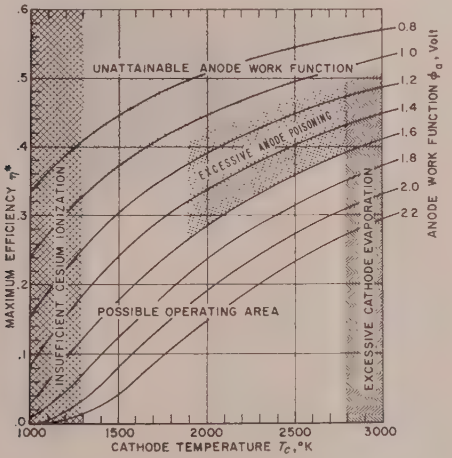

FIG. 8. Practical range of anode work function and cathode temperature, showing maximum efficiency attainable if $\phi_c \leqslant \phi_c^*$.

Next, we note that very low-work-function anode surfaces are usually complex chemical systems, such as Cs on AgO on Ag.[15] Such work functions are difficult to achieve and to maintain, since they are easily poisoned. Hence, we postulate that very low anode work functions are only practical with cathode temperatures below 1900°K, at which temperature the evaporation rate of tungsten reaches a value of 1 atom layer per year.[14] We therefore exclude the region ($T_c > 1900$°K, $\phi_a < 1.6$ v), the latter value being the work function of an anode coated with a monatomic layer of cesium.

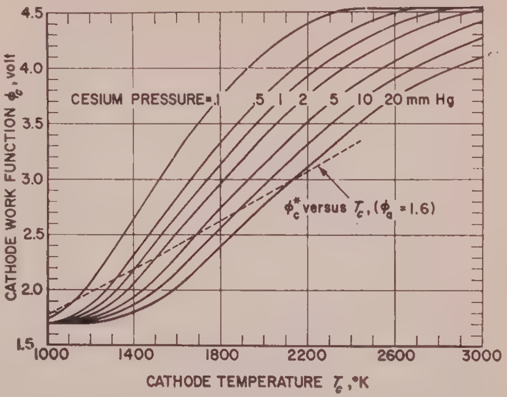

FIG. 9. Work function of cesium coated tungsten cathode. (The dotted line shows the critical cathode work function ϕ_c^*.)

If the four regions enumerated above are removed from Fig. 3, we are left with the unshaded area shown in Fig. 8. The highest efficiencies are seen to occur under two distinct operating conditions. The left peak corresponds to operation with low work functions, moderate cathode temperatures, and generally low cesium pressures; whereas the right peak represents the goal of those who feel that very low anode work functions would be too difficult to maintain, and who favor operation at moderate work functions, high temperatures, and relatively high cesium pressures.

Finally, let us examine the important case in which cesium not only coats the anode, but also serves to modify the work function of the cathode. This has been referred to as a self-healing cathode, since the atoms evaporating from its surface are continuously replenished. For a tungsten cathode in equilibrium with

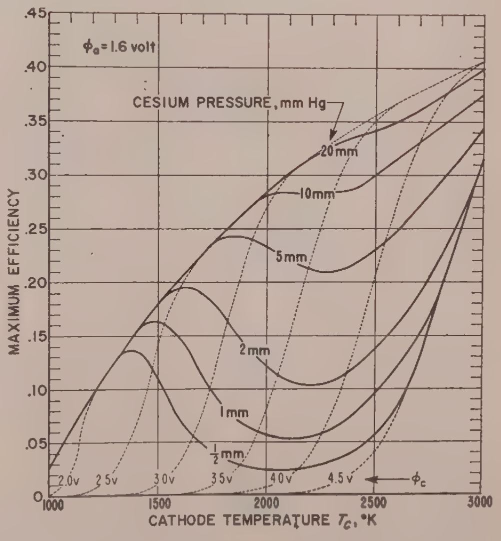

FIG. 10. Effect of cesium pressure and cathode temperature on maximum efficiency of diode.

---

[13] S. Datz and E. H. Taylor, J. Chem. Phys. **25**, 389 (1956).

[14] C. D. Hodgman, *Handbook of Chemistry and Physics* (Chemical Rubber Publishing Company, Cleveland, Ohio), 39th ed., p. 2748.

[15] K. G. Hernqvist, M. Kanefsky, and F. H. Norman, RCA Rev. **19**, 244 (1958).

TABLE I. Optimum performance of converter with tungsten cathode, at various cesium pressures.

μ_a	Cesium arrival rate	atom/cm² sec	5×10^{19}	1×10^{20}	2×10^{20}	5×10^{20}	1×10^{21}
p_{Cs}	Cesium pressure (approx.)	mm Hg	0.5	1	2	5	10
T_{Cs}	Cesium reservoir temperature	°C	235	255	278	309	335
T_c	Cathode temperature	°K	1375	1480	1620	1830	2080
ϕ_c	Cathode work function	v	2.250	2.380	2.560	2.795	3.090
ϕ_a	Anode work function	v	1.600	1.600	1.600	1.600	1.600
J	Current density	amp/cm²	1.297	2.090	3.448	8.098	17.077
V	Load voltage	v	0.592	0.711	0.882	1.094	1.358
V_w	Lead wire voltage	v	0.058	0.069	0.078	0.102	0.132
P	Power density	w/cm²	0.768	1.486	3.043	8.855	23.192
q_e	Electron cooling	w/cm²	3.225	5.507	9.789	25.189	58.892
q_r	Radiative cooling	w/cm²	1.881	2.846	4.582	8.672	16.421
q_c	Conductive cooling	w/cm²	0.476	0.734	1.282	2.835	5.680
q_T	Total heat input	w/cm²	5.582	9.087	15.653	36.696	80.993
η	Efficiency	%	13.75	16.35	19.44	24.13	28.64

cesium vapor at a pressure p_{Cs}; the dependence of work function ϕ_c on temperature T_c has been computed by Wilson,[16] by extrapolating the measurements of Taylor and Langmuir.[17] Recent measurements indicate that cesium coatings on other refractory metals (Mo, Ta) show a similar behavior. After suitable interpolation, Wilson's data may be crossplotted in the convenient form shown in Fig. 9. On the same figure, the dotted line shows the critical cathode work function ϕ_c^*, for an anode work function of 1.6 v. This line is the solution of Eq. (27), and was transposed from Fig. 4. Below that line, the maximum efficiency for a given cesium pressure and cathode temperature is given by the envelope of Fig. 1 [Eq. (26)]. Above the dotted line, the maximum efficiency is computed by inserting the appropriate cathode work function from Fig. 9 into Eq. (21). The results of these computations, for an anode work function 1.6 v, are illustrated by Fig. 10. It should be emphasized again that these results are predicated on an electrode spacing close enough so that the plasma resistance may be neglected.

Inspection of Fig. 10 leads to some interesting conclusions about the performance of thermionic converters with cesium coated tungsten cathodes:

(1) At certain cathode temperatures (e.g., 2000°K) the cesium pressure has a very pronounced effect on maximum efficiency.

(2) For most cesium pressures, efficiency is strongly dependent on cathode temperature.

(3) At each cathode temperature, there is a cesium pressure beyond which there is no advantage in operating. For example, at $T_c=1700$°K, increasing p_{Cs} above 5 mm Hg does not improve the efficiency, and may in fact be harmful by increasing electron collisions.

(4) At most cesium pressures, there is a critical temperature at which the efficiency reaches a peak. For example, at a cesium pressure of 1 mm Hg the efficiency reaches a peak of 16.4% at a cathode temperature of 1480°K. At higher temperatures η'' drops off rapidly, and does not regain its peak value until $T_c=2740$°K. In general, there is little advantage in operating the cathode above that critical temperature.

Finally, Table I summarizes the optimum operation of converters with cesium coated cathodes, for the conditions corresponding to the various peaks in Fig. 10.

ACKNOWLEDGMENTS

The author is greatly indebted to A. E. Kunen and C. L. Eisen of Republic Aviation Corporation; to the former for his support and encouragement, and to the latter for many helpful discussions.

---

[16] V. C. Wilson, J. Appl. Phys. **30**, 475 (1959).

[17] J. B. Taylor and I. Langmuir, Phys. Rev. **44**, 423 (1933).

JOURNAL OF APPLIED PHYSICS VOLUME 32, NUMBER 8 AUGUST, 1961

Increase in Dielectric Constant during Switching in Lithium Selenite and Triglycine Sulfate

Ennio Fatuzzo
Laboratories RCA Ltd., Zurich, Switzerland

(Received January 23, 1961)

The dielectric constant of lithium selenite and triglycine sulfate was measured during switching up to frequencies of 100 Mc. The increase in dielectric constant during switching was found to decrease with frequency ν as $1/\nu$ at low frequencies and as $1/\nu^2$ at high frequencies. A model to explain the experimental results is given and discussed. It is shown that information about the domain wall mass can be obtained from this kind of measurement.

I. INTRODUCTION

IN 1954 Drougard *et al.*,[1] using a bridge method, found that when the small signal dielectric constant in $BaTiO_3$ is measured during switching, it increases many times with respect to its normal value. In 1956 they proposed a model[2] with which they were able to explain some, but not all, of their experimental results.

In 1958 Husimi[3] found that not only the dielectric constant, but also the second harmonic distortion, increases in $BaTiO_3$ during switching. Instead of the bridge method he used a circuit which gave an ac output voltage whose peak amplitude was proportional to the modulus $|\epsilon_s|$ of the dielectric constant of the ferroelectric [Fig. 1(a)]. Figure 1(b) represents the peak amplitude V of the ac output vs time; i.e., the envelope of the curve in Fig. 1(a). It thus shows the dependence of $|\epsilon_s|$ on time (as obtained by Husimi[3]) when switching occurs between t_a and t_b. We define ϵ_N as the dielectric constant of the ferroelectric without switching, which we assume to be real. A measure of the increase of the dielectric constant is defined as $\langle\Delta\epsilon\rangle = |\epsilon_s| - \epsilon_N$, and the maximum of $\langle\Delta\epsilon\rangle$ reached during switching as $\langle\Delta\epsilon\rangle_{\max}$; V_N is the output voltage corresponding to ϵ_N and $\Delta V_{\max}$ is the one corresponding to $\langle\Delta\epsilon\rangle_{\max}$ [Fig. 1(b)].

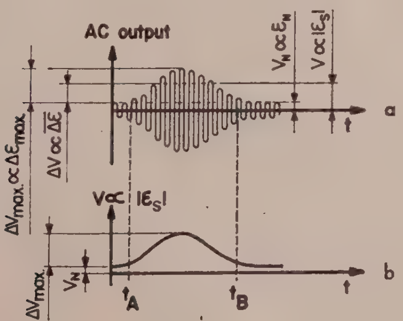

Fig. 1. (a) Alternating current output vs time. (b) Peak amplitude vs time or envelope of the curve of (a).

Prutton[4] found that the dielectric constant increases during switching also in guanidine aluminum sulfate hexahydrate (GASH).

Drougard and Young,[5] measuring $BaTiO_3$ at extremely low frequencies (1 cycle in 3 hr), found a *decrease* of dielectric constant during switching, a result in contrast to the increase of dielectric constant at normal frequencies which the authors explained by piezoelectric strains.

In the present paper we report the measurements of the increase in dielectric constant during switching found in two new materials: lithium selenite and triglycine sulfate (TGS). The effect was measured as a function of frequency up to 100 Mc with an arrangement similar to that of Husimi.[3] The experimental results are given in Sec. II; in Sec. III a model is described, and in Sec. IV a comparison is made between model and experiments.

II. EXPERIMENTAL RESULTS

A. Description of the Circuit

The circuit used in our measurements is shown in Fig. 2. The signal generator S provides a sine wave of small amplitude ($\cong$1 v) and of frequency range between 100 cycle/sec and 250 Mc for measuring the dielectric constant. The voltage generator P provides pulses of variable amplitude and duration, and of repetition rate of about 50 sec^{-1}, for switching the ferroelectric. The ferroelectric crystal F is connected between A and B. Due to the switching, at point B a voltage (switching pulse) appears on which the high-frequency sine wave is superimposed. The amplitude of this sine wave at point B is proportional to the modulus of the admit-

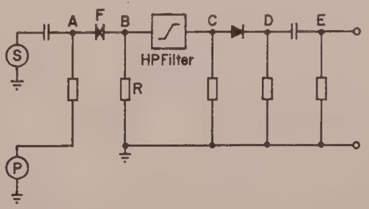

Fig. 2. Diagram of the circuit used in our measurements.

---

[1] M. E. Drougard, H. L. Funk, and D. R. Young, J. Appl. Phys. **25**, 1166 (1954).

[2] R. Landauer, D. R. Young, and M. E. Drougard, J. Appl. Phys. **27**, 752 (1956).

[3] K. Husimi, J. Appl. Phys. **30**, 978 (1959).

[4] M. Prutton, Proc. Phys. Soc. (London) **70**, 702 (1957).

[5] M. E. Drougard and D. R. Young, Phys. Rev. **94**, 1561 (1954).

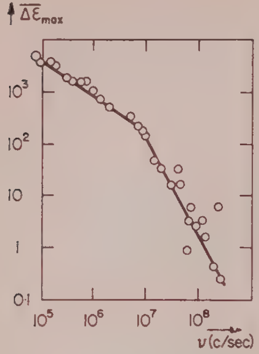

FIG. 3. $\langle\Delta\epsilon\rangle_{\max}$ vs ν in triglycine sulfate.

tance of F, providing this admittance is much less than that of R. At point C the signal has been filtered, so that only the ac sine wave is present [cf. Fig. 1(a)]. At each instant the signal at point D is proportional to the absolute value of the dielectric constant $|\epsilon_s|$ of the ferroelectric F. At very high frequencies (>100 Mc), however, the cable which connects point A to the generator introduces an inductive component, and accurate measurements can no longer be made.

To make the measurements accurately at every frequency, the ferroelectric F was replaced by a set of condensers so as to obtain a calibration curve of *output voltage* vs *capacitance* C. With the help of this calibration curve it is easy to calculate the modulus of the dielectric constant of the crystal, once the output voltage is known. During the measurements of dielectric constant the switching pulse could be observed across the resistance R.

B. Measurements

The present experiments were made under conditions different from those of references 1 and 3:

(a) The crystal was switched with square pulses instead of sine wave, because the mechanism of switching with pulses has been studied rather extensively in TGS[6,7] and in $LiH_3(SeO_3)_2$.[8]

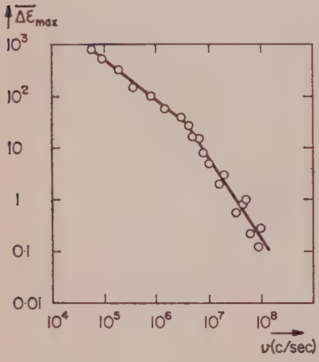

FIG. 4 $\langle\Delta\epsilon\rangle_{\max}$ vs ν in lithium selenite.

(b) The signal at point C was rectified, so that at D one could observe the envelope of the voltage which appeared at point C. This allowed accurate measurements up to high frequencies, as will be seen from the following considerations.

At frequencies of the order of 10 Mc or more the voltage $\Delta V_{\max}$ (see Fig. 1) is much smaller than the voltage V_N (measured without switching). Thus $\Delta V_{\max}$ is the difference between two large quantities, V and V_N. To improve the accuracy of this measurement, we filtered off the dc component V_N (due to the normal dielectric constant) and amplified the remaining pulse $\Delta V_{\max}$ alone [see Fig. 1(b)].

We restricted ourselves to measurements in which the crystals were switched with rather low fields (<5 kv/cm) so as to have switching times of the order of 100 μsec or longer. Experiments using shorter switching times and higher frequencies will be the subject of separate work.

1. $\langle\Delta\epsilon\rangle_{\max}$ vs Frequency ν

$\langle\Delta\epsilon\rangle_{\max}$ was measured as a function of frequency ν; the results are shown in Fig. 3 for TGS and in Fig. 4 for lithium selenite. Both curves are composed of two parts having different slopes. Although there are small differences between different samples, both in TGS and in lithium selenite the slope of the low-frequency part is about 1 and the slope of the high-frequency part is about 2.

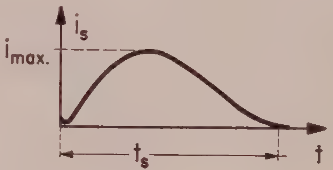

FIG. 5. Switching current i vs time t.

2. $\langle\Delta\epsilon\rangle$ vs Switching Current i

We also measured the dependence of $\langle\Delta\epsilon\rangle$ on the switching current i for different switching times and different measuring frequencies ν. The switching current varies with time, as shown in Fig. 5. With a double-trace oscilloscope the switching current i and the output curve of Fig. 1(b) could be shown simultaneously. The two traces could always be rather well superimposed, showing that:

$$\langle\Delta\epsilon\rangle \propto i. \tag{1}$$

These measurements were only accurate at low frequencies, since for frequencies higher than 1 Mc, $\langle\Delta\epsilon\rangle$ could not be measured very accurately.[9]

---

[6] C. F. Pulvari and W. Kuebler, J. Appl. Phys. **29**, 1742 (1958).

[7] E. Fatuzzo and W. J. Merz, Phys. Rev. **116**, 61 (1959).

[8] E. Fatuzzo, Helv. Phys. Acta **33**, 21 (1960).

[9] For switching times shorter than 100 μsec, relation (1) is no longer valid.

3. $\langle\Delta\epsilon\rangle_{\max}$ *and* $i_{\max}$ *vs Voltage* V *of the Applied Pulses*

By varying the voltage V of the applied pulses, one changes both $i_{\max}$ and $\langle\Delta\epsilon\rangle_{\max}$. In Fig. 6, $i_{\max}$ is plotted vs $\langle\Delta\epsilon\rangle_{\max}$ *with* V *as a parameter* and $\nu=50$ kc. In the course of the discussion we shall have to deal with the quantity $\rho=\langle\Delta\epsilon\rangle_{\max}V/i_{\max}$. In Fig. 7 this quantity is plotted vs the voltage V of the applied pulses.

4. *Second Harmonic Distortion* δ

No extensive studies of the increase in second harmonic distortion during switching were made; we did, however, obtain a few results which deserve to be mentioned. Measurements were made at a fixed frequency of $\nu=100$ kc; the low pass filter of Fig. 2 was substituted by a band pass filter centered on a frequency of 200 kc, while the frequency of the generator S was set to 100 kc. The 200-kc ac signal was due to the second harmonic distortion introduced by the ferroelectric and was displayed on the screen of an oscilloscope as a function of time. The maximum δ reached by the 200-kc signal is plotted in Fig. 8 as a function of the peak voltage E_1 of the signal generator S. From this it can be shown that:

$$\delta\propto E_1^{1.8}. \tag{2}$$

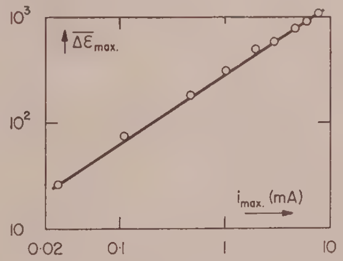

FIG. 6. $\langle\Delta\epsilon\rangle_{\max}$ vs $i_{\max}$ with V as a parameter.

III. PROPOSED MODEL

A. Increase in Dielectric Constant

Before describing a model which explains the increase in dielectric constant during switching, it is necessary to review the mechanism by which polarization reverses. It is assumed that the nuclei of the domains are formed according to a statistical process. The time t_n necessary to form *all* the nuclei (from the first to the last) is given by the exponential law[7,10,11]

$$1/t_n=(1/t_0)\exp(-\alpha/E). \tag{3}$$

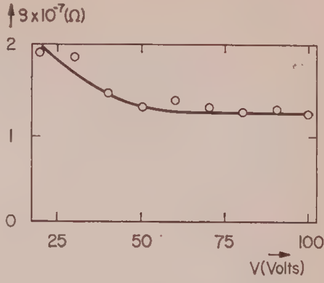

FIG. 7. ρ vs V.

After formation, each nucleus grows predominantly in the direction of the applied field. If v is the average velocity of growth, t_d the time necessary for one nucleus to grow through the sample, E the applied field, μ the forward mobility, l the thickness of the sample, and V the applied voltage, one finds [cf. Eq. (5) of reference 7]

$$v=l/t_d=\mu E=\mu V/l. \tag{4}$$

This model does not necessarily exclude a certain amount of sideways motion, provided this is "apparent" sideways motion; in other words, provided it is due to the following effect: new nuclei of domains prefer to form at the edge of an existing domain rather than elsewhere. After their formation, these domains grow mainly in the direction of the field. The successive formation of new domains at the edge of existing ones gives the impression of a sideways motion ("apparent" sideways motion). This mechanism of "apparent" sideways growth of domains is not unknown in ferroelectrics; it has been observed[12,13] in $BaTiO_3$ at very low switching speeds. Although it is not known which mechanism of sideways growth takes place at higher switching speeds in TGS and $LiH_3(SeO_3)_2$, we shall assume that, if there is any sideways motion at all, this is of the "apparent" type.

With this assumption we shall have to deal just with domains growing in the forward direction because, as already stated, the apparent sideways growth consists of many forward growing domains.

We assume that the equation of motion of one domain wall during its forward growth is (cf. Kittel[14] for the case of sideways motion)

$$m\ddot{x}+\beta\dot{x}+kx=2P_sE, \tag{5}$$

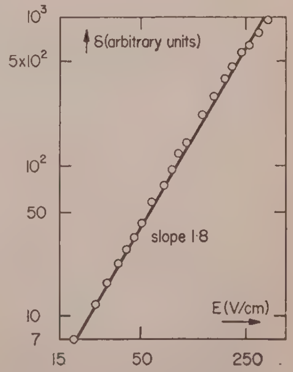

FIG. 8. Second harmonic distortion δ vs E_1.

---

[10] W. J. Merz, Phys. Rev. **95**, 690 (1954).
[11] W. J. Merz, J. Appl. Phys. **27**, 938 (1956).
[12] R. C. Miller and A. Savage, Phys. Rev. **115**, 1176 (1959).
[13] R. C. Miller and G. Weinreich, Phys. Rev. **117**, 1460 (1960).

where m is the effective mass per unit area of the domain wall, P_s the spontaneous polarization of the material, x the length of the nucleus (see Fig. 9), $\beta\dot{x}$ a damping force per unit area, and (kx) a restoring force per unit area. The damping force assumed here is supported by a certain amount of experimental evidence[7]; it can be explained by the interaction of the switching dipoles with adjacent unswitched ones at the domain boundary.

The restoring force can be described as a kind of "surface tension" of the domain boundary and is caused by the fact that both the depolarizing and the surface energy increase with increasing x.

Equation (5) is only a first approximation since it is strictly valid just for a cylindrical domain, and we have clear indications[7,10,11] that the domains are not cylindrical. However, in order to obtain reasonable equations, we must assume Eq. (5) in the first place.

It is also assumed that the restoring force is very small compared to the driving force $2P_sE$. We then obtain from Eq. (5) for the stationary condition

$$v=\dot{x}\cong 2P_sE\beta^{-1}, \tag{6}$$

and hence [cf. Eq. (4)]

$$\mu=2P_s\beta^{-1}. \tag{7}$$

In our experiments a constant field E_0 is applied (to switch the crystal); on this field a sine wave ΔE_0 of angular frequency $\omega=2\pi\nu$ is superimposed (to measure the dielectric constant). In Eq. (5), E must therefore be substituted by $(E_0+\Delta E_0)$, where $|\Delta E_0|=|E_1\times\exp(j\omega t)|$ is much smaller than E_0. Then Eq. (5) becomes

$$\ddot{x}+\gamma\dot{x}+\omega_0^2x=2P_sm^{-1}[E_0+E_1\exp(j\omega t)], \tag{8}$$

with

$$\gamma=\beta m^{-1} \tag{9}$$

and

$$\omega_0^2=km^{-1}. \tag{10}$$

If we assume that the domain wall motion is very much damped, similarly to a viscous drag, it follows that

$$\omega_0\ll\gamma. \tag{11}$$

The increase in dielectric constant during switching may be explained in the following way: during switching, there is a certain number of domains which are growing; on the "top" of these domains there is a finite divergence of the polarization (Fig. 9). The ac field (which measures the dielectric constant) makes this charge oscillate while the domain is growing. This fact produces an increase in the observed dielectric constant, which may be treated quantitatively in the following way.

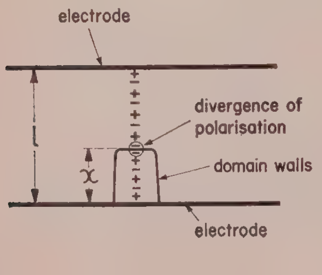

FIG. 9. Divergence of the polarization arising during the growth of a domain.

Starting from Eq. (8), and with no additional assumption besides the ones already made, a number of conclusions may be drawn. The detailed calculations are made in Appendix A, and the results are given below. Let $\Delta\epsilon_i$ be the increase in dielectric constant during switching. It can be shown (see Appendix A) that $\Delta\epsilon_i$ is not an explicit function of the time, but depends on time because it is proportional to the switching current i. This dependence of $\Delta\epsilon_i$ on i is expressed by the following formula (see Appendix A):

$$\Delta\epsilon_i=\Delta\epsilon(i/i_{\max}). \tag{12}$$

Here $\Delta\epsilon$ is the maximum increase in dielectric constant achieved during the switching; i.e., the increase in dielectric constant when the switching current reaches its maximum $(i=i_{\max})$. The real and imaginary part of $\Delta\epsilon$ can be separated by writing

$$\Delta\epsilon=\Delta\epsilon'-j\Delta\epsilon''.$$

It can be shown (see Appendix A) that:

$$\Delta\epsilon'=\{32\pi P_s^2t_d(\omega_0^2-\omega^2)/t_slm[(\omega_0^2-\omega^2)^2+\omega^2\gamma^2]\}, \tag{13}$$

$$\Delta\epsilon''=\{32\pi P_s^2t_d\gamma\omega/t_slm[(\omega_0^2-\omega^2)^2+\omega^2\gamma^2]\}. \tag{14}$$

If $|\Delta\epsilon|=[(\Delta\epsilon')^2+(\Delta\epsilon'')^2]^{\frac{1}{2}}$ is the absolute value of $\Delta\epsilon$, we obtain from Eqs. (13) and (14):

$$|\Delta\epsilon|=\frac{32\pi P_s^2t_d}{t_slm}\frac{1}{[(\omega_0^2-\omega^2)^2+\omega^2\gamma^2]^{\frac{1}{2}}}=\frac{C}{[(\omega_0^2-\omega^2)^2+\gamma^2\omega^2]^{\frac{1}{2}}}, \tag{15}$$

where

$$C=32\pi P_s^2t_d/t_slm. \tag{16}$$

If $\tan\delta=|\Delta\epsilon''/\Delta\epsilon'|$ is a kind of loss tangent, we obtain from Eqs. (13) and (14)

$$|\Delta\epsilon''/\Delta\epsilon'|=\tan\delta=\gamma\omega/|\omega_0^2-\omega^2|. \tag{17}$$

Equations (15) and (17), however, are too complicated to be compared directly with the experimental results and therefore must be simplified by making some approximations. Dealing first with Eq. (17) and taking into account the assumption $\omega_0\ll\gamma$ already made, it is easy to see that

$$\left.\begin{aligned}&|\Delta\epsilon''/\Delta\epsilon'|=\tan\delta\ll1\quad\text{when}\quad\omega\gg\gamma\\&|\Delta\epsilon''/\Delta\epsilon'|=\tan\delta\cong1\quad\text{when}\quad\omega\cong\gamma\\&|\Delta\epsilon''/\Delta\epsilon'|=\tan\delta\ll1\quad\text{when}\quad\omega_0^2/\gamma\ll\omega\ll\gamma\end{aligned}\right\}. \tag{18}$$

Now, considering Eq. (15), if one defines

$$K=C\gamma^{-1}=32\pi P_s^2t_d/t_slm\gamma \tag{19}$$

and remembers that $\omega_0 \ll \gamma$ (viscous drag motion), one can approximate Eq. (15) by

$$\left.\begin{aligned} |\Delta\epsilon| &\cong K/\omega \quad \text{if} \quad \omega_0^2/\gamma \ll \omega \ll \gamma \\ |\Delta\epsilon| &\cong C/\omega^2 \quad \text{if} \quad \omega \gg \gamma \end{aligned}\right\}. \tag{20}$$

This result will be discussed in Sec. IV.

From Eqs. (5) and (9) it follows that

$$\gamma = \beta m^{-1} = 2P_s \mu^{-1} m^{-1}. \tag{21}$$

Although we know P_s and μ for TGS,[7] we are unable to calculate γ because we do not know the wall mass m. However, we can calculate the coefficient K from Eqs. (19), (4), and (21):

$$K = \frac{32\pi P_s^2 t_d}{t_s l m \gamma} = \frac{32\pi P_s^2 (l/\mu E)}{t_s l m 2 P_s \mu^{-1} m^{-1}} = \frac{16\pi P_s}{t_s E}. \tag{22}$$

For TGS one obtains (with $P_s = 6\times 10^3$ esu; $E = 3$ esu, and $t_s = 10^{-3}$ sec)

$$K = 10^8 \text{ sec}^{-1} \tag{23}$$

and, for lithium selenite (with $P_s = 5\times 10^4$ esu; $E = 10$ esu, and $t_s = 10^{-2}$ sec):

$$K = 2.5\times 10^7 \text{ sec}^{-1}. \tag{24}$$

B. Second Harmonic Distortion

The increase in second harmonic distortion during switching does not follow from Eq. (8). It can be explained either by adding a small quadratic restoring force $\omega'^2 x^2$ or a small quadratic damping term $\gamma \dot{x}^2$ to Eq. (8). The two cases will be considered separately.

1. Second Harmonic Distortion Caused by a Nonlinear Restoring Force

In this case Eq. (8) can be rewritten as

$$\ddot{x} + \gamma x + \omega_0^2 x + \omega'^2 x^2 = 2P_s m^{-1} [E_0 + E_1 \exp(j\omega t)], \tag{25}$$

where $E_1 \ll E_0$.

If the oscillatory solution is of the form

$$\Delta x = K_1 e^{j\omega t} + K_2 e^{2j\omega t}, \tag{26}$$

by neglecting higher than second-order terms one obtains

$$\left.\begin{aligned} K_1 &= \frac{2P_s E_1}{m} \frac{1}{(\omega_0^2 - \omega^2) + j\omega\gamma} \\ K_2 &= \frac{\omega'^2 K_1^2}{4\omega^2 - \omega_0^2 - 2j\omega\gamma} = f(\omega) E_1^2 \end{aligned}\right\}, \tag{27}$$

where $f(\omega)$ is a function of frequency alone. Hence

$$\Delta x = \frac{2P_s E_1}{m} \frac{e^{j\omega t}}{(\omega_0^2 - \omega^2) + j\omega\gamma} + f(\omega) E_1^2 e^{2j\omega t}. \tag{28}$$

The second term is proportional to the second harmonic distortion δ, where

$$\delta = f(\omega) E_1^2. \tag{29}$$

2. Second Harmonic Distortion Caused by a Nonlinear Viscous Force

In this case Eq. (8) can be rewritten as

$$\ddot{x} + \gamma\dot{x} + \gamma'\dot{x}^2 + \omega_0^2 x = 2P_s m^{-1} [E_0 + E_1 \exp(j\omega t)]. \tag{30}$$

Treating this equation as in Sec. IIIB1, one obtains

$$\Delta x = \frac{2P_s E_1}{m} \frac{\exp(j\omega t)}{(\omega_0^2 - \omega^2) + j\omega\gamma} + f(\omega) E_1^2 e^{2j\omega t}, \tag{31}$$

and hence again

$$\delta = f(\omega) E_1^2. \tag{32}$$

IV. COMPARISON BETWEEN MODEL AND EXPERIMENT

In this section we shall consider the experimental results of Secs. IIB1, 2, and 3, and we shall try to compare them with the theoretical predictions of our model.

A. $\langle\Delta\epsilon\rangle_{\max}$ vs Frequency ν

We see from Eq. (20) that $|\Delta\epsilon|$ decreases proportionately to $1/\omega$ for $\omega \ll \gamma$ and to $1/\omega^2$ for $\omega \gg \gamma$; at about $\omega \cong \gamma$ there is a change in slope. This is precisely what happens in Figs. 3 and 4: $\langle\Delta\epsilon\rangle_{\max}$ decreases first proportionally to $1/\omega$ and then to $1/\omega^2$ and there is a change in slope at a frequency $\nu_0 \cong 10^7$ cycles/sec. It is therefore very tempting to identify Eq. (20) with the curves of Figs. 3 and 4, and to identify the change in slope of these curves with that of Eq. (20). In this case we have:

$$\gamma = 2\pi\nu_0 \cong 6\times 10^7 \text{ sec}^{-1}. \tag{33}$$

It is shown in Appendix B that the experimental quantity $\langle\Delta\epsilon\rangle_{\max}$ is then given by

$$\langle\Delta\epsilon\rangle_{\max} \cong |\Delta\epsilon|. \tag{34}$$

Thus the theoretical values of Eq. (20) are directly comparable with the experimental results.

Table I lists the values for K, the slopes m of the low-frequency part of the curve $\log\langle\Delta\epsilon\rangle_{\max}$ vs $\log\nu$, and the slope n of the high-frequency part. The experimental values are obtained from an average on all the curves like Figs. 3 and 4 which we measured on different samples. The theoretical values are obtained from Eqs. (23) and (24) for K and from Eq. (20) for m and n.

TABLE I. Values for K, the slope m, and the slope n.

	TGS		$LiH_3(SeO_3)_2$	
	Theor.	Exptl.	Theor.	Exptl.
K	10^8	5×10^8	2.5×10^7	2×10^7
m	1	0.7	1	0.6–0.8
n	2	1.8	2	1.9

The slight disagreement between theoretical and experimental values of m and n is probably due to the fact that Eq. (8) has to be modified if the growing domains are not of cylindrical shape.

If one substitutes the experimental value of γ derived from Eq. (34) into Eq. (21), one obtains for the effective mass of the domain wall in TGS ($P_s=2\mu$ coul/cm^2; $\mu=2$ cm^2/v sec)

$$m=4\times10^{-7}\ \text{g/cm}^2. \tag{35}$$

Since there is no published experimental information about wall mass in ferroelectrics, this value can only be examined on a general basis.

Kittel[14] estimated the mass of sideways moving domain walls in BaTiO$_3$ by taking into account the energy required to move the Ti ions alone. He found $m=10^{-10}$ g/cm^2. If his calculation is repeated for the case of TGS a somewhat similar figure is found, which is therefore three orders of magnitude different from the value of Eq. (35). Such a discrepancy suggests that the assumptions made in arriving at Eq. (35) are not fulfilled in the experiment and an alternative explanation has to be sought.

We have measured the increase in dielectric constant during switching up to a maximum frequency $\nu_{\max}=10^8$ cycles/sec; i.e., up to an angular frequency $\omega_{\max}\cong6\times10^{+8}$ sec^{-1}. If we now assume that

$$\gamma\gg\omega_{\max}=6\times10^8\ \text{sec}^{-1} \tag{36}$$

so that in all measurements we have

$$\omega<\omega_{\max}\ll\gamma,$$

then, taking this into account, we have, from the first of Eq. (20),

$$|\Delta\epsilon|\cong K/\omega \tag{37}$$

and from the first of Eq. (18),

$$|\Delta\epsilon''/\Delta\epsilon'|=\tan\delta\gg1;$$

that is,

$$\Delta\epsilon''\gg\Delta\epsilon' \tag{38}$$

and hence also

$$|\Delta\epsilon|\cong\Delta\epsilon''. \tag{39}$$

From Eq. (39) and (37) it follows that

$$\Delta\epsilon''\cong K/\omega. \tag{40}$$

Since we have [cf. Eq. (67)]

$$\langle\Delta\epsilon\rangle_{\max}=|\epsilon_s|-\epsilon_N=[(\Delta\epsilon'+\epsilon_N)^2+(\Delta\epsilon'')^2]^{\frac{1}{2}}-\epsilon_N,$$

with the help of Eq. (38) we can neglect $\Delta\epsilon'$ and write

$$\langle\Delta\epsilon\rangle_{\max}\cong[\epsilon_N{}^2+(\Delta\epsilon'')^2]^{\frac{1}{2}}-\epsilon_N. \tag{41}$$

Equation (41) can be simplified considering the two cases $\Delta\epsilon''\ll\epsilon_N$ and $\Delta\epsilon''\gg\epsilon_N$.

We have therefore

$$\left.\begin{array}{ll}\langle\Delta\epsilon\rangle_{\max}\cong\Delta\epsilon'' & \text{if}\quad \Delta\epsilon''\gg\epsilon_N\\ \langle\Delta\epsilon\rangle_{\max}\cong(\Delta\epsilon'')^2/2\epsilon_N & \text{if}\quad \Delta\epsilon''\ll\epsilon_N\end{array}\right\}. \tag{42}$$

By taking into account both Eq. (40) and Eq. (39) we can rewrite Eq. (42) as follows:

$$\left.\begin{array}{ll}\langle\Delta\epsilon\rangle_{\max}\cong K/\omega & \text{if}\quad |\Delta\epsilon|\gg\epsilon_N\\ \langle\Delta\epsilon\rangle_{\max}\cong(K^2/2\epsilon_N)(1/\omega^2) & \text{if}\quad |\Delta\epsilon|\ll\epsilon_N\end{array}\right\}. \tag{43}$$

Also in this case, therefore, we find that $\langle\Delta\epsilon\rangle_{\max}$ is proportional first to $1/\omega$ and then to $1/\omega^2$. In this case the change in slope occurs when $|\Delta\epsilon|=\epsilon_N$; i.e., when the dielectric constant doubles during switching, and the model also fits with the curves of Figs. 3 and 4.

In this case, by substituting Eq. (36) into Eq. (21) and calculating m we obtain

$$m<3\times10^{-8}\ \text{g/cm}^2,$$

which is in agreement with Kittel's[14] calculations.

B. $\langle\Delta\varepsilon\rangle$ vs Current i

From Eq. (12) it follows that

$$|\Delta\epsilon_i|\propto i.$$

On the other hand it can be shown [see Eq. (73)] that

$$|\Delta\epsilon_i|\cong\langle\Delta\epsilon\rangle,$$

and hence we have

$$\langle\Delta\epsilon\rangle\propto i,$$

which fits the experimental results of Sec. IIB2.

C. $\langle\Delta\varepsilon\rangle_{\max}$ and $i_{\max}$ vs Voltage V of Applied Pulses

From Eq. (15) it follows that, if ω is kept constant and V is varied, the product

$$\frac{|\Delta\epsilon|t_s}{t_d}\propto\frac{|\Delta\epsilon|\mu E}{i_{\max}}\propto\frac{|\Delta\epsilon|\mu V}{i_{\max}}$$

should remain constant, since $i_{\max}t_s=\text{const}$, and $1/t_d\propto\mu E$. Assuming that the mobility μ is constant, one finds that the product [see, for instance Eq. (34)]

$$\rho=|\Delta\epsilon|V/i_{\max}\cong\langle\Delta\epsilon\rangle_{\max}V/i_{\max}$$

should remain constant as a function of V. Figure 7 shows that ρ is constant as predicted by our model, except for small values of V, at which ρ rises. This rise might be due to the fact that at these values $\langle\Delta\epsilon\rangle_{\max}<\epsilon_N$, and that the contribution of ϵ_N to the total dielectric constant ϵ_s cannot simply be subtracted. Another reason for this rise might be a nonconstant mobility μ.

---

[14] C. Kittel, Phys. Rev. 83, 458 (1951).

D. Second Harmonic Distortion

To explain the increase in the second harmonic distortion during switching it was necessary to assume some nonlinear terms in the equation of motion, which gave [Eqs. (29) and (32)]

$$\delta \propto E_1^2.$$

The experimental results gave [Eq. (3)]

$$\delta \propto E_1^{1.8}.$$

It can be shown that a nonlinear term in the viscous force implies a field-dependent mobility μ.

E. Interpretation of the Drougard-Funk-Young Measurements

With the apparatus used it is not possible to measure $\Delta\epsilon'$ and $\Delta\epsilon''$ separately but only to obtain $|\Delta\epsilon| = [(\Delta\epsilon')^2 + (\Delta\epsilon'')^2]^{\frac{1}{2}}$. On the other hand, Drougard *et al.*[1] measured $\Delta\epsilon'$ and $\Delta\epsilon''$ separately on $BaTiO_3$ up to frequencies of 600 kc. If

$$\bar{\sigma} = \omega\epsilon_0\Delta\epsilon'' \qquad (44)$$

is the conductivity of the sample, they found experimentally (using our notation) that

$$\Delta\epsilon' = K'/\omega^2, \qquad (45)$$

where $K' = 2\times10^{15}\ \mathrm{sec}^{-2}$, and that

$$\bar{\sigma}/\Delta\epsilon' = \omega^2\tau\epsilon_0, \qquad (46)$$

with $\tau = 5\times10^{-6}$ sec. From Eqs. (44), (45), and (46) it follows that

$$\Delta\epsilon'' = K'\tau\omega. \qquad (47)$$

Drougard *et al.* made their measurements with ω varying in the range of 6×10^5 to $3.6\times10^6\ \mathrm{sec}^{-1}$. It is of interest to interpret their experiments in terms of the second proposed model given in Sec. IVA. This restricts the value of γ by the condition [see Eq. (36), which is valid also for $BaTiO_3$ if we assume a similar value for the wall mass]

$$\gamma \gg 6\times10^8\ \mathrm{sec}^{-1}.$$

To explain Drougard, Funk, and Young's experiments it is necessary to make some assumptions as regards the value of ω_0. It is possible to fit the results of Drougard *et al.* with those of the explanation proposed if we take, for example,

$$\omega_0 \cong 10^7\ \mathrm{sec}^{-1}.$$

With these values of ω_0 and γ, we can establish that in the range of frequencies used by Drougard *et al.* the following conditions apply:

$$\omega_0^2/\gamma \ll \omega \ll \gamma;\quad \omega \ll \omega_0.$$

Under these conditions, Eqs. (13) and (14) can be written [see also Eq. (16)]

$$\Delta\epsilon' \cong (C\omega_0^2/\gamma^2)(1/\omega^2) \qquad (48)$$

$$\Delta\epsilon'' \cong K/\omega. \qquad (49)$$

These provide the correct frequency dependence for $\Delta\epsilon'$ and $\Delta\epsilon''$ in agreement with the empirical equations (45) and (47). It remains to be verified that the constant K' and $K'\tau$ are in agreement with the theoretical values given in Eqs. (48) and (49); i.e.,

$$\left.\begin{aligned} K' &= 2\times10^{15}\ \mathrm{sec}^{-2} = C\omega_0^2/\gamma^2 \\ K'\tau &= 10^{10}\ \mathrm{sec}^{-1} = K \end{aligned}\right\}. \qquad (50)$$

Unfortunately, K' cannot be calculated because the value of ω_0 and γ is not known. The value of $K'\tau = K$, however, can be calculated from Eq. (22), if we introduce the values for t_s and E at the moment of switching. With $E = 1\mathrm{kv/cm} = 3$ esu, $t_s = 10^{-4}$ sec, and $P_s = 6\times10^4$ esu, we obtain

$$\tau K' = K = 10^{+10}\ \mathrm{sec}^{-1}.$$

It is apparent, therefore, that at least the second part of Eq. (50) is justified by our theory.

V. CONCLUSIONS

We have measured the increase in dielectric constant up to high frequencies and found that the frequency dependence of $\langle\Delta\epsilon\rangle_{\max}$ changes from $\langle\Delta\epsilon\rangle_{\max} \propto 1/\omega$ at low frequencies to $\langle\Delta\epsilon\rangle_{\max} \propto 1/\omega^2$ at high frequencies. A model was developed which explains both our experimental results and those of Drougard *et al.*[1] In particular, this model explains the change from the inverse linear to the inverse quadratic behavior at the frequency ν_0; it will be possible to confirm that the second of the proposed models is correct by extending the measurements to higher frequencies.

ACKNOWLEDGMENTS

We wish to thank Dr. W. J. Merz and Dr. J. C. Anderson for many helpful discussions, and H. Roetschi for his technical assistance.

APPENDIX A

In this appendix the derivation of Eqs. (12), (13), and (14) from Eq. (8) is shown. Integrating Eq. (8), we find the solution of the differential equation which can be written in the simple form

$$x = x_0(t) + \Delta x, \qquad (51)$$

if we define

$$\Delta x = \frac{2P_sE_1}{m}\,\frac{\exp(j\omega t)}{(\omega_0^2 - \omega^2) + j\omega\gamma} \qquad (52)$$

and

$$x_0(t) = A\epsilon^{-\gamma t/2}\sinh[\tfrac{1}{2}(\gamma^2 - 4\omega_0^2)^{\frac{1}{2}}t + \varphi] + (2P_sE_0/m\omega_0^2).$$

Here A and φ are determined by the following boundary

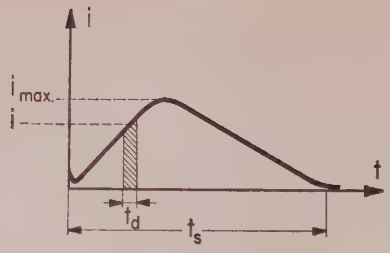

FIG. 10. Fraction of domains which are actually growing at a certain time.

conditions:

$$(x)_{t=0}=0;\quad (\dot{x})_{t=0}=0.$$

We shall now show that the increase in dielectric constant during switching $\Delta\epsilon_i$ is proportional to Δx. Let σ be the base area of a growing domain. If the height of the domain increases from x to $x+\Delta x$ while its base remains constant, the charge Δq collected at the electrode, due to the growth of this single domain, is

$$\Delta q=2\sigma(\Delta x/l)P_s. \tag{53}$$

If n is the number of domains per unit area whose length is varying under the influence of the alternating field ΔE_0, one finds [Eq. (53)]

$$\frac{\Delta\epsilon_i}{4\pi}\cong n\frac{\Delta q}{\Delta E_0}=\frac{2n\sigma P_s}{l}\frac{\Delta x}{\Delta E_0}=\frac{2n\sigma P_s}{l}\frac{\Delta x}{E_1\exp(j\omega t)}$$

and, with Eq. (52),

$$\Delta\epsilon_i=\frac{16\pi P_s^2}{lm}(n\sigma)\frac{1}{(\omega_0^2-\omega^2)+j\omega\gamma},$$

where n is the number of domains per unit area which are in the process of growing; n does not contain the domains which are not yet formed or have already grown through the sample. We now calculate $(n\sigma)$, which is the fractional number of domains in the process of growing. Since the polarization is reversed at a slow rate (small field) the switching current i is at each instant proportional to the *rate* of nucleation,[7] and the fractional number $(n\sigma)$ is equal to the shaded area of Fig. 10 divided by the total area Θ.

$$n\sigma=it_d/\Theta\cong 2it_d/i_{\max}t_s,$$

where t_s is the total switching time.

Equation (54) can now be written as

$$\Delta\epsilon_i=\frac{32\pi P_s^2t_di}{t_slmi_{\max}}\frac{1}{(\omega_0^2-\omega^2)+j\omega\gamma}. \tag{55}$$

If we write

$$\Delta\epsilon=\frac{32\pi P_s^2t_d}{t_slm}\frac{1}{(\omega_0^2-\omega^2)+j\omega\gamma}, \tag{56}$$

we have from Eq. (55)

$$\Delta\epsilon_i=\Delta\epsilon(i/i_{\max}). \tag{57}$$

If we separate the real and imaginary part in Eq. (56) we can write

$$\Delta\epsilon=\Delta\epsilon'-j\Delta\epsilon'', \tag{58}$$

where

$$\Delta\epsilon'=\frac{32\pi P_s^2t_d}{t_slm}\frac{\omega_0^2-\omega^2}{[(\omega_0^2-\omega^2)^2+\omega^2\gamma^2]}, \tag{59}$$

$$\Delta\epsilon''=\frac{32\pi P_s^2t_d}{t_slm}\frac{\gamma\omega}{[(\omega_0^2-\omega^2)^2+\omega^2\gamma^2]}. \tag{60}$$

Equations (59), (60), and (57) are identical to Eqs. (13), (14), and (12), respectively.

APPENDIX B

In this Appendix the assumption of Eq. (34),

$$\langle\Delta\epsilon\rangle_{\max}\cong|\Delta\epsilon|, \tag{34}$$

is justified. From Eq. (18) we have

$$\Delta\epsilon''\gg\Delta\epsilon' \quad \text{when} \quad \omega_0^2/\gamma\ll\omega\ll\gamma, \tag{61}$$

$$\Delta\epsilon''\ll\Delta\epsilon' \quad \text{when} \quad \omega\ll\gamma, \tag{62}$$

and therefore we can approximate the equation

$$|\Delta\epsilon|=[(\Delta\epsilon')^2+(\Delta\epsilon'')^2]^{\frac{1}{2}}$$

with the following two relations:

$$\left.\begin{array}{ll}|\Delta\epsilon|\cong\Delta\epsilon'' & \text{when} \quad \omega_0^2/\gamma\ll\omega\ll\gamma\\ |\Delta\epsilon|\cong\Delta\epsilon' & \text{when} \quad \omega\gg\gamma\end{array}\right\}. \tag{63}$$

The total dielectric constant ϵ_s of the ferroelectric during switching is given by

$$\epsilon_s=\epsilon_N+\Delta\epsilon_i, \tag{64}$$

where ϵ_N is the normal dielectric constant without switching and $\Delta\epsilon_i$ is the increase in dielectric constant during switching. In the Introduction we have defined $\langle\Delta\epsilon\rangle$ as

$$\langle\Delta\epsilon\rangle=|\epsilon_s|-\epsilon_N,$$

and therefore from Eq. (64)

$$\langle\Delta\epsilon\rangle=|\epsilon_N+\Delta\epsilon_i|-\epsilon_N. \tag{65}$$

When $i=i_{\max}$ we have $\langle\Delta\epsilon\rangle=\langle\Delta\epsilon\rangle_{\max}$ and $\Delta\epsilon_i=\Delta\epsilon$, so that Eq. (65) can be written

$$\langle\Delta\epsilon\rangle_{\max}=|\epsilon_N+\Delta\epsilon|-\epsilon_N. \tag{66}$$

Substituting Eq. (58) into Eq. (66), we have

$$\langle\Delta\epsilon\rangle_{\max}=|\epsilon_N+\Delta\epsilon'-j\Delta\epsilon''|-\epsilon_N$$

and hence

$$\langle\Delta\epsilon\rangle_{\max}=[(\Delta\epsilon'+\epsilon_N)^2+(\Delta\epsilon'')^2]^{\frac{1}{2}}-\epsilon_N. \tag{67}$$

Recalling Eq. (62), we shall neglect $\Delta\epsilon''$ in Eq. (67) when $\omega \gg \gamma$, so that we can write Eq. (67) as follows:

$$\langle \Delta\epsilon \rangle_{\max} \cong \Delta\epsilon' \quad \text{when} \quad \omega \gg \gamma. \tag{68}$$

On the other hand, we see from Figs. 3 and 4 that

$$\langle \Delta\epsilon \rangle_{\max} \gg \epsilon_N \quad \text{when} \quad \omega \ll 2\pi\nu_0. \tag{69}$$

Recalling Eq. (67) [and also Eq. (33)], we can rewrite Eq. (69) as follows:

$$[(\Delta\epsilon' + \epsilon_N)^2 + (\Delta\epsilon'')^2]^{\frac{1}{2}} - \epsilon_N \gg \epsilon_N \quad \text{when} \quad \omega \ll 2\pi\nu_0 = \gamma. \tag{70}$$

Equation (70) can be true only when $\Delta\epsilon'$ and/or $\Delta\epsilon''$ are much larger than ϵ_N, but since from Eq. (61), $\Delta\epsilon'' \gg \Delta\epsilon'$, then

$$\Delta\epsilon'' \gg \epsilon_N \quad \text{when} \quad \omega_0^2/\gamma \ll \omega \ll \gamma. \tag{71}$$

Substituting Eqs. (71) and (61) into Eq. (67), we obtain

$$\langle \Delta\epsilon \rangle_{\max} \cong \Delta\epsilon'' \quad \text{when} \quad \omega_0^2/\gamma \ll \omega \ll \gamma. \tag{72}$$

By comparing Eq. (63) with the two Eqs. (68) and (72), it follows that

$$\langle \Delta\epsilon \rangle_{\max} \cong |\Delta\epsilon|,$$

which is valid for ω varying in the range from ω_0^2/γ to $+\infty$, except for a small interval around $\omega \cong \gamma$. A very similar argument can prove that

$$\langle \Delta\epsilon \rangle \cong |\Delta\epsilon_i|. \tag{73}$$

JOURNAL OF APPLIED PHYSICS VOLUME 32, NUMBER 8 AUGUST, 1961

Dislocation Etch Pit Formation in Sodium Chloride

S. Mendelson
Columbia University, New York, New York

(Received March 3, 1961)

Dislocation etch pits can be formed on (100) surfaces of NalC crystals by etching in a solution of $FeCl_3$ in glacial acetic acid. Observations and arguments are enumerated to illustrate the reliability of the etching technique to reveal dislocations at positions where they intersect the crystal surface. The difference in shape of etch pits at edge and screw dislocations is consistent with that expected due to their different angles of inclination. Etch pit formation depends on variables of the etching solution and procedure. Insufficient $FeCl_3$ in solution results in wide, indistinctly shaped pits, whereas excessive $FeCl_3$ results in small pits with rounded corners. NaCl in the solution decreases the etching rate, while the presence of water increases the etching rate and results in more shallow pits. The added salt in the solution is believed to act as an inhibitor which poisons the dissolution process in the same manner as that proposed by Gilman *et al.* [J. J. Gilman, W. G. Johnston, and G. W. Sears, J. Appl. Phys. **29**, 747 (1958)] for LiF. Agitation increases the size of the pits for a given etching time.

INTRODUCTION

ETCHANTS for rocksalt have been reported by Amelinckx[1] and Moran.[2] Both of these are alcohol-base etchants, require short etching times, and are found to be rather sensitive to atmospheric variables. Gilman and Johnston[3] developed two etchants to reveal dislocations on (100) faces of LiF. These are dilute FeF_3 solutions. One is a water-base solution which distinguishes between annealed and fresh dislocations; the other is a glacial acetic acid etch which attacks all dislocations equally well. Etchants to reveal dislocations (too numerous to list here) have also been developed for many metals and semidonductor materials as well as other alkali halide crystals.

Sodium chloride slips on the {110}, ⟨110⟩ system.[4] A characteristic of this system is that there are always four slip systems which are equally stressed relative to an applied load in the [001] direction. The flow characteristics of NaCl are similar to LiF. However, NaCl is much softer and more sensitive to environmental factors.

The crystals used in this work were high-purity optical crystals purchased in random sizes from the Harshaw Chemical Company, Cleveland, Ohio. The crystals are rather soft and must be handled with great care; however, they cleave readily on (100) planes. Large crystals were cleaved with a hardened chisel ground at an angle of 30°. Smaller crystals were cleaved with a razor blade.

RESULTS AND DISCUSSION

Etching Technique

The etchant developed and studied in this work is not sensitive to atmospheric humidity. It has an acetic acid base and, as in the case of the etchant used on LiF, attacks all dislocations equally well. The best etch pits are obtained when the solution consists of 4 g of

---

[1] S. Amelinckx, Acta Met. **2**, 848 (1954).

[2] P. R. Moran, J. Appl. Phys. **29**, 1768 (1958).

[3] J. J. Gilman and W. G. Johnston, *Dislocations and Mechanical Properties of Crystals* (John Wiley & Sons, Inc., New York, 1957), p. 116.

[4] E. Schmid and W. Boas, *Plasticity of Crystals* (F. A. Hughes and Company, Ltd., London, 1950).

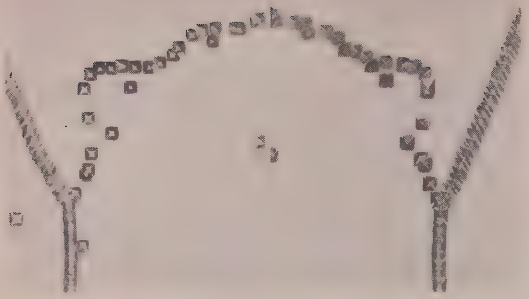

FIG. 1. Etch pits on matched opposite sides of a cleaved crystal. 300×.

ferric chloride per liter of glacial acetic acid and is moderately agitated for about 30 sec. After the crystal has been etched it is rinsed in acetone and dried in a jet of warm air.

Etch pits on (100) surfaces of NaCl crystals appear at positions where dislocations intersect the surface. They are pyramidal in shape, with the edges of their bases parallel to [100] directions of the crystal. The surfaces to be etched in NaCl need not be freshly cleaved, although they must be protected from dust, moisture, scratches, and oil. Best contrast is obtained when oblique reflected light is used in examining the surface of the etched crystal.

Correspondence of Etch Pits and Dislocations

In studies of flow using an etch pit method, many of the arguments depend on the reliability of the etching technique to reveal dislocations. Thus it is desirable to assess the action of the present etchant on sodium chloride crystals. The arguments used here are similar to those presented by Gilman and Johnston[3] to support the hypothesis that, indeed, all dislocations are revealed by the etching techniques. The following circumstantial evidence strongly suggests that this is so:

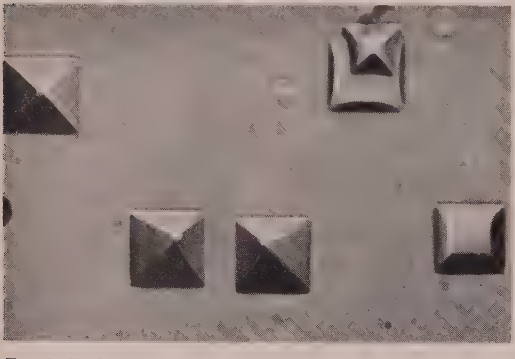

FIG. 2. Etch pit shapes produced by edge and screw dislocations in NaCl. 800×. Upper left, edge dislocation; lower center, screw dislocations on half loop; lower right, flat-bottomed pit; upper right, dislocation moved during etching.

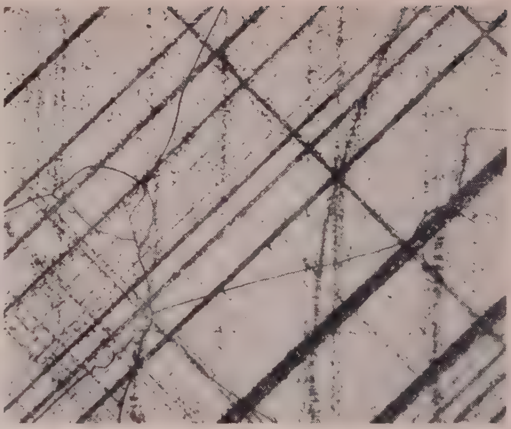

FIG. 3. Glide bands in a deformed NaCl crystal. Etch pits in diagonal bands are at edge dislocations, whereas those in vertical and horizontal bands are at screw dislocations. 28×.

(a) The pits can be matched on the separated faces of a cleaved crystal. Figure 1 shows an example of the almost identical patterns of pits in the matched halves.

(b) The tips of the pits continue deeper into the specimen as the crystal is progressively etched, and the number of pits remain relatively constant.

(c) A pit remains pyramidal during the etching only as long as a dislocation line remains at its bottom. If for any reason the dislocation which is being etched moves or disappears, the pit does not etch deeper but grows laterally to form a "flat-bottomed" pit. An example of this is shown in Fig. 2.

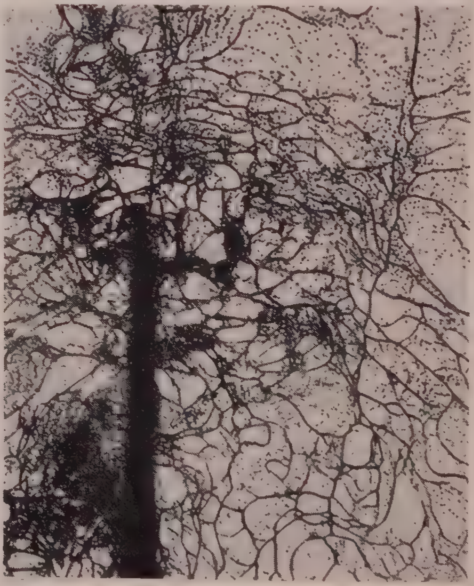

FIG. 4. Polygonization of deformed region around a crack after annealing at 600°C for 3 hr. 50×.

(d) The etch pits are distributed as would be expected if they were associated with dislocations. They appear in glide bands when a crystal has yielded plastically (see Fig. 3), and form into subgrain boundaries as in other crystalline materials when annealed after deformation (see Fig. 4).

(e) Both screw and edge dislocations are attacked by the etchant. The glide plane in NaCl is {110} and the glide direction is ⟨110⟩; therefore edge and screw dislocations which lie in glide bands on (100) faces can be distinguished as shown in Fig. 5. The pits at screw dislocations lie in bands parallel to ⟨100⟩ edges, while the edge dislocation pits lie in bands parallel to ⟨110⟩ directions (see Figs. 3 and 6). In Fig. 6 the rosette was formed by rolling a $\frac{1}{4}$-in. steel ball across the crystal surface.[3] The glide systems are distinguishable by the orientation of the rosette arms. Screw bands are vertical and horizontal, whereas edge bands are diagonal.

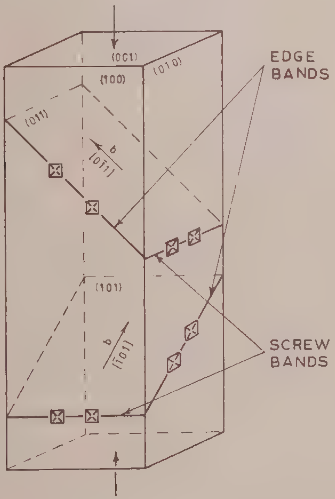

FIG. 5. Schematic of slip systems and their glide band traces on the surface of an NaCl crystal. Edge bands are parallel to ⟨110⟩ and screw bands are parallel to ⟨100⟩ directions.

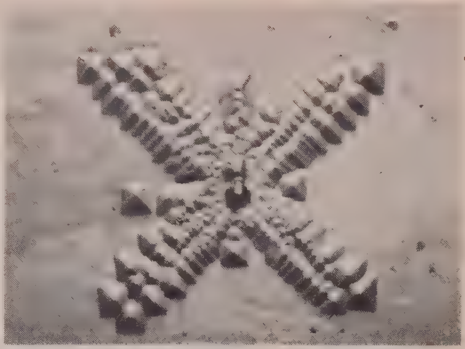

FIG. 6. Rosette formed by rolling a $\frac{1}{4}$-in-diam steel ball along the surface of an NaCl crystal. Glide systems are distinguishable by the orientation of the rosette arms. Screw bands are vertical and horizontal. Edge bands are diagonal. 1000×.

(f) Gilman and Johnston[3] and Amelinckx[5] were first to show that edge and screw dislocations can be distinguished directly from the shape of the pit in rock-salt-type crystals. The sense toward which the deepest point of the pit is displaced with respect to the center of the periphery is also the sense of inclination of the line (see Fig. 7). The pits are symmetric at edge dislocations and asymmetric at screw dislocations. This is a result of the fact that the edge dislocation lines lie normal to the plane of observation, (100), while the screw dislocation lines lie in planes at 45° to it. An example of this is shown in Fig. 2. In this figure, the pair of pits in the lower center have a double asymmetric displacement of the deepest point. First, the displacement normal to the line joining the pits is an indication that both dislocations intersect the surface obliquely at the same angle. Second, the displacements toward each other indicate that their dislocation lines bend toward each other. Finally, the deepest points of these pits show small tails bending into each other, and this reflects the position of the dislocation line. These features and the [100] orientation of the line joining the pair indicate that the pits are at the end of a screw dislocation loop of about 15 μ in diameter.

(g) Formation of an etch pit at a dislocation site in NaCl does not seem to require the precipitation of an impurity as is generally the case in most metals; i.e.,

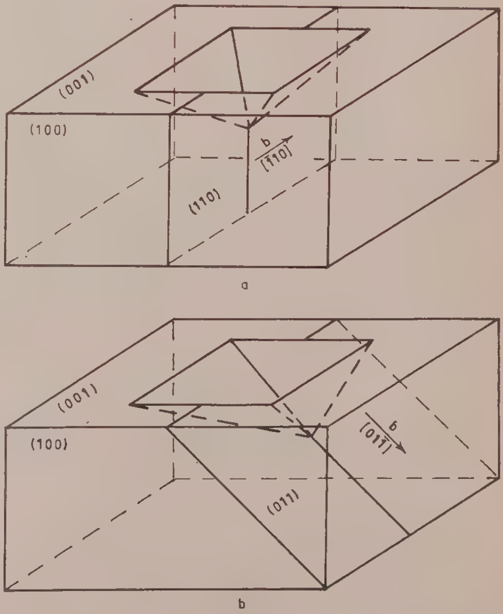

FIG. 7. Effect of inclination of the dislocation line on the shape of the etch pit. (a) Dislocation line is normal to the surface: edge dislocation. Etch pit is a symmetric pyramid. (b) Dislocation line is oblique to the surface: screw dislocation. Etch pit is an asymmetric pyramid with the point of the pit displaced towards the edge which is above the dislocation line.

---

[5] S. Amelinckx, Nuovo cimento 7, Suppl. 2, 569 (1958).

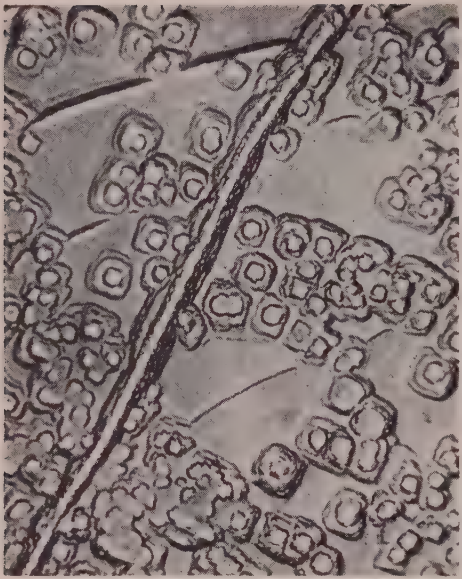

FIG. 8. Effect of etching on a very humid day.

dislocations in glide bands can be etched immediately after deformation.

(h) The etchant is sensitive to defects in the crystals other than dislocations, for example, evaporation pits and point defect clusters. At these defects the etches produce flat-bottomed pits which can be distinguished easily from the pointed pits that appear at dislocations. The fact that several kinds of defects are revealed by the etchant suggests that the etchant would be sensitive to more than one kind of dislocation, and hence to all dislocations.

(i) Edge-dislocation etch pits of one sign in glide bands correlate with the birefringence predicted due to the asymmetric stress field around the edge dislocation.[6] Since this observation is independent of the etching behavior, it may be the strongest evidence that the etch pit technique reveals a true picture of dislocations in sodium chloride.

Variables of Etchant and Etching Procedure

The nature of the etch pit depends on several characteristics of the etching process. These have been studied, and the results are described below.

Effect of $FeCl_3$

The nature of the etch pit depends on the concentration of $FeCl_3$. Pure glacial acetic acid produces very wide, indistinctly shaped pits. As the concentration of $FeCl_3$ is increased, the pits become smaller and have steeper sides. At the critical concentration the pits are sharp pyramids. At greater concentration the etch pits appear small with rounded corners. These effects are exactly what Gilman *et al.*[7] found as the effect of FeF_3 concentration in the etchant for LiF.

Effect of NaCl *Concentration*

There was no observable deleterious effect on the shape of the etch pits after using the etchant a large number of times. However, the etching rate does decrease, and this again was observed in LiF.[7]

Effect of Agitation

The best shaped pyramidal pits are obtained when the solution is moderately agitated for about 30 sec. Etching in a still solution produces small pits with rounded corners, and the size of the pits for a particular etching time is proportional to the speed of agitation. This was also observed in LiF.[7]

Effect of Moisture Content

The etching behavior is not affected by moisture present in solution; however, etching on days when the humidity is much greater than about 90% produces shallow, more rounded and stepped pits (see Fig. 8). This is due to the slow rate of drying on the more humid days and not to any changes in the etching behavior. Small traces of water in the etching solution have no effect on the shape of the etch pits but they do shorten the etching time. Larger quantities of water in solution further reduce the etching time and produce more shallow etch pits. The relative difference in etch pit shapes when water is in solution can be seen by a double etching technique. This is shown in Fig. 9. The crystal was first etched in a solution having about 3% water for several seconds and then immediately transferred to an anhydrous etching solution for 30 sec. The small, dark pits are deep pyramids formed by the anhydrous solution. These lie at the bottom of larger, more shallow, overlapping pits which formed in the first etchant.

Etching Mechanism

Cabrera[8] presented a theory to elucidate the mechanism of the formation of an etch pit at a dislocation site. He has demonstrated that dislocations are regions of undersaturation and thus dissolution should be preferential at the dislocations relative to the perfect lattice. The essential arguments presented by Cabrera are: (a) dislocations are preferential sites for nucleation of a unit pit one molecule deep; (b) the nucleation of many unit pits at a dislocation can result in an etch pit; and (c) the formation of a visible dislocation etch

---

[6] S. Mendelson, J. Appl. Phys. (to be published).

[7] J. J. Gilman, W. G. Johnston, and G. W. Sears, J. Appl. Phys. **29**, 747 (1958).

[8] N. Cabrera in *Semiconductor Surface Physics*, edited by R. H. Kingston (University of Pennsylvania Press, Philadelphia, Pennsylvania, 1957), p. 327.

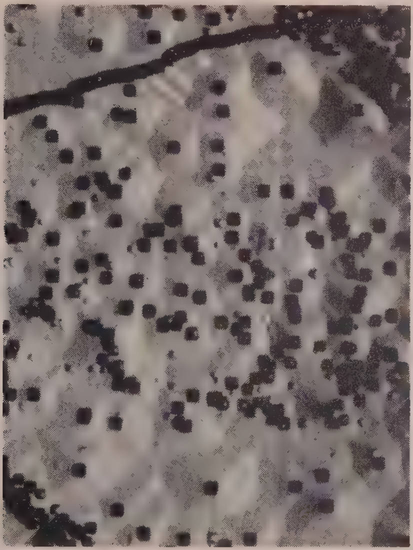

FIG. 9. Double etching technique. Specimen was first etched in an etching solution having about 3% water for several seconds and then immediately transferred to an anhydrous solution for 30 sec. The small, dark pits are deep pyramids formed in the anhydrous solution. These lie at the bottom of larger, more shallow, overlapping pits formed in the first etchant. 100×.

pit depends on the relative nucleation rate for unit pits at a dislocation, v_n, and the rate of motion of the steps across the crystal surface, v_s. Visible pits are obtained when $v_n/v_s \gtrsim 0.1$.

v_n is a small quantity (related to the undersaturations at the dislocation) determined by the surface energy and shear modulus of the crystal (being greater in crystals of low surface energy and large shear modulus), and thus is not altered by changes in the solution at constant temperature. v_s, on the other hand, is determined by the rate of solution and is very high for a pure strong solvent, thus giving a small ratio. The local undersaturations, and consequently this ratio, can be maintained by poisoning the solution with an inhibitor which decreases v_s. Gilman and Johnston[3] have shown that very dilute solutions of ferric fluoride give good etch pits. In this case the ferric ion acts as the inhibitor and its quantity determines the magnitude of v_s. The ferric ion is believed to adsorb onto the advancing dissolution step and poison the dissolution process.[7]

In the etch for NaCl used in this work, the observations indicate that ferric chloride in solution with glacial acetic acid probably behaves in a similar manner, although the relative concentrations of the poison in these solutions differ by several orders of magnitude.

SUMMARY

Sharp, pyramidal dislocation etch pits can be formed at dislocations intersecting the (100) surfaces with a solution having 4 g of $FeCl_3$ per liter of glacial acetic acid.

The reliability of the etch pit method is supported by the following observations:

(1) The pits on cleaved halves of a crystal can be matched;

(2) The tips of pits continue deeper into the specimen as the crystal is etched;

(3) The pits remain pyramidal during the etching only as long as a dislocation line remains at its bottom;

(4) Etch pits are distributed in glide bands when a deformed crystal is etched;

(5) The etch pits form into subgrain boundaries when the crystal is annealed after deformation;

(6) Edge dislocation etch pits in a glide band correlate with the birefringence predicted due to the asymmetric stress field around the edge dislocation.

The difference in shape of etch pits at edge and screw dislocations is consistent with that expected, due to their different angles of inclination.

Etch pit formation depends on variables of the etching solution and procedure. Insufficient $FeCl_3$ in solution results in wide, indistinctly shaped pits, whereas excessive $FeCl_3$ results in small pits with rounded corners. NaCl in the solution decreases the etching rate, whereas the presence of water increases the etching rate and results in more shallow pits. Agitation also increases the size of the pits for a given etching time.

The added salt in the solution is believed to act as an inhibitor which poisons the dissolution process in the same manner as that proposed by Gilman *et al.* for LiF.

ACKNOWLEDGMENTS

The author wishes to thank Dr. E. S. Machlin of Columbia University and Dr. W. G. Johnston of the General Electric Research Laboratories, Schenectady, New York, for their advice and interest in this work.

JOURNAL OF APPLIED PHYSICS VOLUME 32, NUMBER 8 AUGUST, 1961

Zero-, First-, and Second-Order Theories of a General Thermocouple

A. H. BOERDIJK
N. V. Philips' Gloeilampenfabrieken, Eindhoven, The Netherlands

(Received February 3, 1961)

The thermocouple to be dealt with has two bars of arbitrary shape. Each of the properties of the materials (the thermal resistivity κ, the electrical resistivity ρ, and the Seebeck coefficient S) is represented by a finite number of terms of a MacLaurin series in T (the temperature) and u (a position coordinate). A method is described to obtain a theory of arbitrary order t. Such a theory is based on a solution $T=f(u)$ which satisfies the basic nonlinear differential equation (obtained by application of thermodynamics of irreversible processes) and the boundary conditions if all terms of order $>t$ are neglected. The order of a term is equal to the sum of the orders of all partial differential quotients of κ, ρ, and S with respect to T and u occurring in that term. The method is applied to obtain the electrical output power and the thermal output powers as functions of the electrical current and the temperatures of the junctions in theories of order zero, one, and two. The zero-order theory is identical with the common theory of thermocouples with constant properties κ, ρ, and S. In the first-order theory an expression is obtained for the efficiency for production of cold. This efficiency can be improved by suitable temperature dependence of S and by suitable place dependence of S. Finally the accuracy of approximation is discussed.

I. NOTATION, DEFINITIONS

We will consider a couple consisting of two bars, a and b (Fig. 1). At one side the bars are connected to an external electrical circuit by leads 3 and 4. At the other side the bars are joined by lead 5. We suppose that all leads are of the same material, which perfectly conducts heat and electricity, and that leads 3 and 4 have equal temperatures. Part of these leads will be referred to as "junction 2." Lead 5 will be referred to as "junction 1." Symbols relating to junctions will be distinguished by subscripts 1 and 2 and symbols relating to bars by subscripts a and b. The couple is thought to be surrounded by a perfect insulator for heat and electricity which restricts external electrical current to leads 3 and 4 and external heat exchange to junctions 1 and 2.

Each bar has an arbitrary shape. Denoting by O_1 and O_2 the surfaces in contact with junctions 1 and 2, respectively, and by O_3 the remaining part of the surface of the bar, we use a position coordinate u satisfying the following conditions: $\nabla^2 u=0$ inside the bar and on its surface, $u=0$ on O_1, $u=1$ on O_2; ∇u on O_3 is tangent to O_3. We define a characteristic length l by

$$l=\int_{O_1} |\nabla u| dO_1. \quad (1)$$

Each of the bars is inhomogeneous, with the restriction that the composition is a function of u only. The material of each bar may be anisotropic, with the restriction that at any point the direction of ∇u is a symmetry axis of the angular distribution of the properties. In this case the values of the properties occurring in the equations are those measured in the direction of ∇u. Thermal expansion is neglected.

We denote by κ the thermal resistivity (for zero electrical current), T the absolute temperature, Δ the difference T_2-T_1, p the quantity $\kappa^{-1}(dT/du)$, ρ the (isothermal) electrical resistivity, S the absolute Seebeck coefficient, I the electrical current, i the quotient I/l, W_e the electrical output power, W_1 and W_2 the thermal output powers at the junctions 1 and 2, respectively, and V the voltage W_e/I. Efficiencies for generation of heat and cold from electricity and for generation of electricity from heat or cold are denoted, respectively, by

$$\varphi_h=-W_2/W_e, \quad \varphi_c=W_1/W_e,$$
$$\varphi_e=-W_e/W_2, \quad \varphi_e'=W_e/W_1, \quad (2)$$

for the case $T_2 \geqslant T_1$.

Generally, κ, ρ, and S are functions of T and u. We suppose that the values of these quantities and of their partial differential quotients with respect to T and u are given in a fixed reference point $u=u_r$ at a fixed reference temperature $T=T_r$ (which is not necessarily equal to the actual temperature at the reference point), and that the dependence of κ, ρ, and S on T and u in the relevant region of these variables can be described by a finite number of terms of MacLaurin series in the variables $T-T_r$ and $u-u_r$. For instance,

$$\kappa=\kappa_r+(T-T_r)(\partial\kappa/\partial T)_r+(u-u_r)(\partial\kappa/\partial u)_r + \tfrac{1}{2}(T-T_r)^2(\partial^2\kappa/\partial T^2)_r+\cdots. \quad (3)$$

The order of a term is equal to the sum of the orders

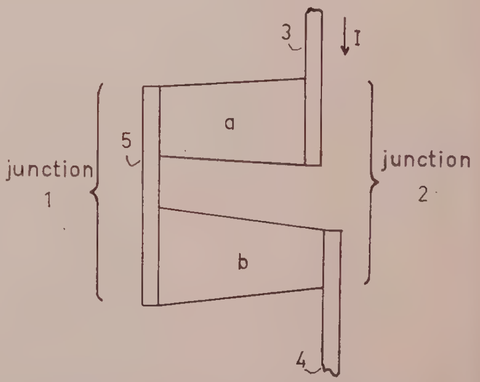

FIG. 1. Thermocouple consisting of bars a and b with junctions 1 and 2, and electrical leads 3, 4, and 5.

of all partial differential quotients of κ, ρ, and S with respect to T and u occurring in that term.

II. BASIC EQUATIONS, PREVIOUS WORK

It has been shown[1] that application of thermodynamics of irreversible processes to the thermocouple defined in Sec. I leads to

$$W_e=IV=-W_1-W_2, \qquad (4)$$

$$W_1=I(S_a-S_b)_1T_1+p_{1a}l_a+p_{1b}l_b, \qquad (5)$$

$$W_2=I(S_b-S_a)_2T_2-p_{2a}l_a-p_{2b}l_b. \qquad (6)$$

The temperature distribution is determined by

$$\frac{1}{\kappa}\frac{d^2T}{du^2}-\frac{1}{\kappa^2}\frac{\partial\kappa}{\partial T}\left(\frac{dT}{du}\right)^2-\frac{1}{\kappa^2}\frac{\partial\kappa}{\partial u}\frac{dT}{du}+T\frac{\partial S}{\partial T}\frac{dT}{du}i+T\frac{\partial S}{\partial u}i+\rho i^2=0, \qquad (7)$$

for bar a, and for bar b by the corresponding equation with replacement of i by $-i$, with the boundary conditions $u=0$, $T=T_1$ and $u=1$, $T=T_2$.

The central problem is to find the last pair of terms in (5) and (6) from (7). Sherman, Heikes, and Ure[2] have found a procedure for obtaining numerical solutions for the case of homogeneous bars, using high-speed computer techniques. They take into account the temperature dependences of κ, ρ, and S. In other previous work, e.g., of Burshtein[3] and Ioffe,[4] the cases investigated are of a less general nature, but the results are obtained in analytical form.

III. METHOD FOR OBTAINING A THEORY OF ARBITRARY ORDER

Taking $u_r=1$, $T_r=T_2$ we will try to obtain T for bar a in the form of a MacLaurin series in $(u-1)$:

$$T(u)=T_2=\sum_{s=1}^{s=\infty}\frac{(u-1)^s}{s!}\left(\frac{d^sT}{du^s}\right)_2. \qquad (8)$$

From (7) we find

$$\frac{d^2T}{du^2}=\kappa\frac{\partial\kappa}{\partial T}p^2+\frac{\partial\kappa}{\partial u}p-\kappa^2T\frac{\partial S}{\partial T}pi-\kappa T\frac{\partial S}{\partial u}i-\kappa\rho i^2, \qquad (9)$$

and, therefore,

$$\left(\frac{d^2T}{du^2}\right)_2=\left[\kappa\frac{\partial\kappa}{\partial T}p^2+\frac{\partial\kappa}{\partial u}p-\kappa^2T\frac{\partial S}{\partial T}pi-\kappa T\frac{\partial S}{\partial u}i-\kappa\rho i^2\right]_2. \qquad (10)$$

We can find d^3T/du^3 by differentiation of (9) with respect to u. The quantity dp/du occurring in the expression so obtained can be eliminated using the equation

$$dp/du=-\kappa Tpi\partial S/\partial T-Ti\partial S/\partial u-\rho i^2, \qquad (11)$$

which follows also from (7). In this way we can go on as far as we like, expressing the values of the derivatives of T with respect to u occurring in (8) in T_2, p_2, i, and in the values of κ and ρ, and of the partial differential quotients of κ, ρ, and S with respect to T and u at the point $u=1$, at the temperature T_2.

If we neglect terms of order $>t$ we find

$$d^sT/du^s\equiv 0, \quad s\geqslant 3(t+1). \qquad (12)$$

Results so obtained are part of a theory of order t. In such a theory the number of differential quotients in (8) is finite as indicated by (12).

At the stage at which we are now (8) contains the variables i and p_2. We could consider these quantities as independent variables and calculate Δ from p_2 and i by means of (8). Generally it is more advantageous to have Δ instead of p_2 as independent variable, since in most cases I and Δ are given and, moreover, all relevant information is contained in an I, Δ diagram.[5]

To express p_2 in i and Δ we proceed as follows. The term for which $s=1$ in (8) contains $(dT/du)_2$ and this is by definition equal to κ_2p_2. Taking $u=0$ in (8) and solving for p_2 occurring in this term we obtain

$$p_2=\frac{1}{\kappa_2}\left\{\Delta+\sum_{s=2}^{s=3t+2}\frac{(-1)^s}{s!}\left[\frac{d^sT}{du^s}\right]_2\right\}. \qquad (13)$$

The right-hand side of (13) also contains p_2, but every term containing p_2 also contains a factor of which the order is at least one. So (13) can be used to find p_2 in a theory of arbitrary order by iteration. To start we need the expression for p_2 in the zero-order theory. In this theory (7) can be solved by elementary methods leading to

$$p_2=\kappa_2^{-1}\Delta-\tfrac{1}{2}\rho_2 i^2. \qquad (14)$$

If we eliminate p_2 from the term for which $s=1$ in (8) we obtain T as an explicit function of u:

$$T(u)=T_2+\Delta(u-1)+\sum_{s=2}^{s=3t+2}\frac{1}{s!}\left[\frac{d^sT}{du^s}\right]_2\times\{(u-1)^s+(-1)^s(u-1)\}, \qquad (15)$$

which is an algebraical expression in u of degree $3t+2$. The square brackets are used to indicate that p_2 has been eliminated from the differential quotients. In the theory of order t, (15) satisfies the differential equation (7) as well as the boundary conditions $u=0$, $T=T_1$ and $u=1$, $T=T_2$.

---

[1] A. H. Boerdijk, J. Appl. Phys. **30**, 1080 (1959).

[2] B. Sherman, R. R. Heikes, and R. W. Ure, J. Appl. Phys. **31**, 1 (1960).

[3] A. I. Burshtein, Soviet Phys.—Tech. Phys. **2**, 1397 (1957).

[4] A. F. Ioffe, *Semiconductor Thermoelements and Thermoelectric Cooling* (Infosearch, Ltd., London, England, 1957).

[5] A. H. Boerdijk, J. Appl. Phys. **31**, 1141 (1960).

Differentiating (15) with respect to u and taking $u=0$ we obtain

$$p_1=\frac{1}{\kappa_1}\left\{\Delta-\sum_{s=2}^{s=3t+2}\frac{(-1)^s(s-1)}{s!}\left[\frac{d^sT}{du^s}\right]_2\right\}. \qquad (16)$$

The relations (13) and (16) can be used to express p_{1a} and p_{2a} in T_2, i, Δ, and in the values of κ and ρ, and of the partial differential quotients of κ, ρ, and S with respect to T and u at the point $u=1$ at the temperature T_2. To obtain p_{1b} and p_{2b} we have to replace, in (13) and (16), i by $-i$ and subscripts a by b.

Next we substitute the expressions for p_{1a}, p_{2a}, p_{1b}, and p_{2b} in (5) and (6). We express $(S_a-S_b)_1T_1$ in (15) in S_{2a}, S_{2b}, T_2, and Δ. In this way we obtain from (4), (5), and (6) relations expressing $W_j(j=e$, 1 or 2) in the independent variables I and Δ. All terms contain, as far as I and Δ are concerned, only products of non-negative powers of I and Δ. The relations can be considered as an expansion of W_j in MacLaurin series in I and Δ. From (4), (5), and (6) it follows that W_{ja}/l_a is, as far as I and l_a are concerned, a function of I/l_a only. The corresponding statement is true for W_{jb}. Following the procedure for obtaining the expressions for W_j, it is not difficult to prove by induction that W_j is of the form

$$W_j=\sum_{n=0}^{n=t+1}\sum_{m=0}^{m=3t+2}\{l_a^{-m+1}F_{jmna}-(-l_b)^{-m+1}F_{jmnb}\}I^m\Delta^n. \qquad (17)$$

Each F_{jmn} is the sum of a finite number of terms of order $\leqslant t$ of the form k_jK, where k_j contains the sign and the numerical coefficient (generally a proper fraction), and K is a product of which possible factors are T_2, the values of κ, ρ, and S and of the partial differential quotients of κ, ρ, and S with respect to T and u, at the point $u=1$ at the temperature T_2.

The theory of order t is identical with that of order $t+1$ but for the terms of order $t+1$.

The representation (17) depends on the chosen values of T_r and u_r. We can change over to an arbitrary other pair of values T_r and u_r by elementary transformations. This generally leads to a different set of coefficients k_j.

From (17) it follows that in a theory of order t the analytical expressions for W_j can be compiled in a table, listing for each m and n all corresponding sets of quantities k_e, k_1, k_2, and K. We have

$$k_e+k_1+k_2=0. \qquad (18)$$

This relation can be used to find k_e from k_1 and k_2.

Theories of orders zero and one can be found with a little effort with paper and pencil. In the second-order theory, the number of terms to be dealt with is already so large that handling of terms has to be organized. We used a system of small cards containing one term per card. About 500 cards have been used to obtain the second-order theory (Tables II and IV). For higher order theories an electronic computer will be indispensable.

IV. ZERO-ORDER THEORY

A. Output Powers

The zero-order theory deals with a thermocouple of which κ, ρ, and S are independent of T and u. It is elementary and old. We will need some special results for comparison purposes. We will not restrict ourselves to the case in which T_2 is constant, and define a constant temperature by

$$T=T_1+\alpha\Delta, \quad (0\leqslant\alpha\leqslant 1). \qquad (19)$$

Table I gives the output powers W_j. Note the occurrence of α. By way of example we will, in this simple case, write out the equations represented by Table I:

$$W_e=(S_a-S_b)I\Delta-(\rho_a/l_a+\rho_b/l_b)I^2, \qquad (20)$$

$$W_1=T(S_a-S_b)I+\tfrac{1}{2}(\rho_a/l_a+\rho_b/l_b)I^2 +(l_a/\kappa_a+l_b/\kappa_b)\Delta-\alpha(S_a-S_b)I\Delta, \qquad (21)$$

$$W_2=-T(S_a-S_b)I+\tfrac{1}{2}(\rho_a/l_a+\rho_b/l_b)I^2 -(l_a/\kappa_a+l_b/\kappa_b)\Delta+(\alpha-1)(S_a-S_b)I\Delta. \qquad (22)$$

TABLE I. Complete list of zero-order coefficients $k_jK(j=e$, 1 or 2) of the terms $I^m\Delta^n$ (I is the current, $\Delta=T_2-T_1$ the temperature difference of the junctions) occurring in the MacLaurin series expansion of the electrical output power W_e and the thermal output powers W_1 and W_2, respectively. The properties of the materials (thermal resistivity κ, electrical resistivity ρ, and Seebeck coefficient S) are independent of temperature and place. The temperature $T=T_1+\alpha\Delta$ is kept constant.

m	n	k_e	k_1	k_2	K
1	0	0	$+1$	-1	TS
2	0	-1	$+\frac{1}{2}$	$+\frac{1}{2}$	ρ
0	1	0	$+1$	-1	κ^{-1}
1	1	$+1$	$-\alpha$	$+\alpha-1$	S

B. Efficiency for Production of Cold

We restrict ourselves to a couple with the optimal value of l_a/l_b. This is given by

$$l_a/l_b=(\kappa_a\rho_a/\kappa_b\rho_b)^{\frac{1}{2}}. \qquad (23)$$

We take $\alpha=\frac{1}{2}$ and suppose $S_b-S_a>0$. For a value of I given by

$$I=(T-\tfrac{1}{2}\Delta_m)(S_b-S_a)(\rho_a/l_a+\rho_b/l_b)^{-1}\Delta/\Delta_m, \qquad (24)$$

φ_c is maximal and given by

$$\varphi_c=(\Delta_m/2\Delta)-\tfrac{1}{2}. \qquad (25)$$

In these equations Δ_m is the maximal value of Δ occurring for $W_1=0$, given by

$$\Delta_m=2T[1+\{1-(1+2r)^{\frac{1}{2}}\}r^{-1}]=2qT, \qquad (26)$$

where

$$r=\tfrac{1}{2}T(S_b-S_a)^2[(\rho_a/\kappa_a)^{\frac{1}{2}}+(\rho_b/\kappa_b)^{\frac{1}{2}}]^{-2}=\tfrac{1}{2}zT. \qquad (27)$$

The quantities z, q, and r are performance indices.

V. FIRST-ORDER THEORY

A. Output Powers

The first-order terms describe in a first approximation the effects caused by the temperature coefficients $\partial\kappa/\partial T$, $\partial\rho/\partial T$, and $\partial S/\partial T$ and by the place dependences $\partial\kappa/\partial u$, $\partial\rho/\partial u$, and $\partial S/\partial u$.

Table II gives the output powers W_j for the case of a reference temperature $T=T_2$ and a reference point $u=1$. Note that all six partial differential quotients occur in the table. Products of partial differential quotients do not occur. This means that all effects of temperature coefficients and inhomogeneities are additive and can be dealt with separately.

The average value κ_{av} of κ in the field defined by $T_1\leqslant T\leqslant T_2$ and $0\leqslant u\leqslant 1$ is

$$\kappa_{\text{av}}=\kappa_2-\tfrac{1}{2}(\partial\kappa/\partial T)\Delta-\tfrac{1}{2}\partial\kappa/\partial u, \tag{28}$$

and depends on $\partial\kappa/\partial T$, $\partial\kappa/\partial u$, and Δ. This is caused by the asymmetrical position of the reference values in this field. Corresponding statements are true for ρ and S. To study the effects of the temperature coefficients and the place dependences *per se* we will eliminate these undesired effects. This can be done by taking a reference point $u=\frac{1}{2}$ and a reference temperature $T=\frac{1}{2}(T_1+T_2)$. Table III gives the output powers W_j for this case. Compared with Table II there are less terms and some of the remaining terms have other coefficients.

It is of interest to compare Table III with Table I, taking $\alpha=\frac{1}{2}$. The couples represented by these tables have the same κ_{av}, ρ_{av}, and S_{av}. Consequently all differences in behavior are caused by the temperature coefficients and the place dependences only. Ioffe[4] and Sherman[2] have investigated to some extent the question whether average values of κ, ρ, and S can be used in a refined theory. The answers can be found from Table III and appear to depend on the special equation to be considered.

TABLE II. Complete list of zero- and first-order coefficients k_jK ($j=e$, 1 or 2) of the terms $I^m\Delta^n$ (I is the current, $\Delta=T_2-T_1$ the temperature difference of the junctions) occurring in the MacLaurin series expansion of the electrical output power W_e and the thermal output powers W_1 and W_2, respectively. All quantities (temperature T, thermal resistivity κ, electrical resistivity ρ, Seebeck coefficient S, and the first-order partial differential quotients of κ, ρ, and S with respect to T and a position coordinate u) are those at a reference point $u=1$ at a reference temperature $T=T_2$.

m	n	k_e	k_1	k_2	K
1	0	0	+1	−1	TS
1	0	0	−1/2	+1/2	$T\partial S/\partial u$
2	0	−1	+1/2	+1/2	ρ
2	0	0	+1/12	−1/12	$\kappa^{-1}\rho\partial\kappa/\partial u$
2	0	+1/2	−1/3	−1/6	$\partial\rho/\partial u$
3	0	0	+1/12	−1/12	$\kappa\rho T\partial S/\partial T$
3	0	−1/12	+1/24	+1/24	$\kappa\rho\partial S/\partial u$
4	0	−1/12	+1/24	+1/24	$\kappa\rho\partial\rho/\partial T$
5	0	0	+1/240	−1/240	$\kappa^2\rho^2\partial S/\partial T$
0	1	0	+1	−1	κ^{-1}
0	1	0	+1/2	−1/2	$\kappa^{-2}\partial\kappa/\partial u$
1	1	+1	−1	0	S
1	1	0	−1/2	+1/2	$T\partial S/\partial T$
1	1	−1/2	+2/3	−1/6	$\partial S/\partial u$
2	1	+1/2	−1/3	−1/6	$\partial\rho/\partial T$
3	1	0	−1/24	+1/24	$\kappa\rho\partial S/\partial T$
0	2	0	+1/2	−1/2	$\kappa^{-2}\partial\kappa/\partial T$
1	2	−1/2	+2/3	−1/6	$\partial S/\partial T$

TABLE III. Complete list of zero- and first-order coefficients k_jK ($j=e$, 1 or 2) of the terms $I^m\Delta^n$ (I is the current, $\Delta=T_2-T_1$ the temperature difference of the junctions) occurring in the MacLaurin series expansion of the electrical output power W_e and the thermal output powers W_1 and W_2, respectively. All quantities (temperature T, thermal resistivity κ, electrical resistivity ρ, Seebeck coefficient S, and the first-order partial differential quotients of κ, ρ, and S with respect to T and a position coordinate u) are those at a reference point $u=\frac{1}{2}$ at a reference temperature $T=\frac{1}{2}(T_1+T_2)$.

m	n	k_e	k_1	k_2	K
1	0	0	+1	−1	TS
2	0	−1	+1/2	+1/2	ρ
2	0	0	+1/12	−1/12	$\kappa^{-1}\rho\partial\kappa/\partial u$
2	0	0	−1/12	+1/12	$\partial\rho/\partial u$
3	0	0	+1/12	−1/12	$\kappa\rho T\partial S/\partial T$
3	0	−1/12	+1/24	+1/24	$\kappa\rho\partial S/\partial u$
4	0	−1/12	+1/24	+1/24	$\kappa\rho\partial\rho/\partial T$
5	0	0	+1/240	−1/240	$\kappa^2\rho^2\partial S/\partial T$
0	1	0	+1	−1	κ^{-1}
1	1	+1	−1/2	−1/2	S
1	1	0	+1/6	−1/6	$\partial S/\partial u$
2	1	0	−1/12	+1/12	$\partial\rho/\partial T$
1	2	0	+1/6	−1/6	$\partial S/\partial T$

Table III does not contain $\partial\kappa/\partial T$. So this quantity plays no role in this theory as a whole. It is sufficient to use, as far as κ as a function of T is concerned, the average value of κ in the range $T_1\leqslant T\leqslant T_2$. At the same time this is the only reason for the occurrence of $\partial\kappa/\partial T$ in Table II. No corresponding statement is true for any of the other five partial differential quotients.

If we consider the equation for W_e alone, we find that this quantity depends on κ, ρ, S, $\partial\rho/\partial T$, and $\partial S/\partial u$. Consequently, for calculation of W_e in the first-order theory it is sufficient to use for ρ as a function of u the average value of ρ in the range $0\leqslant u\leqslant 1$, and for S as a function of T the average value of S in the range $T_1\leqslant T\leqslant T_2$, whereas for κ as a function of T and u it is sufficient to use κ_{av}. The use of the average values just mentioned in a zero-order theory is equivalent with application of the first-order theory.

B. Efficiency for Production of Cold

For the couple represented by Table III, φ_c can be obtained as follows. First we need equations corresponding to (23) and (24) for optimizing φ_c. In principle these equations can be obtained from (23) and (24) by application of a correction found from the first-order theory. This correction contains first-order terms only. Since we are dealing with a maximum of φ_c this correction gives rise to a correction in φ_c of second-order terms only. Because these terms are not of interest here it is sufficient to use Eqs. (23) and (24) without correction. In this way we find from Table III

$$\varphi_c=\frac{\Delta_m}{2\Delta}-\tfrac{1}{2}+\tfrac{1}{2}\frac{q}{1+q}A+\frac{1}{30}$$

$$\times\left\{\frac{5+10q}{1+q}\Delta+\frac{q}{1+q}\frac{\Delta^3}{\Delta_m^2}\right\}B+\frac{1}{12}\frac{1-q}{1+q}C, \quad (29)$$

where

$$A=(S_b-S_a)^{-1}\left\{\frac{\partial S_b}{\partial u}-\frac{\partial S_a}{\partial u}\right\},$$

$$B=(S_b-S_a)^{-1}\left\{\frac{\partial S_b}{\partial T}-\frac{\partial S_a}{\partial T}\right\}, \quad (30,31)$$

$$C=\left[\kappa_b^{\frac{1}{2}}\rho_a^{\frac{1}{2}}\left\{\frac{1}{\rho_a}\frac{\partial\rho_a}{\partial u}-\frac{1}{\kappa_a}\frac{\partial\kappa_a}{\partial u}\right\}\right.$$

$$\left.+\kappa_a^{\frac{1}{2}}\rho_b^{\frac{1}{2}}\left\{\frac{1}{\rho_b}\frac{\partial\rho_b}{\partial u}-\frac{1}{\kappa_b}\frac{\partial\kappa_b}{\partial u}\right\}\right]$$

$$\times\{\kappa_b^{\frac{1}{2}}\rho_a^{\frac{1}{2}}+\kappa_a^{\frac{1}{2}}\rho_b^{\frac{1}{2}}\}^{-1}. \quad (32)$$

Considering first the effects of the temperature coefficients we note that φ_c is not only independent of $\partial\kappa/\partial T$ as could be expected, but also of $\partial\rho/\partial T$. The effects of the only remaining temperature coefficients of S_a and S_b are described by the fourth term of (29). The efficiency will be higher than that of the couple of Table I if $\partial S_b/\partial T-\partial S_a/\partial T>0$. This means that the total Thomson heat developed in the bars is negative. In this way part of the Joule heat is compensated directly at the place where it is developed.

Next we will consider the effects of the place dependences of κ, ρ, and S. An important question is whether it is possible to increase φ_c by such place dependences. It is necessary to give this question a precise meaning. We will compare φ_c of the inhomogeneous couple with φ_c of the best available homogeneous couple. In the general case, each of the bars of the inhomogeneous couple contains a continuous range of compositions. We suppose that each of these compositions *per se* is available for construction of a homogeneous couple. This couple will have the highest possible value of φ_c if we choose the pair of available compositions with the highest index of performance. At this stage of the procedure the differences between the two couples are of two kinds. The inhomogeneous couple is not only inhomogeneous but it generally contains a range of compositions with lower indices of performance. The latter kind of difference may cause φ_c of the inhomogeneous couple to be lower. It counteracts a possible gain in φ_c by the place dependences *per se*. Therefore we have to eliminate this kind of difference. This can be done by restricting the inhomogeneities in such a way that all pairs of available compositions have the same index of performance. This leads to

$$2(S_b-S_a)^{-1}\frac{\partial S_a}{\partial u}+\kappa_b^{\frac{1}{2}}\rho_a^{\frac{1}{2}}\left\{\frac{1}{\rho_a}\frac{\partial\rho_a}{\partial u}-\frac{1}{\kappa_a}\frac{\partial\kappa_a}{\partial u}\right\}$$

$$\times\{\kappa_b^{\frac{1}{2}}\rho_a^{\frac{1}{2}}+\kappa_a^{\frac{1}{2}}\rho_b^{\frac{1}{2}}\}^{-1}=0, \quad (33)$$

$$2(S_a-S_b)^{-1}\frac{\partial S_b}{\partial u}+\kappa_a^{\frac{1}{2}}\rho_b^{\frac{1}{2}}\left\{\frac{1}{\rho_b}\frac{\partial\rho_b}{\partial u}-\frac{1}{\kappa_b}\frac{\partial\kappa_b}{\partial u}\right\}$$

$$\times\{\kappa_b^{\frac{1}{2}}\rho_a^{\frac{1}{2}}+\kappa_a^{\frac{1}{2}}\rho_b^{\frac{1}{2}}\}^{-1}=0. \quad (34)$$

If these conditions are fulfilled φ_c of the homogeneous couple is given by (25). The efficiency of the inhomogeneous couple can be found by substitution of (33) and (34) in (29). We find

$$\varphi_c=\frac{\Delta_m}{2\Delta}-\tfrac{1}{2}+\frac{1}{6}\frac{1+2q}{1+q}(S_b-S_a)^{-1}\left\{\frac{\partial S_b}{\partial u}-\frac{\partial S_a}{\partial u}\right\}, \quad (35)$$

from which it follows that the inhomogeneous couple has a higher φ_c if $\partial S_b/\partial u-\partial S_a/\partial u>0$. This again means that part of the Joule heat is compensated directly at the place where it is developed. It is clear that, all other circumstances being equal, an inhomogeneous couple can have a higher efficiency φ_c than a homogeneous one.

VI. SECOND-ORDER THEORY OF OUTPUT POWERS

The second-order terms can be divided into two groups. The first group describes the second-order effects due to the existence of the partial differential quotients $\partial\kappa/\partial T$, $\partial\kappa/\partial u$, $\partial\rho/\partial T$, $\partial\rho/\partial u$, $\partial S/\partial T$, and $\partial S/\partial u$. In this group we have squares of first-order partial differential quotients such as $(\partial S/\partial T)^2$ and interaction terms such as $(\partial\kappa/\partial T)(\partial S/\partial u)$. The second group describes in a first-order approximation the effects due to the existence of second-order partial differential quotients such as $\partial^2S/\partial T\partial u$.

Table IV[6] gives the second-order terms of the output powers W_j for the case of a reference point $u=1$ and a reference temperature $T=T_2$. Tables II and IV together give the complete second-order theory of output powers. Note that all nine possible partial differential quotients of second order occur in Table IV. Of the squares of the first-order partial differential quotients that of $\partial\rho/\partial u$ is absent; Of the fifteen possible interactions the product $(\partial\kappa/\partial T)(\partial\rho/\partial u)$ is absent.

VII. ACCURACY OF APPROXIMATION

By ϵ we define the smallest quantity for which for both bars at the reference point $u=1$; at the reference temperature $T=T_2$ the conditions

---

[6] Table IV has been deposited as Document No. 6685 with the ADI Auxiliary Publications Project, Photoduplication Service, Library of Congress, Washington 25, D. C. A copy may be secured by citing the Document number and by remitting $1.25 for photoprints or $1.25 for 35-mm. microfilm. Advance payment is required. Make checks or money orders payable to: Chief, Photoduplication Service, Library of Congress.

$$T|Z^{-1}\partial Z/\partial T| \leqslant \epsilon, \quad |Z^{-1}\partial Z/\partial u| \leqslant \epsilon, \qquad (36, 37)$$

$$T^2|Z^{-1}\partial^2 Z/\partial T^2| \leqslant \epsilon^2, \quad T|Z^{-1}\partial^2 Z/\partial T\partial u| \leqslant \epsilon^2, \qquad (38, 39)$$

$$|Z^{-1}\partial^2 Z/\partial u^2| \leqslant \epsilon^2, \qquad (40)$$

are satisfied for $Z=\kappa$, $Z=\rho$, and $Z=S$. We suppose that for both bars and the same reference values I and Δ satisfy the conditions

$$\kappa\rho I^2/l^2 T \leqslant 1, \quad |\kappa SI/l| \leqslant 1, \quad |\Delta/T| \leqslant 1. \qquad (41)$$

Using these equations we can interpret each of the first- and second-order terms occurring in W_j as a correction to one of the eight terms $l_a\Delta/\kappa_a$, $l_b\Delta/\kappa_b$, $\rho_a I^2/l_a$, $\rho_b I^2/l_b$, TS_aI, TS_bI, $S_aI\Delta$, and $S_bI\Delta$ occurring in the zero-order equations (20), (21), and (22) for W_j. We express the total correction to each one of these eight terms in a fraction of the same term. In this way we find that for the set of first-order terms of Table II none of these fractions exceeds 2ϵ and that for the set of second-order terms of Table IV none of these fractions exceeds $2\epsilon^2$. We conjecture that for the set of terms of order t none of these fractions exceeds $2\epsilon^t$. If this is true the relative error in each one of the eight terms mentioned above, after taking into account all corrections following from the theory of order t will not exceed $2\epsilon^{t+1}/(1-\epsilon)$. The relative error in W_j itself depends on the signs and the relative magnitudes of these eight terms. This error will generally be larger than $2\epsilon^{t+1}/(1-\epsilon)$.

ACKNOWLEDGMENT

We wish to thank P. G. van Vliet for checking Tables II and IV.

JOURNAL OF APPLIED PHYSICS VOLUME 32, NUMBER 8 AUGUST, 1961

Nanosecond Triggering of Air Gaps with Intense Ultraviolet Light

Terry F. Godlove
Nucleonics Division, U. S. Naval Research Laboratory, Washington, D. C.

(Received March 13, 1961)

Measurements are presented of the breakdown time of a conventional two-electrode air gap. The applied voltage is maintained below the sparking threshold and breakdown is caused by the emission of a 6-nanosec burst of photoelectrons from the cathode, which produces space-charge distortion of the electric field. An auxiliary trigger spark provides the necessary light and results in cathode emission up to ~10 ma/cm². The dominant wavelength region is found to be ~1100 A because of the relatively low air absorption and high photoelectric yield in this region. For a fixed gap spacing and using the highest light intensity available, the time delay is typically found to decrease from $\sim 5t_-$ to a minimum delay t_- as the main gap voltage is increased from ~8% below threshold up to threshold. The minimum delay ranges from 10–60 nanosec for the gap spacings studied and agrees with calculated values of gap spacing/electron drift velocity. The techniques developed have direct application to the triggering of conventional spark-gap switches and to pulsed light sources and may provide an additional tool for investigating some of the basic parameters of gaseous electronics.

I. INTRODUCTION

ULTRAVIOLET illumination has long been used in the study of electric sparks to facilitate breakdown of a gap by means of photoelectric emission from the cathode. The intensity of illumination has usually been held to a level low enough so as to eliminate any distortion of the electric field resulting from space charge effects. For example, Bandel[1] and Fisher and Bederson[2], using initial currents $<10^{-11}$ amp, measured the time lag for breakdown of a 1-cm gap in air. They found time lags in the range 10–60 μsec for applied voltages within 0.1% of V_s, the sparking threshold. Such time lags have been interpreted as being indicative of the necessity of positive ion current to complete the discharge. The drift time of a positive ion is ~12 μsec for a 1-cm air gap, whereas the electrons created in the initial avalanche are collected in ~0.1 μsec.

Many measurements have also been made using the sudden application of a known overvoltage. In this case it is found that the time lag decreases rapidly with increasing overvoltage. Time lags in the nanosecond (10^{-9} sec) region have been obtained with an overvoltage the order of 50–100%. Work up to about 1954 on spark breakdown in uniform fields in air has been summarized in several reference works.[3] It is sufficient here to point out that the unique feature of the present measurements is the combination of voltage $<V_s$ and enough illumi-

---

[1] H. W. Bandel, Phys. Rev. **95**, 1117 (1954).

[2] L. H. Fisher and B. Bederson, Phys. Rev. **81**, 109 (1951).

[3] J. M. Meek and J. D. Craggs, *Electrical Breakdown of Gases* (Oxford University Press, London, 1953); L. B. Loeb, *Basic Processes of Gaseous Electronics* (University of California Press, Berkeley, California, 1955), Chaps 8 and 9; F. Llewellyn-Jones, *Ionization and Breakdown in Gases* (John Wiley & Sons, Inc., New York, 1957); and in *Handbuch der Physik*, edited by S. Flügge (Springer-Verlag, Berlin, 1956), Vol. 22, pp. 1–52.

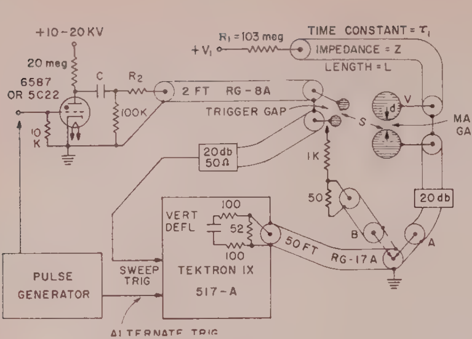

FIG. 1. Schematic and block diagram of the trigger gap circuit and the main gap circuit. The main gap spacing is d and the distance between the trigger spark and the cathode of the main gap is s. The unspecified parameters are: $C=67$–500 $\mu\mu$f; $R_2=50$–5000 ohm; $L=12$–30 ft; repetition rate $=1$–10 pps; $Z=13$ or 52 ohm. Direct vertical plate connection to the oscilloscope is used as shown. The connection marked A is the normal one; connection B is used to locate the trigger pulse at "time zero."

nation to give time lags comparable to the time required for one electron avalanche. This method necessarily involves distortion of the electric field by the space charge of the emitted electrons. Distortion results in an increase in the avalanche multiplication factor, exp $(\int_0^d \alpha dx)$, where α is the Townsend ionization coefficient and d is the gap spacing.

The interpretation of the measurements reported here is complicated by the presence of field distortion. No attempt is made to analyze the time lag results theoretically, except to point out in Sec. V that the initial currents approach a space-charge limiting condition. Many calculations have been given for the so-called static lowering of the breakdown voltage based on distortion, but such calculations assume a breakdown time much longer than the time scale used in the present measurements. It is only in the last few years that calculations have been undertaken to obtain complete solutions for the dynamic case; that is, solutions which can predict gap current vs time, taking into account secondary effects and space-charge distortion. Miyoshi[4] has given some analytic solutions for a 1-cm air gap and Ward[5] has programmed the partial differential equations for electronic computation.

In addition to the general interest in this type of work as a possible new method for investigating discharge processes, there is a strong practical aspect to these measurements. The circuit described herein can be used for triggering a conventional spark-gap switch, resulting in the following properties: (a) breakdown time≈electron drift time; (b) time jitter as low as 1 nsec; (c) stable voltage range up to ~6%; and (d) complete electrical isolation between the trigger circuit and the main gap circuit. The last property is unique among high-current switches and is of value in cases where the overvoltage pulse which is usually used as a trigger produces deleterious effects in the main output circuit.

With regard to the previous use of intense illumination, White[6] and Rogowski and Wallraff[7] years ago observed a lowering of breakdown potential using the light from a nearby spark. However, even though White's trigger spark used a stored energy of 70 joules, it had a relatively long duration (~1 μsec) and did not have the peak intensity which is necessary to produce immediate breakdown. Thus, he required an overvoltage of 30–50% in order to obtain time lags of 30–40 nsec.[8] The circuit described in Sec. II was developed to yield maximum peak light intensity for a very short duration and requires only ~10^{-2} joule energy per pulse.

Section III gives the time lag measurements. Section IV describes some electrometer measurements which confirm the high uv intensity and indicate the dominant wavelength; Sec. V gives a space-charge calculation; Sec. VI gives a summary and some aspects of the practical application of this method of triggering.

II. APPARATUS

Figure 1 shows the essential components of the trigger gap circuit and the main gap circuit. The pulses in both circuits are shaped using the principle of reflection from an open-ended transmission line. The somewhat arbitrary 2-ft length of the trigger pulse-forming line was chosen to be a reasonable approximation to a delta function.

Attention was given to the bandwidth and accurate impedance matching of the circuits because of the extremely short rise time of the pulses, especially at low values of V_s. The viewing system, consisting of 50 ft of RG-17A cable and the modified Tektronix model 517A oscilloscope, has a time constant of 1 nanosec and a rise-time to 95% amplitude of 3 nanosec. The latter figure is partly caused by cable dispersion. These figures were obtained by testing with a mercury switch-pulse generator, which was known to have a rise time <1 nsec.[9] In addition, all attenuators[10] were similarly tested and produced no observable distortion in the mercury-switch pulses.

The main gap electrodes were $\frac{3}{4}$-in.-diam hemispheres made of brass or type 304 stainless steel. One set of measurements (see Fig. 3, $V_s=11.89$ kv) was done using each material; no significant difference in the time delay was found. The trigger gap electrodes were made of brass, $\frac{1}{8}$ in. in diameter. The gap spacing was normally ~0.8 mm. To ensure fast breakdown of the trigger gap, a small (~0.2 mm) point was added to the negative trigger electrode, as shown in Fig. 1.

---

[4] Y. Miyoshi, Phys. Rev. **117**, 355 (1960).

[5] A. L. Ward, Bull. Am. Phys. Soc. **6**, 390 (1961).

[6] H. J. White, Phys. Rev. **48**, 113 (1935); **49**, 507 (1936).

[7] W. Rogowski and A. Wallraff, Z. Physik **97**, 758 (1935).

[8] This was pointed out by Professor L. B. Loeb in *Spark Breakdown in Uniform Fields* (Tech. Rept. Physics Branch, Office of Naval Research, Washington 25, D. C., July, 1954), p. 48; and in *Handbuch der Physik*, edited by S. Flügge (Springer-Verlag, Berlin, 1956), Vol. 22, p. 478.

[9] I. A. D. Lewis and F. H. Wells, *Millimicrosecond Pulse Techniques* (McGraw-Hill Book Company, Inc., New York, 1954), p. 103.

[10] Reference 9, p. 124.

The operation of the trigger gap circuit is sketched in Fig. 2. The lower curve shows the gap voltage vs time assuming no breakdown. The slope of the fall in voltage is exaggerated. The basic idea is to overvolt the gap in a time shorter than the time it takes to break down. The limiting breakdown time of the type 6587 hydrogen thyratron was measured in some previous experiments and known to be ~10 nsec. Thus, aside from this limitation, the rise of voltage on the trigger gap depends on R_2 and the combination of capacitor C and the cable capacitance in series. For the typical values $C=67$ μμf and $R_2=330$ ohm, $\tau_2=10$ nsec. The time required to break down depends on the amount of overvoltage, with 50–100% being typical in this work. The overvoltage was always adjusted to yield minimum variation in amplitude from pulse to pulse. This resulted in some time jitter, but it did not affect the measurements since the oscilloscope was triggered by the trigger-gap pulse itself. The start of the sweep was stable to <1 nsec. For practical triggering applications, the combination $R_2=50$ ohm, $C=100$ μμf, and a high overvoltage has been used successfully and results in over-all jitter <2 nsec. The current following the trigger pulse varies inversely with R_2. However, the time delay measurements were found to be insensitive to changes in the current after the pulse over the range 1%–30% of the peak current.

The amplitude of the trigger pulse was stable to ~5%. Occasional pulses of low amplitude occurred, but these were eliminated by the expedient of measuring the minimum delay time; the method is described in Sec. III. Connection B of Fig. 1 was used to determine "time zero," which was assumed to be the center of the 6-nsec trigger pulse. This was checked frequently. The main gap voltage V_1 was produced by a 50-kv 5-ma power supply which was filtered and backed up by an ac regulator. The uncertainty in relative voltage is ±0.2%; in absolute voltage: ±1%. Checks were made on V_s before, during, and after each series of measurements by turning off the trigger gap and noting the voltage V_1 which caused the main gap to break down spontaneously at a rate ≪ reciprocal of the charging time constant. In most cases, the charging time constant was 35 msec and V_1 was noted at a breakdown rate of the order of 1 cps. The extreme accuracy of voltage needed by Bandel and others is not required in this work. No serious attempt was made to maintain the polish of the electrodes. The delay measurements indicate that only for combinations of voltage and uv intensity such that the delay is very large are such matters as electrode surface condition and extreme voltage stability important. The uncertainty in the time measurements is ±3%. The oscilloscope sweep speeds were checked several times using known lengths of cable.

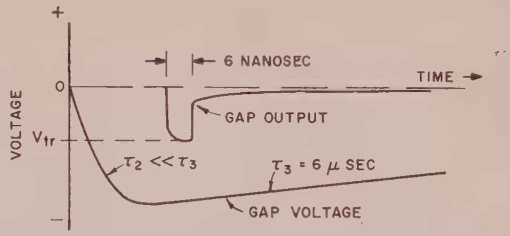

FIG. 2. The lower curve shows the voltage across the trigger gap of Fig. 1 assuming no breakdown. The pulse marked 6 nsec is the output delivered to a 20-db attenuator, which serves as a matched load. The pulse shape shown is obtained with $C=67$ μμf and $R_2=330$ ohm, in which case $\tau_2 \approx 10$ nsec. For all measurements $V_{tr}=5.3\pm0.7$ kv.

In order to make the main gap trigger reliably at voltages near V_s, and in some cases slightly above V_s, the following method was used. The charging time constant τ_1 was computed and the repetition rate was adjusted to make $V<V_1$ (see Fig. 1) by a convenient amount, e.g., 1%. If we denote the repetition period by T, then $V/V_1=1-\exp(-T/\tau_1)$. For $T/\tau_1=4.61$, $V/V_1=0.990$. The most extreme value used was $T/\tau_1=2.30$, in which case $V/V_1=0.90$. The reason for using this method is that for $V\geq V_s$, the time required for the main gap to break down as a result of the natural background current may be less than T, hence the gap will break down spontaneously before the uv flash occurs. The above method ensures that the gap voltage remains in the vicinity of V_s for the shortest possible time. On the other hand, dV/dt is small enough so that V is essentially constant during the measured delay time, which is always <1 μsec.

III. TIME-LAG MEASUREMENTS

The time lag is defined here as the time from the center of the 6-nsec trigger spark to the time at which the main gap current reaches an arbitrary threshold. This threshold is set by the oscilloscope sensitivity and the necessity of some attenuation in order to keep high-voltage pulses out of the oscilloscope. A 20-db attenuator was used throughout and, using the measured deflection sensitivity of 15 v/cm, this gives a minimum observable current of 0.6 amp for 2-mm deflection. The noise level was <1 mm; hence, the sharp break at the beginning of the main gap output pulse was easily located.

The choice of 0.6 amp for the threshold is not critical because di/dt is very large in this region of current. The reason for this is that the gap is highly space-charge distorted; furthermore, the current is not yet so large as to cause any appreciable drop in gap potential which would tend to reduce di/dt. Even at $V_1=6$ kv, 0.6 amp is equivalent to 1% of the peak cathode current. Separate measurements indicated that if the threshold current were to be changed by a factor of 10 in either direction, the delay would not be changed by more than 1 or 2 nsec.

Figures 3–7 give the observed time lag vs voltage for the four gap settings studied, plotted in Fig. 3 directly and in Figs. 4–7 as explained below. The error bar at V_s reflects the nonreproducibility in that measurement. For

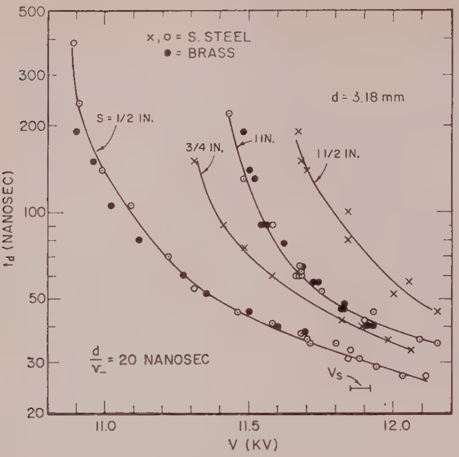

FIG. 3. Time lag vs voltage for $d=3.18$ mm. The open circles and crosses are for stainless steel electrodes, for which $Z=13$ ohm, $L=16.7$ ft, and $V_{tr}=6$ kv. The closed circles are for brass electrodes, for which $Z=52$ ohm, $L=30$ ft, and $V_{tr}=5.5$ kv. The lines have been drawn through the points representing stainless steel. The average V_s for brass was found to be 0.10 kv less than that for stainless steel, which was 11.89 kv. For the purpose of this figure, 0.10 kv was therefore added to each point representing brass. The cluster of points at $V=11.67$ kv and $t_d=61$ nsec is indicative of the fact that this point was used as a periodic check for the over-all stability of the apparatus.

fixed d and s, it was found that t_d approaches a minimum value asymptotically as V increases. The minimum, denoted by t_1, was determined by plotting each curve for several assumed values and selecting the one which gave the best fit to a straight line on the semilog plots. Figures 4–7 show the data plotted in this way. Figure 5 is thus a replot of some of the data of Fig. 3. The uncertainty in t_1 was determined by selecting those values of t_1 which gave a curvature unwarranted by the experimental accuracy and the number of datum points for a given curve. In making the above analysis, the smaller values of t_d were given the greatest weight.

Except for $d=1.59$ mm, the values of t_1 as determined in the above manner agree with the values of $t_-=d/v_-$ within an experimental uncertainty of $\pm10\%$. In making this comparison, the drift velocity was taken to be $v_-=1.26\times10^7$ cm/sec at $V/d=30$ kv/cm.[11] The reason for the straight line behavior must await a detailed theory of the complete dynamic process.

The pulse-to-pulse variation (jitter) in the time lag requires some discussion. In general, the closer the voltage to V_s and the smaller the separation, the less the jitter. To be more quantitative, for all combinations of V and s such that $t_d \lesssim 2t_-$, the jitter was rarely more than 2 nanosec. On the other hand, the jitter was very large under conditions corresponding to the maximum delays observed. In all cases the ***minimum*** delay for given V and s was recorded and plotted. In addition to the jitter arising from the discharge processes, there was a second cause of jitter of experimental origin. This was caused by variations in the uv intensity caused by fluctuations in the amplitude of the trigger gap pulse (V_{tr} of Fig. 2). These fluctuations were mainly a result of the fact that the trigger gap occasionally discharged before the voltage had reached its peak, as discussed in Sec. II. This effect could be observed by using the "alternate trig" of Fig. 1. Such an effect would naturally yield a unique minimum t_d with an occasional pulse having a larger value. The method adopted thus tended to eliminate those pulses which were caused by imperfect trigger operation.

It can be seen that for a given curve the data deviates from a straight line as V decreases. Taking Fig. 6 as an example, the deviation occurs for each value of s at $t_d-t_1\approx100$ nsec, or $t_d\approx140$ nsec. In all cases the deviation occurs at approximately the same value of t_d at which the jitter becomes severe and the average delay deviates from the minimum delay.

Another variable which has a secondary influence on the delay time is the angle between the uv illumination and the electrode axis. The geometry as sketched in Fig. 1 shows the approximate angle which was used (70°) in all measurements except those for $s=\frac{1}{2}$ in. In the latter case, an angle of about 80° had to be used to prevent breakdown from the main electrode to the trigger

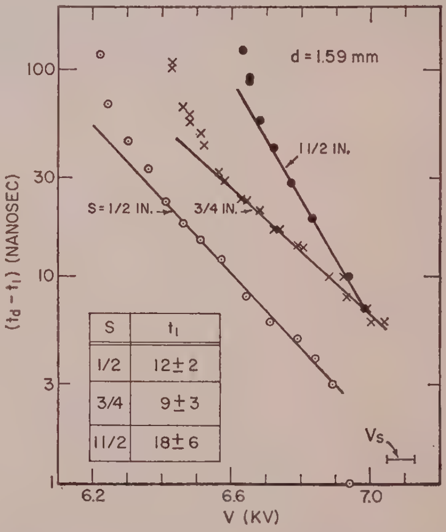

FIG. 4. Time lag vs voltage for $d=1.59$ mm plotted after subtracting a constant t_1 from each set of points as shown. The value of t_1 and its uncertainty was chosen from the best visual straight line fit. Here $Z=13$ ohm (4 cables in parallel), $L=16.7$ ft, and $V_{tr}=6$ kv. Electrode material: stainless steel. The point at $t_d=130$ nsec and $V=6.22$ kv represents the largest reduction in relative voltage, $\Delta V/V_s=12\%$, which was observed. The calculated drift time $d/v_-=10$ nsec.

---

[11] This is an extrapolation of the results of Bradbury and Nielsen as summarized by L. B. Loeb, reference 3, pp. 228–231, assuming $v_-=KE^{\frac{1}{2}}$. This relation appears to be in accord with theory and experiment for the range of E considered here. Bradbury and Nielsen's results give $K=(6.2$ to $6.9)\times10^4$ cm/sec per $(\text{v/cm})^{\frac{1}{2}}$ for $E/p=11$ to 22 v/cm per mm Hg. Our value corresponds to $K=7.3\times10^4$ cm/sec per $(\text{v/cm})^{\frac{1}{2}}$. This is the same value as that chosen for computation by Y. Miyoshi, Phys. Rev. **103**, 1609 (1956).

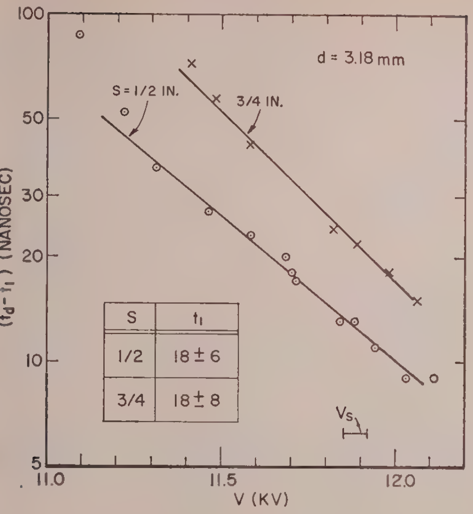

FIG. 5. The data of Fig. 3 plotted according to the method described for Fig. 4. Only points for stainless steel electrodes are used. A similar plot for $s=1$ in. yields $t_1=30\pm5$ nsec.

electrode. Separate measurements indicated that for an angle <80° the variation of t_d with angle was negligible. Between 80° and 100° there was a measurable variation; and beyond ≈100° the delay rapidly increased to large values as a result of shadowing. Therefore, for all measurements involving $s=\frac{1}{2}$ in., the effective uv intensity is slightly less than it would have been if the angle had been maintained constant.

Figure 8 shows some additional measurements of t_d as a function of the separation s at two selected gap spacings, corresponding to the indicated values of V_s. These data are included only to show that t_d is a much more sensitive function of s at low voltages than at high voltages.

IV. ELECTROMETER MEASUREMENTS

In an attempt to obtain more information about the magnitude of the photoelectric currents involved in the work previously described, and also to determine the dominant uv wavelengths, some electrometer measurements were performed. For this work the (approximately spherical) brass cathode was mounted directly on the input connector of a decade shunt, which in turn was mounted on a vacuum tube electrometer. The minimum measurable current was $\sim10^{-14}$ amp. A close-fitting aluminum shield was placed over the cathode and attached to the electrometer guard ring. The shield was covered with black electrical tape except for a $\frac{1}{4}$-in. diam hole through which the uv light from the trigger spark entered.

The results are shown in Figs. 9 and 10. A sketch of the geometry is also shown as an insert in Fig. 9. The trigger circuit of Fig. 1 was used, with $C=67$ μμf, $R_2=330$ ohms, $V_{tr}=4.2$ kv, and repetition rate $=170$ pps. The latter rate was chosen for the convenient range of average current, the duty factor of 10^{-6}, and the fact that the repetition period ≪ the electrometer time constant. A separate check was made on the linearity of current vs repetition rate from 1.7–170 pps. Another check was made on the proportionality between current and $(V_{tr})^2$ and agreement was found within ±20% over a range of a factor of 2. The uncertainty in the relative current measurements of this section is about ±20%; however, the uncertainty in the absolute reproducibility is about a factor of 2.

The data of Fig. 9 is most simply analyzed by direct analogy with a thermionic diode. For a diode, the current varies as exp $(-eV/kT)$, where V is the retarding potential and kT is the thermal energy of the electrons. The diode analogy should be valid provided the observed peak currents of Fig. 9 are much less than the true peak photoemission capability of the brass cathode. This is equivalent to assuming that the peak currents are space-charge limited. That this is indeed the case is supported by the data of Fig. 10, where the two lower curves exhibit a strong saturation effect at small s which is undoubtedly the result of space-charge retardation.

Analyzing Fig. 9 by analogy with a diode yields apparent thermal energies $kT=5.6$, 4.4, and 3.6 ev, respectively, from top to bottom. The former figures are consistent with a photon energy of 10–12 ev, which is the result of evidence discussed below.

The data of Fig. 10 are corrected for the inverse square effect as described in the caption. The open circles represent two series of measurements which showed good agreement with each other, and the crosses represent a third series which differed from the first two as

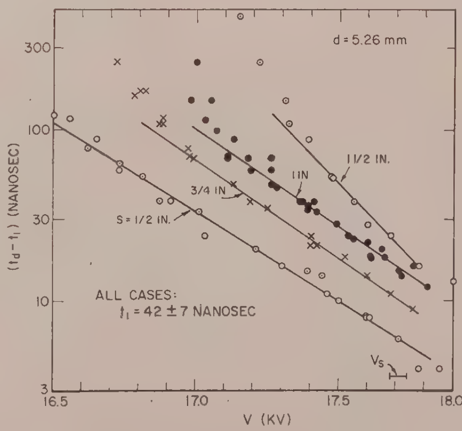

FIG. 6. Time lag vs voltage for $d=5.26$ mm plotted in the manner described for Fig. 4. Here $Z=52$ ohm, $L=11.4$ ft, and $V_{tr}=4.5$ kv. Electrode material: brass. The average V_s was 17.71 kv. The points on the curve labeled $s=\frac{3}{4}$ in. include an addition to the measured voltage of 0.04 kv because the average V_s during that run was lower by that amount. The calculated drift time $d/v_-=39$ nsec.

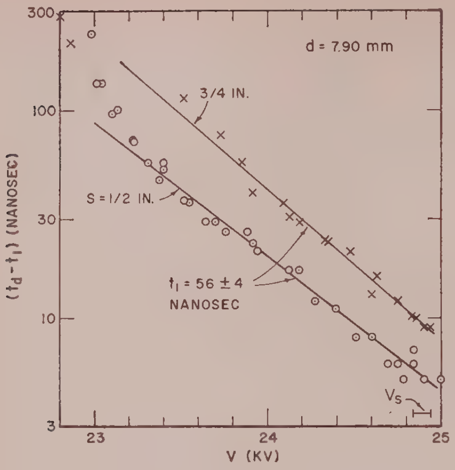

FIG. 7. Time lag vs voltage for $d=7.90$ mm plotted in the manner described for Fig. 4. Here $Z=52$ ohm, $L=11.4$ ft, and $V_{tr}=4.7$ kv. The calculated drift time $d/v_-=61$ nsec.

shown. The discrepancy is probably the result at least in part, of a difference in relative humidity. The upper curve plotted as closed circles represent two series of measurements taken with a "Lyman α" photoionization chamber developed for upper-atmosphere research. It uses a LiF window, contains nitric oxide gas at low pressure, and is sensitive only in the region 1050–1350 A. At 1216 A its efficiency is 0.62 electron/photon. The experimental arrangement and conditions, including the sensitive area, were the same as those used to obtain the other data of Figs. 9 and 10 except that the central wire collector was maintained at +35 v and s was measured from the window of the 1-in. long chamber.

In spite of the discrepancy between the lower curves of Fig. 10 which is noted above, there are three main conclusions to be drawn from these data: (a) except for a slight curvature which is within experimental error, the photoionization chamber data yield an absorption coefficient over a wide range of current which is consistent with the known absorption of N_2, O_2, and water vapor (summarized below) for the wavelength region considered to be important; (b) the photoelectric data yield nearly the same coefficient, provided one assumes that the higher current data are reduced by space-charge; (c) all three curves extrapolate to a peak current of 1 amp, within a factor of 2. Based on this figure and estimates of the quantum efficiency, the source intensity of the trigger spark can be estimated. This is done below.

The available data on uv absorption coefficients in N_2, O_2, and H_2O have been summarized by Weissler[12]. For $\lambda<800$ A, N_2 absorbs very strongly, but for $\lambda>1000$ A, it has little absorption. The O_2 structure is rather complex; however, in the region from ~1000–~1300 A a number of measurements have been made which give absorption coefficients <10 cm^{-1}. In the important region of the H Lyman α line at $\lambda=1216$ A, a coefficient of 0.23 cm^{-1} has been measured. These coefficients all refer to gas at NTP. The data on water vapor indicate (after correction to 50% relative humidity) a coefficient ranging from ~0.1–~2 cm^{-1} in the region from 1000–1800 A.

In view of our rough measurement of $\mu\approx1$ cm^{-1}, the above summary is consistent with the hypothesis that the dominant wavelength in the present work is in the region 1000–1300 A, in the so-called windows of low absorption. The only alternative to this hypothesis is that wavelengths >1700 A are most important. That this is not the case is supported by the attenuation measurements described below.

By using the same experimental arrangement which was used to obtain the lower curves of Fig. 10, photoelectric currents were recorded with and without absorbers of fused quartz and lithium flouride, having thicknesses of 1.2 and 1.0 mm, respectively. The attenuation of quartz was found to be >1000, consistent with its cutoff wavelength at ~1800 A. The attenuation of LiF varied from 12–130 for distances ranging from $s=1$ to $s=4$ cm. The variation with distance is consistent with the space-charge saturation effect noted above. This effect caused the observed photoelectric current without absorber to be less than it would have been without space-charge and hence gave attenuation figures at small s which were too low. In any case, these strong attenuation measurements show that the dominant wavelength cannot be >1700 A and must be near the cutoff in LiF, i.e., 1000–1100 A.[13]

A photon energy of 10–12 ev is also consistent with Weissler's summary of photoelectric yields.[14] The yield from most metals increases rapidly with energy from

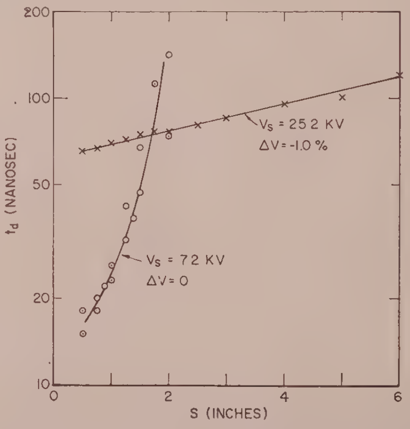

FIG. 8. This shows the marked difference in the behavior of t_d vs s at the two extremes of the voltage range studied. Material: brass. For $V_s=25.2$ kv, $V_{tr}=5$ kv; for $V_s=7.2$ kv, $V_{tr}=6$ kv.

---

[12] G. L. Weissler, in *Handbuch der Physik*, edited by S. Flügge (Springer-Verlag, Berlin, 1956), Vol. 21, p. 326 ff.

[13] E. G. Schneider, Phys. Rev. **49**, 341 (1936).

[14] Reference 12, p. 354.

the order of 10^{-4} electrons/photon near threshold to as high as 0.1 electron/photon for $h\nu=13$ ev on untreated W, Mo, and Ta. At this photon energy the surface condition appears to affect the yield by at most a factor of ~ 2. This is consistent with the results of Sec. III where it was found that the delay time was the same for brass and stainless steel and for polished and unpolished electrodes (except for large values of s corresponding to low initial current and hence long delay time).

On returning to the data of Fig. 10, we now estimate the integrated intensity of the trigger spark into 4π solid angle. The quantum efficiency of the photoionization chamber is estimated to be in the range 0.05–0.005 as a result of attenuation in the LiF window. This is based on our previous conclusion that the dominant wavelength is 1000–1100 A rather than 1216 A, which is the wavelength at which the efficiency was calibrated. This results in an intensity of 1.4×10^{12}–1.4×10^{13} photons/pulse.

With regard to the photoelectric measurements (lower curves of Fig. 10), we assume an extrapolated peak current of 1 amp and a photoelectric yield of 0.05–0.005 (based on Weissler's summary). This gives an intensity of 8×10^{11}–8×10^{12} photons/pulse. Combining both of the above results gives $\sim 3\times10^{12}$ photons/pulse, uncertain by a factor of ~ 5. The corresponding rate of emission is $\sim 5\times10^{20}$ photons/sec.

A direct estimate can be made of the peak photoelectric current density emitted from the cathode of the main gap in the presence of an electric field near threshold, which is strong enough to eliminate the space-charge effect observed in Fig. 10. Taking $s=\frac{1}{2}$ in., we divide the extrapolated peak corrected current of 0.2 amp from Fig. 10 (average of two curves) by $4\pi s^2$ to give 10 ma/cm², or 4×10^8 electrons/cm²/pulse. These figures are uncertain by about a factor of 3, mainly because of the extrapolation.

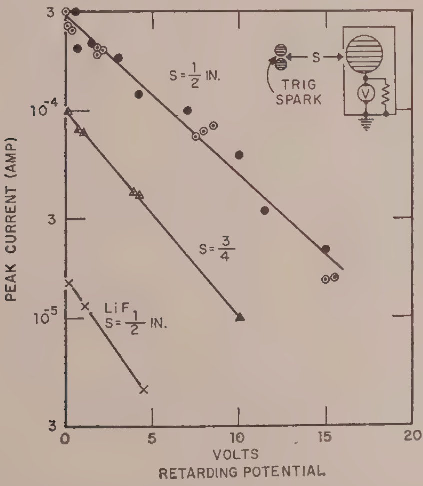

FIG. 9. Semilog plot of electrometer current vs positive retarding potential on a brass cathode. The geometry is sketched in the insert. The uv light from the trigger spark entered through a $\frac{1}{4}$-in. diameter hole in a shield, which was $\frac{1}{8}$ in. from the cathode. The data marked LiF were taken after interposing a 1.0-mm thick LiF filter between the spark and the shield. The trigger spark was operated at 170 pps and $V_{tr}=4.2$ kv. The retarding potential was developed by the photoelectron current passing through shunt resistors of 10^9–10^{12} ohm. The data plotted as closed circles have all been multiplied by 1.40 in order to plot with the open-circle data, which were taken during a different run. Each observed current was multiplied by a duty factor of 10^6.

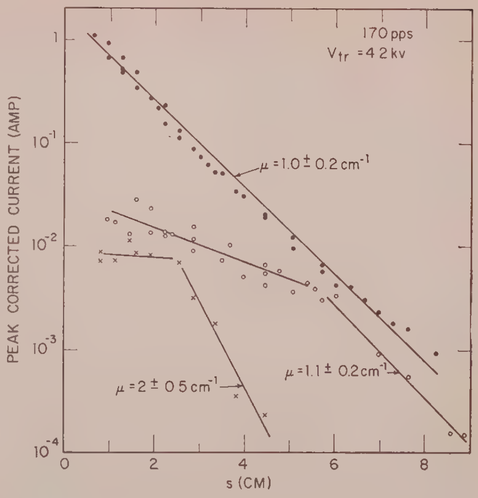

FIG. 10. Crosses and open circles: Electrometer current vs s using the experimental arrangement described for Fig. 9 except that the retarding potential was maintained below 0.7 v. Closed circles: Electrometer current vs s using a "Lyman α" photoionization chamber described in the text. The ordinate in all cases is the observed average current multiplied by $10^6(4\pi s^2/\pi c^2)$, where $c=\frac{1}{8}$ in. = detector aperture radius, to eliminate the inverse square effect (10^6 is the duty factor correction). Note the saturation effect apparent in the lower curves but not present in the photoionization (upper) measurements. The derived absorption coefficient μ is discussed in the text.

V. SPACE-CHARGE LIMITED CURRENT

In this section we calculate the maximum initial current density which is sufficient to break down a gap in the shortest possible time by space-charge distortion. The current density which causes the electric field to be zero at the cathode is therefore required. Suppose that during a brief instant of time after the emission of a step function of photoelectrons the electric field adjusts itself to the current density in a manner analogous to that obtained in a space-charge limited planar diode. On neglecting multiplication effects, Poisson's equation gives $dE/dx=J/\epsilon v_-$ for the one-dimensional case (uniform field), where $J=$ (assumed constant) current density and $\epsilon=8.85\times10^{-12}$ farad/m. Assuming that $v_-=KE^{\frac{1}{2}}$, where K is an empirical constant similar to the electron mobility, one obtains $dE/dx=J/\epsilon KE^{\frac{1}{2}}$. Integrating twice with the boundary conditions $E=0$ at $x=0$ and voltage V at $x=d$ gives the space-charge limited current density J_{sc} in mks units as

$$J_{sc}=(5/3)^{\frac{3}{2}}(2\epsilon K/3)V^{\frac{3}{2}}d^{-\frac{5}{2}}.$$

On using as before[11] $K=7.3\times10^4$ cm/sec per $(\mathrm{v/cm})^{\frac{1}{2}}$, the formula is

$$J_{sc}=0.87\times10^{-8}V^{\frac{3}{2}}d^{-\frac{5}{2}}\mathrm{amp/cm^2},$$

with V in volts and d in cm. Taking as an example $d=8$ mm and $V=25$ kv, $J_{sc}=0.06$ amp/cm². This is only a factor of 6 larger than the experimental value found in Sec. IV, and indicates in a qualitative way the fact that space charge distortion is the primary contributor to the short breakdown times recorded in Sec. III.

A similar derivation assuming $v_-=kE$ has been given by Mott and Gurney[15] for application to space-charge limited currents in crystals. For our case, the latter assumption yields $J_{sc}=4.4\times10^{-11}V^2d^{-2}$ with V in volts, d in cm, and $k=420$ cm/sec per v/cm. This formula gives values of J_{sc} nearly equal to those obtained above for the parameters in which we are interested.

The above derivation, in conjunction with the work of Bandel[1] and others, gives for the space-charge distorted "region" the limits $4\times10^{-6}\lesssim J\lesssim4\times10^{-2}$ amp/cm². The present work demonstrates that initial photoelectric currents in this range can indeed be realized experimentally with relatively simple apparatus. In addition, the $d^{-\frac{5}{2}}$ dependence indicates that much higher initial currents are needed as the gap spacing d is decreased for comparable space-charge distortion. This explains the results of Fig. 8, where it was found that t_d increased much more rapidly with s for a small gap than for a large gap.

VI. SUMMARY AND APPLICATIONS

We have attempted to demonstrate that: (a) A trigger circuit of the type described in Sec. II based on a small gap with a large applied overvoltage and using delay line clipping is able to produce intense short-duration light in the region of ~1100 A. (b) Such light is able to produce photoelectric yields up to ~10 ma/cm² after absorption by 1 cm of air; and the effective absorption coefficient of air for such light is ~1 cm⁻¹. (c) When such light is used as a trigger for conventional air gaps, a lowering of the threshold by as much as 10–12% can be obtained as a result of space-charge distortion of the gap. (d) The time delay between the uv light pulse and the resulting breakdown of the gap yields a straight line when log (t_d-t_-) is plotted vs V for $t_d\lesssim4t_-$; and in this region the time jitter is $<0.1t_-$. (e) The larger the value of d(or V_s) the less sensitive is t_d to variations in light intensity.

Concerning the practical application of this method of triggering, the trigger circuit of Fig. 1 proved to be quite reliable using the combination, $C=100$ μμf, $R_2=50$ ohm, and a small point on the positive (grounded) electrode. With low R_2 the pulse shape is not rectangular but this does not matter for reliable triggering. A trigger pulse longer than 6 nsec may be used; however, it should be emphasized again that high peak intensity is more important than the integrated energy per pulse. In addition, the rise time τ_2 of the trigger gap voltage must be kept short in order to obtain minimum jitter. The circuit of Fig. 1 has been operated at repetition rates as high as 300 pps and may compete favorably with other sources of intense light in the wavelength region of the vacuum ultraviolet unless continuous emission is required.

The advantages of this type of triggering were enumerated in the introduction. The main disadvantage is the voltage range for stable operation, which may vary from ~1%–~6%, depending on V_{tr} and the detailed application. This range can be ascertained from the measurements of Sec. III, once the acceptable limits on time delay have been set. A separation of $s=\frac{1}{2}-\frac{3}{4}$ in. is obviously desirable and can generally be obtained by locating the trigger electrodes in a plane perpendicular to the axis of the main electrodes, in addition to suitable shaping of the electrodes themselves. Note that a window, even of LiF, is not desirable.

ACKNOWLEDGMENTS

The author is indebted to David C. dePackh for many discussions and for pointing out the relevancy of the space-charge limited current. John Negri constructed most of the apparatus used. Several informative discussions were held with Dr. Cabell A. Pearse and Dr. J. McElhinney. Appreciation is also due W. R. Hunter and Dr. T. A. Chubb of the Atmosphere and Astrophysics Division, U. S. Naval Research Laboratory, for the loan of the photoionization chamber, advice concerning its use, and its calibration.

---

[15] N. F. Mott and R. W. Gurney, *Electronic Processes in Ionic Crystals* (Oxford University Press, London, 1948), 2nd ed., p. 172; also see B. Meltzer, J. Electronics and Control 8, 171 (1960).

JOURNAL OF APPLIED PHYSICS VOLUME 32, NUMBER 8 AUGUST, 1961

Study of Electron Bombardment of Thin Films*

G. B. Gilbert, T. O. Poehler, and C. F. Miller
Department of Electrical Engineering, The Johns Hopkins University, Baltimore 18, Maryland

(Received March 20, 1961)

An experimental study has been made of methods by which the physical properties of thin metallic films may be changed. In particular, emphasis has been placed on investigating alterations of the crystal structure of certain films subjected to electron bombardment. The films, after being vapor deposited on amorphous substrates, were bombarded by a 35-kev electron beam in a zone recrystallization process. X-ray diffraction photographs and photomicrographs indicate substantial crystal growth in films of indium, bismuth, and germanium.

INTRODUCTION

THE possibility of growing single-crystal thin films has received the attention of a number of investigators in the past years[1] because of the many desirable device applications. Some success has been achieved in producing single-crystal films, but only under very special conditions. Vapor deposition on an amorphous substrate, such as glass, produces films which are amorphous or have very minute grain size. However, use of a single-crystal substrate often provides sufficient epitaxial[2] force to cause the deposited film to be a single crystal. Thus, numerous experimenters have grown germanium, silicon, and other single-crystal films on single-crystal substrates. The experiments reported here make use only of amorphous substrates for the films. The method used to induce crystal growth is a modification of the normal zone techniques with the required temperature gradient provided by an electron beam.

As in bulk metal crystal growing,[3] the basic problem is establishing the proper temperature gradient and the rate at which it must be moved through the material. While it might be possible to introduce a preferred orientation by some sort of seeding, this is neither necessary nor easily accomplished. The main difficulty is not the lack of nucleation centers for crystal growth, but rather how to get growth from just one of these centers. The proper temperature gradient and speed at which it is moved depend on the physical properties and volume of the material.

While most common methods of crystal growing require that the material pass through a liquid phase, this is not necessary to achieve recrystallization. In many metals it is possible to cause a polycrystalline region, consisting of many small grains, to recrystallize into a single crystal without a change of phase. The mechanisms principally responsible for recrystallization of this type are believed to be the release of strain energy and grain boundary surface tension.[4] When the polycrystalline solid is heated to the recrystallization temperature, strain energy is released, and the grain size increases. Growth of crystals in this manner reduces contamination problems, allows impurity distributions to remain fixed, and prevents undesirable solid phase transformations. Most metals have been observed to recrystallize with this technique, although some reports indicate that materials with highly covalent bonding do not.[5]

In attempting to cause crystallization of a film on a substrate, additional factors are present which influence the success of the process. The forces between the surface of the substrate and the film can be substantial so that, if the substrate is a single crystal, there exists the possibility of growing a single-crystal film on it merely by vapor deposition. However, this technique requires numerous special conditions for crystal growth, including crystalline substrates whose lattice constants are close to those of the deposited material and highly controlled vapor deposition conditions.

If an amorphous substrate is used, then the strong forces tending to bring order to the film do not exist. Films deposited on such substrates tend to be amorphous, or at best polycrystalline, with very small grain size. The use of a strain annealing process similar to that used in bulk materials makes possible crystal growth in these amorphous films. The film in which nucleation and growth of a crystalline phase from an amorphous phase occurs will undergo a release of strain energy which was stored in the original strained matrix of small grains. This release of strain energy, when the solid is heated to a suitable temperature, is believed responsible for the resultant grain growth.[6] The change in energy in forming a crystalline region consists of several terms, one arising from the formation of an interface between regions, another from the change in volume free energy connected with the change in crystal size, and a third from coherence between the two types of grains. When the growing region is in contact with a substrate, the total interfacial energy is the sum of two terms which include the interfacial energy between the crystalline region and the film

---

* This research was supported by the Bendix Radio Division of the Bendix Corporation.

[1] W. C. Dunlap, J. C. Marinace, and R. P. Ruth, Bull. Am. Phys. Soc. **1**, 294 (1956).

[2] M. Davis and R. F. Lever, J. Appl. Phys. **27**, 835 (1956).

[3] W. D. Lawson and S. Nielsen, *Preparation of Single Crystals* (Butterworths Scientific Publications, Ltd., London, 1958), pp. 176–210.

[4] J. E. Burke and D. Turnbull, Progr. in Metal Phys. **3**, 220 (1952).

[5] W. C. Ellis and J. Fageant, J. Metals **6**, 291 (1954).

[6] J. Hollomon, *Thermodynamics in Physical Metallurgy* (American Society for Metals, Cleveland, Ohio, 1950), p. 161.

and substrate, respectively. There is a critical size for the crystalline regions,[7] and all those which exceed this critical dimension will grow, while those which do not will revert to the original small grain size.

It has been shown that the crystalline region which has the minimum energy is a segment of a sphere.[8] This point indicates that a general vacuum annealing of a film will not achieve a significant increase in crystal size, but will eventually result in agglomeration. Experimental evidence has tended to verify this point. A more sophisticated method of zone recrystallization will prevent agglomeration, as well as provide a more suitable method for controlling crystal growth. This method is centered on using an electron beam to provide a high temperature gradient which can move across the face of the film. This moving temperature zone can then be used to cause crystal growth through solid phase recrystallization.

EXPERIMENTAL TECHNIQUE

The basic technique in growing crystalline films has been a zone recrystallization of vacuum evaporated films. The vacuum evaporation methods used have been standard,[9] and have been conducted in a CEC vacuum system at pressures below 10^{-4} mm Hg. The films have been deposited on polished glass substrates located at varying distances from the evaporation source. Numerous methods have been used to vaporize the materials to be deposited, including electron bombardment, resistance heating, and induction heating.

Simplest and most frequently used of these evaporation techniques has been resistance heating. For small quantities of most metals, evaporation may be carried out from coils or boats of refractory metals, and the problem of selecting a suitable host material from which other metals can be evaporated has been thoroughly investigated. However, the results of these investigations are misleading if it is desired to evaporate large quantities of reactive metals such as aluminum. For such materials, only carbon crucibles have been found to be even moderately successful sources.

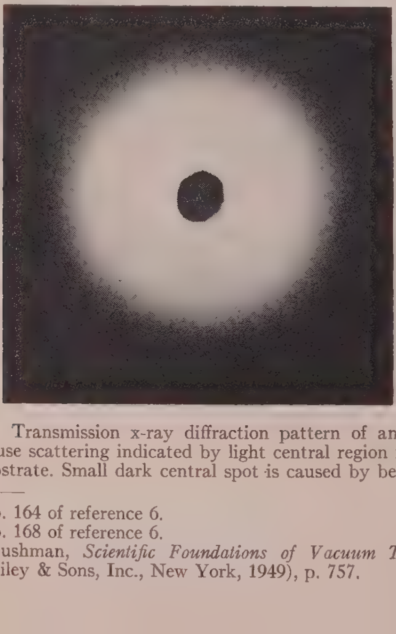

FIG. 1. Transmission x-ray diffraction pattern of amorphous Ge. Diffuse scattering indicated by light central region is due to glass substrate. Small dark central spot is caused by beam stop.

Electron bombardment can also be used to great advantage in the vapor deposition of many types of materials. However, due to vacuum system limitations and the critical nature of a filamentary source of electrons, sufficient rates of deposition were not attained.

To prepare films which will properly adhere to the substrate, the surface must be adequately cleaned. A cleaning process which has been found to be successful includes a chemical cleaning followed by a cleaning in the vacuum chamber. The first phase consists of cleaning the substrate ultrasonically in a detergent solution, followed by rinsing in distilled and then in deionized water. Subsequent cleaning methods used in the vacuum chamber have included heating, use of a glow discharge, and ion bombardment. The method found to be most useful at present has been direct heating of the substrate from a heater mounted in the chamber. This method is particularly attractive since it removes those impurities likely to cause trouble when the film is heated during the zone recrystallization process.

The method used to produce a temperature gradient in the thin films is a unique one in that a beam of medium energy electrons is used. The electron beam is electronically swept in one direction, at a speed high with respect to thermal time constants, to produce an integrated temperature zone. This zone is then slowly deflected in the other direction in the plane of the film in order to stimulate crystal growth. It has been determined that a high speed sweep of about 1 μsec is sufficient to provide an integrated temperature zone. The zone is moved through the film at speeds of from 1–10

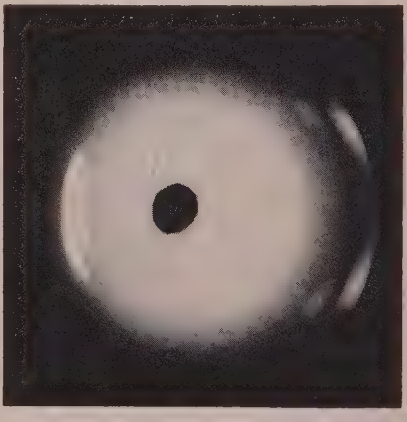

FIG. 2. Transmission x-ray diffraction pattern of textured B film. Although the rings are broken due to texture, they ar quite broad, indicating very small grain size.

---

[7] See p. 164 of reference 6.

[8] See p. 168 of reference 6.

[9] S. Dushman, *Scientific Foundations of Vacuum Technique* (John Wiley & Sons, Inc., New York, 1949), p. 757.

sec/cm. The beam is accelerated by a maximum of 50 kv with a normal operating potential of approximately 35–40 kv. The maximum beam current attainable is approximately 1 ma, although the normal beam current is on the order of 50 μamp. The electron beam is generated by a cold cathode discharge which is magnetically focused on a small aperture at the end of the anode cylinder. On diverging from the aperture, the beam is magnetically focused on the film. Electrostatic deflection plates are used in applying the high-speed horizontal and slow vertical sweep.

Generally, the temperature zone created by the electron beam has been moved through a large homogeneous area of the film. A few attempts have been made to limit the number of nucleation centers encountered initially by the zone by depositing tapered regions of film. These regions were obtained by masking a portion of the slide during deposition. Those initial attempts using this technique did not noticeably improve the resultant crystal size, but it is believed that this method might still be useful in achieving very large crystals. Confinement of the electron beam to a narrow region does serve to inhibit crystal growth in unwanted directions. The zone was generally kept at a temperature slightly below the melting temperature of the material being tested.

Investigation of the results of this type of treatment on various thin films has principally centered on crystal structure changes. X-ray diffraction[10] and photomicrograph studies have been used almost exclusively in determining changes in the films. Both transmission and back reflection have yielded information on the structure of the films. All films which were simply deposited on amorphous substrates were observed to be amorphous, or contain only extremely small grains. Many films deposited were observed to have some texture,[11] that is, an orientation to the small grains of which they were composed. Figures 1 and 2 are representative of the typical diffraction patterns obtained in such films. Photomicrograph studies of the film surfaces have also been used to great advantage in determining certain crystallographic data. The bombardment of the films not only changes the crystalline properties of the films,

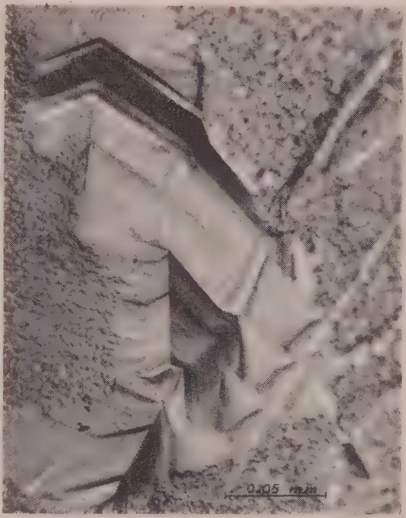

FIG. 4. High magnification photomicrograph of a section of Fig. 3. Note exposed crystal surfaces due to vacuum etching.

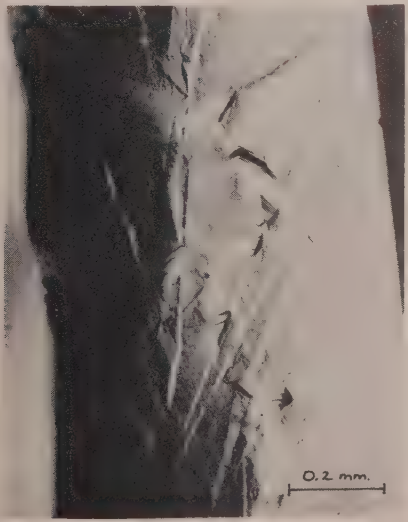

FIG. 3. Photomicrograph of Ge film with sections of bombarded and unbombarded film. Uniform, narrow regions at the edges are unbombarded.

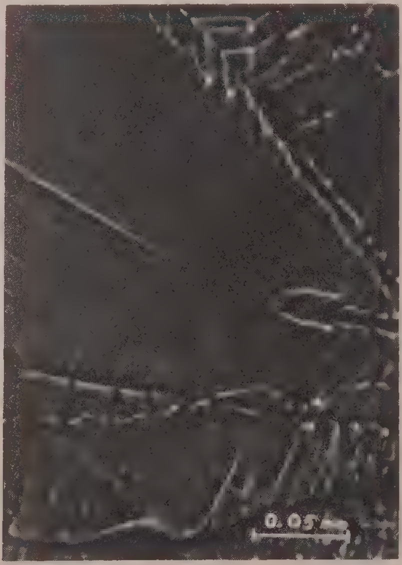

FIG. 5. Photomicrograph of treated Ge film showing grain boundaries and slip bands.

---

[10] B. D. Cullity, *Elements of X-ray Diffraction* (Addison-Wesley Publishing Company, Inc., Reading, Massachusetts, 1956), p. 259.

[11] See p. 272 of reference 10.

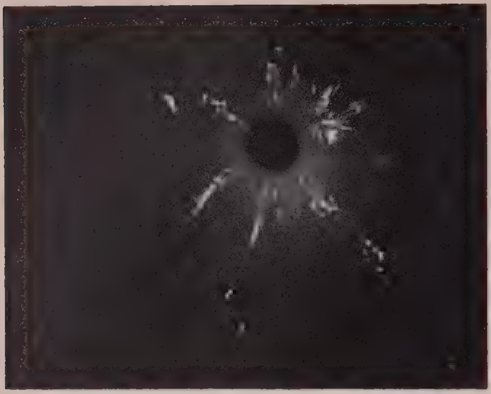

FIG. 6. X-ray diffraction pattern of a treated In film showing significant crystal growth from amorphous state.

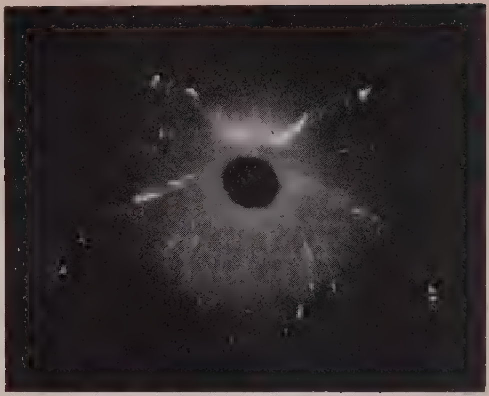

FIG. 7. X-ray diffraction pattern of a treated Bi film.

but also causes a partial etch of the surfaces. Thus, photomicrographs of treated films, as shown in Figs. 3, 4, and 5, give information as to crystal size and probable orientation, without resort to additional chemical etching.

DISCUSSION

Using this recrystallization technique, a number of materials have been treated in an effort to increase the crystal size. Early work was conducted on materials readily evaporated and annealed, including samples of both indium and bismuth. X-ray diffraction analysis indicated that in previously amorphous or textured films, the zone recrystallization process yielded polycrystalline films of significant grain size. Typical diffraction shots of some of these films are illustrated in Figs. 6 and 7. The asterism visible in the diffraction shots is indicative of strain in the crystals. Films of both materials were observed to contain polycrystalline grains at least a millimeter in length. No exhaustive attempts were made to increase the crystal sizes beyond this point, although this is believed to be completely possible.

Several factors seemed to influence the achievement of this crystal growth. First, heating of the substrate during deposition helped prevent blistering during subsequent treatment. The temperature required was dependent on the material being deposited, but appeared to be approximately half the melting point. While this is substantially below the recrystallization temperature, it noticeably aided film adherence. Another factor believed to be of paramount importance in crystal growth was the film thickness. Thin films of thickness of the order of 1000 A were bombarded without any significant success. Conversely, films of 10 000-A thickness or more were successfully recrystallized. It is believed that there may be a critical thickness below which recrystallization is impossible. It is probable that this minimum is a function of the vacuum conditions during deposition and any other factors which influence surface energy. As the conditions lead to a more pure deposit, the surface forces have less tendency to "freeze" the film in its original state. However, under any normal conditions, it appears that recrystallization is possible in films of practical thickness.

Attempts have been made to recrystallize films of other materials, with particular emphasis on germanium. Substantial grain growth has been noted in germanium, although not to quite the grain sizes achieved in other materials. Figure 5 shows crystals with a maximum dimension of 0.3 mm. It is interesting to note that recrystallization occurred in the germanium below its melting point. This contrasts with reports on the improbability of using solid phase recrystallization techniques in covalently bonded metals.

It is expected that future work will proceed in increasing the crystal size in films of germanium and other materials. Investigation of the electrical properties of these films and the influence of film thickness on recrystallization processes is also contemplated.

ACKNOWLEDGMENTS

We wish to thank Professor R. B. Pond, Dr. P. E. Wagner, and Miss E. Harrison for their advice and assistance.

JOURNAL OF APPLIED PHYSICS VOLUME 32, NUMBER 8 AUGUST, 1961

Influence of Deformation and Temperature on the Cobalt Gamma Irradiation of Sodium Chloride. Evidence for Electrical Interaction between Dislocations and Point Defects*

Rohn Truell
Brown University, Providence, Rhode Island

(Received September 19, 1960)

Ultrasonic attenuation measurements in sodium chloride as a function of cobalt 60 gamma-ray irradiation show no appreciable dependence on temperature in the temperature range from room temperature to liquid nitrogen temperature, hence no appreciable thermal activation energy for the process of immobilizing the dislocations. The influence of plastic deformation on the attenuation-irradiation behavior is large; the greater the deformation the more rapid the attenuation change, at least in the deformation range from zero to one percent deformation. The consequences of these effects are discussed in terms of boundary conditions on possible mechanisms for the observed effects.

It is rather well established that the effects of cobalt 60 gamma-ray irradiation on sodium chloride single crystals, as measured by ultrasonic attenuation and velocity, are directly connected with dislocation damping. These effects consist of an attenuation decrease and a corresponding velocity increase as a function of irradiation. The values of the attenuation as well as the velocity depend, among other things, on the dislocation density and on the dislocation loop length. The relationship between the irradiation effects and the dislocation density, loop length, and concentration of defects effective in pinning the dislocations during irradiation has been discussed.[1,2]

It is the purpose of this article to show the influence of deformation and of temperature on the irradiation effects mentioned above. Consider first the effect of varying amounts of deformation on the behavior of attenuation as a function of irradiation. There are several types of deformation experiments that one can perform; one is that of measuring attenuation and velocity as a function of deformation *during* deformation and immediately following such deformation. Such experiments have been described.[3] Another type of experiment is that of deforming a sample and, after removing it from the deforming apparatus, allowing most of the recovery effects to die out. Measurements are then made as a function of some other parameter such as irradiation.

In the case now to be described, a number of samples were deformed by different amounts and then subjected to cobalt 60 gamma irradiation at room temperature and at a rate of 3500 r/hr. The results[4] of attenuation measurements are shown in Fig. 1 where the top curve (No. 1) is that for an undeformed sample and the lower curves are for successively larger deformation extending to a deformation of 1.3% for the bottom curve (No. 7). The most noticeable feature shown by these curves is that deformation before irradiation causes the decrease in attenuation during irradiation to proceed more rapidly the greater the deformation. It is, moreover, evident from Fig. 1 that the difference in the time rates of the change of attenuation with irradiation is rather large—approximately a factor of 5 for the early stages of irradiation.

It has also been found in the course of this work that the attenuation-irradiation results are independent of temperature at least from room temperature to liquid nitrogen temperature.

The results of measurements of attenuation as a function of irradiation, with the sample at liquid nitrogen temperature,[5] are shown in Fig. 2. The data points shown in Fig. 2 are for measurements made on three different samples initially undeformed; the irradiation rate was in all cases 3500 r/hr as it was in the deformation experiments (Fig. 1). In some instances the same sample was irradiated more than once. Following a first irradiation, the sample could be made to recover from the irradiation by allowing the sample to stand for some days in the liquid nitrogen. In any case, the data taken at liquid nitrogen temperature all fell on or very near the solid curve of Fig. 2 as with the three sets of data shown.

The solid curve of Fig. 2 is identical with curve No. 6 of Fig. 1 corresponding to a sample having initially a 1% deformation. In other words, the attenuation-irradiation data taken at liquid nitrogen temperature seems to agree closely with the data for a sample deformed 1% and then irradiated at room temperature.

A sample is deformed by the time it is taken to nitrogen temperature in these experiments because the quartz transducer is bonded tightly to the sodium chloride sample at dry ice temperature and is then lowered from dry ice temperature to liquid nitrogen temperature. The difference in the expansion coefficients

---

* The work described here was supported in part by the Atomic Energy Commission, under contract, and through the cooperation of Brookhaven National Laboratory.

[1] Rohn Truell, J. Appl. Phys. **30**, 1275 (1959).

[2] Charles L. Bauer and Robert B. Gordan, J. Appl. Phys. **31**, 945 (1960).

[3] Bruce Chick, George Anderson, and Rohn Truell, J. Acoust. Soc. Am. **32**, 186 (1960).

[4] See Appendix for discussion of the manner in which data are presented.

[5] Identical results are obtained at dry ice temperature as well.

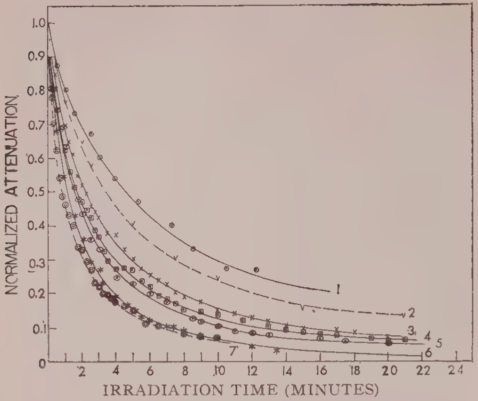

FIG. 1. Attenuation as a function of cobalt 60 gamma-ray irradiation of single-crystal sodium chloride samples which have been deformed by amounts varying from no deformation (top curve) to deformation of 1.3% (bottom curve). Curves are in order of progressively larger deformation from top to bottom.

is about a factor of 5, and the differential contraction between transducer and sample has in this case been definitely shown to cause strain in the sample. The strain is not uniform, but it appears, from the close agreement of the data, that the strain effect is very nearly the same in the several samples irradiated at liquid nitrogen temperature.

While this type of result lacks some of the quantitative features that one would like in such an experiment, nevertheless the fact that the low-temperature data match the room-temperature data (for a deformed sample) shows that there is no thermal activation involved in the process of immobilizing the dislocations and reducing the dislocation damping. In order that a thermal activation exist for this process of reducing or eliminating the dislocation damping, the effect would have to proceed more slowly at low temperature than at room temperature. That this is certainly not the case is shown by the data of Fig. 1 and 2 where (with deformation) the effect at low temperatures can proceed even more rapidly than at room temperature. As far as the writer is aware, this lack of any thermal activation for a dislocation pinning process has not been previously shown.

In examining possible models for the explanation of the observed effects, it seems clear that dislocations are at the center of any model. The evidence for this comes from experiments[6] on the deformation and recovery of NaCl as well as from other experiments[1] on the cobalt gamma-ray irradiation of NaCl.

Any model used to account for the processes which proceed in NaCl under conditions of combined deformation, cobalt 60 gamma-ray irradiation, and recovery following irradiation must take into account the following at least:

(a) The decrease in attenuation with gamma irradiation which is complete before any appreciable color center formation (at least in the visible range) has occurred. By using methods discussed in reference 1, it can be shown from attenuation and velocity measurements that the concentration of effective pinning points *added* during an irradiation period of 20 min does not exceed 10^{11} per cm^3. An equal density of color centers formed in this period would be well below a value that can at present be studied by optical absorption measurements. Consequently, color centers cannot be ruled out as pinning agents.

(b) The effect of deformation in causing the attenuation to decrease more rapidly as a function of irradiation for increasing deformation, at least in the range from 0—1.5%.

(c) The lack of any appreciable temperature dependence of the attenuation-irradiation effect in the temperature range from room temperature to liquid nitrogen temperature.

(d) A velocity change (increase) of approximately 0.3%—0.5% accompanying the attenuation decrease. See reference 1 for details. The amount of the velocity change increases with increasing deformation. The rate at which the velocity changes with time or irradiation for different deformations has not yet been studied.

(e) Following an irradiation, during which the attenuation has reached its lowest level for prolonged gamma irradiation, the attenuation recovers slowly toward higher values and after a number of days the attenuation recovery has reached as much as 90%

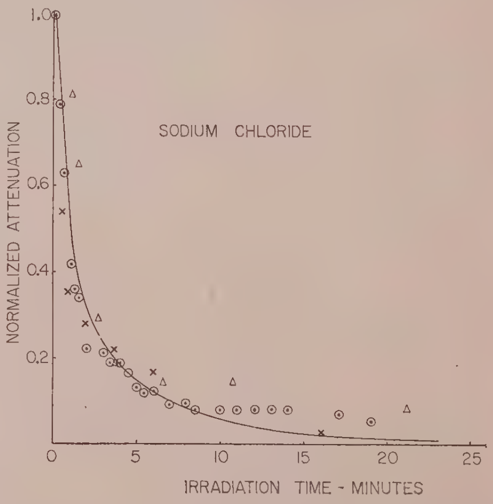

FIG. 2. Attenuation as a function of cobalt 60 gamma-ray irradiation for single-crystal sodium chloride. Data points represent three sets of data taken at liquid nitrogen temperature. Solid curve represents data taken at room temperature on a deformed sample (curve No. 6 from Fig. 1).

---

[6] Amos Picker and Rohn Truell, "Dislocation damping changes in alkali halides during deformation and during recovery following deformation," Masters thesis, Brown University, Providence, Rhode Island, 1960. Also, U. S. Atomic Energy Commission Rept. See also reference 3.

of the original attenuation before irradiation. This recovery takes place at room temperature or at liquid nitrogen temperature. Whether the rate of recovery at different temperatures is the same has not yet been determined.

In accounting for the attenuation decrease and the corresponding velocity increase associated with the immobilization or pinning of dislocations as a function of gamma-ray irradiation, there seem to be the following possibilities.

(1) The ionizing gamma irradiation produces point defects at or very near the dislocations and in sufficient numbers so that little or no migration is necessary in order to have these point defects interact with and pin dislocations. This type of process may include an altering or rearrangement of the charge distribution[7] on and around a dislocation.

(2) The point defects, after being created, move to the dislocations and pin them. In this case, however, one must have a mechanism which can operate with little or no thermal activation energy. An electrical interaction process may be possible but not a thermally activated one unless there are defects in sodium chloride capable of pinning dislocations and capable of moving with activation energies of 0.01 ev or less.

(3) The dislocations themselves move far enough to "pick up" the point defects which then pin them. In NaCl it is possible that even with strains the elastic waves may displace the entire dislocation segments so that they oscillate back and forth with larger amplitude than they could if the ends were strongly pinned.

At the present time, the observations (a)—(e) appear to be consistent with a model involving pinning by means of electrical interaction between point defects and dislocations. There is additional evidence[7–9] supporting an electrical model arising from electrical effects observed during cyclic stressing of sodium chloride as described, for example, in reference 8. It does not, however, seem possible, with the experimental evidence available at present, to select a single model from several possible models, and for this reason no attempt is made now to present and discuss these models. Further experimental evidence, of several types, seems to be necessary to improve the present state of understanding, and current experiments in this laboratory are aimed at obtaining the necessary evidence.

The conclusions of this discussion seem to be as follows:

1. There seems to be very little or no thermal activation for the dislocation pinning process involved in the irradiation of single crystals of sodium chloride by cobalt 60 gamma irradiation in the temperature range from liquid nitrogen to 300°K.

2. Plastic deformation produces a much more rapid pinning of dislocations in sodium chloride under the gamma irradiation. The rate of decrease of attenuation is larger, the larger the initial plastic deformation, at least up to 1.3% deformation.

3. It is not possible at present to specify a single definite model for the observed effects. The combined results of little or no thermal activation together with the plastic deformation effect indicate that the process of pinning may involve electrical interactions between dislocations and the pinning agents.

The author is indebted to Mr. Bruce Chick, Professor Charles Elbaum, Dr. Paul W. Levy of Brookhaven National Laboratory, and Professor Roland Dobbs for comments, suggestions, and for direct help in connection with the deformation and irradiation measurements discussed in this paper.

APPENDIX

The attenuation-gamma–ray irradiation data in the preceeding discussion are normalized, which means that in all cases a value of α is determined for times sufficiently long that the attenuation ceases to change with further irradiation. This value of attenuation, called α_∞, is obtained in either of two equivalent ways; the experiment may be allowed to continue for many hours at the same irradiation rate at which the experiment was carried out and until no further decrease in attenuation occurs. The same result will be obtained by increasing the irradiation rate many times and again irradiating until no further decrease occurs. It has been shown experimentally that the same value of α_∞ is obtained by either method and the latter method is usually used since it is much faster. This residual or background value of attenuation α_∞, which is unaffected by further gamma irradiation, is considered to contain no dislocation damping part. In other words, it is assumed that all dislocations have been pinned or immobilized by the time α_∞ is reached. Consequently,

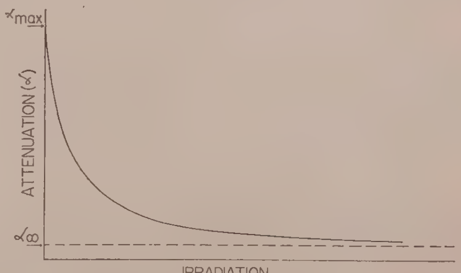

FIG. 3. Curve showing $\alpha_{\max}$ and α_∞ on an attenuation-irradiation plot before normalization.

---

[7] See for example P. L. Pratt, Inst. Metals (London), Monograph and Rept. Ser. No. 23.

[8] S. Amelinckx, J. Vennik, and G. Remaut, J. Phys. Chem. Solids **11**, 170 (1959); **16**, 158 (1960).

[9] J. D. Eshelby, C. W. A. Newey, P. L. Pratt, and A. B. Lidiard, Phil. Mag. **8**, 75 (1958).

α_∞ is subtracted from the measured values of α, and the normalized attenuation is

$$\alpha^* = \left(\frac{\alpha-\alpha_\infty}{\alpha_{\max}-\alpha_\infty}\right),$$

where the quantities are shown in Fig. 3.

In connection with the values of $\alpha_{\max}$ and α_∞ observed during gamma-ray irradiation for varying amounts of deformation, it has been found experimentally that values of $\alpha_{\max}$ and α_∞ do not follow a predictable pattern as a function of deformation but that the difference $(\alpha_{\max}-\alpha_\infty)$ does follow a pattern as a function of deformation. Figure 4 shows a plot of $(\alpha_{\max}-\alpha_\infty)$ as a function of deformation.

The last remarks apply to deformation and gamma-ray irradiation carried out at room temperature. Gamma-ray irradiation is assumed to leave the dislocation density unchanged.

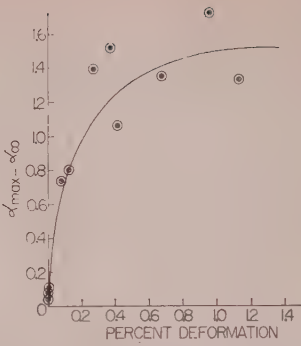

FIG. 4. Attenuation difference $(\alpha_{\max}-\alpha_\infty)$ as a function of the amount of deformation for a set of sodium chloride single-crystal samples irradiated at room temperature.

JOURNAL OF APPLIED PHYSICS VOLUME 32, NUMBER 8 AUGUST, 1961

X-Ray Diffraction Study of Interdiffusion in Cu-Ni Powder Compacts*

BERTINA FISHER AND P. S. RUDMAN
Department of Physics, Technion—Israel Institute of Technology, Haifa, Israel
(Revised February 27, 1961)

Interdiffusion in Cu—Ni powder compacts was studied by x-ray diffraction line shape analysis. Analogues to concentration-penetration plots are obtained. Results obtained at 750°, 850°, 950°, and 1050°C are compared with the conclusion that a single diffusion mechanism dominates in the range 750–950°C with an activation energy of about 26 kcal/mole, and it is concluded that the dominant mechanism is grain boundary diffusion. At 1050°C a new mechanism with a higher activation energy dominates, and it is concluded to be bulk diffusion. Metallographic observation revealed that prior to appreciable interdiffusion, the Cu, presumably by surface diffusion, envelops the Ni particles with subsequent interdiffusion between the Ni-rich core and the Cu-rich shell. This configuration is idealized to a concentric spheres model permitting rigorous solution of the diffusion equation for constant diffusion coefficient. The result of the calculation according to this new model and according to other authors' models are compared with the experimental results with the general certification of the concentric spheres model. The concentric spheres model is shown to predict that the rate of homogenization in the Cu—Ni system should be independent of the Cu particle size.

INTRODUCTION

ALLOY formation by interdiffusion between metallic particles held at temperatures below their melting points is an important powder metallurgical technique. It is important to be able to calculate or to determine the ensuing composition distribution after a given thermal treatment of an initially heterogeneous powder mixture. The calculation requires the solution of the diffusion equation

$$\frac{\partial c}{\partial t} = \nabla(D\nabla c), \tag{1}$$

where c=concentration, D=diffusion coefficient, and t=time.

Even in the simplest case of a binary system exhibiting complete miscibility at the interdiffusion temperature, a reliable, generally applicable solution is not available because: (a) In real systems D is a function of composition and solutions of the diffusion equation are then difficult and generally not available; (b) the appropriate boundary conditions for the solution of the diffusion equation are not known; (c) the individual powder particles are not perfect single crystals and the relative roles of volume and grain boundary diffusion mechanisms is unknown.

Nevertheless several authors[1–3] have constructed

---

* The research reported in this paper represents part of the M.Sc. thesis of Bertina Fisher.

[1] F. N. Rhines and R. A. Colton, Trans. Am. Soc. Metals. **30**, 166 (1942).

[2] P. Duwez and C. B. Jordan, Trans. Am. Soc. Metals **41**, 194 (1949).

[3] S. Weinbaum, J. Appl. Phys. **19**, 897 (1948).

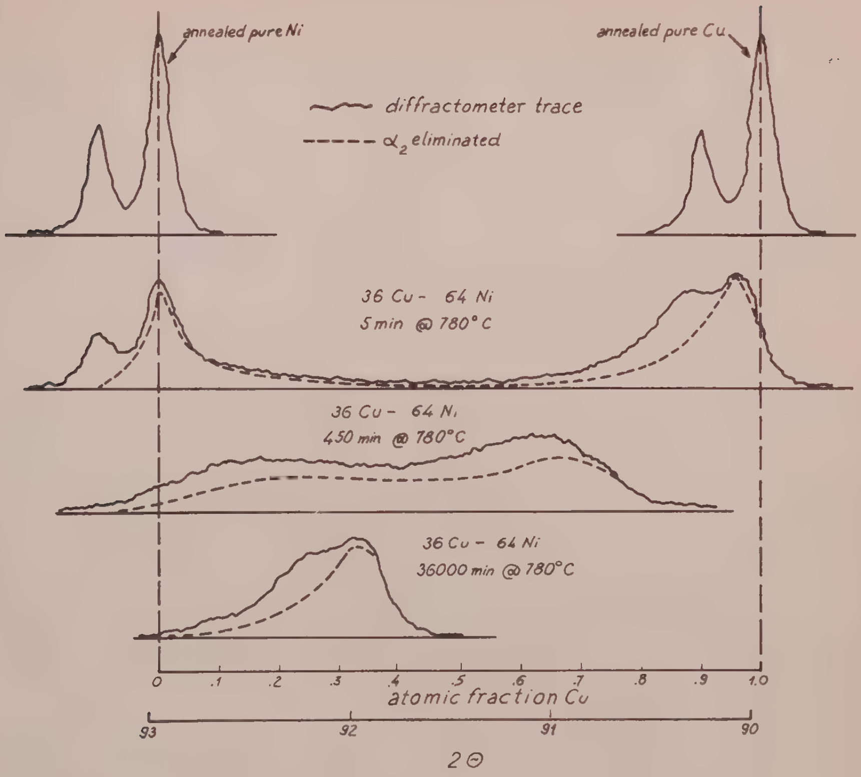

FIG. 1. Diffractometer traces of the CuK_α 311 reflection from interdiffused Cu–Ni powders.

various models and have derived from them some description of the interdiffusion process. All of these investigators chose to test their models by observations of interdiffusion in Cu–Ni powder mixtures. Rhines and Colton,[1] by measuring electrical resistivity, concluded that the time necessary to obtain a given degree of homogeneity is proportional to the square of the interparticle distance, and that the logarithm of this time is proportional to the inverse of the absolute temperature. Duwez and Jordan[2] calculated a measure of the homogenization process using a model due to Weinbaum[3] which assumes that the diffusion coefficient is independent of composition and that the powder mixture is approximated by an alternate packing of cubes. This is a difficult model to generalize to compositions other than the equiatomic. Duwez and Jordan, no doubt realizing this limitation, also considered as a model an alternate layering of infinite sheets of the two components for which the solution was also available. Duwez and Jordan compared their calculations with x-ray diffraction results. The principle of their x-ray diffraction method is that two mutually soluble metals after interdiffusion will present a continuous distribution of lattice parameters and every Bragg reflection will have a shape (intensity vs angle) dependent on the composition distribution. Duwez and Jordan succeeded only in establishing as a measure of diffusion "the most probable composition" and hence their experimental results could only roughly certify their models.

Rudman[4] has described an extension of the Duwez-Jordan x-ray technique which enables the detailed concentration distribution to be determined. The results of the exploitation of this technique in conjunction with metallographic observation to provide a detailed description of the interdiffusion process in Cu–Ni powder mixtures will be presented here.

Sample Preparation

Commercially pure powders (Fisher Scientific Company Catalog No. N-40, nickel, Allied Chemicals and Dye Corporation code 1618, copper) of about 5μ in diameter were used. The unmixed powders were first reduced in a H_2 atmosphere at a low temperature such that insufficient sintering occurred to prevent regaining the powdered state by simply crumbling. After weighing to the desired proportions the powders were thoroughly mixed by tumbling together for about 24 hr. The mixed powders were then cold pressed under 2500 kg/cm^2 into briquettes $2\times1\times0.3$ cm. The interdiffusion anneals were carried out in the range 750°C to 1050°C in a H_2 atmosphere. The furnace was automatically controlled to ±5°C.

---

[4] P. S. Rudman, Acta Cryst. **13**, 905 (1960).

X-Ray Diffraction Results

Figure 1 presents representative changes in the 311-line profile concurrent with interdiffusion. These and all the results utilized here, were recorded with a Philips wide-angle Geiger counter diffractometer. It has been shown[4] that by mathematically eliminating the $K\alpha_2$ component, under the present conditions of high resolution, the remaining $K\alpha_1$ contribution (the dashed curves of Fig. 1) is a reasonable approximation to the pure diffraction profile and is related to the composition distribution by the relation

$$N(c)=Q(\theta)f(\theta), \tag{2}$$

where $N(c)$=number of unit cells of concentration c, $f(\theta)$=pure diffraction line profile,

$$Q^{-1}(\theta)=K(c_Af_A+c_Bf_B)^2LP\mu^{-1},$$

K is constant, f_A, f_B are scattering factors for A and B atoms, respectively, c_A, c_B are concentrations of A and B atoms, respectively, μ is the linear absorption coefficient, and $LP=(1+\cos^2 2\theta)/\sin^2 \cos\theta$.

Interdiffusion is generally described by concentration-penetration curves and it is convenient to present the x-ray results in an analogous manner. We define an effective penetration y:

$$y=\int_0^c N(c)dc \bigg/ \int_0^1 N(c)dc. \tag{3}$$

It has also been shown[4] that this parameter possesses the convenient property that

$$\int_0^1 cdy=\bar{c}.$$

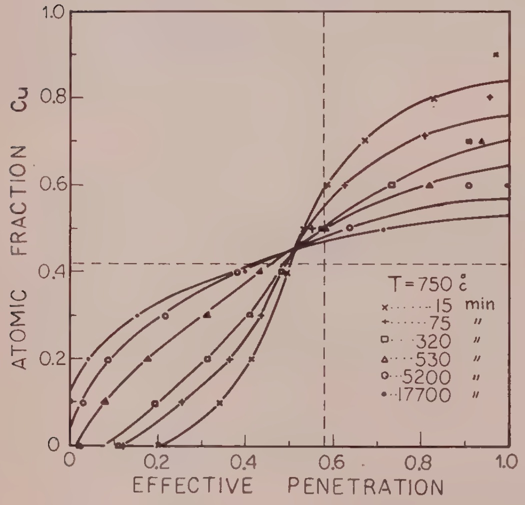

FIG. 2. Concentration-penetration curves for 41%Cu−59%Ni powders interdiffused at 750°C.

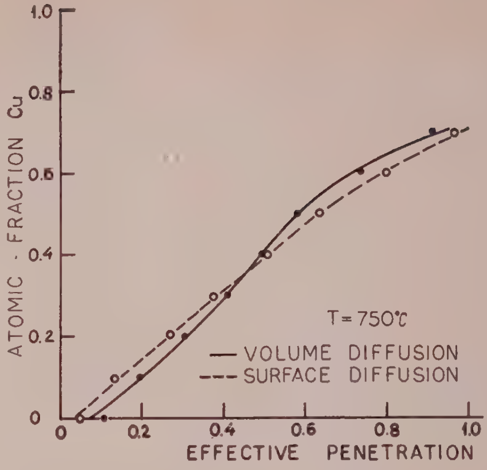

FIG. 3. Concentration-penetration curves for volume and surface diffusion: 41% Cu−59% Ni, T=750°C, t=320 min.

In the present analysis y has been calculated at intervals

$$\Delta y=\int_c^{c+\Delta c}\cdots$$

such that Δc corresponds to a variation of 0.1 atomic fraction Cu. Representative concentration-penetration curves are presented in Fig. 2. The curves have been drawn with a nearly horizontal intercept at $y=1$ although the experimental points indicate a nearly vertical intercept. It is felt, however, that the horizontal intercept is correct and that the tail toward pure Cu is an artifact due to the approximate nature of the determination of the pure diffraction line profile. This effect can be seen from the diffractometer traces of Fig. 1. A perfect instrumental broadening correction would correct the observed line profile of pure Cu to a delta function at 100% Cu while the actual correction leaves apparent intensity to 110% Cu. Thus, in general, the composition limits will always appear wider than reality. The most striking feature of these curves is that Ni quickly contaminates all the Cu such that after 15 min no pure Cu remains, while it is not until after 530 min that all the pure Ni has disappeared.

The curves of Figs. 1 and 2 are representative of interdiffusion in the interior of the specimen. They were obtained by removing the surface layer by mechanical polishing after the diffusion anneal, and then reheating for a few minutes to 500°C to anneal out the thus induced cold work. If this treatment was not performed, a composition distribution representative of surface diffusion processes was obtained. A comparison of the interior and surface distributions is presented in Fig. 3. For all time-temperature combinations of diffusion anneals the surface distribution presented two characteristic features: (a) homogenization proceeds more

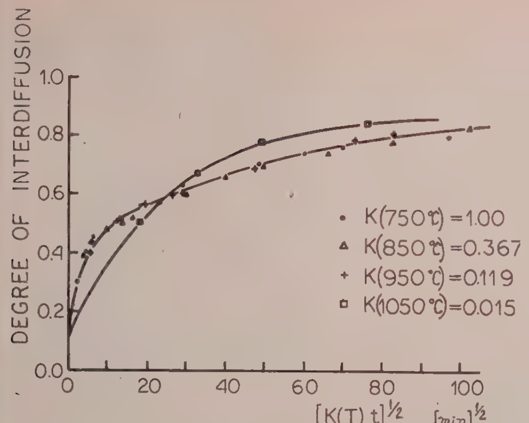

FIG. 4. Degree of interdiffusion: 41% Cu–59% Ni.

rapidly at the surface; (b) the concentration is a linear function of the penetration over most of the region.

The first observation is consistent with the general observation that $D_{\text{surface}}>D_{\text{volume}}$. The linearity is probably also a consequence of this inequality. Since the surface diffusion is so much more rapid than the interior diffusion, the surface distribution can be looked at as a stationary flow between effectively constant composition interior sources.

Comparison of results obtained at different temperatures allows for the determination of D as a function of temperature. It is seen that if the change of variable $z=Dt$ is made in the diffusion equation [Eq. (1)] this equation is transformed to

$$z\frac{\partial c}{\partial z}=\nabla(z\nabla c). \tag{4}$$

Thus, whatever the boundary conditions, a given distribution obtains for $t\alpha\langle D\rangle^{-1}$, where $\langle D\rangle$ is some weighted average of $D(c)$. Hence, the variation of $\langle D\rangle$ with temperature can be obtained from the times necessary to obtain a given distribution at different temperatures. Because of the finite number of concentration-penetration curves at each temperature, it was not possible to find identically shaped curves at different temperatures. The comparison can, however, be made by another method based on the same principle.

Let us define the degree of interdiffusion as m_t/m_∞ such that

$$m_t=\int_{c(y'=0)}^{c0} y'dc, \tag{5}$$

where $y'=0$ defines the Matano interface such that

$$\int_{c(y'=0)}^{c0} y'dc=\int_{c(y'=0)}^{0} y'dc. \tag{6}$$

Physically the degree of diffusion so defined has a very simple meaning. It is the ratio of the net number of atoms that have crossed the Matano interface to a total net number that will have crossed when homogeneity will have been established. According to the foregoing, we can write that m_t/m_∞ is a function of $\langle D\rangle t$. In Fig. 4 is plotted the degree of diffusion as a function of $[K(T)t]^{\frac{1}{2}}$, where $K(T)\propto D(T)$. It is seen that a $K(T)$ can be chosen for each of the three lower temperatures such that a common curve describes the degree of diffusion at each temperature. No $K(T)$ can bring the 1050°C results into coincidence.

By assuming that we can write

$$\langle D\rangle=\langle D_0\rangle \exp[-\langle Q\rangle/RT], \tag{7}$$

the time to obtain a given degree of interdiffusion will vary as

$$\ln t^{\frac{1}{2}}=\text{const}+Q/2RT$$

and in Fig. 5 is plotted $\Delta \ln t^{\frac{1}{2}}=\ln(t_T/t_{750})^{\frac{1}{2}}$ as a function of $1/T$.

As in Fig. 4, the 750°, 850°, and 950°C results are consistent with a common diffusion mechanism and yield an average activation energy:

$$\langle Q\rangle_{750-950°\text{C}}=26 \text{ kcal/mole}.$$

To the extent that it is justifiable in view of its intrinsically different shape to compare the 1050°C degree of interdiffusion curve with the lower temperature ones from the point of view of comparing activation energies, it is seen that $\langle Q\rangle_{950-1050°\text{C}}\simeq 66$ kcal/mole.

It is of interest to compare these numbers with the activation energies for volume diffusion for the Cu–Ni system.[5] The activation energy varies greatly, from 27 kcal/mole for pure Cu to a maximum of 58 kcal/mole for a composition of 0.8 at. fract. Cu. However, since all these values are greater than $\langle Q\rangle_{750-950}$ we conclude that in this temperature range it is not volume diffusion but presumably grain boundary and/or surface diffusion that is the dominant diffusion mechanism. Presumably the reason for the change in shape of the 1050°C degree of interdiffusion curve in Fig. 4 and the apparent tendency to a higher activation energy, $\langle Q\rangle_{950-1050}$,

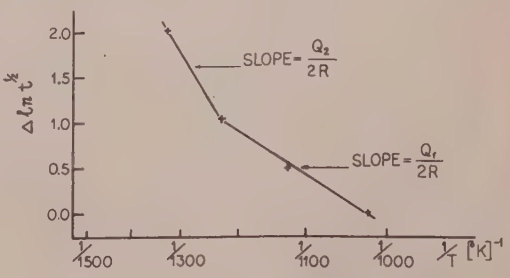

FIG. 5. Plot to obtain activation energies of interdiffusion: 41% Cu–59% Ni.

---

[5] See, C. J. Smithells, *Metals Reference Book* (Interscience Publishers, Inc., New York, 1955), Vol. II.

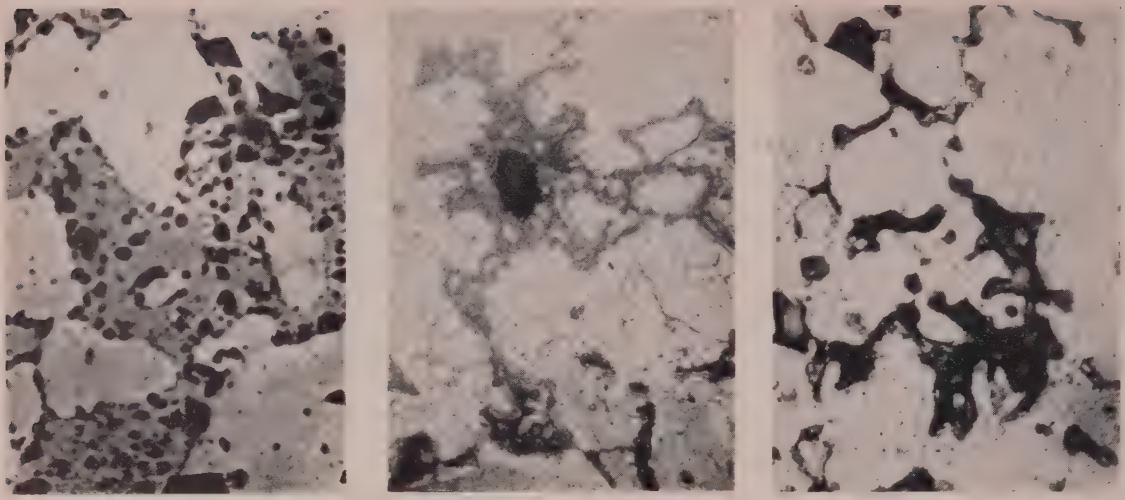
(a) (b) (c)

FIG. 6. Photomicrographs of interdiffused 41% Cu−59% Ni powders; (a) 750°C, $t=10$ min, (b) 750°C, $t=160$ min, (c) 1050°C, $t=10$ min. 533×.

from Fig. 5 is the ascending dominance of volume diffusion as the temperature is raised.

The preceding results provide us with a sufficiently detailed description of the interdiffusion process in these Cu−Ni powder mixtures that we may hope to test the applicability of various models. The model must provide a simplified description of the juxtaposition of particles leading to boundary conditions permitting solution of the diffusion equation. Clearly, the arrangement of the particles can best be observed by direct microscope observation, though none of the previously described models[1–3] are based on microscopic observation.

Metallographic Results and a Model for Interdiffusion

In Fig. 6 are presented typical metallographic results. Fig. 6(a) is representative of a stage prior to appreciable interdiffusion. The individual components, Ni (light) and Cu (dark) are resolved after mechanical polishing only. The apparent voids, primarily in the Cu, are not voids but artifacts of the mechanical polishing. Fig. 6(b) is representative of a stage after appreciable interdiffusion at 750°C. To resolve the components the specimens were electropolished (1:2, nitric acid: methyl alcohol, 20 v, 1.5 amp/cm^2) and after a few seconds the current was interrupted and the copper rich material was etched. This procedure is due to Barnes.[6] Fig. 6(c) is representative of a stage after appreciable interdiffusion at 1050°C.

The following conclusions can be drawn from these photomicrographs:

(a) Prior to any appreciable interdiffusion the nickel particles are enveloped by copper presumably because of the very rapid surface diffusion of Cu.

(b) At 750°C Cu diffuses along grain boundaries in the Ni particles.

(c) At 1050°C no grain boundaries are discernible within the Ni particles. Whether this is because there is no appreciable gain boundary diffusion of Cu to delineate these boundaries or whether the particles have simply eliminated these boundaries by growth is unknown.

Observations (b) and (c) are consistent with the previously given interpretation of the result of Figs. 4 and 5. Observation (a) serves as the basis for a model of interdiffusion in this system. Fig. 7(a) is a schematic simplification of Fig. 6(a), and Fig. 7(b) is the proposed proposed idealized model, a sphere of Ni, of radius given by the measured average Ni particle radius, surrounded by a shell of Cu, the shell thickness being such that the correct ratio Ni:Cu is obtained.

This model has the important advantage that it can be applied to arbitrary composition. An interesting consequence of this model is that it predicts that the rate of interdiffusion should be essentially independent of the Cu particle size, but sensitive to the Ni particle size.

The solution of the diffusion equation according to this model, assuming D independent of composition, requires solving the equation:

$$\frac{\partial c}{\partial t}=D\left(\frac{1}{r}\frac{\partial c}{\partial r}+\frac{\partial^2 c}{\partial r^2}\right) \qquad (7)$$

---

[6] R. S. Barnes, Nature **166**, 1032 (1950).

with boundary conditions

$$\frac{\partial c}{\partial r}=0, \quad \text{at } r=b, \quad \text{all } t.$$

Crank[7] has given the solution to this equation for initial conditions $c(t=0)=f(r)$:

$$c=\frac{3}{b^3}\int_0^b r^2 f(r)dr+\frac{2}{br}\sum_{n=1}^{\infty}\exp[-(Dt)\alpha_n{}^2]\times\frac{\sin\alpha_n r}{\sin^2\alpha_n b}\int_0^b rf(r)\sin\alpha_n r dr, \quad (8)$$

where α_n are positive roots of: $\alpha_n b \cot\alpha_n b=1$,

For comparison of solutions of this equation with the present experimental results, equivolume Cu and Ni fractions were assumed, such that the intitial conditions are

$$f(r)=0 \quad 0<r<a$$
$$f(r)=c_0 \quad a<r<b,$$

where $\frac{4}{3}\pi a^3=\frac{4}{3}\pi(b^3-a^3)$ or $a=b/2^{\frac{1}{3}}$.

In terms of these conditions the solution becomes:

$$\frac{c}{c_0}=\frac{1}{2}+\frac{2b}{r}\sum_{n=1}^{\infty}\exp[-(Dt/b^2)(\alpha_n b)^2]\frac{\sin\alpha_n r}{\sin^2\alpha_n b}\times[(\sin\alpha_n b-\alpha_n b\cos\alpha_n b)/(\alpha_n b)^2-\sin^2\alpha_n b/2^{\frac{1}{3}}+\alpha_n b/2^{\frac{1}{3}}\cos\alpha_n b/2^{\frac{1}{3}}]. \quad (9)$$

In order to compare the results of the respective models, it is convenient to refer all the models to the effective penetration parameter y. Since by definition $N(c)=dN/dc\propto dV/dc$,

$$y=\frac{\int_0^c N(c)dc}{\int_0^1 N(c)dc}=\frac{\int_0^{r(c)} dV}{\int_0^{r(1)} dV}, \quad (10)$$

so that we obtain:

for the laminar model: $c(y)=c(x/a)$
for the concentric spheres model: $c(y)=c[(r/b)^3]$
for the ordered cubes model: $c(y)=\langle c[(x/a)^3]\rangle$,

where $\langle c\rangle$ was taken as the average over positions:

$$x\mathbf{i}+0\mathbf{j}+0\mathbf{k}, \quad x\mathbf{i}+x\mathbf{j}+0\mathbf{k},$$
$$x\mathbf{i}+x\mathbf{j}+x\mathbf{k}.$$

(**i**, **j**, **k** are unit vectors normal to the cube faces.)

In Figs. 8, 9, and 10 are presented the concentration-penetration curves according to these three models.

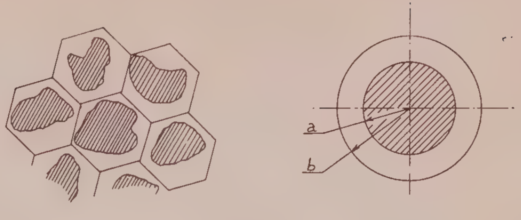

(a) (b)

FIG. 7. Metallographically derived model for interdiffusion in Cu–Ni powder mixtures; (a) schematic simplification of photomicrograph, (b) idealized model.

Comparison of these calculated concentration-penetration curves with the experimental results of Fig. 2 shows that the concentric sphere model is a good approximation to nature. The fact that the experimental curves are representative of only about 40 at. % Cu whereas the calculated curves are representative of 50 at. % Cu should have little effect on the comparison. Although the equiatomic composition was intended for the experimental mixture, apparently the Cu powder absorbed water vapor or underwent some process such that the actual weight of Cu was significantly less than the measured weight.

Although the complexity of the solution appears to obviate the taking of the composition dependence of the diffusion coëfficient into account in any rigorous mathematical way, the validity of the assumption of constant D can be questioned. In the Cu–Ni system, D varies only slightly from 0 to 80 at. % Cu and then rises by an order of magnitude to a maximum at pure Cu. Accordingly, a reasonable approximation seems to be that early in the interdiffusion process the Cu-rich

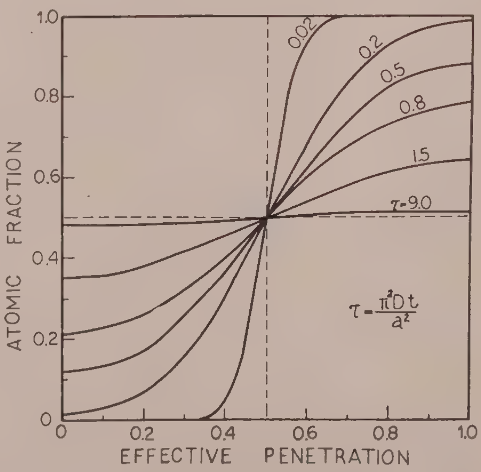

FIG. 8. Concentration-penetration curves for interdiffusion in an equiatomic binary powder mixture according to the laminar model of Duwez and Jordan.

---

[7] J. Crank, *Mathematics of Diffusion* (Oxford University Press, New York, 1956).

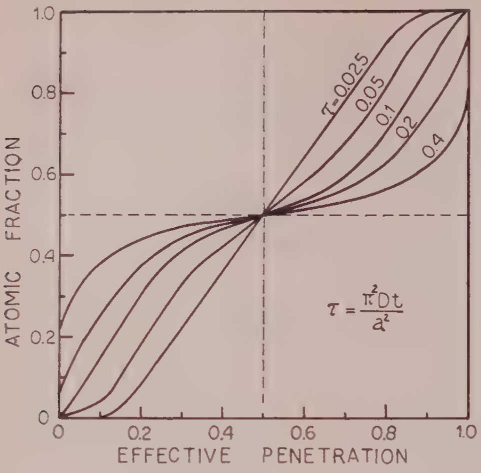

Fig. 9. Concentration-penetration curves for interdiffusion in an equiatomic binary powder mixture according to the ordered cubes model of Weinbaum.

compositions disappear and as far as long diffusion times are concerned, diffusion proceeds with nearly constant D but relative to an effective initial condition of Ni particles enveloped by Cu-rich alloy of approximately 80% Cu. Taking c_0 in Eq. (9) as corresponding to only 80 at. % Cu instead of 100% Cu as used in Fig. 10, we see that the result must simply be Fig. 10 with the ordinate multiplied by 0.8, and we now find excellent agreement between the experimental and the calculated curves. Comparison of Figs. 2 and 10 allows D to be estimated and a value of $\langle D\rangle_{750°\mathrm{C}} \simeq 10^{-11}$ cm²/sec is obtained which is a reasonable value to be expected for grain boundary diffusion at this temperature.

Another basis for intercomparison among the models is on the basis of the degree of interdiffusion curve. In Fig. 11 is presented, for the three models, this variable as a function of an arbitrarily normalized time scale chosen such that the curves intersect at a degree of interdiffusion of about 0.9. As might be expected, when comparison is based on this property which is an integral over the concentration-penetration curve, the differences are much less pronounced. The utility of such a curve is that if the degree of diffusion after a given time is known, the curve can be used to estimate the time to obtain some other degree of diffusion. Or, if the degree of interdiffusion at a given time is known, and the activation energy for diffusion is known, and it is known that the diffusion mechanism does not change with temperature, then the plot may be used to estimate the time to obtain some arbitrary degree of diffusion at another temperature.

A comparison of Fig. 4 with Fig. 11 shows that the agreement between the experimental results and between the calculated result due to the concentric sphere model is poor, the experimental curve rising much more rapidly at short times. This is no doubt due to the rapid transient interdiffusion process that occurs at short times due to the large diffusion coefficient for compositions of greater than 80 at. % Cu, and for this same reason the apparent better agreement with the calculation based on the ordered cubes model is fortuitous.

In principle, for a system where the concentric sphere model is applicable, and D is reasonably constant and known, the degree of interdiffusion can be obtained from such a plot as in Fig. 11 if the inner sphere particle diameter is measured. This cannot be said for the other models since in these cases the laminar thickness or the cube edge is not an experimentally determinable variable, but rather an adjustable parameter.

SUMMARY OF RESULTS

The interdiffusion in a compacted mixture of Cu and Ni powders in the temperature range 750° to 1050°C has been observed by a high-resolution x-ray diffractometer technique of line-shape analysis.[4] The x-ray analysis yields the composition distribution $N(c)$, where $N(c)$ is the number of unit cells of composition c. An effective penetration y has been defined such that

$$y = \int_0^c N(c)dc \Big/ \int_0^1 N(c)dc,$$

and curves of $c(y)$ as a function of y, which are analogous to the usual concentration-penetration plots in diffusion couple studies, were obtained. The degree of interdiffusion has been defined as the ratio of the net number of atoms that have crossed the Matano interface to the net number that will have crossed when complete homogenization will have been obtained. The degree

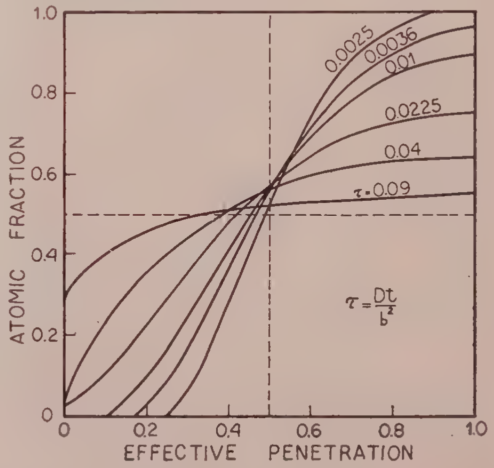

Fig. 10. Concentration-penetration curves for interdiffusion in an equiatomic binary powder mixture according to the concentric sphere model.

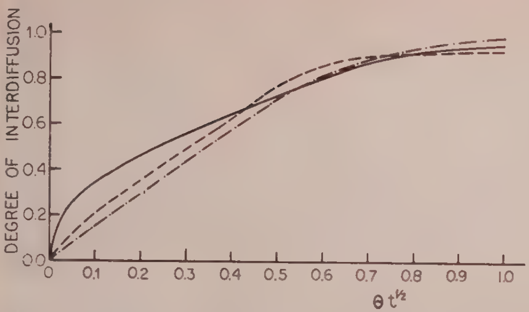

FIG. 11. Degree of interdiffusion according to the different models: ordered cubes model (———), $\theta_1=(\pi^2D/a^2)^{\frac{1}{2}}$; laminar model (—·—·—), $\theta_2=2.5\ (\pi^2D/a^2)^{\frac{1}{2}}$; concentric spheres model (— — —) $\theta_3=2.5(D/b^2)^{\frac{1}{2}}$.

of interdiffusion as a function of time was obtained for diffusion anneals at 750°, 850°, 950°, and 1050°C. From these results it is concluded that in the temperature range 750–950°C there is a common dominant diffusion mechanism. From the value for the average activation energy of about 26 kcal/mole obtained for this range it is concluded that grain boundary diffusion is probably the controlling mechanism because the activation energies for bulk diffusion in the Cu—Ni system vary from 27 to 58 kcal/mole. A significantly different shape for the degree of interdiffusion vs time plot for the 1050°C anneal, and an apparently greater activation energy for this temperature led to the conclusion that at 1050°C a new diffusion mechanism is dominant and it was presumed that it is that of bulk diffusion. These conclusions were substantiated by photomicrographs which show Cu delineated grain boundaries in the Ni particles at 750°C but with no grain boundaries revealed at 1050°C.

Metallographic evidence has been presented showing that, very early in the diffusion anneal the Cu, presumably by surface diffusion, envelops the Ni particles and hence the subsequent interdiffusion is between a Ni-rich core and a Cu-rich shell. This configuration has been idealized to a spherical core-shell model permitting the rigorous solution of the diffusion equation to be given for the case of a composition independent diffusion coefficient. The results of the calculation according to this so-called concentric sphere model, and the result according to a calculation due to Duwez and Jordan[2] for a laminar model, and the result according to a calculation due to Weinbaum[3] for an ordered-cubes model, have been compared with the x-ray derived concentration-penetration curves with essential agreement being obtained for the concentric spheres model. The fact that *D* is not independent of composition in the Cu-Ni system, but rises precipitously at high Cu contents, was qualitatively accounted for as a transient homogenization of the Cu-rich shell to give an effective initial condition for diffusion of a pure Ni core surrounded by a Cu-rich alloy shell.

Although the homogenization transient in the Cu-rich shell does not greatly distort the form of the concentration-penetration curve, it drastically affects the degree of interdiffusion-time plot resulting in a too rapid rise for short annealing times. This fact obviates the hope of being able to utilize a calculation assuming *D* constant to calculate to any precision the degree of interdiffusion in the Cu—Ni system.

It is not known whether the phenomenon of envelopment of the particles of one component by the second component occurs in other interdiffusing powder mixtures. However, in systems where it is found to occur and hence where the concentric sphere model is applicable, this model has several important computational advantages over the other models (exclusive of being more accurate): (a) it is easily extended to arbitrary composition whereas the ordered cubes model is applicable only for the equiatomic composition; (b) it contains no experimentally nonobservable parameters while in both the laminar and in the ordered cubes models the plate and cube dimensions are in fact arbitrary parameters.

A prediction of the concentric spheres model is that the homogenization should be essentially independent of the particle size of the enveloping component (Cu in the present case). Unfortunately it was not possible to check this interesting prediction.

JOURNAL OF APPLIED PHYSICS VOLUME 32, NUMBER 8 AUGUST, 1961

Electron Trajectories in a Nonuniform Axially Symmetric Magnetic Field*

D. A. DUNN AND R. E. HOLADAY†
Stanford Electronics Laboratories, Stanford University, Stanford, California

(Received December 13, 1960)

Electrons injected along the flux lines of a spatially varying, axially symmetric magnetic field that is increasing in the direction of electron motion will follow approximately helical trajectories about the flux lines. If the field increases too rapidly, the electrons will not be able to penetrate the magnetic field beyond a certain point and will be turned back by the magnetic mirror formed by the increasing field. For more slowly varying fields, the electrons can penetrate the mirror with a large fraction of their energy in axial velocity. The equations of motion for electrons in a sinusoidally varying magnetic field have been solved on a computer, and the results are presented in graphical form. An application of this field configuration as a device for converging a hollow cylindrical electron beam has been tested, and measured area convergences of 15 to 1 have been obtained by photographing a movable carbon screen collector that is heated by the beam. The beam is started out with a conventional parallel flow gun immersed in the magnetic field. As the beam leaves the first accelerating electrode it enters the region of increasing magnetic field. It then shrinks in diameter and thickness, and hence in area, approximately in proportion to the increase in the magnetic field. The actual area convergence will be less than this increase by an amount depending on the length and rate of the magnetic field taper.

I. INTRODUCTION

THE idea of increasing the current density in an electron beam by passing it through a region of increasing magnetic field and zero electric field has been suggested by Heil,[1] by Pierce,[2] and by Gittins *et al.*[3] Heil has performed an experiment converging a solid beam in an increasing magnetic field. Gittins *et al.* were also concerned with solid beams. Pierce suggests the use of this technique for converging a hollow beam. The magnetic mirror technique, widely used[4,5] in thermonuclear research to contain a plasma, involves many of the same considerations as the beam converging technique discussed here. Recent studies[6–10] of transverse-field, cyclotron-wave amplifiers can also involve a geometry similar to that studied here. All of these devices require a knowledge of electron trajectories in a spatially varying magnetic field for their design.

The theory of electron trajectories in a static, axially symmetric magnetic field in the absence of space charge can be carried out exactly, if the field variation in space is specified. In this paper the theory is worked out for trajectories in a sinusoidally varying unidirectional field; the equations are solved on a computer. The application of the results of this theory to an electron-beam converging device is worked out, and the results of experiments on a convergent hollow-beam electron gun are presented. The zero space-charge theory is shown to give an adequate picture of the performance of the beam up to quite high space-charge conditions.

The qualitative picture of a hollow-beam converging device of this type is one of a beam starting in the axial direction in a weak axial uniform magnetic field and then shrinking in thickness and diameter as the field increases, as shown in Fig. 1. Individual electrons oscillate about the flux lines in the absence of space charge. The effect of space charge is to add a radial electric field that increases as radius increases; this space-charge field may be expected to cause a net rotation and shearing of the outer electrons with respect to the inner electrons about the main axis of the beam. The instabilities of this type of space-charge flow have been treated by Kyhl and Webster.[11]

The basic limitations on this type of beam converging device, apart from space charge, can be expressed as limitations on the beam entrance velocity for a given field shape. The velocity must be greater than some minimum value in order to penetrate the increasing field. For very long gradual tapers this mirroring velocity is low. For entrance velocities higher than the mirroring value, the radial perturbation increases with increasing velocity and, for a beam of prescribed thickness at the exit of the converging region, a maximum entrance velocity for the prescribed perturbation is determined. These limitations are readily seen from the graphical computer results for single electron trajectories in an increasing field, and from the photographs of beam density vs radius that are presented.

II. ELECTRON TRAJECTORIES IN AN ARBITRARY, AXIALLY SYMMETRIC MAGNETIC FIELD

Although it is difficult to solve for electron trajectories in an arbitrary, axially symmetric magnetic field, it is possible to define a potential function that is of con-

---

* This work was carried out under a U. S. Air Force contract.

† Present address: Litton Industries, San Carlos, California.

[1] O. Heil (unpublished).

[2] J. R. Pierce, *Theory and Design of Electron Beams* (D. Van Nostrand Company, Inc., New York, 1954), 2nd ed., p. 164.

[3] J. F. Gittins, P. G. R. King, and C. P. Lea-Wilson, Services Electronics Research Labs. Tech. J. **5**, 119–126 (1955).

[4] R. F. Post, Revs. Modern Phys. **28**, 338–362 (1956).

[5] L. Spitzer, Jr., *Physics of Fully Ionized Gases* (Interscience Publishers, Inc., New York, 1956).

[6] R. Adler, G. Hrbek, and G. Wade, Proc. I. R. E. **47**, 1713–1723 (1959).

[7] A. E. Siegman, J. Appl. Phys. **31**, 17–26 (1960).

[8] E. I. Gordon, Proc. I. R. E. **48**, 1158 (1960).

[9] E. I. Gordon, J. Appl. Phys. **31**, 1187–1190 (1960).

[10] A. E. Siegman, Proc. I. R. E. **48**, 1750–1755 (1960).

[11] R. L. Kyhl and H. F. Webster, IRE Trans. on Electron Devices **ED-3**, 172–183 (1956).

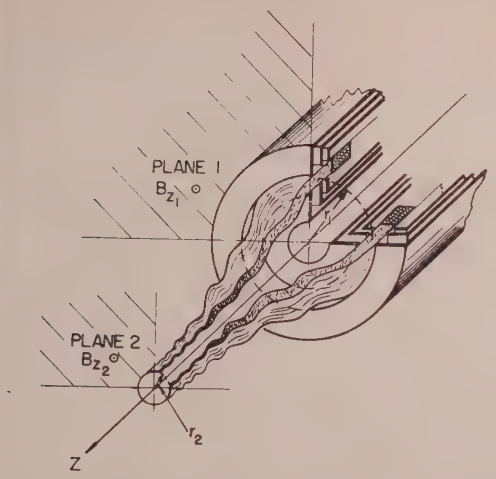

FIG. 1. Hollow cylindrical electron beam emerging from a parallel-flow immersed gun at radius r_1 at plane 1. The magnetic field in the gun is B_{z1} and the magnetic field increases to a value B_{z2} at plane 2. The beam approximately follows the flux lines emerging at radius r_2 at plane 2.

siderable help in understanding the types of trajectories to be expected.[12,13]

If the magnetic field is axially symmetric and the electric field is zero, the equations of motion and the field itself can be written in terms of a single component of the magnetic vector potential A_θ.[14]

$$\ddot{r}+\dot{\theta}[\eta A_\theta+\eta r(\partial A_\theta/\partial r)-r\dot{\theta}]=0, \tag{1}$$

$$(d/dt)(r^2\dot{\theta}-\eta r A_\theta)=0, \tag{2}$$

$$\ddot{z}+\eta\dot{\theta}r(\partial A_\theta/\partial z)=0, \tag{3}$$

where $\eta=(e/m)$. Equation (2) can be integrated to give

$$p_\theta=r^2\dot{\theta}-\eta r A_\theta, \tag{4}$$

where p_θ is a constant that can be evaluated, if the initial conditions are specified. mp_θ may be considered to be an extended definition of angular momentum which remains constant in the presence of axially symmetric magnetic fields.[15] A potential U can be defined in terms of p_θ as follows:

$$U=\frac{1}{2\eta r^2}(p_\theta+\eta r A_\theta)^2=\frac{r^2\dot{\theta}^2}{2\eta}. \tag{5}$$

It is convenient to use this definition of potential and to use Eqs. (4) and (5) to substitute for $\dot{\theta}$ in Eqs. (1) and (3). The following form, essentially as obtained by Glaser,[13] is the result:

$$\ddot{r}+\eta(\partial U/\partial r)=0, \tag{6}$$

$$\ddot{z}+\eta(\partial U/\partial z)=0. \tag{7}$$

Following Glaser, it is convenient to note that the total energy may be obtained by multiplying Eq. (6) by $\dot{r}$ and Eq. (7) by $\dot{z}$, adding, and integrating to get

$$\tfrac{1}{2}(\dot{r}^2+\dot{z}^2)+\eta U=\eta H_0, \tag{8}$$

where H_0 is a constant which may be shown to be equal to the total energy and U is a potential corresponding to the $\dot{\theta}$ energy. For example, if $U=H_0$ it is seen from Eq. (8) that the sum of the axial and radial velocity energies is zero and all the energy is in spinning motion. This is the mirroring condition.

Another case of interest is that of trajectories not far from a magnetic flux line. If a flux line is defined by the radius r_e and the vector potential at r_e is defined as $A_{\theta e}$, then

$$r_e A_{\theta e}=r_e(0)A_{\theta e}(0)=\text{const}, \tag{9}$$

where $r_e(0)$ and $A_{\theta e}(0)$ are the values of these quantities at $z=0$. If a trajectory starts on a flux line with $r(0)=r_e(0)$ and $A_\theta(0)=A_{\theta e}(0)$, and if $\dot{\theta}(0)=0$, Eq. (5) can be written in terms of r_e as follows:

$$U=(\eta/2)A_{\theta e}^2(0)r_e^2(0)(r)^{-2}[(A_\theta r/A_{\theta e}r_e)-1]^2. \tag{10}$$

Now if A_θ near the flux line can be taken as varying linearly with r, corresponding to an axial magnetic field that is independent of r near the flux line,

$$A_\theta\cong A_{\theta e}(r/r_e), \tag{11}$$

and Eq. (10) can be written in the form

$$U\cong(\eta/2)A_{\theta e}^2(0)[r_e^2(0)/r_e^2][(r/r_e)-(r_e/r)]^2. \tag{12}$$

Near the flux line it is convenient to write

$$r/r_e=1+\delta. \tag{13}$$

It is convenient to define the axial cyclotron frequency ω_{cz} in terms of the axial magnetic field B_z and the quantities defined above. Then, along a flux line,

$$\begin{aligned}\omega_{cz}&=\eta B_z=\eta(r)^{-1}(\partial/\partial r)(rA_\theta)\\&=\eta(r)^{-1}(\partial/\partial r)[(r^2/r_e)A_{\theta e}]\\&=2\eta(A_{\theta e}/r_e)=2\eta[A_{\theta e}(0)r_e(0)/r_e^2],\end{aligned} \tag{14}$$

and U in terms of ω_{cz} and δ is

$$U\cong(\omega_{cz}^2 r_e^2/2\eta)\delta^2. \tag{15}$$

If the field changes only slowly with z such that $(\partial U/\partial z)\ll(\partial U/\partial r)$, $\ddot{z}\cong 0$, and the only equation of motion is Eq. (6), which can be written

$$\begin{gathered}(\ddot{r}/r_e)+(\eta/r_e^2)(\partial U/\partial\delta)=0,\\ \delta+\omega_{cz}^2\delta=0,\end{gathered} \tag{16}$$

which indicates simple harmonic motion in radius at the "local" cyclotron frequency, as long as the field is

---

[12] C. C. Wang, Proc. I. R. E. **38**, 135–147 (1950).

[13] W. Glaser, *Grundlagen der Electronenoptik* (Springer-Verlag, Berlin, 1952).

[14] K. R. Spangenberg, *Vacuum Tubes* (McGraw-Hill Book Company, Inc., New York, 1948).

[15] W. W. Harman, *Fundamentals of Electronic Motion* (McGraw-Hill Book Company, Inc., New York, 1953).

TABLE I.

Figure No.	R	βr_0	N_0	γ_0
3	10	0.1	3.33	0
4	10	0.1	2.00	0
5	10	0.1	1.00	0
6	10	0.3	3.33	0
7	10	0.3	2.00	0
8	10	0.3	1.00	0
9	10	0.6	0.952	0
10	30	0.1	2.00	0
11	30	0.1	1.00	0
12	30	0.1	0.500	0
13	30	0.3	0.500	0
14	30	0.3	0.333	0
15	10	0.5	2.00	0
16	10	0.5	2.00	+0.1
17	10	0.5	2.00	−0.1

not changed too rapidly. To this approximation there is no z acceleration, and consequently there is no change in the z velocity.

To obtain more details of the electron motion, it is convenient to choose a specific field-vs-distance variation and compute the trajectories. This process is carried out in the next section for a sinusoidal field variation.

III. ELECTRON TRAJECTORIES IN A SINUSOIDALLY VARYING, UNIDIRECTIONAL AXIALLY SYMMETRIC MAGNETIC FIELD

The equations of motion can be solved exactly for specific field variations such as a sinusoidal variation in the z direction. The proper form of A_θ to go with an axial field that is a constant plus a cosine function of z, and hence is the sum of two fields that separately satisfy Laplace's equation, is

$$A_\theta \cong (A_1\beta r/2) - A_2 I_1(\beta r)\cos\beta z. \tag{17}$$

For small βr, as is the case in many practical geometries, only the first term of a series expansion of $I_1(\beta r)$ need be retained. This linear approximation is accurate to within 10% for $\beta r < 1$. Then, to this approximation

$$A_\theta \cong (\beta r/2)(A_1 - A_2\cos\beta z). \tag{18}$$

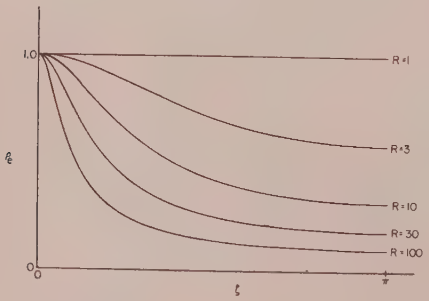

FIG. 2. Sinusoidally varying axial magnetic field of the form $[B_z/B_z(0)] = \{[(R+1)/2] - [(R-1)/2]\cos\zeta\}$ has flux lines of radius $\rho_e = (r_e/r_0)$ that vary as a function of ζ in the manner shown.

Going with this A_θ are the following fields:

$$B_\theta = 0, \tag{19}$$

$$B_z = (r)^{-1}(\partial/\partial r)(rA_\theta) = \beta(A_1 - A_2\cos\beta z), \tag{20}$$

$$B_r = -(\partial A_\theta/\partial z) = (\beta^2 r A_z/2)\sin\beta z, \tag{21}$$

In the following, trajectories are found for particles traveling in the field represented by Eqs. (18)–(21). It is convenient to normalize the equations of motion (1)–(3) in terms of the following parameters:

$$\rho = r/r_0, \tag{22}$$

$$\zeta = \beta z, \tag{23}$$

$$\tau = \omega_0 t, \tag{24}$$

$$r_0 = \text{value of radius for } t = z = 0, \tag{25}$$

$$\omega_0 = \eta B_z(0)/2 = (\eta\beta/2)(A_1 - A_2), \tag{26}$$

$$B_z(0) = \text{value of field for } z = 0, \tag{27}$$

$$R = \frac{B_z(\pi)}{B_z(0)} = \frac{A_1 + A_2}{A_1 - A_2} = \frac{\text{maximum field}}{\text{minimum field}}, \tag{28}$$
$$= \text{“condensation ratio.”}$$

In terms of these parameters, the equations of motion (1)–(3) can be rewritten as follows for the field described by Eqs. (18)–(21):

$$\frac{d^2\rho}{d\tau^2} = \frac{1}{\rho^3} - \rho\left(\frac{R+1}{2} - \frac{R-1}{2}\cos\zeta\right)^2, \tag{29}$$

$$\frac{d^2\zeta}{d\tau^2} = \frac{(\beta r_0)^2}{2}(R-1) \times \sin\zeta\left[1 - \rho^2\left(\frac{R+1}{2} - \frac{R-1}{2}\cos\zeta\right)\right], \tag{30}$$

$$\frac{d\theta}{d\tau} = -\frac{1}{\rho^2} + \frac{R+1}{2} - \frac{R-1}{2}\cos\zeta. \tag{31}$$

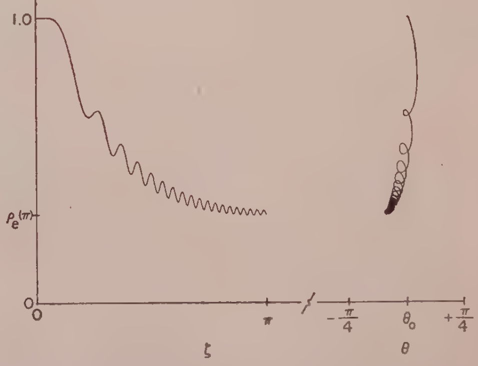

FIG. 3. Electron trajectory shown in the $\rho-\zeta$ plane and the $\rho-\theta$ plane for $R=10$, $\beta r_0 = 0.1$, $\gamma_0 = 0$, and $N_0 = 3.33$.

These equations can be solved for various values of entrance velocity. It is convenient to express the axial entrance velocity u_0 in terms of the quantity N_0, defined as follows:

$$N_0=\omega_0 d/\pi u_0, \tag{32}$$

where d is the value of z for which $\zeta=\pi$. The number of cyclotron wavelengths N in the distance d is

$$N=\frac{1}{2\pi}\int_0^d \frac{\eta B_z(z)}{u(z)}dz, \tag{33}$$

where $u(z)$ is the axial velocity. If the beam retains most of its axial velocity, $u(z)\cong u_0$, and

$$N\cong\frac{1}{2\pi}\int_0^\pi \frac{\eta B_z(\zeta)d}{\pi u_0}d\zeta \qquad (34)$$

$$\cong\frac{d}{2\pi^2}\int_0^\pi \frac{2\omega_0}{u_0}\left(\frac{R+1}{2}-\frac{R-1}{2}\cos\zeta\right)d\zeta \qquad (34)$$

$$\cong\frac{\omega_0 d}{\pi u_0}\left(\frac{R+1}{2}\right)\cong N_0\left(\frac{R+1}{2}\right).$$

For a constant field, $R=1$, and N is exactly N_0:

$$N=N_0=\omega_0 d/\pi u_0, \tag{35}$$

N_0 is the number of cyclotron wavelengths in the distance d measured at the entrance value of magnetic field and of axial velocity. If we multiply N_0 by $(R+1)/2$, we get the number of cyclotron wavelengths in the distance d that corresponds to a beam traveling at the velocity u_0 at all values of z.

The radial entrance velocity can conveniently be specified by the parameter γ_0, defined as follows in terms of the radial entrance velocity u_{0r}:

$$\begin{aligned}&\gamma_0=d\rho/d\tau \quad \text{at} \quad t=z=0,\\ &\gamma_0=u_{0r}/\omega_0 r_0=[(u_{0r}/u_0)/\beta r_0 N_0].\end{aligned} \tag{36}$$

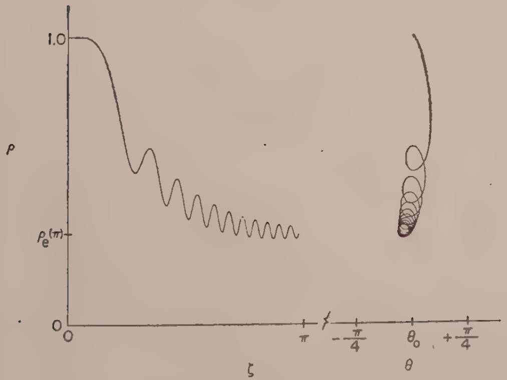

FIG. 4. Electron trajectory. Parameters as in Fig. 3 except $N_0=2$, corresponding to a higher entrance velocity.

From Eqs. (29)–(31), particle trajectories in the form $\rho(\zeta)$ and $\rho(\theta)$ can be computed for various values of R, βr_0, N_0, and γ_0. A tabulation of the cases presented is given in Table I by figure number. Figure 2 is a plot of the flux lines passing through $\rho(0)=1$ as a function of R for the sinusoidal field variation used here. It will be noted that the flux lines themselves do not have a sinusoidal shape. Figures 3–17 show particle trajectories

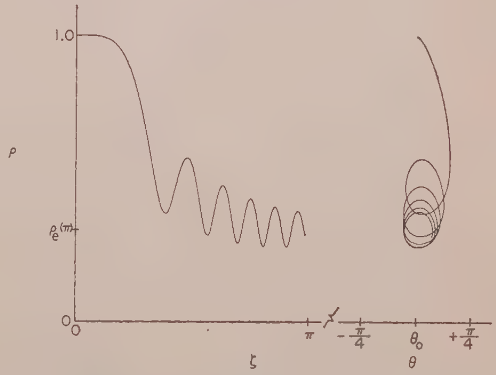

FIG. 5. Electron trajectory. Parameters as in Fig. 3 except $N_0=1$.

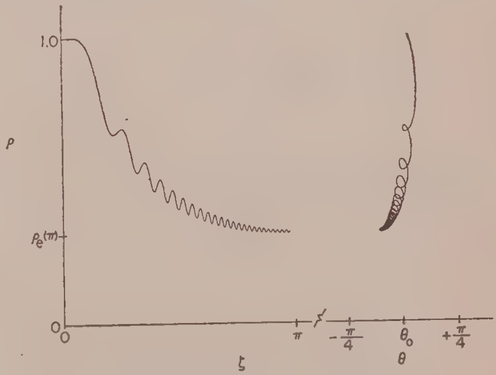

FIG. 6. Electron trajectory for $R=10$, $\beta r_0=0.3$, $\gamma_0=0$, and $N_0=3.33$.

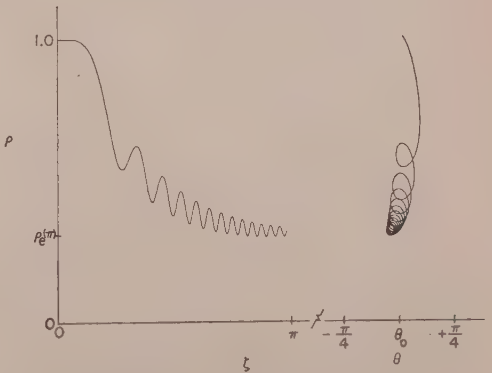

FIG. 7. Electron trajectory. Parameters as in Fig. 6 except $N_0=2$.

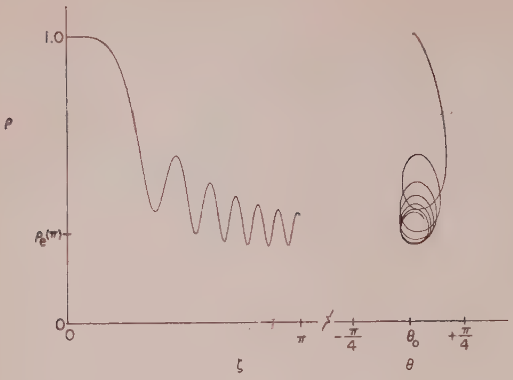

FIG. 8. Electron trajectory. Parameters as in Fig. 6 except $N_0=1$.

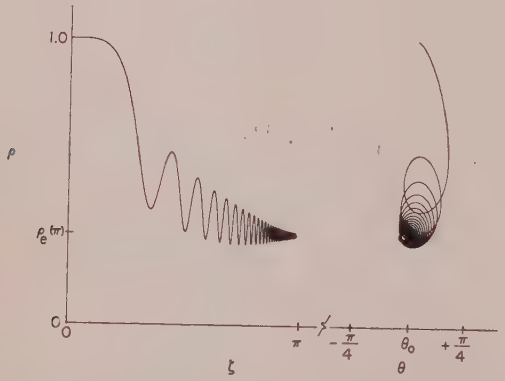

FIG. 9. Electron trajectory for $R=10$, $\beta r_0=0.6$, $\gamma=0$, and $N_0=0.952$. Mirroring just occurs for this value of N_0. Higher entrance velocity electrons pass through.

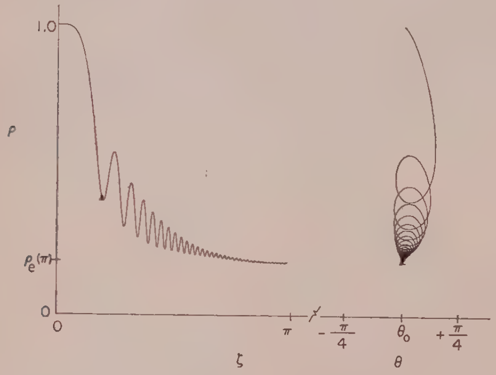

FIG. 10. Electron trajectory for $R=30$, $\beta r_0=0.1$, $\gamma_0=0$, and $N_0=2$.

in the ρ-z and ρ-θ planes. In addition to these trajectories, the value of N_0 for mirroring N_{0m} was computed for each set of the other parameters. The mirroring condition for particles injected along a flux line with $\gamma_0=0$ was found to be one of a minimum velocity or a maximum number of cyclotron wavelengths N_{0m}. For lower velocities, the electron would not penetrate the field but would, at some point, convert all its axial velocity into rotational velocity and then return to the region of weaker field. The computer setup used to find these trajectories was not very accurate in its determination of N_{0m}, but the form of the variation and the approximate numerical value is thought to be correct.

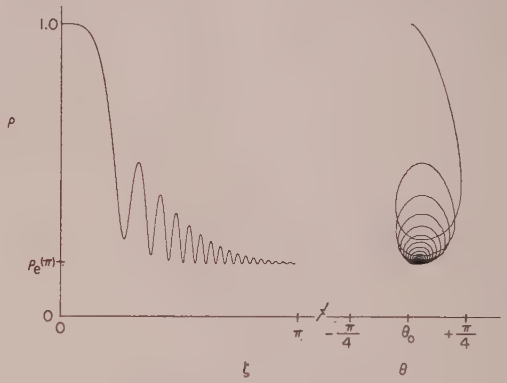

FIG. 11. Electron trajectory. Parameters as in Fig. 10 except $N_0=1$.

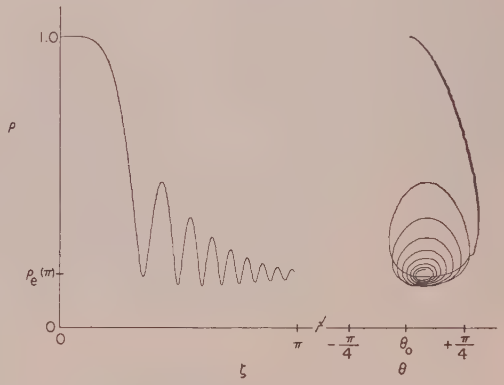

FIG. 12. Electron trajectory. Parameters as in Fig. 10 except $N_0=0.5$.

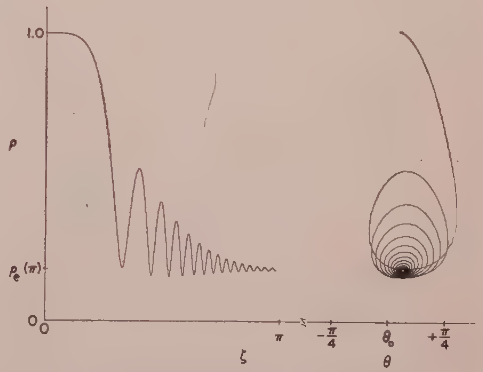

FIG. 13. Electron trajectory for $R=30$, $\beta r_0=0.3$, $\gamma_0=0$, and $N_0=0.5$.

These results are summarized graphically in Fig. 18, a plot of the mirroring value of N_0, N_{0m}, as a function of βr_0 for $R=10$ and $R=30$.

The final radial perturbation at $\zeta=\pi$ can be measured from Figs. 3 through 14; the result is plotted in Figs. 19 and 20 as a function of N_0 for various values of βr_0 and R. What is plotted is the radial perturbation in the outward direction $+\delta(\pi)$ and the inward perturbation $-\delta(\pi)$ divided by the final normalized radius of the flux line $\rho_e(\pi)$. It is seen that a given final beam perturbation can be obtained at progressively higher values of N_0 (lower values of injection velocity) as βr_0 is decreased. For a given condensation ratio R, βr_0 specifies the shape of the taper and small βr_0 corresponds to a long, gradual taper.

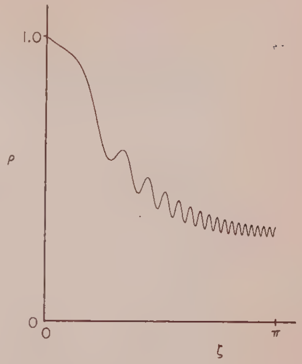

FIG. 17. Electron trajectory. Parameters as in Fig. 15 except $\gamma_0=-0.1$. For an electron injected with a significant inward radial velocity, mirroring does not occur. The optimum injection direction for minimum ripple and spinning energy is not the direction of the flux lines at the entrance plane.

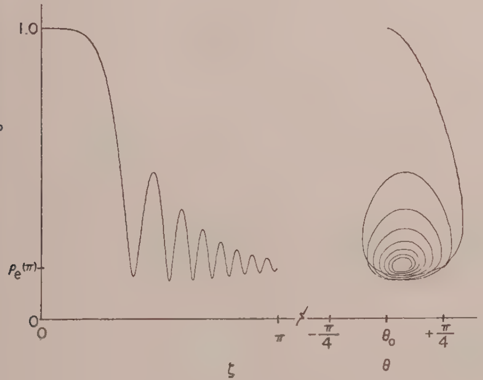

FIG. 14. Electron trajectory. Parameters as in Fig. 13 except $N_0=0.333$.

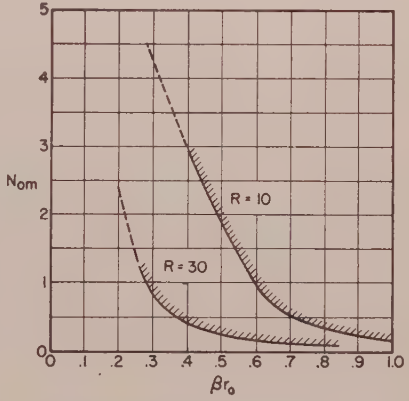

FIG. 18. Plot of the mirroring value of N_0, N_{0m}, as a function of βr_0 for two values of R with $\gamma_0=0$. For values of N_0 less than N_{0m}, mirroring does not occur.

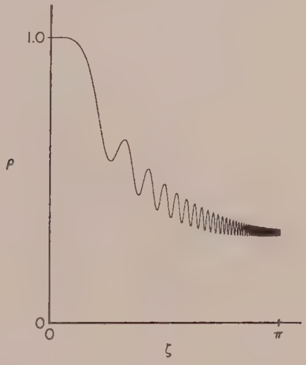

FIG. 15. Electron trajectory for $R=10$, $\beta r_0=0.5$, $N_0=2$, and $\gamma_0=0$. Mirroring just occurs.

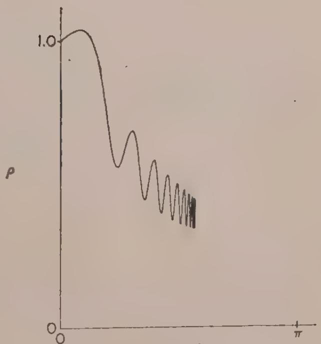

FIG. 16. Electron trajectory. Parameters as in Fig. 15 except $\gamma_0=+0.1$. For an electron injected with a significant outward radial velocity, mirroring occurs much closer to the injection position.

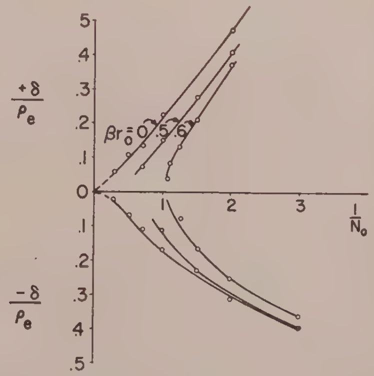

FIG. 19. Plot of the radial perturbation (δ/ρ_e) at the exit plane as a function of $(1/N_0)$ for three values of βr_0 and for $R=10$.

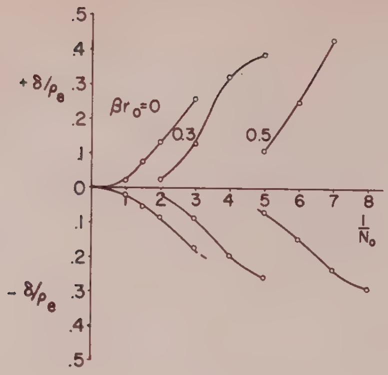

FIG. 20. Plot of the radial perturbation (δ/ρ_e) at the exit plane as a function of ($1/N_0$) for three values of βr_0 and for $R=30$.

IV. DESIGN CRITERIA FOR A HIGH AREA-CONVERGENCE, HOLLOW-BEAM ELECTRON GUN

A specific application of the calculations above is in connection with a hollow-beam electron gun. A hollow beam can be generated by a parallel-flow gun immersed in a uniform or nearly uniform magnetic field and then passed through a region of increasing axially symmetric field to condense the beam into a smaller-diameter, thinner hollow beam. In principle, very high area convergences are possible by this technique in a reliable and predictable device. No small, accurately machined gun electrodes are required; in fact the beam can be much smaller than the gun. It also appears that the shape of the field is not very critical, provided the flux lines that are to be followed by the beam pass through the final hole through which the beam is to pass. The principal objectionable feature of this type of gun shows up when space charge is included in the design. A certain amount of magnetic field is required to confine the beam in the presence of space charge. It turns out that if this amount of field is used in the weak magnetic field portion of the condenser region, more field than necessary will be present at the high-field end of the condenser. Or, if the field is adjusted to the right value in the high-field region, it will be too weak to overcome space charge in the weak-field region. Consequently, the application of this condensing technique is most appropriate in two situations: (1) when a very small hollow beam is desired, as in very high-frequency microwave tubes, where the principal reason for using the technique is to avoid building a very small gun, and area convergence is not the sole consideration; (2) for high area convergence when the beam to be used is of sufficiently high power that the size and weight of the magnet plus power supplies is much smaller than the beam power supply. In either case a somewhat larger than normal magnet would not be a serious disadvantage.

This excess magnetic field requirement can be understood most simply if idealized performance of the condenser is assumed; i.e., if the electrons follow the flux lines exactly. In this case the area convergence is simply the condensation ratio R. If the planes 1 and 2 are defined as entrance and exit planes of the condenser, respectively, then the current density J_1 is the density at plane 1, J_2 is the density at plane 2, and B_1 and B_2 are the magnetic fields at these planes. Then, if the electrons follow the flux lines,

$$J_2/J_1=B_2/B_1=R. \tag{37}$$

Now the Brillouin field at plane 1 B_{01} for planar geometry is given by Pierce[16] as

$$B_{01}=1.04\times10^{-3}(J_1/V_1^{\frac{1}{2}})^{\frac{1}{2}}, \tag{38}$$

where V_1 is the voltage corresponding to the velocity at plane 1. It is appropriate to use this planar symmetry value of field to estimate the effect of space charge in a hollow beam, if the ratio of thickness to diameter is small. The value of the perturbation due to space charge in planar symmetry has been shown by Dunn and Luebke[17] to be inversely proportional to the square of the field, as follows:

$$\delta_1/y_1=2(B_{01}/B_1)^2, \tag{39}$$

where y_1 is the beam half-thickness and δ_1 is the maximum beam perturbation. The beam has a thickness of δ_1+y_1 at its thickest point.

Then it is evident that, if (B_1/B_{01}) is chosen to give an appropriate value of (δ_1/y_1), the value of (B_2/B_{02}) will be such as to provide a much smaller value of (δ_2/y_2), as follows:

$$\frac{\delta_2}{y_2}=2\left(\frac{B_{02}}{B_2}\right)^2=2\left(\frac{B_{02}}{B_{01}}\frac{B_{01}}{B_1}\frac{B_1}{B_2}\right)^2=2\left(\frac{\delta_1}{y_1}\right)\frac{1}{R}. \tag{40}$$

From a design point of view, (B_2/B_{02}) is larger than necessary by a factor of $R^{\frac{1}{2}}$. Thus, the basic limitation on the usefulness of this technique in a beam converging device is this practical one of an excessive magnetic field which requires an increase in the size and weight

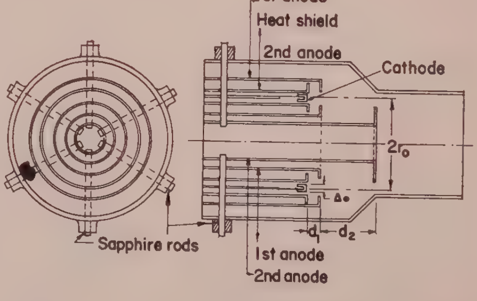

FIG. 21. Two views of the experimental electron gun.

---

[16] See p. 155 of reference 2.

[17] D. A. Dunn and W. R. Luebke, IRE Trans. on Electron Devices **ED-4**, 265–270 (1957).

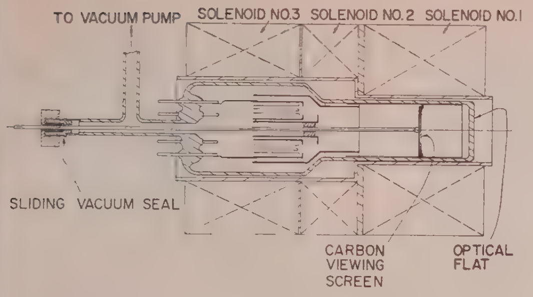

FIG. 22. Cross-section view of the experimental apparatus. A movable carbon viewing screen collected the beam and was heated by the beam so that the beam thickness could be observed through the optical flat. Three solenoids provided a shaped magnetic field.

of the focusing system for a given beam, as compared with the size and weight for a nonconvergent gun.

To compute the actual area convergence, taking into account the ripple produced by passing the beam through the condenser, it is necessary to choose values for the various parameters used in Sec. III. Assume a value of N_0 well below that corresponding to mirroring, and in particular, in order to make the best use of the focusing field, assume a value of N_0 as small as possible consistent with the desired beam ripple. About as far as it is practical to go in this direction is a choice of N_0 such that, neglecting space charge, the beam ripple on both upper and lower electrons is equal to half the final beam thickness. For smaller N_0 and higher beam velocities the ripple will be greater than this amount.

Define $W(\pi)$ as the final thickness in the idealized case, such that if $W(0)$ is the initial thickness,

$$W(0)=R^{\frac{1}{2}}W(\pi). \tag{41}$$

Define $W'(\pi)$ as the final actual thickness. From the theory of Sec. IV, the predicted value of $W'(\pi)/W(\pi)$ is

$$\frac{W'(\pi)}{W(\pi)}=1+\frac{|[\delta_+(\pi)]/[\rho_e(\pi)]|+|[\delta_-(\pi)]/[\rho_e(\pi)]|}{[W(0)/r_0]}. \tag{42}$$

Now, for the maximum ripple condition,

$$W'(\pi)/W(\pi)=2. \tag{43}$$

If N_0 is chosen to give δ_+ and δ_- appropriate to this ripple, the design is then set for minimum magnetic field, and from Eqs. (42) and (43),

$$\frac{\delta_+(\pi)}{\rho_e(\pi)}+\frac{\delta_-(\pi)}{\rho_e(\pi)}=\frac{W(0)}{r_0}. \tag{44}$$

As an example, for the experimental gun to be described in the next section, $[W(0)/r_0]=0.096$. Since the beam thickness is to be twice its idealized value, to get an area convergence of 15 we must choose $R=30$. Then, three different designs, all of which yield the desired ripple, may be compared for different values of βr_0. From Fig. 24, if $\beta r_0=0$, the value of N_0 that yields a total perturbation of 0.096 as required by Eq. (44) for this value of $W(0)/r_0$ is 0.715. If $\beta r_0=0.3$, the correct value of N_0 is seen to be 0.416, and if $\beta r_0=0.5$, N_0 must be 0.218. Further design considerations involve balancing the length of taper βr_0, the value of field for a given entrance velocity N_0, and the ratio of rotational energy to axial energy as determined by how far from the mirroring value N_{0m} the design value of N_0 turns out to be.

V. EXPERIMENTAL HOLLOW-BEAM CONVERGING DEVICE

A hollow cylindrical electron beam was produced by a parallel-flow gun in a region of nearly constant axial magnetic field, and was caused to shrink in diameter and thickness by increasing the magnetic field in the direction of beam travel. Measurements of the beam density at various axial positions were made by observing a carbon screen heated by the beam.

Figure 21 shows two views of the electron gun used for this experiment. All of the concentric cylinders were supported from the rear by insulating sapphire rods so that no angular variations in the beam were introduced by the gun itself. The dimensions were as follows:

$2r_0=1.3$ in. (mean cathode diameter),

$\Delta_0=0.0625$ in. (cathode thickness),

$d_1=0.190$ in. (cathode to first anode spacing),

$d_2=0.500$ in. (first anode to second anode spacing).

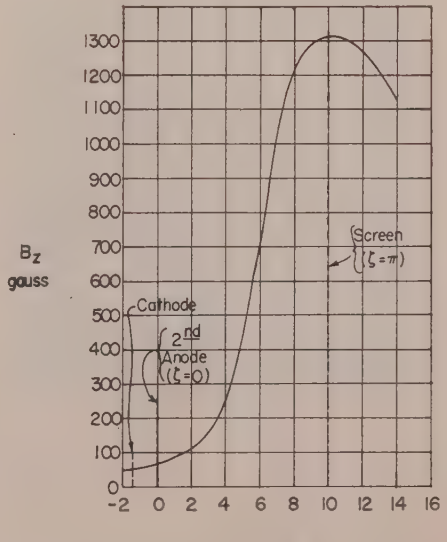

FIG. 23. Typical plot of magnetic field vs axial distance that could be produced in the experimental tube of Fig. 22.

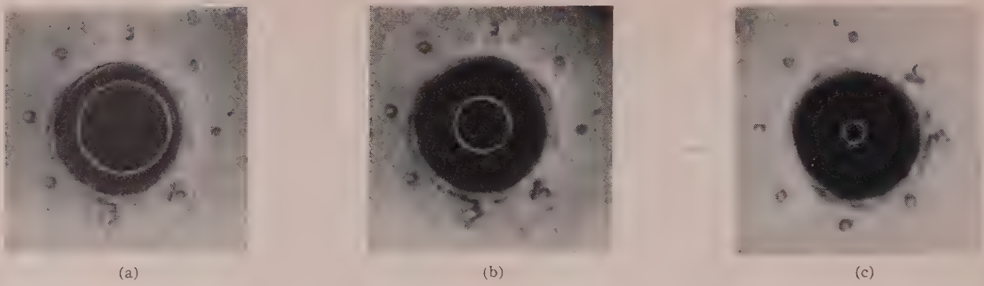
(a) (b) (c)

FIG. 25. Three photographs of the beam for smaller condensation ratios. (a) Uniform magnetic field of 500 gauss. 330 v, 100 ma. (b) $R=3.92$. Field increasing from 250 to 980 gauss. 300 v, 100 ma. (c) $R=10$. Field increasing from 150 to 1500 gauss. 200 v, 20 ma. These photographs were taken with a different carbon viewing screen without the three support wires that show in Fig. 24.

The perveance per square at the first anode was 0.25×10^{-6}. This is the value of $(I/V^{\frac{3}{2}})$ per square having sides equal to Δ_0.

This gun was mounted in a beam tester that included a movable carbon viewing screen which could be observed through an optical flat at the end of the tube, as shown in Fig. 22. The three solenoids could be adjusted to provide various shaped fields. An example is shown in Fig. 23 of a plot of magnetic field as a function of distance. It is seen that the field between cathode and second anode increases slightly. The value of R is seen to be about 20. It was found that by increasing the field between cathode and anode slightly, as was done here, a better-defined beam was obtained after convergence. The effect is analogous to that obtained by injecting the beam deliberately inward as in Fig. 17. A photograph of a high-current beam produced in this field configuration is given in Fig. 24. The measured ratio of fields gives a value of $R^{\frac{1}{2}}=4.5$. The value of $R^{\frac{1}{2}}$ calculated from the measured image dimensions is 4.4. The results for smaller-area convergences were similarly in accord with the zero space-charge theory, up to fairly high values of perveance. Here the perveance was 2.5×10^{-6}. When the perveance was increased to 20×10^{-6}, beam breakup was observed, probably as a result of limiting perveance conditions due to space-charge potential depression being exceeded for the geometry used. For lower-area convergences the value of limiting perveance was increased, as would be expected from the fact that the ratio of beam to outer wall diameter was increased.

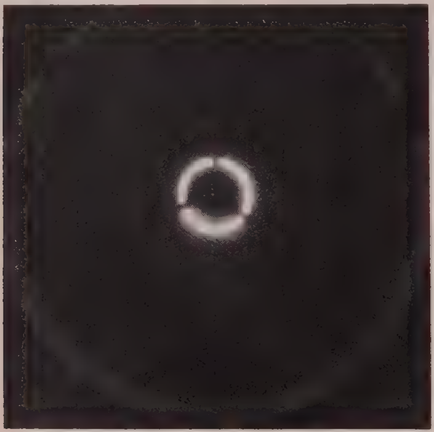

FIG. 24. Photograph of the beam when operated in the field of Fig. 23 at a voltage of 400 v and a current of 20 ma. For this field and voltage, $N_0=1.9$, $\beta r_0\cong0.5$, and $R\cong20$. The beam image is interrupted in three places by the viewing screen support. The beam itself is continuous.

Figure 25 shows three photographs of the beam for smaller condensation ratios. The largest beam outline is for a uniform magnetic field of 500 gauss, a voltage of 300 v, and a current of 100 ma. The next smaller beam outline is for a value of $R=3.92$ with the field increasing from 250 to 980 gauss, a voltage of 200 v, and a current of 50 ma. The smallest beam outline is for a value of $R=10$ with the field increasing from 150 to 1500 gauss, a voltage of 200 v, and a current of 20 ma. All of these photographs yield measured beam areas within 20% of the predicted values.

VI. CONCLUSIONS

A zero space-charge theory for electron trajectories in a sinusoidally varying magnetic field has been presented. An experimental hollow-beam gun has been built and tested operating into an increasing magnetic field with a variation that was approximately sinusoidal The beam behavior was found to be quite accurately predicted by the zero space-charge theory up to quite high values of beam current. Some of the aspects of the design of a high-area-convergence, hollow-beam gun using this principle have been presented. It has been shown that this technique is particularly suited to very high-average power tube designs where the higher than normal magnetic field requirement required by thi technique is not objectionable.

Letters to the Editor

Monotonic Trap Distributions

Richard H. Bube
RCA Laboratories, Radio Corporation of America, Princeton, New Jersey
(Received April 6, 1961)

MONOTONIC trap distributions, such as density of traps essentially independent of trap depth, or density of traps decreasing exponentially with trap depth, have been assumed for some time as an aid to mathematical analysis of problems involving trapping phenomena. Rose,[1] indeed, considered an effectively uniform trap distribution essential to obtain the experimentally observed variations of decay time and photocurrent as a function of light intensity; he showed how a uniform distribution of traps could give rise to a photocurrent varying as the half or first power of the light intensity, and how an exponential trap distribution could lead to photocurrent vs light curves with exponents between 0.5 and 1.0.

Actual measurements of trap distributions in a variety of materials have seemed to fail to substantiate the assumption of a monotonic trap distribution. Measurements of thermally stimulated current, for example, have usually indicated a finite number of fairly discrete trap levels.[2] Theoretical investigations have shown that a great variety of observed photoconductivity phenomena can be described by a band model with only two discrete levels with suitable properties.[3] One question which has not been suitably answered is whether or not monotonic trap distributions are ever observed in real crystals.

Using a technique involving the measurement of decay time of photoconductivity, DeVore[4] showed that monotonic trap distributions with approximately exponential variations of trap density with trap depth were indicated for CdS:Cl:Cu powder photoconductor samples and for CdSe:Cl:Cu sintered layers. This paper reports similar measurements made by means of the technique of thermally stimulated current, which agree with those of DeVore on the powders and sintered layers described by him, and which also show similar effects in certain crystalline photoconductors. Basically equivalent results have also been reported by Niekisch using an ac technique.[5]

Two typical results of such thermally stimulated current curves are shown in Fig. 1. Approximately exponentially varying trap distributions are found for a CdS:Cl:Cu sintered layer and a CdS:I:Cu crystal prepared by chemical transport through the vapor phase.[6] In the latter case, thermal quenching of photoconductivity occurs above a certain temperature, and the lifetime of free electrons decreases markedly. Correction for this decrease in lifetime has not been attempted, but an indication of where it sets in is given in the figure.

All the materials in which evidence of a monotonic trap distribution has been found have in common a high degree of imperfection. This is certainly true of photoconducting powders and sintered layers, which not only contain high concentrations of impurities, but also have large surface-to-volume ratios. The trap densities N_t indicated in Fig. 1 are the total trap densities; they are in the range of 10^{17} cm^{-3}. The CdS:I:Cu crystal of Fig. 1 contains about 10^{18} to 10^{19} impurities cm^{-3}; the crystal color is black, and the spectral response is peaked at 7000 A.

The monotonic trap distribution, however, is not to be associated only with high impurity concentrations; discrete trap depths have been observed for trap densities as high as 10^{19} cm^{-3} in well-crystallized GaAs, for example. Such a monotonic distribution is to be associated rather with a poor over-all crystallinity, with many deviations from the structure of a perfect crystal, so that the distribution of traps is given by primarily statistical considerations. If the energy to form a trap of a given depth is roughly proportional to the trap depth, a statistical determination of trap density vs depth will naturally lead to a near-exponential variation.

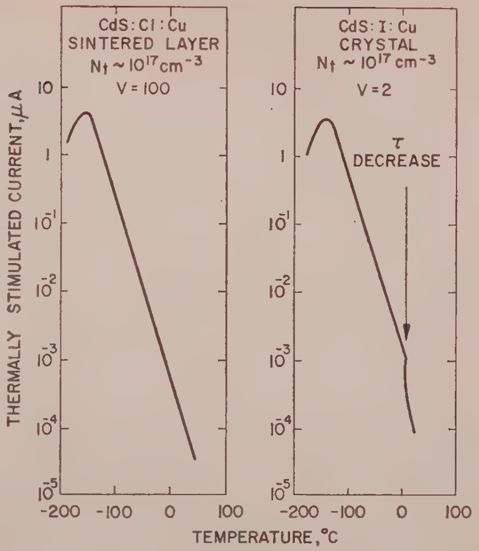

FIG. 1. Thermally stimulated current as a function of temperature for a CdS:Cl:Cu sintered layer, and a CdS:I:Cu crystal grown by vapor phase chemical transport. Total trap densities and applied voltages are indicated for each sample. Heating rate of 0.5°/sec was used. The apparent maximum arises from the brief period of decay in the dark before the beginning of the heating period; the true distribution would not contain such a maximum.

Such considerations lead to the suggestion that the monotonic trap distribution is the background distribution of traps in any crystal. The perfection of the crystal structure then determines whether this monotonic background or discrete imperfection trapping levels will predominate in measurements of trap distribution. Even when present only as a background, however, the monotonic trap distribution can be important in determining the photoconductivity characteristics of insulators. Photoconductivity measurements provide one of the most sensitive available techniques for the detection of low level densities.

---

[1] A. Rose, RCA Rev. **12**, 362 (1951); L'Onde elec. **34**, 645 (1954).

[2] R. H. Bube, J. Chem. Phys. **23**, 18 (1955); Proc. I.R.E. **43**, 1836 (1955); Phys. Rev. **106**, 703 (1957); R. H. Bube and L. A. Barton, RCA Rev. **20**, 564 (1959); R. H. Bube, J. Appl. Phys. **31**, 315 (1960); R. H. Bube and H. E. MacDonald, Phys. Rev. **121**, 473 (1961); J. Blanc, R. H. Bube, and H. E. MacDonald, J. Appl. Phys. (to be published).

[3] C. A. Duboc, Brit. J. Appl. Phys., Suppl. **4**, S107 (1955); G. Wlerick, Compt. rend. **238**, 2514 (1954); H. J. Dirksen and O. W. Memelink, Appl. Sci. Res. **4B**, 205 (1954); M. Schön, Physica **20**, 930 (1954); H. A. Klasens, J. Phys. Chem. Solids **7**, 175 (1958); R. H. Bube, J. Phys. Chem. Solids **1**, 234 (1957).

[4] H. B. DeVore, RCA Rev. **20**, 79 (1959).

[5] E. A. Niekisch, Ann. Physik **15**, 279, 288 (1955); Z. Naturforsch. **9a**, 700 (1954).

[6] Crystal grown by E. L. Lind; see R. Nitsche, J. Phys. Chem. Solids **17**, 163 (1960).

Ferrimagnetic Resonance of Single-Crystal Barium Ferrite in the Millimeter Wave Region

Franklin F. Y. Wang
Long Range Research, A. O. Smith Corporation, Milwaukee, Wisconsin
AND
Koryu Ishii and James B. Y. Tsui*
Electrical Engineering Department, Marquette University, Milwaukee, Wisconsin
(Received February 20, 1961)

POLYCRYSTALLINE barium ferrite ($BaFe_{12}O_{19}$) has been recently used in microwave studies[1,2] to utilize its high crystalline anisotropy. This letter reports some recent ferri-

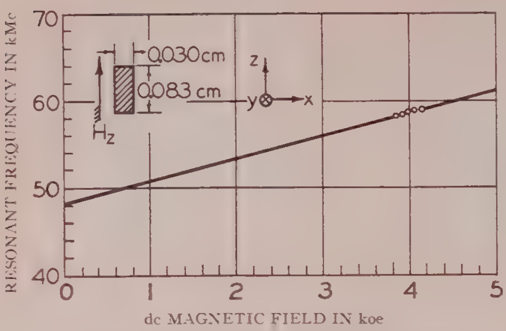

FIG. 1. Ferrimagnetic resonance frequency of single-crystal barium ferrite and the applied magnetic field.

magnetic resonance experiments on single-crystal barium ferrite at frequencies greater than 50 kMc.

Single crystals were grown by the oxide and flux method.[3] Slabs were cut from the crystals to make a test specimen of 0.030×0.083×0.531 cm. Crystals were cut so that their easy axes (crystal axes) were coincident with the E direction during the test. The test specimen was placed in a rectangular waveguide of TE_{10} mode (Fig. 1). Reflex klystron QK295 was employed as the signal source.

Weiss and Anderson[1] have derived an equation relating the resonant frequency to the applied dc field for a hexagonal crystal with high anisotropy along the hexagonal axis, such as barium ferrite ($BaFe_{12}O_{19}$), as follows:

$$f^2=\gamma_e^2[H_x(H_x-AM_z)+(H_z+AM_z)^2]. \qquad (1)$$

H_x, H_z are the applied dc magnetic field components, M_x, M_z are the magnetization components, in the x and z directions, and $A=2K_1/M_s^2$, where M_s is the saturation magnetization and K_1 is the first-order anisotropy constant. The literature[4] lists M_s for $BaFe_{12}O_{19}$ to be 380 gauss, and K_1 to be $+3.3\times10^6$ erg/cm^3. The equivalent anisotropy field H_A along the crystal axis at saturation can be calculated from the relation $H_A=AM_z=AM_s$, and the field was found to be 17.4 koe.

When the applied magnetic field is along the crystal axis, Eq. (1) becomes

$$f=\gamma_e(H_z+AM_z) \qquad (2)$$

for $H_x=0$. The demagnetization field in the z direction, which is not included in Eqs. (1) and (2) in Weiss-Anderson's treatment, is found to be 0.096 koe, estimated according to Osborn's formula.[5] It is negligible as compared to H_z. Our results (Fig. 1 and Table I) showed that the resonant frequency varies linearly with the applied dc magnetic field. They confirm the theory as suggested by Weiss and Anderson.[1] By the standard method of correlation analysis,[6] our data fit a linear regression equation of f versus H_z excellently with a correlation coefficient of 0.988 and the standard error of estimate 0.056 kMc. A comparison of the regression equation and Eq. (2) established that the anisotropy field H_A was 18.4 koe; the effective gyromagnetic ratio γ_e was 2.62; and from γ_e, the effective spectroscopic splitting factor g_e was found to be 1.87. The variance of results to the reported values[7] and the above expected values lies in the fact that point defects do exist in all ferrite single crystals, and their effects on magnetic properties are not taken into account.

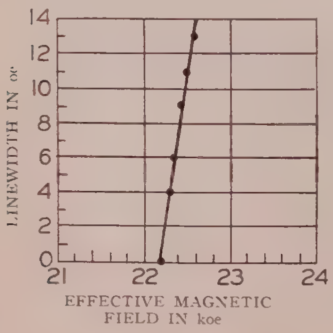

FIG. 2. Linewidth of single-crystal barium ferrite and effective magnetic field.

Linewidths measured on this sample were remarkably small. They were in the neighborhood of 10 oe, as shown in Fig. 2. For operating frequencies of greater than 50 kMc, such narrow linewidths were not reported previously in the literature, to our knowledge. Empirically, the linewidth is related to the effective field H_{eff}, where $H_{\mathrm{eff}}=H_z+H_A$, by a linear equation,

$$\Delta H=0.034H_{\mathrm{eff}}-763 \text{ oe}. \qquad (3)$$

Galt[8] derived a linear relationship between the linewidth and the effective field, involving the damping parameter. The presence of an anisotropy field in the present case makes it too complex to calculate the damping parameter from the above observed relationship [Eq. (3)].

TABLE I. Resonant frequency of single-crystal barium ferrite and the applied magnetic field.

Resonant frequency f (kMc)	Applied magnetic field H_A (koe)
58.2	3.844
58.4	3.886
58.6	3.964
58.8	4.042
59.0	4.140

The apparent density of the single crystal is 5.13 g/cm^3, which is 97% of the true x-ray density, 5.28 g/cm^3. One can speculate that the linewidth could be further decreased if the single crystal could attain a density closer to its x-ray density. The thin slab shape of the sample is used in this experiment for the purpose of excluding the line-broadening effects due to scattering of energy by imperfections from the uniform precession to degenerate spin waves. A detailed summary of this investigation will be reported in a later publication.

* Supported in part by A. O. Smith Corporation, Milwaukee, Wisconsin.

[1] M. T. Weiss and P. W. Anderson, Phys. Rev. **98**, 925 (1955).

[2] M. T. Weiss and F. A. Dunn, IRE Trans. on Microwave Theory Tech. **MTT-6**, 331 (1958).

[3] J. P. Remeika, J. Am. Chem. Soc. **78**, 4259 (1956).

[4] J. Smit and H. P. J. Wijn, *Ferrites* (John Wiley & Sons, Inc., New York, 1959), p. 204.

[5] J. A. Osborn, Phys. Rev. **67**, 351 (1945).

[6] M. Ezekiel, *Methods of Correlation Analysis* (John Wiley & Sons, Inc., New York, 1941), pp. 146–151.

[7] F. K. DuPre, D. J. DeBitetto, and F. G. Brockman, J. Appl. Phys. **29**, 1127–1128 (1958).

[8] J. K. Galt, Proc. Inst. Elec. Eng. **104**, Part B, Suppl. No. 5, 189–197 (1957).

Stored Energy in Fuel-Bearing Graphite

A. H. WILLIS, J. M. BAUGNET, AND R. C. DE BEUKELAER
Centre d'Etude de l'Energie Nucleaire, Mol, Belgium

(Received March 9, 1961)

THE irradiation effects accompanying neutron bombardment of graphite have been extensively studied[1,2] and are therefore rather well known. Much less is known, however, about fission product damage to graphite,[3] particularly with regard to Wigner energy storage, for which no data have previously been reported. To support an existing reactor program, it was necessary to determine whether such fission-product damage could contribute to Wigner energy storage in irradiated, fuel-bearing graphite. We obtained an energy storage that was 20 or more times the amount which would have been expected from neutron damage alone.

In this experiment a 92-g sample of Pechiney graphite, having a density of 1.75±0.04 g/cm^3, was impregnated by a solution impregnation technique with 1.61 g of uranium-235 (0.0332 g/cm^3) in the form of UO_2. The resulting UO_2 particle size is so small that virtually all of the fission products recoil into the graphite matrix. This sample, 25 mm in diameter and 100 mm long, was sealed in an aluminum container and had a thermocouple located at its center. It was irradiated to 1.3×10^{18} nvt (thermal) in a water-cooled loop in the BRI reactor at a nominal temperature of 32°C (maximum temperature 36°C). Post-irradiation calorimetric measurements indicated that 31.2±3.2 cal/g of stored energy had accumulated during exposure to 3 MWD/T. Neutron bombardment alone would have yielded approximately one calorie per gram of stored energy.

For the calorimetric tests we employed the dipping technique,[4] wherein the sample is inserted into a massive furnace-calorimeter consisting of a copper cylinder, which provides a uniform axial surface temperature, surrounded by thermal insulation. Calorimeter measurements were made (1) before irradiation (for reference), (2) after irradiation to measure Wigner energy release, and (3) twice after the energy release to examine the reproducibility of the experimental procedure. The furnace was maintained at its reference temperature 200°C, for several hours before the test was conducted. Among the four calorimeter tests, only the Wigner energy release measurement produced a result that was substantially different from the others, and in this case the maximum sample temperature exceeded the furnace temperature by 11.5°C.

The stored energy in neutron bombarded material has been attributed to the trapping of atoms carbon displaced from their normal lattice positions, and one MWD/T of exposure results in 0.45 cal/g of energy storage, or 5×10^{-6} displaced atoms per carbon atom.[1] Thus one can estimate that each fission event produced 30 000 displaced carbon atoms. This larger energy storage could also have resulted from (1) a larger number of displaced atoms; (2) a different process for energy storage because of the higher density of damage in the case of fission fragments, or (3) a different type of damage that is a consequence of the high charge of fission fragments. The energy storage process is currently being examined further. The results of the present and the further tests will be described more completely in another report.

---

[1] G. R. Henning and J. E. Hove, Proc. Geneva Conf. 7, 666 (1955).
[2] H. M. Finniston and J. P. Howe, Prog. Nuclear Energy 5, Ser. 2, 551 (1959).
[3] R. J. Harrison, USAEC Report ORNL-1722 (1954).
[4] J. C. Bell and J. H. W. Simmons, USAEC Report TID-7565 (Part I) (1959), p. 83.

Peltier Coefficient at High Current Levels*

John R. Reitz
Case Institute of Technology, Cleveland, Ohio
(Received April 10, 1961)

The optimum thermoelectric materials are extrinsic semiconductors with carrier concentrations[1] in the range 10^{19} electrons (or holes) per cm^3. To maximize the performance of a thermocouple, one leg is made of *p*-type material, the other of *n*-type material. The junction between the two legs thus assumes the character of a *p*-*n* junction and is shown schematically in Fig. 1. To the left of the junction the current is carried primarily by holes, whereas to the right it is carried primarily by electrons. For the direction of current shown, hole-electron pairs must be thermally created, and the junction is a heat-absorbing junction.

The thermal energy required to make a hole-electron pair is just the vertical projection of the transition arrow shown in the figure, and this is seen to be in accord with the usual definition of the Peltier coefficient[2]

$$\pi_{12}=T(S_2-S_1), \qquad (1)$$

where

$$S=(1/e)(Ak-\zeta/T). \qquad (2)$$

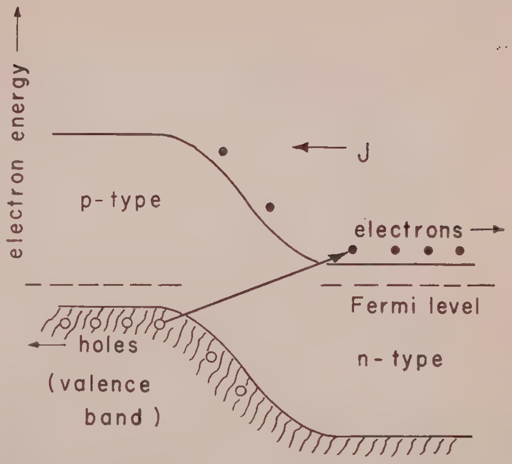

FIG. 1. An isothermal junction between *p*-type and *n*-type semiconductors at low current density. This is a heat-absorbing junction for direction of current shown.

Here S is the Seebeck coefficient, T is the absolute temperature of the junction, k is Boltzmann's constant, and ζ (the chemical potential) measures the position of the Fermi level relative to the carrier band edge. A is a number which depends upon the precise mechanism of charge carrier scattering ($A=2$ for scattering by acoustical phonons). The quantity AkT may be regarded as the average thermal energy of charge carriers emitted from the junction.

Of course the transition shown in Fig. 1 does not occur; the junction is too wide. Electron-hole pairs are created by vertical transitions across the full energy gap after which the created carriers diffuse and drift in the isothermal junction region. The net thermal energy absorbed per pair is the same as indicated, but the transport of charge through the junction is impeded by the rectifying contact. The situation is improved by replacing the junction with a metal weld as shown in Fig. 2, but a single metal cannot in general eliminate the rectifying contacts at both surfaces. In Fig. 3 we show the establishment of ohmic contacts[3] at both surfaces by using a low work function metal in contact with the *n*-type material and a high work function metal in contact with the *p*-type material.

The importance of an ohmic contact for many semiconductor applications is well known, but its importance for high-current Peltier junctions has apparently not received adequate discussion. At appreciable current levels a rectifying contact is accompanied by a voltage drop across the contact; this may be interpreted in terms of a contact resistance, but actually it is a reduction in

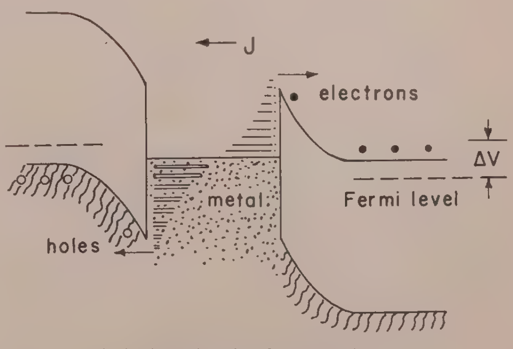

FIG. 2. An isothermal semiconductor-metal-semiconductor junction at high current density.

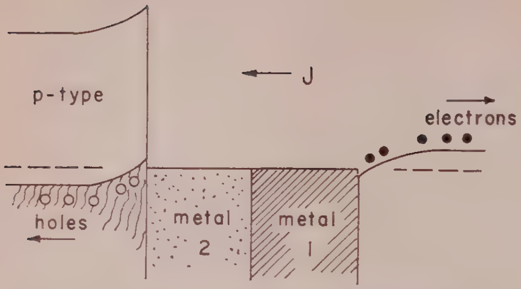

FIG. 3. An ohmic junction at low or high current density. Metal 1 has a low work function and metal 2 has a high work function.

Peltier coefficient of the heat-absorbing junction and an increase in Peltier coefficient of the heat-producing junction. This statement follows from an examination of Fig. 2 where, as usual, the voltage drop across the junction (ΔV) is depicted as a shift in Fermi level. The net thermal energy to create an electron-hole pair is thus reduced by an amount $e\Delta V$. Note that at the heat-absorbing junction, current flows through the rectifier in the "reverse" direction, but at the heat-producing junction its passage is in the "forward" direction. Thus the presence of a rectifying contact reduces the efficiency of the thermocouple as the current density is increased. Since current densities in power generating thermocouples may run as high as several hundred amperes per cm², the effect appears to be important.

The rectifying contact can probably not be eliminated completely in practical thermocouples. The choice of semiconductor for a thermoelectric application is controlled by its figure of merit, or *materials parameter*, and the choice of junction metal is limited by considerations of chemical compatibility and stability. The ohmic contact to the *n*-type material offers the most difficulty, particularly for high-temperature junctions. The harmful effects of the rectifying contact can be partially compensated, however, by changing the carrier concentration of the semiconductor. Thus, to gain back the appropriate Peltier coefficient at the heat-absorbing junction, the doping level of the crystal should be decreased. The optimum concentration of charge carriers is therefore different at high current from its value at low current, and in some cases the difference would appear to be substantial.

---

* Supported in part by the U. S. Atomic Energy Commission, and in part by the National Carbon Company, a division of Union Carbide Corporation.

[1] C. Zener, *Thermoelectricity*, edited by P. H. Egli (John Wiley & Sons, Inc., New York, 1960), p. 8.

[2] See, e.g., A. H. Wilson, *The Theory of Metals* (Cambridge University Press, New York, 1953), 2nd ed., p. 232.

[3] A good discussion of ohmic contacts is given by L. V. Azaroff, *Introduction to Solids* (McGraw-Hill Book Company, Inc., New York, 1960), p. 343.

Maser Action in Emerald

F. E. GOODWIN
Hughes Research Laboratories Malibu, California

(Received March 23; in final form, May 24, 1961)

THE paramagnetic resonance spectra of emerald (chromium-doped beryl) have been reported by Geusic *et al.*[1] The stable physical properties and zero-field splitting at 53.6 kMc make this material especially attractive for use in solid-state-maser amplifiers in the millimeter-wave region. Bogle[2] has shown that emerald may also be of importance at X band and L band because of favorable cross-relaxation effects. The spin Hamiltonian of emerald is identical to that for ruby,

$$\mathcal{H}=g\beta\mathbf{S}\cdot\mathbf{B}+D\left[S_z^2-\frac{5}{4}\right],$$

except that the D factor is greater by 4.66. Therefore, the wealth of experimental and computed data available for ruby masers is useful in predicting the operation of emerald masers.[3,4]

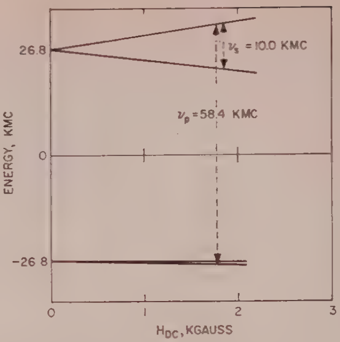

FIG. 1. Energy-level diagram for emerald maser (θ = 90 deg).

This correspondence reports the successful operation of synthetic emeralds in a single-cavity reflection-type maser amplifier operating at 10 kMc. The c axis was oriented at 90 deg with respect to a magnetic field of 1900 gauss and a pump frequency of 58.4 kMc was used (see Fig. 1). The particulars of operation are given in Table I. The expected magnetic $Q(Q_M)$ can be approximated from

$$Q_M=\frac{h\Delta\nu_m}{8\pi\langle\mu^2\rangle(n_2-n_1)F}\cong\frac{kT\Delta\nu_m}{\pi N_0\langle\mu^2\rangle(\nu_p-2\nu_s)F}.$$

For the values given in Table I, $Q_M\cong 180$, which is in approximate agreement with the experiment value:

$$Q_M\cong 2\nu_m/G^{\frac{1}{2}}B\cong 160.$$

The cavity, with dimensions of 0.140×0.280×0.280 in., was constructed of copper and filled with three emerald slabs allowing a TE_{011} resonance. The c axis was in the plane of the crystal slabs and perpendicular to the magnetic field (see Fig. 2). Pump power was introduced into the cavity through the signal iris.

Slabs of beryl were used as seeds on which to grow the emerald material. When the emerald had grown to a thickness of 0.050 in., the samples were removed. As is typical of early growth, these crystals exhibited a number of imperfections, as was evidenced by microscopic twinning and spontaneous nuclei. The filling factor of 80% was a result of these imperfections. The crystal axis exhibited a spread of 3 deg within the sample which caused broadening of the paramagnetic resonance linewidth to 300 M for θ=90 deg and to 500 Mc for θ=55 deg, values five to eigh times greater than that for ruby.

TABLE I. Particulars of operation for the emerald maser.

Signal frequency (ν_s)	10.0 kMc
Pump frequency (ν_p)	58.4 kMc
Magnetic field (H_{dc})	1900 gauss
Orientation H_{dc} to c axis	90 degrees
Temperature (T)	4.2°K
Power gain (G)	16 db
Bandwidth (B, 3 db)	20 Mc
Voltage gain bandwidth	126 Mc
Paramagnetic linewidth ($\Delta\nu_m$)	300 Mc
Filling factor (F)	80%
Magnetic Q (expected)	180
Magnetic Q (measured)	160
Concentration (ions/cm³)	2.5×10^{19}
Average (squared) dipole moment of the maser transition $\langle\mu^2\rangle$	4×10^{-40} erg²/gauss²

The maser performance obtained indicates that the broadenin of the spectral lines due to microscopic spreading of the c axi does not destroy the maser properties at θ=90 deg; however preliminary attempts to achieve maser action at θ=55 deg wer not successful. Crystals of a longer growth cycle are being synthesized; it is expected that the later samples will be relatively fre

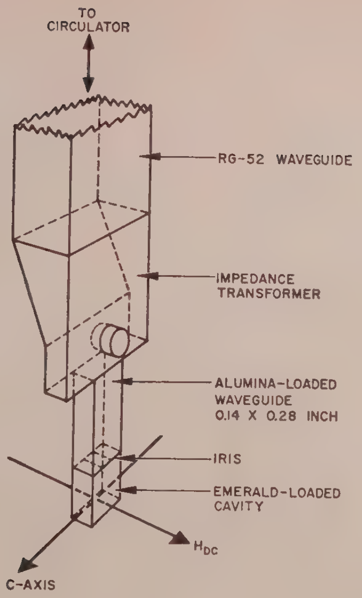

FIG. 2. Configuration of emerald-loaded maser cavity.

of polycrystalline effects and will exhibit narrower linewidths and superior maser characteristics.

The author wishes to thank Dr. R. H. Hoskins for his spectral analysis, G. E. Moss for the development of the experimental maser, and Chatham Research Laboratories for providing the emerald crystals.

---

[1] J. E. Geusic, Martin Peter, and E. O. Schultz-du Bois, Bell System Tech. J. **38**, 291–296 (1959).
[2] G. S. Bogle, Proc. Inst. Radio Engrs. **49**, 573–590 (1961).
[3] W. S. Chang and A. E. Siegman, Technical Report No. 156-2, Stanford Electronics Laboratory, Stanford, California, September 30, 1958.
[4] E. O. Schultz-du Bois, Bell System Tech. J. **38**, 271–290 (1959).

Announcements

Pittsburgh Diffraction Conference

The annual Pittsburgh Diffraction Conference will be held November 1–3, 1961, at Mellon Institute, Pittsburgh, Pennsylvania. Sessions will be devoted to metals and alloys, instrumentation, structures, polymers and fibers, refractories, and electron probe including special sessions on electron diffraction and x-ray diffraction microscopy. The evening meeting will be addressed by Dr. Peter J. W. Debye, emeritus professor of Chemistry, Cornell University. Further information can be obtained from T. B. Massalski, Mellon Institute, 4400 Fifth Avenue, Pittsburgh 13, Pennsylvania.

New Pamphlet

A new pamphlet entitled "Instructions for filing and using solid state abstracts on cards" by Geoffrey Knight, Jr., president of Cambridge Communications Corporation, is now available. This pamphlet describes Dr. Knight's fundamental classification system···filing and use of the cards, together with general information about solid state abstracts on cards.

The new pamphlet is one of the many extra services designed by Dr. Knight to facilitate communication of scientific achievement among scientists. Requests on business letterhead for a complimentary copy of "Instructions for filing and using solid state abstracts on cards" should be addressed to Dept. M, Cambridge Communications Corporation, 238 Main Street, Cambridge 42, Massachusetts.

Seventh Annual Conference on Magnetism and Magnetic Materials

The American Institute of Electrical Engineers and The American Institute of Physics in cooperation with The Office of Naval Research and The Metallurgical Society of A.I.M.E. announce the Seventh Annual Conference on Magnetism and Magnetic Materials November 13–16, 1961, Hotel Westward Ho, Phoenix, Arizona.

The Conference will continue to emphasize the value of bringing together those interested in both basic and applied work from the many disciplines having contact with magnetism. Contributed papers are solicited on basic theoretical and experimental investigations, potential engineering applications, and apparatus and techniques which utilize recent advances in magnetism. Invited papers will be presented by eminent scientists and engineers, both from America and from abroad. Programs, containing abstracts of all papers, will be distributed before the meeting.

For further information, contact the Local Conference Committee Chairman: Peter B. Myers, Motorola Semiconductor Products Division, 5005 East McDowell Road, Phoenix, Arizona.

Cover Photograph

The cover photograph shows the (111) face of a 99.999% copper crystal which was etched to form pits at dislocation-surface intersections. The sharp-bottom pits indicate that the dislocation remained in one position. The flat-bottom pits indicate that the dislocation has moved from its initial position since etching was begun. The large flat-bottom pit in the center of the photograph locates the initial position of a dislocation. The dislocation was then subjected to a stress in one direction of 6 g/mm², and the crystal re-etched. The dislocation was moved to the position of the intermediate size flat-bottom pit to the left. The same stress, 6 g/mm², was then applied in the opposite direction and the crystal re-etched. The final position of the dislocation is denoted by the small sharp-bottom pit to the right. The sides of the pits define the slip directions. The other large sharp-bottom pits locate dislocations which were not moved by the applied stress; the other large flat-bottom pit indicates a dislocation which was moved out of the field of view by the applied stress.

A more complete treatment will appear in "The elastic-plastic transition in copper crystals as determined by an etch pit technique," by F. W. Young, Jr., in the September issue of this Journal.

JOURNAL OF APPLIED PHYSICS VOLUME 32, NUMBER 8 AUGUST, 1961

Proceedings of the Electron Microscope Society of America

The Annual Meeting of the Electron Microscope Society of America was held at the
Pittsburgh Hilton Hotel, Pittsburgh, Pennsylvania,
on August 23, 24, 25, and 26, 1961.

Titles and abstracts of the papers are given below

PROGRAM

Session AI, Lattice Defects and Radiation Damage

A1. On the Reliability of Information Deduced from Dislocation Patterns in Thin Metal Foils.* J. SCHMITZ AND H. G. F. WILSDORF, *The Franklin Institute Laboratories, 20th and The Parkway, Philadelphia 3, Pennsylvania.*—Attention has been given to the changes in dislocation patterns which occur when preparing a thin foil suitable for diffraction electron microscopy. Aluminum single crystals with a predetermined orientation were deformed about 10% in tension and subsequently thinned by an electrolytic technique. It was observed that practically all dislocations were intertwined and occurred as tangles, provided the thickness of the specimens was greater than 1500–2000 A. At a specimen thickness of less than 1000 A, the dislocations appeared as straight lines and singly. These experimental observations can be explained with the help of dislocation theory using the concepts of image forces and line energy of a dislocation.

* This research was supported by Wright Air Development Division.

A2. Dislocation Substructures in Deformed and Recovered Molybdenum. R. BENSON AND G. THOMAS, *Inorganic Materials Research Division, Lawrence Radiation Laboratory, University of California, Berkeley, California.*—Preliminary observations of thin films prepared from bulk polycrystalline molybdenum have been made in order to develop a theory of strain hardening and recovery in BCC metals. The dislocation structure has been observed as a function of strain at room temperature and as a function of annealing temperature for a constant annealing time and constant prestrain. The foils were prepared by electropolishing and were examined in a Hitachi H.U. 10-electron microscope. Stacking faults were not observed during this investigation, which would indicate that molybdenum has a high S.F.E. At strains of 1 to 3%, many dislocation nodes, straight dislocation segments, and jogged dislocations were observed. At least two slip systems operate even at the lowest strains and, by interactions of type

$$\frac{a}{2}(11\bar{1})+\frac{a}{2}(1\bar{1}1)-->a(100),$$

relatively immobile $\langle 100\rangle$ segments are formed. At macroscopic strains of about 3 to 5% a cell structure develops, which consists of very dense subboundaries of dislocations. There are many dislocation loops in specimens deformed >3%, probably as a result of interactions between moving dislocations. In specimens annealed in the range 300–700°C, there is evidence of dislocation annihilation, loop formation, and the breaking up of networks. At 900°C there is a large decrease in the dislocation density with the formation of regular networks. The results are discussed in terms of the relationship between the dislocation substructure, flow stress and recovery.

A3. Dislocation Behavior in Beryllium Single Crystals.* F. WILHELM AND H. G. F. WILSDORF, *The Franklin Institute Laboratories, 20th and The Parkway, Philadelphia 3, Pennsylvania.*—Single crystals of Be of commercial purity (>99%) have been deformed by compression, the basal plane lying under 45° against the compression axis. Subsequently, the crystals were cut with the help of an electrolytical technique and thinned down to 2500 A by a similar method for investigation by diffraction electron microscopy. The most startling result, found in furnace-cooled specimens, was the presence of small precipitates 50–300 A in diameter with an average distance of 700 A. It was seen clearly that the dislocations are pinned by the precipitates. The theory of dispersion hardening gives an agreeable value for the yield stress of these crystals. The dislocation patterns allow some deductions of possible dislocation reactions which are necessary to explain the brittle behavior of this material.

* This research was supported by the U.S. Air Force, monitored by Nuclear Metals, Inc.

A4. Dislocation in Thin Films of Copper-Gold. S. BORGESE AND B. H. KEAR, *The Franklin Institute Laboratories, 20th and The Parkway, Philadelphia 3, Pennsylvania.*—Observations on dislocation configurations in thin films of plastically deformed Cu_3Au will be described. In fully ordered and partially ordered Cu_3Au, dislocations exist in pairs, probably connected by a strip of antiphase domain boundary, whereas in disordered crystals the dislocations are not paired. Differences in the dislocation configurations in fully ordered and disordered crystals have been correlated with the well-known differences in slip-line structure. The transformation from the ordered to the disordered state has also been studied using a hot stage in the electron microscope. The structural changes accompanying the transformation will be described.

A5. Cine Film of Dislocation Structures and Other Imperfections in Graphite Single Crystals.* R. SPRAGUE, *Research Laboratory, National Carbon Company, Division of Union Carbide Corporation, Parma 30, Ohio.*—The study of graphite single crystals by electron microscopy has received much attention recently.[1] By means of cine photography the viewer can gain much greater feeling for the process of dislocation motion and interaction. The RCA EMU-3B viewing screen was photographed directly using a Bolex 16-mm camera and Tri-X negative film. In this film crystal step edges are seen to act as sources for dislocation motion and grain boundaries as dislocation sinks. The motion of a decorant $FeCl_3$ also is observed and influenced by the electron beam.

* This research was sponsored in part by the Air Research and Development Command and the Air Material Command, U. S. Air Force.

[1] R. Bacon and R. Sprague, J. Appl. Phys. 31, 1831 (A) (1960).

A6. Dislocation and Plastic Flow in MgO. W. ELKINGTON AND G. THOMAS, *Inorganic Materials Research Division, Lawrence Radiation Laboratory, University of California, Berkeley, California.*—It has been proposed elsewhere that strain hardening in crystals of the NaCl structure results from defects left in the wake of moving dislocations. Washburn *et al.* have shown by transmission electron microscopy of thin flakes of deformed MgO that the predominant defects left in the slip bands are plus-minus pairs of edge dislocations. For the purpose of testing the validity of a proposed mechanism of formation of such plus-minus pairs and to determine the dislocation substructure as a function of stress and temperature, the following work has been done. Thin slabs of MgO were deformed by pinpoint bending at various temperatures and stresses. The samples were then thinned by polishing in hot orthophosphoric acid and examined in transmission in a Hitachi H.U. 10-electron microscope. The results obtained will be discussed in terms of the dislocation arrangements as a function of stress and temperature.

A7. Some Observations of Fission Fragment Damage in Metals. T. K. Bierlein and B. Mastel, *Hanford Atomic Products Operation, Richland, Washington.*—Electron microscopy of thin films and foils irradiated in close proximity to a fissionable source has permitted study of fission fragment damage to fissionable and nonfissionable material. The interaction of fission fragments with material thin enough for transmission microscopy manifests itself as regions or tracks having a lower atomic packing density than the matrix. Such damaged regions, approximately 150 A in diameter and less than 5 μ in length, appear to be a function of the material and the distance between the fission fragment and the free surface of the material. Results on typical evaporated multilayered films of the type carbon-UO_2-X, and carbon-X-UO_2 are presented (where X = Ge, Pt, and Pd, and UO_2 is the source of fission fragments). Similar damage is reported in prethinned aluminum foils, in which discrete regions free of UO_2 show fission fragment tracks. Dislocations in irradiated UO_2 coated aluminum foils have been observed to interact with fission fragment tracks. The importance of free surfaces on the damage introduced in bulk aluminum specimens by fission fragment bombardment is illustrated by surface replicas.

A8. Electron Microscopy of Fission Damage in Metal Matrices. J. J. Kelsch, O. F. Kammerer, and P. A. Buhl, *Brookhaven National Laboratory, Upton, New York.*—Direct observation of the effects of fission events has been made in thin films of Al, Cu, Pt, and U by transmission electron microscopy. A very thin layer (10 to 20 A thick) of U^{235} was incorporated between evaporated metal films. The samples were exposed to a total thermal neutron flux of 2.8×10^{15} n/cm^2. The fission fragments produced tracks in the matrix, the characteristic appearance of which is strongly influenced by the thickness of the matrix. The mechanism of track formation is discussed from the viewpoint of dissipation of thermal energy of the fission fragments in thin films of evaporated metals.

Session BI, General Biological Ultrastructure

B1. Nephrotoxic Nephritis. I. The Fine Structure of the Canine Glomerulus. Henry Z. Movat, Jan W. Steiner, Dieter Huhn, and Douglas D. McGregor, *Department of Pathology, University of Toronto, Toronto, Canada.*—This presentation will deal with the fine structure of the glomerulus in dogs and a correlation between light and electron microscopy will be attempted. The material fixed in buffered osmium tetroxide and potassium permanganate was stained with silver methenamine, protargol, uranyl acetate, lead hydroxide, and phosphotungstic acid (PTA). The latter gave the best definition of basement membrane. The various structures will be described in the following order: epithelium, endothelium, basement membrane, and axial region. Evidence will be presented for and against the existence of an axial (mesangial, intercapillary) region. In the opinion of the authors, the cells in the axial region are modified endothelial cells concerned with the elaboration of those portions of the basement membrane which anchor capillary loops to the axial tree of the glomerulus.

B2. Nephrotoxic Nephritis. II. The Fine Structure of the Glomerulus in Acute Nephrotoxic Nephritis of Dogs. Dieter Huhn, Douglas D. McGregor, Jan W. Steiner, and Henry Z. Movat, *Department of Pathology, University of Toronto, Toronto, Canada.*—Dogs injected with a moderately potent rabbit-anti-dog kidney serum developed immediate proteinuria (Phase I) followed in a few days by diminuation or cessation of proteinuria and followed again by re-appearance of severe proteinuria (Phase II). If potent sera were injected, the proteinuria was continuous due to direct transition of Phase I into Phase II. The fine structural alterations will be shown in detail. The changes are: first a swelling ("Quellung") and sometimes splitting of the basement membrane, then formation of intracapillary protein deposits. The latter may abut on the basement membrane or may lie between proliferated endothelial cells. Endothelial cells show an increase in cytoplasmic organelles and particularly of pinocytic vesicles. Epithelial cells show, at times, fusion of their foot processes, protein absorption (hyaline) droplet formation, and like endothelial cells, an increase of endoplasmic reticulum. Immuno-histochemical studies are in progress and some preliminary findings pertinent to the pathogenesis of the disease will be presented.

B3. Electron Microscopic Studies of Fibrilogenesis during Repair of Connective Tissue in the Dermis and Tendon of the Rabbit. Neil V. P. Fernando and Henry Z. Movat, *Department of Pathology, University of Toronto, Toronto, Canada.*—Incisions were made in the skin, and the Achilles tendons of rabbits were severed and the regenerating connective tissue examined by light and electron microscopy at various time intervals. In the tendon extravascated serum and blood is found between the two cut edges on the 3rd day. In this one encounters islets of ground substances and newly formed delicate collagen fibrils. At 5 and 7 days both ground substance and fibrils increase, along with the increase in the number of fibroblasts. The latter are distributed haphazardly first, but gradually align themselves along the axis of the tendon. At 3 and 6 weeks there is little ground substance but still numerous cells. The fibroblasts are first irregular and plump, but later elongated and compressed between the fibrils. The newly formed fibrils were found only extracellularly. They were found both adjacent to fibroblast and at quite a distance from them. Fibrils apparently within the cytoplasm were always in a niche. Thus sectioning in a different plane may mimic intracellular location. The newly formed fibrils measure only a fraction of the thickness of the mature fiber. This was seen better in the skin where mature fibrils are displaced during the incision and come to be intermingled with the serum clot and later with the newly formed connective tissue. These newly formed fibrils already have the normal periodicity of collagen and not merely $\frac{1}{3}$ of that observed by others. It would appear that the fibroblast secretes a soluble protein (presumably the tropocollagen macromolecule) which is polymerized into fibrils in the milieu of the ground substance.

B4. Studies of Bright's Disease. I. Fine Structure of the Glomerulus in Acute Glomerulonephritis. Henry Z. Movat, Jan W. Steiner, and Dieter Huhn, *Department of Pathology, University of Toronto, Toronto, Canada.*—In addition to the known hypertrophy and hyperplasia of endothelial cells in acute glomerulonephritis, electron micrographs show an increase in the number of their cytoplasmic organelles. The basement membrane changes are threefold: (1) generalized swelling ("Quellung") of the basement membrane, (2) focal bulges towards the endothelium, and (3) outpouchings towards the epithelium. Whereas the protrusions towards the endothelium may or may not be of an identical electron density as the basement membrance, the outpouchings are denser than the basement membrane, from which they are well demarcated. These additions to the basement membrane are identical to those of foreign protein nephritis of rabbits demonstrated with immuno-histochemistry by Vasquez *et al.* (58th Annual Meeting, American Association of Pathologists, 1960) and probably represent antigen-antibody complexes. The epithelium shows fusion of its foot processes over the the above outpouchings. It also shows swelling and homogenization of the cytoplasm (regressive changes) and an increase in the number and size of organelles.

B5. Studies on Bright's Disease. II. Fine Structure of the Glomerulus in Lipoid Nephrosis. Jan W. Steiner and Henry Z. Movat, *Department of Pathology, University of Toronto, Toronto, Canada.*—The initial changes of lipoid nephrosis are characterized by a "Quellung" of the basement membrane, fusion of foot processes, and other cytoplasmic changes of epithelial cells together with the formation of deposits of an exogenous electron-dense material on the luminal side of the basement membrane. Progression to chronic glomerulonephritis is associated with (1) an accentuation of the latter changes together with a proliferative response on the part of endothelial cells, and (2) a parallel process leading to increased prominence of the axial areas of the glomerulus due to hyperplasia of axial cells and the laying down of new basement membrane material between these cells. Both the above alterations contribute to the gradual narrowing and finally total occlusion of capillary lumina. An acidophilic exudate accumulates between the basement membrane and epithelial cells in most adults. This change is responsible for the apparent thickening of the basement membrane as seen in the light microscope. The exudate does occur in the child and adolescent.

B6. Observations on the Ultrastructure of the Pars Distalis of the Pituitary Gland of the Salamander (*Triturus Viridescens*). Robert R. Cardell, Jr., *Department of Physics, Edsel B. Ford Institute for Medical Research, Henry Ford Hospital, 2799 W. Grand Boulevard, Detroit 2, Michigan.*—Pituitary glands of *Triturus viridescens* were exposed surgically, fixed *in situ* with buffered 1% osmium tetraoxide (*p*H 7.4), embedded in either methacrylate or vestopal *W*, and sectioned on an ultramicrotome for study with an electron microscope. Advantages of using vestopal as the embedding medium are pointed out. The structure and ultrastructure of the sinusoids and perisinusoidal spaces, and the relationship of the pituitary cells to the vascular system are presented. Three distinct cell-types of the *pars distilis* are recognized. One acidophilic cell-type and two types of basophils are described and their ultrastructure discussed. Further, the gonadtrophic and thyrotrophic cell-types are identified and the ultrastructure of the gonadotrophic granules presented. Information is given on the method of hormone secretion in the pituitary gland.

B7. Distribution of Lingnin in Some Woods. I. Sachs, J. Pew, and I. Clark, *U. S. Forest Products Laboratory, Madison, Wisconsin.*—After chemical treatment to remove the cellulose and hemicellulose supporting framework of wood cells, much of the lignin appears in the compound middle lamella. However, considerable lignin, uniformly distributed, is evident in the secondary wall with a definite increase in the tertiary wall.

B8. A Possible Structure of Crystals from *Bacillus Thuringiensis* Berliner. L. W. Labaw, *National Institutes of Health, Bethesda, Maryland.*—The crystals formed in *B. thuringiensis* Berliner were examined using the shadowed carbon replica technique with pepsin digestion. The gross features of these crystals were described by Hannay and Fitz-James (1955). The rectangular cross section of the crystals perpendicular to the long axis of the bipyramid, together with the separation of the rows of molecules on the faces about three times that of the molecules in the rows, suggests that the structure can be approximated by a cubic close packing of spheres. The faces of the crystal would be the (221) planes of a face centered cubic structure having a tetramolecular unit cell of about 110 A on an edge. The molecular diameter would be about 80 A and the rows of molecules on the (221) faces would be separated by about 250 A. There are also membranes in cultures which have undergone autolysis apparently made up on one side of spheres or hemispheres about 65 A in diameter in hexagonal array.

B9. An Electron Microscope Study of Tobacco Sheet. Charles Gadziala, *American Machine & Foundary Company, Research & Development Division, 689 Hope Street, Springdale, Connecticut.*—Methods used in the study of the structure of homogeneous tobacco are discussed. The preshadowed negative replica technique was used to examine the surface of the finished sheet. These replicas reveal the distribution of various substances used in the tobacco mixture. Cross sections of the sheet, embedded in "Araldite," give additional information about air bubbles and distribution of adhesive binder. Problems in embedding and sectioning this type material are discussed.

B10. Reversal of Mitochondrial Membrane and Its Physiological Significance. Satish Chandra, *Sloan-Kettering Institute for Cancer Research, 410 East 68th Street, New York 21, New York.*—An electron microscope study of mitochondria in hamster liver cells has revealed that at some points the outer membrane of these organelles is continuous with the inner membrane. Also, at such points the discontinuous components of the membrane pairs have free endings. The outer and the inner membranes of a mitochondrion, therefore, are not two different and distinct entities, as has been conventionally assumed, but a part of the same unit. Such a morphological structure makes the intramitochondrial substance accessible to the cytoplasmic substance through the inter-membrane channel. This structure will also facilitate the swelling of a mitochondrion either by an unfolding of the cristae, or a sliding of the two membranes, or by these processes occurring simultaneously. The physiological significance of the observed structure will be discussed.

Session AII, Metallurgical Studies

I1. Some New Developments in Electron Metallography in England. J. Nutting, *Department of Metallurgy, University of Leeds, Leeds 2, England.*—An account will be given of the application of thin-foil techniques to the study of a number of new metallurgical problems, notably radiation damage, stacking fault energies of alloys, and precipitation and fracture mechanisms.

A9. Structure of Precipitation-Hardened Alloys. G. Thomas, *Inorganic Materials Research Division Lawrence Radiation Laboratory, University of California, Berkeley, California.*—A review of the work which has been done using thin film transmission electron microscopy will be given. This will include (1) a description of dispersion-hardened alloys with a discussion of zones and partial coherency, (2) the evidence for dislocation-precipitate interactions and their impact upon theories of hardening, (3) precipitation upon dislocations, and (4) the general relationships between microstructure and properties. The discussion will be concerned mainly with nonferrous alloy systems.

A10. An Electron Microscope Study of a Gold-1.5% Cobalt Alloy. P. Gaunt and J. Silcox,* *Cavendish Laboratory, University of Cambridge, Cambridge, England.*—When a gold 1.5% cobalt alloy is aged for periods of the order of 5 min at 565°C after quenching from 880°C, particles of ferromagnetic cobalt precipitate in the nonferromagnetic gold matrix. The form of these precipitates has been studied by transmission electron microscopy and the observations suggest that most of the particles are in the form of disks in (100) planes which are arranged in sheets also on (100) planes. The contribution to the coercivity of the alloy from these particles due to shape anisotropy is small and the origin of the high coercivity must be due to some other type of anisotropy.

* Now at Department of Engineering Physics, Cornell University, Ithaca, New York.

A11. Electron Transmission Studies of Fe-Cr-Ni Alloys. John Dash and Henry M. Otte, *RIAS, 7212 Bellona Ave., Baltimore 12, Maryland.*—Partially transformed high purity Fe-Cr-Ni alloys have been examined by electron microscopy and selected area diffraction of suitably thinned samples. Results obtained from a 15/10 and an 18/12 alloy show that the dislocation density in the martensite is exceedingly high. A few dislocations may be seen in the adjoining austenite which before transformation contained essentially none. No twins or twin faults were found in the martensite. Diffraction patterns from the epsilon phase (hcp) were obtained; these patterns showed spots from twinned austenite as well as from the hcp structure. Observations on the relation between the austenite, the martensite and the epsilon phase will be presented and interpretations discussed.

A12. Interaction of Slip Lines and γ' Particles in a Nickel-Base Alloy. G. I. Madden, W. C. Bigelow, and D. L. Sponseller, *Department of Chemical and Metallurgical Engineering, The University of Michigan, Ann Arbor, Michigan.*—Specimens of a nickel-base alloy aged for different periods at temperatures in the range from 1400°F to 1600°F, have been subsequently subjected to tensile deformation at room temperature, and examined by electron microscopy to study the interaction between slip lines and the γ' particles as a function of particle size and aging treatment.

A13. Electron Metallographic Studies of Torsional Fatigue in Single Crystal Copper. Harry M. Bendler, *Research Laboratories, General Motors Corporation, Twelve Mile and Mound Roads, Warren, Michigan.*—Oriented single crystals of high purity copper were cycled at varying amplitudes in torsion. The development of slip bands on crystals having axial orientations of [100] and [111] was observed using two-stage carbon replicas. An analysis was made of the resolved shear stresses on the possible slip systems. An observed slip band could, in general, be identified with that slip system having the greatest resolved shear stress. In regions where the resolved shear stress had similar values on different slip systems interactions were observed between the slip systems. The details of these interactions as revealed by the slip bands will be discussed.

A14. Study of the Recrystallization Temperature of Metals Used for Shadowing Replicas. Charles F. Cook, Jr., *U. S. Army Signal Research and Development Laboratory, Fort Monmouth, New Jersey.*—A serious deterrent to high resolution electron microscopy using preshadowed carbon replication techniques is the tendency for shadowing materials to recrystallize. This recrystallization can occur due to improper handling outside the microscope or to high beam current densities while in the electron microscope. It is the purpose of this paper to report some results of a study of the recrystallization temperature of some of the noble metals and their alloys commonly used as shadowing metals. It has been found that the recrystallization temperature of the above metals when used in replica techniques are considerably lower than the Tammann temperature. For example, the recrystallization of a 20–40 A layer of platinum on a carbon substrate is approximately 350°C.

A15. Electron Diffraction and Microscopy Studies on Evaporated Cr Films. H. W. Treupel and S. Clarke, *IBM Command Control Center, Federal Systems Division, Kingston, New York.*—Thin Cr films ($\sim$1000 A thick) have been vacuum deposited at high evaporation rates (225 A/sec and 1000 A/sec) and 190°C substrate temperature. NaCl, which had been previously coated with a thin SiO layer, was used as a substrate. These Cr films were found to have polycrystallinity in some areas and single crystallinity in others. Transmission micrographs and diffractographs, using the selected area technique, show that two adjacent areas of different crystallinity have sharp boundaries. In other Cr-film samples, prepared in the same manner but at 25°C substrate temperature, preferred orientation on different lattice planes occurs and multiple scattering could be observed in the diffractographs. Highly intense (110), (200), and (310) Laue reflexes act as primary beams for the multiple scattering in the different film portions. When deposited at 320°C substrate temperature, under otherwise the same preparation conditions, single crystallinity only was observed in Cr-film samples. Multiple scattering also occurred when portions of these films were superimposed with a small misaligning angel.

Symposium SI, Ultrastructure of Protein Fibers—Collagen, Muscle and Karatin

S1. Introduction. R. Borasky.

S2. Physical, Chemical, and Mechanical Properties of Protein Fibers. Alfred E. Brown and John Menkart, *Harris Research Laboratories, Inc., Washington, D. C.*—The protein fibers form a class of their own, in contrast with other organic natural and synthetic fibers, in two important aspects of behavior: (1) their mechanical properties, particularly their long-range elasticity; and (2) their high moisture-sorbing capacity. These two characteristics are important not only for the use of fibrous proteins as textile materials, but also for their functions in biological systems. The relationship of these physical and mechanical properties to the chemical composition and molecular structure of the protein fibers forms the main theme of this paper. The fibrous proteins fall into four groups differing in the arrangement of their polypeptide chains:

(a) the coiled or α-pattern, typified by wool keratin, myosin, fibrinogen; (b) the extended β-pattern, typified by silk fibroin, feather keratin, stretched wool; (c) the special case of collagen; and (d) the random coil, obtained by the denaturation of globular proteins, which can, by drawing, be transformed into the β-configuration; all the regenerated protein fibers (peanut, zein, casein, egg albumen) fall into this category.

The α-proteins, keratin and myosin, and collagen, will be discussed in some detail by the three other participants in the symposium. Therefore, they will be referred to only for comparison purposes. Two other protein fibers, silk and regenerated zein, will be discussed in detail to show the relationship between chemical composition and molecular structure on the one hand, and the various properties of the fibers on the other.

In the case of silk, the molecular organization has become well understood in recent years, largely as the result of the elegant work of Smith and co-workers at the Shirley Institute in Manchester. The crystalline portion of the structure consists of a simple sequence of amino acid residues with small side chains [Ser. Gly. (Ala. Gly.) n]; the bulkier residues are restricted to the less organized regions. Silks differ in the degree of crystallinity, and the more crystalline ones form fibers which are stronger and less extensible than the more amorphous ones. Like all protein fibers, the silks are weaker wet than dry, but this weakening is least in the more crystalline silks, which suggests that the intermolecular bonds in the crystalline region of the fiber are unaffected by water. Similarly, the weakening caused by elevated temperature in water is least in the more crystalline silks. On the other hand, the differences in moisture sorption across the whole spectrum are slight.

It is only natural that much effort has been directed to the production of textile fibers from various proteins in an attempt to simulate the desirable properties of the natural protein fibers, wool and silk. Denaturation is utilized to convert globular proteins to extended molecular configurations. These proteins can be utilized to prepare either "wool-like" or "silk-like" fibers, and the factors involved in this choice are the chemical structure, the ease with which the flexible protein molecules are transformed from their natural configuration to an optimum configuration for fiber construction, and the extent to which this optimum configuration can be stabilized in the fiber.

The regenerated protein fibers, with their lack of crystallinity, are weak when wet. This problem has proved to be the greatest barrier to their commercial acceptance despite much effort to overcome it. The influence of cross-linking treatments, which help to strengthen protein fibers and improve other properties, will be discussed in detail.

S3. Collagen. EMIL BORYSKO, *Ethicon Inc., Somerville, New Jersey.*—Comparative electron and optical microscopic studies were made of so-called "insoluble" collagen fibrils obtained from a number of different tissues and species, using the swelling of the fibrils in dilute acid media as one of the principle tools for obtaining information about their fine structure. The fibrils varied in their reaction to the swelling media, some increasing manyfold in volume while others showed no perceptible change. Rat tail tendon collagen dissolved completely in the acid media. Collagen fibrils varied in diameter in both the swollen and unswollen states within a single tissue, between tissues, and between different species. The larger swollen fibrils had an optically visible dense central core, excluding the possibility that the fibrils were hollow. The presence of a dense central core in the smaller fibrils was established electron microscopically. In the case of beef leg tendon fibrils, the swelling of the fibrils involved the lateral dimension only, the length of the fibrils remaining constant. The swelling of the fibrils did not change the 640-A dimension of the periodic structure. In highly swollen fibrils, the periodic structure was obliterated. The fine structure of the swollen fibrils was quite variable, depending on the degree of swelling and the types of artifacts produced during the preparation of the grid. Preparative artifacts were minimized by fixing the swollen fibrils with 50% formalin overnight prior to drying them on the grid. Highly swollen fibrils were made up of anastomosing filaments ranging in diameter from about 50 A down to, or below, the resolving limits of the microscope. These filaments did not exhibit any periodic structure, nor were they oriented in any particular direction. The ends of the swollen fibrils were usually square, showing no tendency to broom or fibrillate. In the swollen state, the fibrils could be easily digested by enzymes to which they were normally resistant in the unswollen state. The enzymes did not destroy the fundamental collagen unit since fibrils and tactoids with 640-A periodicity, SLS, and FLS forms could be reconstituted from the enzymic solutions. Optical and electron microscopic examinations of thin sections of swollen and unswollen collagen fibrils provided additional support for the data obtained from whole mounts as well as giving information concerning the arrangement and size distribution of the fibrils in several collagenous tissues.

S4. Organization of Protein Fibers in Muscle. WILLIAM H. JOHNSON, *Department of Physiology, University of Illinois, Urbana, Illinois.*—Many differences exist in the organization and fine structure of intracellular fibrous protein systems found in various types of muscles. Only a relatively small variety of muscles has been studied thoroughly, so that the range of types available for comparison is somewhat limited.

Vertebrate striated muscle are the best known. The contractile system of such muslces consists of small filaments (ca. 50 A in diameter), found in both the *A* and *I* bands of the sarcomere, and larger filaments (ca. 120 A in diameter) found only in the *A* band. The latter interdigitate with the smaller filaments in the lateral portions of the *A* band. The relative arrangement of these filaments in the living muscle is still open to question; Huxley has found that, under certain conditions, the filaments are packed in an ordered hexagonal array. The protein myosin has been localized in the *A* band, while actin, the second member of the contractile protein complex, actomyosin, is located in both bands.

The above pattern of filament organization seems to be common to all striated muscles studied so far. The question arises as to whether or not this pattern (and that of protein segregation) is common to all contractile systems. A different pattern of fine structure is seen in insect flight muscles, although the major features of *A-I* band organization are present.

Among the nonstriated muscles, a variety of fibrous structures are seen. In lamellibranch nonstriated muscles, two sizes of filaments are also present within the cells, one ca. 500 A in diameter and the other ca. 50 A. The former contains a third protein, paramyosin, which is now clearly implicated in tonic contractile responses of these muscles. The smaller filaments are extracted by solutions which extract myosin, and thus may contain this protein. Such solutions, however, also remove a surface layer from the large filaments, leaving a large core of dense material. Solutions which extract paramyosin remove most of the remainder of the large filaments, leaving behind a fibrous backbone, the structure of which depends on the species or type of muscle from which the filaments came. Recent studies in our laboratory of partially extracted and intact fibers from two species indicate that, although the backbone structure of the large filaments may differ from muscle to muscle, the structural organization in the presence of paramyosin is much the same. When this protein is present, the filaments often exhibit the unique periodic structure described some time ago by Hall, Jakus, and Schmitt. Similar patterns have also been observed in crystals of paramyosin by Hodge.

In lamellibranch muscles, the arrangement of small filaments is not comparable to that observed in striated muscles. The former are arranged in the form of a stocking-like network around the large filaments. A further difference between striated and lamellibranch muscles is evident in the large filament system. These filaments, in the latter case, form a system which is mechanically continuous throughout the length of the muscle; in contrast, the large *A*-band filaments in skeletal muscles are not continuous. Other studies of the behavior of these fibrous systems in lamellibranch muscles suggest that the coupling between large and small filaments is quite close, although points of attachment have not been resolved in the electron microscope.

Little is known about the arrangement and fine structure of filaments within vertebrate and invertebrate smooth muscles. Filaments can be detected, but they are small and hard to resolve. The study of the organization of such systems remains one of the challenging problems of electron microscopy.

S5. Keratin. HAROLD P. LUNDGREN, *Western Regional Research Laboratory,* 800 Buchanan Street, Albany 10, California.*—In review of keratin structure, it is helpful to begin with consideration of the generation of hair and wool in the fiber follicle. Fibrous prekeratin material is first detected as "wispy filaments" within the keratinogenic cells that are formed at the base of the follicle. These filaments measure 70 to 80 A in width and become oriented parallel with the direction of the fiber that is forming as the cells push outwards in the follicle. The filaments transform into keratin by incorporation of disulfide crosslinks. This is accomplished by interaction with a nonfibrous material high in sulfur in the reduced (thiol) state, which is deposited, at least in part, between the filaments as a "cementing material." Most of each cell is eventually transformed into adherent fibrils closely aligned, dried, and with the sulfur almost entirely oxidized to the disulfide state. In this process the transformed cell (called the spindle cell because of its elongated spindle-like shape) adheres closely to its neighbors through a thin structured membrane with an irregular area of contact to form the continuous cortex which makes up about 90% of a typical fine wool fiber. In crimped fibers the cortex has bilateral structure, in one part of which the fibrous components are arranged in fairly regular discrete units (macrofibrils) whereas these are more extensively fused in the other part less accessible to most chemical reagents. Simultaneously with the formation of the cortex, other cells in the follicle transform into flattened cells that become the scales (or cuticle) surrounding the cortex. The cuticle itself is complex, consisting of three easily distinguishable components, a very thin chemically resistant outer sheath called the epicuticle, and the underlying exocuticle and endocuticle. Emerging from the follicle is an extremely heterogeneous assembly of components uniquely "suited" for such purposes as warmth, protection, and tactile purposes.

Research is extending and refining our knowledge of these structures, as well as providing information on the underlying details of the fine structure of the individual components. Except for moisture, nuclear remnants, pigments, and traces of waxes, the whole of the fiber is protein. The proteins from each part may be quite different. Some components have been isolated and their composition studied and, in time, the amino acid sequences will be determined. Also being studied are the molecular-kinetic properties and effects of chemical modification. Among techniques employed on the intact fiber as well as on isolated components are infrared and ultraviolet absorption, nuclear magnetic resonance, and the methods of rheological testing.

In similar studies, but in a more limited way than in the case of hair and wool, information is developing on the details of structure of other keratins including those of feathers, skin, horn, hoof, etc.

Despite the apparent structural heterogeneity of most keratins as they occur naturally, there has been little modification in our knowledge of the broad aspects of the polypeptide configurations of keratins, at least in the crystalline regions, as first established by Astbury in his classical studies of 30 years ago. Astbury classified the mammalian keratins by their characteristic x-ray patterns and correlated these with their extensibility and elasticity. The polypeptide chains of the mammalian keratins (similar to those in a number of other fibrous proteins, including myosin, epidermin, and fibrinogen) occur in nature in a regularly folded α form from which they may be extended into the relatively straight β form. More recently the α folding has been shown to consist of internally hydrogen-bonded helical units. On the other hand, the keratins of feathers, claws, beaks, scales of birds and reptiles occur typically in the β form naturally, but this β form is about 7% shorter than mammalian β keratin. Critical study recently of some of these keratins has shown evidence for a certain proportion of α chains. Cumulating information on the macro- and microstructures and on the physical and chemical behavior of keratins should in time make it possible to describe uniquely each morphologically distinct unit in keratins in terms of the proportion of helically coiled structures, random coils, and extended chains in the amorphous as well as in crystalline areas, and also to define the amino acid sequences, the location of disulfide crosslinking, hydrogen bonding, and other interactions in the fibrous structural components and in the nonfibrous cementing proteins.

* A laboratory of the Western Utilization Research and Development Division, Agricultural Research Service, U. S. Department of Agriculture.

Special Session on Techniques*

T1. Simple Grid-Coating Technique. ROBERT F. BILS, *Department of Biology, Massachusetts Institute of Technology, Cambridge 39, Massachusetts.*—By the use of a multiperforate-grid-holder coating grids with collodion, Formvar, or carbon is simplified. This inexpensive holder is an electroplated nickel sheet* approximately 3-by-6 cm and 2–3 mm thick, having conical holes slightly smaller than the grids. The coated grids are left on the holder for carbonization and storage.

* Available from Perforated Products, Inc., Brookline 46, Massachusetts.

T2. Uniform Method of Producing Contrast Differences by Vertical Metal Evaporation. BOLIVAR J. LLOYD, JR., *National Cancer Institute, Bethesda 14, Maryland.*—In pursuing studies of hamster skin collagen, a method has been developed for electron microscopy, producing uniform contrast differences by vertical metal evaporation. After vertical evaporation of 2.5 mg of chromium onto a specimen of unstained collagen from a height of 20 cm, fibrils examined in the electron microscope are outlined sharply at their edges. The 640-A period as well as smaller subperiods can be identified in many instances. The amount of metal used is rather critical. Short shadows beneath particles are seen especially where specimens rise above the surface of the substrate. A few viruses, *T*-2 bacteriophage, and thin sections of tissue have been examined using this method.

T3. Simple Method for Bridging the Gap between Light and Electron Microscopy in Histological Work. NILS H. BJÖRKMAN,* *Department of Anatomy, School of Medicine, University of Washington, Seattle 5, Washington.*—Sections from tissue embedded in epoxy resin and cut on a Porter–Blum microtome are valuable for low-magnification electron microscopy. Thin (200–500 A) sections have poor contrast at low magnification, and it is difficult to obtain large areas without sectioning defects. For initial magnifications of 200–1000 diam, 0.3- to 0.5-μ-thick sections give high contrast. Large sections of that thickness are easily obtained and can be picked up conveniently on wide meshed grids. Adjacent sections may be prepared so that one can be used for light microscopy and the other for electron microscopy. Electron micrographs of such thick sections are much crisper than photomicrographs at the same magnification. This method of direct comparison is helpful in the interpretation at the transition between light and electron microscopy.

* International Postdoctoral Research Fellow of the National Institutes of Health.

T4. A Method for the Quantitative Estimation of Cyto-Plasmic Structures. ALDEN V. LOUD, *Detroit Institute of Cancer Research, Detroit 1, Michigan.*—For studies correlating cell structure and function by means of electron microscopy it is desirable to have a systematic technique for the quantitative estimation of cytoplasmic components seen in electron micrographs. A simple sampling procedure has been devised by which the total cell area and areas occupied by formed inclusions (nuclei, mitochondria, lipid bodies, etc.) may be estimated. The difference between these values represent the remainder of the cytoplasm, in which the principal structures are the irregularly shaped and dispersed membranes of the endoplasmic reticulum. A quantitative measure of these membrane profiles has been obtained by counting their intersections with the lines of a uniform grid superimposed on the micrograph. The statistical error of estimation is readily calculated.

T5. Accessories for Electron Diffraction with the RCA EMD-3 Diffraction Camera and the EML Electron Microscope. J. A. AMY, *Convair-Astronautics, San Diego, California.*—A description is given of a convenient, flexible sample-holder for the RCA model EMD-3 diffraction chamber and of a beam-stop for the RCA model EML electron microscope.

T6. Determination of Exposure in the Electron Microscope.* ARTHUR L. COHEN, *Oglethorpe University, Atlanta, Georgia.*—Both photometric (light intensity on the screen) and electrometric (beam current) measurement have been used satisfactorily for determining exposure for electron micrographs. Photometric determination was made by matching the reflection of a variable light source in the viewing port glass with the background intensity of the screen fluorescence. While exposure could be duplicated by any individual, the calibration factor varied from user to user. Later an electrometer connected to the screen was used to determine exposure by measuring beam current. Suitable electrometers with low-impedance pathways to ground are available, and simple means of connecting the screen to the meter are described.

* Supported by grants from the National Science Foundation and the National Institutes of Health.

T7. Method of Exposure Control for Electron Microscopy. GAROLD F. OSBORNE, *The Bendix Corporation, Kansas City 41, Missouri.*—A method for controlling exposure in electron microscopy is being used in the Bendix Laboratory. The reproduction of film contrast and density, especially for the beginner, can be simplified if a method of exposure control is available. The present method utilizes measurement of the electron-beam current density with a sensitive millimicroammeter. The exposure, *I* density times shutter speed, is plotted against film density for various accelerating potentials. The correct intensity and shutter speed can be taken directly from a chart of kv vs index. This method has been found to be efficient in producing uniform quality micrographs.

T8. Replica Jig for the PVA–Formvar Technique. THOMAS E. REICHARD, *Monsanto Chemical Company, Research and Engineering Division, Dayton, Ohio.*—A device is described which greatly improves the speed and reliability of the two-stage polyvinyl–Formvar replica technique. This "replica jig" holds the PVA first-stage replica flat and seals off the desired area against an O ring so that the Formvar second stage can be applied with a controlled, uniform thickness.

T9. Water-Flow Fail-Safe Control for RCA-EMU-3 Series Microscopes. R. A. Schlegel, C. E. Powell, and C. B. Reimer, *Lilly Research Laboratories, Physicochemical Research Division, Indianapolis 6, Indiana.*—The device to be described protects an RCA-EMU-3 electron microscope in the event that an insufficient rate of *flow* (rather than pressure) occurs in the water supply. If the flow becomes insufficient for proper cooling of the diffusion pump, the fail-safe is actuated and serves the same function as though the "standby" switch were manually depressed. That is, the high voltage is turned off if the microscope happens to be in use at the time of failure; heater voltage for the diffusion pump is cut off; and all the motorized valves in the vacuum system cycle to the closed positions. A red light and audible alarm are actuated until the operator corrects the malfunction.

T10. Simple Gauge for Magnification Calibration of the Electron Microscope. Charles B. Reimer, *Lilly Research Laboratories, Physicochemical Research Division, 731 South Alabama Street, Indianapolis 6, Indiana.*—A simple annular gauge will be described which enables the microscopist to adjust quickly ($\frac{1}{2}$ hr), and accurately ($\pm 3\%$), all the magnification control circuit elements for preselected values of magnification. In use, a projected shadow of the gauge is superimposed upon the image of a diffraction grating. Circuit elements are adjusted to give a preselected integral number of grating spacings between grating lines tangent to the inner or to the outer diameter of the gauge shadow. An equation is given relating the physical size of the gauge to its placement within the geometry of the microscope, to the spacing of the grating used, and to the magnifications desired. The gauge remains as a permanent attachment within the microscope. Once the initial calibration is made, the operator can rapidly and precisely check or readjust at any time the entire magnification range of the instrument by eye, without taking a micrograph.

T11. Photography in Electron Microscopy—A Survey. John S. Odell, *LogEtronics Inc., 500 East Monroe Avenue, Alexandria, Virginia.*—This paper will briefly summarize the results of a survey of information from a representative sample of electron microscopists with emphasis on the photographic aspects of their operations. The information reviewed will include the number of microscopes; the annual production of negatives and prints; an analysis of print problems; negative and print size, emulsion type, magnification, etc; and an analysis of darkroom production with respect to time, personnel, man-hours, test prints, etc.

Symposium SII, Contribution of Electron Microscopy to Polymer Morphology

S6. Introduction to the Problem. Charles W. Hock, *Hercules Powder Company, Wilmington, Delaware.*

S7. X-Ray Diffraction Applied to Polymers. N. M. Walter, *American Viscose Corporation, Marcus Hook, Pennsylvania.*

S8. The Study of Spherulites. Douglas Keith, *Bell Telephone Laboratores, New York 14, New York.*

S9. Electron Diffraction Applied to Single Crystals. W. D. Niegisch, *Union Carbide Plastics Company, Bound Brook, New Jersey.*

S10. Morphology of Polymers. Phillip Geil, *DuPont Experimental Station, Willmington 98, Delaware.*

Session BII, Neoplasms and Related Topics

B11. An Electron Microscopic Study of a Series of Mouse Leukemias. Albert J. Dalton, *National Cancer Institute, Bethesda, Maryland.*—Samples of lymph node, thymus, spleen and bone marrow from mice carrying the Moloney, Friend, and Gross induced leukemias and from strain AKR and Figge substrain C3H mice with spontaneous leukemias were examined in thin section with the electron microscope. In the induced leukemias, characteristic particles were observed in all tissues examined and in all the leukemias characteristic particles were identified in the dilated cisternae of the megakaryocytes of spleen and/or bone marrow. The greatest number of particles was found in the induced leukemias, the least in the spontaneous leukemia of AKR mice. Particles in the megakaryocytes of leukemic Figge subline C3H mice occurred primarily within the specific granules. The majority of these particles did not possess dense central nucleoids. A comparison of the fine structural features, including size of the particles associated with this series of leukemias will be given.

B12. Demonstration of Virus in Human Autopsy Material with Electron Microscopy. R. C. Reynolds, F. J. Luibel,* and E. Sanders, *The University of Texas Southwestern Medical School, Dallas, Texas.*—The electron microscopy of virus particles in tissue culture cells and experimental animals has been well described, but descriptions of these particles in human autopsy material are scarce. We have recently examined post mortem tissues from three infants, two of them dying with generalized salivary gland virus infections and one dying with disseminated herpes simplex virus, by means of electron microscopy. In the two infants with salivary gland infections, typical inclusion-bearing giant cells were found in the kidneys and pancreas. The ultrastructure of the bulls-eye-shaped virus particles is easily demonstrated in the cytoplasm and nuclei of these cells. Typical virus particles of herpes simplex were somewhat more difficult to find, but were clearly demonstrated by electron microscopy in sections of the liver. Hematoxylin and eosin stained sections and electron photomicrographs will be presented.

* Research Fellow (CF-11, 763), National Cancer Institute, Public Health Service.

B13. Electron Microscopic Study of an Osteolytic Virus Associated with Mongoloid Deformity in Hamsters. Satish Chandra, Helene W. Toolan, A. R. T. Denues, and Frances C. Mottram, *Sloan-Kettering Institute for Cancer Research, 410 East 68th Street, New York 21, New York.*—Cell-free filtrates of several transplantable human tumors when injected into newborn hamsters produce an abnormality that resembles Mongolism.[1] The deformity is the result of a minimal infection by a virus[2] that causes lytic lesions of bones and early changes in the Kupffer cells as observed in the light microscope.[3] Two distinct viruses of this kind have been recognized thus far.[4] Electron microscope studies of liver, kidney, and bone from animals 2–4 days old infected when newborn with the H-1 virus have revealed virus particles ca. 15 mμ in diameter enclosed by a smooth membrane in the cytoplasm of the infected cells. The significance of the enclosed space (the viroplasm or the grey body as it has been called by some) in relation to the formation of virus particles will be discussed.

[1] H. W. Toolan, Science **131**, 1446–48, (1960).
[2] H. W. Toolan, *et al.* Proc. Natl. Acad. Sci. U. S. **46**, 1256–58 (1960).
[3] G. Dalldorf, Bull. N. Y. Acad. Med. **36**, 795–803 (1960).
[4] G. Dalldorf (In Press).

B14. Studies on Swiss Mice Transplantable Lymphomas. ETIENNE DE HARVEN* AND CHARLOTTE FRIEND, *Laboratoire de Microscopie Electronique de l'Institut d'Anatomie, Université Libre de Bruxelles, Brussels, and the Virus Study Section, Sloan Kettering Institute for Cancer Research, New York, New York.*—Swiss mice transplantable lymphomas were studied with the electron microscope. Ninety-eight samples of lymphomatous tissue have been examined so far, and typical particles were observed in 71 cases. Serial transplantation of the tumors does not seem to "dilute" the particles, since in one of the lymphomas they are still present after 23 passages. These "lymphoma particles" (LP) are always located within the cytoplasmic matrix in which they form large inclusion bodies. They consist of two concentric spherical membranes or shells, an outer and an inner one, whose diameters are respectively around 69 and 52 mμ. Morphologically, LP's are identical to the intracytoplasmic particles described by several authors in mouse mamary carcinoma. In this last tumor, however, the intracytoplasmic particles bud at the cell membrane and form more complex extracellular particles. In Swiss mice transplantable lymphomas this budding phenomenon is relatively rare. So far, the biological activity of LP's is unknown, since it has not yet been possible to transmit the lymphoma by means of cell-free filtrates of lymphomatous tissue. Although the oncogenic property of LP's is still unknown, these particles do not inhibit the mitotic activity of the lymphoblasts. In numerous cases indeed, LP's were observed in those cells at the different phases of their mitotic activity. The contrast of LP's is greatly enhanced after different "electron staining" procedures including potassium permanganate, uranyl acetate, and lead hydroxyde. It seems, on the contrary, almost specifically decreased by chromyl chloride treatment. The significance of these various affinities will be discussed, and a classification of virus-like particles associated with mouse tumors and averaging 100 mμ in diameter will be presented.

* Aided by a grant of the Leukemia Society, New York.

B15. Correlative Light, Phase, Fluorescence, and Electron Microscopy of Mouse Embryo Cells Infected with Polyoma.* ELIZABETH BERECZKY, LEON DMOCHOWSKI, AND CLIFFORD E. GREY, *Section of Virology and Electron Microscopy, The University of Texas M. D. Anderson Hospital and Tumor Institute, and Department of Microbiology, Baylor University College of Medicine, Texas Medical Center, Houston, Texas.*—The nature and sequence of changes in polyoma-infected mouse embryo cells have been studied by light, phase contrast, fluorescence, and electron microscopy. After initial enlargement and change in the shape of nuclei, small dark granules, increasing in number, appear in the enlarged nuclei. Two types of inclusions develop in different nuclei, one composed of dense, homogeneous material, the other consisting of dense strands of amorphous scattered material. Following increase in size and density of the inclusions, they occasionally appear in the cytoplasm, then lysis of the cells takes place. The inclusions stain yellow for DNA with acridine-orange dye. The staining is not affected by DNase but is removed by pepsin followed by DNase. By the Feulgen method, the inclusions stain pink and later lavender-pink. In the electron microscope, the inclusions contain characteristic polyoma particles, frequently in an orderly array. The significance of these observations as to the chemical nature of polyoma virus will be discussed.

* These studies have been supported by U. S. Public Health Service grants and by an American Cancer Society grant.

B16. Studies on Mammary Glands and Mammary Tumors of Mice Bearing Grafts of Pituitary Tumors and Injected with the Bittner Virus.* LEON DMOCHOWSKI, CLIFFORD E. GREY, JACOB FURTH, AND K. YOKORO, *Section of Virology and Electron Microscopy, The University of Texas M. D. Anderson Hospital and Tumor Institute; Department of Microbiology, Baylor University College of Medicine, Texas Medical Center, Houston, Texas; and Roswell Park Memorial Institute, Buffalo, New York.*—Yokoro, Furth, and Takemoto reported the induction of mammary tumors in LAF1 low-cancer-strain mice (incidence less than 1%) given grafts of functional mammotropic pituitary tumors and the mammary tumor-inducing (Bittner) virus. Electron microscopy studies of such mammary tumors will be presented and the presence of numerous characteristic virus particles shown. The virus particles are present in much greater numbers in these mammary tumors than in spontaneous mammary tumors of virus-carrying C_3H strain mice. Similar studies of mammary glands in LAF1 mice with grafts of pituitary tumors and treated with the Bittner virus showed the presence of only a small number of virus particles. No virus particles could be observed in the pituitary tumors grafted in LAF1 mice, either treated or untreated with the Bittner virus. Similarly, no virus particles could be observed in mammary glands of LAF1 mice treated with virus alone. The implications of these observations will be discussed.

* Supported in part by a U. S. Public Health Service grant and by an American Cancer Society grant.
[1] K. Yokoro, J. Furth, and H. Takemoto, Proc. Am. Assoc. Cancer Research **3**, 281 (1961).

B17. Electron Microscopy of Amnion Cells Treated with Ribonucleic Acid from Human Leukemic Cells. S. DE CARVALHO, A. R. TAYLOR, MARY H. JONES, AND G. T. TRUFFELLI, *Cancer Research Laboratory, Rand Development Corporation, Cleveland, Ohio, and Research Division, Parke, Davis & Company, Detroit, Michigan.*—Primary caesarean amnion cell cultures inoculated with a ribonucleic acid (RNA), obtained from human leukemic and tumor cells either by exhaustive fluorocarbon extraction or by a phenol method, show a cytopathogenic effect within 16 to 48 hr.[1] The degree of cytolysis is dependent upon the concentration of RNA in the inoculum; 200–300 μg/ml produces complete lysis in 24–48 hr, while 0.3–3.0 μg/ml produces varying degrees of lysis. Examination of thin sections of RNA-treated amnion cells, osmic acid fixed and embedded in Vestopal, at 15, 24, 36, and 48 hr after inoculation revealed that the ribonucleoprotein (RNP) granules of the cytoplasm become progressively more aggregated. In the nucleus dense, irregular accumulations of granular material occur along the inner membrane surface. Viral-like particles approximately 60 to 80 mμ in diameter are formed in the cytoplasm in or near the nuclear membrane. Control cultures inoculated with medium without RNA were sectioned for comparison.

[1] J. Lab. Clin. Med. **55**, 694 (1960).

B18. The Cell Base in the Striated Duct of Normal Human Submaxillary Gland. BERNARD TANDLER, *Sloan-Kettering Division of Cornell University Medical College, New York 21, New York.*—Surgical specimens of normal human submaxillary gland were examined with the electron microscope. A striking feature of the striated duct epithelium is the multitudinous complexly folded membranes at the cell base. Although in thin sections these membranes appear to be intracellular, they are in reality intercellular as is demonstrated by numerous desmosomes which are studded on the membranes. The desmosomes are similar to those described in other epithelia, but a further substructure has been resolved. The characteristic appearance of the striated duct epithelium is due to the complex interlocking of adjacent cells, analogous to Rhodin's[1] demonstration in kidney tubules. True inflections of the plasma membranes into the cytoplasm are occasionally observed. The inflections always end blindly. A row of vesicles sometimes is seen in apparent continuity with the blind endings of the inflections. Similar rows of vesicles are also found scattered through the basal cytoplasm. The significance of the morphological findings will be discussed.

[1] J. Rhodin, Intern. Rev. Cytol. **7**, 485–534 (1958).

B19. Induced Squamous Metaplasia in the Rat Urinary Bladder. John J. Ghidoni and Boris Gueft, *Albert Einstein College of Medicine, Eastchester and Morris Park Roads, Bronx 61, New York.*—The normal transitional epithelium has an ultrastructure similar to that reported for mice. Lysosomes are frequently encountered. Noncornifying metaplastic epithelium is 4–6 cells deep. Cytoplasmic vesicles, plasma membrane interdigitations, and desmosomes are rare. Scattered tonofilaments add to the cytoplasmic density. Collapsed superficial cells have pyknotic nuclei and closely approximated tonofilaments. The layers of the 8–12 cell cornified epithelium roughly correspond to those of skin. Desmosomes and tonofilaments are abundant. Dense keratohyalin granules are intimately associated with bundles of tonofilaments. The superficial granular layer cells are enlarged and have "washed out" nuclei. The cornified layer starts abruptly. The cornified cells are composed of closely packed bundles of 75–100 A filaments bounded by plasma membranes. No nuclei or organelles are discernible. The "hollow tube" keratin pattern is present; however, much unexplained fine detail resides within this pattern.

B20 Viral-Like Inclusions in Human Liver Biopsies from Patients with Infectious Hepatitis. Alton R. Taylor, Wilton A. Rightsel, Ruth A. Keltsch, Mary H. Jones, I. William McLean, Jr., Edwin Kerr,* and Richard S. McCaughey,† *Research Division, Parke Davis & Co., and Wayne State University College of Medicine, Detroit, Michigan*—Punch liver biopsy specimens from three clinically confirmed cases of infectious hepatitis were found to contain many cells with viral-like particles. In cells only slightly involved, the ribosomal or Palade granules normally associated with the reticular and mitochondrial membranes appear to become more densely stained. They coalesce or aggregate into groups of 4, 6, or 8 to form scattered islets of 20- to 40-mμ granules, in many of which the appearance of the aggregating microsomal elements is retained.[1] These scattered groups of granules appear to form larger masses of more densely staining particles filling large areas in the cytoplasm. In this formation of larger aggregates the reticular membranes become smooth and free of granules; mitochondria appear swollen, lose their cristae and structure, and eventually become vacuolated.[2] A later stage of infection or lesion formation appears where the particles or granules are somewhat less densely stained and close packed. The cytoplasm of whole groups of cells often is filled completely with granules. The nucleus does not appear to be involved, at least in the early stages. Virus particles, 10 to 20 mμ, similar to those in the liver biopsy specimens, have been obtained from Detroit-6 tissue culture cells and fluids which were infected initially with virus isolates from blood of humans with infectious hepatitis.

* Fruehauf Fellow in Gastroenterology, Wayne State University College of Medicine, Detroit, Michigan.

† Department of Medicine, Detroit Receiving Hospital and Wayne State University College of Medicine, Detroit, Michigan.

[1] H. Braunsteiner, K. Fellinger, F. Pakesch, and A. Neumayr, Klinische Wschr. **36**, 379 (1958).

[2] W. G. C. Bearcroft, Nature **190**, 549 (1961).

Symposium SII (*continued*), Contributions of Electron Microscopy to Polymer Morphology

S11. Fiber Microscopy. Frederick Morehead, *American Viscose Corporation, Marcus Hook, Pennsylvania.*

S12. Electron Diffraction Applied to Synthetic Fibers. R. G. Scott, *DuPont Experimental Station, Wilmington, Delaware.*

Session AIII, Industrial Applications

A16. Electron Microscope Studies on Polyethylene and Polypropylene. G. W. Bailey, *Esso Research Laboratories, Humble Oil and Refining Company, P. O. Box 551, Baton Rouge, Louisana.*—Replication techniques are being used to relate the microstructural characteristics and physical properties of polyethylene and polypropylene. This study included polymer particles and molded pads. Low penetrating power and damage from heating prevents the direct examination of polymer particles in the microscope. Replication, however, has given us details of the surface structure of these particles. The spherulitic structure of these polymers in molded form has been determined by replicating etched or fractured surfaces. Marked differences in the spherulitic structure of polyethylene and polypropylene have been observed. The effect of molecular weight on spherulitic structure of both polymers has also been established.

A17. Particle Diameter Determination of Film-Forming Latexes by Electron Microscopy of the Deformed Particles. E. B. Bradford and J. W. Vanderhoff, *The Dow Chemical Company, Midland, Michigan.*—The flattening of film-forming latex particles upon drying makes their particle diameter determination difficult. Bromination and high-energy irradiation have been used to prevent this deformation; however, neither technique is universally applicable, e.g., certain acrylate copolymer particles are unaffected by bromination and are degraded by high-energy irradiation. This paper concerns the measurement of shadowed, flattened latex particles. Monodisperse polystyrene spheres of known diameter are used to determine the magnification and shadow angle of each exposure. From these measurements the original diameter of the deformed particle can be calculated, assuming that (1) the configuration of the flattened particle is a segment of a sphere,

(2) the calibration particles do not deform upon drying, and (3) the substrate is level over the area of the exposure. The applicability of this technique is demonstrated by measurements of heat-deformed monodisperse polystyrene particles. The results for various film-forming latexes are presented.

A18. Study of Synthetic Rubber Latices by the Electron Microscope. W. Rupar and J. M. Mitchell, *Polymer Corporation Limited, Sarnia, Ontario, Canada.*—In emulsion polymerization the number and size of the latex particles govern not only the colloidal behavior of the reacting system but also are a major factor in determining the rate at which conversion of the monomer progresses. Because of the importance of these factors a wide variety of synthetic latices have been studied with the electron microscope. The changes in the latex particles—from the swollen monomer polymer particles at low conversion to the final latex particles after removal of the unreacted monomer—have been observed for a typical SBR system. The effect of various post polymerization treatments on the size and size distribution of the latex particles has also been observed. Representative electron photomicrographs are included as are a discussion of the methods used in the study and the significance of the data obtained in relation to specific latex properties.

A19. An Electron Stain to Reveal Hydroxyl-Ion Distribution on Corroded Glass Surfaces. Carl W. Melton and Charles M. Schwartz, *Battelle Memorial Institute, 505 King Avenue, Columbus 1, Ohio.*—An electron staining method has been developed to reveal the distribution of hydroxyl ion on the surface of corroded glass. A chemical reaction is involved which deposits MnO_2 and metallic silver at the site of hydroxyl-ion concentration. Light and electron micrographs of stained pecimens will be shown.

A20. Insulating Organic Deposits on Precious Metal Electrical Contacts. Saul W. Chaikin and Donald K. Stellman, *Stanford Research Institute, Menlo Park, California.*—Contacts in hermetically sealed relays can acquire insulating deposits merely upon storage. An investigation of this phenomenon in controlled laboratory experiments revealed that pure organic vapors and vapors from outgassing in plastic insulation can react spontaneously at some precious metal surfaces to form minute, but significant, deposits of insulating organic polymer. Replica methods have permitted following the gradual buildup of these otherwise invisible deposits over a period of many months. This study has emphasized gold and palladium as contact metals; palladium is considerably more reactive than gold in developing surface deposits from organic vapors. Pure hydrocarbons (ethylbenzene, limonene, and octene-1) were studied, as well as insulating materials (Kel-F and Teflon). The mechanism of formation of the deposits is presumed to be catalytic, and electron microscope evidence is presented to support this. The occurrence of the phenomenon was confirmed by viewing the organic deposit directly, in the electron microscope, as it formed on fine wires over a two-month period.

A21. Electron Microscopic Examination of High-Altitude Particulate Material. Douglas S. Hallgren, *Ernest F. Fullam, Inc., P. O. Box 444, Schenectady 1, New York,* and James P. Friend, *Isotopes Inc., Westwood, New Jersey.*—A study has been made of high-altitude particulate material collected in high-altitude aircraft. A collection device attached to the nose of U-2 aircraft allowed samples to be collected at known altitudes without contamination from ground level materials. Large numbers of particles were collected, many of which were identified as ammonium sulfate and ammonium persulfate by electron diffraction. From the parameters of the collection device and from the size distribution of the particles collected, an estimate was made of the total stratospheric burden of these materials.

Session BIII, Studies on DNA and RNA—Proteins—Techniques

B21. Visibility Studies on DNA Stained with Uranyl Salts. Michael Beer and C. Richard Zobel, *The Johns Hopkins University, Baltimore 18, Maryland.*—DNA fibrils, when stained in solutions of uranyl acetate or uranyl nitrate at *p*H 3.5, are detectable in the electron microscope. When the DNA is obtained from solutions with a concentration of 1 mg/ml the fibrils are aggregates readily visible by staining. When the solutions have a DNA concentration below 5γ/ml, many of the fibrils have diameters near 20 A and probably are single molecules. For these, an attachment of three to four uranyl ions per base pair leads to about 7% contrast at 50 kv with an objective aperture of 3.5×10^{-3}. With two uranyl ions per base pair DNA is still detectable, but with one or less uranyl ion per base pair the molecule is not detectable by the methods used. The significance of these results in cytological and molecular studies is discussed.

B22. On the Electron Microscopy of DNA in Protein Films. A. Kleinschmidt, *Institute of Hygiene, University Frankfurt am Main, Frankfurt am Main (Germany).*—Pure DNA, mixed with cytochrome *C* (0.01%) and ammonium acetate (1 *M*) solution, can be spread on the watery surface of a Langmuir trough. Using a quantitative method for the preparation and the transfer to carbon—Formvar support it is possible to demonstrate morphologically: (a) the equal distribution of a multiplicity of single incoherent DNA threads. The contrast arises by depositing platinum along the unbranched macromolecules. The analysis of the lengths also shows the statistical distribution of molecular weights; (b) some morphological effects of physical or chemical agents on the DNA threads; (c) by the use of subcellular components (e.g., of bacteria as DNA participants in the mixed protein film) the possible intracellular structure of continuity of extremely long and rather closely packed threads.

B23. Helix⇄Coil Transformations of Anisometric Macromolecules. Robert V. Rice, *Mellon Institute, Pittsburgh 13, Pennsylvania.*—Thermal-phase transformation of three-stranded helices (collagen) and two-stranded helices (DNA) was previously studied. TMV-RNA, a one-strand helix, has now been studied by the Hall mica replica technique. From salt solutions at room temperature RNA appears as irregularly contoured rods (weight average particle length, 1170 A; diameter, 30 A). This morphology appears to be consistent with a recently proposed model for RNA in solution. Only globules were obtained from hot salt or pure water solutions of RNA above its melting temperature. Only globules were seen from solutions of weakly ionized synthetic polyelectrolytes or water-soluble polymers. Upon cooling previously heated RNA salt solutions the rod-shaped morphology reappeared. Apparently macromolecules with appreciable secondary bonding retain their (helical) structures when prepared below their melting temperature, but the free-draining random coils become compacted particles of maximum density when prepared by usual drying techniques.

B24. Fine Structure of Keratin.* G. E. Rogers, *Division of Protein Chemistry, C.S.I.R.O., 343 Royal Parade, Parkville N.2, Melbourne, Australia.*—Electron microscopy of ultrathin sections of araldite embedded keratinous structures,[1,2] e.g., porcupine quill, wool, and hair, has consistently revealed their α-keratin content to consist of microfibrils 70–80 A in diameter, which are aligned with the fiber axis and embedded in an apparently amorphous protein matrix rich in sulfur. The question arises as to whether the microfibril itself possesses substructure resolvable by electron microscopy rather than consisting simply of tightly packed protein α-helices. High-resolution electron micrographs of sections post-strained with lead hydroxide have revealed a number of subfibrils $\sim$20 A in diameter within each microfibril. Consideration of this result together with recent x-ray studies indicates that each subunit consists of 3 α-helices.[3]

* This paper to be read by Harold P. Lundgren in Symposium SI.

[1] G. E. Rogers, J. Ultrastructure Research **2**, 309 (1959).

[2] G. E. Rogers, Ann. N. Y. Acad. Sci. **83**, 378 (1959).

[3] R. D. B. Fraser, T. P. MacRae, and G. E. Rogers (to be published).

B25. Observation of Myosin in the Electron Microscope. F. D. Carlson and C. Richard Zobel, *The Johns Hopkins University, Baltimore 18, Maryland.*—Shadow-cast preparations of myosin from rabbit skeletal muscle have been observed in the electron microscope under high-resolution conditions. Rodlike particles of varying widths and lengths have been observed. Estimates of the degree of aggregation have been inferred from dimensional analysis of the rod-like particles. Depending on the solvent from which the myosin has been cast and the substrate on which the particles are supported, particles with minimum widths of approximately 20 and 40 A have been observed. The state of the myosin in the various solvents has been determined by centrifugation.

B26. Advantages of a Phosphate Buffer for OsO_4 Solutions in Fixation. G. Millonig, *The Rockefeller Institute,* New York 21, New York.*—Since the sodium mono- and diphosphate exists as an effective buffer system in the body fluids of animals, it has seemed reasonable to test it as a vehicle for OsO_4 in fixation of biological tissues. An isotonic ($\Delta = -0, 56°$) solution at *p*H 7.3 of the following composition was tested sol. *A*: 2.26% $NaH_2PO_4 \cdot H_2O$; sol. *B*: 2.52% NaOH; sol. *C*: 5.4% glucose ($\Delta = -0, 56°$); sol. *D*: 41.5 ml sol. A+8.5 ml sol. *B* (essentially according A. v. Muralt); Fixative: 45 ml sol. D+5 ml sol. C+0.5 g OsO_4. It has been found that this solution is stable for several weeks, if stored in the refrigerator in a clean bottle. In comparative studies, mainly with the veronal-acetate buffer+osmium and on different animal tissues, the phosphate buffer seems to prevent extraction of the cytoplasmic matrix, preserves the glycogen and fibrillar elements and gives an uniform fixation at different levels in the tissue block.

B27. Concentration of Small Cells for Ultrathin Sectioning.* Arthur L. Cohen and Joseph M. Harb, *Oglethorpe University, Atlanta, Georgia.*—For ultrathin sectioning, small cells and particles are usually concentrated into a pellet by centrifugation. This method is impracticable if the cells are few in number, tend to stick to the sides of the vessel, form a very fragile pellet, or are damaged by this treatment. For all these reasons we found it necessary to develop another method for our studies on the ultrastructure of Myxomycete swarm cells. Small disks punched out of membrane filter (27 A, Gelman Instrument Company, Chelsea, Michigan) are placed on a simple holder, and the suspension of fixed cells concentrated on the filter by suction. The cells are held in place on this filter by the final addition of a drop of egg albumin which is coagulated by the fixative. The disk is dehydrated, embedded, and sectioned in the usual manner.

* Supported by grants from the National Institutes of Health and the National Science Foundation.

Session AIV, Instrumentation and Electron Diffraction

A22. Improved Method for Astigmatism Correction. Donald O'Hara and Michael Beer, *Thomas C. Jenkins Department of Biophysics, Johns Hopkins University, Baltimore 18, Maryland.*—Accuracy of astigmatism compensation depends on the closeness with which the pole piece astigmatism is known. Since the absolute error in determining the magnitude of astigmatism increases with the magnitude, a more accurate method for measuring the pole piece astigmatism would be to compensate partially with a precisely known astigmatism and to measure the small resultant. Then a subtraction of the corrective astigmatism from the resultant would give the angle and magnitude of the uncompensated astigmatism. By considering astigmatism as a vector with length equal to the magnitude of the astigmatism, A, and with an angle, 2ϕ, twice that measured on the photographic plate, it is possible to add superimposed astigmatisms vectorially. This allows calibration of the compensation controls for the value of A_e and $2\phi_e$, produced at each setting and consequently allows accurate determination and rapid correction of the pole piece astigmatism.

A23. A Three-Specimen Holder for the RCA EMU-3 Electron Microscope. Douglas S. Hallgren, *Ernest F. Fullam, Inc., P. O. Box 444, Schenectady 1, New York.*—A specimen holder has been built which permits examination of three specimens without breaking vacuum. This sample holder has been found to be useful in comparing several similar samples. Insertion of a switch in the line to the plate drive mechanism of the microscope allows double exposures to be made. This makes it possible to superimpose a grating replica on an unknown sample for more accurate measurement of particles or structures. In electron diffraction a calibration pattern can be superimposed without having the interference of the calibration pattern during the scanning.

A24. Effect of Polyester Embedments on Microscope Maintenance. Robert E. Druce, Max R. Clevenger, and Frank N. Low, *Department of Anatomy, Louisiana State University School of Medicine, 1542 Tulane Avenue, New Orleans 12, Louisiana.*—The relative effects of methacrylate and polyester sections on cleaning problems in two microscopes indicate that methacrylate produces a higher contamination rate. A yellowish-brown deposit on objective aperture and pole piece, traceable to methacrylate sublimation, was conspicuous in an RCA-EMU-3C, while contamination was barely visible in an RCA-EML-1B after comparable exposure to polyester preparations. Cleaning procedures in the latter were reduced. Polyesters possess a thermostable, insoluble matrix that renders mounted sections amenable to clearing by heat (200–250°C) and organic solvents (acetone/ether, CCl_4, etc.). Mixtures containing the polyester Selection 5003 and *n*-butyl methacrylate in 50/50 or 60/40 proportions withstand clearing without damage to tissue fine structure. Heavy metal compounds in organic reagents stain sections effectively. In these preparations methacrylate removal by heat and solvent clearing is indicated by minimal contamination problems during one year of use.

A25. Sputtering Experiments on Thin Films Inside the Electron Microscope. Helmut R. Poppa, *Convair-Astronautics Division, General Dynamics Corporation, Department 592–50, P. O. Box 166, San Diego 12, California.*—Provisions have been made to expose thin film specimens consecutively and repeatedly to the imaging electron beam and to a beam of noble gas ions inside an electron microscope. Ions of well-defined energies were provided by a low-voltage discharge-ion gun attached to the specimen chamber of the electron microscope. Electron microscopy and selected-area electron diffraction were used to record structural changes of the films and electron absorption measurements were employed to monitor film thicknesses to a high degree of accuracy. The following applications will be mentioned: (1) measurement of sputtering yield constants of polycrystalline silver for low ion energies, (2) thickness reduction (polishing) and disintegration of polycrystalline and single crystalline silver films by sputtering, (3) micromachining of silver films by selective ion etching.

A26. A Split Specimen Holder Heating Stage for the RCA EMU-3.* R. Sprague, *Research Laboratory, National Carbon Company, Division of Union Carbide Corporation, Parma 30, Ohio.*—A simple heating stage for the RCA EMU-3B has been constructed which permits heating of the specimen directly. A split specimen holder forms the two poles for the electrical resistance heating of conductive specimens or the resistance heating of standard EM specimen grids for nonconductive specimens. Problems such as temperature control, outgassing, sputtering of metals onto the specimen, and calibration attempts will be discussed.

* This research was sponsored in part by the Air Research and Development Command and the Air Material Command, U. S. Air Force.

A27. Study of the Rate of Contamination in Reflection Electron Diffraction. Eiji Yoda and Benjamin M. Siegel, *Department of Engineering Physics, Cornell University, Ithaca, New York.**—Investigations of reactions occurring at surfaces of solids by electron diffraction is severely limited by contamination layers which form on any surface exposed to an electron beam in a conventional vacuum system. To overcome this limitation we have designed a chamber, cooled to −165°C, which surrounds the specimen. By carefully stopping the chamber to provide minimal apertures for the electron beam, the rate of contamination has been reduced as much as 100×. The factors controlling the rate of contamination on various surfaces (e.g., alkali halides, metal single crystals) under varying conditions have been studied by observing the decay of intensity of given electron diffraction spots during exposure to the electron beam.

* Supported in part by the Advance Research Project Agency of the Department of Defense.

A28. Electron Diffraction Studies of Condensing Semiconductor Films. G. G. Via, *IBM Command Control Center, Federal Systems Division, Kingston, New York.*—Nucleation and epitaxial growth of germanium and silicon films were studied by electron diffraction during the actual film deposition. The specially built reflection-diffraction apparatus was equipped with two electron-bombardment evaporation sources, an adjustable sample holder providing a controlled substrate temperature, and outside screen photography of the electron diffraction pattern. Titanium getter pumps and liquid-nitrogen traps aided in obtaining a vacuum of 5×10^{-8} mm Hg during evaporation. The growth of evaporated Ge on Ge, Si on Si, and Ge as well as Si on CaF_2 was investigated. In all cases, single-crystalline wafers with well-prepared surfaces were used as substrates. At a sufficiently high substrate temperature ($T_{Ge}>560$°C, $T_{Si}>800$°C), Kikuchi lines and well-developed Laue spots indicated a nearly perfect single-crystalline deposit even on CaF_2, if the film was grown on a clean (111) plane. The conditions leading to a less perfect growth will be discussed in detail.

Session BIV, Virology—Structure, Development, and Reactions

B28. Detection of Poliovirus Particles in Monkey Kidney Cells. Heather Donald Mayor and Liane E. Jordan, *Baylor University College of Medicine, Houston 25, Texas.*—Stuart and Fogh[1,2] have demonstrated polivirus particles in ultrathin sections of infected FL and HeLa cells. Although poliovirus propagates readily in monkey kidney cells there have been no reports demonstrating virus particles in thin sections of these cells. This is not surprising as monkey kidney cells release poliovirus rapidly and the fixative osmium tetroxide penetrates most tissues very slowly. The present study of ultrathin sections of monkey kidney cells infected with poliovirus (types 1 and 2 virulent and attenuated) has revealed cytoplasmic arrays of spherical particles with diameters approximately 27 mμ. Similar particles were found occasionally in "blebs" at the cell walls. Particles were detected only when infected cultures were incubated at 30°C. At this temperature fully infective poliovirus is formed but its release is inhibited. Particles were not encountered in control preparations or when infected cultures were incubated at 37°C. Preliminary observations using acrolein fixation will also be reported.

[1] D. C. Stuart, Jr., and J. Fogh, Exptl. Cell Research **18**, 378–381(1959).
[2] J. Fogh and D. C. Stuart, Jr., Virology **11**, 308–311, 1960.

B29. Observations on the Structure of Influenza Virus. Dan H. Moore, Maurice C. Davies, S. Levine, and M. E. Englert, *The Rockefeller Institute, New York 21, New York, Lederle Laboratories, Pearl River, New York.*—The fine structure of influenza virus has been studied, and a correlation has been made between structural elements found and the known chemical and biological properties of this virus. Most particles of standard virus were spherical and contained a dense nucleoid surrounded by a zone of lesser density, which in turn was enclosed within a complex structure consisting of an osmophilic dense shell covered with protruding spines somewhat similar to those of a minute echinoderm. Preparations of incomplete virus differed markedly from preparations of standard virus in being void of nucleoids, irregular in shape, and of a wide range in size. Negative staining with phosphotungistic acid gave no evidence for the existence in intact virus of the soluble antigen or hemagglutinin particles observed after splitting the virus with ether. The lipid fraction, which constitutes about one-third of the volume of the virus, seems to be located, from osmium staining, in the inner dense portion of the spiney coat. In a standard virus particle with an average diameter of 115 mμ the nucleoid occupies about 2%, the intermediate zone about 30% to 35%, and the fringed coat the remaining two-thirds of the total volume.

B30. Adsorption and Penetration of Mammalian Viruses into Their Hosts Observed by Electron Microscopy. Samuel Dales, *The Rockefeller Institute, New York 21, New York.*—Early stages of virus-host cell interaction were examined using two model systems, of which one comprised adenovirus 7 and HeLa cells and the other vaccinia and strain L cells. A technique, based on negative staining, was developed for visualizing in three dimensions the contact between virus and shell membrane and the observations obtained using this method were correlated with those made on thinly sectioned cells. After contact is established between the capsomeres and the cell surface the membrane invaginates below the virus particle and eventually enfolds it. Thus virus particles are taken into the cytoplasm within small vesicles and, presumably, transported in them to sites of viral multiplication. Damaged or incomplete virus particles, present in small proportion in purified preparations, are also adsorbed onto the cell membrane and phagocytozed.

B31. Coliphage *T2* Infection of Normal and Plasmolyzed Cells of *Escherichia coli*.* EUGENE H. COTA–ROBLES, *Division of Life Sciences, University of California, Riverside, California.*—Sections of normal *Escherichia coli* infected with coliphage *T2* present a characteristic pattern yet a wide variety of structural units. The cell wall and cytoplasmic membrane are well defined as is the granular nature of the cytoplasm. Lysing cells reveal that lysis results from a relatively small tear in the retaining envelopes. The cytoplasmic constituents leaving the lysing cell demonstrate a fibrillar pattern. The structure remaining after lysis consists of the cell wall and cytoplasmic membrane. The cytoplasmic membrane is often seen projecting into the cytoplasmic space in a defined manner. Such projections are large and demonstrate an organized vesicular arrangement. In contrast to the above findings, if cells are plasmolyzed prior to virus infection the cells appear normal, suggesting that such cells can not be effectively infected with *T2*. Virus attachment is occasionally observed yet the virus is electron dense indicating that it still retains its DNA.

* This work was supported in part by the Cancer Research Coordinating Committee of the University of California and the American Cancer Society.

B32. Specific Agglutination of Phages and Polio Virus by Antibody Molecules as Seen in the Electron Microscope.* THOMAS F. ANDERSON, NOBUTO YAMAMOTO AND KLAUS HUMMELER, *The Institute for Cancer Research and Children's Hospital, Philadelphia, Pennsylvania.*—When bacteriophages *P22* and *P221* are separately mixed with homologous rabbit antisera or gamma globulin and mounted on grids with potassium phosphotungstate, the negatively stained particles are aggregated and have a fuzzy appearance. Under high resolution the fuzziness is seen to be due to the attachment to the particles of thin fibers which form connecting bridges between them and at the same time keep the particles from touching each other. Other fibers are seen to form loops on the surfaces of individual particles. The fibers appear to range from 100 to 200 A in length and from 20 to 30 A in width. The reactive sites appear to be located at their tips where there is no marked thickening of the structure. Since neither attached fibers nor aggregation of particles is seen in preparations with heterologous sera, it seems clear that the fibers are antibody molecules specifically attached to haptenic groups on the surface of the phage particles. Similar results were obtained with the virus of poliomyelitis and its antibodies.

* This work was supported in part by the National Science Foundation and the Office of Naval Research.

B33. Studies on Fine Structure of Foot-and-Mouth Disease Virus. SYDNEY S. BREESE, JR., AND RODES TRAUTMAN, *Plum Island Animal Disease Laboratory, A.D.P.R.D., A.R.S., U.S.D.A., Greenport, New York.*—Foot-and-mouth disease virus (FMDV), type A, from infected guinea-pig foot-pad vesicular fluid was examined for fine structure in both phosphotungstic acid and uranium shadowed preparations on carbon coated grids. The virus was prepared for electron microscopy by CsCl isodensity ultracentrifugation to give a light-scattering virus zone which was removed and dialysed against NH_4OAc, *p*H 7.3. Phosphotungstic acid penetration was less than with many other viruses, hence shadowed specimens were also used extensively to study the structure. Regular polyhedral models of 12, 20, 32, and 42 subunits were constructed and analyzed for distinguishing features exhibited by both virus and model. Mixtures of FMDV and bacteriophage ϕ×174, which have approximately the same diameters, revealed that FMDV had smaller and more numerous subunits than the 12 of ϕ×174. The icosahedral model with 42 subunits was favored over the modified dodecahedral model of 32 subunits for FMDV, although there was no unequivocal evidence that these represented the ultimate structure of FMDV.

B34. Structure and Development of Vesicular Stomatitis Virus. A. F. HOWATSON AND G. F. WHITMORE, *Department of Medical Biophysics, University of Toronto, 500 Sherbourne Street, Toronto 5, Canada.*—Vesicular stomatitis virus grown on *L* cells cultivated in suspension was partially purified by differential centrifugation and examined by the negative contrast method. The typical virus particle is in the form of a right circular cylinder of average diameter 68 mμ and length 141 mμ, topped at one end by a hemispherical cap, the total length being 175 mμ. There are indications in many particles of a central cylindrical hole of diameter 17 mμ and variable length extending from the plane end of the particle. Thin sections of infected cells show many protuberances at the cell surface. Some of these can be distinguished from the type of protuberance that occurs in control as well as in infected cells by their high density, uniform diameter, and fairly uniform length; these are interpreted as virus particles in the process of development. Particles of similar appearance but unattached to the cell surface are seen in the vicinity of infected cells; these are interpreted as mature virus particles.

B35. Morphology of the Development and Release of Vesicular Stomatitis Virus. R. S. STONE, M. I. SELLERS, AND T. HIRAMOTO, *University of California School of Medicine, Department of Pathology, University of California Medical Center, Los Angeles 24, California.*—Vesicular stomatitis virus, New Jersey type, was grown in HeLa cell cultures and in cultures of mouse embryo brain. In addition the pathogenesis of vesicular stomatitis injection was studied *in vivo* in mice at the fine-structure level. In tissue cultures test-tube-shaped viral particles, having one rounded and one flattened end, 170×60 mμ, are present free in the cytoplasm and in vesicles. The virus has a peripheral double contour and a central-electron dense core. Also present are circular cross sections 60 mμ in diameter. In occasional instances a spiral structure has been identifiable. This possession of structural polarity is apparently unique to this animal virus.

B36. Cell Surface Reaction to *B*-Virus Infection. JOHN MATHEWS AND DARWIN A. BUTHALA, *The Upjohn Company, Kalamazoo, Michigan.*—Monolayers of HeLa, rabbit kidney, and rat embryo kidney cells grown on glass cover slips were infected with *B*-virus. At appropriate times after infection the cell monolayers were washed, fixed and dehydrated. Chromium-shadowed carbon replicas were prepared. Electron-microscopic observation revealed progressive changes in cell surface morphology. Emergence of virus was noted at a time and site characteristic for each of the cell lines. Released virus was observed to accumulate on certain cell structures.

B37. Intracellular Development of *B*-Virus. DARWIN A. BUTHALA AND JOHN MATHEWS, *The Upjohn Company, Kalamazoo, Michigan.*—By using the techniques of thin sectioning and electron microscopy, the various stages of intracellular development of *B*-virus in Chang human liver and rat embryo kidney cells were investigated. The progressive development of intranuclear viral crystaloids made up of structures composed of a single wall surrounding a central nucleoid was observed. Subsequent stages of the release of intranuclear virus into the cytoplasm, the progressive development of virus at the cell membrane and the release of mature virus into the extracellular milieu completed the cycle.

Symposium SIII, The Fine Structure of Viruses

S13. Recent Advances in Fine Structure. A. F. HOWATSON, *Department of Medical Biophysics, University of Toronto, 500 Sherbourne Street, Toronto 5, Canada.*—During the past few years improvements in the techniques of replication, shadow casting and thin sectioning have enabled the high resolving power of the electron microscope to be applied more effectively to the study of the structure of viruses and macromolecules. Recently "negative contrast" obtained by the use of heavy metal salts such as phosphotungstate has proved to be a powerful tool for demonstrating biological structures. Some examples of the type of information obtained by this technique will be discussed.

S14. Animal Virus Structure. PETER WILDY, *Department of Virology, University of Glasgow, Glasgow, Scotland.*—Animal virus particles have for some time been known to occur in three main shapes; (1) as bricks (e.g., the pox group); (2) as approximate spheres (e.g., the enteroviruses); and (3) as rods (e.g., the nuclear polyhedrosis viruses). Until recently, little was shown of their chemical structure or detailed morphology. Now, owing largely to advances in preparative techniques, we are amassing information upon both the chemical nature of viral components and the way these are fitted together. Though this information is at present patchy and is restricted to rather few virus species, patterns are emerging which have features in common, not only within the field of animal viruses, but also within plant viruses and some bacteriophages.

At its simplest, the infective virus particle (*the virion*) comprises nucleic acid (believed to carry genetic information) encased in a protective protein coat (the *capsid*). This coat appears to be composed of a number of morphological subunits (the *capsomeres*) which are packed in a symmetrical way. More elaborate virions may be embellished with additional layers, envelopes, which do not appear to possess symmetry.

Two forms of symmetry have been recognized in the capsids of animal viruses; (a) helical symmetry (e.g., the myxoviruses) and (b) cubic symmetry (e.g., polio virus, tipula iridescent virus). Little is yet known of the symmetry resident in the brick-shaped virons.

The only type of cubic symmetry so far encountered in animal virus is 5:3:2 symmetry. This requires a multiple of 60 protein subunits in the capsid. The number of capsomers comprising capsids of several viruses has now been estimated, and in no instance has it been a multiple of 60. This appears to be because each capsomere is composed of a number of symmetrically arranged protein subunits. There are a limited number of ways in which capsomers of this sort may be packed in accordance with 5:3:2 symmetry. The arrangements most commonly encountered give rise to a series of potentially icosahedral bodies with capsomeres situated on the corners and on the edges. The total number of capsomers comprising members of this series is given by the formula $10(n-1)^2+2$, where n is the number of capsomeres between and including these on any adjacent fivefold axes. Several capsids in this series have been found.

The study of virus structure becomes meaningful only when considered in terms of function. The viral growth cycle is conveniently summarized by the following stages: (1) attachment of the virion to the cell; (2) penetration of the genetic material; (3) eclipse phase, in which infectivity disappears; (4) independent synthesis of viral components; (5) assembly of new viral components; and (6) release of new virions.

With animal viruses, the mechanisms underlying these events are incompletely understood and their elucidation is currently the central problem in virology. Electron microscopy of thin sections has provided some interesting information on the assembly process with some viruses. On the other hand, studies of fine structure in virus particles have now raised a number of interesting points concerning the way correct assembly of components may be specified, and these will be discussed.

S15. Electron Microscopy of Nucleic Acids and Proteins. C. E. HALL, *Department of Biology, Massachusetts Institute of Technology, Cambridge, Massachusetts.*—This discussion is concerned mainly with the determination of size, shape, and morphological features of nucleic acids and proteins with the electron microscope principally through the use of the shadow-casting process. These observations may be of interest here in that they deal with virus components or substances like the components of viruses. Native DNA has been observed as single-stranded, double-stranded, and in some instances as pairs of double strands side by side. Heat denatured DNA assumes a random coil configuration but the separated strands recombine to form rigid rods when cooled slowly. Similarly, synthetic polynucleotides in single strand, random-coil configuration can be induced to form double or triple stranded rods under certain conditions. The size and shape of protein molecules can be measured within certain tolerances down to molecular weight 40 000. One of the smallest viruses, bacteriophage ϕX-174, consists of a single-stranded DNA surrounded by a protein shell, showing evidence that the protein molecules are packed over the surface with icosahedral symmetry.

S16. Structures of Bacteriophages and Their Variations.* THOMAS F. ANDERSON, NOBUTO YAMAMOTO, AND DONALD H. WALKER, JR., *The Institute for Cancer Research, Philadelphia 11, Pennsylvania.*—Until now three main structural classes of bacteriophage have been discovered: (1) Some, such as the well-known *T* phages, contain double helices of DNA enclosed in polyhedral head membranes to which functional appendages or tails are attached which facilitate the injection of DNA into host cells. (2) Others, such as ϕX-174 and *f2*, contain single-stranded DNA or RNA enclosed in small protein capsids made up of discreet numbers of capsomers. Finally (3), some, such as the phage discovered by Kottmann, are shaped like tiny bacilli, but little more is known about them. The general uniformity of structure of a given bacteriophage is most striking. Indeed, when major variations in size are found, as in *P*1, many questions as to their significance arise. A second striking fact is that unrelated phages, like *T*2 and *P*2, for example, often have very similar devices for infecting host cells. This could imply that during evolution the same improbable devices have been invented independently for each phage type. Recently, however, two morphologically and serologically unrelated bacteriophages (*P*22 and *P*221) have been observed to exchange genetic information. So, instead of each type having to make all its evolutionary inventions itself, a bacteriophage might well be able to acquire and utilize genetic descriptions of inventions developed by other types. Such exchanges of genetic information could account for the fact that similar morphological features are found in a great variety of phage types.

* This work was supported in part by the National Science Foundation and the Office of Naval Research.

S17. Correlation of Biochemical and Biophysical Properties of Viruses with Their Structure. PAUL KAESBERG, *Department of Biochemistry, University of Wisconsin, Madison, Wisconsin.*—Much detailed structural information is now known concerning tobacco mosaic virus (TMV), including its molecular weight, the molecular weight of its nucleic acid and the molecular weight, amino acid sequence, and arrangement of its protein subunits. Electron micrographs of TMV are, in general, in agreement with the results of other biophysical studies but do not show as much detail as might be expected from the available resolving power. Considerably less is known concerning spherical plant viruses, both from the point of view of physico-chemical measurements and of electron microscopy. Many spherical viruses appear polyhedral in shape in electron micrographs of shadowed preparations. Negative staining shows that this structure is a consequence of protuberances on the surfaces of the viruses. Except in the case of turnip-yellow mosaic virus and one or two other viruses these protuberances are not sufficiently clear to be countable, but their number is smaller than the number of subunits obtained from chemical or biophysical analyses.

Several viruses cause the production of viruslike particles which lack nucleic acid. Electron micrographs confirm other physical studies which indicate that these particles are hollow protein shells.

Negative staining and positive staining experiments with uranyl acetate show that the bromegrass mosaic virus consists of protein subunits which form a shell surrounding a core of nucleic acid disposed in such a way as to leave a small central cavity in the virus.

Session AV, Specimen Preparation and Replicating Techniques

A29. Ultrathin Sectioning of Microcrystals for the Electron Microscopy of Their Structure. JOHN H. L. WATSON AND ROBERT R. CARDELL, JR., *Edsel B. Ford Institute for Medical Research, Detroit 2, Michigan.*—Application of well-known ultrathin sectioning techniques to the sectioning of single microcrystals of alpha iron in investigations of a nonbiological nature have already been reported from this laboratory. The work has been extended to colloidal crystal systems of *b*-FeOOH to derive information concerning their packing in sediments, the shape and dimensions of their cross sections, and their fine structure. The "schiller layers" of the tetragonal *b*-FeOOH have been demonstrated to be cubic packing of microcrystals of square cross section (670 Au side), separated from each other by about 60 Au in the final preparation. The single microcrystals themselves are deduced to be a cubic packing of long rods of square cross section, (25 Au side). Both longitudinal and transverse sections gave consistent observations, and showed that while the elongated sides of the crystals were smooth, the ends were tapered and uneven. The crystal growth was concluded to be more rapid in the long direction and of equal but slower rates in the other two directions. The technique has also been applied briefly to $H_2WO_4 \cdot H_2O$.

A30. X-Ray Diffraction Analysis of Methacrylate Embedded Specimens. JONATHAN PARSONS, ROBERT R. CARDELL, JR., AND JOHN H. L. WATSON, *Department of Physics, Edsel B. Ford Institute for Medical Research, Henry Ford Hospital, 2799 West Grand Boulevard, Detroit 2, Michigan.*—In the application of biological techniques of ultrathin sectioning to the study of the structure of colloidal crystals and other materials the question arises as to whether or not the structure of the crystals is altered in any way during the usual methacrylate embedding processes. X-ray diffraction patterns are made of the crystalline materials before and after they have been embedded in methacrylate. Comparison of the two patterns indicates whether changes have occurred. No changes have been noted in applications of the embedding techniques with tungstic acid monohydrate, ferric monohydroxy oxide, or human bone.

A31. Studies Concerning the Operation of the Thermal Precipitator. H. FROULA AND A. F. BUSH, *Department of Engineering, University of California, Los Angeles 24, California.*—Thermal precipitation is a phenomenon in which aerosol particles located between two surfaces at different temperatures are driven toward and deposited upon the colder surface. Thermal precipitators, utilizing this phenomenon, have been used for collecting aerosol particles for light and electron microscopy although thermal precipitation itself has not been fully understood. At the 1958 meeting of this society, one of us (H. F.) described a very flexible experimental thermal precipitator. The present paper is concerned with research done with this device during the past three years and with the use of thermal precipitation in microscopic studies of aerosols.

A32. A Technique for Handling and Mounting Fine Particles for Electron Microscope Examination. C. R. MORELOCK AND A. S. HOLIK,* *General Electric Research Laboratory, Schenectady, New York.*—It is often necessary to determine the size, shape, and population density of very fine particles with the electron microscope. A technique is described which utilizes the electrostatic properties of Dow Saran Wrap for handling fine particles and their subsequent mounting on carbon films.

* Speaker

A33. High-Temperature Replication and Vacuum Firing of Kaolinite. R. Borasky and C. A. Sorrell,* *Electron Microscope Laboratory and Department of Geology, University of Illinois, Urbana, Illinois.*—In order to obtain a replica representative of the surface of a material at an elevated temperature, oriented aggregates were heated on molybdenum boats in high vacuum and shadowed with platinum while hot. Carbon was evaporated normal to the surface after cooling, replicas were stripped by hydrofluoric acid treatment and placed on coated grids, and observations were made with the electron microscope. A kaolin with appreciable potash content was heated to 1063° and 1260°C for 20 hr in vacuum and replicated while hot. Control samples were fired in air for the same time at the same temperatures and replicated by conventional techniques. Vacuum firing results in much better phase development than does equivalent air firing, possibly because of greater volatility of impurities. X-ray investigations agree with electronoscopic observations and indicate that time is an important factor in development of cristobalite in the presence of impurities.

* Present address: Department of Geology, Miami University, Oxford, Ohio.

A34. A Modified Platinum-Carbon Replica Technique and an Application to the Study of Diamond Powders. M. Kranitz and M. Seal, *Engelhard Industries, Inc., 497 Delancy Street, Newark 5, New Jersey.*—A method of simultaneous evaporation of carbon and platinum is described in which the usual solid carbon-platinum rods are replaced by plain carbon rods with insert tips. The tips are pellets of porous carbon on which platinum has been deposited. Pellets of this type are widely used as catalysts and are commercially available. The pellets are used once only. They are small, do not need sharpening, are easy to replace, and are economical in the use of platinum. Carbon and iridium may also be evaporated together in a similar way. An application of the method to the study of diamond powders is also described.

A35. A New Method for Producing Platinum Preshadowed Carbon Substrates. Charles F. Cook, Jr., *U. S. Army Signal Research and Development Laboratory, Fort Monmouth, New Jersey.*—A novel approach to the evaporation of platinum and carbon will be described. The technique is capable of producing, routinely, preshadowed carbon replicas with a resolution of better than 30 A. The technique consists of evaporating platinum in wire form from a specially shaped carbon rod which later is evaporated to coat the shadowed specimen without breaking the vacuum or rotating the specimen.

A36. Improved Two-Stage Carbon Method for Replicating Fracture Surfaces. J. A. Coles and A. W. Danko, *Composition and Performance Department, Westinghouse Electric Corporation, East Pittsburgh, Pennsylvania.*—In replicating the rough surfaces of fatigue-fracture copper alloys and fractured ceramic samples for electron microscopy, a simple rotating method was developed for applying the carbon substrate. As it was imperative that the sample surfaces be not destroyed, the two-stage carbon method was used in this study rather than the direct carbon-replication technique. Parlodion with ethyl acetate as a solvent instead of the regular isoamylacetate produced a stronger replica that resisted tearing during stripping. Several thin layers of Parlodion were used to build up thick layers. The stripped replicas were then rotated with a small motor while being shadowed at 30° with carbon. This filled in the undercuts nicely and strengthened the carbon substrate for the Jaffe process. Electron micrographs of fatigue-fractured copper surfaces and fractured ceramic samples will be shown to illustrate the success of the technique.

Session BV, General Intracellular Morphology

B38. A study of Ultrastructure in the Mosaic Embryo of the Snail, *Ilyanassa obsoleta*. R. Weymouth and J. N. Cather, *Department of Zoology*, and W. C. Bigelow, *Department of Chemical and Metallurgical Engineering, The University of Michigan, Ann Arbor, Michigan.*—Fine structural details of unfertilized eggs, zygotes, and developing embryos of *Ilyanassa* have been investigated. Distribution of mitochondria, endoplasmic reticular elements, duetoplasmic inclusions and microvillous projections have been followed to the veliger stage. Particular attention has been directed to the differentiation of the shell gland which originates from cell 2*d*. An attempt is being made to correlate ultrastructural and cytochemical localizations which can be detected at different stages in development of the shell gland.

B39. Electron Microscopy of Internal Structure of *Actinomycetes*. O. F. Edwards,* H. Haines, and M. Hotchkiss, *Department of Microbiology, University of Kentucky, Lexington, Kentucky.*—Previously we have examined unsectioned cultures of *Actinomycetes*. Fragmenting strains had heavily electron dense hyphae, but those of the nonfragmenting type had areas of greater and lesser electron density indicative of internal structure. Cell walls were not demonstrable, and structures resembling septa were rarely seen. We have continued these studies on thin slices cut on a Porter-Blum microtome. Cultures were fixed either in Palade's 1% buffered OsO_4 or in Tokuyasu and Yamada's mixed OsO_4 and $KMnO_4$ solutions, dehydrated in ethyl alcohol series and embedded in *n*-butyl-methacrylate. Distinct cell walls were found on both types. Septa were never found at the site of branching, although they were present elsewhere. Nonfragmenting types showed a core of electron dense material. Fragmenting types showed an area of electron dense material surrounded by an area of less dense protoplasm. Similar structures have been interpreted by others as chromatinic material in a nuclear vacuole.

* Speaker.

B40. Variations of Reproduction in *Toxoplasma Gondii*. Mary Ann Gavin, *Opthalmology Branch, National Institute of Neurological Diseases and Blindness, National Institutes of Health, Bethesda, Maryland.*—Toxoplasma organisms of the Beverly strain were studied in mouse peritoneal exudate three to five days after inoculation. The organisms are predominantly intracellular and occupy a vacuole separated by a membrane from the host cell cytoplasm. In this study, special attention was given to multiplying forms of toxoplasma and the following modes of proliferation were observed (a) *Binary fission*—a longitudinal cleavage resulting in two organisms of equal size and composition. (b) *Endodyogeny*—the production within one parental organism of usually two daughter cells. They develop from protuberances of the parent nucleus into whole organisms with the usual cell constituents. (c) *Multiple budding*—a rosette configuration in which the cytoplasmic matrix of four or more radially oriented organisms is surrounded by a common single membrane.

B41. Observations on Alterations of the Fine Structure of Absorptive Cells in the Small Intestine of the Mouse in Response to 3-kr X Irradiation. J. C. Hampton and H. Quastler, *Department of Pathology, University of Texas Medical Branch, Galveston, Texas, and Biology Department, Brookhaven National Laboratory, Upton, New York.*—The fine structure of the absorptive cells in the intestinal mucosa appeared to be normal through 36 hr post-irradiation, and the absorptive activity, as judged by the uptake of corn oil, was within normal limits. During the interval between 36 and 72 hr post-irradiation corn oil continued to be absorbed but in diminishing amounts. Observation of specimens fixed 3–5 days after treatment revealed that: (1) Small amounts of corn oil were absorbed, but little or no corn oil was discharged into the lamina propria. (2) Mitochondria were reduced in number, and the internal structure was modified. (3) Only a small amount of endoplasmic reticulum and associated particles remained. These observations indicate that radiation at 3 kr inhibits absorption and active transport of corn oil and RNP synthesis.

B42. Electron Microscopy of "Foam Cells" in the Spleen. J. M. Hill, Alice Smith, and Olga Fiorello, *Wadley Research Institute and Blood Bank, Dallas, Texas.*—Recently we have encountered an accumulation of a lipoid-laden reticuloendothelial cell in certain of the surgically excised spleens of patients with hematological disorders necessitating prolonged dosage of steroid hormones given in appreciable or even massive amounts. A brief background as to clinical findings, conventional tissue morphology, and histochemical studies is given for what we believe to be a new entity, previously undescribed, with distinguishing features of its own. In the thin sections examined with the electron microscope emphasis is placed on the large phagocytic reticuloendothelial cells which can be seen to contain characteristic "onion-ring" structures considered to be lipoid in nature. Electron micrographs present shapes, variable sizes, cytoplasmic distribution, and the suggested relation of these "onion rings" to cytoplasmic organelles in the reticuloendothelial cell. Biochemical correlation to the pathological picture is presented with the results of chemical analyses of fat in these infiltrated spleens with comment as to probable pathogenesis of this disorder.

B43. Cytologic Changes Produced by Low Doses (7r) of X Rays on Primary Oocytes of the Four-to-Six–day-Old Mouse. D. F. Parsons, *Biology Division, Oak Ridge National Laboratory, Oak Ridge, Tennessee.*—An exceptional radiosensitivity of primary oocytes of the mouse has been reported by Oakberg,[1] Peters and Borum,[2] and other workers. In the four–six-day-old RF mice the nuclei of the oocytes are in a resting phase of meiotic prophase. The chromosomal material is dispersed throughout the nucleus. Cytologic changes in the interval 6–48 hr after irradiation will be described. At this dose, few cells show marked changes at 6 hr, but at 8–10 hr dense aggregates appear in the nucleus. In the cytoplasm mitochondria show alteration of structure, and the ground substance becomes dense. At 12 hr many oocytes are necrotic, but the surrounding follicular cells are usually intact. Fine structure changes in the nucleoli, chromosomes, mitochondria, etc., will be described. The significance of these findings in relation to possible "targets" in the cell will be discussed.

[1] E. F. Oakberg, Proc. Tenth Intern. Congr. Genet. **2**, 207 (1958).

[2] H. Peters, and K. Borum, Intern. J. Radiation Biol. **3**, 1 (1961).

B44. Electron Microscope Observations of Spermatogenesis in Cestodes. Benjamin Rosario, *Department of Pathology, University of Texas Medical Branch, Galveston, Texas.*—Two tapeworms, *Hymenolepis nana* and *Hymenolepis diminuta*, were studied with reference to sperm development. Preliminary observations have shown that primary spermatocytes undergo several nuclear divisions to produce a large multinucleate cell. Several stages in the development of spermatozoa were observed in each of these large cells. Mitochondria were characteristically found in large numbers near the plasma membrane. Mature spermatozoa were elongated cylindrical cells enclosed in a plasma membrane showing helical striations at about 30° to the central axis. A clear division of sperm into a head and tail has not been observed. The nucleus was elongated, was variable in position and overlapped the more centrally placed axial filaments. The usual array of nine pairs of axial filaments, surrounding a central pair, was found to be connected to the central pair by fine strands. In longitudinal section the central pair of filaments appeared as a tightly wound helix.

B45. Cortical Changes in Fertilized Eggs of *Rana pipiens*.* Norman E. Kemp, *Department of Zoology, The University of Michigan, Ann Arbor, Michigan.*—Eggs when extruded from the cloaca possess a layer of cortical granules close to the surface. Low, irregularly distributed microvilli extend outward and contact the underside of the vitelline membrane. Around the microvilli there is a narrow perivitelline space containing a few small granules. Cortical granules remain intact up to 10–15 min after fertilization at room temperature (about 25°C), but by 20 min most of them have moved up to the surface and extruded their contents into the perivitelline space. After receiving this granular discharge from the egg, the perivitelline space widens and the egg becomes free to rotate so that its animal pole is oriented upward. Following the wave of breakdown of cortical granules, the cortical cytoplasm regenerates a new surface layer, which may prevent any residual cortical granules from reaching the surface.

* This work was supported by grants from the U. S. Public Health Service, the National Science Foundation and the Michigan Memorial, Phoenix Project.

B46. Comparative Light and Electron Microscopical Study of the Ganglia of the Cockroach, *Periplaneta americana*. C. E. Challice and R. C. B. Hartland–Rowe, *University of Alberta, Calgary, Alberta, Canada.*—This study represents an attempt to find out more of the relationship between structure and function in the ganglia of the cockroach *Periplaneta americana.* Of particular interest is the morphology of the neurosecretory system which displays a marked 24-hr rhythm. This rhythm dictates the diurnal locomotor activity of the insect.

ABSTRACTS OF CONTRIBUTED SCIENTIFIC EXHIBITS

E1. Electron Microscopy of Unbroken DNA Molecules. Michael Beer and Doris Naimark, *The Johns Hopkins University, Baltimore, Maryland,* and A. D. Hershey, *Carnegie Institution of Washington, Cold Spring Harbor, New York.*—Unbroken DNA molecules can be transferred to supporting membranes having appropriate adsorption properties. Molecules 60 microns long have been recorded in serial exposures. Length measurements indicate that the DNA of T_2 phage is one double-stranded fiber of molecular weight about 120×10^6.

E2. Dislocations in the Pseudo-Binary Alloy System Bi_2Te_3-Sb_2Te_3. James N. Bierly, *The Franklin Institute, 20th and Parkway, Philadelphia 3, Pennsylvania.*—Alloys of the pseudo-binary system Bi_2Te_3-Sb_2Te_3 all have a layered structure which is very convenient for the preparation of thin foils. Examinations of this series of alloys by the electron microscope shows unique patterns of dislocations and networks which are preferentially situated in the cleavage plane. Both hexigonal and circular loops occur in certain alloys which appear to be vacancy loops.

E3. Spore Surface Fine Structure of *Actinomycetes.* Charles B. Reimer, Richard A. Schlegel, Calvin E. Higgins, *Lilly Research Laboratories, Physicochemical Research Division, 731 South Alabama St., Indianapolis 6, Indiana.*—The spores of a number of different actinomycete species show a high degree of ordered structure of cell wall particles in the 10^6 molecular weight range. Profound species differences are apparent.

E4. Electron Microscopy of *Saccharomyces.** Tadashi Hirano and Carl C. Lindegren, *Biological Research Laboratory, Southern Illinois University, Carbondale, Illinois.*—The electron micrographs of this exhibit present examples of organelles as seen in different structures during growth. The best mitochondrial preparations were obtained from cultures inoculated on nutrient agar medium and incubated for 30 days at 25°C. Potassium permanganate fixation has been effective for the fixation of mitochondria of *Saccharomyces.*

* This work was supported by a research grant from the U. S. Public Health Service.

E5. Surface of Magnetic Recording Tape. Saul W. Chaikin and Donald K. Stellman, *Stanford Research Institute, Menlo Park, California.*—Important factors pertaining to magnetic tape performance are surface roughness, and concentration and orientation of magnetic particles. Replicas depicting these characteristics were made by a two-stage process polyvinyl alcohol shadowed with palladium and carbon. With certain tapes direct replicas were made by evaporating metal, then carbon, on the tape and stripping with hydrochloric acid, then a solvent.

E6. Automatically Dodged Electron Micrograph Prints. O. Eugene Sedberry, *LogEtronics Inc., 500 East Monroe Avenue, Alexandria, Virginia.*—This exhibit will demonstrate the results achieved by using a photoelectronic device for producing automatically dodged enlargements of electron micrograph negatives. Dodged and undodged enlargements of negatives exhibiting over-all unevenness and problems associated with reproduction of detail will be included as well as a schematic diagram of the equipment.

E7. Electron Micrographs of Whole Mounts of Spores and Swarm Cells of the Myxomycete, *Reticularia lycoperdon.* Arthur L. Cohen, *Oglethorpe University, Atlanta, Georgia.*—All photographs were taken with the Philips 75 B electron microscope. 1. Empty spore case of *R. lycoperdon*, unshadowed. 75 kv, condenser set near crossover. EKC fine-grain positive film developed in Microdol 5 min. Original magnification =3600×. Print magnification =3200×. Electron micrographs 2–4. The following were taken on EKC 649 film developed in EKC developer D8 diluted 1 to 2 with water, 8 min at 20°C. All specimens chrome shadowed. 2. Germinated spores of *R. lycoperdon.* 75-kv accelerating voltage, original magnification =2400×. Print magnification —30 000×. 3. Swarm cell of *Reticularia* after escaping from spore. Suspension fixed by 2-min exposure to fumes of osmium tetroxide. Original magnification =900×. Print magnification =12 000×. Note small bacterium near tip of flagellum. 4. Detail of unidentified bacterium and flagellum of *Reticularia.* Original magnification =3000×. Print magnification 38 500×.

E8. Fine Structure of Keratin. G. E. Rogers, *Division of Protein Chemistry, C.S.I.R.O., 343 Royal Parade, Parkville N.2, Melbourne, Australia.*—High-resolution electron micrographs of cross sections of araldite-embedded α-keratins poststained with lead hydroxide have revealed the presence of a number of subfibrils within each 80 A-diam microfibril.

E9. Demonstration of Viruses in Human Autopsy Material with Electron Microscopy. E. Sanders, F. J. Luibel, and R. C. Reynolds, *The University of Texas Southwestern Medical School, Department of Pathology, Dallas, Texas.*—Representative electron micrographs from three fatal cases of viral diseases will be shown. The tissue is from human autopsy material fixed in formalin. The viruses demonstrated include the salivary gland virus and the herpes simplex virus. An additional finding in one case was that of *pneumocystis carinii*, and this organism also is shown.

E10. Mechanism of Cutting in Ultramicrotomy. Victor A. Phillips, *General Electric Research Laboratory, Schenectady, New York.*—Slices cut from relatively perfect metal crystals exhibit surface features and internal defects characteristic of the shear nature of the cutting process. The mechanism of cutting therefore can be studied by analysis of transmission electron micrograph detail. Microslip lines are a prominent feature on many micrographs of face-centered cubic metals and arise when crystallographic slip occurs on a single plane parallel to the cutting shear plane.

E11. Some Theoretical and Practical Shadow-Casting Profiles. Claude Bugenis and Luther E. Preuss, *Physics Department, Edsel B. Ford Institute for Medical Research, Detroit 2, Michigan.*—Shadow-cast, planar surface concentrations are theoretically predictable through extension of Knudsen's law. Gross condensand profiles for practical shadowing sources were plotted by radiotracer surface scanning Experimental source geometries (point, directed, extended, cylindrical, etc.) were compared with those assumed in the cosine law. Significant differences were observed between theory and experiment.

E12. Effects of Fixatives, Embedding Materials, and Procedures on Ultrastructural Images. Hilton H. Mollenhauer, C. Willard Lewis, Jr., and W. Gordon Whaley, *The Plant Research Institute, University of Texas, Austin 12, Texas.*—The growing complexity of processing biological materials by chemical fixatives and in plastic embedding media for electron microscopy suggested a comparative survey of a variety of methods utilizing different specimens. The results indicate marked differences in ultrastructural images.

E13. Dislocations in Graphite.* R. Sprague, *Research Laboratory National Carbon Company, Division of Union Carbide Corporation, Parma 30, Ohio.*—This exhibit illustrates the formation of dislocation networks, moiré patterns, and dislocation in interactions. The diagonal line running through the picture is a grain boundary. Several dislocations are seen to be continuous through the grain boundary indicating that the imperfections exist on different levels of the crystal. Magnification on the print is 18 000 diam.

* This research was sponsored in part by the Air Research and Development Command and the Air Material Command, U. S. Air Force.

E14. Electron Micrographs of Tissues Embedded in Selectron. Max R. Clevenger and Frank N. Low, *Department of Anatomy, Louisiana State University School of Medicine, 1542 Tulane Avenue, New Orleans 12, Louisiana.*—Chemically and thermally stable mixtures of polyesters (Selectron) and methacrylate yield embedding media that are prepared without difficulty, section well, and respond to clearing and staining techniques. Selectron is widely miscible, and several combinations are practical, including polymerization with water-soluble glycol methacrylate.

E15. Electron Diffraction and Microscopy Studies on Evaporated Cr Films. H. W. Treupel and S. Clarke, *IBM Command Center, Federal Systems Division, Kingston, New York.*—In transmission micrographs and diffraction diagrams it is shown that in Cr films, vacuum-deposited on NaCl covered with SiO and prepared under certain conditions, polycrystallinity and single crystallinity with a sharp boundary occurs in adjacent areas in different portions of the film sample. Multiple scattering is demonstrated in diffractographs of other thin Cr films.

E16. Structures Affecting the Permeability of Wood to Liquids. W. A. Côté, Jr., A. C. Day, and R. L. Krahmer, *Wood Products Engineering Department, State University College of Forestry, Syracuse 10, New York.*—Bordered, half-bordered, and simple pit pairs are recognized as communication channels between cells in wood. Comparison of their fine structure in conifers and hardwoods is made possible by electron microscopy. The mechanism of pit aspiration is demonstrated.

E17. Scanning X-Ray Microanalysis. T. Ichinokawa and S. Shirai, *Akashi Seisakusho, Ltd., Naka 8th Building, Marunouchi, Tokyo.*—By using a scanning type x-ray microanalyzer having a specially designed gas flow counter, we observed the carbon distribution on the surface of a metal specimen as an image on the display tube. We also tried some other applications on metal, mineral, and biological specimens.

E18. Fine Structure of Particles Associated with Tumors of Known or Suspected Viral Etiology. Albert J. Dalton and Robert F. Zeigel, *National Cancer Institute, Bethesda, Maryland.*—Electron micrographs of thin sections of tissue from a series of mouse leukemias (Moloney, Friend, Gross, AKR, and Figge) and from mice carrying polyoma and "K" viruses will be demonstrated. The figures were chosen with the primary aim of illustrating similarities and differences between particles associated with this series of disease entities.

E19. High Resolution Electron Microscopy of Bacteriophages. H. Fernández-Morán, *Mixter Laboratories for Electron Microscopy, Massachusetts General Hospital, Boston.*

Index of Authors of Contributed Papers

Anderson, T. F.—B32
Amy, J. A.—T5
Bailey, G. W.—A16
Beer, M.—A22, B21
Bendler, H. M.—A13
Benson, R.—A2
Bereczky, E.—B15
Bierlein, T. K.—A7
Bigelow, W C.—A12, B3
Bils, R. F.—T1
Björkman, N. H.—T3
Borasky, R.—A33
Borgese, S.—A4
Bradford, E. B.—A17
Breese, S. S. Jr.—B33
Buhl, P. A.—A8
Bush, A. F.—A31
Buthala, D. A.—B36, B37
Cardell, R. R., Jr.—A29, A30, B6
Carlson, F. D.—B25
Cather, J. N.—B38
Chaikin, S. W.—A20
Challice, C. E.—B46
Chandra, S.—B10, B13
Clark, I.—B7
Clarke, S.—A15
Clevenger, M. R.—A24
Cohen, A. L.—B27, T6
Coles, J. A.—A36
Cook, C. F., Jr.—A14, A35
Cota-Robles, E. H.—B31
Dales, S.—B30
Dalton, A. J.—B11
Danko, A. W.—A36
Dash, J.—A11
Davies, M. C.—B29
DeCarvalho, S.—B17
de Harven, E.—B14
Denues, A. R. T.—B13
Dmochowski, L.—B15, B16
Druce, R. E.—A24
Edwards, O. F.—B39
Elkington, W.—A6
Englert, M. E.—B29
Fernando, N. V. P.—B3
Fiorello, O.—B42
Friend, C.—B14
Friend, J. P.—A21
Froula, H.—A21
Furth, J.—B16
Gadziala, C.—B9
Gaunt, P.—A10
Gavin, M. A.—B40
Ghidoni, J. J.—B19
Grey, C. E.—B15, B16
Gueft, B.—B19
Haines, H.—B39
Hallgren, D. S.—A21, A23
Hampton, J. C.—B41
Harb, J. M.—B27
Hartland-Rowe, R. C. B.—B46
Hill, J. M.—B42
Hiramoto, I.—B35
Holik, A. S.—A32
Hotchkiss, M.—B39
Howatson, A. F.—B34
Huhn, D.—B1, B2, B4
Hummeler, K.—B32
Jones, M. H.—B17, B20
Jordon, L. E.—B28
Kammerer, O. F.—A8
Kear, B. H.—A4
Kelsch, J. J.—A8
Keltsch, R. A.—B20
Kemp, N. E.—B45
Kerr, E.—B20
Kleinschmidt, A.—B22
Kranitz, M.—A34
Labaw, L. W.—B8
Levine, S.—B29
Lloyd, B. L., Jr.—T2
Loud, A. V.—T4
Low, F. N.—A24
Luibel, F. J.—B12
Lundgren, H. P.—B24
Madden, G. I.—A12
Mastel, B.—A7
Mathews, J.—B36, B37
Mayor, H. D.—B28
McCaughey, R. S.—B20
McLean, I. W., Jr.—B20
McGregor, D. D.—B1, B2
Melton, C. W.—A19
Millonig, G.—B26
Mitchell, J. M.—A18
Moore, D. H.—B29
Morelock, C. R.—A32
Mottram, F. C.—B13
Movat, H. Z.—B1, B2, B3, B4, B5
Odell, J. S.—T11
O'Hara, D.—A22
Osborne, G. F.—T7
Otte, H. M.—A11
Parsons, D. F.—B43
Parsons, J.—A30
Pew, J.—B7
Poppa, H. R.—A25
Powell, C. E.—T9
Questler, H.—B41
Reichard, T. E.—T8
Reimer, C. B.—T9, T10
Reynolds, R. C.—B12
Rice, R. V.—B23
Rightsel, W. A.—B20
Rogers, G. E.—B24
Rosario, B.—B44
Rupar, W.—A18
Sachs, I.—B7
Sanders, E.—B12
Schlegel, R. A.—T7
Schmitz, J.—A1
Schwartz, C. M.—A19
Seal, M.—A34
Sellers, M. I.—B35
Siegel, B. M.—A27
Silcox, J.—A10
Smith, A.—B42
Sorrell, C. A.—A33
Sponseller, D. L.—A12
Sprague, R.—A5, A26
Stellman, D. K.—A20
Steiner, J. W.—B1, B2, B4, B5
Stone, R. S.—B35
Tandler, B.—B18

Taylor, A. R.—B17, B20
Thomas, G.—A2, A6, A9
Toolan, H. W.—B13
Trautman, R.—B33
Treupel, H. W.—A15
Truffelli, G. T.—B17
Vanderhoff, J. W.—A17
Via, G. G.—A28
Watson, J. H. L.—A29, A30
Weymouth, R.—B38
Whitemore, G. F.—B34
Wilhelm, F.—A3
Wilsdorf, H. G. F.—A1, A3
Yamamoto, N.—B32
Yoda, E.—A27
Yokoro, K.—B16
Zobel, C. R.—B21, B25

Index of Invited Speakers

Anderson, T. F.—S16
Borasky, R.—S1
Borysko, E.—S3
Brown, A. E.—S2
Geil, P.—S10
Hall, C. E.—S15
Hock, C. W.—S6
Howatson, A. F.—S13
Johnson, W. H.—S4
Kaesberg, P.—S17
Keith, D.—S8
Lundgren, H. P.—S5
Menkart, J.—S2
Morehead, F.—S11
Niegisch, W. D.—S9
Nutting, J.—I1
Scott, R. G.—S12
Walker, D. H., Jr.—S16
Walter, N. M.—S7
Wildy, P.—S14
Yamamoto, N.—S16

Index of Contributors to Scientific Exhibits

Beer, M.—E1
Bierly, J. N.—E2
Bugenis, C.—E11
Chaikin, S. W.—E5
Clarke, S.—E15
Clevenger, M. R.—E14
Cohen, A. L.—E7
Côté, W. A., Jr.—E16
Dalton, A. J.—E18
Day, A. C.—E16
Fernández-Morán, H.—E19
Hershey, A. D.—E1
Higgins, C. E.—E3
Hirano, T.—E4
Ichinokawa, T.—E17
Krahmer, R. L.—E16
Lewis, C. W., Jr.—E12
Lindegren, C. C.—E4
Low, F. N.—E14
Luibel, F. J.—E9
Mollenhauer, H. H.—E12
Naimark, D.—E1
Phillips, V. A.—E10
Preuss, L. E.—E11
Reimer, C. B.—E3
Reynolds, R. C.—E9
Rogers, G. E.—E8
Sanders, E.—E9
Schlegel, R. A.—E3
Sedberry, O. E.—E6
Shirai, S.—E17
Sprague, R.—E13
Stellman, D. K.—E5
Treupel, H. W.—E15
Whaley, W. G.—E12
Zeigel, R. F.—E18

Progress of the Hughes Infrared Systems and Guidance Heads Department reflects Hughes' overall growth. In the past ten years, employment has risen from under 2,000 to over 30,000 in semi-autonomous divisions concerned with Engineering, Research, Commercial Products, Ground Systems, Communications and Manufacturing. The infrared activity includes these typical projects:

---

1. Air-To-Air Missiles
2. AICBM
3. Air-To-Air Detection Search Sets
4. Satellite Detection & Identification
5. Infrared Range Measurement
6. Detection Cryogenics
7. Detector Application Physics
8. Optical Systems Design

These activities have created a number of new openings for graduate engineers and physicists with analytical and inventive abilities.

You are invited to investigate these openings if you have several years of applicable experience in infrared, optics or electronics, and can assume responsibility for systems analysis and preliminary design.

The importance of infrared development at Hughes is shown in substantial development contracts and in the fact that Hughes is investing its own funds in further exploration.

We invite your earliest inquiry. Wire collect, or airmail resume directly to:
Mr. William Craven, Manager,
Infrared Systems and
Guidance Heads Department,
Hughes Aerospace Engineering Division,
Florence and Teale Streets,
Culver City 67, California.

At Hughes, all qualified applicants will receive consideration for employment without regard to race, creed, color or national origin.

We promise that you will hear from us within one week!

Creating a new world with Electronics

HUGHES

HUGHES AIRCRAFT COMPANY
AEROSPACE DIVISIONS

Write for reprints of these important technical papers, written by Hughes staff members... Infrared Search-Systems Range Performance; R. H. Genoud/Missiles Seekers and Homers; W. A. Craven, et al. Servomechanisms Design Considerations for Infrared Tracking Systems; J. E. Jacobs/Simulation of Infrared Systems; H. P. Meissinger.

——New Scientific Literature

SYNTHESIS OF OPTIMUM CONTROL SYSTEMS

By SHELDON S. L. CHANG, New York University. Available in September, 1961.

A second-year-graduate-level text bridging the gap between a standard text on the subject and the current literature on optimum control. It may also be used as a supplementary text for a one year graduate course, and as a reference book for industry. The book is designed to equip students with advanced design techniques for high performance systems where the ultimate in response is required.

PROCEEDINGS OF THE SIXTH SYMPOSIUM ON MAGNETISM AND MAGNETIC MATERIALS

Edited by J. A. Osborn, Westinghouse Electric Corp. 408 pages, $10.00.

A compilation of recent work in the field of magnetism and magnetic materials, in this book contains a collection of technical papers presented at the annual symposium sponsored by the American Institute of Electrical Engineers and the American Institute of Physics. Topics include ordered spin systems, computer devices, metallic films, nuclear hyperfine fields, ferromagnetic resonance, high coercive materials, exchange interactions, fine particles, magnetization processes, anistropy, domain walls, microwave devices, and oxides.

LINEAR VACUUM TUBE AND TRANSISTOR CIRCUITS:

A Unified Approach to Linear Active Circuits

By A. J. COTE, Jr. and J. BARRY OAKES, The Johns Hopkins University. *The McGraw-Hill Electrical and Electronic Engineering Series.* Available in August, 1961.

This senior-graduate level text presents a basic approach to the analysis and synthesis of linear vacuum tube and transistor circuits, and emphasizes the difference and similarities between these devices. This viewpoint permits the designer to select the optimum combination of external passive elements that will make the best use of the device employed in a particular application.

Send for copies on approval

MH

McGraw-Hill Book Company, Inc.

330 West 42nd Street New York 36, N. Y.

Proceedings of Alloyd's Symposia on Electron Beam Technology

1st Symposium	**96 pp**	**microfilm only**	**$ 5.00**
2nd Symposium	**135 pp**		**$10.00**
3rd Symposium	**378 pp**		**$15.00**

The only comprehensive reviews of activities in the field of Electron Beam technology. They include papers which discuss Electron Beams in melting refining, evaporation, welding machining, irradiation, microelectronics and recording, etc.

Available on prepaid order basis from the ALLOYD ELECTRONICS CORPORATION, 37 Cambridge Parkway, Cambridge 42, Massachusetts.

SCIENTISTS ENGINEERS

CALIFORNIA

offers you and your family

- A world center of the electronics-missile-space industries for CAREER ADVANCEMENT
- The High Sierra and the Pacific Ocean for RECREATION
- And for your children some of the nation's FINEST PUBLIC SCHOOLS
- World Famous Universities for ADVANCED STUDY
- MAJOR CULTURAL CENTERS

while living in such places as

Exciting San Francisco
Fabulous Southern California
Cultural Palo Alto

Companies pay interview, relocation and agency expenses

Submit resume in confidence to:

PROFESSIONAL and TECHNICAL RECRUITING ASSOCIATES
(a Division of the Permanent Employment Agency)
Suite A
825 San Antonio Road
Palo Alto, Calif.

MIKROS

10 to 40 KV
REGULATED
RF-DC
POWER
SUPPLY

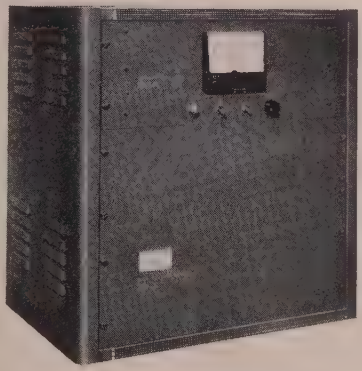

ENGINEERED TO MEET THE EXACTING REQUIREMENTS OF ELECTRON MICROSCOPY—A compact, air-insulated, RF-type, DC high voltage supply providing exceptional advantages in reliability, simplicity of design and ease of operation. Originally developed for use with the advanced Mikros electron microscope, the unit offers new high levels of performance for insulation leakage tests, electron gun research, electrostatic spraying, electron optical examinations and many other research laboratory applications.

OUTPUT RANGE—10 to 40 KV, continuously variable
CURRENT—0.5 MA, continuous
LOAD REGULATION—0.5%
LINE REGULATION—0.05%
RIPPLE—less than 0.5%
INPUT POWER—117 V, 60 cps, 3 amp, single-phase

Dimensions: 23"x22"x15". Price $575, f.o.b. factory. Availability 15 days . . . Write for technical literature.

VISIT OUR DISPLAY
Booth 20—ELECTRON MICROSCOPE SOCIETY SHOW—Pittsburgh, Pa.
Booth 4—VACUUM SCIENCE and TECHNOLOGY SHOW—Washington, D.C.

MIKROS INC.
7620 S. W. Macadam Avenue
Portland 19, Oregon
A Subsidiary of Electro Scientific Industries

THE CENCO LAB JACK

Imitation is the sincerest form of flattery and the Cenco Lab Jack has been overwhelmed with it. While some who have followed offer sound design, or others decent quality, none (as yet) has equalled Cenco's design and quality at the same price.

Developed in collaboration with Dr. Aaron B. Lerner of Yale University, the Cenco Lab Jack's simple, efficient design and precision construction are still its outstanding features. It will hold 100 lbs. easily, with complete stability at all elevations between 3 and 10¼ inches. Its scissors action permits steady, level, and quick raising or lowering—a feature especially noticeable when maneuvering fragile glassware.

With over 25,000 in use throughout the world today, we find only one trouble with the Cenco Lab Jack. It lasts too long.

NO. 19089-001-Cenco—Lerner Lab Jack................$34.00

CENTRAL SCIENTIFIC
A Division of Cenco Instruments Corporation
1700 West Irving Park Road,
Chicago 13, Illinois

Mountainside, N. J.
Montreal
Santa Clara
Somerville, Mass.
Toronto
Los Angeles
Birmingham, Ala.
Ottawa

cenco

Vancouver
Houston
Cenco S.A., Breda, The Netherlands
Tulsa

announcing

1" & 2" ULTRA-HIGH VACUUM VALVES

and COMPLETE LINE of MATCHED FITTINGS

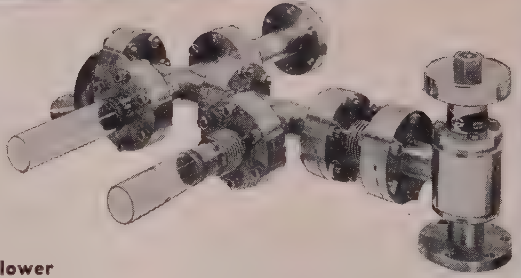

- Bakeable to 450° C
- Useful to 10^{-10} mm Hg or lower
- Conductance variable from 60 liter/sec to 10^{-13} liter/sec with 2" valve; from 10 liter/sec to less than 10^{-14} liter/sec with 1" valve
- Constructed entirely of low vapor pressure metals insuring minimum contamination
- Available from stock

WRITE OR PHONE FOR COMPLETE SPECIFICATIONS

GP Granville-Phillips Company

P. O. Box J-198 Pullman, Washington • telephone LOgan 4-1130

PHYSICAL METALLURGIST
CHEMIST

Important new, long-range projects at the IBM Thomas J. Watson Research Center at Yorktown, N. Y., have created an outstanding opportunity for a person with an advanced degree or equivalent experience in physical metallurgy or chemistry. The person who can fill this position must be able to take charge of a semi-conductor crystal-growing activity and carry out program of research on related problems. Experience should include preparation of solid state materials and a background in semiconductor physics.

This is a unique opportunity for work in advanced areas of entirely new research projects at IBM that promise to open up exciting new fields of discovery.

IBM's new Thomas J. Watson Research Center at Yorktown is located in pleasant, rural Westchester County countryside, just 35 miles from New York City. The Research Center, featuring the most modern facilities, was designed to provide the best possible working environment for scientists and engineers engaged in advanced studies. The location provides excellent schools and housing. IBM offers a fully paid benefits program that is setting the pace for industry today. All qualified applicants will receive consideration for employment without regard to race, creed, color or national origin.

Please write, outlining your experience, qualifications and background, to:

Mr. John B. Farrington, Dept. 579H
Thomas J. Watson Research Center
P. O. Box 218
Yorktown Heights, New York

IBM®

International Business Machines Corporation

Special Supplement—October Issue—Journal of Applied Physics

SEMICONDUCTING COMPOUNDS

The complete Proceedings of the recent "Conference on Semiconducting Compounds" held June 14–16 at the General Electric Research Laboratory, Schenectady, N. Y. will be published as a special Supplement to the regular October issue of JAP.

The Conference, under the joint sponsorship of the U. S. Air Force Office of Scientific Research and the General Electric Company was the first in its field. The conference synthesized a large body of existing experimental information, relative to energy band structure, transport (including tunneling) and optical, galvanomagnetic and resonance phenomena. Emphasis was placed on 3–5 and 2–6 compounds with some discussion of the 2–5 and 5–6 materials. Over 50 papers were presented and will be published in the Special October supplement.

Advertising in the Supplement will be accepted and interested manufacturers should write to Mr. T. Vorburger, Advertising Manager, JAP, 335 East 45th St., New York 17, N. Y. for details. Closing date for advertising is September 3rd.

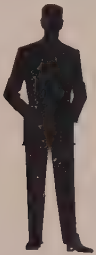

Are you this man?

APPLIED RESEARCH PHYSICIST: Honeywell offers a challenging career opportunity to an experienced PhD or MS. Individual will conduct an experimental research and development program in solid state materials and processes for high accuracy inertial instruments. Areas of investigation will include: stability of materials in the micro-strain region; deposition of metallic coatings; ultra-precision gauging, shaping and surface finishing techniques; voltage breakdown phenomena in high vacuum. All qualified applicants will receive consideration for employment without regard to race, creed, color or national origin. Send resume to: Mr. Clyde W. Hansen, Technical Director, Honeywell Aero, 2615-A Ridgway Road, Minneapolis 40, Minnesota.

Honeywell

H Military Products Group

Gaertner Ellipsometer uses polarized light to study ultra-thin films

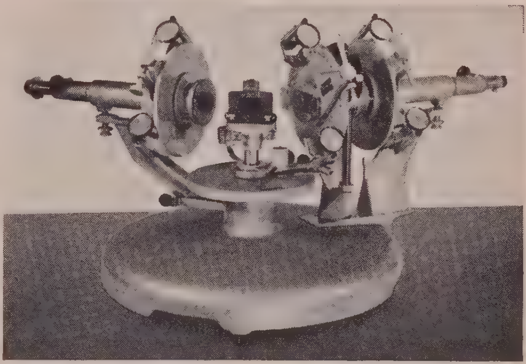

L119 Ellipsometer with L118TN Tronstad and Nakamura Biplate Assembly

This Ellipsometer, or polarizing spectrometer, is one of many fine optical and measuring instruments designed and manufactured by Gaertner Scientific Corporation. The instrument is a basic research tool for investigating and measuring ultrathin films, and is of particular interest to those working in the field of solid state physics. Using the methods of Drude, Rothen, Tronstad and others, it permits precise determination of film thickness from a few angstroms to 200 angstroms, or approximately to one-tenth of a microinch. It is also adaptable to the study of birefringence, index of refraction, and other characteristics and phenomena associated with thin films and surfaces.

Gaertner Ellipsometers are, in effect, dual-purpose tools. They can be readily converted to a spectrometer by adding an entrance slit to the collimator, and Gauss eyepiece and adapter to the telescope.

Gaertner offers a wide range of precision optical and measuring instruments to scientists in all fields. Our services include modifications of these instruments to meet unusual needs, complete design and manufacture of special instruments and optical systems, and manufacture of assemblies and instruments from customer sketches and drawings. **Write for information on optical or measuring instruments used in your field. Bulletin 203-58 describes Gaertner Ellipsometers.**

Gaertner
SCIENTIFIC CORPORATION
1246 Wrightwood Avenue • Chicago 14, Illinois

INDEX TO ADVERTISERS

Name	*Page*
AEROSPACE CORPORATION	iv
ALLOYD ELECTRONICS CORP.	xviii
ALPHA SCIENTIFIC LABS., INC.	v
ARNOLD ENGINEERING CO.	xi
BECKMAN & WHITLEY, INC. Manufacturers of high-speed research cameras—both framing and sweeping-image type; specialized meteorological instruments; heat-flow transducers; and explosive-actuated mechanisms.	Cover 2
BELL TELEPHONE LABORATORIES	iii
CENTRAL SCIENTIFIC CO. Manufacturers of Cenco physical apparatus and instruments to meet all requirements of University, College and High School Physics Laboratories. Specializing in high vacuum pumps and development of instruments and apparatus for various sciences.	xix
FISHER SCIENTIFIC CO.	x
GAERTNER SCIENTIFIC CORP. Spectroscopes, spectrometers, spectrographs, spectrophotometers, heliostats, measuring microscopes, comparators, cathetometers, reading telescopes, interferometers, chronographs, dividing machines, etc.	xxi
GENERAL RADIO CO. Manufacturers of electronic measuring instruments; vacuum-tube voltmeters, amplifiers, and oscillators; wave analyzers, noise meters and analyzers, stroboscopes, laboratory standards of capacitance; inductance and frequency; impedance bridges, decade resistors and condensers, air condenser and variable inductors; rheostats, variacs, transformers; other laboratory accessories.	Cover 3
GRANVILLE–PHILLIPS COMPANY	xx
HAMNER ELECTRONICS CO., INC.	xxiv
HUGHES AIRCRAFT CO.	xvii
I.B.M. CORP.	xx
KEITHLEY INSTRUMENTS, INC. Vacuum tube electrometers, microammeters, kilovoltmeters, static detectors, meg-meg-ohm-meters, high gain dc amplifiers, dc vacuum tube voltmeters, high input impedance ac isolation amplifiers.	vii
LINCOLN LABORATORY, M.I.T.	xii
LOS ALAMOS SCIENTIFIC LAB.	vi
McGRAW–HILL BOOK CO., INC.	xviii
MIKROS INC.	xix
MINNEAPOLIS HONEYWELL REGULATOR COMPANY	xxi
NRC EQUIPMENT CORP. Manufacturers of standard and special high vacuum components, equipment, and systems including mechanical booster, and diffusion pumps; gauges; valves; seals; connectors; melting and heat-treating furnaces; coaters; impregnators; gas in metal analyzers; driers and freeze driers; altitude chambers and leak detectors.	xiv
PERMANENT EMPLOYMENT AGENCY	xviii
RAMO–WOOLDRIDGE LABS. Research, development, and manufacture in the field of electronic systems for commercial and military applications, and in the field of guided missiles.	Cover 4
SPERRY RAND RESEARCH CENTER	viii
SYLVANIA ELECTRONICS SYSTEMS Amherst Laboratories	xvi

INDEX—*Continued*

Name *Page*

TEKTRONIX, INC. xiii
Manufacturers of Cathode-Ray Oscilloscopes, Auxiliary amplifiers, square-wave generators, vacuum-tube characteristic-curve tracers, L.C. Meters, constant-amplitude generators, operational accessories.

VARIAN ASSOCIATES INSTRUMENT DIVISION ix

WELCH SCIENTIFIC CO., W. M. .. xvi
Manufacturers of high-vacuum pumps, both mechanical and diffusion; vacuum gauges; electrical measuring instruments; physics equipment; and other items for the physical and chemical laboratories.

POSITION OPEN

PHYSICIST WANTED FOR PROCESS DEVELOPMENT

A new, exciting challenge is offered to a Physicist or Electronics Engineer who has an interest in the use of high voltage and electrostatic force for new processes. This man would have responsibility to determine feasibility; to assess development prospects; and would have a hand even in final application to manufacture.

An M.S. or Ph.D. in Physics or EE, and a good theoretical background in electrical field theory and electronics is required. Experience in industrial process development is desirable, and would extend the assignment responsibilities, but is not a specific necessity. Salary will be determined by the qualifications of the applicant.

This position is open at Owens-Illinois Technical Center, a new, modern, well-equipped research facility in Toledo, Ohio, a community of 350,000 people. Owens-Illinois has 69 plants and employs 35,000 people. O-I manufactures Duraglas containers, Libbey table glassware and Kimble laboratory glassware, as well as corrugated boxes, closures and blown plastic containers.

Send resumé to T. C. Baker, Chief, Physics Section, Owens-Illinois, 1700 N. Westwood, Toledo, Ohio.

TUBULAR SLIDE CONTACT **RHEOSTATS**
RESISTORS
Toroidal *Winding Machines*
REX RHEOSTAT CO.
149-a Babylon Tpke. Roosevelt, L. I., N. Y.

PHYSICIST or PHYSICAL CHEMIST

One of the nation's leading manufacturers of paper and paper products has an opening in its research laboratories for a STAFF SCIENTIST to work on projects dealing with the theory and application of electrophotographic phenomena and solid state physics as they apply to photoelectric papers and processes.

Prefer a Ph.D with concentration in solid state physics or physical chemistry; however, will consider an M.S. with experience.

Qualified candidates should send a complete resume of educational background and work experience to:

G. HUGH MEILINGER
EMPLOYMENT SUPERVISOR
THE MEAD CORPORATION
CHILLICOTHE, OHIO

All replies will receive immediate and confidential attention.

INSTRUMENTATION ENGINEER OR PHYSICIST

Unique opportunity for research-oriented instrumentation engineer or physicist. Degree in physics or electrical engineering, with background and experience in electronics and instrumentation desired; specific experience in optics and surface-optical measurements preferred. Challenging assignments include developing and designing new instruments for specialized measurements of optical, electrical, dimensional and thermal properties of alloy and specialty steels in well-established research laboratory, with opportunity for developing steel-plant control systems.

Pioneering opportunity for the right man. Salary and position commensurate with qualifications.

Please send resume including educational background, work experience, and salary required to **Box 861-A,** *JAP 335 East 43 St., New York 17, N. Y.*

HAMNER

A-8 DESIGN
ULTRA HIGH SPEED, NON-OVERLOAD
LINEAR AMPLIFIERS

Unexcelled A-8 Characteristics . . . PLUS

- NEW LAYOUT WITH FINE GAIN CONTROL
- OPTIONAL PICK-OFF GATE FOR FAST COINCIDENCE WORK
- YOUR CHOICE OF PULSE ANALYZING SECTION

The A-8 Design Amplifier has found wide usage in nuclear physics laboratories where one or more of the following three conditions exist:

1. Very large overload signals will be present.
2. Counting rates up to 250kc will be present.
3. It is required to do medium-fast coincidence work on pulses having slow risetimes.

In these three areas, the A-8 design represents a great improvement over previous units.

These results are achieved through the use of double differentiation with two delay lines, thus providing for fast baseline recovery even under high-duty cycle operation. Overload performance is enhanced by preventing the Amplifier from overloading before differentiation and by not allowing overload to occur inside a feedback loop.

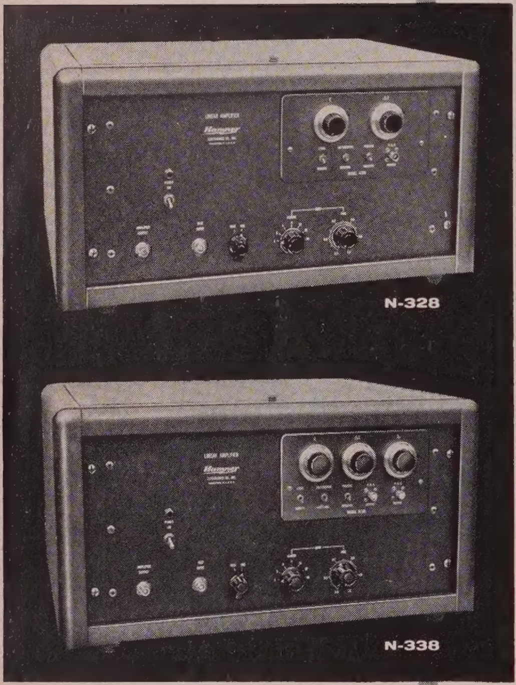

N-308
AMPLIFIER ONLY

Maximum Gain: 7000 in main Amplifier (additional gain of 1, 3 or 10 in Pre-Amp).

Gain Stability: 0.25%/day.

Risetime: About 0.2 μs.

Linearity: 0.1% Integral Linearity, 3-100 volts into 10K or greater load.

Overload Recovery: About 8 μs for 4000 times overload.

Maximum Counting Rate: About 250,000 CPS.

N-318
AMPLIFIER WITH INTEGRAL DISCRIMINATOR

Amplifier Section: See details on N-308.

Discriminator Section: This Discriminator is based on the P. R. Bell Design.

Range: 4-100 volts by 10-turn helipot.

Linearity: Better than 0.5%, 3-100 volts.

Stability: Better than 50 mv/day.

Resolving Time: About 1.2 μs.

Output Pulse: 1 μs wide, +50 volts high into 10K load.

N-328
AMPLIFIER WITH PULSE-HEIGHT ANALYZER

Amplifier Section: See details on N-308.

Output Pulse-Height: (25 volts, positive or negative by switch.)

Baseline:
Control—By 10-turn helipot.
Range—3-100 volts by 10-turn helipot.
Linearity—0.1%, 3-100 volts.
Stability—Better than 50 mv/day.

Window:
Control—By 10-turn helipot.
Width—0-10 volts by 10-turn helipot (0-20, 30, 40 or 50 volts at slight extra cost).

N-338

Amplifier with Integral Discriminator similar to N-318, and independent Pulse-Height Analyzer similar to N-328.

N-670 COINCIDENCE PICK-OFF. In Coincidence Work, the time of the pulse zero crossover is largely independent of pulse-height. For this reason, it is well related in time to the event causing the pulse and is useful for coincidence studies. Coincidence resolving times of from 30-100 mμs can be successfully used. The N-670 is an optional subchassis which detects the zero crossing and presents an output for coincidence work.

Hamner

HAMNER
ELECTRONICS CO., INC.
P. O. Box 531, Princeton, N. J.
PEnnington 7-1320

New TUNED AMPLIFIER and NULL DETECTOR

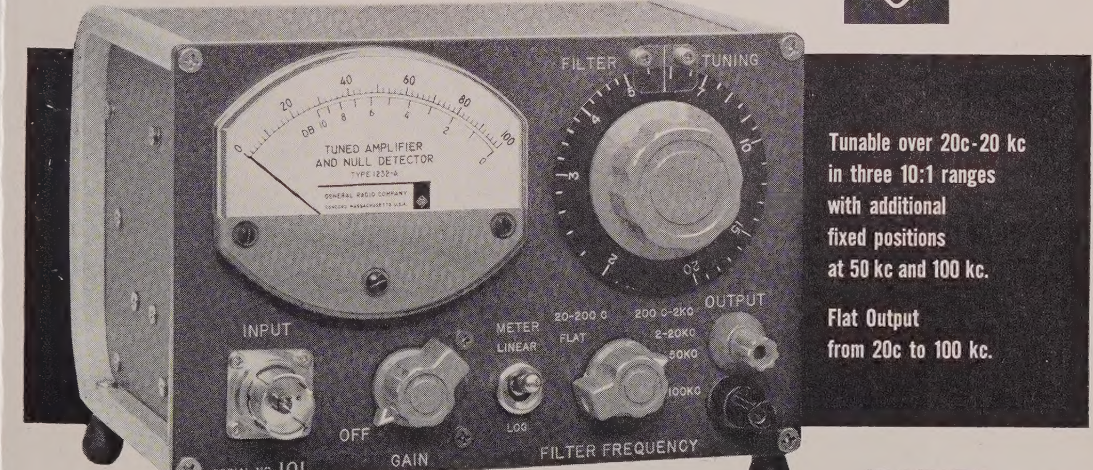

Tunable over 20c-20 kc in three 10:1 ranges with additional fixed positions at 50 kc and 100 kc.

Flat Output from 20c to 100 kc.

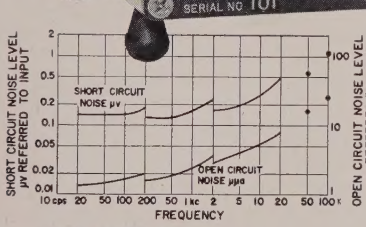

LOW NOISE

Short-circuit noise is typically less than 0.2μv for most of tuned range; less than 2μv for "flat" 20c-100 kc position. Open circuit noise is typically less than 0.2μv.

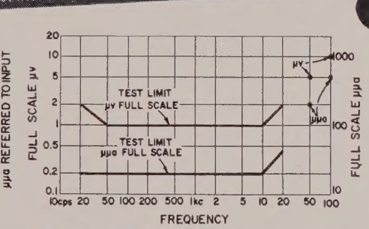

HIGH SENSITIVITY

At least 1μv full scale over major portion of tuned range. In flat position, sensitivity is 20μv full scale.

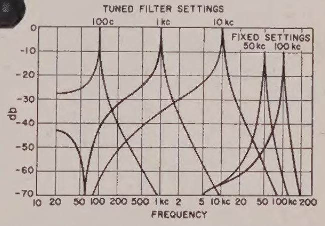

EXCELLENT SELECTIVITY

Bandwidth at any frequency is about 5%. 2nd-harmonic rejection is at least 35 db. On all ranges above 200 cps, 60-cycle rejection is at least 60 db.

★ Useful as a tuned amplifier, audio amplifier, or null detector.

★ As a general-purpose amplifier, output is constant within ±3 db from 20 cps to 100 kc ("flat" position).

★ High Gain — 120 db for tunable settings; 100 db for flat 20-c to 100-kc position; 106 db at 50 kc; and 100 db at 100 kc.

★ Meter switch provides either linear or logarithmic response. Compression adds 40 db to upper portion of meter scale for null measurements — does not affect sensitivity of bottom end of meter scale.

★ Fully transistorized — small and compact, width 8 inches, height 6 inches, depth 7½ inches.

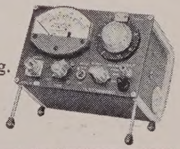

★ Front legs extend to permit tilting of panel for easier viewing.

★ Panel extensions available for rack mounting.

OTHER DATA

INPUT IMPEDANCE: 50 KΩ to 1MΩ depending on gain control setting
OUTPUT: 1 volt in 10,000 ohms
DISTORTION: (In flat position) less than 5%
POWER REQUIREMENTS: 12 volts, dc, from 9 mercury cells; estimated operating cost is 0.4 cent/hr. for 1500 hours
TYPE 1232-A — PRICE: $360.

Write for Complete Information

GENERAL RADIO COMPANY

WEST CONCORD, MASSACHUSETTS

The Best Instruments In Electronics

NEW YORK, WOrth 4-2722
NEW JERSEY, Ridgefield, WHitney 3-3140

CHICAGO
Oak Park
VIllage 8-9400

PHILADELPHIA
Abington
HAncock 4-7419

WASHINGTON, D.C.
Silver Spring
JUniper 5-1088

SAN FRANCISCO
Los Altos
WHitecliff 8-8233

LOS ANGELES
Los Angeles
HOllywood 9-6201

IN CANADA
Toronto
CHerry 6-2171

Research is the
investigation of natural phenomena,
motivated
by a desire for basic understanding

Anyone actually doing research can easily define the term. Unfortunately, ever since research became an institutional status symbol, the word has rapidly been losing most of its meaning as a descriptive noun. Nowadays we see the word—along with its prestigious modifiers "basic" and "fundamental"—being applied to such unlike pursuits as the study of strange particle decays and the improvement of deodorants.

All of this poses more than just an interesting problem in semantics to the serious researcher—trained for, skilled in and devoted to understanding the first principles of natural phenomena—who is looking for a situation in which he can make a significant contribution to his chosen scientific field.

Where can he find such a situation?

To be sure, much of the basic research in the United States today is being carried on in universities and allied quasi-academic institutions. Another large fraction of it is done in certain research and development companies where the "development" activities are so advanced, and are being done by such competent technical people, that they could easily pass for research in most other companies. There are perhaps half a dozen firms like this in the entire country—places where basic research has always been considered a vital part of the technical program, enjoying the understanding, the support and the general environment required for creative work of high quality. We respectfully submit that Ramo-Wooldridge is one of these organizations.

During the past five years the Research Laboratory in R-W (and in its sister corporation, Space Technology Laboratories) has made notable contributions in such diverse fields as superconductivity, plasma physics and magnetohydrodynamics, millimeter waves and nuclear reactor kinetics. This breadth of activities reflects the varied interests of members of the Laboratory staff, and illustrates Ramo-Wooldridge's guiding principle that a necessary (although not sufficient) condition for worthwhile research is the definition and selection of problems by the scientists who are to work on them.

Ramo-Wooldridge's technical efforts are now directed toward the broad and challenging new field of extending man's intellectual powers. Basic research to support these activities ranges from problems of pure mathematics to studies in advanced areas of current experimental and theoretical physics.

We would be glad to discuss details of our programs with research scientists holding PhD degrees. All qualified applicants will receive consideration for employment without regard to race, creed, color or national origin. Address Dr. Burton D. Fried, Director, Research Laboratory, or Mr. Theodore Coburn at

RAMO-WOOLDRIDGE

A DIVISION OF

Thompson Ramo Wooldridge Inc.

8433 FALLBROOK AVENUE • CANOGA PARK, CALIFORNIA

10-1A